Investigating the role of SNORD116 in cardiac development and disease

By

Terri-Lea Holmes, MSci

A thesis submitted for the degree:

Doctor of Philosophy

Norwich Medical School
The University of East Anglia, Norwich, UK

Date of submission: 31st January 2023

Declaration

I declare that the contents of this thesis entitled "Investigating the role of SNORD116 in cardiac development and disease" was undertaken and completed by myself, unless otherwise acknowledged and has not been submitted in an application for another degree or qualification in this or any other university or institution.

This thesis is approximately 70,000 words in length

Terri-Lea Holmes

Acknowledgements

Firstly, and foremostly I must thank my supervisor James Smith for his brilliance both as a scientist and as a mentor. His patience and encouragement were crucial in helping me to complete this thesis. He has taught me how to achieve excellence both as a researcher and as a human, and I aspire to have the same impact on others that he has had on me.

I must also thank Ben Johnson for his wonderful support, friendship, and humour, which kept me optimistic and motivated through the many challenges of lab life. I would also like to acknowledge the other researchers of the Bob Champion Building, who have cultivated an open and uplifting environment where it is easy to feel welcome and reassured.

Thank you also to Georgina Ducker and Chetan Mukhtyar of Rheumatology, and Ramez Nassif and his team in ENT at the Norfolk and Norwich University Hospital. I would not have my life, much less my thesis, without their excellent care.

Finally, thank you to my friends and family for their ceaseless support through some of the most challenging years of my life so far. Thank you Tom for your insight and patience. Thank you to my sister Cassandra for your unconditional love and motivation. Thank you to my fathers Antony and Marc for your calm wisdom and guidance. And thank you to my mother Katherine for everything you have done. You are my greatest champion and my loudest advocate.

Abstract

Heart disease is a condition that affects millions of people and contributes to countless deaths worldwide. The underlying pathophysiology is highly complex and involves many intricate cellular processes and elaborate signalling pathways. Non-coding RNA, specifically small nucleolar RNA (snoRNA) has recently been implicated in the pathogenesis of many different human diseases including cardiovascular disease. The snoRNA SNORD116 was recently found at elevated levels in a human induced pluripotent stem cell (hiPSC) model of cardiac disease. SNORD116 has previously been associated with the congenital disease Prader-Willi Syndrome (PWS), where it is implicated in the dysregulation of various cellular, metabolic and developmental pathways.

This work presents the use of hiPSCs as a model of heart development and disease. The focus of this work is to understand the function of SNORD116 in a cardiac context, and to investigate how SNORD116 may influence disease phenotypes. This research indicates that SNORD116 is elevated during key points of cardiomyocyte development, and is dysregulated in response to cardiac stress. SNORD116 was shown to be involved in modulating the metabolism of cells, potentially impacting how they respond to disease stimuli. Moreover, results presented here demonstrate how SNORD116 may directly interact with the mRNA of the desmosomal armadillo protein PKP1, and how this may impact cardiac development and function.

Chapter 1 Table of Contents

List of Figures

List of Tables

List of Accompanying Material

Publications

Johnson BB, Reinhold J, **Holmes TL**, Moore JA, Cowell V, Bernardo AS, Rushworth SA, Vassiliou V, Smith JGW. *Modelling Metabolic Shifts during Cardiomyocyte Differentiation, Iron Deficiency and Transferrin Rescue Using Human Pluripotent Stem Cells*. Metabolites. 2021 Dec 22;12(1):9. doi: 10.3390/metabo12010009. PMID: 35050131; PMCID: PMC8778576. T.L.H. CREDIT; Investigation; Writing—review and editing

James V, Nizamudeen ZA, Lea D, Dottorini T, **Holmes TL**, Johnson BB, Arkill KP, Denning C, Smith JGW. *Transcriptomic Analysis of Cardiomyocyte Extracellular Vesicles in Hypertrophic Cardiomyopathy Reveals Differential snoRNA Cargo*. Stem Cells Dev. 2021 Dec 15;30(24):1215-1227. doi: 10.1089/scd.2021.0202. PMID: 34806414; PMCID: PMC8742282. T.L.H. CREDIT; Writing—original draft preparation.

Poster Presentations

Holmes TL, Johnson BB, Denning C, James V, Smith JGW. *Cardiomyocyte communication in apical hypertrophic cardiomyopathy*. International Society for Stem Cell Research (ISSCR) 2020, Jun 23 – 27, Virtual Meeting.

Holmes TL, Johnson BB, Smith JGW. *Exosomal and cellular long non-coding RNAs in a human induced pluripotent stem cell-derived cardiomyocyte model of hypertrophic cardiomyopathy*. 4th Annual Symposium, London Stem Cell Network (LSCN) 2021, 19th October, Crick Institute London.

Holmes TL, Johnson BB, Price J, Papadopoulou C, Clarke E, Anderson J, James V, Denning C, Peffers MJ, Smith JGW. *Investigating the role of SNORD116 in Hypertrophic Cardiomyopathy.* British Society for Cardiovascular Research (BSCR) Autumn Meeting 2022, 5th September Queen's University Belfast.

Grants

Denning C, James V, Peffers MJ, Smith JGW. £970K BHF Special Project Grant, SP/F/22/150044. "Do snoRNAs govern genotype-phenotype interactions in hypertrophic cardiomyopathy?" T.L.H. CREDIT; Pilot Data; Named PDRA.

Definitions/abbreviations

αSMA	Alpha smooth muscle actin
AA	Alpha actinin
ACLY	ATP citrate lyase
ACTC	Cardiac alpha actin
ADP	Adenosine diphosphate
AGN	4-[2-[5,6-Dihydro-5,5-dimethyl-8-(4-methylphenyl)-2-naphthalenyl]ethynyl]benzoic acid
ANK	Ankyrin
ARVC	Arrhythmogenic right ventricular cardiomyopathy
ASE	Anti-sense element
ATP	Adenosine triphosphate
ATP2A2	ATPase Sarcoplasmic /Endoplasmic Reticulum Ca^{2+} Transporting 2
BAX	Bcl2-associated X protein
BCL2	B cell lymphoma 2
BDNF	Brain Derived Neurotrophic Factor

KCNJ	Potassium Inwardly Rectifying Channel Subfamily J
KEGG	Kyoto encyclopaedia of genes and genomes
KO	Knockout
LB	Luria broth
LC-MS/MS	Liquid chromatography tandem mass spectrometry
LDHA	Lactate dehydrogenase A
LVH	Left ventricular hypertrophy
LVOT	Left ventricle outflow tract
MHRA	Medicines and healthcare products regulatory agency
MI	Myocardial infarction
mRNA	Messenger ribonucleic acid
MSC	Mesenchymal stem cell
Mt	Matrigel
mTOR	Mechanistic target of rapamycin

BLAST	Basic local alignment search tool
BMP	Bone morphogenic factor
BSA	Bovine serum albumin
Ca^{2+}	Calcium ion
CACNA	Calcium voltage-gated channel
CD	Cluster of differentiation
cDNA	Copied deoxyribonucleic acid
CF	Cardiac fibroblast
CHIR	CHIR99021
CM	Cardiomyocyte
CMR	Cardiac magnetic resonance
CMT	Cardiac microtissue
CO_2	Carbon dioxide
COL	Collagen
COX1	Cytochrome c oxidase subunit 1
CRISPR	Clustered regularly interspaced palindromic repeats
Ct	Cycle threshold
DAPI	4′,6-diamidino-2-phenylindole
DCM	Dilated cardiomyopathy

MYBPC	Myosin binding protein C
MYH	Myosin heavy chain
MYL	Myosin light chain
NAD	Nicotinamide adenine dinucleotide
NCBI	National centre for biotechnology information
NHEJ	Non-homologous end-joining
NNUH	Norfolk and Norwich University Hospital
O_2	Oxygen
OCM	Orange cell mask
OCR	Oxygen consumption rate
OE	Overexpression
PAM	Protospacer adjacent motif
PB	PiggyBac
PBS	Phosphate buffered saline
PCR	Polymerase chain reaction
Pen Strep	Penicillin streptomycin
PFK	Phosphofructokinase
PGC1a	Pparg coactivator 1 alpha
Pi	Phosphate

DMEM	Dulbecco's Modified Eagle Medium
DMSO	Dimethyl sulfoxide
DNA	Deoxyribonucleic acid
DOX	Doxorubicin
DSC	Desmocollin
DSG	Desmoglein
DSP	Desmoplakin
DTT	Dithiothreitol
E8	Essential 8
ECAR	Extracellular acidification rate
ECG	Electrocardiogram
ECL	Enhanced chemiluminescence
ECM	Extracellular matrix
EDTA	Ethylenediaminetetraacetic acid
ESC	Embryonic stem cell
FAO	Fatty acid oxidation
FBS	Fetal bovine serum
FCCP	Carbonyl cyanide-4-(trifluoromethoxy) phenylhydrazone
FGF	Fibroblast growth factor

PKA	Protein kinase A
PKP	Plakophilin
PPAR	Peroxisome proliferator-activated receptor
PWS	Prader-Willi Syndrome
rcf	Relative centrifugal force
RNA	Ribonucleic acid
ROCK	Rho kinase
ROS	Reactive oxygen species
RPM	Rotations per minute
RPMI	Roswell Park Memorial Institute Medium
rRNA	Ribose ribonucleic acid
RT	Reverse transcription
RYR	Ryanodine
SDS	Sodium dodecyl sulfate
SERCA	Sarco/endoplasmic reticulum Ca^{2+}-ATPase
SNHG	Small nucleolar host gene
SNORA	Small nucleolar RNA H/ACA class
SNORD	Small nucleolar RNA C/D class
snoRNA	Small nucleolar ribonucleic acid

GAPDH	Glyceraldehyde 3-phosphate dehydrogenase
gDNA	Genomic deoxyribonucleic acid
GFP	Green fluorescent protein
GSK	Glycogen synthase kinase
HCl	Hydrochloric acid
HCM	Hypertrophic cardiomyopathy
HDR	Homology-directed repair
hEHT	Human engineered heart tissue
HFEA	Human fertilisation and embryology authority
hiPSC	Human induced pluripotent stem cell
HK	Hexokinase
I/R	Ischemia/Reperfusion
IAA	Iodoacetamide
IPA	Ingenuity pathway analysis
ISO	Isoprenaline
ITR	Inverted terminal repeat
JUP	Plakoglobin

snoRNP	Small nucleolar ribonucleoprotein
SNRPN	small nuclear ribonucleoprotein polypeptide N
SNURF	SNRPN Upstream Reading Frame
TC	Tissue culture
TCA	The citric acid cycle
TFA	Trifluoroacetic acid
TGF	Tissue growth factor
TNF	Tumour necrosis factor
TNNI	Slow skeletal troponin
TNNT	Cardiac troponin
TTN	Titin
UEA	University of East Anglia
VEGF	Vascular endothelial growth factor
VF	Ventricular fibrillation
VT	Ventricular tachycardia
VTN	Vitronectin
WT	Wild type

Chapter 2 Introduction

2.1 SNORD116

2.1.1 Small Nucleolar RNA

Whilst 40% of the human genome is predicted to be transcribed into RNA, only 2% of the transcriptome is translated into protein (1). The remaining ~38% consists of non-coding RNA, which is becoming one of the most rapidly expanding fields of research in genetics and disease. Non-coding RNAs have been shown to take part in various biological processes including DNA methylation (2), RNA processing and modification (3,4), and protein translation, trafficking, and activation (5,6).

SNORD116 (formally known as HBII-85) is a specific type of non-coding RNA called a small nucleolar RNA (snoRNA). The first snoRNAs identified – U3, U8 and U13 – were found to localise to the nucleolus (7–9), hence their nomenclature. However, subsequent studies have demonstrated snoRNAs can localise to multiple different cellular and extracellular regions (10,11). There are two families of snoRNA categorised according to the presence of consensus sequence motifs. These are the C/D box (SNORD) snoRNAs and the H/ACA box (SNORA) snoRNAs (12). SNORD116 is a member of the C/D box family. The C box consists of the consensus sequence RUGAUGA (where R is a purine base), and the shorter D box sequence is CUGA. Many C/D box snoRNAs also contain an additional pair of often less well conserved C and D motifs, denoted C' and D'. Figure 2-1 shows how internal base-pairing between the C and D motifs within the snoRNA allows the formation of a stem loop structure.

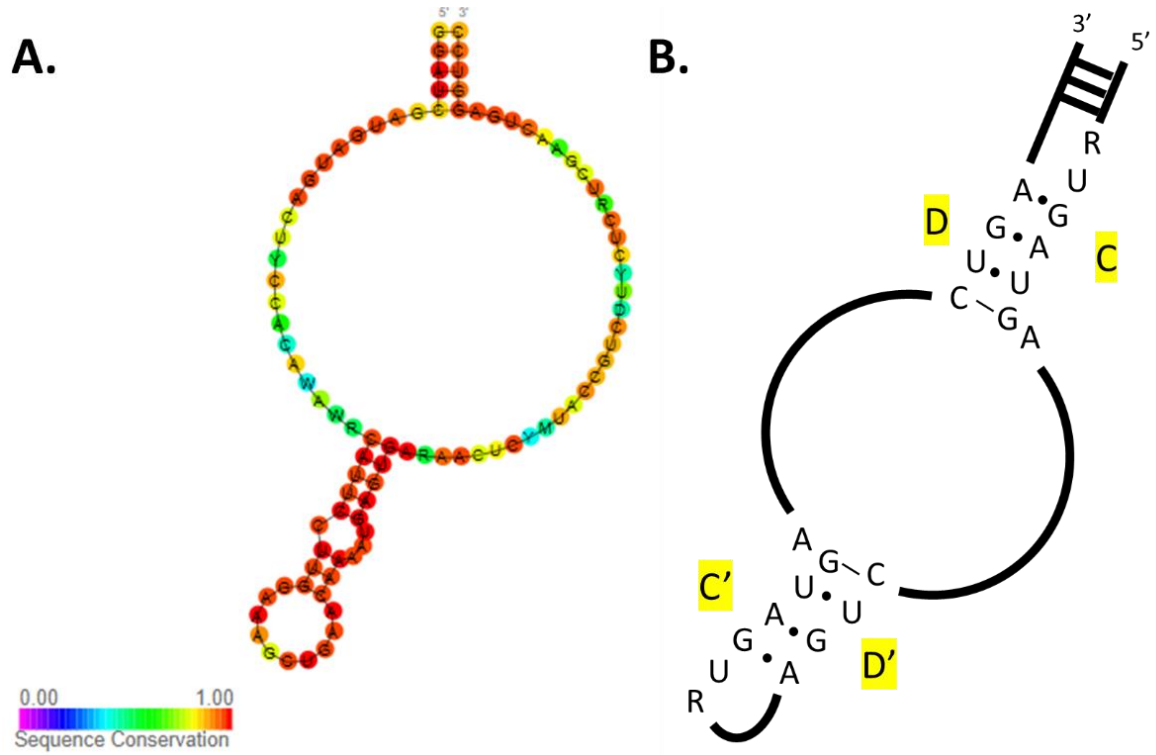

Figure 2-1. SnoRNA secondary structure.
A. Predicted secondary structure of SNORD116 with each base colour coded according to sequence conservation (violet = 0%, red = 100. Generated by Rfam, reference number RF00108 (470)(447).
B. Schematic of general snoRNA secondary structure with C/D boxes highlighted. Generated in MS PowerPoint.

Canonically, C/D box snoRNAs function to facilitate the 2'-O-methylation of ribose molecules in ribosomal RNA. Targeting is achieved through complementary base-pairing between the target RNA and an anti-sense element (ASE) or guide sequence located upstream of the D (or D') box within the snoRNA (13). A snoRNA ribonucleoprotein complex (snoRNP) forms upon association of the C and D motifs with partner proteins Snu13, Nop56, Nop58 and the methyltransferase fibrillarin (14–16). SnoRNA-mediated methylation of rRNA can have different cellular consequences depending on the target. For example, SNORD42A was found to methylate the U116 base in 18S rRNA. Upon SNORD42A knockout in a human cell line, U116 methylation was decreased, which lead to an overall decrease in protein translation and diminished cell proliferation (17). In another example, a study in zebrafish showed that knockdown

of the C/D box snoRNA U26 caused loss of methylation of a ribose base within the in 28S rRNA, and lead to developmental abnormalities (18).

SnoRNAs are not limited to the methylation of rRNAs. There are examples of snoRNAs regulating gene expression through the methylation of mRNA. One study found that the snoRNA SNORD89 targets the mRNA of the proapoptotic gene Bim, causing its methylation. This caused the downregulation of Bim protein levels which led to a reduction of apoptosis (19). Another study found that the C/D box snoRNAs U32A and U51 were responsible for the methylation of PXDN mRNA (20). Combined knockout of U32A and U51 caused a decrease in PDXN mRNA but an increase in PDXN protein levels. The results suggested that snoRNA-mediated methylation increased the stability of the mRNA but inhibited its translation.

In addition to methylation, snoRNAs have also been shown to affect the splicing of target genes. One study showed that overexpression of SNORD88C caused alternative splicing of the *FGFR3* gene, resulting in reduced levels of the ∆8-10 isoform of FGFR3 (21). Interestingly, evidence has shown that SNORD115 – a snoRNA located within the same gene cluster as SNORD116 – may regulate the alternative splicing of serotonin receptor 2C (5-HT_{2C}R) (22). There are two alternative 5' splice sites in exon V of *5-HT_{2C}R* pre-mRNA, resulting in two potential isoforms: exon Va and exon Vb. Only mRNAs containing exon Vb encode a functional protein (23). SNORD115 was shown to promote inclusion of exon Vb by binding to and blocking a silencer located within exon Vb (22,24). However, a recent study conducted using a SNORD115 knockout mouse model demonstrated no conclusive evidence that SNORD115 is capable of regulating 5-HT_{2C}R alternative splicing, suggesting this mechanism may be specific to human cells (25).

In humans, SNORD116 is encoded on chromosome 15 as shown in Figure 2-2. The SNORD116 locus is a ~60,000 bp cluster of 30 paralogue sequences, each ~100 bp in length. These paralogues can be divided by sequence similarity into three groups: group I (SNORD116-1 to SNORD116-9), group II (SNORD116-10 to SNORD116-24) and group III (SNORD116-25 to SNORD116-30) (26). Orthologues of the SNORD116 cluster have been found in other species including mouse, rat, chimpanzee, macaque, and rabbit, but no orthologues have been found outside of the class Mammalia (27). In mice, the SNORD116 cluster is located on chromosome 7 and consists of ~180,000 bp. Within this cluster are 17 SNORD116 paralogues nearly identical in sequence (26). The majority of snoRNAs are usually located within the intron of a host gene (28). According to the RefSeq database (29), SNORD116 is located within the host gene Small Nucleolar RNA Host Gene 14 (SNHG14) alongside several other snoRNAs such as SNORD115, and ubiquitin protein ligase E3A (UBE3A). SNHG14 also shares a promoter with the SNRPN (small nuclear ribonucleoprotein polypeptide N) and SNURF (SNRPN Upstream Reading Frame) genes. Unlike canonical snoRNAs, SNORD116 does not show sequence complementarity to other non-coding RNAs and has not been shown to modify rRNAs, so is therefore classed as a non-canonical or orphan SNORD (30). Despite this, SNORD116 has been shown to associate with the snoRNP methyltransferase fibrillarin (31), suggesting it may engage in RNA methylation.

In an effort to better understand the function of SNORD116, a study using the now defunct bioinformatic software snoTARGET searched for potential SNORD116 targets based on complementarity with its predicted ASE (32). Half of the targets showed potential binding sequences within exons of genes that undergo alternative splicing, and many were located close to alternatively spliced junctions. This indicated that, similar to SNORD115, SNORD116 could play a role in regulating the alternative splicing of target genes.

2.1.2 SNORD116 in Prader-Willi Syndrome

In the literature, SNORD116 has been investigated mostly in the context of its role in the congenital disorder Prader-Willi Syndrome (PWS). PWS is a multisystem disorder characterised by a number of physical and behavioural abnormalities. It has a reported international prevalence of 1 in 30,000 births (33), classing it as a rare disease. Presenting in early infancy, PWS patients experience abnormalities in a range of biological systems from appetite control to sleep regulation. Motor, language and cognitive development are generally delayed, and the majority of patients suffer with growth hormone deficiency and infertility (33). PWS is currently one of the leading genetic causes of obesity in children (34).

The disease itself arises due to loss of expression of genes within the locus 15q11.2-q13 on the paternally inherited chromosome 15, which is shown in Figure 2-2. Many of the genes within this locus (including SNORD116) are paternally imprinted. This means that the maternal copy of the gene is silenced, in this case via histone methylation (35,36). There are two types of deletion that have been observed in PWS patients: Type I (~6.6Mb) spans the entire 15q11.2-q13 region whereas Type II (~5.3 Mb) spans from the MKRN3 gene to the HERCC2 gene (37). Patients with the Type II deletion perform better in behavioural and academic assessment than Type I individuals (38). Importantly, SNORD116 expression is lost in both types of PWS. Chromosome deletion is not the only cause behind loss of expression of this region; approximately 25% of PWS cases are caused by maternal disomy of chromosome 15, where there are two silenced maternal copies of the chromosome, and the paternal copy is not present (39). Crucially, smaller microdeletions specifically within the SNORD116 locus have been shown to cause PWS, thus reinforcing the implication of the snoRNA in PWS pathogenesis (40–42).

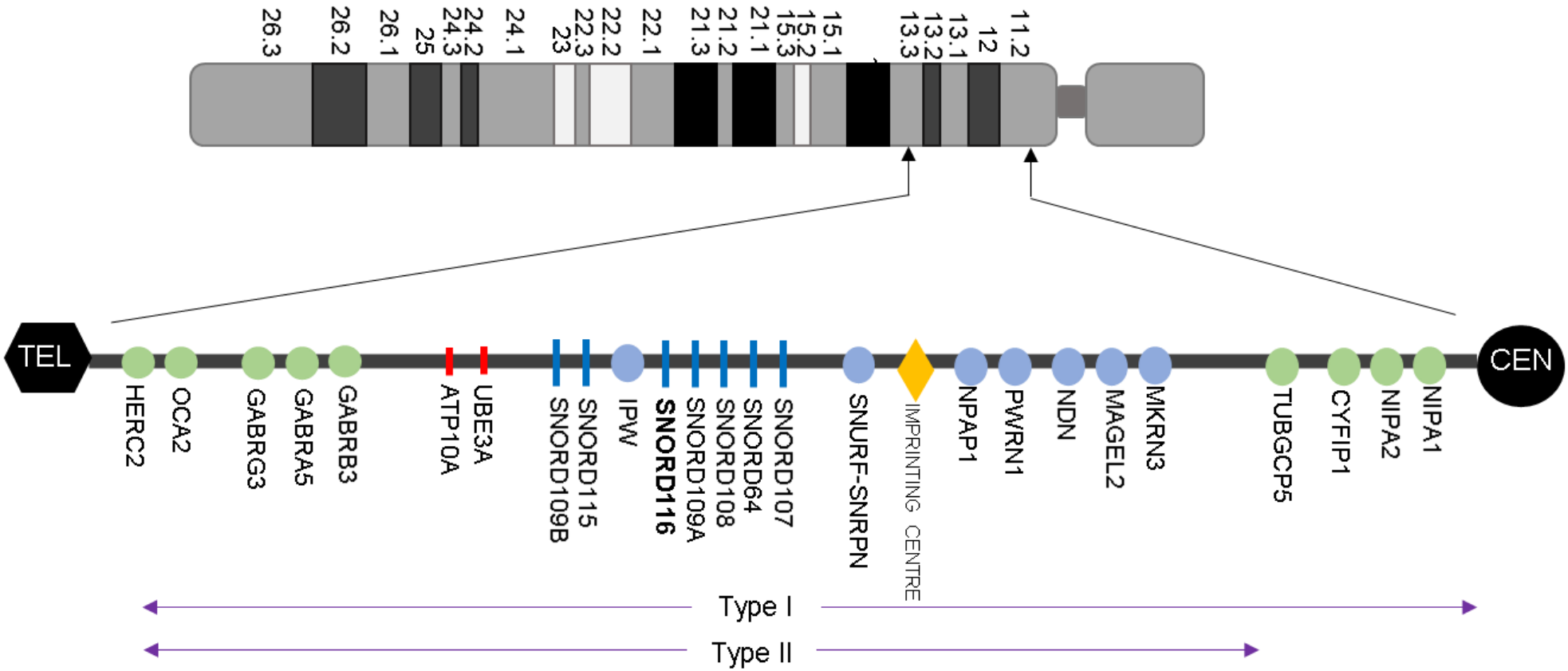

Figure 2-2. Map of chromosome region 15q11.2-q13.
Genes coloured blue are paternally imprinted and associated with Prader-Willi Syndrome. Genes coloured red are maternally imprinted and associated with Angelman Syndrome. Genes coloured green are non-imprinted. The purple arrows indicate regions that are deleted in type I and type II PWS. Adapted from Gabriel *et al.*, 1999 and Stefan *et al.*, 2005. Generated using MS PowerPoint.

Extensive effort has been put into generating mouse models to investigate PWS. The mouse orthologue of 15q11.2-q13 is similar to its human counterpart. Located on chromosome 7C, this region in mice contains homologues of genes found in the human 15q11.2-q13 region, with the exceptions of C15ORF2, SNORD108 and SNORD109A/B which are absent in mice (43). The mouse orthologues appear in the same order but are reversed in sequence (telomere to centromere). Many of the orthologues (including the snoRNAs) maintain the same paternal imprinting pattern seen in humans. In developing mice embryos, SNORD116 is expressed predominantly in the brain and spinal cord (44), suggesting it plays a role in the development of these structures. In the adult mouse SNORD116 expression is highest in specific regions of the brain, namely the hypothalamus (45). However, in humans, SNORD116 expression is detected not only in the brain, but also in other tissues including the heart, ovary, prostate, thyroid and kidney (46,47). This indicates that SNORD116 may function in tissue-specific ways that are unique to humans. It is important to note that not all the SNORD116 transcripts are expressed equally. Demonstrative of this, group 1 (SNORD116-1 to SNORD116-9) were found to have a 20-fold higher expression in human hypothalamic tissue than the other two groups (46).

Deletion of the entire region corresponding to 15q11.2-q13 in mice resulted in neo-natal lethality, with the affected pups displaying hypotonia and failure to thrive (48) The mutant mice also showed lower levels of vital metabolites including plasma triglycerides, liver glycogen, glucose and glucagon. The authors postulated that the mice survived *in utero* due to plasma exchange with the placenta, but post-birth the dysregulation of hormone pathways important in feeding and metabolism resulted in lethality (48). This was a notable indication that SNORD116 may have a metabolic role.

Several clinical cases of PWS have been identified involving microdeletions of the SNORD116 cluster (49), which led to the hypothesis that selective loss of SNORD116 contributes to the PWS phenotype. A SNORD116$^{m+/p-}$ mouse model was generated using loxP/CRE recombinase (27,49,50), which caused growth retardation but only ~15% neonatal lethality. The majority of mutant mice survived to adulthood, although remaining smaller in weight than their wild-type counterparts. The mRNA and protein levels of IGF-1 (an important growth hormone) were lower in the mutant mice liver tissue but in pituitary tissue, levels were comparable to wild type. This suggests that the SNORD116 knockout caused a growth hormone deficiency secondary to a hypothalamic dysregulation that could explain the growth retardation.

The mutant mice displayed phenotypes seen in PWS patients such as increased anxiety/fear, motor learning deficiency and hyperphagia, but key characteristics such as obesity, lower muscle tone and infertility were not observed. This could suggest that loss of SNORD116 alone may not be sufficient to induce the full phenotype of PWS in mice. However, it also reflects the limitations of using animal systems to model PWS. As stated previously, SNORD116 expression is not detected highly outside the central nervous system of mice, whereas in humans it is expressed in other tissues. For example, humans express SNORD116 in gonadal tissue, suggesting it may be involved in reproductive processes. This differential expression pattern may explain why loss of SNORD116 expression causes infertility in humans but not in mice. Due to the differences between human and mouse expression, extensive research into SNORD116 has also been conducted using primary human tissue and cell lines.

A study performed transcriptional analysis on hypothalamic tissue samples from the brains of four PWS patients compared to four age-matched controls (51). In total, 658 genes were significantly differentially expressed. In terms of obesity-related gene changes, Agouti-related protein (AgRP) expression was found to be 3-fold higher in the PWS samples. Given Agrp is an appetite stimulant (52), its upregulation is likely an important contributor to the obesity phenotype in PWS patients. Several inflammation-related genes were also found to be upregulated including TNFα and S100b. Genes important in neurone development and maintenance, namely *BDNF* and *TrkB*, were found to be downregulated in PWS. Disruption of these genes caused developmental and behavioural problems in mice and humans similar to those seen in PWS (53). In the same study, the SNORD116 cluster was deleted using CRISPR-Cas9 in a neuroblastoma cell line, resulting in reduced neuronal differentiation, cell proliferation, and survival compared to the WT line (51). However, treatment of the knockout line with BDNF resulted in a ~13% higher percentage of neurites compared to untreated cells. This indicated that loss of SNORD116 could cause neurodegeneration via reduction of the BDNF signalling pathway.

A transcriptome-wide search for alternative splicing revealed that genes involved in microglial and inflammatory processes showed the highest level of alternative splicing in PWS neurones (54). The study concluded that genes in the 15q11.2-q13 region – particularly the snoRNAs – may be in part responsible for regulation and / or splicing of genes important to neurone survival.

As this study demonstrates, much of the research into PWS using human tissue has focused on brain tissue and neurological cell types. This coheres with the high level of SNORD116 expression in the brain, however it fails to explore the other systems that are affected by SNORD116, for example in cartilage. A recent study showed that cartilage extracted from osteoarthritic mice showed a higher level of SNORD116 compared to controls (55). The upregulation of SNORD116 in osteoarthritis was confirmed in a separate study in which osteoarthritis was induced in mice through surgical destabilisation of the medial meniscus (56). These results show that SNORD116 is clearly capable of playing a role in diseases outside of the nervous system.

Clinical assessment of PWS patients has shown that other systems are affected by the loss of SNORD116, particularly the cardiovascular system. Although much of the cardiac dysfunction in PWS patients is associated with obesity-related factors, there are broader effects on the cardiovascular system that can present in advance of the onset of obesity in PWS patients (57). The most prevalent cause of death in PWS adults is cardiovascular disease resulting from complications that can present in early childhood (58–61). Echocardiogram testing on children with PWS found that over half of the patients exhibited cardiac dysfunction, which was not seen in any of the healthy age-matched controls (62). Studies have shown that left ventricular mass and internal diameter are reduced in PWS individuals, and even when compared to obese controls PWS patients have decreased cardiac muscle mass causing decreased cardiac output efficiency (57,63,64). This indicates that SNORD116 may have a specifically cardiac function, leading to cardiovascular defects when its expression is disrupted.

2.1.3 SNORD116 in the heart

Although there is considerable clinical evidence suggesting that SNORD116 has a function in the heart, there is a distinct lack of research exploring this. Previous work has shown that cardiac stress caused increased packaging of SNORD116 into exosomes, which are important vesicles involved in paracrine and autocrine signalling (65–67). The exosomes released from two isogenic lines of human induced pluripotent stem cell-derived cardiomyocytes (hiPSC-CMs) were compared. The lines were genetically identical except that one contained a genetic mutation (*ACTC1*-E99K) causing Hypertrophic Cardiomyopathy (HCM). Transcriptomic analysis of exosome content revealed that multiple SNORD116 paralogues were packaged at a >2-fold higher abundance in the HCM line compared to the non-mutant line. Both lines were subjected to electrical pacing of 1 V/2 Hz with a 2ms impulse duration for 24 hours to increase their contraction rate. This caused an increase in overall exosome output, but importantly SNORD116 levels were increased relative to the number of exosomes released. Interestingly, the stress induced by electrical pacing compounded the effect of the genetic mutation, causing an even greater level of SNORD116 packaging (65). Overall, the presence of both cardiac stresses combined caused SNORD116-23, SNORD116-25 and SNORD116-29 to be packaged 8-fold, 10-fold and 11-fold higher compared to unstressed controls (65). These results implicate a cardiac signalling role of SNORD116 that may contribute to cardiovascular conditions.

A poster presentation at the International Society for Stem Cell Research 2022 conference presented work demonstrating the role of SNORD116 in response to myocardial infarction in mice (Poster number 863) (68). The research presented used a mouse model wherein SNORD116 had been conditionally knocked out in cardiac tissue. Mice lacking cardiac SNORD116 expression underwent less pathological remodelling after surgery-induced myocardial infarction. These mice also developed less

fibrotic scar tissue compared to their wild-type littermates. When subjected to ischaemia, SNORD116$^{-/-}$ myocardial tissue showed improved recovery to diastolic baseline compared to SNORD116-expressing myocardium. Additionally, proteomic analysis of left ventricle tissue showed that the expression of several metabolism-related proteins was dysregulated by the loss of SNORD116, suggesting a role in cardiac metabolism.

Although limited, current research into the role of SNORD116 in the heart suggests an exciting novel signalling pathway that merits further investigation. However, it is important to understand the molecular and physiological changes that occur during heart disease in order to understand the potential involvement of SNORD116.

2.2 Heart disease

In 2020, one in every five deaths in the United States occurred as a result of heart disease (69). Heart and circulatory diseases are estimated to generate an annual healthcare cost of £9 billion in the UK (70). The term 'heart disease' generally refers to any abnormality or ailment occurring in the heart or its associated blood vessels, impairing the function of the organ. There are many different forms of heart disease that can arise due to various factors both genetic and environmental, but all result in diminished cardiac function, poor health, and reduced quality of life. As one of the leading causes of death in the western world, there is a substantial demand for research into the molecular and signalling mechanisms that underlie cardiovascular disease. Although there are many different cell types that populate the heart and may contribute to disease, this work will focus largely on cell types that compose the heart musculature – namely the cardiomyocytes and cardiac fibroblasts. Further work should be done exploring the other major cell types, including the vasculature, from which many forms of heart disease such as coronary heart disease can arise.

Most forms of heart disease are characterised by changes in gene transcription and metabolism. These changes reflect a shift away from adult-associated characteristics to more foetal-like phenotypes. Generally, most forms of heart disease coincide with a reactivation of the foetal gene program (71–74). In addition, cardiomyocyte metabolism shifts from primarily fatty acid oxidation, or FAO, to relying more on glycolytic metabolism (75). Foetal cardiomyocytes are exposed to a low oxygen environment and rely heavily on oxygen-independent forms of metabolism such as glycolysis (76). However, during peri- and post-natal development, cardiomyocytes undergo a metabolic switch to (FAO) (77,78). Compared to glycolysis, FAO yields more ATP per mole of substrate oxidised, and is therefore better able to support the greater energy demands of the post-natal heart (79). The regression of

cardiomyocyte metabolism during heart disease contributes to an overall energy deficit wherein cardiomyocytes have a reduced capacity to cope with increased workload and greater energy demands. In this section, various cardiac conditions will be explored to identify commonalities occurring across different pathologies and to better understand the complex mechanisms contributing to heart disease.

2.2.1 Inherited Cardiomyopathies

2.2.1.1 Hypertrophic Cardiomyopathy

There are many forms of heart disease that exist due to genetic variation. Hypertrophic cardiomyopathy (HCM) is one of the more commonly occurring genetic heart diseases, affecting 1 in 500 people (80). The disease is characterised by hypertrophic expansion of the myocardium as shown in Figure 2-3, which is often accompanied by left ventricular outflow obstruction, diastolic dysfunction and cardiac fibrosis (81). HCM

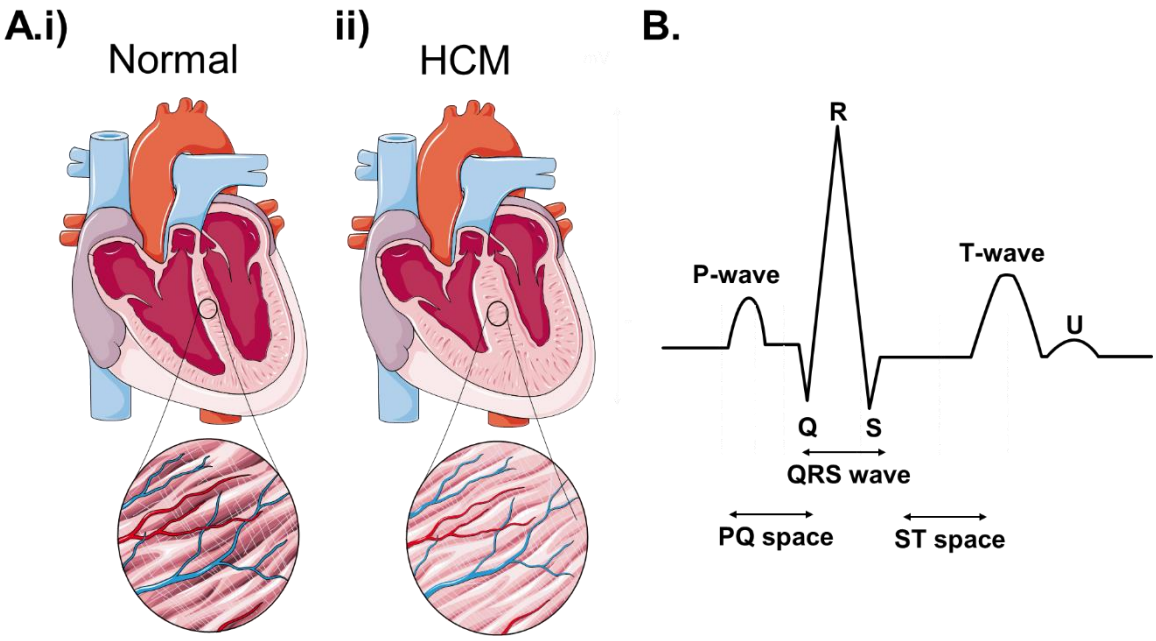

Figure 2-3. Hypertrophic Cardiomyopathy.
A. Diagram depicting the heart and myocardium of a (i) normal and (ii) HCM heart. Generated using Servier Medical Art.
B. Elements of an ECG trace. Generated using MS PowerPoint.

can usually be detected by abnormalities in an electrocardiogram (ECG) trace, shown in Figure 2-3. Commonly observed characteristics include high voltage narrow QRS complexes, deep T-wave inversions and abnormal rhythm (82). Cardiovascular magnetic resonance (CMR) is a 3D imaging technique used to measure the left ventricular size and septal thickness, which in HCM is generally larger than 13-15 mm (83). It is also useful for detecting other HCM-related attributes such as fibrosis and diastolic dysfunction (84). Similarly, echocardiography is an ultrasound technique that can be used in conjunction with ECG and CMR to examine the heart's structure and function.

HCM is an autosomal dominant disorder with a highly variable disease penetrance. The most common symptoms presenting in ~80% of patients are tiredness, shortness of breath and dizziness, along with angina and palpitations (85). Symptoms are often worsened with physical activity, reflecting the limited cardiac output of the diseased heart. HCM can present more severely with symptoms such as syncope, arrythmia and sudden cardiac death. Indeed, HCM is one of the primary causes of sudden cardiac death in young adults and athletes (86). The clinical heterogeneity of HCM is hypothesised to arise from poorly understood genetic and epigenetic mechanisms (87–89).

Over 1,400 unique genetic variants have been associated with HCM (90). The top eight most common pathogenic variants found in HCM patients are in sarcomeric genes (91). Figure 2-4 shows the sarcomere in detail.

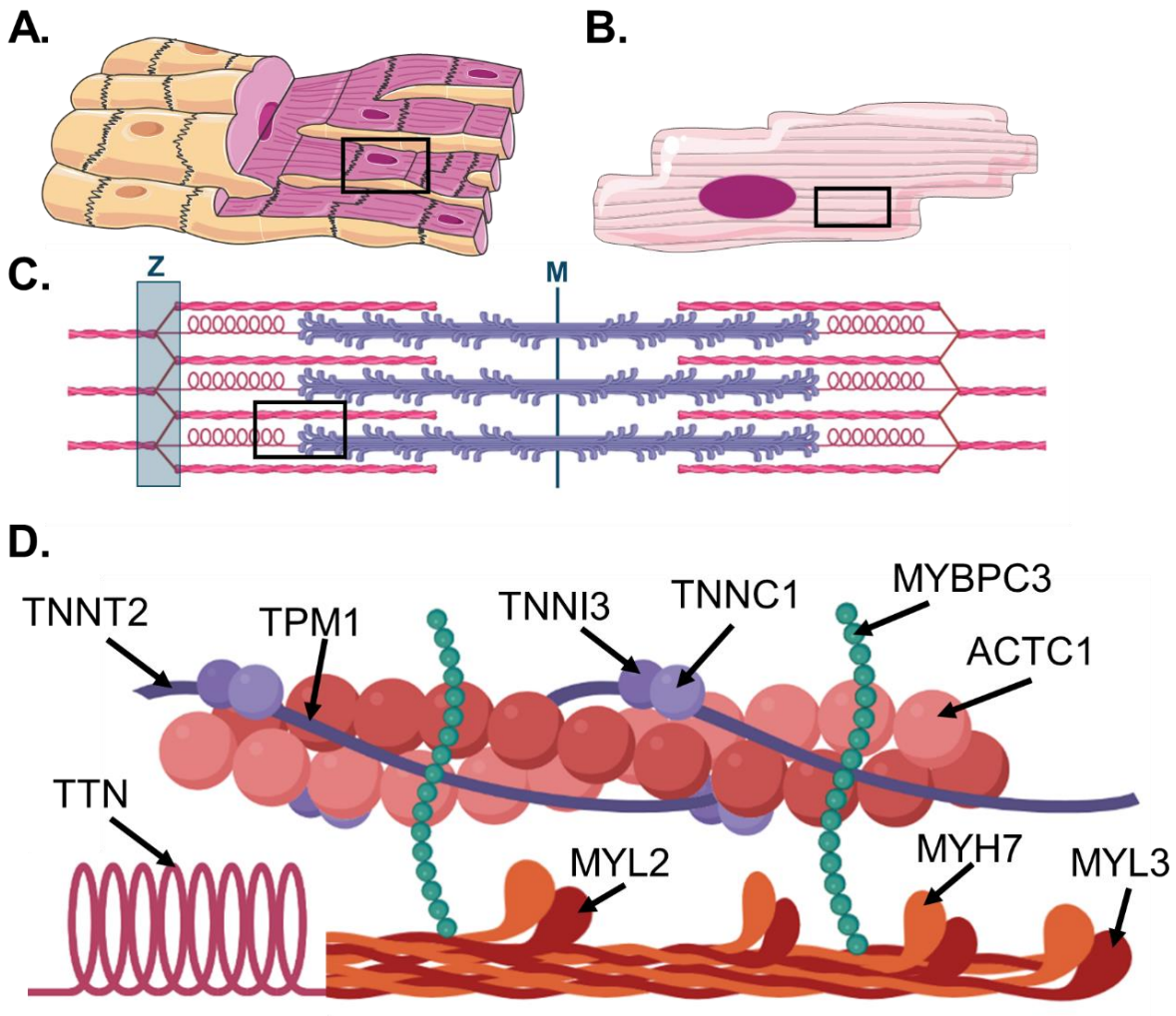

Figure 2-4. Structure of the cardiomyocyte.
A. Heart muscle fibres made up of cardiomyocytes.
B. A single nucleated cardiomyocyte
C. The sarcomere made up of actin (red) and myosin (blue) Z= Z disk, M = M line.
D. Detailed model of the proteins that make up the sarcomere. Components with HCM-causing gene mutations are labelled. Generated using Servier Medical Art.

The two major structures composing the sarcomere are the thick and thin filaments, made up of myosin and actin respectively. The sarcomere is anchored at either end within a dense fibrous structure called the Z-disk. The M-line runs down the centre of the sarcomere and acts an anchorage point for the thick filaments.

According to the sliding filament theory (92,93), during contraction the thick filament is pulled along the thin filament to cause a shortening of the sarcomere in a process called the cross-bridge cycle. This is shown in Figure 2-5. At the start of contraction, calcium-induced-calcium-release from the sarcoplasmic reticulum causes the cytoplasmic Ca^{2+} concentration to increase. Ca^{2+} binds to troponin-C, causing a shift in the complex that exposes myosin binding sites within actin filaments. The subsequent association between myosin and actin causes myosin, which was previously associated with adenosine diphosphate (ADP) and phosphate (Pi), to release the Pi molecule. This induces a conformational change which causes myosin to undergo a power stroke movement, shifting it 5-10 nm closer to sarcomere centre (94). Upon this movement, ADP dissociates from myosin and ATP binds in its place. Myosin detaches from the actin filament and ATP is then hydrolysed, causing another conformation change restoring myosin to its original position.

The process of contraction is highly controlled by the movement of Ca^{2+}. Under low cytoplasmic Ca^{2+} conditions, troponin-C is bound weakly to troponin-I, which is bound strongly to actin and causes tropomyosin to block the myosin binding sites (95). Under high cytoplasmic Ca^{2+} conditions, Ca^{2+} binds to troponin-C, strengthening the binding interaction between troponin-C and troponin-I. This causes troponin-I to pull away from the actin filament, shifting the position of tropomyosin and exposing the myosin-binding sites, allowing the cross-bridge cycle to commence (96).

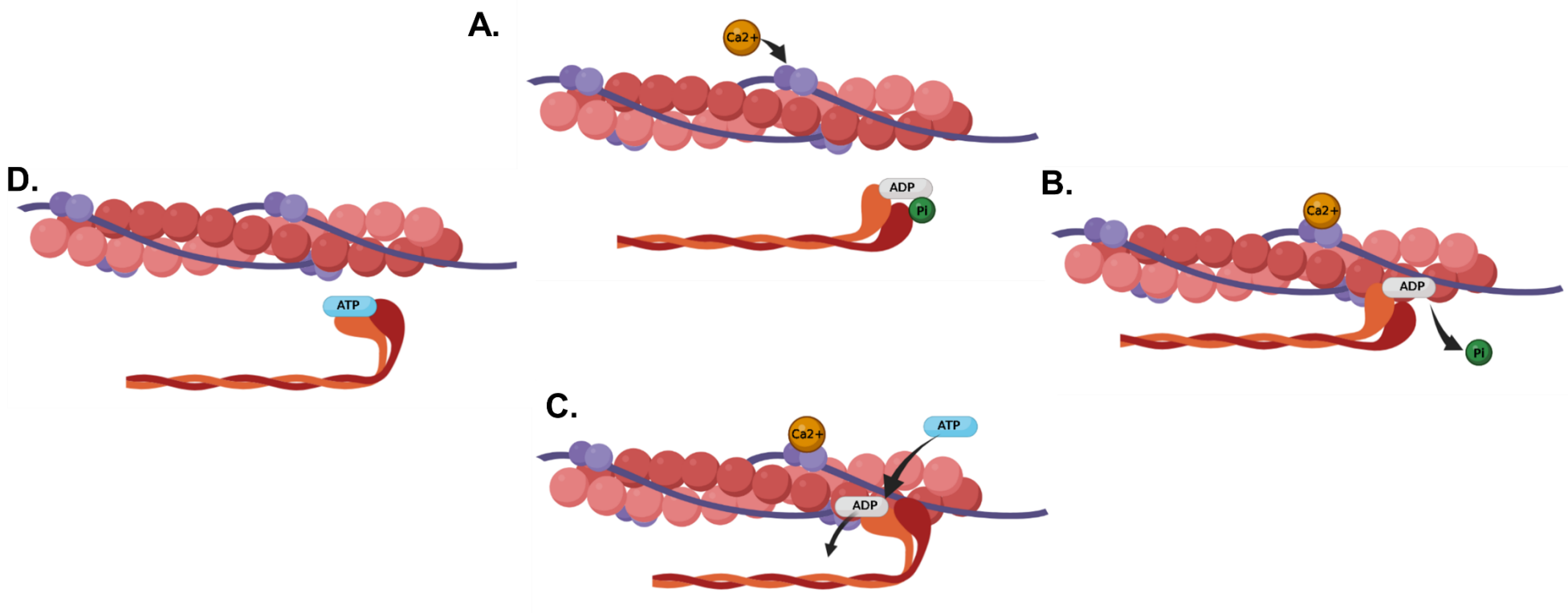

Figure 2-5. The cross-bridge cycle.
A. The cycle begins with myosin dissociated from actin and Ca^{2+} ions binding to troponin-C
B. Myosin is bound to ADP and Pi. Upon Ca^{2+} binding to troponin, myosin binds to the actin filament and releases Pi
C. Release of Pi initiates a power stroke manoeuvre within the myosin filament. ADP dissociates and ATP binds in its place.
D. Myosin dissociates from the actin filament and ATP is hydrolysed. Rendered using Servier Medical Art.

Around 80% of HCM-causing mutations are within the genes for myosin heavy chain 7 (*MYH7*) and cardiac myosin binding protein C (*MYBPC3*) (97). Other most commonly identified genes include *MYL2*, *MYL3*, *TNNT2*, *TNNI3*, *ACTC1* and *TPM1* (98). Mutations in any of these genes can affect the function of the sarcomere and dysregulate processes such as actin-myosin binding, Ca^{2+} sensitivity, generation of the power stroke and the anchorage of the sarcomere itself (99,100). The majority of HCM-linked genetic variants are caused by nucleotide substitution, leading to destabilisation of the protein structure or binding affinity (101). The exception to this is the *MYBPC3* gene, wherein the majority of variants are frameshift mutations that cause truncation and non-functionality of the protein (102).

Biochemical analysis has been undertaken to better understand the molecular consequences of HCM-associated genetic variants. For example, the single nucleotide substitution c.C9123T in the gene for *MYH7* results in the amino acid substitution p.R453C. Investigation into the effect of this mutation showed that the mean velocity of myosin during the power stroke and the ATPase activity of myosin was significantly reduced (103). In addition, a dual-beam optical trap was used to measure the average intrinsic force produced during power stroke by a single myosin molecule. This assay combined a classic *in vitro* motility assay with laser-trap techniques to measure force of myosin motor movement (104,105). Using this assay, the mutant myosin protein was found to generate an intrinsic force that was 50% higher compared to the wild-type (103).

Another well-characterised example is *ACTC1*, the gene encoding cardiac alpha actin. There are over ten unique genetic variants within the *ACTC1* gene that have been linked to HCM. These genetic variants are classed

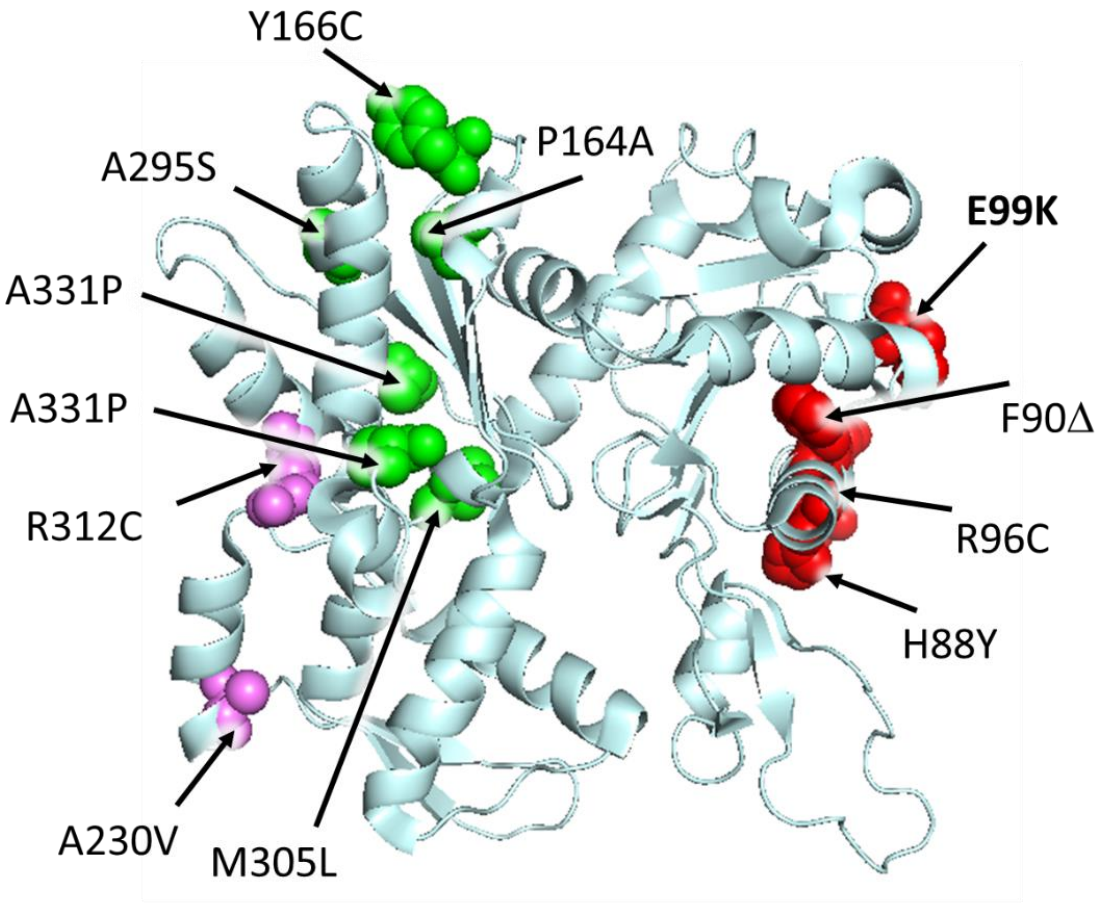

Figure 2-6. Mutations in cardiac actin.
The chain D subunit of the cardiac alpha actin protein is shown in pale blue. Amino acid residues that are known HCM-causing mutations are depicted using colour-coded atomic spheres. Red = M-class mutations, green = T-class mutations, pink = MT-class mutations. Crystal structure obtained from PDB entry 5NOJ. Rendered using PyMOL .

according to which binding interactions they affect. M-class mutations affect the actin-myosin binding interaction, whereas T-class mutations affect the actin-tropomyosin binding interaction (106). MT-class mutations affect both. The location of these mutations within the actin protein is shown in Figure 2-6 (107). The E99K mutation within *ACTC1* is one of the better characterised M-class variants, and has been identified in two separate families affected by familial HCM (108,109). The glutamate-99 residue within actin is one of several believed to make up a secondary myosin binding site. The substitution of glutamate with lysine was found to cause a reduction in the binding affinity of actin to myosin (110). When bound to myosin, the presence of the E99K mutation in actin did not reduce the maximal ATPase activity of myosin but did reduce its

affinity to ATP (110,111). It also caused a reduction in the velocity of the myosin power stroke (110–112). Mouse-model (113) and patient-derived (114) muscle filaments from E99K$^{+/-}$ cardiac tissue exhibited greater calcium sensitivity and impaired fibre relaxation compared to wild-type. Overall, the effects of sarcomeric mutations generally cause an increase in Ca^{2+} sensitivity and filament activation coupled with decreasing the efficiency of the cross-bridge cycle, leading to impaired sarcomeric function and a hypercontractile phenotype (115–117).

Although HCM is often classed as a genetic disease, 30-60% of patients do not have an identifiable mutation (118–120). Even in cases attributed to specific gene mutations, the type of variant can sometimes correlate with a higher risk of increased disease severity (121), but this is not always the case (120). Gene mutations can also have conflicting molecular consequences. For example, the p.R453C mutation in *MYH7* caused a hypercontractile phenotype in some models (103), and a hypocontractile phenotype in others (122). Further complicating the matter is the existence of genotype-positive phenotype-negative individuals who do not present with HCM symptoms despite having a mutation (123). This demonstrates that HCM is a multifactorial disease where there are a number of complex signalling pathways and molecular mechanisms contributing to the disease pathogenesis. However, HCM is a useful disease to model when investigating cardiomyopathy as it often co-presents with other characteristics of heart disease such as fibrosis, and recapitulates key metabolic and gene changes seen universally in cardiovascular disease.

An *in vitro* model of HCM was developed using isogenic lines of iPSC-derived cardiomyocytes, wherein the disease line was developed from a phenotype and genotype-positive male patient with the heterogenous *ACTC1*-E99K mutation. CRISPR-Cas9 editing was used to correct the substitution and generate a WT isogenic control line. Exosomes released

from these cardiomyocytes were subjected to transcriptomic analysis, which identified SNORD116 to be packaged to a higher level by HCM iPSC-CMs. This identified the snoRNA as a potential pathogenic signalling molecule, thereby suggesting a possible connection between SNORD116 and the various molecular mechanisms of HCM.

2.2.1.2 Dilated Cardiomyopathy

Dilated Cardiomyopathy (DCM) is also a commonly occurring cardiomyopathy that can be both familial and non-familial (69). Overall, where HCM is characterised mainly by diastolic dysfunction (the filling of the ventricles with blood), DCM is characterised by systolic dysfuction (the pumping of blood out of the heart). The DCM heart is characterised by left ventricle dilation where the wall of the left ventricle becomes progressively weak and thin. This leads to impaired systolic function which can progress into heart failure (124). Non-familial, or acquired DCM can develop due to various conditions such as hypertension, myocarditis, toxicity and drug use (124). Around 20-40% of DCM cases have a genetic cause (124–126) and there are over 50 genes that have been identified with DCM-causing mutations (127). Unlike familial HCM which is caused predominantly by sarcomeric gene mutations, DCM shows a much wider genetic heterogeneity. Inherited DCM is mostly autosomal dominant, but autosomal recessive and X-linked variants have been identified (128). Maternally-inherited mitochondrial gene mutations have also been shown to cause DCM (127).

Interestingly, around 35-40% of DCM-causing mutations are in sarcomeric genes, with the majority of these occurring within titin (*TTN*) (127,129). Titin is a giant protein of ~33,000 amino acids that anchors in the Z-disk and M-line, and is required for sarcomere assembly (130,131). Most DCM-linked *TTN* mutations cause protein truncation (129). Truncated proteins are typically more likely to be degraded,

leading to decreased titin protein levels that could disrupt sarcomere assembly (129,132). However, immunohisto-chemical studies have suggested that truncated titin is capable of incorporating into the sarcomere at the Z-disk but not the M-line (129). As the M-line portion of titin is implicated in sensing and modulating sarcomeric force (133–135), loss of titin at this region may disturb the regulation of contraction force leading to the DCM phenotype.

As stated previously, DCM genetic variants are not restricted to the sarcomere. Many different components of cardiomyocyte function can be affected by DCM variants including the cytoskeleton, desmosomes, ion channels and mitochondria. In a study focused on myocardial tissue from idiopathic DCM patients, 22% were found to have genetic variants in mtDNA (136). This was coupled with enlarged mitochondria and abnormally arranged cristae. Further biochemical study showed a significant decrease in cytochrome-c oxidase and NADH dehydrogenase activity. This dysregulation of energy production likely contributes to an energy deficit and poor cardiac output of the DCM heart.

Outside of genetic variants, DCM has a disruptive effect on the cardiac transcriptome as a whole. Meta analysis of RNA expression comparing 41 DCM and 21 non-failing left ventricle tissue found 789 dysregulated genes (137). *MYH6*, CACNA1D, *ATP2A2* and *NKX2-5* are examples of cardiac genes that were downregulated in DCM. KIF1C, a microtubule motor protein, and GAPDHS, an enzyme important in glucose metabolism, were found to be upregulated. Pathway analysis of the differential gene expression revealed that congestive heart failure, cardiac hypertrophy and actin cytoskeleton signalling were among the top pathways predicted to be activated by DCM. The results indicated that multiple pathways are affected by DCM, from microtubule management to metabolism.

Overall, despite key differences between HCM and DCM, both diseases are alike in the overall impairment of cardiac output and disruption to cardiomyocyte function, and both cardiomyopathies often lead to the progression of heart failure. Although SNORD116 has not specifically been linked with DCM, there is a growing number of non-coding RNAs that have been identified as contributing to DCM pathogenesis (138). As such, although unexplored it is possible that SNORD116 may contribute to the underlying mechanisms common in both HCM and DCM cardiomyopathies.

2.2.1.3 Arrhythmogenic Right Ventricular Cardiomyopathy

Arrhythmogenic right ventricular cardiomyopathy (ARVC), sometimes called right ventricular dysplasia, is a genetic cardiomyopathy with an incidence rate of 0.02-0.05% of the population (139). The disease is characterised by loss of the ventricular myocardium and substitution with fibrofatty tissue (140). Dysplasia of the myocardium is attributed to increased inflammation and the death of cardiomyocytes (141). As shown in Figure 2-7, the fibrofatty scar progresses from the epicardial layer across the myocardium towards the endocardium predominantly in the right ventricle wall. This results in thinning and dilation of the ventricles, presenting similarly to a DCM phenotype (142). The most common symptom of ARVC is arrythmia, although patients can experience palpitations, dyspnoea, syncope and – similar to HCM – sudden cardiac death, particularly in young athletic individuals (143). The disease is commonly diagnosed through genetic screening and/or ECG, and right ventricular outflow tract tachycardia is a hallmark of ARVC (144–146).

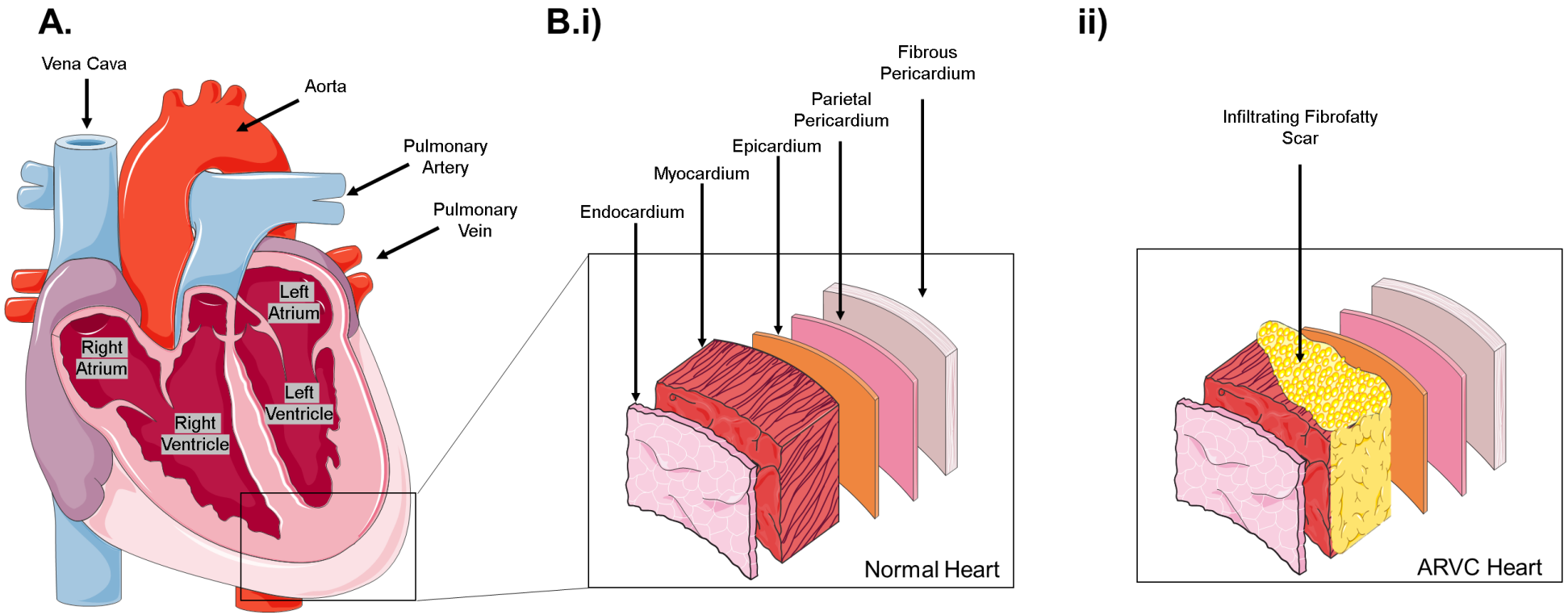

Figure 2-7. Layers of the heart in normal health and ARVC.
A. The adult human heart with the chambers and major blood vessels labelled
B. The layers that make-up the heart in (i) normal health versus (ii) the presence of the fibrofatty scar in an ARVC heart.
Figure generated using Servier Medical Art.

Several genetic variants have been linked to ARVC, and these are almost exclusively found in desmosomal genes. The desmosome is a sophisticated protein structure that connects the intermediate filaments within a cell's cytoplasm to that of neighbouring cells. In cardiomyocytes, desmosomes are one of three important cell junctions present in the intercalated disc. Together with adherens junctions and gap junctions, these structures comprise the *area composita*, working interdependently to regulate the structural integrity and conductivity of myocardial tissue (147). Cadherins, armadillo proteins and plakins are the three major protein families that populate the desmosome. The cadherins desmoglein-2 (DSG2) and desmocollin-2 (DSC-2) are the two cardiac isoforms that link desmosomes between cardiomyocytes via their extracellular domains, as shown in Figure 2-8.

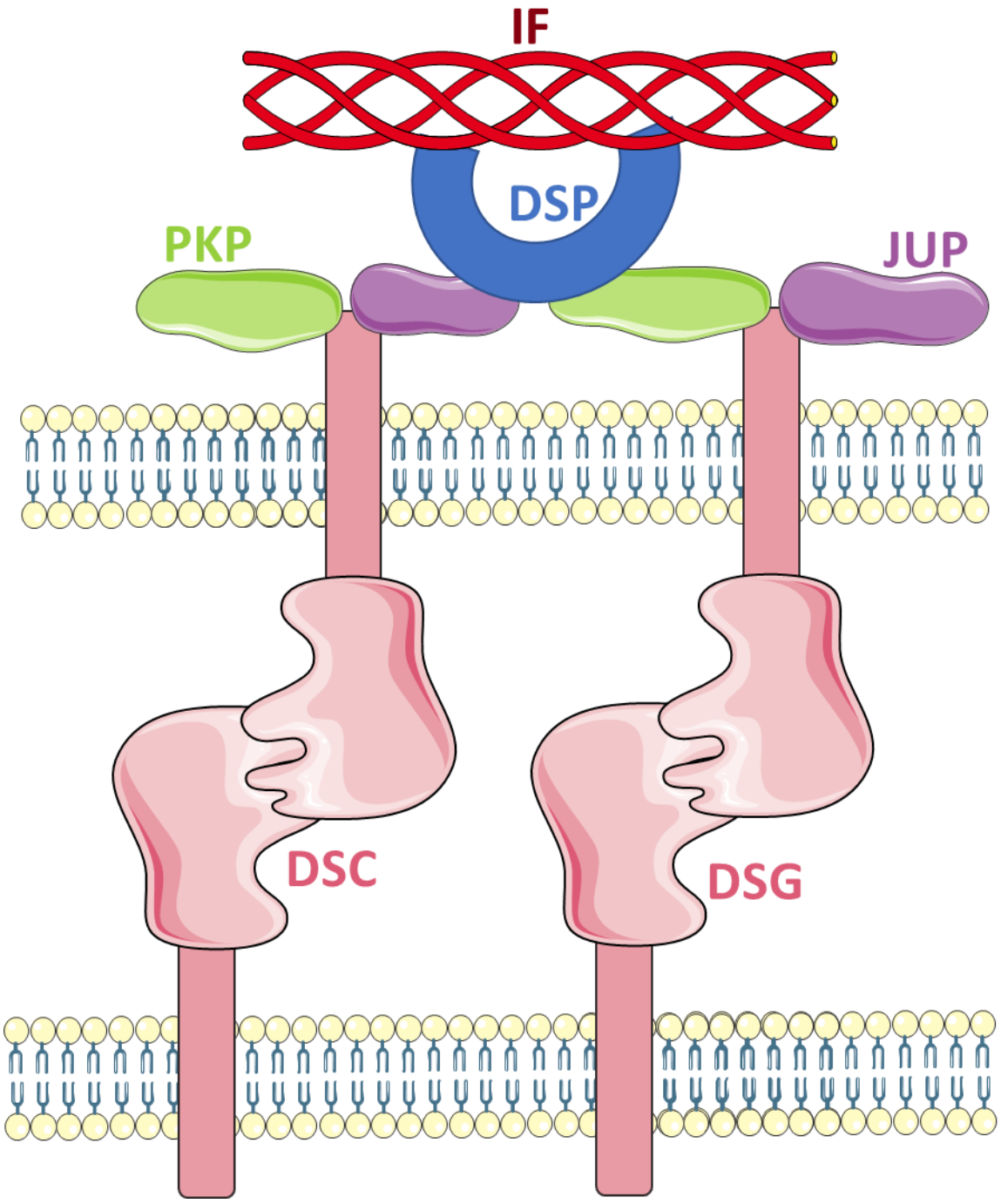

Figure 2-8. Structure of the desmosome.
The key components of the desmosome are shown. DSC = desmocollin, DSG = desmoglein, JUP = plakoglobin, PKP = plakophilin, DSP = desmoplakin, IF = intermediate filament. Figure generated using Servier Medical Art.

Via intracellular subunits, the cadherins interact with the desmosome armadillo proteins, namely plakoglobin (JUP) and plakophilin (PKP). *PKP2* is the plakophilin isoform predominantly expressed in the heart (148). Other plakophilin isoforms include *PKP1*, *PKP3* and *PKP4*. *PKP1* expression is generally restricted to epithelial cell types (149), whereas the other isoforms are expressed in multiple different tissues (150). The armadillo proteins connect the desmosome to the cytoskeleton via the plakin protein desmoplakin (DSP). DSP is vital in connecting the desmosome to the intermediate filaments and other intracellular organelles such as the sarcomere (150–152).

Desmosomal genes with ARVC-causing mutations include *DSP* (153), *PKP2* (154), *DSG2* (155) and *DSC2* (156). Approximately 50-70% of ARVC cases are caused by mutations in the *PKP2* gene (154,157,158).

Many of the *PKP2* variations linked with ARVC are frameshift mutations, resulting in the production of a truncated protein which is degraded by the cell, resulting in decreased PKP2 levels (154,159,160). This reduction is coupled with a reduction in other desmosome components such as JUP (159,160). In these cases, the disease phenotype is believed to arise from haploinsufficiency of PKP2 leading to poor desmosome assembly, cardiomyocyte death and subsequent fibrofatty replacement. Transcriptomic analysis on a conditional cardiac *PKP2* knockout mouse model showed that calcium signalling was dysregulated by loss of *PKP2* (161). Genes important in calcium cycling including ANK2, *RYR2*, CASQ2 and *CACNA1C* were downregulated upon loss of *PKP2*. Concurrently, *PKP2* knockout cardiomyocytes exhibited increased calcium transient duration and an increased propensity to develop arrhythmias. Other pathways found to be affected by loss of *PKP2* were p53 signalling, regulation of actin cytoskeleton and cell cycle (161).

Interestingly, PKP2 has also been found to localise to the nucleus in both desmosome-forming and non-desmosome-forming cell types, although its expression was restricted to the karyoplasm and was absent from nucleoli and condensed chromatin (162). Discovery of this led to sequence analysis which found that there are two isoforms of *PKP2*: *PKP2a* and *PKP2b* (162). *PKP2b* is longer than *PKP2a* due to an additional 132 bp between exons 5 and 6, translating to 44 additional amino acids between arms 2 and 3 of the protein (162). Similarly, *PKP1* also has two splice variants denoted *PKP1a* and *PKP1*b. The latter is longer due to the addition of 63 bp between exons 6 and 7, which translates to an additional 21 amino acids between arms 3 and 4 of the protein. Details of this are shown in Figure 2-9. In various desmosome-forming and non-desmosome forming cell types, *PKP1a* can localise to both the desmosome and the nucleus, however *PKP1b* is highly restricted to the nucleus (149). This is not the case for *PKP2*, for which both isoforms have been shown to localise to both the desmosome and the nucleus in various cell types (162). However, multiple studies have shown that *PKP2b* is not expressed in the heart (163,164), implicating *PKP2a* as the dominant cardiac splice variant.

Although PKP2 has been shown to complex with the ribosomal RNA polymerase III (165), the exact nuclear role of PKP2 is yet to be elucidated. However, it could be conceived that in addition to it's structural role in the desmosome, loss of PKP2 in the nucleus may result in the disruption of gene regulatory pathways that could contribute to the ARVC phenotype.

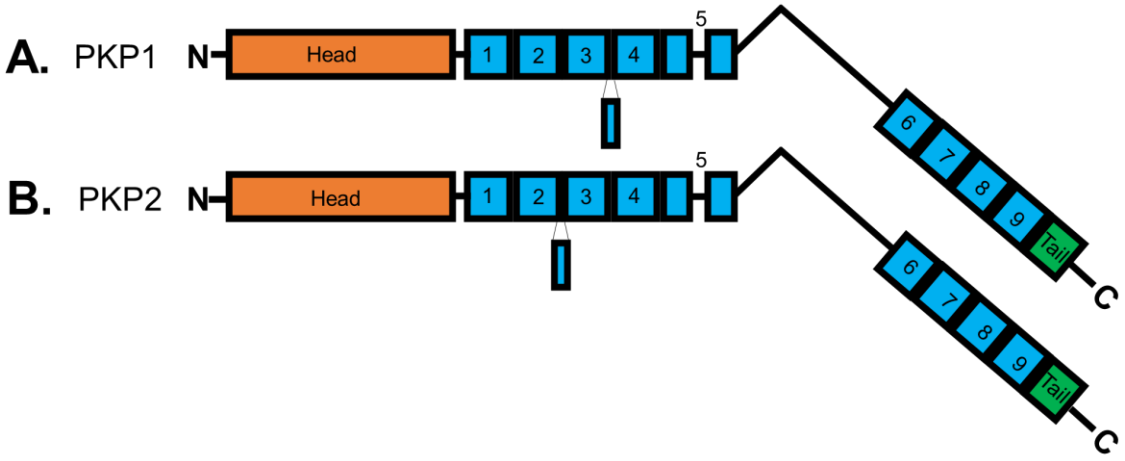

Figure 2-9. Isoforms and splice variants of plakophilin
The different protein domains of (A) PKP1 and (B) PKP2. The "a" isoform of each is shown, with the additional amino acids of the "b" isoform denotated at their corresponding locations. Figure adapted from Desai et al., 2009. Rendered in MS PowerPoint.

The cardiac desmosome is important not only in cell-cell and cell-matrix communication, but is also crucial to mechanical safeguarding and transduction of force thorough the myocardium, as well as participating in internal signalling pathways (154). Destabilisation of desmosomal proteins in both the desmosome and the nucleus is likely to cause a reduction in structural integrity, functional signalling and survivability of the cardiomyocyte population, leading to ARVC pathogenesis.

This section has explored some of the more commonly occurring forms of inherited cardiomyopathies. Although the underlying molecular mechanisms behind these diseases are complex and unique, there are some key commonalities across the different examples that contribute to harmful morphological changes and reduced cardiac output. SNORD116 signalling has currently only been implicated HCM and the cardiac response to ischemia, however its mechanism remains undefined. As such, SNORD116 may contribute to some of the molecular and signalling mechanisms common across multiple disease states.

2.2.2 Drug induced cardiomyopathy

2.2.2.1 Doxorubicin

In addition to genetic variants, cardiomyopathies can arise from exposure to drugs and toxins. Doxorubicin was first discovered as daunorubicin (or daunomycin), an anticancer compound identified from soil microbes (166). The level of cardiotoxicity caused by daunorubicin was intolerably high (167), therefore small changes were made to the molecule resulting in the new compound Adriamycin (168), later renamed to doxorubicin. Despite these modifications, doxorubicin was still found to cause fatal cardiotoxicity in large cumulative doses (169). One study found that 30% of patients receiving doxorubicin therapy developed cardiotoxicity as a result, and 70% showed ~50% reduction in left ventricular ejection fraction within the first year of treatment (170). Another study found that 5% of patients developed congestive heart failure in response to doxorubicin therapy (171). Extensive research has been undertaken to better understand the molecular mechanisms behind doxorubicin-induced cardiomyopathy.

The chemotherapeutic mechanism of doxorubicin is its inhibition of topoisomerase II (172), leading to the accumulation of DNA damage and ultimately cell death. Doxorubicin cardiotoxicity is associated with increased cardiomyocyte apoptosis, increased oxidative stress, reduced mitochondrial biogenesis and disruption of calcium handling (173). Many of the hallmarks of heart failure are seen in doxorubicin-induced cardiomyopathy including chamber dilation, enlarged heart size, interstitial fibrosis and cardiomyocyte death (174,175). Doxorubicin is believed to contribute to increased oxidative stress through a number of mechanisms such as the activation of ROS-generating molecules, including NOX2 and Rac1 (176,177), as well as the downregulation of antioxidant processes (178). Additionally, as a quinone molecule, doxorubicin is capable of engaging in redox cycling, wherein a single-

electron transfer by mitochondrial enzymes generates a semiquinone radical (179). This generation of ROS is believed to partially contribute to the chemotherapeutic activity of doxorubicin, but is also hypothesised to promote oxidative stress in cardiomyocytes due to their enrichment of mitochondria and increased oxidative phosphorylation (178,180,181).

Molecular docking analysis demonstrated that doxorubicin binds to and inhibits the glycolysis enzyme phosphofructokinase (PFK) (182). PFK-deficient mice develop cardiac hypertrophy and left ventricular dysfunction (183,184). The same study showed that doxorubicin also binds to and inhibits α-enolase, a glycolytic enzyme shown to be important in doxorubicin-induced cardiomyocyte death and mitochondrial dysfunction (185). The overlapping symptoms between doxorubicin-induced cardiomyopathy and other forms of cardiovascular disease suggest that there could be similar underlying mechanisms playing a wider role in progressive heart failure.

2.2.2.2 Isoprenaline

A common problem encountered in heart disease is an energy deficit resulting from a reduced capacity to produce ATP, leading to cardiac dysfunction (75,186,187). This means that under stressful conditions, cardiomyocytes struggle to meet the energy demands of the body. Isoprenaline, or isoproterenol, is a non-selective β-adrenergic receptor agonist. Some of the earliest examples of clinical applications of isoprenaline as a cardiac stimulant was its use on German soldiers during World War II (188). Isoprenaline has been used since the 1960s as a treatment for heart block and bradycardia (189,190). It works by binding to the β-adrenoreceptor and causing a conformational change resulting in the release of the Gα protein. Gα activates adenyl cyclase which converts ATP to cAMP which activates protein kinase A (PKA). PKA then mediates a number of pathways within the cell including the release of

Ca^{2+} from the sarcoplasmic reticulum (191). This results in an increased contraction rate in cardiomyocytes.

As contraction is an active process, an increased contraction rate will naturally increase the workload of the cardiomyocytes. Therefore, as a method of applying cardiac stress, isoprenaline is often useful in animal and cell models when investigating the response to increased cardiac demand. Short-term (<24hrs) exposure to isoprenaline results in tachycardia, and also an increase in arrythmias (192,193). However, long-term exposure causes over-stimulation of the β-adrenoreceptors which leads to serious pathological outcomes including increased cell death, cardiac hypertrophy, myocardial infarction and fibrosis (194,195). Sustained stimulation of β-adrenergic receptors induces multiple mechanisms that contribute to the hypertrophic phenotype including enhanced protein synthesis, elevated oxidative stress and stimulation of the mTOR/pI3K signalling pathway (196). Long-term isoprenaline exposure was shown to decrease the abundance of sarcomeric proteins including *MYL2* and *MYL3*, both examples of genes with mutations contributing to familial HCM (197). There was also a marked decrease in fatty acid oxidation and mitochondrial proteins, suggesting a metabolic mechanism contributing to the hypertrophic phenotype.

Isopranline causes cardiac stress by increasing the workload of the cardiomyocytes. Doxorubicin causes cardiotoxicity through the excessive production of free radicals and increased oxidative stress within cardiomyocytes. Doxorubicin has the added toxicity of causing DNA damage and the accumulation of toxic adducts in the heart, whereas isoprenaline induces cardiac damage progressively through sustained β-adrenoreceptor activation (198). Both forms of drug-induced cardiomyopathy have been used as viable strategies of modelling heart disease both *in vivo* and *in vitro*, and therefore would be effective tools in the investigation of the role of SNORD116 in cardiovascular disease.

2.2.3 Myocardial Infarction and Cardiac Fibrosis

A myocardial infarction (MI) is defined by the sudden and often irreversible damage to the heart muscle tissue as a result of ischaemia caused by loss of adequate blood supply (199). According to the British Heart Foundation, there are ~100,000 hospital admissions each year due to an MI event (200). Men are more than twice as likely to suffer an MI compared to women (200), and the average age of first event is 55-60 years (201). There are a number of criteria used to diagnose MI including symptoms of ischaemia, elevated cardiac biomarkers, pathological ECG traces, morphological abnormalities and the presence an intracoronary thrombus at angiography (or autopsy) (202). The prognosis is improved if reperfusion is commenced within six hours of the event, and over seven out of ten patients who suffer an MI survive the first event (200). However, repetition of cardiovascular events is common and the one-year survival rate is estimated at 88%, declining with age and the presence of other risk factors such as hypertension, diabetes, and chronic heart disease (201).

One of the most common causes of MI is the rupture of an atherosclerotic plaque within a coronary artery (203,204), referred to a type I MI (205). This can cause thrombosis and acute blood vessel closure which cuts off the oxygen and nutrient supply to the area at risk, the location of which is determined by the blood vessel affected. Figure 2-10 shows an example of an apical infarct. Type II MI is characterised by a loss of oxygen supply not attributed to acute atherothrombotic plaque disruption. This can arise due to acute gastrointestinal bleeding or a sustained tachyarrhythmia

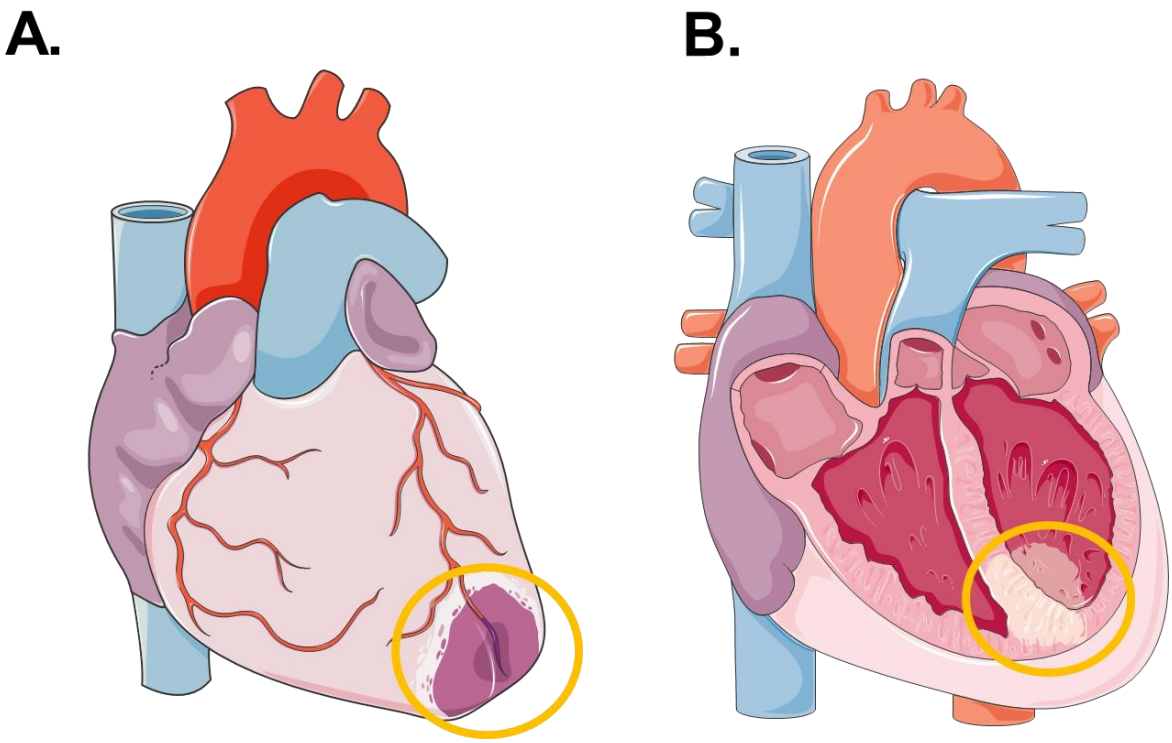

Figure 2-10. Myocardial infarction and cardiac remodelling.
Yellow circles highlights the (A). infarct region and (B) area of remodelling following MI. Rendered using Servier Medical Art.

(205). Other causes include coronary artery disease outside of atherosclerosis, spontaneous coronary dissection, coronary emboli, systemic hypotension and atrial fibrillation (206). Type III MI is classified by presentation of MI in the absence of elevated biomarkers, whereas types IV and V typically arise from coronary intervention (205).

Upon infarction, oxygen is depleted in the affected tissue, forcing the cardiomyocytes to switch from fatty acid oxidation to anaerobic metabolism, as demonstrated by the depletion of glucose and increase in lactic acid production (207). Contraction is quickly inhibited within the infarct (207,208). An inflammatory response is initiated, and the complement cascade is activated, followed by the recruitment of neutrophils and monocytes to the injured myocardium (209,210). Apoptosis begins to occur as early as 20 minutes after ischaemia develops.

Left untreated, an MI will lead to heart failure and cardiomyocyte death. However, correction of the artery occlusion and subsequent reperfusion can in some cases lead to further damage, referred to as myocardial ischaemia-reperfusion (I/R) injury. Illustrating this, pro-apoptotic markers are higher after reperfusion compared to during MI (211). In addition to contributing to atherosclerosis progression, reactive oxygen species (ROS) production is elevated following MI, as demonstrated by the increased expression of the NADPH oxidase Nox2 which was shown to contribute to ROS-induced cardiac damage (212,213). During reperfusion, platelets and macrophages become activated and flood into the infarct causing it to expand in size (214,215). This, coupled with fluid extravasation from the damaged myocardium can lead to oedema (216). The activated immune response further contributes to the increase in ROS production within the infarct (215). ROS also promotes the drastic mishandling of Ca^{2+} in injured cardiomyocytes. Increased ROS in damaged cardiomyocytes has been shown to modify amino acids on *RYR2* receptors, resulting in sarcoplasmic reticulum Ca^{2+} leak and causing the accumulation of intracellular Ca^{2+} (217). This calcium overload damages proteins, organelles, the cytoskeleton and the plasma membrane (218). This leads to further cardiomyocyte loss and can contribute to pathological remodelling and progressive heart failure that follows MI.

Adverse cardiac remodelling almost always occurs after MI in the form of a fibrotic scar and development of interstitial fibrosis (219). Pathological fibrosis involves the overabundant production of extracellular matrix proteins, resulting in excessive stiffness and impaired cardiac function. Remodelling after the loss of cardiomyocytes due to MI-related ischaemia is capitulated by two events: the hypertrophic expansion of surviving cardiomyocytes, and the proliferation and activation of cardiac fibroblasts, the latter of which can be quantified by the increased expression of alpha-smooth muscle actin (aSMA) fibres. The activation of cardiac fibroblasts progresses through three stages beginning with the inflammatory phase, during which the production of interleukins and

TNFα increases fibroblast migration to the infarct area (220,221). This is followed by a proliferative phase which is activated by TGFβ and SMAD2/3 signalling (222,223). There is also a substantial increase in ECM production during this phase (224). The final maturation phase is characterised by the release of anti-inflammatory cytokines, increased generation profibrotic fibres and the formation of fibrotic scar tissue (225). The length of the maturation phase can vary between individuals, but evidence has shown that myofibroblasts can remain active in the infarct area for up to 18 years post-MI (226). As stated previously, research using mouse models have shown that SNORD116 expression is linked to fibrotic scar formation and pathological remodelling following MI (68). This could suggest a pathological role of SNORD116 during cardiac damage and repair.

In addition, SNORD116 was identified in the exosomes of stressed cardiomyocytes (65). During stress, exosomes released from cardiomyocytes may signal to other cell types including cardiac fibroblasts. This could suggest that SNORD116 may act as a disease signal released by cardiomyocytes that plays a part in the communication between cardiomyocytes and cardiac fibroblasts, ultimately contributing to the activation of disease phenotypes in both cell types.

To summarise, heart disease is one of the biggest killers in the developed world and effectuates a gruelling burden on the healthcare system. There are many different forms that heart disease can take, influenced by internal and external factors. Each form of heart disease presents unique challenges to both the patients experiencing them and the medical staff administering treatment. However, there are some overarching commonalties that appear in most forms of heart disease. Gene transcription programs undergo significant change and often revert to foetal expression patterns. Metabolism undergoes a similar shift toward foetal-like characteristics, adopting carbohydrates as the primary source

of ATP production as opposed to the more efficient fatty acid oxidation. Understanding these patterns and themes will support the elucidation of SNORD116's role in cardiovascular disease. However, effective models of heart disease must be developed in order to undertake this investigation.

2.3 Modelling heart disease using induced pluripotent stem cells

2.3.1 Generation and culture of induced pluripotent stem cells

Stem cells are undifferentiated cells that have the potential to differentiate down multiple cell lineages. There are different types of stem cells that exist that can be used for a variety of research and medical purposes. Adult stem cells reside in a variety of niches throughout the human body. Examples include haemopoietic stem cells within the bone marrow, neural stem cells in the brain, and intestinal stem cells in the crypts of the gut (227,228). Mesenchymal stem cells (MSCs) are adult stem cells that reside in the bone marrow stroma and various other niches within the body. They can be isolated, cultured and differentiated into multiple specialised cell types including chondrocytes, osteocytes, adipocytes and muscle cells (229). Despite the name, MSCs can also be induced to trans-differentiate along non-mesodermal lineages such as neural and endothelial (230,231). Compared to other cell types, MSCs are relatively easy to isolate and culture (232). However, the pluripotency of MSCs is still under debate and they are officially classed as multipotent due to their restricted differentiation capacity (233). In addition, long-term culture of MSCs can be problematic due to the induction of cellular senescence after relatively few passage numbers. This can lead to phenotypic changes and inhibit differentiation capacity (234,235).

Embryonic stem cells (ESCs) are pluripotent stem cells isolated from the inner cell mass of human or animal blastocysts. When separated from the developing embryo, ESCs can be maintained in culture indefinitely in an undifferentiated state whilst maintaining their capacity to differentiate along all three germ lineages (236). Research using human ESCs is highly regulated and subject to restrictive legislation. International organisations such as the International Society for Stem Cell Research

publish guidelines advising scientific policy and ethical standards for using ESCs for research purposes (237). In the UK, the Human Fertilisation and Embryology Authority (HFEA) is an independent regulator that controls licencing and monitoring of ESCs in clinical and research settings (238), and there are numerous government agencies such as the Medicines and Healthcare products Regulatory Agency (MHRA) providing governmental restriction and oversight. Although their unlimited capacity for self-renewal and differentiation makes ESCs an enticing tool for disease modelling, the ethical and practical difficulties concerning the acquisition, isolation and use of ESCs can restrict their implementation in research.

Induced pluripotent stem cells (iPSCs) provide a strategy to overcome the restrictions surrounding ESCs while preserving the capacity for self-renewal and pluripotency. The first iPSCs were developed by the Yamanaka group in 2006, who were able to reprogram adult mouse fibroblasts into an induced pluripotent state using four key reprogramming factors (Oct4, Sox2, c-Myc, and Klf4) via retroviral infection (239). Since then, there have been a variety of different methods developed to reprogram human cells into iPSCs (240), which can then be used in research for the purposes of disease modelling, drug testing, generating transgenic lines etc. Although still regulated under the Human tissue Authority and subject to ethical standards of practice, iPSCs do not require the use or destruction of an embryo and are therefore exempt from restrictive regulation on embryonic research. In addition, iPSCs have the same pluripotent capacity as ESCs as demonstrated by the generation of entirely iPSC-derived animals (241,242), and have been shown to share highly similar transcriptional and epigenetic profiles (243–246).

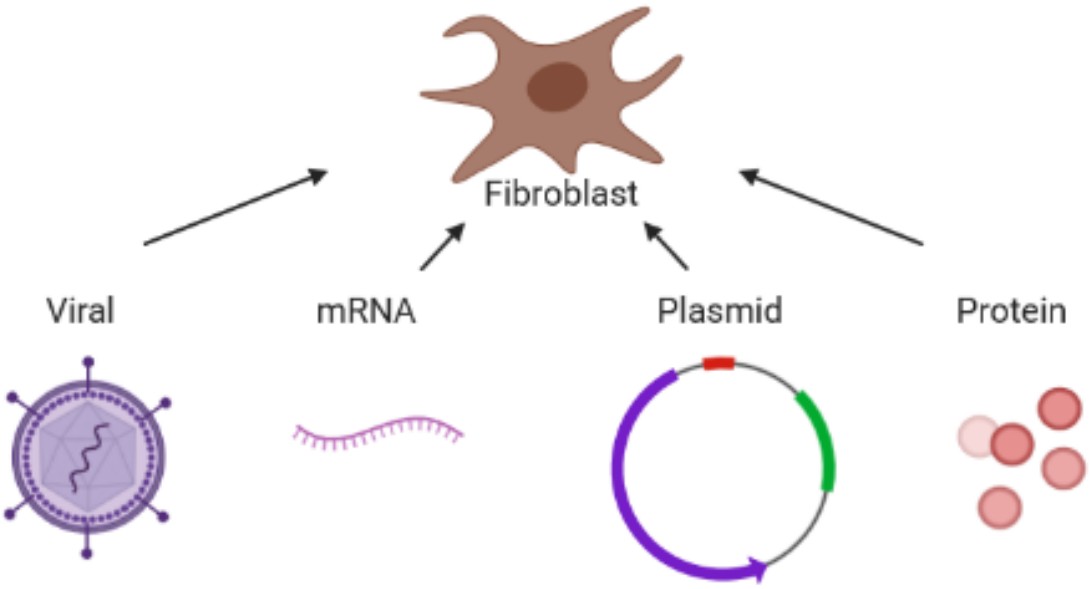

Figure 2-11. Methods of reprogramming iPSCs.
Viral methods (lentiviral, adenoviral and retroviral) involve infecting the cells with a virus that contains the DNA/RNA encoding the reprogramming factors. MRNA transfection involves transfecting the cells with mRNA encoding the reprogramming factors. Episomal plasmids can be constructed that encode the reprogramming factors, which can be transfected into cells. Alternatively, the reprogramming factors can be obtained as purified recombinant proteins and introduced to the cells. Generated using BioRender.com.

The two main strategies of reprogramming somatic cells into iPSCs are referred to as integrating and non-integrating. Integrating strategies involve using retroviral and lentiviral vectors that insert into the target cell genome. A single polycistronic vector or multiple single-gene vectors can be constructed and used to package the reprogramming factors in the form of DNA code. Retroviruses can only infect proliferating cells and are prone to incomplete silencing and insertional mutagenesis. Lentiviruses are preferred over retroviral infection as they can infect non-proliferating cells and have a larger cloning capacity (247). During the development of these methods, there was concern around the integration of viral genomes into human cells. The vector may integrate into an important gene locus such as a tumour suppressor or oncogene, leading to a cancerous or otherwise aberrant phenotype in the infected cells. To mitigate this, Cre-mediated excision of integrated loxP-containing

lentiviral reprogramming vectors in iPSCs can be performed (248), but this still leaves a loxP scar that may affect pluripotency or cell function.

Non-integrating methods of reprogramming were therefore developed. Replication-incompetent adenoviruses have been used to successfully reprogram mouse (249) and human (250) cells into iPSCs. This method of reprogramming involves generating an adenovirus containing the cDNA of Oct4, Sox2, c-Myc, and Klf4, which the virus injects into the nuclei of target cells where the genes are expressed for several days (250,251). Adenoviral reprogramming avoids the pitfalls of integrating viral methods but is much less efficient (240). An alternative is the Sendai virus, a non-integrating RNA virus that does enter the nucleus, instead injecting RNA into the cytoplasm of target cells where it is translated into protein (252,253). The Sendai virus has a higher reprogramming efficiency than an adenovirus, but cells must be cultured for at least ten passages before the virus is completely absent from infected cells (240).

There are several non-viral methods of reprogramming that have been developed. The PiggyBac (PB) transposon system is a footprint-free method of gene delivery (254) that has been used to successfully generate mouse (255) and human (256) iPSCs. Use of this system involves the construction of a transposon containing the genetic code of the reprogramming factors flanked by transposon-specific inverted terminal repeat sequences (ITRs). The transposase enzyme (introduced using the PB transposase expression vector) recognises these ITRs and cuts out the transposon, inserting it into the chromosome at a TTAA site. To remove PiggyBac from the chromosome, the cells must simply be re-transfected with the PB transposase expression vector. The drawback of using PiggyBac is that it is integrating, meaning the transposon may insert into an important gene locus which could disrupt cell behaviour. Sequence verification would be required to ensure that the transposon

has not integrated into an important site, and that it has been fully excised by the transposase.

To completely avoid the risk of insertional mutagenesis, there are several transient episomal methods of delivering the reprogramming factors into target cells. For example, plasmids encoding the reprogramming factors have been used to generate mouse iPSCs (257). However, the cells must be transfected daily for the proteins to be present long enough to induce reprogramming, and even then, the efficiency is very low. A specialised type of plasmid called oriP/EBNA has a more stable in vivo half-life and has been used to reprogram human fibroblasts into iPSCs with an efficiency of ~0.0004% (258). Another study was able to boost this efficiency to 0.009% in peripheral blood cells by including Lin28 and SV40 large T antigen into the oriP/EBNA vectors alongside the reprogramming factors and supplementing the growth media with sodium butyrate (259). Although the use of plasmids is footprint-free, one study has shown that the plasmid can remain in cells after reprogramming is complete (260). An alternative to plasmid transfection is the use of RNA, which is less stable therefore will not persist in cells. Warren et al.(261) were able to reprogram human fibroblasts with an efficiency of 4.4% by transfecting cells with the mRNA of Oct4, Sox2, c-Myc, Klf4 and Lin28, whilst culturing the cells in valproic acid-supplemented media and 5% oxygen. The cells had to be transfected daily for at least seven days for successful reprogramming to occur. Also, the RNAs must be synthetically modified to protect them from endogenous cellular defence mechanisms.

Overall, there are many possible approaches for generating iPSCs, each with their own advantages and disadvantages. Reprogramming efficiency and labour intensity must be weighed against risks such as insertional mutagenesis and the incomplete silencing of reprogramming factors. The application of the iPSCs, be it research or therapy, must be taken into account. Integrational reprogramming is generally not used to generate

iPSCs for therapeutic purposes as the risk of teratoma formation is unacceptably high. Another disadvantage of iPSCs is that they are sex-biased, as many commercially available lines are typically XY. This could impact their power as a disease model, particularly in diseases where sex is a factor.

However, the value of iPSCs as a research tool is rapidly increasing as their versatility expands. IPSCs can be differentiated into any existing cell type, which makes them incredibly useful as a tool for modelling disease. Multiple cardiac cell types can be derived from iPSCs in both two-dimensional and three-dimensional culture. This allows the modelling of both heart development and heart disease using human cells. As stated in previous sections, SNORD116 is a challenging snoRNA to investigate as it seems to exhibit expression patterns that are unique to humans, implying that it could have human-specific functions. The sequence variability between different SNORD116 paralogues also appears unique to humans, which suggests animal models could be limited in the investigation of human-specific paralogues. Additionally, development and disease of the heart can vary significantly between human and animal models in size, time, contraction output and gene/protein isoform expression (262–264). For these reasons, iPSCs represent a promising strategy for the investigation of SNORD116 in human heart development and disease.

2.3.2 Using iPSCs to model heart development

During embryogenesis, the circulatory system is the first functional unit to develop in the embryo (265). Early embryos consist of three germ layers: the ectoderm, endoderm and mesoderm. The mesoderm develops into the paraxial mesoderm which gives rise to the somites (skeletal muscle progenitors), and the lateral plate or splanchnic mesoderm which gives rise to cardiac precursors. Nodal, BMP4 and Wnt signalling are important in the specification of splanchnic mesoderm (265). However, the development of cardiac progenitor cells requires the subsequent downregulation of Wnt and TGFβ signalling (266).

Heart development begins around 3 weeks post-conception in humans, commencing with the formation of the primary heart field that makes up the cardiac crescent within the mesoderm (267). Figure 2-12 depicts how the three-dimensional heart structure develops (266). As embryogenesis occurs, cardiac progenitor cells from the primary heart field generate the straight heart tube along the embryo midline. The secondary heart field is a region of the mesoderm medial to the primary heart field. The straight heart tube is elongated through the addition of cells from the secondary heart field. The structure loops and gives rise to the outflow tract and right ventricle. As development continues, the four-chambered heart structure begins to take shape. A cell protrusion from the from the embryonic heart tube forms the proepicardial organ from which the epicardium – the outer layer of the heart – is derived (268). Vasculogenesis of cardiac mesoderm precursors gives rise to the endocardium (269).

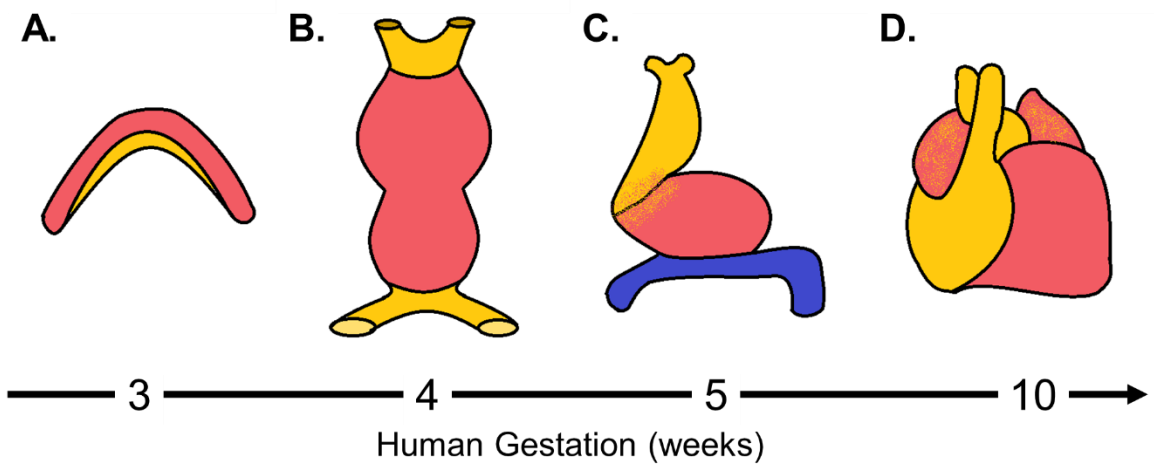

Figure 2-12. Human heart development.
Heart development begins at 3 weeks with (A) the cardiac crescent. The embryo folds ventrally causing the cardiac fields to meet and form (B) a straight heart tube. The heart tube begins to loop rightward and caudally forming (C) the looped heart tube. The chambers start to form as septations occurs forming (D) the septated heart. Pink shading represents first heart field derivatives, yellow shading represents second heart field derivatives, blue shading represents proepicarium derivatives. Adapted from Doyle *et al.*, 2015

There are many key transcriptional changes that control cardiac specification and development. The transcriptional factors *GATA4* and TBXT regulate the onset of cardiac differentiation, and *NKX2-5* is critical for the differentiation of the myocardium (265). Mutations in these genes lead to congenital heart defects such as atrial/ventricular septal defects, tetralogy of Fallot and DiGeorge syndrome (270–273). As the heart develops, cardiac progenitors specialise into cells that make up the different layers of the heart. Cardiomyocytes develop and form the myocardium, and genes encoding structural proteins such as actin and myosin are expressed. These genes have different isoforms that are associated with different stages of heart development. For example, foetal cardiomyocytes primarily express slow skeletal troponin I (*TNNI1*), whereas adult cardiomyocytes preferentially express cardiac troponin I (*TNNI3*) (274).

2.3.2.1 Cardiomyocyte differentiation

Since the 2000s, a multitude of ESC and iPSC-derived cardiomyocyte (iPSC-CM) and cardiac fibroblast (iPSC-CF) differentiation protocols have been published (275–279). Many of the established cardiac differentiation protocols involve the use of small molecules to recapitulate the key signalling events that occur during embryogenesis. The initial activation of Wnt signalling followed by Wnt inhibition is a widely used method of inducing general cardiac mesoderm development. IPSC-CM differentiation continues along the mesodermal pathway to form differentiated contractile cardiomyocytes, whereas iPSC-CF differentiation diverges along an epicardial progenitor cell type before forming cardiac fibroblasts. The protocol laid out in Burridge et al.(280) became a standard protocol for iPSC-CM differentiation, which has since been adapted to include small molecule activators/inhibitors and various growth factors to improve cardiomyocyte purity, specificity, and maturation (281–283). The stage of differentiation can be monitored by measuring changes in gene expression, protein expression and metabolism, as the cells develop from undifferentiated stem cells into differentiated contractile cardiomyocytes.

During the development of cardiomyocytes, their metabolism undergoes notable changes, particularly on the shift from glycolysis to fatty acid oxidation. A summary of the changes in metabolism that occur during cardiomyocyte differentiation is shown in Figure 2-13.

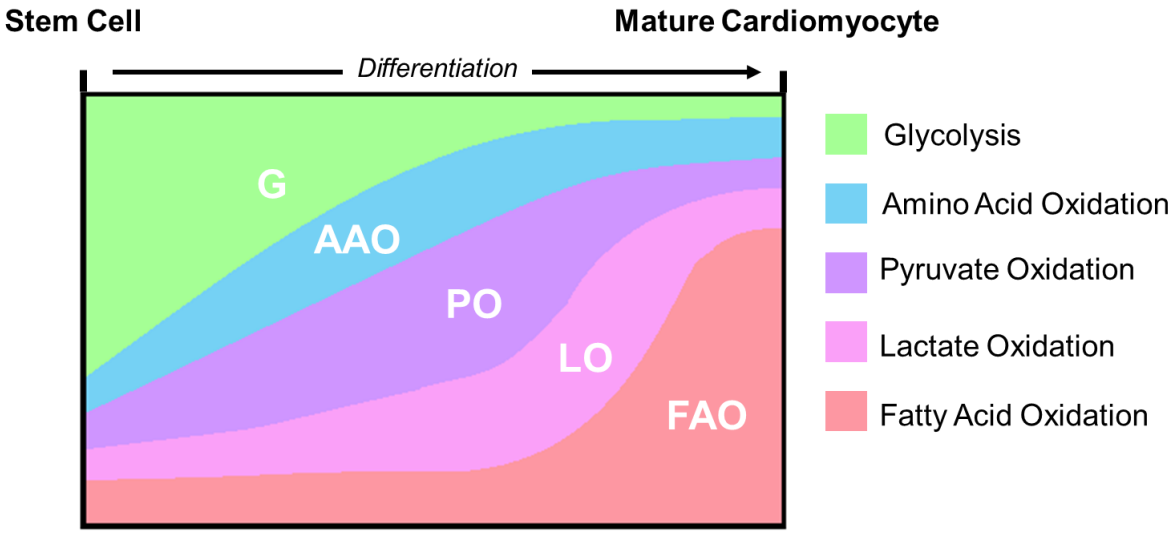

Figure 2-13. Key forms of metabolism used by cells during cardiomyocyte differentiation.
The chart represents the level of reliance the cells have on each of the different forms of metabolism: glycolysis (G), amino acid oxidation (AAO), pyruvate oxidation (PO), lactate oxidation (LO) and fatty acid oxidation (FAO). Stem cells rely mostly on glycolysis for ATP production. As the cells differentiate into, oxidative phosphorylation of substrates increases,. Mature cardiomyocytes predominantly perform oxidative phosphorylation. Figure adapted from Morita et al., 2020

In vivo, studies have shown that the alpha, gamma and delta isoforms of peroxisome-proliferator-associated receptor (*PPARa*, *PPARy* and *PPARd*) may be important in regulating this metabolic switch during cardiac development (284,285). *PPARa* has been shown to function in the developing heart specifically in the regulation of mitochondrial and fatty acid oxidation enzymes (286). In contrast, *PPARy* has been found to have a relatively low expression level in the heart (287,288), however may still be important for cardiomyocyte survival and differentiation (289). *PPARd* has also been shown to contribute to cardiomyocyte metabolic development: when activated, *PPARd* increases fatty acid oxidation and contractile force generation, whereas it's absence leads to reduced fatty acid oxidation (285,290).

Differentiated iPSC-CMs are distinct from primary cardiomyocytes in several ways, and lack the maturity of adult cardiomyocytes (291–294). Morphologically, iPSC-CMs are round or polygonal instead of the traditional rod-shape of primary cardiomyocytes (295), and they lack the T-tubule network that is important in heart muscle contraction (296). iPSC-CMs also exhibit a greater extent of sarcomeric misalignment than adult cardiomyocytes (291). There is less co-localisation of ion channels and less uniform calcium release (297) resulting in longer action potentials, spontaneous contraction and a negative force-frequency relationship (296). A summary of the differences is presented in Table 2-1.

Table 2-1. Summary of the key phenotypic differences between adult cardiomyocytes and iPSC-derived cardiomyocytes.

Phenotypic property	IPSC-derived Cardiomyocyte	Primary Cardiomyocyte
Cell size	Smaller	Larger
Cell morphology	Rounded	Circular
Sarcomeric alignment	Disarray	Aligned
Spontaneous contraction	Yes	No
Resting membrane potential	Less negative	More negative
T-tubules	Absent	Present
Primary metabolism	Glycolytic	Fatty acid oxidation
Nuclei number	Mono-nuclear	Poly-nuclear

Many methods have been developed to improve the maturation of iPSC-CMs so that they more closely resemble primary adult cardiomyocytes and are therefore an improved biological model for cardiac development and disease. Modulating the metabolism of cardiomyocytes has been shown to change their maturity. As stated previously, cardiomyocytes undergo a metabolic switch away from glycolysis and towards fatty acid oxidation as they develop from foetal to adult (77,78). IPSC-CMs cultured in glucose-rich media have been shown to emphasise phenotypes associated with immaturity such as reduced contraction, rounded morphology, sarcomeric disarray and glycolysis-reliant metabolism when compared to iPSC-CMs cultured in low glucose or glucose-free media (298–302). Consequentially, fatty acid-based media has become a standard medium for post-differential iPSC-CM culture as a strategy for improving maturity and better recapitulation of the adult cardiomyocyte metabolism and phenotype.

2.3.2.2 Cardiac fibroblast differentiation

Similarly to cardiomyocytes, cardiac fibroblasts originate from progenitor cardiac cells emerging from the mesoderm. However, cardiac fibroblasts originate from the epicardium (303–305). The presence of epicardial cells expressing the transcription factor TCF21 is required for cardiac fibroblast generation during heart development (303). Although evidence has also shown that some cardiac fibroblasts originate from endocardial progenitors, as well as the neural crest (305–307), the majority of cardiac fibroblasts present in the developed heart appear to arise from epicardial origins (308).

In contrast to the differentiation of iPSC-CMs, there is a limited number of protocols focused on the derivation of cardiac fibroblasts from iPSCs. Until recently, cardiac fibroblasts were not considered to be distinct from fibroblasts of non-cardiac origin. However, transcriptomic studies have

revealed that cardiac fibroblasts share greater similarity with cardiomyocytes than they do with non-cardiac fibroblasts (309,310). This discovery has emphasised the importance of cell specificity and encouraged the development of iPSC-derived cardiac-specific fibroblasts.

To achieve iPSC-CF differentiation *in vitro*, small molecules are used on iPSCs to induce the progression of cardiac progenitors through mesodermal and epicardial stages of cardiac fibroblast development (279). Wnt signalling activators such as CHIR are used to induce mesoderm development causing a reduction in pluripotency marker expression and an increase in TBXT and *GATA4*. Wnt signalling is then inhibited to generate cardiac progenitor cells. Once these cells develop, Wnt signalling is re-activated and retinoic acid supplementation is used to induce the mesothelium-epicardium transition to generate epicardial progenitor cells (311). Epicardial cells are transitioned into cardiac fibroblast using Fibroblast Growth Factor (FGF) and the inhibition of TGFβ signalling. Multiple studies have shown that iPSC-CFs more closely resemble primary cardiac fibroblasts than they do iPSC-CMs or primary non-cardiac fibroblasts (312,313).

To summarise, iPSCs can be differentiated successfully *in vitro* to generate both cardiomyocytes and cardiac fibroblasts.

2.3.3 Using iPSCs to model heart disease

As stated previously, there are many different forms of heart disease that are generally united by common overarching features such as transcriptional and metabolic changes. This section will briefly outline how different strategies involving iPSC-derived cells can be used to model heart disease.

2.3.3.1 Drug induced cardiac stress

There are forms of cardiomyopathy that directly arise from the use of pharmaceutical agents such as doxorubicin-induced cardiomyopathy. IPSC-CMs have been used to investigate the molecular pathways underlying doxorubicin cardiotoxicity. Multiple studies have demonstrated that pathological phenotypes associated with doxorubicin cardiotoxicity such as apoptosis, ROS production, aberrant mitochondrial biogenesis and calcium mishandling can be induced in iPSC-CMs through the supplementation of doxorubicin in the culture media (314,315). Additionally, isoprenaline has also been used in the context of iPSC-CMs to model the effects of cardiac hypertrophy and increased cardiac workload (316,317). This is particularly useful in investigating arrhythmogenic disorders as isoprenaline increases the frequency of arrhythmogenic events in iPSC-CMs (318).

Not only is this useful in the design of improved drugs with reduced cardiotoxic effects, but it also allows the modelling of these aspects of heart disease *in vitro* using human cardiomyocytes.

2.3.3.2 Hypoxia-induced cardiac stress

During MI, cardiomyocytes are disconnected from the oxygen supply, leading to metabolism changes, myofibril degradation and apoptosis.

During I/R injury, the re-introduction of oxygen to the infarct causes increased damage and promotes pathological remodelling. These circumstances can be partially re-created *in vitro* using iPSC-CMs through modification of the culture conditions by incubating iPSC-CMs in a hypoxic atmosphere (319–321). Hypoxia causes an increase in DNA damage, ROS production, increased apoptosis and sarcomeric disarray in iPSC-CMs. Contraction frequency is also reduced, coupled with an increase in calcium overload and arrythmia (319,322–324). In the adult heart, MI causes a switch from oxygen-dependent fatty acid oxidation to anaerobic glycolysis. Because the metabolic profile of iPSC-CMs is generally closer to foetal-like glycolytic metabolism than fatty acid oxidation, iPSC-CMs are more resistant to hypoxic stress than adult cardiomyocytes (319,320). Recently, fatty acid-driven maturation of iPSC-CMs has shown to be effective in increasing their susceptibility to the effects of hypoxia and allowing the switch from FAO to glycolysis to occur (325). Additionally, metabolism as measured by the oxygen consumption rate (OCR) is decreased in both fatty acid-matured and glucose-fed iPSC-CMs under hypoxic conditions (325).

Hypoxia also causes changes to gene transcription in iPSC-CMs that mimic events during MI. Cardiac structural genes such as *TNNT2*, *MYBPC3*, *RYR2* and *ATP2A2* are downregulated (326) Additionally, *VEGFA*, a pro-angiogenic grown factor released during MI, is upregulated in hypoxic iPSC-CMs (327–329). Genes important in mitochondrial function, metabolism and glucose transportation are also commonly dysregulated in hypoxic iPSC-CMs (325–328). This shows that iPSC-CMs can be used as a model for cardiac damage occurring during and after MI that contribute to progressive heart failure.

2.3.3.3 Fibrotic stress

Fibrosis is one of the hallmarks of heart failure and often occurs conjointly with many forms of heart disease (330–333). During fibrosis, inflammatory signalling causes the activation of fibroblasts into myofibroblasts. However, this process can also happen naturally as the heart ages (334). Modelling the development of cardiac fibroblasts and how they change during disease is crucial in understanding how fibrosis occurs, and how its harmful effects can be mitigated.

IPSC-derived cardiac fibroblasts have been shown to be less susceptible to spontaneous activation into myofibroblasts compared to primary cardiac fibroblasts during passaging in culture (312,335). However, upon treatment with TGFβ, iPSC-CFs significantly upregulate myofibroblast markers aSMA and POSTN, and the expression of ECM genes such as *COL1A1*, COL3A1, COL4A2, and FN1 also increase (312,313). Doxorubicin was used to induce a fibrotic phenotype IPSC-CFs, which could then be alleviated through treatment with the clinical fibrosis treatment pirfenidone (312). This shows that iPSC-CFs can be used to model fibrosis *in vitro*.

Co-culture of iPSC-CMs and iPSC-CFs shows improved maturity and contractility within the iPSC-CM population (313,336). This demonstrates that not only are iPSC-CFs useful in investigating the role of cardiac fibroblasts in heart disease, but can lead to improved multi-cellular models of heart disease that better explore cross-talk between the different populations within the heart.

2.3.3.4 Genetic variants

Inherited cardiomyopathies contribute to a not-insignificant number of cardiovascular disease cases. Although there are many animal models

that provide an excellent approach to investigating heart disease, the numerous discrepancies in genotype and phenotype can result in certain aspects remaining less well-explored. To overcome this, models using human iPSC-derived cardiac cell types have been generated using a number of different strategies. Due to its high incidence rate among the population and variety in sarcomeric gene mutations, HCM is one of the more commonly modelled inherited cardiomyopathies.

One method of modelling genetic heart diseases such as HCM *in vitro* is the use of iPSC lines that have HCM-causing mutations. This is often achieved through the reprogramming of primary somatic cells donated by patients with a specific genetic variant(s). These iPSCs can be differentiated into cardiomyocytes to investigate the effect of these variants on cardiomyocyte function. In many cases, these iPSC models can successfully recapitulate the phenotypes seen in the clinic such as hypertrophy, impaired metabolism, calcium dysregulation and contractile arrythmia (122,337–340). In addition, the amenability of iPSCs to genetic modification expands the scope of disease modelling.

2.3.3.5 CRISPR-Cas9 modification

The CRISPR-Cas9 complex, composed of a Cas9 endonuclease and a RNA guide, allows precise editing of specific DNA sequences within a genome. An overview of the complex is shown in Figure 2-14. Gene knockout is achievable by designing a guide to target a gene of interest and allowing endogenous DNA repair pathways to fix the double stranded break caused by Cas9. The most common repair pathway – Non-Homologous End Joining (NHEJ) – is error-prone and introduces insertion / deletion (indel) mutations. This disrupts the reading frame of the gene meaning the transcript can no longer be expressed.

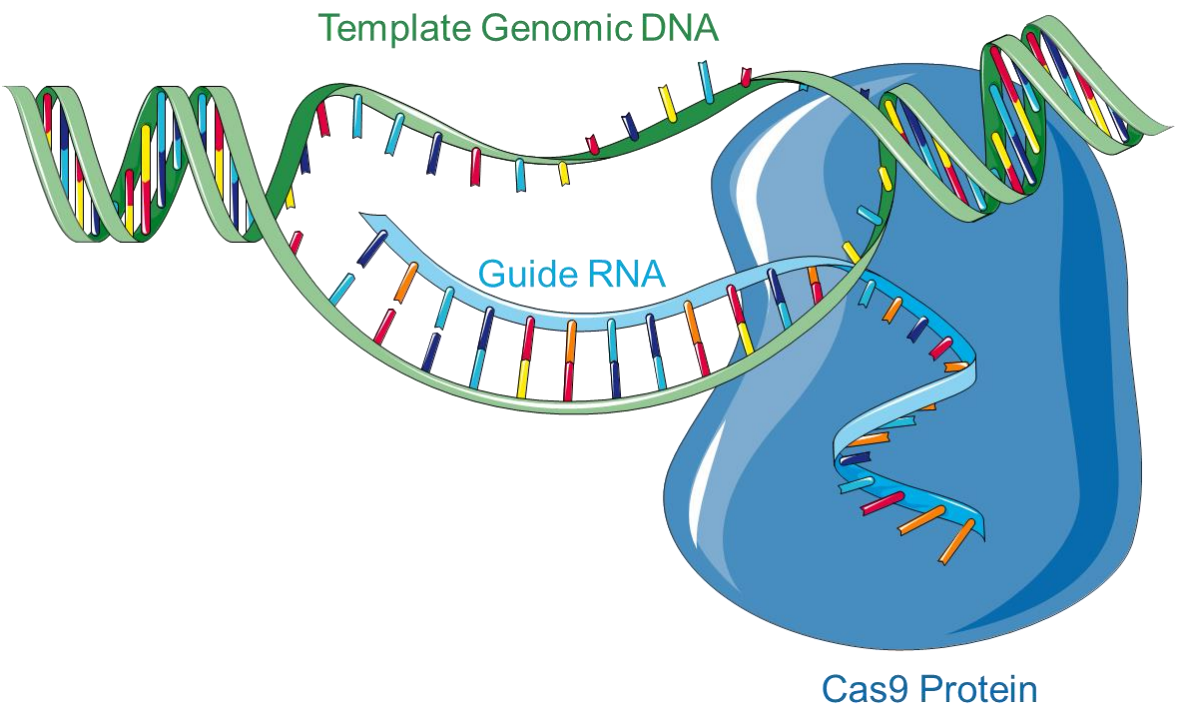

Figure 2-14. CRISPR-Cas9 complex.
The Cas9 enzyme forms a ribonucleoprotein complex with the guide RNA and the template genomic DNA. The enzyme catalyses a double stranded break at the target site.

CRISPR-Cas9 can also be used to generate knock-in mutations by exploiting another endogenous DNA repair pathway, Homologous Recombination (HR). For this to work, a construct must be designed wherein the sequence to be knocked-in is flanked by regions that are homologous to the sequences flanking the site of the break. The repair machinery recognises the regions of homology and inserts the construct into the target site and repairs the break. The construct should also include a positive selection marker such as a gene for antibiotic resistance to enable easier identification of successful recombinants. This method of Homology-Directed Repair (HDR) can be used to insert or correct specific gene mutations that are linked with disease (341–343).

One challenging aspect of modelling HCM is the prevalence of phenotypic and epigenetic variation between different individuals with the same genetic mutation (344). IPSC-models can overcome this obstacle through

the generation of isogenic controls (345–347). This is most often used in cases where the disease is caused by a single point mutation; the CRISPR/Cas9 system can be calibrated to remove the mutant nucleotide and replace it with the wild-type base-pair. This would produce a cell line that is genetically identical to the disease line except at the target site, thus providing a control which accounts for any genetic variation between cell lines.

CRISPR-Cas9 genome editing has been used on human iPSCs to generate models for HCM by introducing specific mutations into sarcomeric genes (348–350). A study by Cohn et al. demonstrated the use of CRISPR in the generation of four mutant iPSC lines, two within the *MYH7* gene (R403Q and V606M) and two within the *MYBPC3* gene (W792fsX41 and R502W59) (350). The same study also described the use of isogenic controls, wherein an almost genetically identical cell line is created with the mutation corrected to wild-type. Cohn et al. differentiated these iPSCs into cardiomyocytes (iPSC-CMs) and used them to generate human cardiac microtissue (CMT). These were used to show that all four mutations resulted in hypercontractility compared to their wild-type controls (350). In a similar study, Mosqueira et al. used CRISPR to introduce the R453C mutation in the *MYH7* gene (348). The study found the mutant iPSC-CMs showed an increase in oxygen consumption and ATP production, despite no significant increase in mitochondria. In addition, human engineered heart tissues (hEHTs) generated from the iPSC-CMs showed the mutant lines produced lower force generation and a hypocontractile phenotype compared to wild-type controls (348).

Other HCM-related genetic variants have been modelled using iPSC-CMs. The E99K mutation in the gene for cardiac alpha actin (*ACTC1*) has been identified in a number of patients with severe HCM. A 2007 study by Monserrat et al. found that out of 72 patients with the E99K mutation, 62 exhibited a HCM phenotype, although severity varied (109). Smith et al.

developed an in vitro model of the E99K mutation using iPSCs derived from a heterozygous E99K patient with severe HCM (340). These iPSC-CMs displayed the typical HCM characteristics including hypercontractility, increased brain natriuretic peptide (BNP) expression and calcium mishandling, indicating that this system can be used to successfully model HCM (340). In addition, it was this model of HCM that led to the identification of SNORD116 as a potential pro-pathogenic signal during cardiac stress (65).

Disease-causing genetic variants are a method of inducing cardiac stress through internal cellular pathways as opposed to external stimuli. IPSC-CM models allow the *in vitro* modelling of phenotypes that are common to both genetic and non-genetic forms of heart disease.

2.4 Summary and aims

SNORD116 appears to adopt expression patterns that could suggest species-specific (and even tissue-specific) functions. Although animal models have led to interesting insights into SNORD116 functionality, the specific role of SNORD116 in the context of the human heart warrants the use of human cell models. As outlined here, there are numerous strategies for modelling cardiomyocyte development and cardiac stress using iPSCs. These models can be implemented in the investigation of SNORD116 in human cardiac tissue. In addition, these models can be harnessed as platforms in the manipulation of SNORD116 expression in order to elucidate the function of SNORD116. The work presented in this thesis explores the hypothesis that SNORD116 plays a pathological role in cardiac cells and may contribute to molecular phenotypes seen in HCM.

The overall aim of this work is to investigate the role of SNORD116 in cardiomyocytes.

- AIM 1: Investigate the expression of SNORD116 during cardiac differentiation using hiPSCs.
- IAIM 2: investigate the effect of cardiac stress on SNORD116 expression.
- AIM 3: Investigate the effect of modulating SNORD116 expression in cardiac cell types.
- AIM 4: Analyse the expression of SNORD116 in clinical samples from HCM patients.

Chapter 3 Methods

3.1 Materials

All reagents and materials used to complete this work are shown in Table 3-1 and described in the methods section below. The reagents were obtained from the manufacturers as detailed.

Table 3-1. Materials used with their manufacturer and catalogue number.

Product	Manufacturer	Catalogue Number
Plastics		
1.5mL 1.5 ml TubeOne® Microcentrifuge Tubes, Natural (non-sterile)	Starlab	S1615-5550
10mL serological pipette	Starstedt	86.1254.001
24 Well Cell Culture Plate, Flat Bottom with Lid, Tissue Culture Treated, Non-pyrogenic Polystyrene	Corning Incorporated	3526
25mL serological pipette	Starstedt	86.1685.001
5mL Polystyrene Round-Bottom Tube	Falcon	352054
5mL serological pipette	Starstedt	86.1253.001
6-well Clear TC-treated Multiple Well Plates, Individually Wrapped, Sterile	Corning Incorporated	3516
96 Well Assay Plate, Black Plate, Clear Bottom with Lid, Tissue Culture Treated Polystyrene	Corning Incorporated	3603
96 well plate, polystyrene, High Bind, white flat bottom wells, non-sterile, white	Corning Incorporated	3922
96 Well TC-Treated Microplates	Corning Incorporated	3598
BD Discardit™ 20mL Syringe	Becton Dickinson	300296
BD Vacutainer 6ml EDTA Purple Blood Collection Tubes	Beckton Dickinson	367863

BioLite 24 Well Multidish	Thermo Fisher Scientific	930186
Cell Strainer, 70 um	Falcon	352350
Cellstar 15mL tube	Greiner	188 271-N
EDTA tubes	Sarstedt	6.265 374
LightCycler® 480 Multiwell Plate, 384, white	Roche Diagnostics	04729749001
Millex® Syringe-driven filter unit, 0.22um pore size	Sigma-Aldrich	SLGVV255F
MS Columns	Miltenyi Biotec	130042201
Nunc™ EasYFlask™ 25 cm^2 Nunclon™ Delta Surface	Thermo Fisher Scientific	156340
Nunc™ Biobanking and Cell Culture Cryogenic Tubes, 1.8mL	Thermo Sientific	368632
Protein LoBind® Tubes	Eppendorf	E0030108132
Röhre 50mL tube	Sarstedt	62.547.254
Transfer pipette	Fisher Sceintific	2600111
Medias		
Advanced DMEM	Gibco	12634010
B27™ supplement (50x)	Gibco	17504044
B27™ Supplement, minus Vitamin A 50x)	Gibco	12587010
B-27™ Supplement, minus insulin (50x)	Gibco	A1895601
Bovine serum albumin (BSA) solution. 7.5% in DPBS	Sigma-Aldrich	A8412
DMEM	Gibco	11995040
DPBS	Gibco	14190094
EDTA	Sigma-Aldrich	E9886
Essential 8™ Basal Medium	Gibco	A1516901
Essential 8™ Supplement (50x)	Gibco	A1517101
Fetal Bovine Serum (FBS), qualified, heat inactivated	Gibco	16140071
GlutaMAX™ (100x)	Gibco	35050061

HBSS, minus Calcium Chloride, minus Magnesium Chloride, minus Magneisum Sulfate (1x)	Gibco	14175095
Luria Broth (LB) Agar	Invitrogen	22700025
Luria Broth (LB) Base	Invitrogen	12795027
Neural Maintenance Basal Media	Axol	ax0031b
Neural Maintenance Medium Supplement	Axol	ax0031a
Neural Plating Medium	Axol	ax0033
NeurOne Supplement A	Axol	ax0674a
NeurOne Supplement B	Axol	ax0674B
OptiMEM®	Gibco	31985047
Penicillin-Streptomycin	Gibco	15140122
RPMI 1640	Gibco	11875
RPMI 1640 Medium, no glucose	Gibco	11879020
Reagents		
(±)-Sodium 3-hydroxybutyrate (B-OBH)	Sigma-Aldrich	54965-10G-F
30% Acrylamide/Bis Solution	Bio-Rad	1610156
Acrilamide Bis-Acrylimide solution 30%	BioRad	1610168
Activin A	R&D Systems	338-AC-010
Agarose	Fisher Scientific	BP1356-100
AGN 193109 Sodium Salt	Santa Cruz Biotechnology	sc-210768
Ammonium Bicarbonate	Fluka Chemicals	40867
Ammonium Persulfate (APS)	Thermo Scientific	17874
Ampicillin	Sigma-Aldrich	A9393-5G
BsaI-HF	New England BioLabs	R3733
Biolog MAS	Biolog	72303
Biolog MitoPlate S-1	Biolog	14105
Biolog Redox Dye Mix MC	Biolog	74353

CD14 MicroBeads, human	Miltenyi Biotec	130050201
Cell Dissociation Buffer, Enzyme-Free, PBS-Based	Gibco	13151041
CellMask™ Orange Plasma membrane Stain	Invotrogen	C10045
CellTiter-Glo® 2.0	Promega	G9242
Chemgene	Medimark Scientific	XTM309
CHIR-99021 (CT99021) HCl	Selleck Chemicals	S2924
Chloroform	Fisher Scientific	15498679
Citric Acid	Sigma-Aldrich	251275-5G
CloneR™	Stem Cell Technologies	05888
Collagenase Type 2	Worthington Biochem	LS004174
Coomassie Brilliant Blue R-250 Dye	Thermo Fisher Scientific	20278
D-(+)-Galactose	Sigma-Aldrich	G5388-100G
D-(+)-Glucose	Sigma-Aldrich	G7528-250G
DAPI	Thermo Fisher Scientific	62248
Dimethyl sulfoxide (DMSO)	Fisher Scientific	67685
Dithiothreitol (DTT)	Sigma-Aldrich	3483-12-3
Doxorubicin hydrochloride	Sigma-Aldrich	25316-40-9
ECL Extra	Expedeon	ECLA0250
Ethanol absolute, (200 Proof), Molecular Biology Grade	Fisher Scientific	16695992
Exo-spin™ Exosome Isolation Kit	Cell Guidance Systems	EX01-8
Formaldehyde solution 4%, buffered, pH 6.9	Sigma-Aldrich	1.00496.8350
Gel Loading Dye Purple (6X)	New England BioLabs	B7024S
GeneRuler 1kb DNA Ladder	Thermo Fisher Scientific	SM0311
Glycerol	Fisher Scientific	56-81-5
Glycine	Fisher Scientific	56-40-6
Goat serum	Sigma-Aldrich	G9023
HISTOPAQUE®	Sigma-Aldrich	10771

Iodoacetamide (IAA)	Sigma-Aldrich	144-48-9
Isoprenaline hydrochloride	Sigma-Aldrich	I5627-5G
IWR	Sigma-Aldrich	I0161-25MG
L-Ascorbic acid 2-phosphate	Sigma-Aldrich	A8960-5G
LB Agar	Invitrogen	11518916
LB Broth base	Invitrogen	12780052
L-Carnitine	Sigma-Aldrich	541-15-1
L-Glutamine	Sigma-Aldrich	G3126-100G
LumiBlue ECL Extreme	Expedeon	ECLM0100
Matrigel hESC-Qualified	Corning Incorporated	54277
Milk Powder	Thermo Scientific	16694685
NotI-HF	New England BioLabs	R3189S
Oleic Acid	Sigma-Aldrich	O1383-1G
P3 Primary Cell 4D-Nucleofector® X Kit L	Lonza	V4XP-3024
PacI	New England BioLabs	R0547S
Palmitic Acid	Sigma-ALdrich	P0500-10G
Phosphate Buffered Saline (PBS) tablets	Gibco	18912014
Phusion High-Fidelity DNA Polymerase	New England BioLabs	M0530L
Precision Plus Protein™ Standards Dual Colour Prestained	Bio-Rad	161-0374
Propan-2-ol	Fisher Scientific	67630
Proteinase K	Thermo Fisher Scientific	EO0491
qPCRBIO cDNA Synthesis Kit	PCR Biosystems	PB30.11-10
qPCRBIO SyGreen Mix Lo-ROX	PCR Biosystems	PB20.11-05
RapiGest	Waters	186001861
rCutSmart Buffer	New England BioLabs	B6004S
Recombinant Human BMP4	R&D Systems	314-BP-010
Recombinant Human FGF Basic (FGF2)	R&D Systems	233-FB-025

Retinoic Acid	Alfa Aesar	44540
Revert™ 700 Total Protein Stain	LI-COR Biosciences	926-11011
SalI-HF	New England BioLabs	R3138S
Saponin	Sigma-Aldrich	47036-50G-F
SB 431542	Tocris	1614
SDS Solution, 10% Sodium Dodecyl Sulfate Solution	Fisher Scientific	151-21-3
Seahorse XF Base Medium	Agilent	1033335-100
Seahorse XF Cell Mito Stress Test Kit	Agilent	103015-100
Sodium DL-lactate	Sigma-Aldrich	71720-5G
Sodium pyruvate	Sigma-Aldrich	P4562-5G
SureBond-XF	Axol	ax0053
SYBR® Safe DNA gel stain	Invitrogen	S33102
T4 DNA Ligase	New England BioLabs	M0202
Technisolv®	VWR Chemicals	83811.360
TEMED	Fisher Scientific	BP150-100
TransBlot® Turbo™ Mini-size nitrocellulose	BioRad	1704156
TransBlot® Turbo™ Mini-size transfer stacks	BioRad	1704158
Transforming Growth Factor-β1 human (TGFβ)	Sigma-Aldrich	T7039-2UG
Trifluoroacetic acid (TFA)	Sigma-Aldrich	76-05-1
TRIS, 0.5M buffer soln., pH 7.8	Fisher Scientific	77-86-1
Tris-Base	Sigma-Aldrich	77-86-1
TRIS-HCL 1.5M PH 8.8	Fisher Scientific	50-843-294
Triton™ X-100 solution	Sigma-Aldrich	93443-100ML
TrypLE Express, minus phenol red	Gibco	12604021
Trypsin/Lys-C Mix, Mass Spec Grade	Promega	V5071
TWEEN®20	Sigma-Aldrich	P1379-100ML

ViaFect™ Transfection Reagent	Promega	E4983
Vitronectin (VTN-N) Recombinant Human Protein, Truncated	Gibco	A14700
XhoI	New England BioLabs	R0146S
Y-27632 dihydrochloride (ROCK inhibitor)	MedChemExpress	HY-10583
Antibodies		
Anti-Alpha-Smooth Muscle Actin primary antibody	Invitrogen	14-9760-82
Anti-Ki67 primary antibody	Abcam	ab15580
Anti-Plakophilin 2/PKP2 primary antibody	Abcam	ab223757
Anti-Sarcomeric Alpha Actinin primary antibody	Abcam	ab9465
APC anti-human CD16 Antibody	BioLegend	302012
Donkey anti-Mouse IgG (H+L) Highly Cross-Adsorbed Secondary Antibody, Alexa Fluor™ 647	Invitrogen	A-31571
FITC anti-human CD14 Antibody	BioLegend	367116
Goat anti-Mouse IgG (H+L) Cross-Adsorbed Secondary Antibody, Alexa Fluor™ 488	Invitrogen	A-11001
Goat anti-Mouse IgG (H+L), Superclonal™ Recombinant Secondary Antibody, HRP	Invitrogen	A28177
Goat Anti-Rabbit IgG H&L Secondary antibody (Alexa Fluor® 594)	Abcam	ab150080
PKP1 Monoclonal Primary antibody	Invitrogen	10B2

All primers were obtained from Sigma-Aldrich (St. Louis, Missouri, United States) in powder-form and made up to 100uM using nuclease-free water. Primers were used at a working concentration of 10uM unless stated otherwise. Sequences are shown in Table 3-2.

Table 3-2. Primer Sequences

Gene	Forward Primer	Reverse Primer
Primers used in RT-qPCR (5'3')-		
GAPDH	GTCTCCTCTGACTTCAACAG CG	ACCACC CT GTTGCTGTA G CCAA
18S	ATCGGGGATTGCAATTATTC	CTCACTAAACCATCCAATCG
Nanog	GGA CAC TGGCT GAATCCTTCC	CTCGCTGATTAGGCTCCAACC
GATA4	TCAAACCAGAAA ACGGAAGC	GCATCTCTTCACTGCTGCTG
NKX-25	G AGCTGCGCGCAGAGC	CAGCGCGCACAGCTCTT
TTN	GTAAAAAGAGCTGCCCCAG TGA	GCTAGGTGGCCCAGTGCTACT
TTN-N2BA	GCCACAGTAACTGTGACAG AGG	GGCTGCCTTACCCACAAAAG
PPARa	CGTCCTGGCCTTCTAAACG TA	AGATATCGTCCGGGTGGTTG
PPARy	CGCCCAGGTTTGCTGAATG T	CTCAGGGTGGTTCAGCTTCA
PPARd	GCCCAGTACCTCTTCCCCA A	TTTCGGTCTTCTTGATCCGCT
Ki67	TCCTTTGGTGGGCACCTAA AGACCTG	TGATGGTTGAGGTCGTTCCTTGATG
LDHA	GGATCTCCAACATGGCAGC CTT	AGACGGCTTTCTCCCTCTTGCT
ACLY	GCTCTGCCTATGACAGCAC CAT	GTCCGATGATGGTCACTCCCTT
TNNI1	AGTCACCAAGAACATCACG GAGAT	GCAGCGCCTGCATCATG
COL1A1	TCTGCGACAACGGCAAGGT G	GACGCCGGTGGTTTCTTGGT
Agrin	CATGGCTGTGTTCTTCATGT GTT	GGTCATTCTGAGACAAGGACGACT
TBX20	CGTCCCTGTGGACAACAAG A	GACCCTCGATTTGGGGTTGT
aSMA / ACTA2	CCAGAGCCATTGTCACACA C	CAGCCAAGCACTGTCAGG
Caspase 3	GAGCTGCCTGTAACTTG	ACCTTTAGAACATTTCCACT
Cyclin D2	GTTCCTGGCCTCCAAACTC A	CTTGATGGAGTTGTCGGTGTAAAT
SNORD116-1	TGGATCGATGATGAGTCC	TGGACCTCAGTTCCGATGAGA
SNORD116-23	TGGATCGATGATGACCTCA ATACATG	TGGACCTCAGTTTGACGAGGACGA CG
SNORD116-24	TGGATCGATGATGACTTTTA TACATG	GGACCTCAGTTCAACGAAGATGAC GG
SNORD116-25	GATGATGACTTTAAAATGGA TCTCAT	CAGCTCACAGAAGTGGCACAGAAG TG
SNORD116-29	ATGATGACTTAAAAAAATGG AAACCTTG	ACAGAAGTGTCTTGGTCACTCATTT T
RYR2	TTGTTATGGCTCAGCTGTTT G	GCCTGGATGACAGTGTGAGA
ACTC1	CCAGCCCTCCTTCATTGGT	GGTGCCTCCAGATAAGACATTGTT
MYH6	TCAGCTGGAGGCCAAAGTA AAGGA	TTCTTGAGCTCTGAGCACTCGTCT
MYH7	CCATTGGGGACCGCAGCAA GA	GCGGATTTGCCCAGGTGGTTG
HK2	GAGTTTGACCTGGATGTGG TTGC	CCTCCATGTAGCAGGCATTGCT

COX1	TCCTTATTCGAGCCGAGCTG	GGGCTGTGACGATAACGTTG
PGC1a	AGGCTAGTCCTTCCTCCATGC	GTTGGCTGGTGCCAGTAAGAG
BAX	TGGCAGCTGACATGTTTTCTGAC	TCACCCAACCACCCTGGTCTT
BCL2	CGGAGGCTGGGATGCCTTTG	TTTGGGGCAGGCATGTTGAC
TNFa	AGGCAGTCAGATCATCTTC	TTATCTCTCAGCTCCACG
PTX3	AGAGAGAGTTGAGACCAATC	AAACAATTGTCCCTCTGTTC
PKP1	GAAACAACAACTATGACTGCC	TAGCATCTTTCTTGCTCTTG
PKP2	GTAAAAGAGCAA TACCAGGAC	CTAAGGATGCTTCTTGTGTG
PKP3	AGATCTTCTACAACGCCAC	CTCTTGTCCTCGCATTTG
PKP4	CCCATCAATAGACAGCATTC	CCTCCATCTTCACTTTGTTG
Primers used in Plasmid Design (5'-3')		
SNORD116 Left HA	TCGCGAGTCGACACCCCAGGGAGGGACACACA	TCGCGATTAATTAAAGCACGTGGGGCAGAGGAAT
SNORD116 Right HA	TCGCGAGCGGCCGCGTTATCTGGGACATGACAGT	TCGCGACTCGAGTCCTGATAAGAAGTTATGAG
SNORD116 Upstream Guide	ACCGACGTGCTGAATGAGAGTGG	AAACCCACTCTCATTCAGCACGT
SNORD116 Downstream Guide	ACCGGAGCCATCCATAAGTTATCT	AAACAGATAACTTATGGATGGCTC
SNORD116-23 Overexpression Insert	TCGCGAGGTACCTGGATCGATGATGACCTCAATACATGCATTCCTTGGAAAGCTGAACAAAATGAGTGAAAACTCTATACCG	TCGCGACTCGAGTGGACCTCAGTTTGACGAGGACGACGGTATAGAGTTTTCACTCATTTTGTTCAGCTTTCCAAGGAATGCA
Cassette Primer Pair	TAAGGCAGGTCACGCAGTCAG	ATGTAGCCATTGCCGTCCTT
M13	ACTGGCCGTCGTTTTAC	CAGGAAACAGCTATGAC
SNORD116 5' Screening Primer Pair 1	TGTTCTTGAGCTGTCCGGTT	CGCTCACCTGTGGGAGTAAC
SNORD116 5' Screening Primer Pair 2	CCAGGAGTGGTGGCTGTTAG	CGCTCACCTGTGGGAGTAAC
SNORD116 5' Screening Primer Pair 3	ACTGTCTCTGGGCTTGATGC	TCACGCAGCCACAGAAAAGA
SNORD116 5' Screening Primer Pair 4	TGTGTCCTGTCTGCTTGGTC	TAGGGGGCGTACTTGGCATA
SNORD116 3' Screening Primer Pair 1	CGCAACCTCCCCTTCTACGA	CACCGCATACCCCTTAGTCG
SNORD116 3' Screening Primer Pair 1	AAATGGCTCTCCTCAAGCGT	CCCGGTGAACATCCCATTCA
SNORD116 Arm-spanning primer pair	TGTTCTTGAGCTGTCCGGTT	CACCGCATACCCCTTAGTCG

3.2 Cell Culture

All cell/tissue culture and incubation were carried out under normal atmospheric pressure. Cells were incubated at 37°C, 5% CO_2 and 20% O_2 (unless stated otherwise) in the HERACELL 150i CO2 incubator (Thermo Fisher Scientific, Waltham, Massachusetts, United States). All tissue culture was carried out in the Scanlaf Mars Safety class 2 MBSC4C safety cabinet (Labogene, Allerød, Denmark).

3.2.1 Human iPSC culture

IPSCs were cultured on vitronectin (VTN)-coated plastic in Essential 8™ (E8) media. VTN was obtained from Gibco (Waltham, Massachusetts, United States) and diluted to 1% in phosphate buffered saline solution (PBS). Table 3-3 shows the volume of VTN-PBS used to coat each type of culture surface. All culture surfaces were coated under 1% VTN-PBS for 1 hour at room temperature.

Table 3-3. Volumes of VTN used to coat various culture surfaces

Culture Surface	Surface Area	Volume of VTN
T25 flask	25 cm^2	4mL
6-well	10 cm^2	2 mL
24-well	2 cm^2	0.5mL
96-well	0.3 cm^2	0.05 mL

IPSCs were cultured in Essential 8™ (E8) media (Gibco, Waltham, Massachusetts, United States). E8 media was comprised of 1X E8 supplement made up in in E8 basal media (Gibco, Waltham, Massachusetts, United States).

Table 3-4 shows the volume of media that was used to feed cells in various culture surfaces.

Table 3-4. Volumes of media used to feed cells in various culture surfaces

Culture Surface	Surface Area	Volume of media
T25 flask	25 cm^2	4mL
6-well	10 cm^2	2 mL
24-well	2 cm^2	0.5mL
96-well	0.3 cm^2	0.1 mL

For long-term storage and preservation, iPSCs were stored in 1.8mL cryogenic tubes as 1mL aliquots of 1 million cells per aliquot in a suspension composed of 50% E8 media, 30% Fetal Bovine Serum (FBS) (Gibco, Waltham, Massachusetts, United States) and 20% Dimethyl sulfoxide (DMSO) (Thermo Fisher Scientific, Waltham. Massachusetts, United States).

To thaw iPSCs, frozen cryovials were placed in a Grant Sub 6 unstirred water bath (Grant Instruments Ltd, Cambridge, United Kingdom) at 37^{O}C for 60 seconds. The cell solution was transferred to a 10% FBS in PBS solution and spun in an Eppendorf Centrifuge 5804 (Eppendorf, Hamburg, Germany) at 160 rcf for 4 minutes. The supernatant was removed and the cells were resuspended in pre-warmed E8 media supplemented with 10uM Y-27632 dihydrochloride (ROCK inhibitor) (MedChemExpress, New Jersey, United States). ROCK inhibitor was made up into a 10mM stock solution in sterilised water and stored at -80^{o}C.

IPSC media was changed every 24 hours and the cells were grown to 80% confluence before passaging. To passage iPSCs, the media was

removed and the cells were washed with PBS. To dissociate the cells, 0.2mL/cm^2 TrypLE Express (Gibco, Waltham, Massachusetts, United States) was added to the cells which were then incubated at 37^{o}C for 2-5 mins. The cells were suspended in PBS and counted using the Neubauer-improved counting chamber haemocytometer (Marienfeld Superior, Lauda-Königshofen, Germany). Then the cells were spun down in an Eppendorf Centrifuge 5804 at 160 rcf for 4 minutes. The supernatant was removed and the cell pellet was resuspended in pre-warmed E8 media supplemented with 10uM Y-27632 dihydrochloride (ROCK inhibitor) (MedChemExpress, New Jersey, United States). An aliquot of cells corresponding to 1/10th of the cell suspension was transferred to a new culture surface pre-coated with VTN as described previously.

3.2.2 IPSC-CM differentiation and culture

IPSCs were differentiated into cardiomyocytes using a protocol developed and kindly shared by Andreia Bernardo (Francis Crick Institute/ Imperial College London) (Dark *et al*. manuscript in preparation, patent submission WO2020245612). IPSCs were passaged twice after thawing as described previously and seeded onto a Matrigel (Mt)-coated surface at a seeding density of 20,000 cells/cm^2. Matrigel was obtained from Corning Incorporated (New York, United States). Matrigel was thawed overnight at 4^{o}C and aliquoted into 250mL aliquots that were stored at -80^{O}C. To coat a surface, Matrigel was diluted to a 1% solution in sterile PBS and added to the culture surface in the same surface-to-volume ratios used for VTN (see Table 3-3). The surface was incubated at room temperature for 1 hour before a wash with PBS.

The media was changed 24 and 48 hours after seeding. 72 hours after seeding, the differentiation protocol was initiated. The cells were fed with a media comprised of RPMI 1640 (Gibco, Waltham, Massachusetts,

United States) supplemented with 1X B27™ minus insulin (Gibco, Waltham, Massachusetts, United States), 2uM CHIR-99021 (CHIR) (Selleck Chemicals, Houston, Texas, United States), 5 ng/mL BMP4 (R&D Systems, Minneapolis, Minnesota, United States), 5 ng/mL FGF2 (R&D Systems, Minneapolis, Minnesota, United States), 5 ng/mL Activin A (R&D Systems, Minneapolis, Minnesota, United States) and 100nM AGN (Santa Cruz Biotechnology, Dallas, Texas, United States). After 24 hours the media was changed for RPMI 1640 supplemented with 1X B27™ minus insulin and 100nM AGN. After 24 hours the media was changed for RPMI 1640 supplemented with 1X B27™ minus insulin, 100nM AGN, 65 ug/mL ascorbic acid (Sigma-Aldrich, St. Louis, Missouri, United States) and 1uM IWR (Sigma-Aldrich, St. Louis, Missouri, United States). After 48 hours, the media was changed for RPMI 1640 supplemented with 1X B27™ minus insulin, 100nM AGN and 65 ug/mL ascorbic acid. After 48 hours the media was changed for fresh media of the same composition. After 48 hours the media was changed for RPMI 1640 supplemented with 1X B27™ minus vitamin A, 100nM AGN and 65 ug/mL ascorbic acid. After 48 hours the media was changed for RPMI 1640 minus glucose supplemented with 1X B27™ minus vitamin A, 100nM AGN, 65 ug/mL ascorbic acid and 4mM lactate (Sigma-Aldrich, St. Louis, Missouri, United States). After 48 hours the media was changed for fresh media of the same composition. After 48 hours the media was changed for RPMI 1640 supplemented with 1X B27™ minus vitamin A, 100nM AGN and 65 ug/mL ascorbic acid.

The following day (15 days after initiation of the differentiation protocol), the iPSC-CMs were dissociated using collagenase. Collagenase Type 2 was obtained from Worthington Biochem (Lakewood New Jersey, United States) and made up at 200 units per mL in HBSS (Gibco, Waltham. Massachusetts, United States). IPSC-CMs were washed twice in HBSS and collagenase was added to the cells at 0.1mL/cm^2. The cells were incubated for 2-4 hours at 37^{o}C. The dissociated cells were transferred into a suspension of 10% FBS in PBS and spun down in an Eppendorf

Centrifuge 5804 at 100 rcf for 15 minutes. The supernatant was discarded and the cells were resuspended in RPMI 1640 media supplemented with 1X B27™ and 10% FBS. The iPSC-CMs were plated onto a VTN-coated surface at a density of 150,000-250,000 cells/cm^2 or a split ratio of 1:2. After 24 hours the media was changed for RPMI 1640 media supplemented with 1X B27™ (referred to as RPMI/B27 media).

For maturation in a fatty acid-based media, iPSC-CMs were cultured in a media called GFAM using a recipe from Correia *et al.*, (2017) (300) comprised of glucose-free RPMI/B27 supplemented with, 10mM galactose (Sigma-Aldrich, St. Louis, Missouri, United States), 100uM oleic acid in BSA (Sigma-Aldrich, St. Louis, Missouri, United States), and 50uM Palmitic acid in BSA (Sigma-Aldrich, St. Louis, Missouri, United States). Oleic acid was initially reconstituted in DMSO to make a 1M stock solution. A 5uL aliquot of this stock was added to 45uL of 7.5% BSA (Sigma-Aldrich, St. Louis, Missouri, United States). The resulting 50uL solution was then added to 50mL to make the fatty acid media. Palmitic acid was initially reconstituted in DMSO to make a 0.1M stock solution. A 25uL aliquot of this stock was added to 225uL of 7.5% BSA. The resulting 250uL solution was then added to make the fatty acid media.

For culture in high glucose media, iPSC-CMs were cultured in a media using a recipe from Ng *et al.,* (2018) (302) composed of glucose-free RPMI/B27 supplemented with 22mM glucose (Sigma-Aldrich, St. Louis, Missouri, United States). A 1M stock of glucose was made up by dissolving 3.6g D-(+)-Glucose powder in 25mL sterile water.

3.2.3 IPSC-CF differentiation and culture

IPSCs were differentiated into cardiac fibroblasts using a method based on the protocol developed by Zhang *et al* (313). IPSCs were passaged as described previously and seeded at a density of 20,000 cells/cm^2 into a

Mt-coated 6-well plate. After 48 hours, the media was changed for RPMI 1640 supplemented 1X B27™ minus insulin and 2uM CHIR (Selleck Chemicals, Houston, Texas, United States). After 48 hours the media was changed for RPMI 1640 supplemented 1X B27™ minus insulin and 2uM IWR. After 48 hours the media was changed for RPMI 1640 supplemented 1X B27™ minus insulin. After 24 hours, the media was removed and the cells were washed with 0.5ml/cm^2 PBS. To dissociate the cells, 0.2mL/cm^2 TrypLE Express (Gibco, Waltham, Massachusetts, United States) was added to the cells which were then incubated at 37°C for 5-15 mins. The dissociated cells were suspended in PBS and spun down in an Eppendorf Centrifuge 5804 at 200 rcf for 5 minutes. The supernatant was discarded and the cell pellet was resuspended in a media composed of advanced DMEM (Gibco, Waltham, Massachusetts, United States) supplemented with 2uM CHIR and 2uM retinoic acid (Alfa Aesar, Ward Hill, Massachusetts, United States). The cells were seeded in a split ratio of 1:4. For the following three days the media was changed every day for fresh media of the same composition. On the fourth day the media was changed for advanced DMEM. This media was changed every day for three days. Thirteen days after initiation of the differentiation, the cells were passaged once again in the same manner as described previously. The cells were re-seeded in a split ratio of 1:4 in a media composed of advanced DMEM supplemented with 10% FBS, 1% penicillin streptomycin (pen strep) (Gibco, Waltham, Massachusetts, United States), 1% GlutaMAX™-100X (Gibco, Waltham, Massachusetts, United States), 10ng/mL FGF2 and 10uM SB431542 (Tocris, Bristol, United Kingdom). The media was changed for new media of the same composition every day for the following five days. From the 18th day onwards, the cardiac fibroblasts were maintained in a media composed of advanced DMEM supplemented with 10% FBS. 1% pen strep and 1% GlutaMAX™-100X. This media is referred to as fibroblast media. Media was typically changed every 2-3 days.

In order to induce activatory conditions, iPSC-CFs were cultured in serum-free media and TGFβ-supplemented media. Serum-free media was composed of advanced DMEM supplemented with 1% pen strep and 1% GlutaMAX™-100X. TGFβ-supplemented media was composed of advanced DMEM supplemented with 1% pen strep, 1% GlutaMAX™-100X and 10ng/uL TGFβ (Sigma-Aldrich, St. Louis, Missouri, United States). A 10ug/uL stock of TGFβ was made up in sterile water.

3.2.4 Neural cell differentiation and culture

Human iPSC-Derived Neural Stem Cells (NSCs) were obtained from Axol (Cambridge, United Kingdom) (product code ax0015). The NSCs were thawed as described previously in 3.2.1 into a T25 flask pre-coated with 1% Matrigel. The NSCs were thawed into a media composed of Neural Maintenance Basal Media (Axol, Cambridge, United Kingdom) supplemented with 1.5% Neural Maintenance Medium Supplement (Axol, Cambridge, United Kingdom), 4ug/mL FGF2 (R&D Systems, Minneapolis Minnesota, United States), 1 % pen strep (Gibco, Waltham, Massachusetts, United States), and 0.1% ROCK inhibitor (MedChemExpress, New Jersey, United States). The day after thawing, the media was changed once every 24 hours for four days. The culture media was composed of Neural Maintenance Basal Media supplemented with 1.5% Neural Maintenance Medium Supplement, 4ug/mL FGF2, and 1% pen strep to allow the cells to reach confluence. On the 5th day, the cells were dissociated with TripLE and seeded into a 24-well plate coated with SureBond-XF (Axol, Cambridge, United Kingdom) at a density of 188,000 cells per 24-well. To coat the plate with SureBond-XF, the SureBond-XF stock solution was diluted 1 in 200 in DPBS (Gibco, Waltham, Massachusetts, United States) and used to coat the surface with 200 uL/cm^2. The plate was incubated for 4 hours at 37^{o}C followed immediately by cell seeding.

3.2.5 Hypoxic cell culture

To culture cells in hypoxic conditions, media was pre-conditioned for 24-hours in hypoxic conditions. To achieve hypoxic conditions, a HERACELL 150i CO2 incubator (Thermo Scientific, Waltham, Massachusetts, United States) was used with the temperature set to 37°C, CO_2 was set to 5% and O_2 was set to 2%.

3.2.6 Doxorubicin treatment

A 10mM stock of doxorubicin (Sigma-Aldrich, St. Louis, Missouri, United States) was made up my dissolving 5.8mg doxorubicin hydrochloride in 1mL sterile water. Aliquots of 50uL of this stock was stored at -20°C. The appropriate volume of this stock was added to the media used to feed cells for treatment with doxorubicin. Aliquots were not re-frozen once thawed.

3.2.7 Isoprenaline treatment

A 10mM stock of isoprenaline (Sigma-Aldrich, St. Louis, Missouri, United States) was made up my dissolving 2.5mg isoprenaline in 1mL sterile water. Aliquots of 50uL of this stock was stored at -20°C. The appropriate volume of this stock was added to the media used to feed cells for treatment with isoprenaline. Aliquots were not re-frozen once thawed.

3.3 Transfection of cells

3.3.1 Transfection of iPSC-CMs

IPSC-CMs were transfected according to methods adapted from Bodbin *et al.,* 2020 (351). IPSC-CMs were dissociated using collagenase and re-

plated as described previously in 3.2.2. After 24 hours following dissociation, the media was changed for media composed of RPMI/B27 supplemented with 10% FBS. The following day, the cells were transfected. The total volume of transfection solution came to 30uL/cm^2. The transfection solution made up 10% of the total media given to the cells. The other 90% was composed of RPMI/B27 supplemented with 10% FBS. On the day of transfection, the cells were fed with 270uL/cm^2 of RPMI/B27+10% FBS, onto which the transfection solution was added. To make the transfection solution, 300ng/cm^2 of plasmid was combined with ViaFect™ (Promega, Madison, Wisconsin, United States) in a 6:1 ratio of ViaFect™ volume (in uL) to plasmid mass (in ug). The solution was incubated at room temperature for 5 minutes. Opti-MEM (Gibco, Waltham, Massachusetts, United States) was then added to the solution to make it up to 30uL/cm^2 and incubated at room temperature for 15 minutes. After incubation, the transfection solution was added to the cells which were then incubated at 37^{o}C for 24 hours. The following day, the media was changed for RPMI/B27. The cells were typically analysed 72 hours post-transfection. Cells were transfected with an empty control plasmid with no gene expression to provide a transfection control. Cells were transfected with a GFP-expressing plasmid to estimate transfection efficiency.

3.3.2 Transfection of iPSC-CFs

IPSC-CFs were transfected using the same method that was used to transfect iPSC-CMs. IPSC-CFs were dissociated using Gentle Cell Dissociation Buffer (Gibco, Waltham, Massachusetts, United States) as described previously in 3.2.3. The cells were seeded in fibroblast media. The following day, the cells were transfected. The total volume of transfection solution came to 30uL/cm^2. The transfection solution made up 10% of the total media given to the cells. The other 90% was composed of RPMI/B27 supplemented with 10% FBS. On the day of transfection, the cells were fed with 270uL/cm^2 of RPMI/B27+10% FBS,

onto which the transfection solution was added. To make the transfection solution, 300ng/cm^2 of plasmid was combined with ViaFect™ in a 6:1 ratio of ViaFect™ volume (in uL) to plasmid mass (in ug). The solution was incubated at room temperature for 5 minutes. Opti-MEM was then added to the solution to make it up to 30uL/cm^2 and incubated at room temperature for 15 minutes. After incubation, the transfection solution was added to the cells which were then incubated at 37°C for 24 hours. The following day, the media was changed for fibroblast media. The cells were typically analysed 72 hours post-transfection.

3.3.3 Transfection of neural progenitor cells

NSCs were seeded into a SureBond-XF-coated plate at a density of 94,000 cells/cm^2 as described previously in 3.2.4. The following day the cells were transfected. On the day of transfection, the cells were fed with 270uL/cm^2 of media that was composed of Neural Maintenance Basal Media supplemented with 1.5% Neural Maintenance Medium Supplement, 1 % pen strep, 2% NeurOne Supplement A (Axol, Cambridge, United Kingdom) and 10% FBS. onto which the transfection solution was added. To make the transfection solution, 300ng/cm^2 of plasmid was combined with ViaFect™ in a 6:1 ratio of ViaFect™ volume (in uL) to plasmid mass (in ug). The solution was incubated at room temperature for 5 minutes. Opti-MEM was then added to the solution to make it up to 30uL/cm^2 and incubated at room temperature for 15 minutes. After incubation, the transfection solution was added to the cells which were then incubated at 37°C for 24 hours. After 24 hours, the media was changed for 250uL/cm^2 of media composed of Neural Maintenance Basal Media supplemented with 1.5% Neural Maintenance Medium Supplement, 1 % pen strep and 2% NeurOne Supplement A. The cells were analysed after 72 hours.

3.3.4 Transfection of hiPSCs

IPSCs were dissociated as described previously in 3.2.1. Dissociated iPSCs were counted and 1 million cells per sample were transfected. Transfection of stem cells was carried out using the P3 Primary Cell 4D-Nucleofector® X Kit L (Lonza, Basel, Switzerland) in the Amaxa™ 4D-Nucleofector™ (Lonza, Basel, Switzerland). The plasmid solution was composed of 1000ng of plasmid per sample. The P3 solution was composed of 85% P3 buffer (Lonza, Basel, Switzerland) and 15% P3 supplement (Lonza, Basel, Switzerland). 1 million iPSCs were resuspended in 100uL P3 solution. The cell solution was added to the plasmid solution and gently mixed using a pipette. The cell solution was then transferred to a Nucleofector® cuvette (Lonza, Basel, Switzerland). The cuvette was placed into the Amaxa™ 4D-Nucleofector™ and tranfected using program number CA-137. The cuvette was then incubated for 5 minutes at 37^{o}C. After incubation the cells were resuspended in E8 media supplemented with 0.1% ROCK inhibitor and transferred to a Matrigel pre-coated plate at a density of 50,000-250,000 cells/cm^{2}.

3.4 Cell viability

Cell viability was analysed using CellTiter-Glo® 2.0 (Promega, Madison, Wisconsin, United States). The cells were washed with 300uL/cm^{2} DMEM (Gibco, Waltham, Massachusetts, United States). The cells were incubated at room temperature for 30 minutes in 150uL/cm^{2} DMEM. Meanwhile, the CellTiter-Glo® 2.0 was also incubated at room temperature for 30 minutes. After incubation, 150uL/cm^{2} of CellTiter-Glo® 2.0 was added to the cells which were then protected from light using foil. The cells were incubated at 37^{o}C on a shaker for two minutes. The cell solution was then transferred to a white 96-well assay plate

(Corning, New York, United States) and incubated at room temperature for 10 minutes while protected from light. The luminescence was measured using the FLUOstar OPTIMA microplate reader (BMG Labtech, Ortenburg, Germany).

3.5 Substrate metabolism analysis

For iPSC-CMs, substrate usage was analysed using the Biolog MitoPlate assay (Biolog, Hayward California, United States) (352). The wells of the MitoPlate S-1 plate (Biolog, Hayward California, United States) were hydrated in 30uL assay mix composed of sterile water supplemented with 2X Biolog MAS (Biolog, Hayward California, United States), 6X Redox Dye MC (Biolog, Hayward California, United States) and 1,200ug/mL saponin, (Sigma-Aldrich, St. Louis, Missouri, United States). The plates were incubated for 1 hour at 37^{o}C. The cells were suspended in a cell solution of 2 x 10^{6} cells/mL in 30uL of MAS buffer. The cells were pipetted into each well of the MitoPlate. The MitoPlate was read for 6 h with 5 min intervals at OD590 using a OmniLog plate reader (Biolog, Hayward California, United States). Results were calculated using the OmniLog Data Analysis 1.7 software before being exported to Microsoft Excel.

The Biolog MitoPlate assay was adapted for use with iPSC-CFs in the absence of the MitoPlate S-1 plates. Instead, a standard 96-well plate (Corning, New York, United States) was used. The iPSC-CFs were seeded into the plate at a density of 20,000 cells per well as described previously in 3.2.3. On the day of analysis, the cells were fed assay media that was composed of sterile water supplemented with 1X Biolog MAS (Biolog, Hayward California, United States), 3X Redox Dye MC (Biolog, Hayward California, United States), 600 ug/mL saponin, (Sigma-Aldrich, St. Louis, Missouri, United States), and a metabolic substrate. The concentration of substrate was 100mM for all substrates tested except oleic acid, which was 0.1mM. The MitoPlate was read for 6 h with 5 min intervals at OD590

using a OmniLog plate reader (Biolog, Hayward California, United States). Results were calculated using the OmniLog Data Analysis 1.7 software before being exported to Microsoft Excel.

3.6 Seahorse analysis

The OCR and ECAR of hiPSC-CMs was analysed using the XF Cell Mito Stress Kit on the Seahorse XF Analyser (Agilent Technologies, Santa Clara, California, USA). This was carried out with the help of Katherine Hampton, MSc. IPSC-CMs were seeded at a density of 30,000 cells per well of a VTN-coated 96-well Seahorse XF Cell Culture Microplate (Agilent Technologies, Santa Clara, California, USA) and transfected as previously described in 3.3.1. The cells were analysed 72-hours post-transfection. In preparation for the assay, XF flux cartridges (Agilent Technologies, Santa Clara, California, USA) were hydrated with XF Calibrant (Agilent Technologies, Santa Clara, California, USA) overnight at 37°C. Flux cartridges were loaded with Oligomycin (2 µM), carbonyl cyanide-4-(trifluoromethoxy) phenylhydrazone (FCCP) (1 µM), and Rotenone (0.5 µM) (all from Agilent Technologies, Santa Clara, California, USA). The assay was performed in Seahorse XF Media (Agilent Technologies, Santa Clara, California, USA), which is supplemented with 1 mM Sodium pyruvate, 2 mM l-Glutamine, and 10 mM Glucose. Following the seahorse assay, the Seahorse plate was washed with PBS and fixed at room temperature in 4% formaldehyde solution (Sigma-Aldrich, St. Louis, Missouri, United States) for 10 min, then stained with 1ug/mL DAPI (Thermo Fisher Scientific, Waltham, Massachusetts, United States) for 15 min. Cell count was calculated using automated nuclei counting on the EVOS M5000 imaging system (Thermo Fisher Scientific, Waltham, Massachusetts, United States). All results were normalised to output cell count.

3.7 Exosome analysis

3.7.1 Exosome isolation

Exosomes were isolated from cell culture media using the Exo-spin™ exosome isolation kit (Cell Guidance Systems, Cambridge, United Kingdom). 12mL of media was harvested from iPSC-CMs and spun at 300 x g for 10 minutes in the Eppendorf 5810R benchtop centrifuge (Eppendorf, Hamburg, Germany). The supernatant was transferred to multiple 1.5mL microcentrifuge tubes (Starlab, Brussels, Belgium) and spun at 16,000 x g for 30 minutes in the Eppendorf 5424R benchtop microcentrifuge (Eppendorf, Hamburg, Germany). The supernatant was collected and Exo-spin™ Buffer (Cell Guidance Systems, Cambridge, United Kingdom) was added in a 2:1 ratio of buffer to sample. The solution was mixed by inverting and the sample was incubated at 4°C overnight. After incubation, the solution was spun at 16,000 x g for 1 hour to pellet the exosomes. The supernatant was aspirated and the exosome pellet was resuspended in 100uL PBS. 15 minutes before use, the Exo-spin™ column was equilibrated by adding 250uL PBS and centrifuging at 50 x g for 10 seconds. This was performed twice for each column. After equilibration, the columns were loaded with the 100uL exosome suspension and centrifuged at 50 x g for 60 seconds. The exosomes were eluted into a sterile microcentrifuge tube by applying 200uL PBS to the column and spinning at 50 x g for 60 seconds. Exosomes were stored at -80°C before analysis. According to the product brochure (Cell Guidance Systems, Cambridge, United Kingdom), particles of a diameter range of 30nm – 300nm are isolated using this protocol.

3.7.2 Exoview analysis

Exosomes were transported on dry ice for analysis on the Exoview™ R100 and all subsequent sample handling and analysis was performed by the team at Nanoview Biosciences (Brighton, Massachusetts, United States).

The following methods were adapted from the manufacturer's instructions and from Breitwieser *et al.,* (2022) (353). The Exoview™ R100 is an automated imaging platform that uses a multiplexed array to capture, quantify and characterise extracellular vesicles. The Exoview™ human tetraspanin cargo kit (Nanoview Biosciences, Brighton, Massachusetts, United States) contains microarray chips coated with antibodies against the exosome markers CD9 (HI9a), CD63 (H5C6) and CD81 (JS-81) (353–355). 40uL of sample were loaded onto the chips and incubated overnight at room temperature. Following incubation, the chips were submerged in 1000 µL of solution A (Nanoview Biosciences, Brighton Massachusetts, United States). The chips were then washed three times in 750uL of solution A. The chips were incubated for 5 minutes between each wash. In parallel, the antibody detection mixture was prepared as a twofold concentrate by diluting anti-CD9 (CF®-488-labeled), -CD63 (CF®-647-labeled) and -CD81 (CF®-555-labeled) antibodies 1:500 in blocking buffer (antibody and blocking buffer both from (Nanoview Biosciences, Brighton, Massachusetts, United States). After washing, 250 µL of the antibody mixture were added to the chips and incubated for one hour at room temperature in a light-protected environment. Unbound antibodies were washed out by adding 500 µL of solution A, and three more washes were carried out as described previously. Excess detergent was removed by washing three times with Solution B (Nanoview Biosciences, Brighton, Massachusetts, United States). The chips were washed in Milli-Q water before quantification and analysis in the Exoview™ R100.

3.8 Video capture and contraction analysis

All cells were recorded on the EVOS™ M5000 imaging system (Thermo Fisher Scientific, Waltham, Massachusetts, United States). All cells were recorded at 37°C, 5% CO_2 and 20% O_2 using the EVOS™ Onstage Incubator (Thermo Fisher Scientific, Waltham, Massachusetts, United States). Each well was recorded three times at different locations to gain

three technical replicates. Recordings were taken using the 10x objective in the brightfield channel. Each recording was taken for at least 20 seconds per replicate. The recordings were converted into TIFF image stacks using VideoLAN Client (VLC) media player (Paris, France). The recordings were analysed in ImageJ (356) using the software plugin MUSCLEMOTION (357). MUSCLEMOTION uses pixel movement to detect contraction. Contraction data is plotted as a trace which the software then analyses to provide output data. The extent of the movement of pixels during a contraction event is plotted on the y axis, and the time in milliseconds is plotted on the x-axis. The difference between the baseline and the peak is calculated to give an amplitude value referred to as contraction amplitude. The distance in milliseconds between each peak is converted into Hz (peaks per second) to give contraction frequency. Then the average time between peaks is calculated. The time between each peak is calculated as a percentage of the average time between peaks. Any value that is smaller than 80% or greater than 120% of the average is deemed an outlier and classed as an "arrhythmogenic-like event". The number of arrhythmogenic-like events is calculated as a percentage of the total number of events.

3.9 Immunocytochemistry

3.9.1 Fixing and staining cells

Prior to fixation, cells were washed with 0.25mL/cm^2 PBS. Cells were fixed in 0.1mL/cm^2 4% formaldehyde solution (Sigma-Aldrich, St. Louis, Missouri, United States) for 10 minutes at room temperature. Cells were washed three times for 5 minutes in PBS and permeabilised using 0.1% Triton-X100 (Sigma-Aldrich, St. Louis, Missouri, United States) for 15 minutes at room temperature. Cells were washed three times for 5 minutes in PBS then incubated at room temperature for 1 hour in 4% goat serum blocking solution (Sigma-Aldrich, St. Louis, Missouri, United States). Primary antibodies used are stated in Table 3-1 and were diluted

to 1 in 200 in 4% goat serum. Cells were incubated overnight at 4°C in primary antibody. To obtain a secondary control to evaluate fluorescence due to non-specific binding and background fluorescence, cells were incubated in 4% goat serum without the primary antibody. Afterwards, cells were washed three times for 5 minutes in 0.1% PBS-Tween (Tween-20, Sigma-Aldrich, St. Louis, Missouri, United States). Cells were incubated for 1 hour at room temperature in secondary antibody. Secondary antibodies used are stated in Table 3-1 and were diluted 1 in 1000 in 4% goat serum. Cells were washed three times in 0.1% PBS-Tween. Cells were stained with 1ug/mL DAPI (Thermo Fisher Scientific, Waltham, Massachusetts, United States) in PBS for 15 minutes at room temperature. For cells stained with Orange Cell Mask (OCM) (CellMask™ Orange Plasma membrane Stain, Invitrogen, Waltham, Massachusetts, United States), the stain was added alongside the DAPI stain at a concentration of 5ug/mL. After staining, the cells were washed three times for 5 minutes with 0.1% PBS-Tween and stored under 0.5mL/cm^2 PBS in parafilmed plates wrapped in foil at 4°C before imaging.

3.9.2 Imaging fixed cells

Fixed cells were imaged using the EVOS M5000 imaging system (Thermo Fisher Scientific, Waltham, Massachusetts, United States). The microscope was equipped with light cubes outlined in Table 3-5 and objectives outlined in Table 3-6.

Table 3-5. Light cubes used for imaging on the EVOS M5000 microscope

Light cube	Colour	Excitation (nm)	Emission (nm)	Compatible dyes	Category number
DAPI	Blue	357/44	447/60	DAPI, Hoechst, NucBlue, Alexa Fluor 350, BFP	AMEP4950
GFP	Green	470/22	525/50	GFP, Alexa Fluor 488, Calcein, SYBR Green, FITC, Fluo-4,	AMEP4951

				MitoTracker Green, pHrodo Green	
Texas Red	Red	585/29	628/32	Texas Red, Alexa Fluor 568/594, MitoTracker Red CMXRos, mCherry, pHrodo Red, Cy3.5, CellTracker Red CMTPX	AMEP4955

Table 3-6. Objectives used for imaging on the EVOS M5000 microscope

Objective	Objective type	Category number
4x	Plain fluorite	AMEP4680
10x	Plain fluorite	AMEP4681
20x	Plain fluorite	AMEP4682

All images taken within the same experiment (including any secondary controls) were taken using the same exposure settings. Images were saved as TIFF image files.

3.9.3 Image analysis

Images were processed and analysed using the image analysis softwares ImageJ (356) and CellProfiler (358). To quantify mean fluorescence using CellProfiler, images were split into their individual channels and converted to greyscale. Cells were identified by smoothing and masking the image followed by the module IdentifyPrimaryObjects. The following settings were used to identify cells: 40-400 pixel diameter, global thresholding strategy, manual thresholding method, thresholding smoothing scale of 0. Nuclei were identified using the IdentifyPrimaryObjects module with the following settings: 15-70 pixel diameter, adaptive thresholding strategy, Otsu thresholding method, two-class thresholding, 0 threshold smoothing scale, 1.0 threshold correction factor, 0-1.0 threshold bounds, size 50 adaptive window, identification of clumped objects determined using intensity. Mean intensity was measured using the MeasureObjectIntesity module. Background intensity was measured by

using the module MeasureImageIntensity on images taken of the secondary control. The number of nuclei was counted using the IdentifyPrimaryObjects and MeasureObjectsSizeShape modules. The perinuclear region was determined by outlining the nuclei using the IdentifyPrimaryObjects module followed by expanding the nuclei by 10 pixels using the ExpandOrShrinkObjects module, then masking and removing the nuclei leaving just the expanded region around the nuclei. The intensity of this region was measured using the MeasureObjectIntenstiy module. Results were exported to Excel using the ExportToSpreadsheet module.

3.10 Clinical blood sample analysis

3.10.1 Blood extraction

Patients were consented and their blood collected by Cardiology nurses Emma Hughes and Caroline Hall of the Norfolk and Norwich University Hospital. 6mL of blood was collected into a purple EDTA haematology tube (Beckton Dickinson, Franklin Lakes, New Jersey, United States). Blood was processed within 30 minutes of collection.

3.10.2 Blood processing and separation

Blood was handled in sterile conditions under a vented Scanlaf Mars Safety class 2 MBSC4C safety cabinet (Labogene, Allerød Denmark). Blood was diluted 1:1 with PBS and separated using HISTOPAQUE® (Sigma-Aldrich, St. Louis, Missouri, United States). 8mL of histopaque was used for every 6mL undiluted blood. The diluted blood was pipetted gently onto the histopaque and spun in an Eppendorf Centrifuge 5804 (Eppendorf, Hamburg, Germany) at 400 rcf for 15 minutes with 0 brake and 0 acceleration. This separated the blood into three layers: a top layer of serum, a middle layer of white blood cells and the remaining

components including red blood cells resided in the bottom layer. The serum was collected into 1.8mL cryovials (Thermo Fisher Scientific, Waltham, Massachusetts, United States). The white blood cells were harvested using a transfer pipette (Thermo Fisher Scientific, Waltham, Massachusetts, United States). The isolated white blood cell solution was made up to 50mL in PBS and spun down in an Eppendorf Centrifuge 5804 (Eppendorf, Hamburg, Germany) at 400 rcf for 5 minutes. The supernatant was discarded, and the cell pellet was resuspended in 1mL MACS buffer. MACS buffer was made of PBS supplemented with 0.5% BSA (Sigma-Aldrich, St. Louis, Missouri, United States) and 2mM EDTA (Sigma-Aldrich, St. Louis, Missouri, United States) and filtered using a 22um pore-size syringe driven filter (Sigma-Aldrich, St. Louis, Missouri, United States) before use. 500uL of the white blood cell suspension was collected for cell sorting, the remaining 500uL was fixed using 10mL 4% formaldehyde solution (Sigma-Aldrich, St. Louis, Missouri, United States) at room temperature for 10 minutes. The cells were washed 3 times by spinning at 400 rcf for 5 minutes and resuspending in 20mL PBS before a final resuspension in 10mL MACS buffer. The fixed white blood cells were stored at 4^{o}C before antibody staining and analysis by flow cytometry.

3.10.3 RNA analysis of serum

For whole serum RNA analysis, 200uL of serum was lysed according to the method outlined in 3.11 RNA expression analysis.

The ExoQuick® Exosome Isolation and RNA Purification Kit (for Serum & Plasma) (System Biosciences, Pao Alto, California, United States) was used for the analysis of RNA within serum exosomes. 500uL of serum was centrifuged at 3,000 x g for 15 minutes. The supernatant was transferred to a new tube and 120uL of ExoQuick® (System Biosciences, Pao Alto, California, United States) was added to the serum and mixed through

inversion. The solution was incubated at 4°C overnight, then the precipitated exosomes were pelleted by centrifuging at 1,500 x g for 30 minutes. The supernatant was aspirated, and the exosomes were resuspended in 350uL lysis buffer (System Biosciences, Pao Alto, California, United States). The solution was vortexed for 15 seconds and incubated at room temperature for 5 minutes. 200uL absolute ethanol (Thermo Fischer Scientific, Waltham, Massachusetts, United States) was added and the solution was transferred to a ExoRNA isolation spin column (System Biosciences, Pao Alto, California, United States). The column was centrifuged at 13,000 RPM for 1 minute. The column was washed twice by adding 400uL Wash Buffer (System Biosciences, Pao Alto, California, United States) and centrifuged at 13,000 RPM for 1 minute, followed by a spin at 13,000 RPM for 2 minutes to dry the matrix. To elute the RNA, 30uL nuclease-free water was added to the column and incubated for 4 minutes, followed by centrifuging at 13,000 RPM for 1 minute.

3.10.4 Flow cytometry to characterise cell surface marker expression

Cells were strained using a 70um cell strainer (Corning, New York, United States) and then spun in an Eppendorf Centrifuge 5804 (Eppendorf, Hamburg, Germany) at 400 rcf for 5 minutes. The cell pellet was resuspended in 1mL MACS buffer and separated into four 250uL aliquots. To stain cells for CD14, 1uL CD14-FITC conjugated antibody (Invitrogen, Waltham, Massachusetts, United States) was added to a 250uL cell suspension. To stain for CD16, 1uL CD16-PE conjugated antibody (Invitrogen, Waltham, Massachusetts, United States) was added to a 250uL cell suspension. To dual stain for both CD14 and CD16, 1uL of each antibody was added to 250uL cell suspension. The final 250uL cell suspension was left unstained. After incubation at room temperature for 30 minutes, 250uL MACS buffer was added to each aliquot. The cells were analysed using the CytoFLEX Flow Cytometer (Beckman Coulter, Brea,

California, United States). Analysis was carried out using the CytExpert software (Beckman Coulter, Brea California, United States). Forward and side scatter were used to determine the leucocyte population, and the unstained sample was used to set the gate for background fluorescence.

3.10.5 Cell sorting

$CD14^+$ white blood cells were isolated using Magnetic-Activated Cell Sorting (MACS) technology. A 50uL aliquot of human CD14 MicroBeads (Miltenyi Biotec, Bergisch, Gladbach, Germany) was added to the 500uL white blood cell suspension and incubated at 4°C for 20 minutes. In parallel, the MS column (Miltenyi Biotec, Bergisch, Gladbach, Germany) was loaded into the MiniMACS™ Seperator (Miltenyi Biotec, Bergisch Gladbach, Germany) and equilibrated with 500uL MACS buffer. The white blood cell suspension was added to the column. The column was washed three times with 500uL MACS buffer. To elute the $CD14^+$ cells, the column was removed from the MiniMACS™ separator and eluted using 1mL MACS buffer. The cells were spun into a pellet at 400rcf for 5 minutes in the Eppendorf 5424R benchtop microcentrifuge (Eppendorf, Hamburg, Germany). The supernatant was discarded and the cells were lysed for RNA.

3.11 RNA expression analysis

3.11.1 RNA isolation

For analysis by RT-qPCR, cells were lysed and RNA was extracted using the Macherey-Nagel™ NucleoSpin™ RNA Mini Kit for RNA purification (Macherey-Nagel, Nordrhein-Westfalen, Germany). Cells were washed with 0.25mL/cm^2 PBS and lysed with 350mL LBP (Macherey-Nagel, Nordrhein-Westfalen, Germany). The lysate was transferred to a gDNA removal column (Macherey-Nagel, Nordrhein-Westfalen, Germany) and spun at 11,000 x g for 30 seconds in the Eppendorf 5424R benchtop

microcentrifuge (Eppendorf, Hamburg, Germany). 100uL binding solution (Macherey-Nagel, Nordrhein-Westfalen, Germany) was added to the flow-through, which was then was transferred to an RNA bidning column and spun at 11,000 x g for 15 seconds. The column was washed with 200uL Wash Buffer 1 (Macherey-Nagel, Nordrhein-Westfalen, Germany) and spun at 11,000 x g for 15 seconds. The flow-through was discarded. 650uL of Wash Buffer 2 was added to the column and spun at 11,000 x g for 15 seconds. The flow-through was discarded. The column was spun at 11,000 x g for 2 minutes to dry the matrix. The RNA was eluted by adding 30uL sterile water to the column and incubating at room temperature for 4 minutes before spinning at 11,000 x g for 1 minute.

For analysis by RNA-seq, RNA was isolated using the miRNeasy Micro Kit (Qiagen, Hilden, Germany). Cells were washed with 0.25mL/cm^2 PBS then lysed with 500uL QIAzol Lysis Reagent (Qiagen, Hilden, Germany). 100uL chloroform (Thermo Fisher Scientific, Waltham, Massachusetts, United States) was added to the lysate which was mixed vigorously before incubation at room temperature for 2 minutes. The solution was spun at 12,000 x g at 4^{o}C for 15 minutes using the Eppendorf 5424R benchtop microcentrifuge (Eppendorf, Hamburg, Germany). The upper aqueous phase was transferred to a new collection tube and 525uL ethanol absolute was added (Thermo Fisher Scientific, Waltham, Massachusetts, United States). The solution was mixed and transferred to an RNeasy MinElute spin column in a 2 ml collection tube and spun at 8,000 x g for 15 seconds. The flow-through was discarded. 700uL of RWT buffer (Qiagen, Hilden, Germany) was added to the spin column and spun at 8,000 x g for 15 seconds. The flow through was discarded. 500uL of RPE buffer (Qiagen, Hilden, Germany) was added to the column and spun at 8,000 x g for 15 seconds. The flow-through was discarded. 500uL of 80% ethanol (Thermo Fisher Scientific, Waltham, Massachusetts, United States) was added to the spin column and spun at 8,000 x g for 2 minutes. The flow-through was discarded. The column was then spun at 12,000 x g for 5 minutes to dry the matrix. The RNA was eluted by adding

20uL sterile water to the column and incubating at room temperature for 4 minutes before spinning at 12,000 x g for 1 minute.

The concentration of RNA was quantified using the NanoDrop 2000 Spectrometer (Thermo Fisher Scientific, Waltham, Massachusetts, United States). The machine was cleaned with 5uL nuclease-free water then blanked with 1µl nuclease free water. 1µl of each sample was analysed to measure the RNA concentration and purity. Sample purity was measured using the ratio of absorbance at 260nm to absorbance at 280nm. A 260/280 ratio of 1.7 to 2.3 was considered sufficiently pure. RNA was stored at -80^{o}C.

3.11.2 CDNA synthesis

RNA was reverse transcribed into cDNA using the qPCRBIO cDNA synthesis kit (PCR Biosystems, London, UK). Each 20µl reaction contained 4µl of 5X cDNA Synthesis Mix (PCR Biosystems, London, United Kingdom), 1µl of 20X RTase (PCR Biosystems, London, United Kingdom) and 15uL RNA. Each RNA sample was diluted to an equal concentration with nuclease free water The PCR tubes were placed into a Thermocycler (Bio-Rad, Watford, United Kingdom) and run on a pre-defined program consisting of 1hr at 42ºC, 10 minutes at 85ºC, to denature the RTase, and then a return to 4ºC until the samples were removed and stored at -20ºC until analysis.

3.11.3 Real-time quantitative PCR

Real time quantitative PCR (qPCR) was performed on a Roche LightCycler® 480 (Roche, Basel, Switzerland) using SYBR-green technology. Samples were analysed on 384-well LightCycler® plates (Roche, Basel, Switzerland). Each well contained a 5uL solution composed of 2.5uL SyGreen Mix (PCR Biosystems, London, United

Kingdom), 0.5uL primer mix, 1uL nuclease-free water and 1uL cDNA. Each sample was analysed with three technical replicates. Once all samples were plated, the plate was sealed and centrifuged at 1000 rpm for 1 minute. The plate was placed in a Roche LightCycler® 480 (Roche, Basel, Switzerland) for qPCR and run on a pre-programmed cycle. This program consisted of 2 minutes of pre-amplification at 95°C, followed by 35 amplification cycles of 95°C for 15 seconds, 60°C for 10 seconds and72°C for 10 seconds. To obtain a melt curve, the plate was heated to 95°C for 5 seconds, followed by 65°C for 1 minute, followed by 97°C for 30 seconds. The plate was cooled to 40°C at the end of the program.

3.11.4 Expression fold change

The output from the LightCycler® is the cycle threshold (Ct) value. The Ct value for each gene of interest was normalised to a housekeeping gene. To determine the relative expression of each gene the ΔCt value for a specific gene was quantified by subtracting the average Ct of the housekeeping gene from the average Ct of the gene of interest. The ΔΔCt could then be calculated by subtracting the ΔCt of the test condition from the control condition. The fold change in expression was then determined relative to control by $2^{-\Delta\Delta Ct}$.

3.11.5 RNAseq

RNA was shipped on dry ice to the University of Cambridge. All subsequent analysis was carried out by Harris Papadopoulou and the Bennet group at the University of Cambridge Department of Medicine. All bioinformatic and statistical analysis was carried out by Dr Jonathan Price of the University of Cambridge Department of Medicine using the software R (359). Results were converted to lists of differentially expressed genes alongside their log fold changes and p-value, as well as normalised counts

of mRNA. Any further analysis was carried out by myself using Microsoft Excel (Alburquerque New Mexico, USA).

3.12 Protein expression analysis

3.12.1 Flow cytometry to quantify internal protein fluorescence

To quantify the level of aSMA by flow cytometry, cells were dissociated using TrypLE as previously described. Dissociated cells were resuspended in 1mL PBS and spun at 200 rcf for 5 minutes in an Eppendorf 5424R benchtop microcentrifuge (Eppendorf, Hamburg, Germany). The cell pellet was resuspended in 200uL 4% formaldehyde solution (Sigma-Aldrich, St. Louis, Missouri, United States) and fixed at room temperature for 10 minutes. 800uL PBS was added to the suspension which was then spun at 200 rcf for 5 minutes. The cells were washed twice more using 1mL PBS. The cells were permeabilised by suspending them in 200uL 0.1% Triton-X100 (Sigma-Aldrich, St. Louis, Missouri, United States) for 15 minutes at room temperature. Cells were washed three times for 5 minutes with 1mL 0.5% PBS-Tween (Tween-20, Sigma-Aldrich, St. Louis, Missouri, United States) then incubated at room temperature for 30 minutes in 200uL 4% goat serum blocking solution (Sigma-Aldrich, St. Louis, Missouri, United States). Mouse anti-aSMA primary antibody (Invitrogen, Waltham, Massachusetts, United States) was diluted 1 in 1000 in 4% goat serum. Cells were incubated in primary antibody at 4^{o}C overnight. To obtain a secondary control, cells were incubated in 4% goat serum without primary antibody. The cells were washed three times for 5 minutes with 1mL 0.5% PBS-Tween. The anti-mouse 488-conjugated secondary antibody (Invitrogen, Waltham, Massachusetts, United States) was diluted 1 in 1000 in 4% goat serum. The cells were incubated in secondary antibody at room temperature for 30 minutes. The cells were washed three times for 5 minutes with 1mL 0.5% PBS-Tween and then

resuspended in 500uL MACS buffer. Cells were protected from light and stored at 4°C until analysis.

Protein quantification by flow cytometry was carried out on the CytoFLEX Flow Cytometer (Beckman Coulter, Brea California, United States). Analysis was carried out using the CytExpert software (Beckman Coulter, Brea, California, United States). Forward and side scatter were used to eliminate debris. The secondary control was used to determine background fluorescence and set the gate.

3.12.2 Protein extraction

Cells were lysed using SDS lysis buffer composed of sterile water supplemented with 0.1mM Tris (pH 6.8) (Thermo Fisher Scientific, Waltham, Massachusetts, United States), 2% SDS (Thermo Fisher Scientific, Waltham, Massachusetts, United States), 0.1M DTT (Sigma-Aldrich, St. Louis, Missouri, United States) and 14% glycerol (Thermo Fisher Scientific, Waltham, Massachusetts, United States). Cells were lysed with 0.2mL/cm^2 SDS lysis buffer and stored at -20°C until analysis.

3.12.3 Pierce assay

Protein concentration was determined using the Pierce™ BCA protein assay kit (Thermo Fisher Scientific, Waltham, Massachusetts, United States). 25uL of each sample was pipetted into a well of a 96-well microplate (Corning, New York, United Stated). WR assay mix was made up by mixing 50 parts of BCA Reagent A with 1 part of BCA Reagent B. 200uL of WR was added to the sample. Three technical replicates were performed per sample. The plate was placed on a shaker for 30 seconds and then incubated for 30 minutes at 37°C. Absorbance at 562nm was read using the FLUOstar OPTIMA microplate reader (BMG Labtech, Ortenburg, Germany). A concentration curve based on pre-mixed

albumin standards was used to determine the protein concentration of the sample.

3.12.4 Western blotting

To separate proteins according to size, an 8% acrylamide gel was made by mixing 4.6mL of sterile water with 2.7mL 30% acrylamide mix (Bio-Rad, Watford, United Kingdom), 2.5mL 1.5 M Tris (pH 8.8) (Thermo Fisher Scientific, Waltham, Massachusetts, United States), 100uL 10% SDS (Thermo Fisher Scientific, Waltham, Massachusetts, United States), 100uL 10% ammonium persulfate (Thermo Fisher Scientific, Waltham, Massachusetts, United States, and 6uL TEMMED (Thermo Fisher Scientific, Waltham, Massachusetts, United States). The gel was submerged in western running buffer composed of 250mM Tris-Base (Sigma-Aldrich, St. Louis, Missouri, United States), 2M glycine (Thermo Fisher Scientific, Waltham, Massachusetts, United States) and 1% SDS (Thermo Fisher Scientific, Waltham, Massachusetts, United States). The same amount of protein per sample (up to 15uL) was loaded onto the gel alongside 5uL of Precision Plus Protein™ Standards (Bio-Rad, Watford, United Kingdom). The gel was run at 180V for 30 minutes using the PowerPac™ Basic power supply (Bio-Rad, Watford, United Kingdom). The proteins were transferred onto a nitrocellulose membrane in 1X Bio-Rad transfer buffer (Bio-Rad, Watford, United Kingdom) using the Trans-Blot® Turbo™ System (Bio-Rad, Watford, United Kingdom). The mixed molecular weight 7m program was implemented. For western normalisation, the Revert™ 700 total protein stain was used (LI-COR Biosciences, Lincoln, New England, United States). The membrane was washed twice with 5mL water then incubated for 5 minutes at room temperature in 5mL Revert™ total protein stain (LI-COR Biosciences, Lincoln, New England, United States). The membrane was washed twice with Revert™ total protein wash buffer (LI-COR Biosciences, Lincoln, New England, United States) then imaged using the Odyssey CLx Imaging System (LI-COR Biosciences, Lincoln, New England, United States) in the

700 nm channel. After imaging the membrane was washed in 5mL water then transferred to 10% milk solution (Thermo Fisher Scientific, Waltham, Massachusetts, United States) and blocked for 3 hours at room temperature. The PKP1 primary antibody (Invitrogen, Waltham, Massachusetts, United States) was made up to 2ug/mL in 5mL 10% milk solution. The membrane was incubated overnight at 4^{o}C in the primary antibody solution. The membrane was washed twice for 5 minutes in 5mL 0.1% PBS-Tween (Sigma-Aldrich, St. Louis, Missouri, United States), then left in 0.1% PBS-Tween for 30 minutes. The Goat anti-mouse secondary antibody conjugated to Horse Radish Peroxidase (Thermo Fisher Scientific, Waltham, Massachusetts, United States) was diluted 1 in 5000 in 10% milk solution. The membrane was incubated in the secondary antibody solution for 1 hour at room temperature. The membrane was washed twice for 5 minutes in 0.1% PBS-Tween then left at room temperature in 0.1% PBS-Tween for 15 minutes. The Enhanced Chemiluminescence (ECL) Extreme solution (Expedeon, Heidelberg, Germany) was used to visualise protein bands. 500uL of luminol enhancer (Expedeon, Heidelberg, Germany) was mixed with 500uL of peroxide solution (Expedeon, Heidelberg, Germany). The 1mL solution was added to the membrane which was then transferred to the Syngene G:BOX F3 Gel imaging system (Syngene, Bangalore, India). The images were taken using the GeneSys software (Syngene, Bangalore, India). Image analysis and band quantification was carried out using ImageJ (356).

3.12.5 Proteomics

Proteomic analysis was performed on cells 72 hours post-transfection. To extract protein, cells were washed once in 0.25mL/cm^2 room-temperature PBS, followed by two washes of 0.25mL/cm^2 4^{o}C PBS. Cells were the covered in 0.5mL 4^{o}C PBS and scraped using a P1000 pipette. The scraped cells were transferred to a microcentrifuge tube and spun at 900 x g for 5 minutes in a Eppendorf 5424R benchtop microcentrifuge (Eppendorf, Hamburg, Germany). The supernatant was removed and the

cell pellets were stored at -80^{o}C. The pellets were shipped on dry ice to Liverpool university, where all subsequent analysis was carried out by Prof. Mandy Peffers and her team.

The pellets were thawed and suspended in 100uL 25mM ammonium bicarbonate (Fluka Chemicals Ltd., Gillingham, UK). The samples were sonicated three times at an amplitude of 10um for 10 seconds with 50 seconds rest. A Pierce assay was performed as described previously in 3.12.3. 10 ug of sample was taken and the final volume brought up to 160 ul using 25 mM ammonium bicarbonate (Fluka Chemicals Ltd., Gillingham, UK). 10 ul of 1% (w/v) RapiGest (Waters, Elstree, Hertfordshire, UK) was added and heated at 80°C for 10 min.10 ul of 1.84 mg/ml solution of DTT (0.6 mM final) (Sigma-Aldrich, St. Louis, Missouri, United States) was added and incubated at 60°C for 10 min. 10 ul of 6.6 mg/ml solution of IAA (1.5 mM final) (Sigma-Aldrich, St. Louis, Missouri, United States) was added and incubated at RT in the dark for 30 min. Any excess IAA was quenched by adding 9.4 ul of DTT used in the previous step. 10 µl of 0.2 ug/µl trypsin/lys-c (Promega, Madison Wisconsin, United States) was added and samples were incubated for 2 hours at 37°C in the rotating incubator. The same amount of trypsin/lyc-c was added and the samples were incubated overnight at 37°C in the rotating incubator. 1ul of TFA (Sigma-Aldrich, St. Louis, Missouri, United States) was added and samples were then incubated for 30 min at 37°C in the rotating incubator. Samples were centrifuged for 15 min at 13,000 x g at 4°C and supernatant was transferred to a new LoBind tube (Eppendorf, Hamburg, Germany). 5 ul of digest ran on protein gel and stained with Coomassie Blue (Thermo Fisher Scientific, Waltham, Massachusetts, United States).

Protein digests were analysed using liquid chromatography with tandem mass spectrometry (LC-MS/MS) on an UltiMate 3000 Nano LC System (Dionex, Sunnyvale California, United States) coupled to a Q ExactiveTM

Quadrupole-Orbitrap instrument (Thermo Fisher Scientific, Waltham, Massachusetts, United States). 1,500ng of protein was loaded on a 120 minute LC gradient. Raw spectral files underwent spectral alignment, peak picking, peptide quantification and normalisation in Progenesis™ QI 2.0 (Nonlinear Dynamics, Elstree, Hertfordshire, UK). Proteins were identified using the Mascot server Version 2.6.2 (360) and the UniHuman Reviewed database was used with search parameters including: 10.0ppm peptide mass tolerance; 0.01 Da fragment mass tolerance; trypsin enzyme; 1 missed cleavage allowed; fixed modification of carbamidomethylation (cysteine) and variable modification of oxidation (methionine). All statistical analysis was performed by Dr James Anderson using the software package R (359). Results were converted to normalised counts of protein alongside their p-values. Any further analysis was carried out by myself using Microsoft Excel (Alburquerque New Mexico, USA)

3.13 Plasmid design and construction

3.13.1 Genomic DNA isolation

DNA was isolated from cells using the NucleoSpin DNA RapidLyse Mini kit for rapid DNA purification (Macherey-Nagel, Nordrhein-Westfalen, Germany). Cells were lysed in 150uL RLY lysis buffer (Macherey-Nagel, Nordrhein-Westfalen, Germany) supplemented with 10uL liguid proteinase K (Macherey-Nagel, Nordrhein-Westfalen, Germany). The sample was incubated at 56^{o}C for up to 1 hour until the solution was completely lysed. 440uL of RLB buffer (Macherey-Nagel, Nordrhein-Westfalen, Germany) was added and the sample was mixed by pipetting. The sample was loaded onto the NucleoSpin® DNA RapidLyse Column (Macherey-Nagel, Nordrhein-Westfalen, Germany) and spun in a Eppendorf 5424R benchtop microcentrifuge (Eppendorf, Hamburg, Germany) at 11,000 x g for 1 minute. The flow-through was discarded and 500uL of RLW wash buffer (Macherey-Nagel, Nordrhein-Westfalen,

Germany) was added. The column was spun at 11,000 for 1 minute and another 500uL of RLW wash buffer was added. The flow-through was discarded and the column was spun for 2 minutes to dry the matrix. The DNA was eluted by adding 30uL sterile water to the membrane and incubating for 4 minutes before spinning at 11,000 x g for 1 minute. The concentration of DNA was quantified using the NanoDrop 2000 Spectrometer (Thermo Fisher Scientific, Waltham, Massachusetts, United States) as previously described.

3.13.2 PCR amplification of DNA

Target fragment of DNA were amplified using PCR. The Phusion® High-Fidelity DNA Polymerase kit (New England Biolabs, Ipswich Massachusetts, United States) was used for the PCR amplification of DNA fragments. For a 20uL reaction, 4uL 5X Phusion HF buffer (New England Biolabs, Ipswich Massachusetts, United States) was mixed with 0.4uL 10mM dNTPs (New England Biolabs, Ipswich Massachusetts, United States), 1uL 10uM forward primer (Sigma-Aldrich, St. Louis, Missouri, United States), 1uL 10uM reverse primer (Sigma-Aldrich, St. Louis, Missouri, United States) and 0.2uL Phusion enzyme (New England Biolabs, Ipswich Massachusetts, United States). The remaining 13.6uL was comprised of 100ng DNA in nuclease-free water. The PCR tubes were placed into a Thermocycler (Bio-Rad, Watford, United Kingdom) and run on a pre-defined program consisting of an initial denaturation at 98^{o}C for 30 seconds, followed by 30 amplification cycles of 98^{o}C for 10 seconds, 60^{o}C for 30 seconds and 72^{o}C for 30 seconds per kb of template. A final extension of 72^{o}C for 10 minutes was performed after the amplification cycles finished followed by a final hold at 4^{o}C. DNA was stored at -20^{o}C.

3.13.3 Gel electrophoresis

DNA was separated by size using gel electrophoresis. A 1% agarose gel was made up by mixing 1g of agarose (Thermo Fisher Scientific, Waltham, Massachusetts, United States) with 100mL of 1X TAE buffer and heated in a microwave at 800W for 2 minutes until the agarose had dissolved. 1X TAE buffer was composed of 40mM Tris base, 1.3mM EDTA and 20mM acetic acid. After the agarose solution had cooled to a safe handling temperature, 5uL SYBR™ Safe DNA Gel Stain (Thermo Fisher Scientific, Waltham, Massachusetts, United States) was added. The agarose solution was then poured into a 100mL gel mould and allowed to set. The gel was placed in a gel bath and covered with 1X TAE buffer. DNA was mixed with 6X purple loading dye (New England Biolabs, Ipswich Massachusetts, United States) in a ratio of 6:1. Up to 20uL of DNA was loaded into the wells of the gel. Gels were run with 6uL of GeneRuler 1 kb DNA Ladder (Thermo Fisher Scientific, Waltham, Massachusetts, United States) or 6uL 100bp DNA ladder (New England Biolabs, Ipswich Massachusetts, United States) for smaller fragments. Gels were run at 100V for 1 hour using the PowerPac™ Basic power supply (Bio-Rad, Watford, United Kingdom). DNA was visualised using the Syngene G:BOX F3 Gel imaging system (Syngene, Bangalore, India). The images were taken using the GeneSys software (Syngene, Bangalore, India).

3.13.4 DNA extraction from agarose gels

Gel extraction was performed using the NucleoSpin Gel and PCR Clean-up Mini kit (Macherey-Nagel, Nordrhein-Westfalen, Germany). DNA bands were cut from the gel using a sterilised scalpel. 200uL NTI buffer (Macherey-Nagel, Nordrhein-Westfalen, Germany) per 100mg gel was added and incubated at 50°C for 10 minutes until the gel had melted. The sample was loaded onto the NucleoSpin® Gel and PCR Clean-up Column (Macherey-Nagel, Nordrhein-Westfalen, Germany) and spun in a Eppendorf 5424R benchtop microcentrifuge (Eppendorf, Hamburg,

Germany) at 11,000 x g for 30 seconds. 700uL NT3 wash buffer (Macherey-Nagel, Nordrhein-Westfalen, Germany was added to the column and spun at 11,000 c g for 30 seconds. The flow-through was discarded and the wash step repeated. The column was then spun at 11,000 x g for 2 minutes to dry the matrix. DNA was eluted by adding 30uL nuclease-free water to the matrix and incubating for 4 minutes before spinning at 11,000 x g for 1 minute. The concentration of DNA was quantified using the NanoDrop 2000 Spectrometer (Thermo Fisher Scientific, Waltham, Massachusetts, United States) as previously described.

3.13.5 Restriction digest of DNA

The restriction enzymes used are outlined in Table 3-1. Restriction digests were carried out according to the manufacturer's instructions (New England Biolabs, Ipswich Massachusetts, United States). For a 50uL reaction, 5uL 10X rCutSmart Buffer (New England Biolabs, Ipswich Massachusetts, United States) was mixed with 1uL restriction enzyme. The remaining volume was made up with 1ug DNA in nuclease-free water. The solution was incubated at 37^{o}C for 1 hour in a Thermocycler (Bio-Rad, Watford, United Kingdom). Enzyme denaturation was achieved by heating the solution to 65^{o}C for 10 minutes.

3.13.6 Ligation

Ligation reactions were performed using T4 DNA ligase (New England Biolabs, Ipswich Massachusetts, United States). For a 20uL reaction, 2uL 10X T4 ligase buffer (New England Biolabs, Ipswich Massachusetts, United States) was mixed with 1uL T4 ligase (New England Biolabs, Ipswich Massachusetts, United States). The remaining 17uL was made up of vector DNA and insert DNA mixed in a 3:1 molar ratio in nuclease-free water. The NEBioCalculator (https://nebiocalculator.neb.com/) was

used to calculate the amount of vector and insert DNA for each reaction. The solution was incubated at 25°C for 1 hour followed by an overnight incubation at 16°C in a Thermocycler (Bio-Rad, Watford, United Kingdom).

3.13.7 Miniprepping plasmids

Plasmids were transformed into One Shot™ TOP10 Chemically Competent *E. coli* (Invitrogen, Waltham, Massachusetts, United States) using the heat-shock protocol. The vial of bacteria was thawed on ice. 5uL plasmid solution was added to the bacteria and incubated on ice for 30 minutes. The vial was placed in a water bath at 42°C for 30 seconds then transferred to the ice for 2 minutes. 250uL S.O.C medium (Invitrogen, Waltham, Massachusetts, United States) was added to the vial which was then incubated at 37°C for 1 hour with shaking at 225 rpm. Agar plates were made up by dissolving 32 g of LB agar (Invitrogen, Waltham, Massachusetts, United States) with 1L sterile water. This was autoclaved for 15 min at 121°C. Once cooled, ampicillin (Sigma-Aldrich, St. Louis, Missouri, United States) was added to make a final concentration of 100ug/mL. The agar solution was poured into petri dishes at a volume of 15mL per dish and allowed to set. Transformed bacteria was plated onto ampicillin-supplemented agar plates and incubated overnight at 37°C. The following day, colonies were picked into 5mL LB broth and incubated overnight at 37°C while shaking at 180 RPM. LB broth was made up by dissolving 25g LB broth base (Invitrogen, Waltham, Massachusetts, United States) in 1L sterile water and autoclaving for 15 minutes at 121°C.

To isolate plasmid from bacteria, the Wizard® Plus Minipreps DNA Purification System (Promega, Madison Wisconsin, United States) was used to miniprep plasmids. Bacteria were centfuged at 10,000 x g for 5 minutes in a Eppendorf 5810R benchtop centrifuge (Eppendorf, Hamburg,

Germany). The supernatant was discarded and the pellet was thoroughly resuspended in 250uL of Cell Resuspension Solution (Promega, Madison Wisconsin, United States). 250uL Cell Lysis Solution (Promega, Madison Wisconsin, United States) was added and mixed by inverting the solution 4 times. 10uL Alkaline Protease Solution (Promega, Madison Wisconsin, United States) was added and the sample was incubated at room temperature for 5 minutes. 350uL Neutralisation Solution (Promega, Madison Wisconsin, United States) was added and the sample was mixed by inverting 4 times. The sample was centrifuged at 12,000 x g for 10 minutes at room temperature. The cleared lysate was transferred to the Spin Column (Promega, Madison Wisconsin, United States) and spun at 12,000 x g for 1 minute. 750uL of Column Wash Solution (Promega, Madison Wisconsin, United States) was added and spun at 12,000 x g for 1 minute. This was repeated with 250uL Column Wash Solution. The column was spun at 12,000 x g for 2 minutes to dry the column. The plasmid DNA was eluted by adding 50uL nuclease-free water and incubating the column at room temperature for 4 minutes before spinning at 12,000 x g for 1 minute. The concentration of plasmid DNA was quantified using the NanoDrop 2000 Spectrometer (Thermo Fisher Scientific, Waltham, Massachusetts, United States) as previously described.

3.14 Sequencing and bioinformatics

3.14.1 DNA sequencing

Plasmids were sequenced using GENEWIZ Sanger Sequencing Services (Azenta Inc., South Plainfield, NJ, USA).

DNA sequences were obtained from the NCBI database (https://www-ncbi-nlm-nih-gov.uea.idm.oclc.org/) and analysed using SnapGene

software (www.snapgene.com). Sequence alignment and primer design was performed using BLAST (361).

3.14.2 Ingenuity pathway analysis (IPA)

RNAseq and proteomic data was analysed using Ingenuity Pathway Analysis (IPA) software (Qiagen, Hilden, Germany). Information on biological pathways is gathered from publications and stored in the Qiagen Knowledge Base. The IPA software uses this database to analyse the inputted list of DEGs and predict which pathways have been targeted based on the fold changes and statistical significance. Predicted pathways have an associated P-value and Z-score. The P-value is calculated using Right-Tailed Fisher's Exact Test and reflects the likelihood that the association or overlap between a set of significant molecules from the dataset and a given pathway is due to random chance. The Z-score reflects whether the software predicts the pathway to be activated or inhibited based the literature-derived directional effect of one molecule on another molecule or on a process, and the direction of change of molecules in the dataset. The formula for calculating the z-score is as follows:

$$z = \frac{x}{\sigma_x} = \frac{\Sigma_i w_i x_i}{\sqrt{\Sigma_i w_i^2}}$$

Where x = a random variable, σ = the variance, i = the index from 1 to N and $w = \frac{|M_{activating} - M_{inhibiting}|}{M_{activating} + M_{inhibiting} + 1}$

3.15 Statistical analysis

GraphPad Prism software version 5.0 (GraphPad Software, San Diego California, USA) and Microsoft Excel (Alburquerque New Mexico, USA)

were used for data analysis, presentation and statistical analysis. Statistical comparison between two groups was performed using unpaired t-test. No normality test was carried out to check if the data was normally distributed. For comparison of more than two groups, one-way ANOVA followed by Bonferroni's multiple comparison test was used. For comparison of more than two groups and two parameters the two-way ANOVA followed by Bonferroni's multiple comparison test was used. Differences among groups were considered significant when the probability value, p, was less than 0.05 (*P < 0.05, **P < 0.01, ***P < 0.001, ****P<0.0001, ns = not significant). Results are represented showing each sample value and the standard deviation or standard error of mean (SEM). No statistical methods were used to pre-determine sample size. When not otherwise stated, a single biological replicate constituted one sample pooled from two wells of a plate. Technical replicates were achieved by running the same biological sample three times. A hierarchical statistical approach such as nested ANOVA (362) was not used to account for biological and technical replicates.

Chapter 4 Using iPSC-derived models to investigate SNORD116 expression during cardiac development

4.1 Introduction

SNORD116 may influence developmental cardiac processes, thus leading to the increased prevalence of cardiac defects in PWS patients (57,64). The aim of this chapter is to investigate SNORD116 during cardiac differentiation. Many protocols for iPSC-CM differentiation have been developed (275–278). Typically, the process begins with the activation of wnt signalling by the GSK3 inhibitor CHIR99021 (CHIR). This causes an epithelial-to-mesenchymal transition and induces mesoderm formation. Wnt signalling is then inhibited and the cells are maintained in a cardiac-specific media to promote cardiomyocyte differentiation. The key gene expression and metabolism changes that occur during this process are outlined in this chapter.

Studies have shown that iPSC-CM differentiation can benefit from changing the main metabolic substrate from glucose to lactate part-way through the development process (363–365). The Wnt activation/inhibition-based method of cardiomyocyte differentiation can give rise to a mixed population that includes non-cardiomyocyte populations such as cardiac fibroblasts and smooth muscle cells. Unlike the other cell types, cardiomyocytes can use lactate as an energy source in the absence of glucose. This ability has been exploited to improve the purity of the cardiomyocyte population and reduce the number of contaminating cell types by changing the media from glucose-based to lactate-based (366). In addition to improving the purity of cardiomyocyte cultures, a recent study found that cell proliferation markers are upregulated in a lactate-rich environment, in addition to genes associated with stemness and progeneration (367). Another study found that

transient lactate exposure in developing cardiomyocytes caused numerous transcriptomic changes that promoted maturity (290). Forcing early cardiomyocytes to metabolise lactate simulates *in utero* conditions where lactate levels are typically high (368), thus potentially promoting a foetal-like proliferative phenotype that may assist the development process. This chapter explores the effectiveness of lactate as a metabolic selection tool during iPSC-CM differentiation.

Changing metabolic substrate availability is not the only method to induce a proliferative phenotype in cardiomyocytes; Wnt signalling can be manipulated to induce proliferation (369,370). Buikema *et al.*, 2020 demonstrated that the activation of Wnt signalling through CHIR supplementation was effective in causing the rapid expansion of low-density iPSC-CMs (370). In this study it was found that cell-cell contact had an inhibitory effect on iPSC-CM proliferation, although removing cell-cell contacts alone was not sufficient in inducing cell-cycle re-entry, which was only achieved with the addition of CHIR. Although the expansion of iPSC-CMs has obvious commercial applications, it may also be a useful tool in investigating the effect of pro-proliferative, de-differentiating signalling in developing cardiomyocytes.

IPSC-CMs are typically differentiated and maintained in a glucose-based media. However, studies have shown that transitioning differentiated iPSC-CMs from glucose-based to fatty acid-based media can induce a more mature phenotype (371–374). Greater maturity would improve the iPSC-CM model as it captures the later stages of cardiac development when the cells are utilising a form of metabolism that is more physiologically relevant to the adult human heart. To implement this, differentiated iPSC-CMs were maintained in a glucose-free fatty acid-rich media. Gene expression was analysed to evaluate the effects of glucose-based media versus glucose-free fatty acid-based media.

In addition to cardiomyocytes, iPSCs can be used to generate cardiac fibroblasts. Zhang *et al* (312) *o*utlines a protocol for generating cardiac fibroblasts from iPSCs. In this protocol, cardiac progenitor cells are differentiated into cardiac fibroblasts via an epicardial progenitor phase. This protocol is the basis for the method used in the differentiation of iPSCs into cardiac fibroblasts as explored in this chapter.

In order to understand the expression of SNORD116 during heart development, it is important to understand how the process of development is modelled *in vitro* using iPSCs. This chapter will describe the process of iPSC-CM and iPSC-CF differentiation, and will define the expression of SNORD116 during these processes.

4.2 The differentiation of iPSCs into cardiomyocytes

To investigate cardiomyocyte differentiation, a recently developed protocol for the derivation of ventricular cardiomyocytes from iPSCs was employed. This method was developed and kindly shared by Andreia Bernardo (Francis Crick Institute/ Imperial College London) and shown to successfully produce cultures of high purity and maturity status iPSC-CMs (Dark *et al*. manuscript in preparation, patent submission WO2020245612). Figure 4-1 outlines this differentiation protocol applied to iPSCs obtained from the Allen Cell Collection of the Coriell Institute. These iPSCs (ID: AICS-0075-085) have been genetically modified so that the cardiomyocyte-specific sarcomeric protein alpha-actinin (AA) is tagged with Green Fluorescent Protein (GFP) resulting in an AA-tagged line that can be used to assess the progress of cardiomyocyte differentiation.

Contractile cardiomyocytes are typically generated between days 5-8 of the protocol. Although the length of the protocol is fifteen days, it can be extended to beyond 30 days to allow maturation to take place. The differentiation is initiated through the activation of Wnt signalling on day 0, which induces mesoderm formation. On day 2, Wnt signalling is inhibited to induce cardiac mesoderm progression. The cells are fed with a cardiac-specific media to promote cardiomyocyte development. Over the course of development, the cells progress through specific stages which can be identified by the expression of cell-type-specific markers.

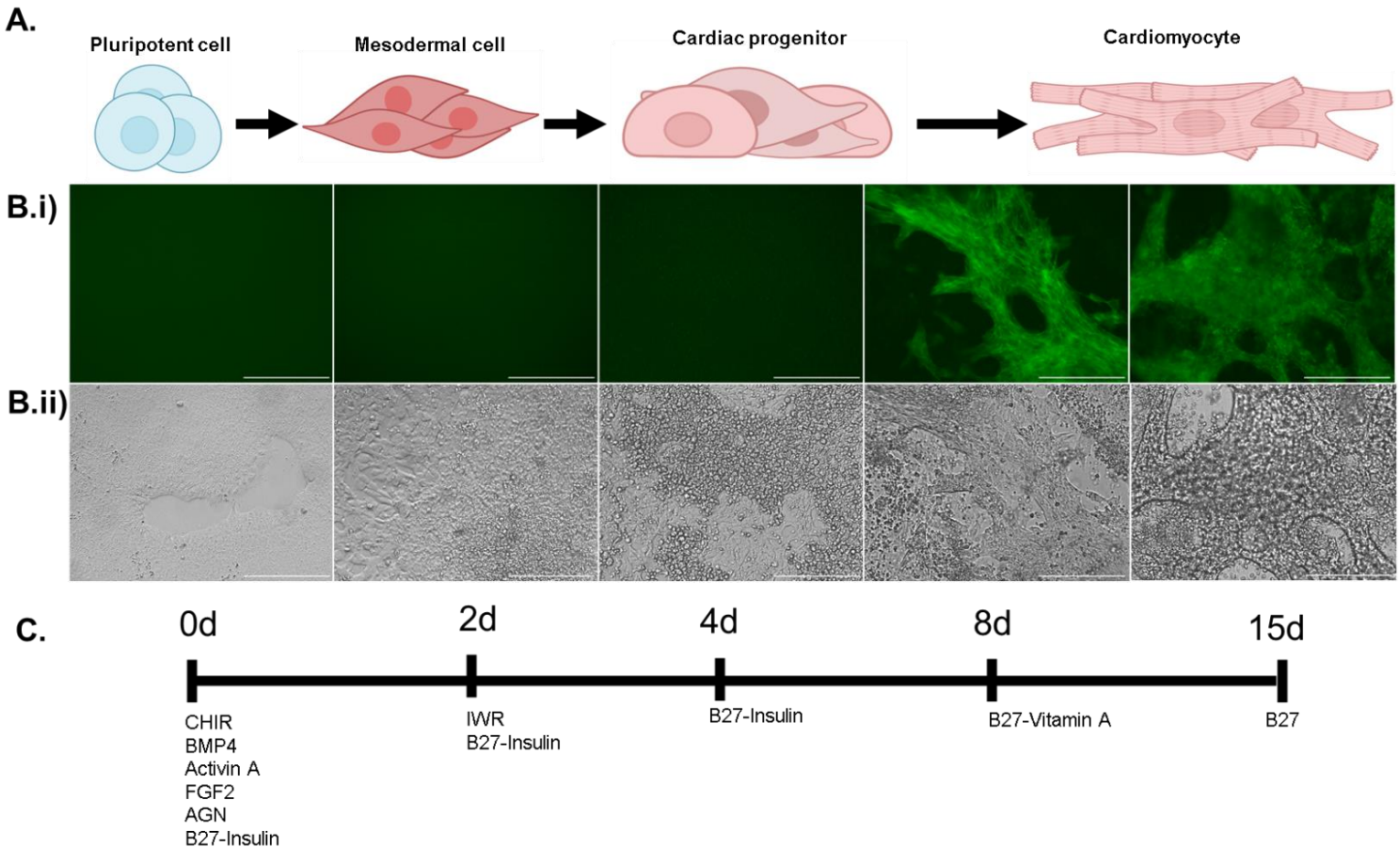

Figure 4-1. Differentiation of iPSCs into cardiomyocytes.
A. The different stages that cells pass through during iPSC-CM differentiation.
B. Images were taken of the AA-tagged hiPSCs in the (i) GFP and (ii) brightfield channels at 20x magnification on days 0, 2, 4, 8 and 15 of the differentiation protocol laid out in Dark et al. Scale bar = 200um.
C. The timeline and corresponding small molecules and factors used at each feeding day during the differentiation protocol.
Generated using MS PowerPoint.

Bulk RNAseq was performed to analyse the expression on days 0, 6, 10 and 15. Figure 4-2 shows the expression of various marker genes during these points in the differentiation. The expression of pluripotency markers SOX2, OCT4 and *nanog* (258,375,376) were downregulated after day 0, indicating that the stem cells underwent differentiation. The transcription factors EOMES, *GATA4* and *NKX2-5* are upregulated between days 6 and 10 and are important for mesoderm development and early cardiogenesis (377–379). The structural sarcomeric genes for cardiac alpha-actin (*ACTC1*), Myosin Heavy Chain 6 (*MYH6*), Myosin Heavy Chain 7 (*MYH7*), slow skeletal troponin (*TNNI1*) and cardiac troponin (*TNNT2*) are upregulated from day 6 onwards. Except for *TNNI1*, the expression of these genes is highest at day 15, although due to variation between samples only *MYH7* expression levels show a statistically significant increase between days 10 and 15. The gene encoding phospholamban (PLN) significantly increases in expression sequentially throughout the differentiation. This protein is essential to the function of cardiomyocytes as it regulates the activity of SERCA, a Ca^{2+}-ATPase pump within the sarcoplasmic reticulum that controls calcium movement within the cell. Overall, these results demonstrate the generation of cardiomyocytes on a transcriptomic level.

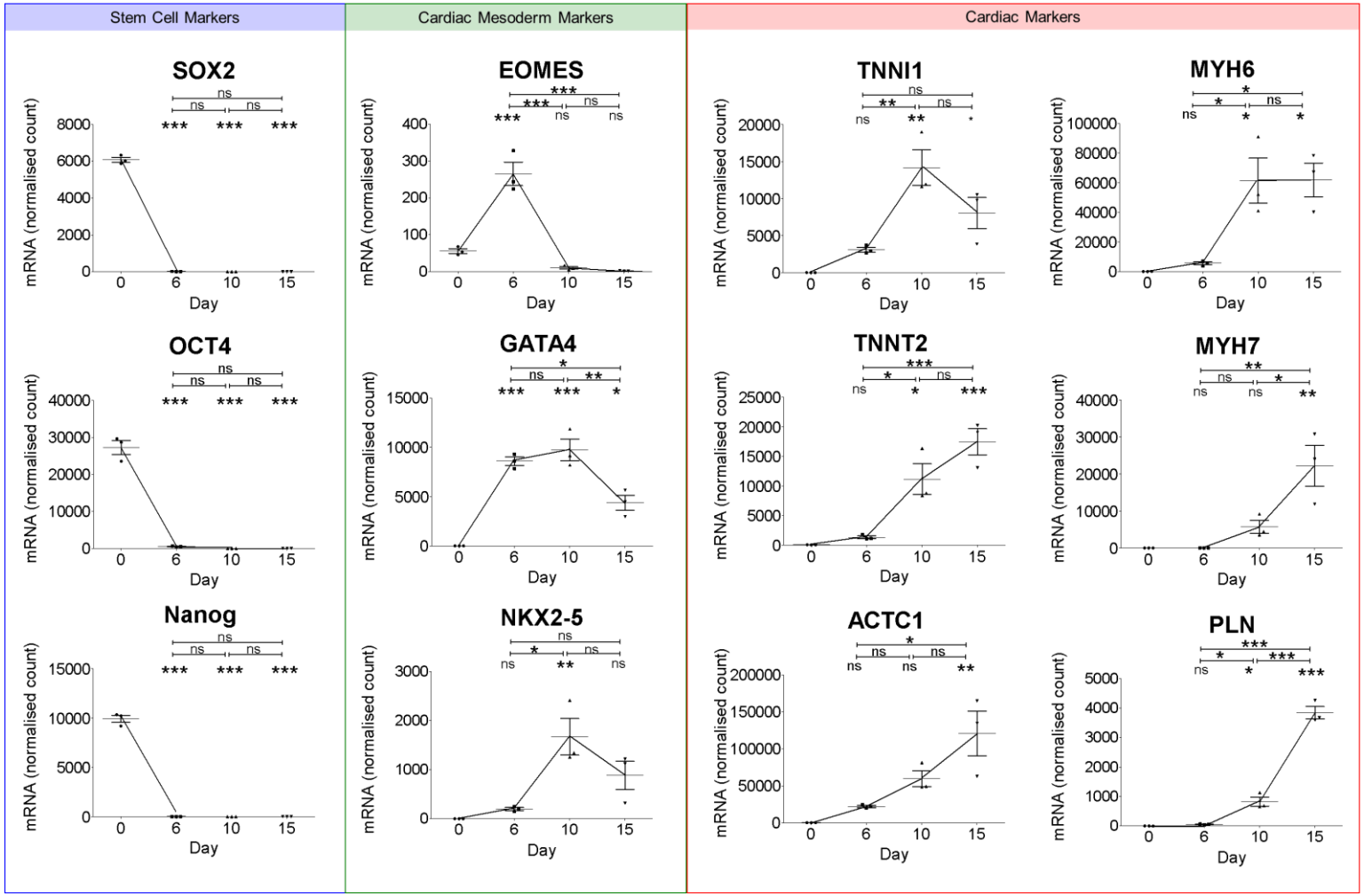

Figure 4-2. Gene expression during iPSC-CM differentiation determined through RNAseq analysis.
The normalised counts of the mRNA of marker genes on days 0, 6, 10 and 15 of iPSC-CM differentiation. Individual replicates are shown as dots, the box and whisker plot shows the mean and SEM. Statistical analysis performed using one way ANOVA. * = P≤0.05, ** = P≤0.01, *** = P≤0.001. N=3.

Although the results obtained through RNAseq provide a detailed transcriptomic report of the later post-progenitor stages of cardiomyocyte differentiation, it does not reveal expression changes during the early stages of differentiation occurring around the initial wnt signalling manipulation events. Therefore, RNA expression was also analysed using RT-qPCR at the earlier days of differentiation (0, 2 and 4) as well as the later days (8 and 15), which is shown in Figure 4-3.

Nanog, *GATA4* and *NKX2-5* all show a similar trend to the RNAseq results in Figure 4-2. *Nanog* expression decreases after day 2 whilst the mesodermal marker *GATA4* is upregulated from day 2 onwards. *NKX2-5* expression is upregulated from day 4 onwards. The structural cardiac gene titin (*TTN*) is also upregulated from day 4 onwards, with its expression increasing in a linear-like fashion. Overall, the results in Figure 4-3are consistent with the results in Figure 4-2 in demonstrating the expected gene expression changes of the various cell type markers during differentiation.

Both *PPARa* and *PPARy* expression levels increase during iPSC-CM differentiation, whereas the expression fold change of *PPARd* does not significantly change from the level of expression in stem cells (relative to GAPDH).

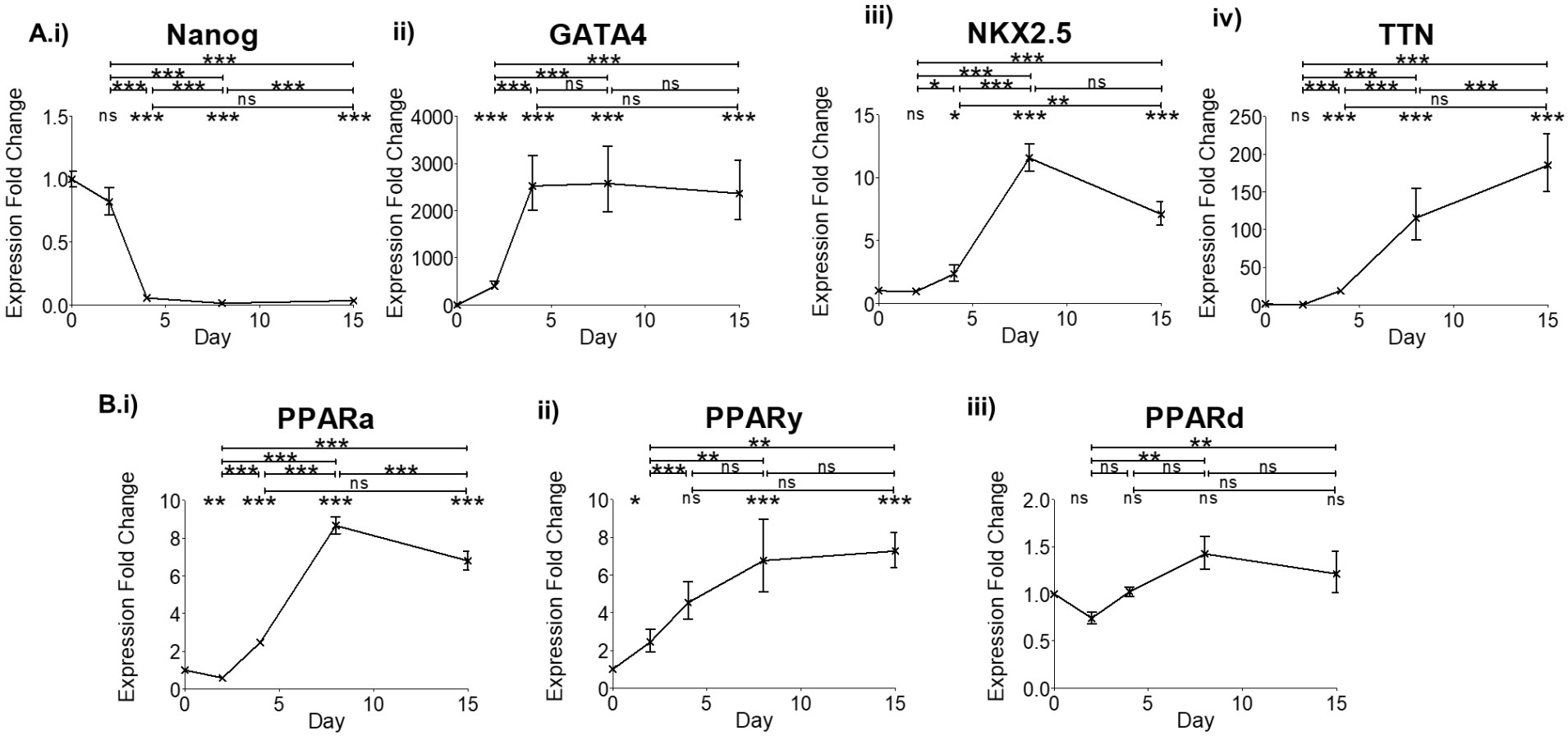

Figure 4-3. Gene expression during iPSC-CM differentiation determined through RT-qPCR.
A. Expression of marker genes (i) *nanog*, (ii) *GATA4*, (iii) *NKX2-5* and (iii) *TTN*. Plotted as fold change relative to day 0, normalised to GAPDH, calculated by ddCt method.
B. Expression of (i) *PPARa*, (ii) *PPARy* and (iii) *PPARd*. Plotted as fold change relative to day 0, normalised to GAPDH, calculated by ddCt method.

Gene expression of the PPAR isoforms was calculated as 2^{-dCT} and plotted on one graph to demonstrate how the different isoforms change relative to each other. This is shown in . Additionally, to better understand the relationship between the three different isoforms and how their expression relates to each other, the expression of *PPARy* and *PPARd* have been plotted as relative to *PPARa* instead of a normal housekeeper.

Relative to GAPDH, *PPARd* shows the highest level of expression of the three isoforms at every time point (except day 8, where there is no significant difference between *PPARa* and *PPARd*). In contrast, *PPARy* shows the lowest level of expression at every time point (although this is not significant between *PPARa* and *PPARy* at days 0 and 2). *PPARa* expression does initially decrease at day 2 compared to day 0, but from day 2 to day 8 the expression of *PPARa* increases significantly and remains at upregulated at day 15. In other words, *PPARa* expression increases as pluripotency (i.e. *nanog*) decreases and cardiac gene expression increases. This aligns with the established finding that *PPARa* is important in cardiac development and cardiomyocyte function (380,381).

When calculated as relative to *PPARa*, *PPARy* expression is highest at day 2 with a 2^{-dCt} of 0.26±0.045 but is otherwise unchanged from the stem cell level of 0.06±0.009. *PPARd* expression is also highest at day 2 (relative to *PPARa*), with a 2^{-dCt} of 8.9±0.8 but the ratio of *PPARd*:*PPARa* decreases as the differentiation progresses. This reflects the increasing levels of *PPARa* (relative to GAPDH) from day 4 onwards, to the point that these two isoforms are expressed at similar levels by day 8.

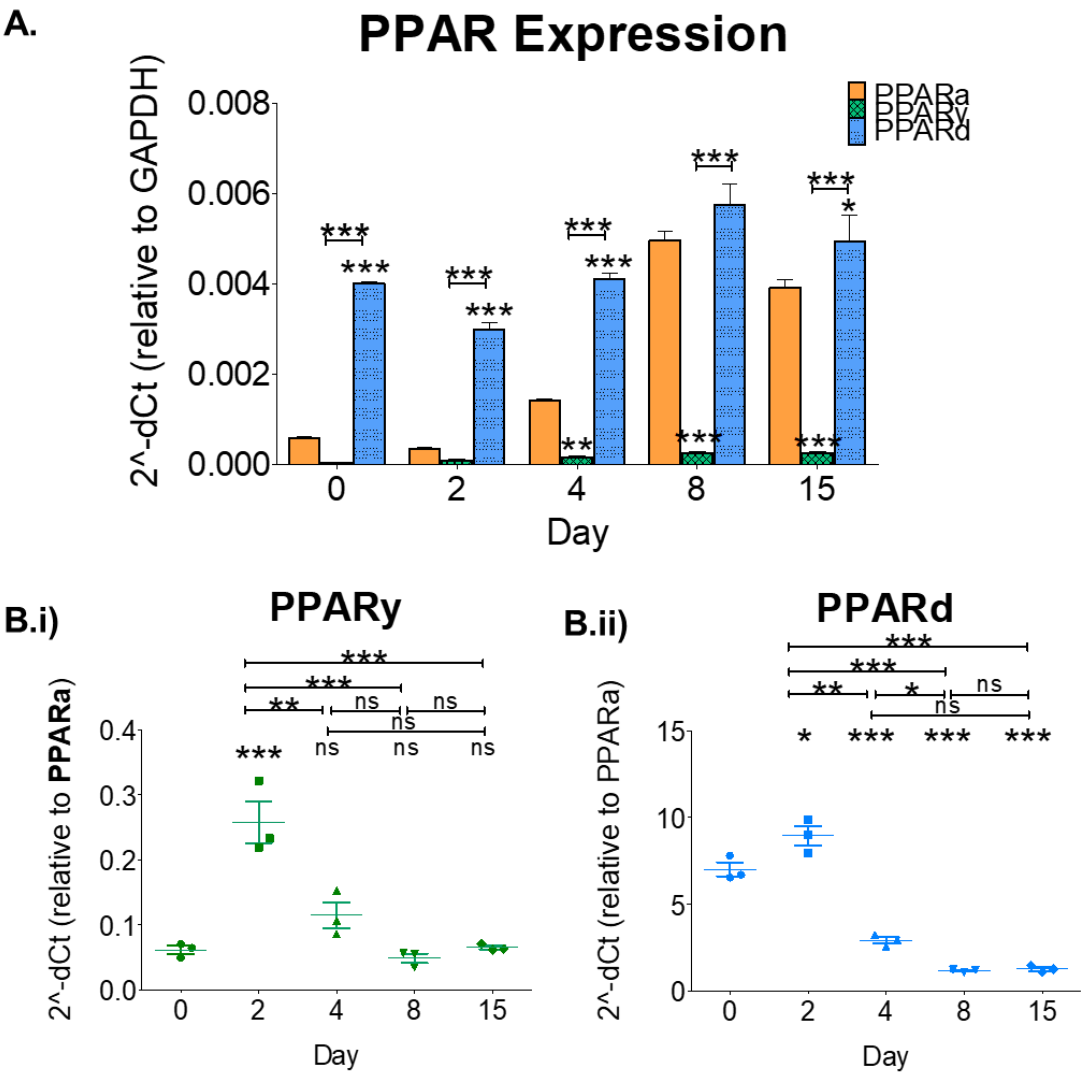

Figure 4-4. Relative expression of the PPAR isoforms in comparison to eachother.
A. Expression of all three PPAR isoforms plotted as 2^-dCt (normalised to GAPDH).
B. Expression of (i) *PPARy* and (ii) *PPARd* plotted as fold change relative to day 0, normalised to *PPARa*, calculated by ddCt method.
Statistical analysis performed using one-way ANOVA. * = P≤0.05, ** = P≤0.01, *** = P≤0.001. N=3. Error bars represent SEM.

The changes in PPAR gene expression could reflect the changing of metabolism as the cardiomyocytes develop. This can also be analysed by measuring the metabolism of various substrates at different points during differentiation. Metabolism was assessed using the Biolog MitoPlate assay, wherein the flow of electrons across the electron transport chain caused the reduction of a dye that turns from colourless to purple. The extent of this colour change reflects the extent of metabolic activity capable of being performed by the cell in the presence of a specific substrate within a given time frame (6 hours).

Overall, 29 substrates were tested and classed into one of four metabolic classes: glycolysis, the citric acid cycle (TCA), amino acid or fatty acid. The results of this are shown in Figure 4-5 and Figure 4-6. Of the 29 substrates assayed, substrates in class TCA are the largest proportion of total substrate metabolism across all four time points, contributing 47-58% of substrate usage. This indicates that out of all of the substrates tested, these substrates are the most easily absorbed and / or metabolised by the cells. Glycolysis makes up 19-28% of substrate use, and amino acids make up 14-21%. Fatty acids are the least-metabolised substrates, making up only 3-8% of total metabolic capacity. This indicates that these substrates are the least readily metabolised. In terms of total metabolic capacity i.e. the sum of the total colour change of all substrates, day 6 cells demonstrated the lowest levels of metabolism, whereas day 10 showed the highest.

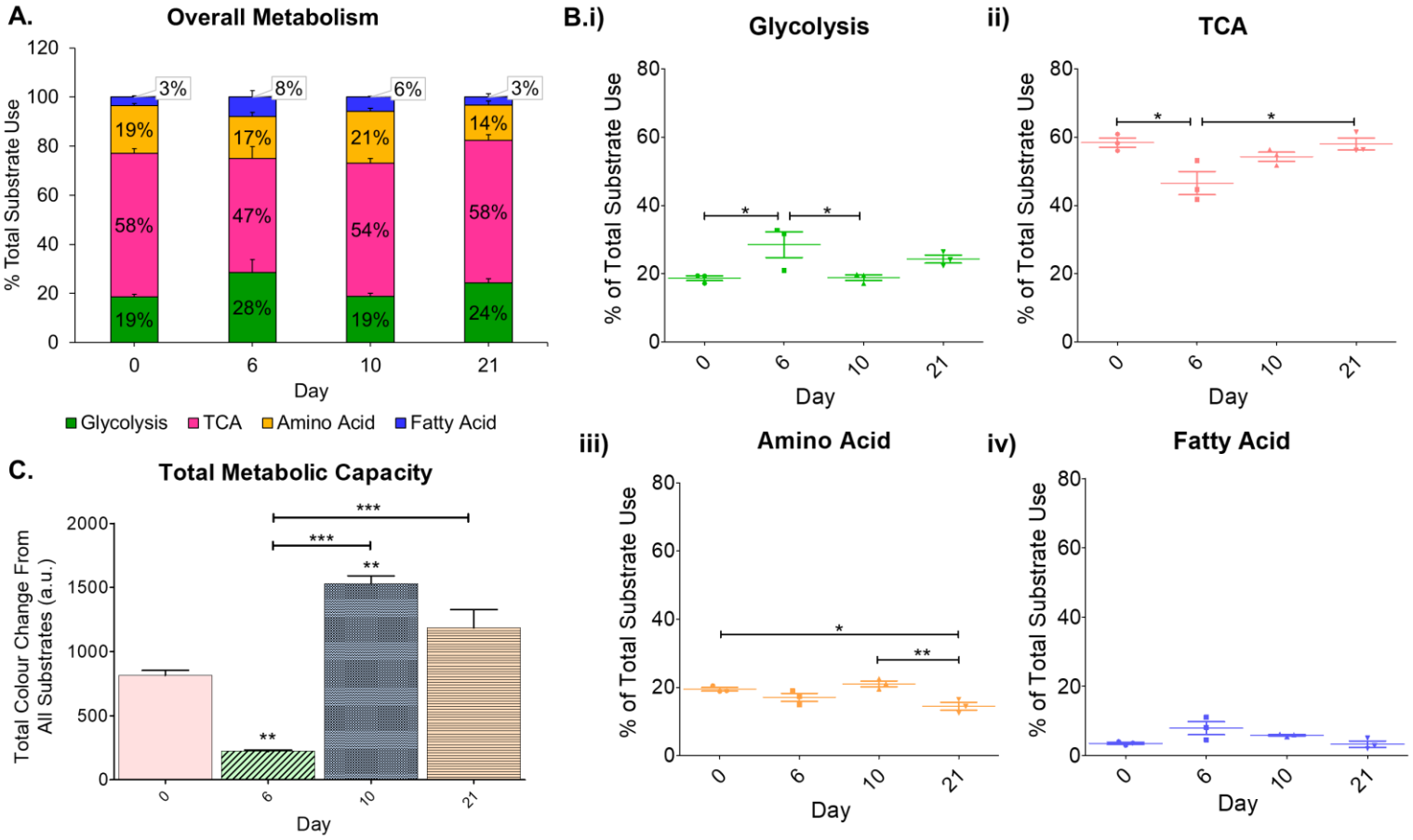

Figure 4-5. Changes in overall metabolism during iPSC-CM differentiation.
A. The percentage usage of each metabolic substrate class (based on total colour change).
B. The percentage usage of each metabolic substrate class, broken down into the individual classes (i) glycolysis, (ii) TCA, (iii) amino acid and (iv) fatty acid.
C. Sum of the total colour change of all substrates at each time point. Statistical analysis performed using one-way ANOVA. * = P≤0.05, ** = P≤0.01, *** = P≤0.001. N=3. Error bars represent SEM.TCA = The citric acid cycle.

Although day 6 shows the lowest overall level of metabolism, it is at this time point that glycolysis is at its highest percentage of substrate use, making up 28±5% of total substrate use. This correlates in a decrease of TCA substrate usage, from 58±2% at day 0 to 47±5% at day 6. Figure 4-6 shows there is no significant increase in total colour change by any of the glycolysis substrates at day 6 compared to day 0, however the TCA substrates citric acid, A-Keto-glutaric acid, fumaric acid and malic acid all yield a significantly smaller colour change at day 6 compared to day 0. Therefore, the increase in glycolysis as a percentage of total metabolism reflects not an increase in glycolytic metabolism per se, but rather a decrease in the capacity for the cells to metabolise the TCA substrates.

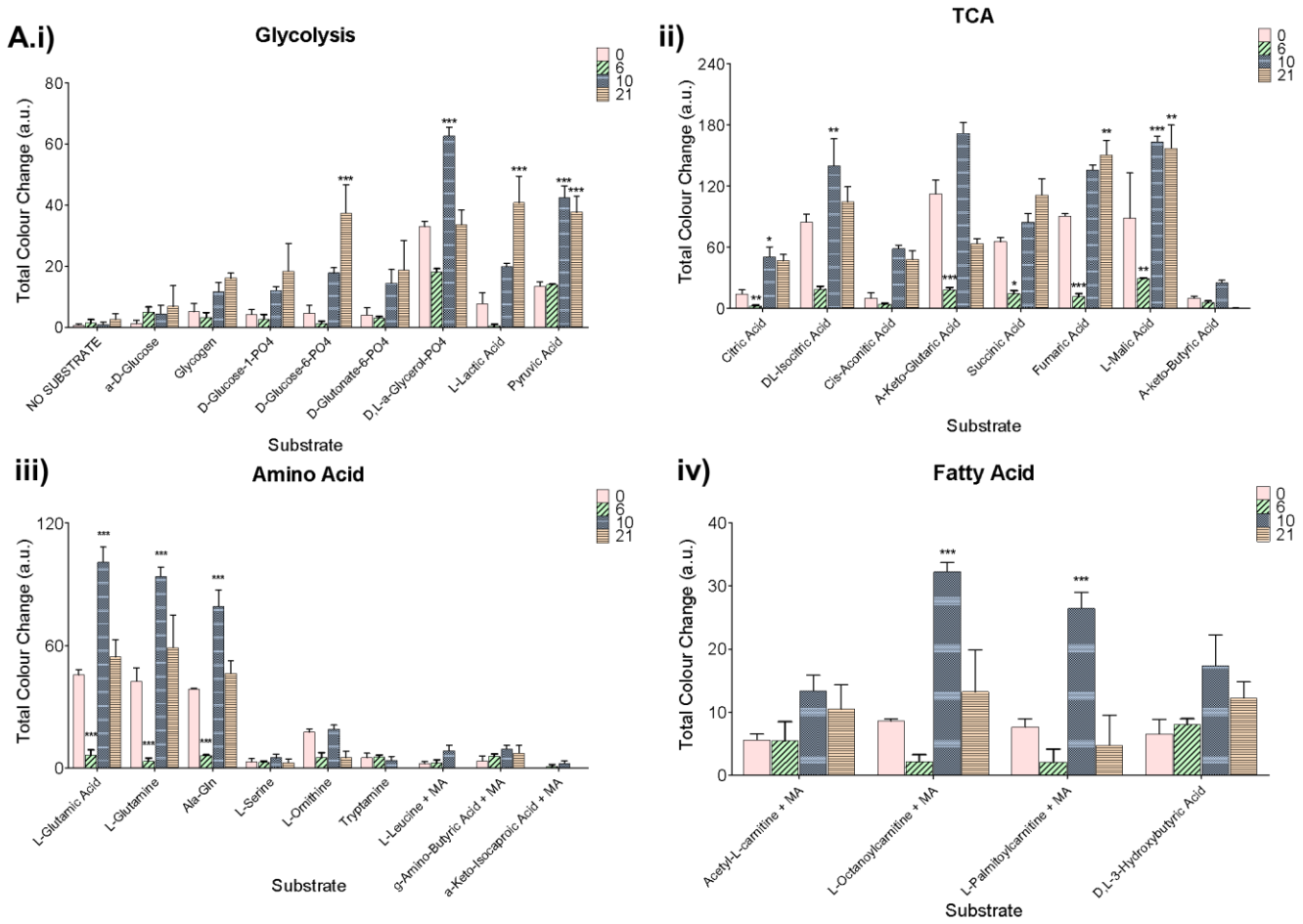

B.

Glycolysis	Day 0	Day 6	Day 10	Day 21
NO SUBSTRATE	1.0	2.1	1.3	3.8
a-D-Glucose	1.0	4.4	3.8	6.1
Glycogen	1.0	0.6	2.3	3.2
D-Glucose-1-PO4	1.0	0.6	2.9	4.3
D-Glucose-6-PO4	1.0	0.3	3.9	8.2
D-Glutonate-6-PO4	1.0	0.7	3.6	4.6
D,L-a-Glycerol-PO4	1.0	0.6	1.9	1.0
L-Lactic Acid	1.0	0.1	2.6	5.3
Pyruvic Acid	1.0	1.0	3.1	2.8
Pyruvic Acid + MA	1.0	0.2	1.3	1.0
TCA				
Citric Acid	1.0	0.2	3.6	3.3
D,L-Isocitric Acid	1.0	0.2	1.7	1.2
Cis-Aconitic Acid	1.0	0.4	5.8	4.7
A-Keto-Glutaric Acid	1.0	0.2	1.5	0.6
Succinic Acid	1.0	0.2	1.3	1.7
Fumaric Acid	1.0	0.1	1.5	1.7
L-Malic Acid	1.0	0.3	1.8	1.8
A-keto-Butyric Acid	1.0	0.6	2.5	0.0
Amino Acids				
L-Glutamic Acid	1.0	0.1	2.2	1.2
L-Glutamine	1.0	0.1	2.2	1.4
Ala-Gln	1.0	0.2	2.1	1.2
L-Serine	1.0	1.0	1.7	0.9
L-Ornithine	1.0	0.3	1.1	0.3
Tryptamine	1.0	1.0	0.7	0.0
L-Leucine + MA	1.0	1.2	4.0	0.0
g-Amino-Butyric Acid + MA	1.0	1.6	2.7	2.1
a-Keto-Isocaproic Acid + MA	1.0	0.9	2.1	1.0
Fatty Acids				
Acetyl-L-carnitine + MA	1.0	1.0	2.4	1.9
L-Octanoylcarnitine + MA	1.0	0.3	3.8	1.5
L-Palmitoylcarnitine + MA	1.0	0.3	3.5	0.6
D,L-3-Hydroxybutyric acid	1.0	1.2	2.6	1.9

Fold Change
0 1 9

Figure 4-6. Changes in individual substrate metabolism during iPSC-CM differentiation.

A. The total colour change of each individual substrate under each metabolic class (i) glycolysis, (ii) TCA, (iii) amino acid and (iv) fatty acid. Statistical analysis performed using two-way ANOVA. * = P≤0.05, ** = P≤0.01, *** = P≤0.001. N=3. Error bars represent SEM. TCA = The citric acid cycle, MA = L-Malic Acid (100uM).

B. Fold change of the total colour change for each substrate at each time point relative to total colour change at day 0.

The glycolysis substrates show the greatest increase in total colour change at day 21 compared to day 0, with an average of 4±2-fold increase in total colour change. This indicates that the differentiated cardiomyocytes have a greater ability to metabolise glycolytic substrates compared to stem cells.

The majority of the amino acid substrates tested do not generate a significantly different colour change across the different time points with the exception of L-glutamic acid, L-glutamine and ala-gln. These show the lowest total colour change (3-6 a.u.) on day 6 and the highest total colour change (80-100 a.u.) on day 10. Day 0 and day 21 yield similar total colour changes for these substrates (40-60 a.u.).

Two of the four fatty acid substrates tested do not generate a significantly different colour change across the time points. However, L-octanoylcartinine and L-palmitoylcartinine do generate a significant increase in total colour change at day 10 of the differentiation compared to the other time points.

Together, these transcriptomic and metabolic results demonstrate the successful implementation of a recently developed method of differentiating hiPSC-CMs, showing characteristic stage-specific marker expression and changes in metabolic capacity. The iPSC-CMs produced were taken forward in the analysis of purity, proliferation and maturity.

4.3 The proliferation and maturation of iPSC-derived cardiomyocytes

According to the protocol (Dark *et al*. manuscript in preparation, patent submission WO2020245612), at day 10 of the differentiation, media is switched from glucose-based to lactate-based in order to select for cardiomyocytes and to promote their development. To assess the effectiveness of this strategy, day 8 iPSC-CMs were dissociated and re-plated at a range of seeding numbers: 5,000, 10,000 and 20,000 per well of a 24-well plate. On day 10 the media was changed to either a glucose-based media (RPMI/B27-Vitamin A) or a lactate-based media (RPMI-glucose/B27-Vitamin A + 4mM lactate). The cells were cultured for four days, with one media change after 2 days. On the fourth day, cell viability was assessed by cell titre-glo and cells were fixed and stained with DAPI and orange cell mask (OCM). The results are presented in Figure 4-7.

At the lower seeding numbers (5,000 and 10,000) there is no difference in cell viability or in cardiomyocyte purity between glucose-treated cells versus lactate-treated cells. However, when seeded at 20,000 cells, there is a significant decrease of 5,000±2,700 in cell number in the lactate-treated cell population compared to the glucose-treated sample. This could indicate the successful elimination of non-cardiomyocyte cell types, or alternatively could reflect a decrease in overall cell viability in response to the change in media. When assessing cardiomyocyte purity by AA expression using CellProfiler (358), cells treated with glucose-based media were comprised of 60±32% AA-expressing cells, which was increased to 91±13% with lactate treatment. This combined with the cell viability data suggests that changing the media from glucose to lactate is a viable strategy for the elimination of non-cardiomyocyte cell types, however this does appear to be cell density-dependent.

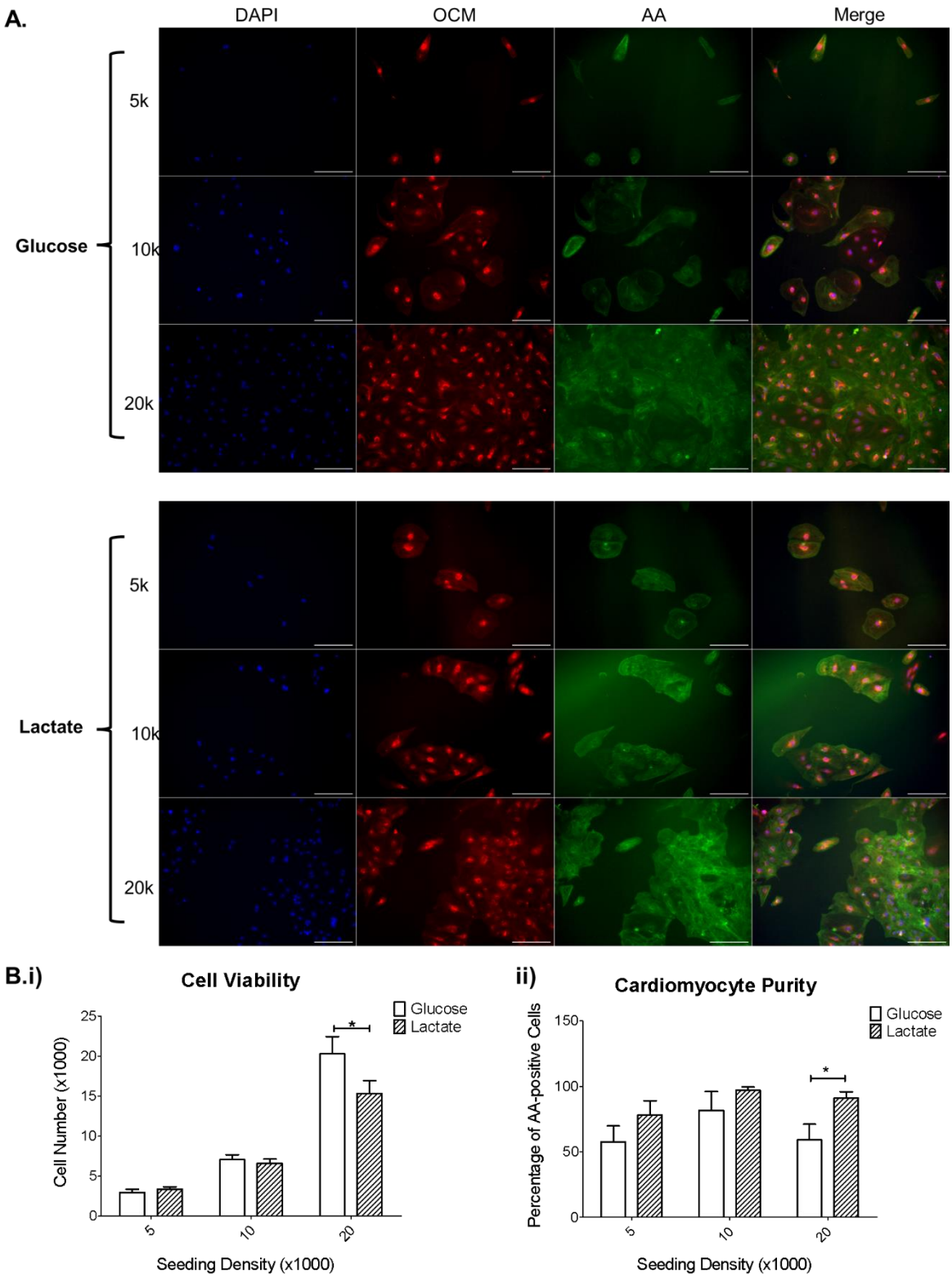

Figure 4-7. Metabolic selection of iPSC-CMs.
A. Cells seeded at 5k, 10k and 20k treated with either glucose or lactate-based media for 4 days. Green = AA, blue = DAPI, red = OCM. Scale bar = 200um. Magnification = 10x.
B.i) Cell viability in response to glucose or lactate-based media, quantified using cell titre-glo. N=3. Error bars represent SEM.
B.ii) The percentage of cells present that are AA-positive, quantified based on GFP expression using Cell Profiler. Statistics calculated using two-way ANOVA. * = P≤0.05. N=3. Error bars represent SEM.

The cell viability data in Figure 4-7 also demonstrates the non-proliferative nature of pure cardiomyocyte cultures beyond day 8, as the cell number of lactate-treated cells did not exceed the seeding number. A key feature of cardiomyocyte development is that they exit the cell cycle so that they can become highly specialised and mature. However, studies have shown that this can be reversed and cardiomyocytes can be made to proliferate through a process of removing cell contacts and activating Wnt signalling (370).

Day 8 iPSC-CMs were dissociated and seeded into 96-well plates in a split ratio of 1:10. After 24-hours they were fed RPMI/B27 supplemented with 2uM CHIR (or a vehicle control). The media was changed for fresh media after two days, and the cells were fixed and stained after four days of treatment. Cell number was quantified using cell titre-glo on days 0, 2 and 4 of treatment. Before treatment began, both cell populations were comprised of 11,000 cells. By day 2, the control population had increased to 12,700±4,100 cells and the CHIR-treated population had increased to almost twice this number, at 24,300±6,300 cells. However, due to variation between replicates, the difference between the control and treated samples was not statistically significant. At day 4 the control sample had grown to a population of 38,200±11,000 whereas the CHIR-treated sample had reached a total of 62,400±3,000 cells. This was significantly higher than the control, indicating that the CHIR treatment did have a positive effect on proliferation. However, cell number alone did not distinguish between cardiomyocytes and non-cardiomyocytes.

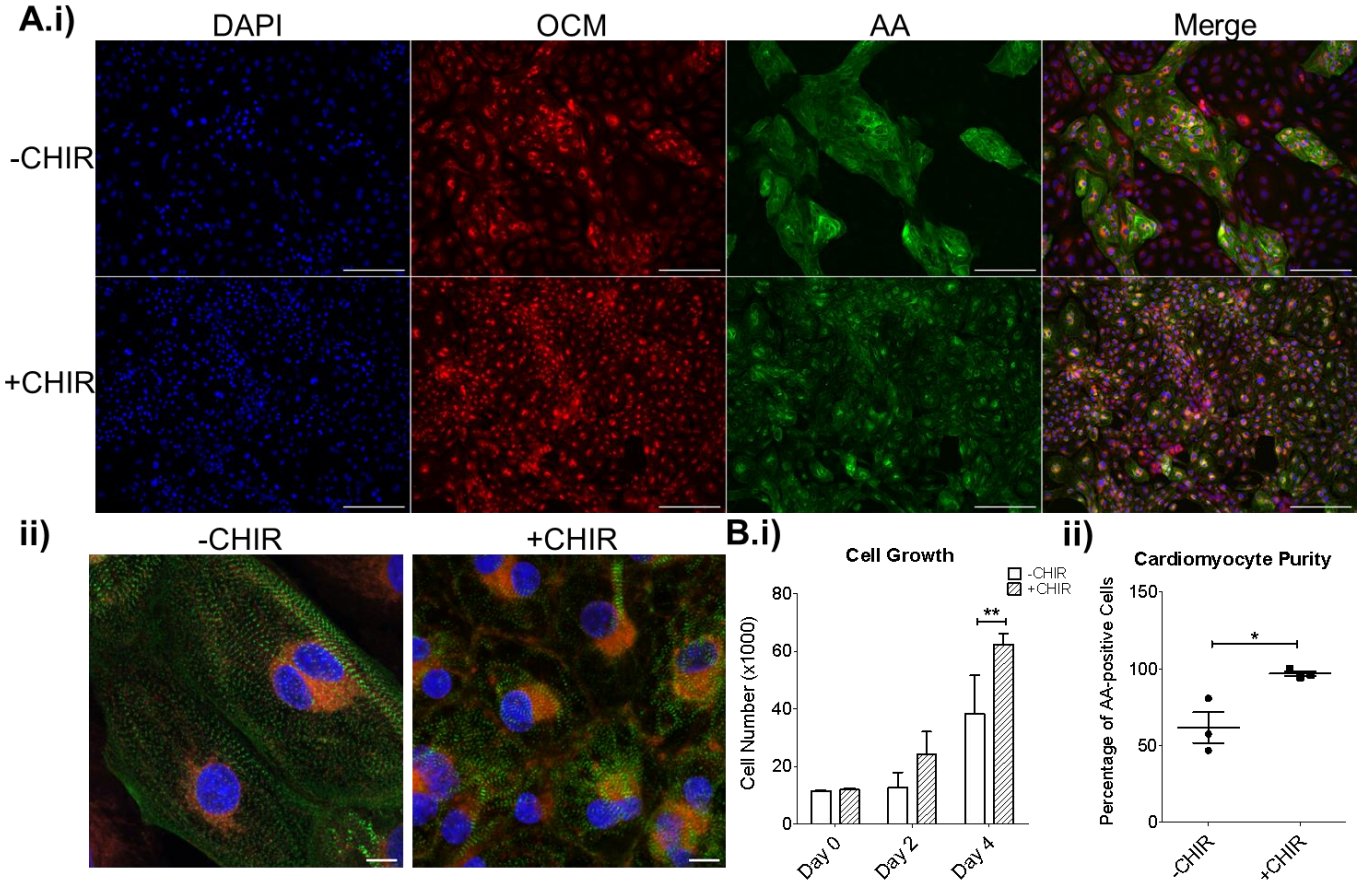

Figure 4-8. Wnt activation and cell proliferation of iPSC-CMs.

A. Cells treated with media supplemented with and without CHIR. Green = AA, blue = DAPI, red = OCM.

A.i) Scale bar = 200um. Magnification = 10x. A.ii) Scale bar = 10um. Magnification = x63

B.i) Cell viability in response to glucose or lactate-based media, quantified using cell titre-glo. Statistics calculated using two-way ANOVA. ** = $P \leq 0.01$. N=3. Error bars represent SEM.

B.ii) The percentage of cells present at day 4 that are AA-positive, quantified based on GFP expression using Cell Profiler. Statistics calculated using unpaired t-test. * = $P \leq 0.05$. N=3. Error bars represent SEM.

The percentage of AA-positive cells present at day 4 of treatment was quantified using immunocytochemistry. The CHIR-treated samples were found to be 97±2% AA-positive, whereas the control samples showed a significantly lower level of purity at 62±14% AA-positive. The CHIR-treated samples had not only a higher cell number but also a higher percentage of cardiomyocytes within the total population. Both CHIR-treated and control samples showed an increase in cell number from day 0 to day 4 (26,700±11,000 in the control and 50,400±3000 with CHIR). The lower level of purity in the control sample could be due to the presence of proliferative non-cardiomyocyte cells outnumbering the non-proliferative cardiomyocytes. This is demonstrated qualitatively in Figure 4-8A by the presence of large numbers of cells that do not express AA. Upon higher magnification, the AA-expression pattern shows greater alignment and organisation in the control cells compared to the CHIR-treated cells. The apparent increased disorganisation in sarcomeric structure may be due to the disassembly of the sarcomere necessary for cell division. It could also reflect a lower level of maturity in these cells compared to the untreated control.

Gene expression at day 4 was analysed by RT-qPCR. The results shown in Figure 4-9 indicate that CHIR treatment may have caused a global downregulation in gene expression, as the majority of genes analysed show a downregulatory trend in response to CHIR. Further replicates are needed to confirm this.

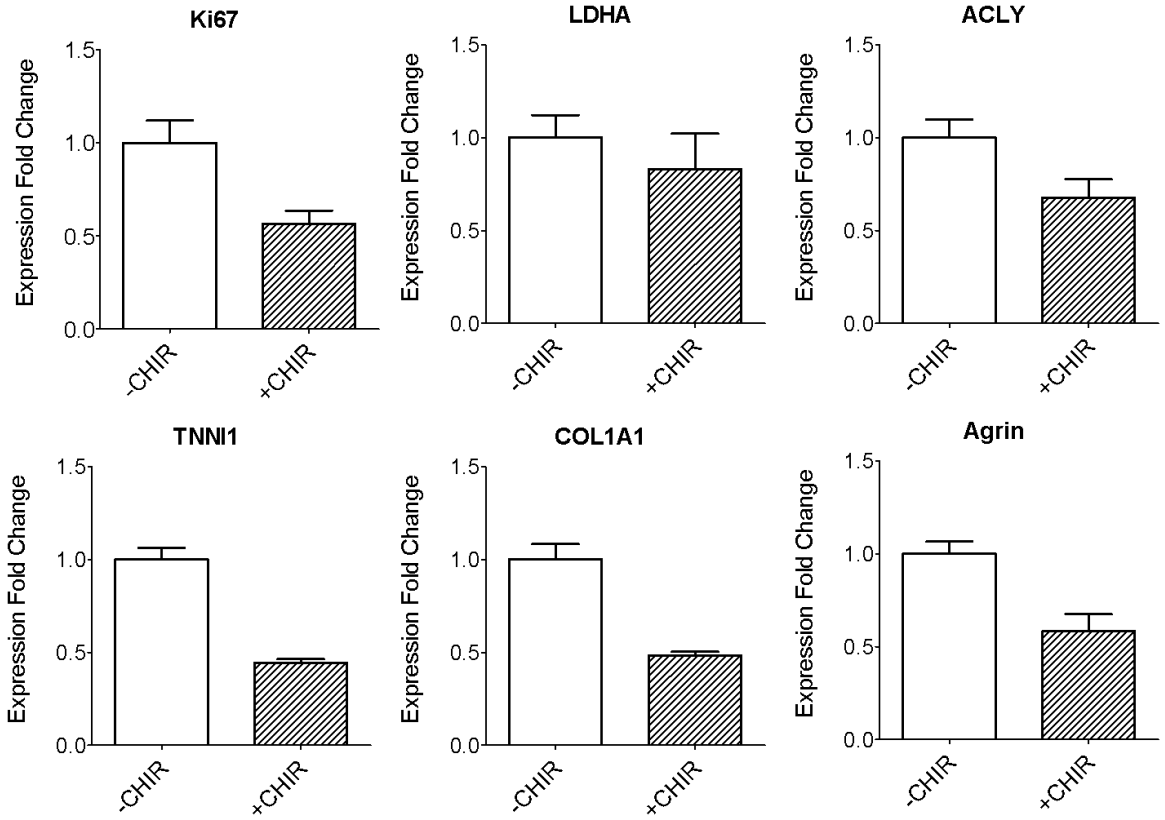

Figure 4-9. Gene expression changes as a result of CHIR treatment.
Gene expression plotted as expression fold change relative to the control, normalised to GAPDH, calculated using the ddCt method. N=1. Error bars represent SEM.

Manipulating Wnt signalling pathways can be used to de-differentiate cardiomyocytes into a proliferative state. However, to influence the cells in the opposite direction and towards maturity, one strategy is to change the type of substrates available for metabolism. Adult cardiomyocytes rely on fatty acid oxidation (FAO), therefore supplying the cells with fatty acid-rich media could induce a metabolic switch from glycolysis to FAO and encourage maturation.

Transcriptomic analysis was carried out to compare the RNA expression between day 20 iPSC-CMs and iPSC-CMs that had been cultured for an additional ten days in a fatty acid-rich media (GFAM). The results are presented in Figure 4-10. Due to an outlier sample in one of the day 30 replicates, there is too great a level of variation for any of the differences to reach statistical significance. Focusing on the structural cardiac genes, all of the genes analysed show an increase in expression between days 20 and 30. The ratio of *MYH7*:*MYH6* increases from 0.8±0.4 at day 20 to 3.2±2.2 at day 30. The ratio of *TNNI3*:*TNNI1* increases from 0.009±0.003 at day 20 to 0.06±0.03 at day 30, and the ratio of *MYL2*:MYL7 increases from 0.09±0.05 at day 20 to 0.37±0.27 at day 30. The cardiac ion channels *CACNA1C* and *RYR2* show an increase of 471±342 and 545±264 from day 20 to day 30, respectively. However, the ventricular cardiac potassium channel *KCNJ2* – associated with mature ventricular cardiomyocytes (382) – does not show a difference in mRNA levels.

The PPAR isoforms show an interesting trend. *PPARa* expression shows a slight decrease from 1690±209 at day 20 to 1462±644 at day 30. *PPARd* shows the opposite trend, increasing from 508±53 to 714±196. *PPARy* also shows an increase in expression from 48±17 to 205±171, although this gene also shows a high level of variation between the day 30 replicates. The cell cycle genes Ki67, CCNB1 and CKDK1 show decreases of 2099±519, 695±231 and 324±134 respectively.

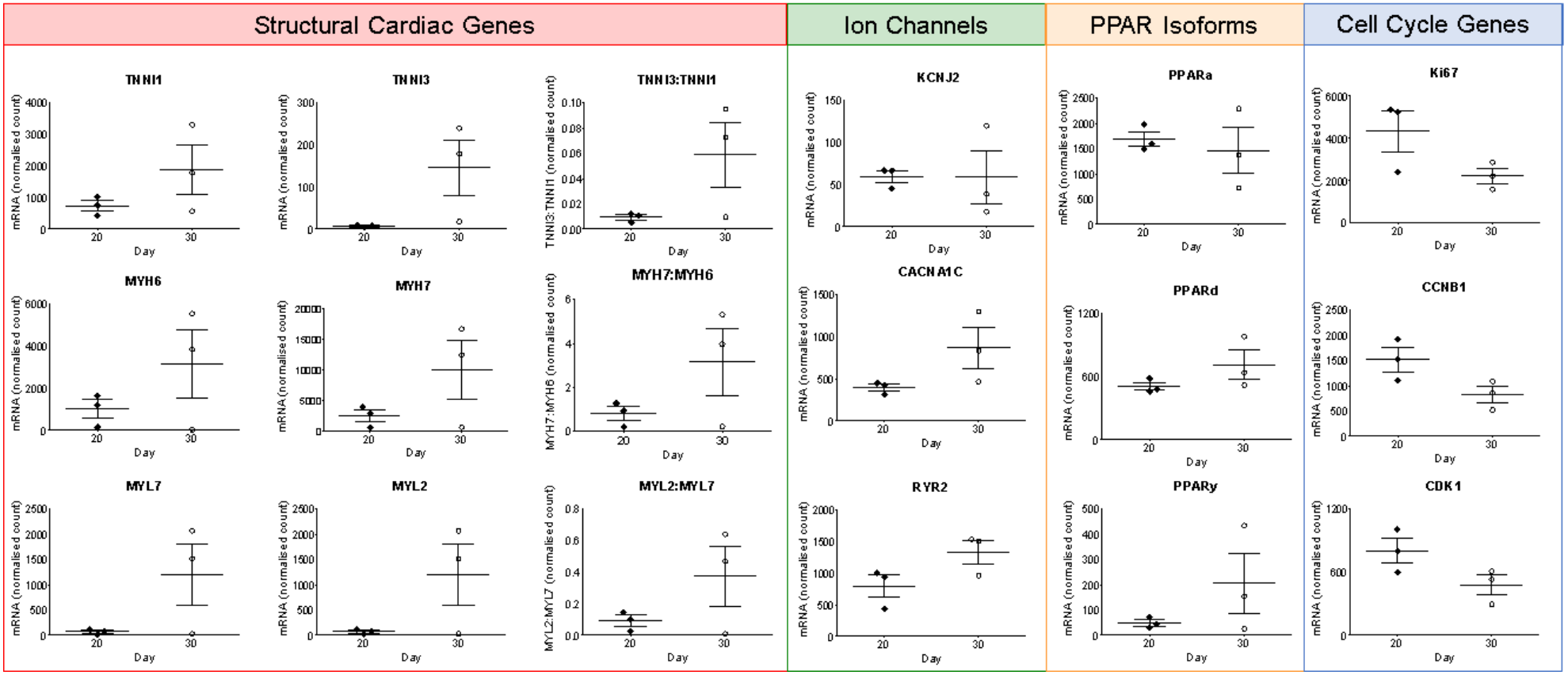

Figure 4-10. Gene expression of iPSC-CMs at day 20 versus day 30.
The normalised counts of the mRNA of genes expressed by iPSC-CMs 20 and 30 days after the start of the differentiation, with the use of GFAM media between days 20 and 30. Genes categorised according to their function. Statistical analysis performed on the normalised counts using unpaired t-test. N=3. Error bars represent SEM.

Overall, the results in Figure 4-10 indicate an increase in genes associated with cardiomyocyte maturity. However, these results are limited in that they lack a day 30 non-fatty acid media control. Based on this data alone it was not clear weather this increase was caused by the addition of fatty acid media or the additional ten days in culture. Therefore, RT-qPCR was used to analyse the effect of additional time in culture as well as fatty acid vs glucose-based media.

RNA was isolated at day 15 of the iPSC-CM differentiation. In addition, iPSC-CMs were dissociated and re-plated at day 15. On day 20, the cardiomyocytes were fed with one of three different medias: normal RPMI/B27 which has a glucose concentration of 11mM (RG), fatty acid-rich media which has a glucose concentration of 0mM (GFAM) and high glucose media which has a glucose concentration of 22mM (HG). The media was changed every other day and RNA was extracted at day 30. Total titin (*TTN*) expression was analysed along with the foetal form *TTN*-N2BA, however neither form shows a significant change in expression under any of the tested conditions and the ratio of *TTN*-N2BA to *TTN* is unchanged. *PPARa* expression is not significantly affected by the tested conditions.

PPARy is the isoform expressed to the lowest level under all tested conditions. *PPARy* expression appears to be downregulated under all media conditions at day 30 compared to day 15, though this is only statistically significant under high glucose conditions. However, this downregulation appears to occur to a lesser extent under GFAM conditions compared to both glucose-containing conditions. The ratio of *PPARy* to *PPARa* is significantly lower at day 30 compared to day 15 under normal and high glucose conditions, but not in fatty acid media.

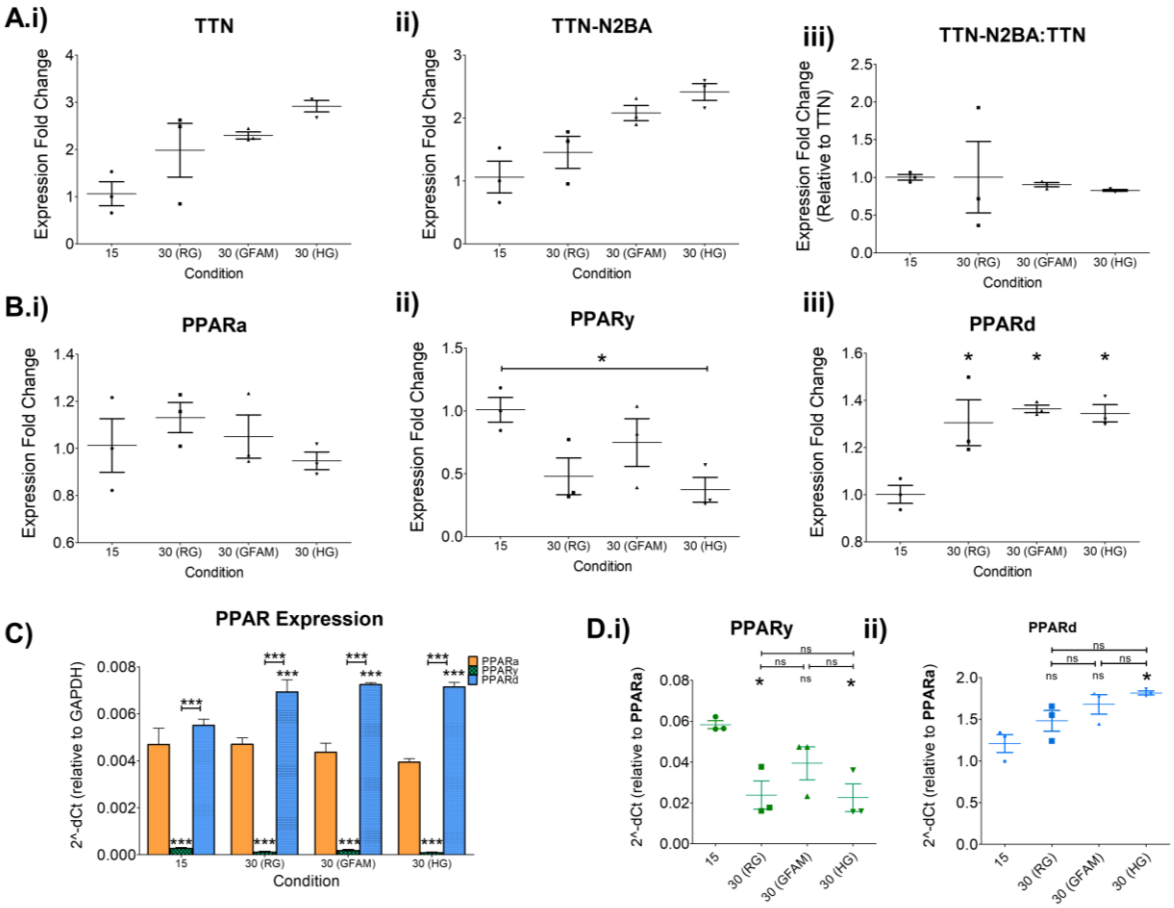

Figure 4-11. Gene expression changes in iPSC-CMs resulting from time in culture in addition to different media conditions.

A. Expression fold change of (i) *TTN* and (ii) *TTN*-N2BA normalised to GAPDH, and (iii) the expression fold change of *TTN*-2BA normalised to *TTN*. Calculated using the ddCt method.

B. Expression fold change of (i) *PPARa*, (ii) *PPARy* and (iii) *PPARd* normalised to GAPDH. Calculated using the ddCt method. Statistics calculated by one-way ANOVA.

C. The expression of each of the PPAR isoforms under each condition, normalised to GAPDH. Plotted as 2^{-ddCt}. Statistics calculated by two-way ANOVA.

D. The expression of (i) *PPARy* and (ii) *PPARd* under each condition, normalised to *PPARa*. Plotted as 2^{-ddCt}. Statistics calculated by one-way ANOVA. * = P≤0.05, ** = P≤0.01, *** = P≤0.001.

N=3. Error bars represent SEM.

At day 30, relative to GAPDH, *PPARd* expression is significantly higher than *PPARa* and *PPARy* expression under all three media conditions. *PPARd* expression is upregulated at day 30 compared to day 15, but its expression does not appear to be affected by the different media conditions. The ratio of *PPARd* to *PPARa* is increased under high glucose conditions, with a value of 1.8±0.03:1.

Overall, culture in fatty acid-based media may have caused an increase in the expression of pro-maturation markers, and appears to have affected metabolic gene expression in a manner that may indicate increased maturation of the cardiomyocytes.

To summarise this section, these results show that cardiomyocyte purity and number can be manipulated by changing the composition of the media supplied to the cells. In addition, changing the type and concentration of substrate available to the cells for metabolism can impact the gene expression profile of the cardiomyocytes. Similar concepts can be used in the differentiation of other cell types, namely cardiac fibroblasts.

4.4 The differentiation and activation of cardiac fibroblasts

In addition to cardiomyocytes, iPSCs can also be differentiated into cardiac fibroblasts. The initiation of cardiac fibroblast differentiation, like cardiomyocyte differentiation, begins with the activation of Wnt signalling followed by its inhibition to induce an epithelial to mesenchymal transition and the development of cardiac progenitor cells. However, after this stage is complete the cells are dissociated and fed with advanced DMEM supplemented with CHIR and retinoic acid. This causes the cells to progress through an epicardial progenitor stage before a second dissociation takes place. The resulting cardiac fibroblast progenitors are stimulated to proliferate and complete differentiation through supplementation with FGF and a TGFβ inhibitor. An overview of this differentiation process is shown in Figure 4-12.

To analyse gene expression changes during differentiation, RNA was isolated from cells at day 0, 4, 8 and 20 of the differentiation process. The expression of various marker genes was analysed by RT-qPCR. The pluripotency marker *nanog* is drastically downregulated from day 4 onwards. The mesoderm markers *TBX20* and *GATA4* are upregulated 1190±180-fold and 1740±240-fold at day 4, respectively. Their expression levels decrease after day 4 but still remain upregulated relative to stem cell levels. The early cardiomyocyte marker *NKX2-5* is upregulated 2-fold at days 4 and 20. Although this upregulation is lower than the 10-fold upregulation seen at day 8 of the cardiomyocyte differentiation, this could indicate the presence of a small cardiomyocyte progenitor population within the differentiating cell population. *COL1A1*, the gene encoding collagen-I subunit A1, is upregulated 29±5-fold from day 4 and remains at this expression level throughout the later time points.

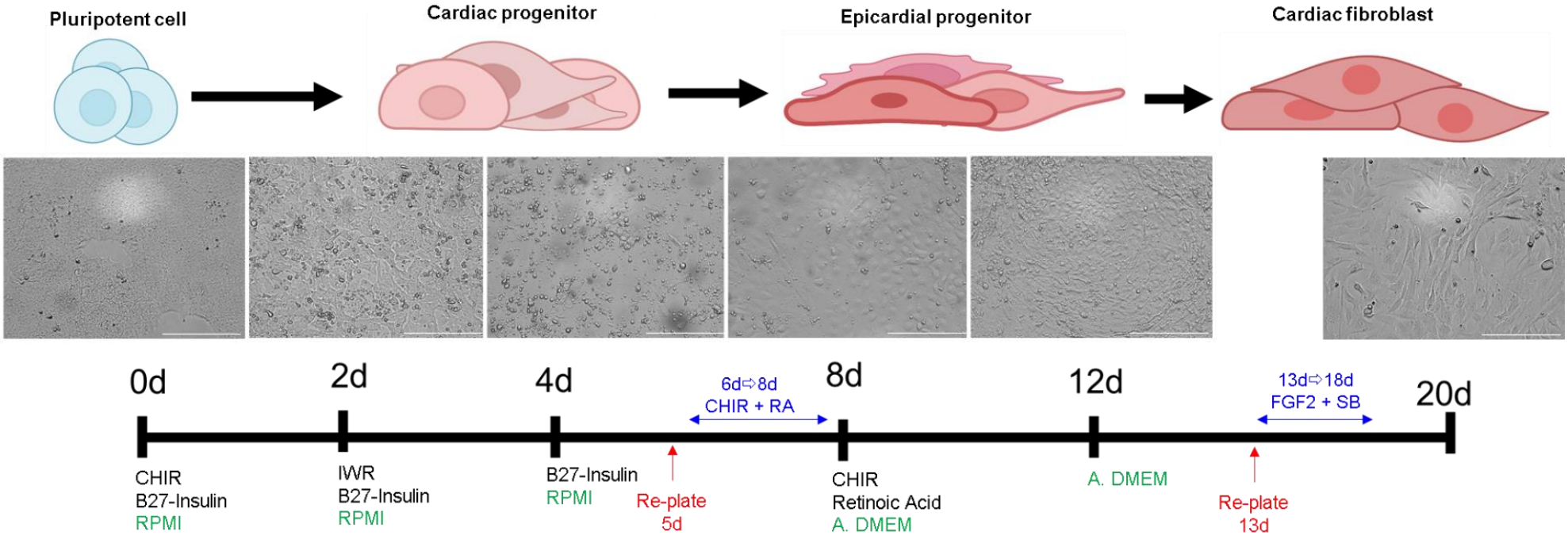

Figure 4-12. Differentiation of iPSCs into cardiac fibroblasts.
Images were taken of the cells in the brightfield channel at 20x magnification on days 0, 2, 4, 8, 12 and 20 of the differentiation protocol. The small molecules and factors used at each time point are listed below the relevant day. The base media is listed in green, points at which the cells are dissociated are indicated in red. The approximate cell stage is depicted above the corresponding images. Scale bar = 200um. (d = day).

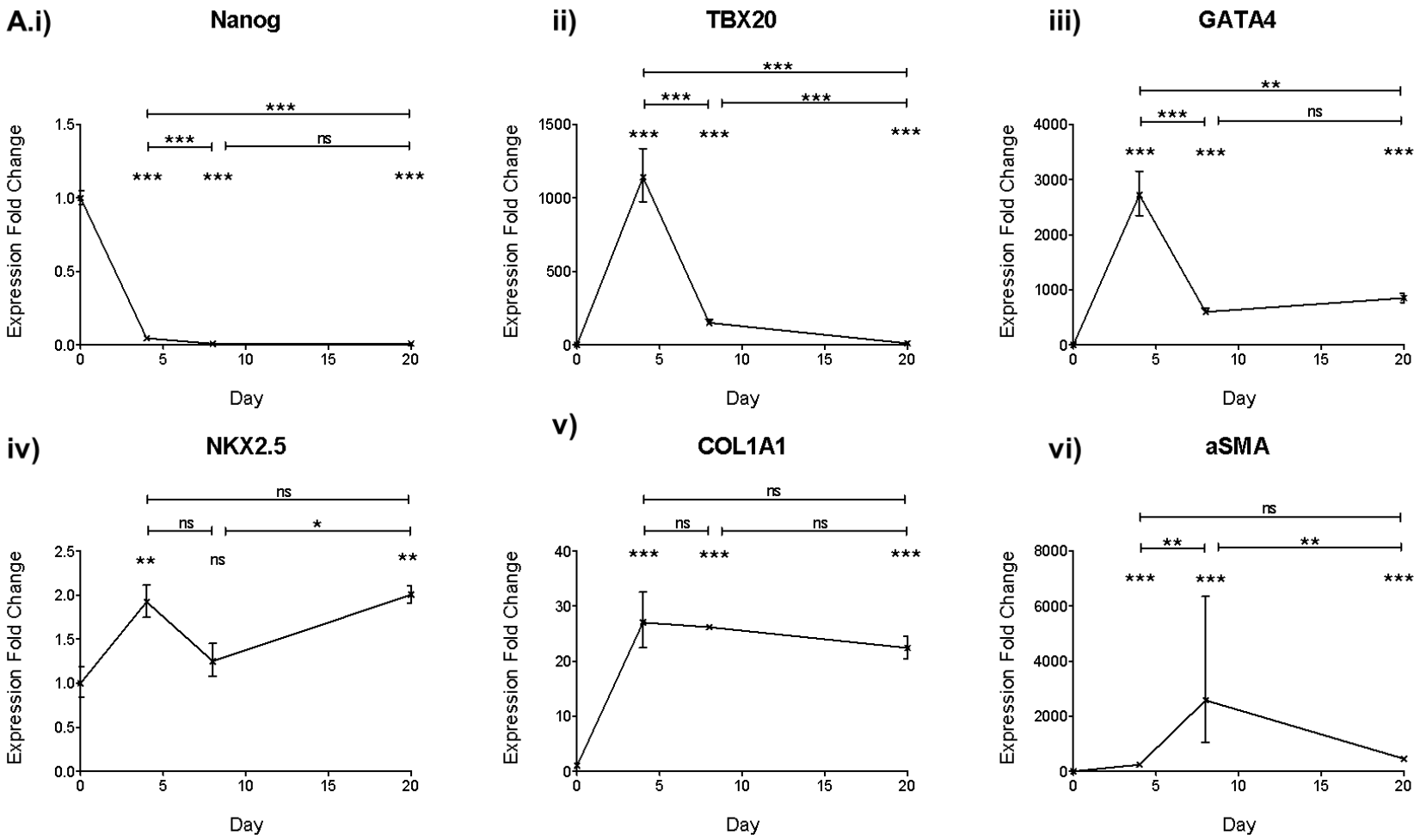

Figure 4-13. Gene expression during iPSC-CF differentiation determined through RT-qPCR

A. Expression of marker genes (i) *nanog*, (ii) *TBX20*, (iii) *GATA4*, (iv) *NKX2-5*, v) COL1A1 and vi) aSMA. Normalised to GAPDH, calculated by ddCt, plotted as fold change relative to day 0. Statistical analysis done by one-way ANOVA. * = P≤0.05, ** = P≤0.01, *** = P≤0.001. N=3. Error bars represent SEM.

The gene for smooth muscle alpha-actin (*aSMA*) is upregulated from day 4 onwards, but peaks at day 8 with an expression fold change of 250±88. Although a marker of activated myofibroblasts, *aSMA* is also important in cell polarity, rigidity and internal cellular communication which may explain why the gene is upregulated part-way through the differentiation.

Once cardiac fibroblasts are differentiated, they can be induced into myofibroblasts in order to model fibrotic activation *in vitro*. This is achieved through a combination of removing serum from the cell media and adding TGFβ. Multiple "activatory" conditions were tested on cardiac fibroblasts to observe the effect on gene expression, the results of which are presented in Figure 4-14. Cells were dissociated on day 22 and re-plated at a split ratio of 1:3. Cells were then fed every other day with either standard media containing 10% serum, 0% serum or 0% serum supplemented with 10ng/uL TGFβ and lysed at day 30. The expression of the fibroblast and myofibroblast markers *COL1A1* and *aSMA* under these conditions were compared to the expression at day 20. *COL1A1* is upregulated under all three conditions at day 30 compared to day 20. At day 30 with 10% serum, *COL1A1* was upregulated 8±2-fold compared to day 20. However, in 0% serum and 0% serum with TGFβ, *COL1A1* was upregulated to an even greater extent (19±0.6 and 23±2-fold higher than day 20 respectively). There was no significant difference between the level of upregulation caused by 0% serum versus 0% serum with TGFβ when compared to day 30 cells in 10% serum, indicating that removing the serum was sufficient to cause *COL1A1* upregulation and that adding TGFβ did not further upregulate *COL1A1*.

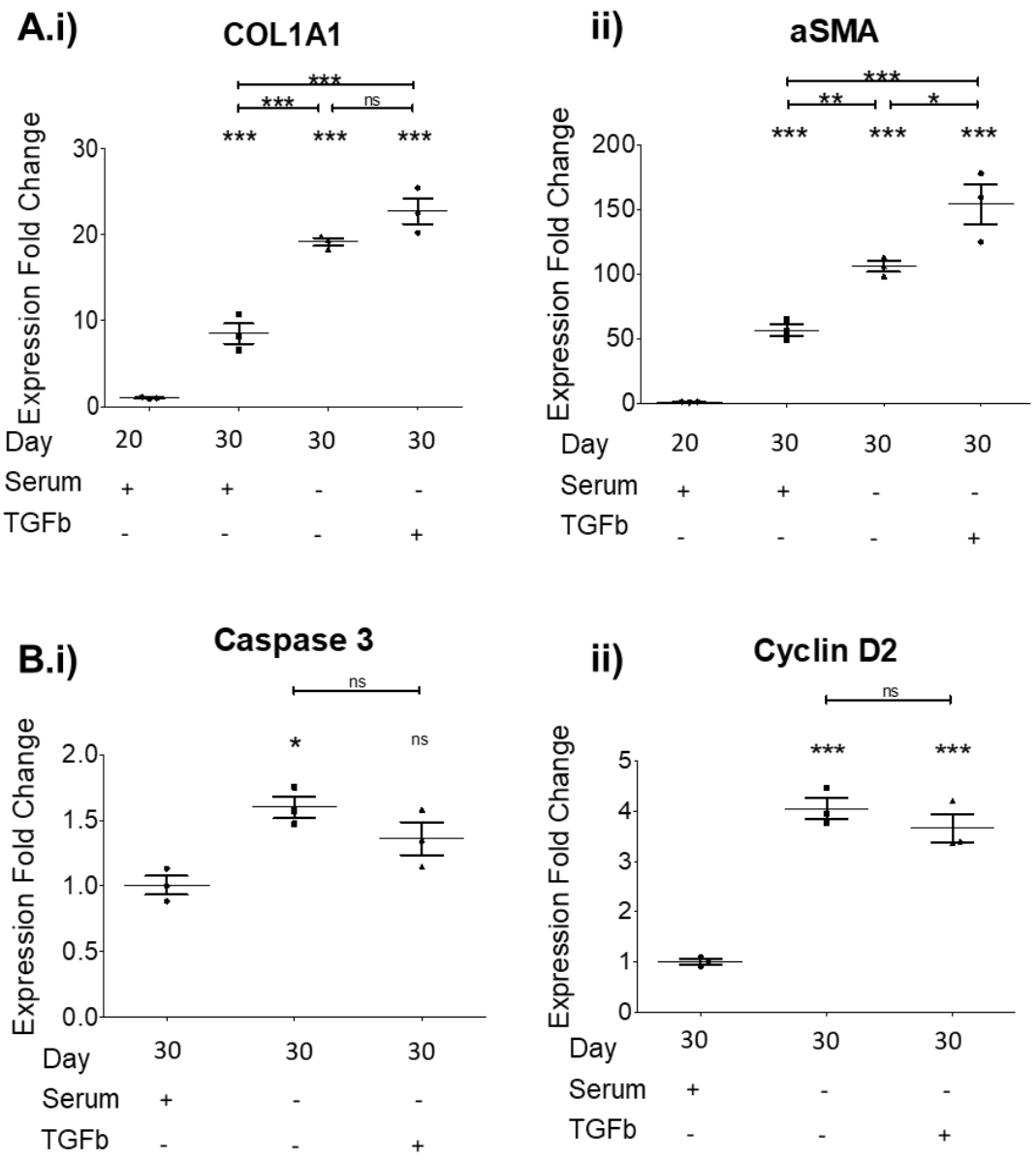

Figure 4-14. Gene expression changes in iPSC-CFs under activatory conditions.
A. Expression of i) COL1A1 and ii) aSMA at day 20 and day 30 with different media conditions. Plotted as fold change relative to day 20 levels.
B. Expression of i) caspase 3 and ii) Cyclin D2 day 30 under different media conditions. Plotted as fold change relative to day 30 levels.
Fold change calculated by ddCt relative to GAPDH, stats calculated by one-way ANOVA. * = P≤0.05, ** = P≤0.01, *** = P≤0.001. N=3. Error bars represent SEM.

Relative to day 20, the expression of *aSMA* was upregulated at day 30 under all tested conditions. At day 30 under 10% serum, *aSMA* was upregulated 56±6-fold compared to day 20. This was increased to 106±6-fold under 0% serum conditions, and increased further to 154±22-fold upon the addition of TGFβ. This shows that dissociation followed by prolonged culture was sufficient to upregulate *aSMA* expression. Removal

of serum from the cells caused a greater level of *aSMA* upregulation, which was compounded by supplementation of TGFβ. Considering increased *aSMA* gene expression as an indicator of myofibroblast activation, then dissociation, extended culture, removal of serum and TGFβ supplementation appear to contribute to the activation of cardiac fibroblasts.

To further asses the effect of removing serum and adding TGFβ to cardiac fibroblasts, the expression of the apoptosis gene caspase 3 and the cell cycle regulator cyclin D2 was evaluated. Compared to normal conditions at day 30, the expression of caspase 3 was slightly upregulated by 1.6±0.1-fold under 0% serum and 1.4±0.2-fold with TGFβ added. The results in Figure 4-14 show that the removal of serum and addition of TGFβ both cause a 4-fold upregulation of cyclin D2 expression compared to 10% serum conditions. However, there is no additive effect of TGFβ to the removal of serum alone, indicating that serum-starving the fibroblasts is sufficient to upregulate cyclin D2 expression.

Overall, these results demonstrate the utilisation of established protocols in the differentiation of cardiac fibroblasts from iPSCs. In addition, these iPSC-CFs can be induced into an activated state through the manipulation of media composition. IPSC-CMs and iPSC-CFs developed using these methods were used to investigate the expression of SNORD116 during cardiac development.

4.5 The expression of SNORD116 during cardiomyocyte and cardiac fibroblast development

SNORD116 is a small nucleolar RNA (snoRNA) with 30 different paralogue sequences (SNORD116-1 to SNORD116-30). Historically, these have been categorised into three groups based on sequence similarity: group I (SNORD1161-SNORD116-9), group II (SNORD116-10 to SNORD116-24) and group III (SNORD116-25 to SNORD116-29). Because there are so many different paralogues of SNORD116, analysing the expression of just one paralogue may not always be sufficient for gaining a comprehensive understanding of SNORD116 activity. In view of this, it was necessary to fully explore the differences between the individual paralogues in order to inform subsequent analysis.

Each of the 30 paralogue sequences were blasted against each other using nucleotide-nucleotide basic local alignment search tool (BLASTn), an online software available through NCBI (383). The software aligns the sequences and calculates the percentage identity i.e. the percentage of identical base pairs within the region of alignment. To account for differences in sequence length, the percentage identity was multiplied by the percentage coverage of the shorter sequence over the longer sequence, which was multiplied by the length difference factor (longer/shorter) to give percentage sequence similarity. Any percentage identity $<$12% is too dissimilar to be detectable by the software. Using this method, the human SNORD116 paralogues were compared to each other and to the 17 mouse SNORD116 paralogue sequences. The results are shown in Figure 4-15 and Figure 4-16. Examples of alignments between SNORD116 paralogues are shown in Figure 4-17.

A.

0% Sequence Similarity 100%

Similarity (%)	S116-1	S116-2	S116-3	S116-4	S116-5	S116-6	S116-7	S116-8	S116-9	S116-10	S116-11	S116-12	S116-13	S116-14	S116-15	S116-16	S116-17	S116-18	S116-19	S116-20	S116-21	S116-22	S116-23	S116-24	S116-25	S116-26	S116-27	S116-28	S116-29	S116-30
S116-1	100.00%	95.88%	96.91%	92.86%	95.88%	94.90%	95.88%	94.85%	96.91%	50.70%	77.55%	80.82%	78.57%	87.76%	85.71%	84.69%	86.73%	86.73%	86.73%	85.71%	85.71%	85.71%	83.67%	82.65%	43.97%	43.64%	35.24%	0.00%	52.95%	0.00%
S116-2	95.88%	100.00%	95.88%	95.92%	94.85%	98.98%	94.85%	95.88%	95.88%	52.55%	60.73%	81.84%	77.55%	88.78%	86.73%	85.71%	87.76%	86.73%	87.76%	86.73%	87.76%	86.73%	85.71%	82.65%	19.95%	46.23%	35.24%	0.00%	53.60%	0.00%
S116-3	96.91%	95.88%	100.00%	95.92%	98.97%	94.90%	98.97%	97.94%	100.00%	50.70%	77.55%	80.82%	78.57%	87.76%	85.71%	84.69%	86.73%	85.71%	86.73%	85.71%	86.73%	85.71%	85.71%	81.63%	34.20%	19.00%	35.24%	0.00%	51.30%	0.00%
S116-4	92.86%	95.92%	95.92%	100.00%	94.90%	95.92%	94.90%	95.92%	95.92%	50.70%	58.67%	79.00%	76.77%	85.86%	83.84%	82.83%	84.85%	83.84%	84.85%	83.84%	84.85%	83.84%	83.84%	80.81%	34.20%	45.00%	35.24%	0.00%	52.11%	0.00%
S116-5	95.88%	94.85%	98.97%	94.90%	100.00%	93.88%	100.00%	96.91%	98.97%	50.70%	78.57%	80.82%	78.57%	87.76%	86.73%	84.69%	86.73%	85.71%	86.73%	85.71%	86.73%	85.71%	86.73%	81.63%	34.20%	19.00%	35.24%	0.00%	51.30%	0.00%
S116-6	94.90%	98.98%	94.90%	95.92%	93.88%	100.00%	93.88%	96.94%	94.90%	52.55%	60.73%	82.00%	77.78%	88.89%	86.87%	85.86%	87.88%	86.87%	87.88%	86.87%	87.88%	86.87%	85.86%	82.83%	34.20%	46.87%	35.24%	0.00%	53.82%	0.00%
S116-7	95.88%	94.85%	98.97%	94.90%	100.00%	93.88%	100.00%	96.91%	98.97%	50.70%	78.57%	80.82%	78.57%	87.76%	86.73%	84.69%	86.73%	85.71%	86.73%	85.71%	86.73%	85.71%	86.73%	81.63%	34.20%	19.00%	35.24%	0.00%	51.30%	0.00%
S116-8	94.85%	95.88%	97.94%	95.92%	96.91%	96.94%	96.91%	100.00%	97.94%	50.70%	77.55%	80.82%	78.57%	87.76%	85.71%	84.69%	86.73%	85.71%	86.73%	85.71%	86.73%	85.71%	85.71%	81.63%	19.95%	45.94%	35.24%	0.00%	53.60%	0.00%
S116-9	96.91%	95.88%	100.00%	95.92%	98.97%	94.90%	98.97%	97.94%	100.00%	50.70%	77.55%	80.82%	78.57%	87.76%	85.71%	84.69%	86.73%	85.71%	86.73%	85.71%	86.73%	85.71%	85.71%	81.63%	34.20%	19.00%	35.24%	0.00%	51.30%	0.00%
S116-10	55.00%	57.00%	55.00%	55.00%	55.00%	57.00%	55.00%	55.00%	55.00%	100.00%	56.62%	71.09%	54.52%	73.07%	74.02%	58.71%	74.02%	73.07%	74.02%	73.07%	73.07%	73.07%	57.66%	56.62%	17.00%	16.00%	38.00%	0.00%	39.56%	0.00%
S116-11	77.55%	59.86%	77.55%	57.00%	78.57%	59.00%	78.57%	77.55%	77.55%	51.39%	100.00%	83.25%	84.04%	87.23%	89.36%	89.36%	88.30%	87.23%	88.30%	89.36%	87.23%	89.36%	88.30%	86.17%	43.76%	16.00%	17.00%	0.00%	54.07%	0.00%
S116-12	80.82%	81.84%	80.82%	79.00%	80.82%	82.00%	80.82%	80.82%	80.82%	71.87%	83.25%	100.00%	85.36%	90.62%	90.62%	88.51%	91.68%	90.62%	91.68%	90.62%	90.62%	90.62%	85.36%	87.47%	0.00%	0.00%	0.00%	12.00%	0.00%	0.00%
S116-13	78.57%	77.55%	78.57%	76.77%	78.57%	77.78%	78.57%	78.57%	78.57%	49.48%	84.04%	85.36%	100.00%	86.17%	86.17%	88.30%	87.23%	86.17%	87.23%	88.30%	86.17%	86.17%	85.11%	89.36%	42.75%	18.00%	19.95%	12.00%	53.39%	0.00%
S116-14	87.76%	88.78%	87.76%	85.86%	87.76%	88.89%	87.76%	87.76%	87.76%	73.86%	87.23%	90.62%	86.17%	100.00%	97.87%	95.74%	98.94%	97.87%	98.94%	97.87%	97.87%	97.87%	92.55%	92.55%	44.77%	44.75%	74.00%	0.00%	56.42%	0.00%
S116-15	85.71%	86.73%	85.71%	83.84%	86.73%	86.87%	86.73%	85.71%	85.71%	74.81%	89.36%	90.62%	86.17%	97.87%	100.00%	95.74%	98.94%	97.87%	98.94%	97.87%	97.87%	97.87%	94.68%	92.55%	44.77%	44.75%	45.79%	0.00%	56.42%	0.00%
S116-16	84.69%	85.71%	84.69%	82.83%	84.69%	85.86%	84.69%	84.69%	84.69%	53.29%	89.36%	88.51%	88.30%	95.74%	95.74%	100.00%	96.81%	95.74%	96.81%	95.74%	95.74%	95.74%	94.68%	96.81%	46.81%	46.78%	44.77%	0.00%	57.59%	0.00%
S116-17	86.73%	87.76%	86.73%	84.85%	86.73%	87.88%	86.73%	86.73%	86.73%	74.81%	88.30%	91.68%	87.23%	98.94%	98.94%	96.81%	100.00%	98.94%	100.00%	98.94%	98.94%	98.94%	93.62%	93.62%	44.77%	44.75%	45.79%	0.00%	56.42%	0.00%
S116-18	86.73%	86.73%	85.71%	83.84%	85.71%	86.87%	85.71%	85.71%	85.71%	73.86%	87.23%	90.62%	86.17%	97.87%	97.87%	95.74%	98.94%	100.00%	98.94%	97.87%	97.87%	97.87%	92.55%	92.55%	45.79%	45.25%	44.77%	0.00%	55.25%	0.00%
S116-19	86.73%	87.76%	86.73%	84.85%	86.73%	87.88%	86.73%	86.73%	86.73%	74.81%	88.30%	91.68%	87.23%	98.94%	98.94%	96.81%	100.00%	98.94%	100.00%	98.94%	98.94%	98.94%	93.62%	93.62%	44.77%	44.75%	45.79%	0.00%	56.42%	0.00%
S116-20	85.71%	86.73%	85.71%	83.84%	85.71%	86.87%	85.71%	85.71%	85.71%	73.86%	89.36%	90.62%	88.30%	97.87%	97.87%	95.74%	98.94%	97.87%	98.94%	100.00%	97.87%	97.87%	92.55%	92.55%	44.77%	44.75%	45.79%	0.00%	56.42%	0.00%
S116-21	85.71%	87.76%	86.73%	84.85%	86.73%	87.88%	86.73%	86.73%	86.73%	73.86%	87.23%	90.62%	86.17%	97.87%	97.87%	95.74%	98.94%	97.87%	98.94%	97.87%	100.00%	97.87%	92.55%	92.55%	44.77%	44.75%	45.79%	0.00%	56.42%	0.00%
S116-22	85.71%	86.73%	85.71%	83.84%	85.71%	86.87%	85.71%	85.71%	85.71%	73.86%	89.36%	90.62%	86.17%	97.87%	97.87%	95.74%	98.94%	97.87%	98.94%	97.87%	97.87%	100.00%	92.55%	92.55%	45.79%	19.00%	45.79%	0.00%	55.25%	0.00%
S116-23	83.67%	85.71%	85.71%	83.84%	86.73%	85.86%	86.73%	85.71%	85.71%	52.34%	88.30%	85.36%	85.11%	92.55%	94.68%	94.68%	93.62%	92.55%	93.62%	92.55%	92.55%	92.55%	100.00%	92.55%	45.79%	45.76%	43.76%	0.00%	57.59%	0.00%
S116-24	82.65%	82.65%	81.63%	80.81%	81.63%	82.83%	81.63%	81.63%	81.63%	51.39%	86.17%	87.47%	89.36%	92.55%	92.55%	96.81%	93.62%	92.55%	93.62%	92.55%	92.55%	92.55%	92.55%	100.00%	75.00%	73.47%	72.00%	70.45%	57.59%	0.00%
S116-25	46.24%	19.00%	33.25%	32.30%	33.25%	32.30%	33.25%	19.00%	33.25%	15.00%	45.26%	0.00%	44.25%	46.31%	46.31%	48.42%	46.31%	47.37%	46.31%	46.31%	46.31%	47.37%	47.37%	75.00%	100.00%	93.88%	89.36%	83.29%	78.12%	76.04%
S116-26	44.37%	47.00%	19.00%	46.50%	19.00%	48.43%	19.00%	46.70%	19.00%	15.00%	17.00%	0.00%	18.95%	44.75%	44.75%	46.78%	44.75%	45.25%	44.75%	44.75%	44.75%	19.95%	45.76%	73.47%	93.88%	100.00%	84.69%	0.00%	78.57%	79.17%
S116-27	34.29%	34.29%	34.29%	33.33%	34.29%	33.33%	34.29%	34.29%	34.29%	34.00%	17.00%	0.00%	19.95%	74.00%	47.37%	46.31%	47.37%	46.31%	47.37%	47.37%	47.37%	47.37%	45.26%	72.00%	89.36%	84.69%	100.00%	0.00%	70.00%	75.00%
S116-28	0.00%	0.00%	0.00%	0.00%	0.00%	0.00%	0.00%	0.00%	0.00%	0.00%	0.00%	12.00%	12.00%	0.00%	0.00%	0.00%	0.00%	0.00%	0.00%	0.00%	0.00%	0.00%	0.00%	70.45%	83.29%	0.00%	62.60%	100.00%	100.00%	69.37%
S116-29	48.21%	48.80%	46.70%	48.22%	46.70%	49.80%	46.70%	48.80%	46.70%	32.20%	48.42%	0.00%	48.46%	50.53%	50.53%	51.58%	50.53%	49.48%	50.53%	50.53%	50.53%	49.48%	51.58%	51.58%	78.12%	78.57%	61.66%	0.00%	0.00%	84.71%
S116-30	31.00%	46.00%	31.00%	32.18%	31.00%	47.00%	31.00%	33.00%	31.00%	18.14%	19.86%	0.00%	0.00%	20.91%	20.91%	20.91%	20.91%	20.91%	20.91%	20.91%	20.91%	20.91%	20.91%	20.91%	73.76%	76.79%	72.75%	59.80%	82.17%	100.00%

B.

	S116-1	S116-2	S116-3	S116-4	S116-5	S116-6	S116-7	S116-8	S116-9	S116-10	S116-11	S116-12	S116-13	S116-14	S116-15	S116-16	S116-17
S116-1	100.00%	95.86%	97.45%	97.53%	96.02%	99.54%	97.22%	97.60%	94.94%	95.18%	94.10%	96.75%	96.99%	97.22%	97.22%	97.30%	96.68%
S116-2	96.83%	100.00%	97.45%	97.14%	99.85%	96.91%	97.22%	97.22%	95.18%	95.02%	94.10%	97.22%	99.38%	98.15%	98.15%	97.22%	97.68%
S116-3	97.45%	96.48%	100.00%	98.22%	96.62%	97.37%	99.77%	98.30%	95.49%	95.33%	94.86%	97.30%	97.91%	98.53%	98.53%	98.15%	96.91%
S116-4	97.53%	96.17%	98.22%	100.00%	96.33%	97.45%	97.99%	99.92%	95.10%	95.02%	94.41%	96.91%	97.14%	97.37%	97.37%	98.53%	97.14%
S116-5	96.99%	99.85%	97.60%	97.30%	100.00%	97.06%	97.37%	97.37%	95.18%	95.02%	94.25%	99.77%	97.06%	97.22%	97.22%	97.37%	97.68%
S116-6	99.54%	95.94%	97.37%	97.45%	96.09%	100.00%	97.14%	97.53%	94.94%	95.18%	94.17%	96.99%	99.30%	98.07%	98.07%	97.22%	96.75%
S116-7	97.22%	96.25%	99.77%	97.99%	96.40%	97.14%	100.00%	98.07%	95.33%	95.25%	94.78%	97.37%	97.99%	98.61%	98.61%	98.07%	96.68%
S116-8	97.60%	96.25%	98.30%	99.92%	96.40%	97.53%	98.07%	100.00%	95.10%	95.02%	94.48%	95.75%	96.06%	96.37%	96.37%	98.61%	97.22%
S116-9	95.90%	95.18%	96.45%	96.06%	95.18%	95.90%	96.29%	96.06%	100.00%	98.01%	95.33%	95.98%	96.06%	96.29%	96.29%	96.37%	95.60%
S116-10	96.14%	95.02%	96.29%	95.98%	95.02%	96.14%	96.21%	95.98%	99.00%	100.00%	96.02%	94.02%	94.71%	94.86%	94.86%	96.29%	95.52%
S116-11	94.10%	94.10%	94.86%	94.41%	94.25%	94.17%	94.78%	94.48%	96.29%	96.99%	100.00%	95.52%	95.60%	95.90%	95.90%	94.86%	93.56%
S116-12	95.67%	94.34%	95.90%	95.52%	94.49%	95.67%	95.83%	95.52%	96.29%	95.55%	94.26%	100.00%	96.91%	97.06%	97.06%	95.90%	95.05%
S116-13	99.46%	95.78%	97.22%	97.30%	95.94%	99.77%	96.99%	97.37%	94.79%	95.02%	94.02%	96.91%	100.00%	97.84%	97.84%	97.06%	96.60%
S116-14	97.14%	96.02%	99.38%	97.91%	96.17%	97.06%	99.30%	97.99%	95.10%	95.10%	94.71%	97.06%	97.84%	100.00%	99.85%	97.84%	96.60%
S116-15	97.30%	96.25%	98.15%	98.53%	96.40%	97.22%	98.07%	98.61%	95.41%	95.33%	94.86%	97.06%	97.84%	99.85%	100.00%	99.85%	96.60%
S116-16	97.30%	96.25%	98.15%	98.53%	96.40%	97.22%	98.07%	98.61%	95.41%	95.33%	94.86%	96.60%	96.60%	96.60%	96.60%	100.00%	96.60%
S116-17	96.68%	96.70%	96.91%	97.14%	96.70%	96.75%	96.68%	97.22%	94.64%	94.56%	93.56%	97.14%	97.30%	97.30%	96.68%	96.60%	100.00%

Figure 4-15. Sequence similarity between the human and mouse isoforms of SNORD116.
The level sequence similarity between each of the SNORD116 paralogue sequences in (A) human and (B) mouse, calculated as a percentage. The colour scale indicates the level of similarity: red = 0% similarity, yellow = 50% similarity, green = 100% identical. S116 = SNORD116.

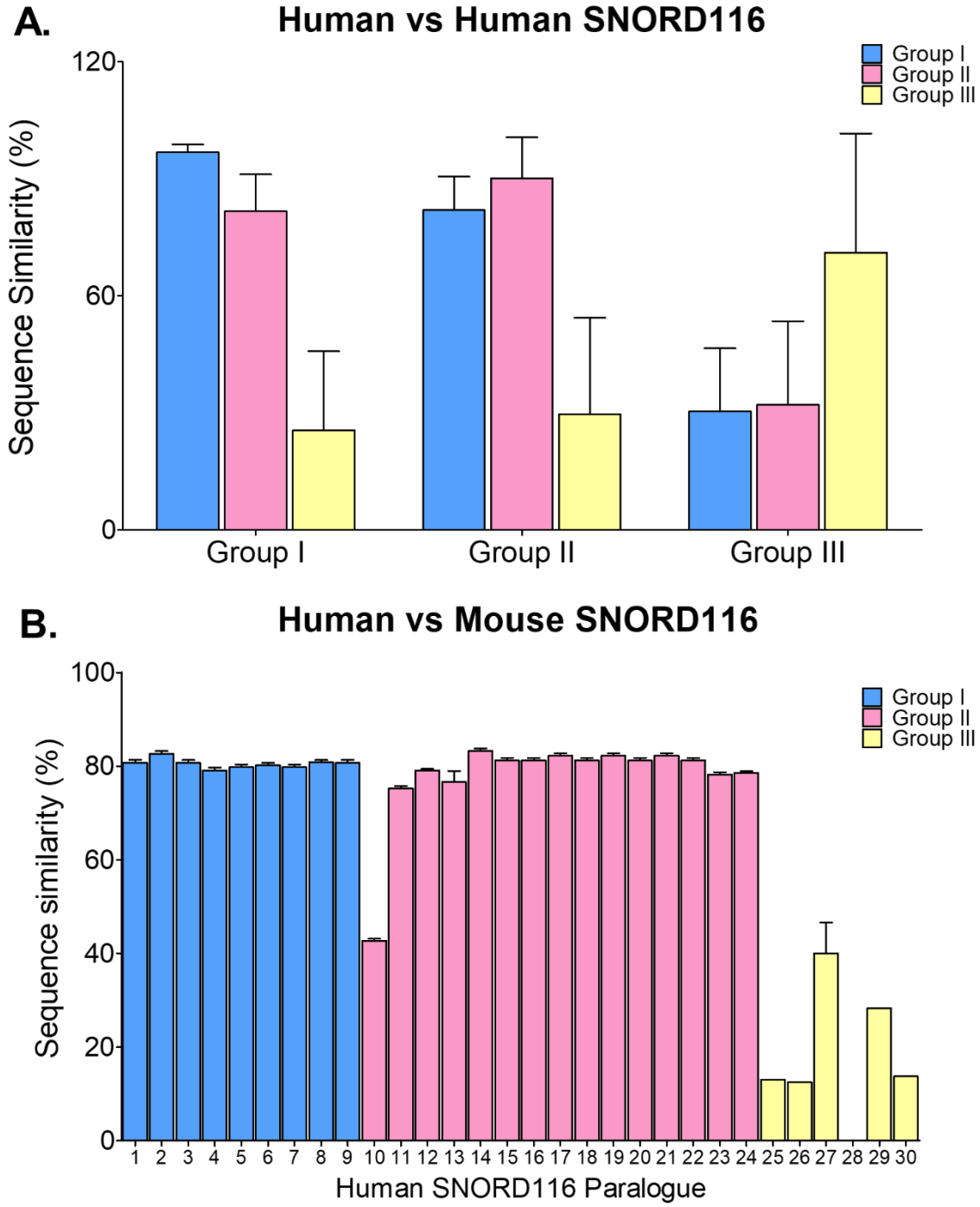

Figure 4-16. Sequence similarity of human and mouse SNORD116.
A. The average sequence similarity of the human SNORD116 paralogue sequences in each group compared to the other groups. Error bars represent standard deviation across the paralogues within the group.
B. The average percentage similarity of each human SNORD116 paralogue compared to each mouse SNORD116 paralogue. Error bars represent standard deviation in % similarity across the 17 mouse paralogue sequences.
Blue = group I, pink = group II and yellow = group III.

Figure 4-17. Sequence alignment between various SNORD116 paralogues. Representative SNORD116 paralogues have been compared to SNORD116-1 to demonstrate how the sequences align. Group I paralogues (SNORD116-1 and SNORD116-2) are blue, Group II paralogues (SNORD116-12) are pink and Group III paralogues (SNORD116-25) are yellow. Alignments generated using BLAST

The similarity between human SNORD116 paralogues ranges from 0-100%. Within group I, the paralogues show a high level of similarity at 97±2% similar to each other. The paralogues in group II are 82±9% similar to each other, with paralogues 10-13 showing the greatest level of discrepancy to the rest of the group. Group III shows the highest level of uniqueness within the group with only 71±31% similarity within the group. Group III also demonstrates the greatest level of dissimilarity to the other groups, with a percentage similarity of 30±16% and 32±21% to groups I and II, respectively. Contrastingly, group I is highly similar to group II with a percentage similarity of 82±9%.

Interestingly, Figure 4-15 shows that the 17 mouse paralogue sequences of SNORD116 are all highly similar to each other and are therefore not categorised into groups. As shown in Figure 4-16B, when compared to the mouse paralogues, the majority of group I and group II paralogues are around 80% similar to mouse SNORD116, with the exception of human SNORD116-10 which is only 43±0.4% similar to mouse SNORD116. However, within group III there is a much greater discrepancy between the human and mouse sequences. SNORD116-28 shows 0% similarity to mouse SNORD116, and the highest level of

similarity is 40±6% between SNORD116-27 and mouse SNORD116. These results further demonstrate the higher level of uniqueness within the paralogues of group III relative to the other groups.

Using methods described previously, iPSCs were differentiated into both cardiomyocytes and cardiac fibroblasts. Different conditions were used to influence the differentiation, maturation, and activation of these cardiac cell types. This was used to investigate the expression of SNORD116 during development. As an alternative to analysing the expression of all 30 paralogues of SNORD116, representative paralogues were selected from each of the three groups. Group I is represented by SNORD116-1, group II by SNORD116-23 and SNORD116-24, and group III by SNORD116-25 and SNORD116-29. Also, SNORD116-23, SNORD116-25 and SNORD116-29 were previously shown to be involved in signalling during cardiac stress (65).

Figure 4-18 shows the expression of these paralogues during cardiomyocyte differentiation. All of the SNORD116 paralogues analysed follow the same general trend. Expression does not change after two days, however on day 4 expression is around 2-fold upregulated relative to stem cell level. After day 4 expression appears to decrease in SNORD116-1, 25 and 29 but remains upregulated in SNORD116-23 and SNORD116-24. However, at day 15, SNORD116 expression has been restored to stem cell levels in all paralogues.

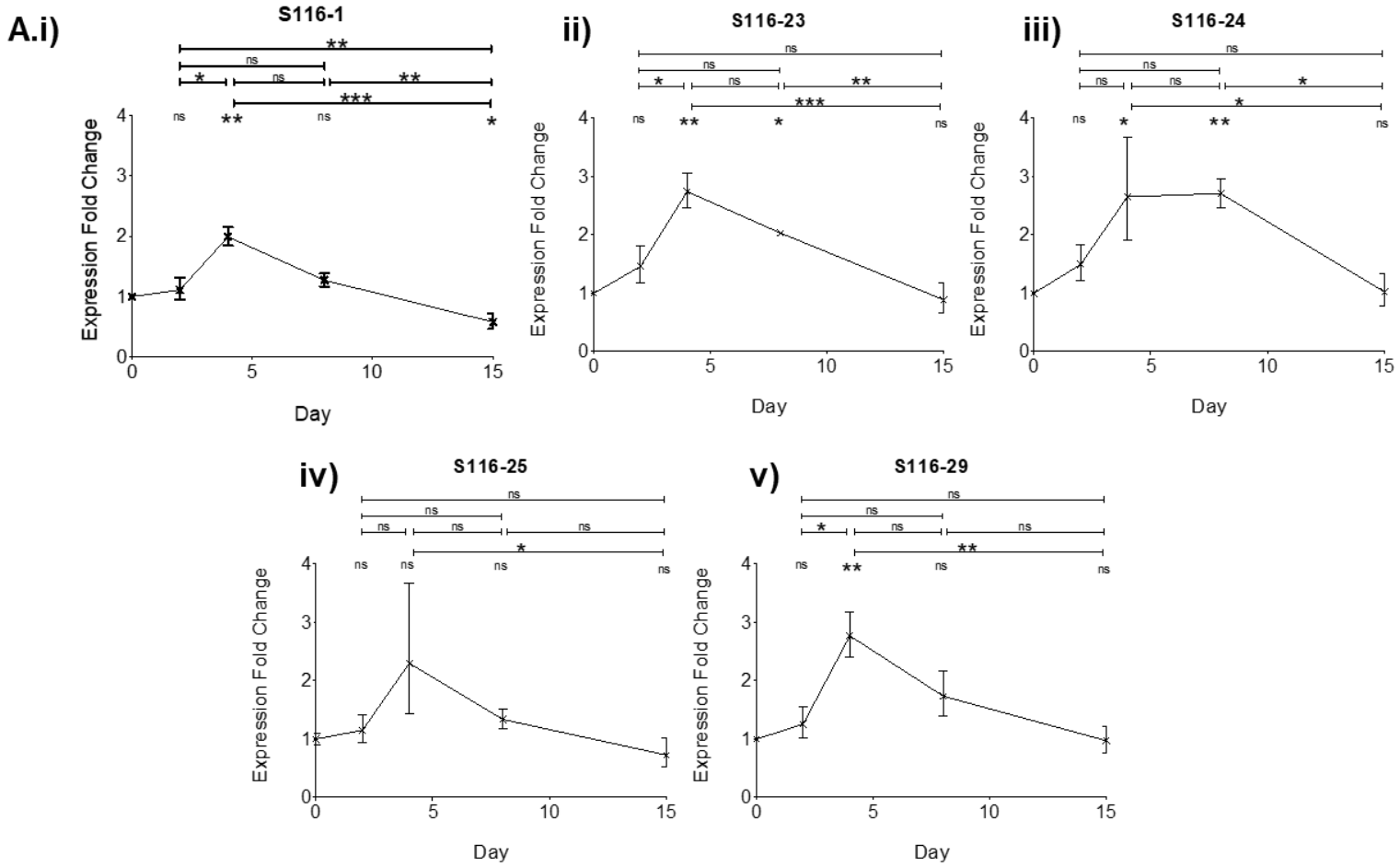

Figure 4-18. The expression of SNORD116 during iPSC-CM differentiation.
The expression of i) SNORD116-1, ii) SNORD116-23, iii) SNORD116-24, iv) SNORD116-25 and v) SNORD116-29 during iPSC-CM differentiation. Plotted as fold change relative to day 0 expression, calculated by ddCt normalised to GAPDH. Statistics calculated by one-way ANOVA. * = P≤0.05, ** = P≤0.01, *** = P≤0.001. N=3. Error bars represent SEM.

As shown in Figure 4-11, changing the media supplied to cardiomyocytes can change their metabolic gene expression, which may influence their state of maturity. Figure 4-19 shows how SNORD116 expression responds to pro- and anti-maturation influences. SNORD116-1, 23, 24 and 29 show no significant expression changes at day 30 compared to day 15 regardless of media composition. However, SNORD116-25 is upregulated 2.5±0.7-fold under high glucose conditions. In addition, SNORD116-1 is upregulated 1.8-fold in response to CHIR.

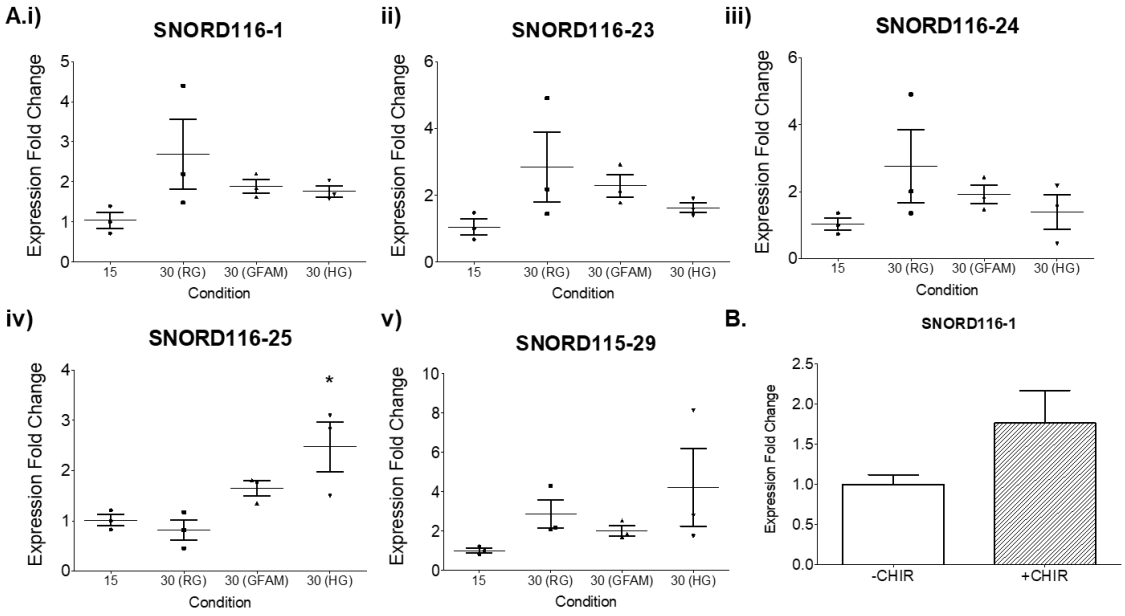

Figure 4-19. The effect of media manipulation on SNORD116 expression in iPSC-CMs.
A. The expression of SNORD116 paralogues i) 1, ii) 23, iii) 24, iv) 25 and v) 29 at day 15 and day 30 in various media conditions. Expression plotted as fold change relative to day 15. Calculated using ddCt normalised to GAPDH. Statistics calculated using one-way ANOVA. * = P ≤0.05. N=3. Error bars represent SEM. RG = regular glucose, GFAM = fatty acid media, HG = high glucose.
B. The expression of SNORD116-1 in response to CHIR. Plotted as fold change relative to control. Calculated by ddCt normalised to GAPDH. N=1. Error bars represent SEM.

SNORD116 expression was also analysed in iPSC-CFs, as shown in Figure 4-20. During cardiac fibroblast differentiation, SNORD116-23, 24 and 29 show an upregulation of around 2-fold at day 4 relative to day 0. SNORD116-1 and SNORD116-25 show no change in expression at day 4. However, across all paralogues at day 8 expression is 0.5-fold that of stem cell levels and remains downregulated at day 20. The key difference between cardiomyocyte differentiation and cardiac fibroblast differentiation is the downregulation of SNORD116 from day 8 to below stem cell levels, which does not occur in the cardiomyocyte time course.

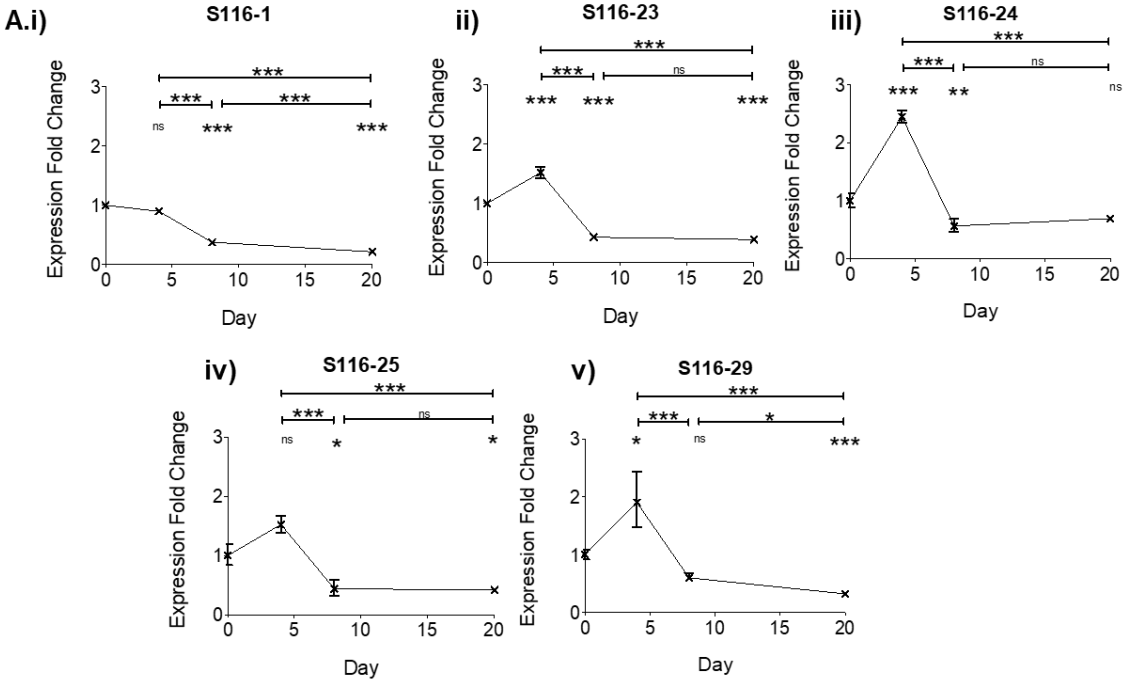

Figure 4-20. The expression of SNORD116 during cardiac fibroblast differentiation. The expression of i) SNORD116-1, ii) SNORD116-23, iii) SNORD116-24, iv) SNORD116-25 and v) SNORD116-29 during iPSC-CF differentiation. Plotted as fold change relative to day 0 expression, calculated by ddCt normalised to GAPDH. Statistics calculated by one-way ANOVA. * = P≤0.05, ** = P≤0.01, *** = P≤0.001. N=3. Error bars represent SEM.

Cardiac fibroblasts were subjected to activatory conditions in order to asses how the expression of SNORD116 was affected. The results are shown in . In cardiac fibroblasts, Figure 4-21 shows that an additional ten days in serum-containing media from day 20 to day 30 does not cause any change to the expression on any of the SNORD116 paralogue sequences. However, upon removal of the serum, SNORD116-1 is upregulated 2.8±0.2-fold. SNORD116-23, 24 and 25 are upregulated 3.6±0.3, 4.2±0.6 and 3.6±0.3-fold, respectively. SNORD116-29 shows the highest upregulation at 5.8±0.5-fold relative to day 20. There is no significant difference in the expression of SNORD116 in 0% serum versus 0% serum supplemented with TGFβ, implying there is no additive effect of the TGFβ on the upregulation of SNORD116 in cardiac fibroblasts in serum-starved conditions.

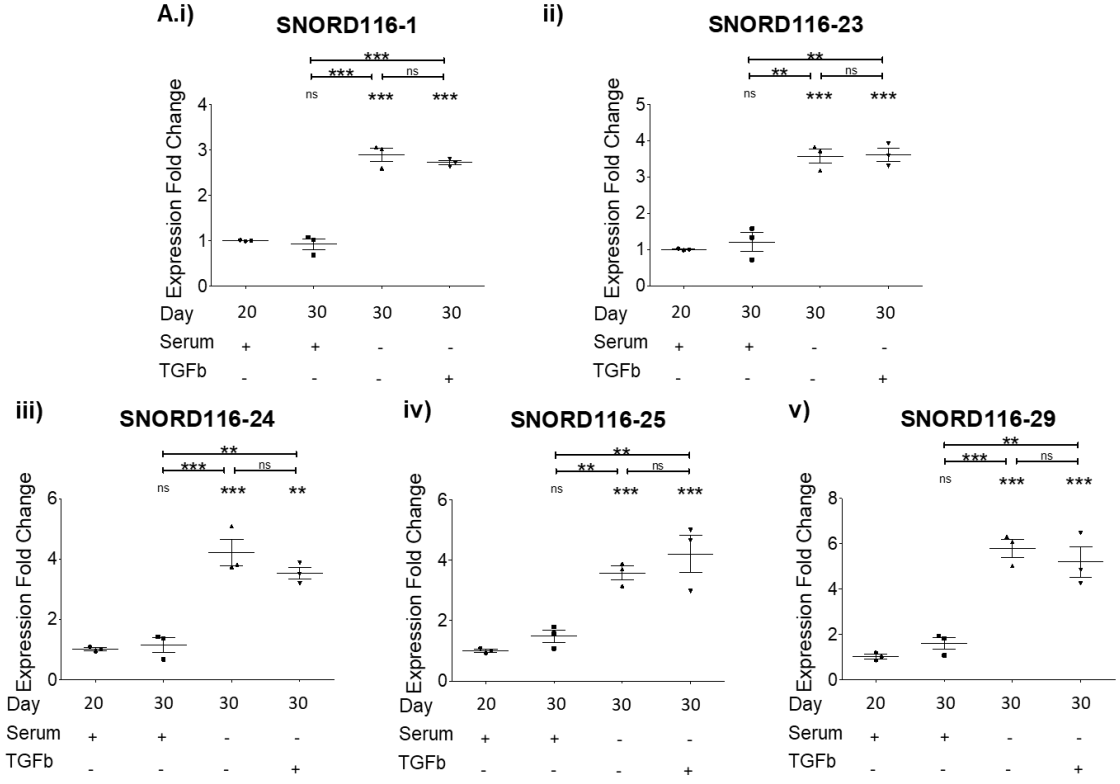

Figure 4-21. The effect of activatory conditions on SNORD116 expression in iPSC-CFs.

Expression of SNORD116 paralogues i) 1, ii) 23, iii) 24, iv) 25 and v) 29 plotted as fold change relative to day 20 CFs in 10% serum media an no TGFβ supplementation. Calculated by ddCt normalised to GAPDH. Statistics calculated by one-way ANOVA. * = P≤0.05, ** = P≤0.01, *** = P≤0.001. N=3. Error bars represent SEM.

The expression of day 30 cardiac fibroblasts was compared to that of day 30 cardiomyocytes in normal glucose conditions. Figure 4-22 shows the expression of all SNORD116 paralogues is higher in cardiomyocytes versus fibroblasts. The expression of SNORD116-1, 23, 24, 25 and 29 is 16±7, 16±8, 12±7, 7±2 and 22±8-fold higher in day 30 cardiomyocytes compared to day 30 cardiac fibroblasts.

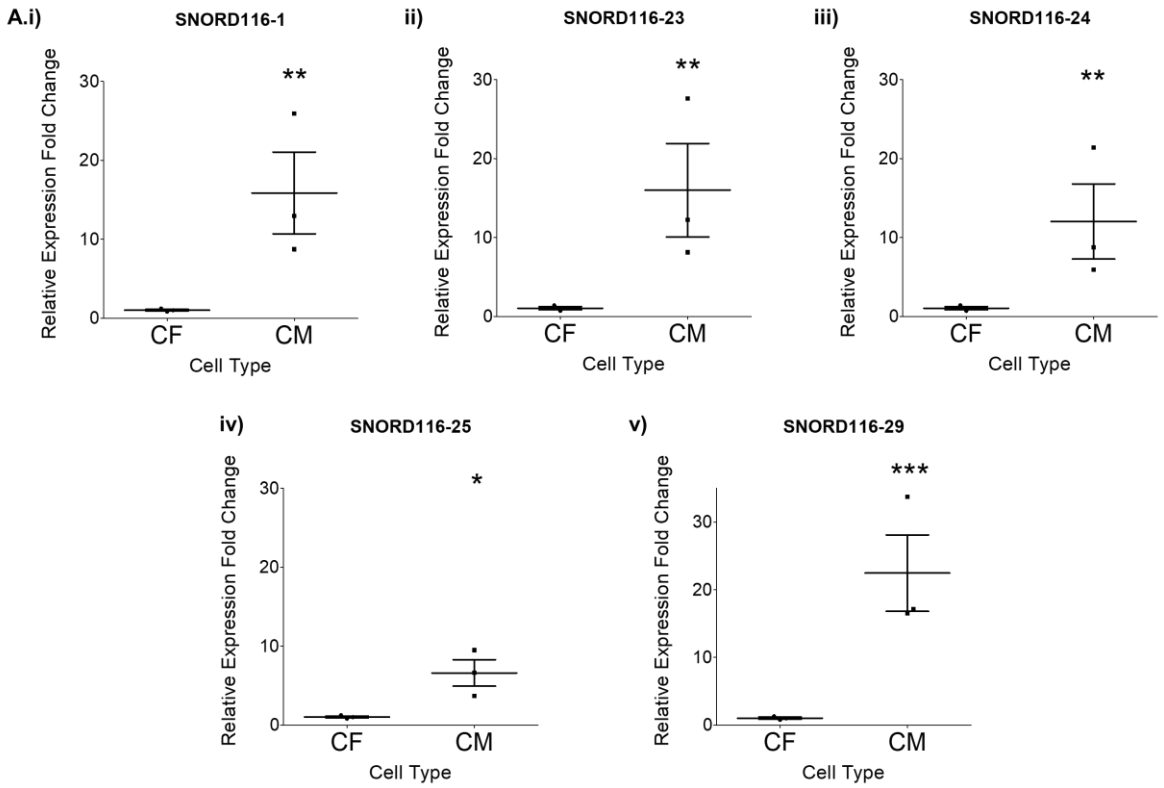

Figure 4-22. SNORD116 expression in cardiomyocytes compared to cardiac fibroblasts.
The expression of SNORD116 paralogues i) 1, ii) 23, iii) 24, iv) 25 and v) 29 in day 30 iPSC-CMs versus day 30 iPSC-CFs. Expression plotted as fold change. Calculated by ddCt normalised to GAPDH. Statistics calculated by unpaired t-test. * = P≤0.05, ** = P≤0.01, *** = P≤0.001. N=3. Error bars represent SEM.

4.6 Discussion

The aim of this chapter was to demonstrate that iPSCs could be successfully differentiated into both cardiomyocytes and cardiac fibroblasts. These processes could be manipulated to affect the results of the differentiation. Importantly, this chapter explores the changes in expression of SNORD116 that occur during cardiac differentiation, an entirely novel finding.

During the differentiation, the expression of pluripotency markers was downregulated. Illustrating the epithelial to mesenchymal transition during mesoderm induction, mesoderm marker expression increased around day 4 of both the iPSC-CM and iPSC-CF differentiation. In iPSC-CM differentiations, cardiomyocyte markers were upregulated from day 4 onwards demonstrating the assembly of the sarcomere and commitment to the cardiomyocyte fate. During cardiac fibroblast differentiation, two key fibroblast marker genes *COL1A1* and *aSMA* are both upregulated post-mesoderm induction. These results demonstrate how gene expression changes can be used to track the different phases of development that cells progress through during differentiation. Similar expression changes have been demonstrated by others for iPSC-CM (384–386) and iPSC-CF differentiation (387,388).

Correia *et al.* demonstrated that fatty acid-based media could induce improved maturity in iPSC-CMs (300). This chapter briefly explored the effect of fatty acid-based media on iPSC-CMs. RNAseq results of day 20 cardiomyocytes compared to day 30 cardiomyocytes cultured in GFAM indicated improved cardiomyocyte maturation through isoform switching of cardiac genes. The predominant myosin heavy chain isoform switched from the foetal-associated *MYH6* to the adult associated *MYH7*. There were also increases in the adult-to-foetal isoform ratio of other cardiac genes including troponin and myosin light chain. A reduction in cell cycle

gene expression indicated the arrest of the cell cycle which is associated with maturation in cardiomyocytes (382) This illustrates the pro-maturation effect of extended culture in fatty acid-based media. However, these results are limited in that they lack an age-matched non-fatty acid control, therefore it is possible that extended time in culture in either media may have influenced the gene expression changes. Additionally, GAPDH was used as the singular housekeeper gene for later RT-qPCR analysis. As GAPDH is a glycolysis-related gene, its expression may have been influenced by the change in media. A housekeeper gene not related to metabolism such as 18S or beta actin would improve this assay. Also, in addition to gene expression, other phenotypic characteristics related to maturity could be investigated. For example, the use of image analysis software to analyse sarcomeric alignment.

Similar to cardiomyocytes, the state of cardiac fibroblasts can be influenced by culture conditions. Dissociation, extended time in culture, removal of serum and TGFβ activation caused compounded upregulatory effects on the expression of *aSMA*, a marker of myofibroblast activation. Caspase 3 was also slightly upregulated, which could indicate a higher level of apoptosis in the fibroblasts upon the removal of serum, however this cannot be confirmed as cell number was not quantified. Cyclin D2 gene expression was also evaluated under activatory conditions. Cyclin D2 is a cell cycle regulator that has previously been shown to be upregulated in murine fibroblasts upon the removal of serum (389). Also, increased levels of cyclin D2 expression have been associated with cell senescence (389). Concurrently, results presented here showed the removal of serum caused an increase in the expression of cyclin D2. However, there is no additive effect of TGFβ supplementation, indicating that serum-starving the fibroblasts is sufficient to upregulate cyclin D2 expression and activate senescence in cardiac fibroblasts. Analysis of cell proliferation would help to confirm this.

Metabolism is a crucial component of cardiomyocyte function, as they are one of the most metabolically active cell types in the body, and dysregulation of cardiomyocyte metabolism is a key hallmark of heart disease. PPAR is a transcription factor, specifically a nuclear receptor that activates genes important in lipid metabolism and homeostasis (381). Each of the three isoforms of PPAR have a slightly different role in lipid metabolism. *PPARa* specialises in fatty acid transport and oxidation, and also activates the expression of enzymes important in ketogenesis (390). *PPARy* regulates adipogenesis and lipid storage, and is mostly active outside the cardiovascular system (390). *PPARd* affects both lipid and glucose metabolism by controlling oxidative phosphorylation (391). Work by Wickramasinghe *et al.* has demonstrated the importance of PPAR activation during cardiomyocyte differentiation and maturation (290). Corroboratively, PPARa and PPARy were shown here to increase during cardiomyocyte differentiation. However, results in this chapter also show that during cardiomyocyte differentiation, *PPARd* expression does not increase relative to GAPDH, although is consistently at a higher expression level than the other two isoforms. This suggests that the role of *PPARd* is important in multiple cell types and may not be unique to cardiomyocytes. Interestingly, *PPARd* is upregulated as the cardiomyocytes age from day 15 to day 30, indicating that older cardiomyocytes may have an increased demand for targets of *PPARd*, potentially such as those involved in oxidative phosphorylation. Increased *PPARd* expression has been associated with increased FAO and therefore metabolic maturity in cardiomyocytes (285,290).

PPARa expression increases as the expression of cardiomyocyte markers such as *TTN* increase, indicating that it contributes to the development and function of cardiomyocytes. This increase in *PPARa* expression correlates with an increase in total metabolic capacity including increased fatty acid substrate usage. Given the role of *PPARa* in fatty acid metabolism, the increase in *PPARa* expression may contribute to the

increase in the capacity for the cells to metabolise these fatty acids, or it may simply facilitate overall substrate absorption and metabolism.

Interestingly, the ratio of *PPARd* to *PPARa* is increased under high glucose conditions. This implies that the high glucose concentration caused a switch in expression from *PPARa* to *PPARd*, which could indicate that the *PPARd* isoform may be important in managing the metabolic stress induced by a high glucose environment. This aligns with other work wherein PPARd has been shown to be important in both fatty acid and glucose metabolism (284,390).

PPARy shows the lowest level of expression of the three isoforms, but does increase in expression during cardiomyocyte differentiation. *PPARy* is downregulated as the cardiomyocytes age from day 15 to day 30 under normal and high glucose conditions, but not fatty acid-rich conditions. This indicates that PPARy expression is important to fatty acid metabolism. This is supported by other studies which have shown PPARy is important in fatty acid transport and adipogenesis (390,392).

Metabolism during early cardiomyocyte development was also analysed through substrate usage. Although TCA substrates were generally the most readily metabolised, there was a significant reduction in the metabolic capacity of several key TCA substrates at day 6 compared to other time points. The citric acid cycle takes place within the matrices of mitochondria (393,394), therefore a reduction in TCA metabolic capacity could reflect a reduction in the number, size or functional output of mitochondria during the mesodermal progenitor phase of cardiomyocyte differentiation compared to other time points. However, the metabolism of three key amino acid substrates was also significantly lower on day 6 compared to the other time points, which could suggest that overall metabolism is lower at this time point. Across all four substrate classes, many of the substrates tested generated the greatest total colour change

on day 10, which could suggest that cells at this time-point have the highest or most versatile metabolism compared to the other time points. Although this likely reflects the increased energy demands associated with contractile cell development, this could also suggest the occurrence of a key switching point in metabolic substrate usage at this stage as the cells become fully specialised.

Clinical evidence suggests that SNORD116 may have a metabolic or developmental function, which could correlate with its potential role in the heart (57,60,62,64). SNORD116 is expressed in various tissues throughout the body, predominantly in the central nervous system, kidneys, thyroid, heart and gonadal organs (47). Group I is generally expressed to the highest levels in all tissues, followed by group II then group III (46). When analysing the sequence similarity between the three groups, group three demonstrated the highest level of uniqueness. The differences in sequence similarity between the three groups may indicate the possibility of paralogue-specific roles of SNORD116. The differences between mouse and human SNORD116 highlight the advantage of using a human iPSC-derived model to investigate the role of SNORD116 in human heart development.

Other than the general expression of SNORD116 in heart tissue, detail into the cardiac-specific expression of SNORD116 is distinctly absent from the literature. Therefore, investigation into the expression of different SNORD116 paralogues in different cardiac cell types was carried out.

The majority of SNORD116 paralogues are upregulated during the mesodermal phase of differentiation, when *GATA4* expression is at its peak and structural cardiac genes are beginning to be expressed. This could indicate that SNORD116 plays a functional role in cardiac mesoderm development. Interestingly, during cardiac fibroblast differentiation, after the mesoderm forming stage occurs, SNORD116 is

downregulated to below stem cell levels, a trend that is not seen in cardiomyocyte differentiation. This indicates that SNORD116 could be involved in cardiac development in a capacity specific to cardiomyocytes.

To model fibrotic activation, iPSC-CFs were fed serum-free and TGFβ-supplemented media. The removal of serum and addition of TGFβ to cardiac fibroblasts caused a compounding up-regulatory effect on the expression of the myofibroblast marker *aSMA*. This suggests that the cardiac fibroblasts were activated by the removal of serum, and further activated by TGFβ. Activation of the fibroblasts through removal of the serum caused SNORD116 to be upregulated. However, the addition of TGFβ did not cause further upregulation of SNORD116. Fibroblasts have previously been shown to become activated into myofibroblasts upon removal of serum alone (395), therefore it may be that this level of activation is enough to upregulate SNORD116. The upregulation of SNORD116 in fibrotic cardiac conditions may indicate that SNORD116 is important in fibrotic signalling.

Media composition was modified in order to investigate how cardiomyocyte proliferation and maturation may alter SNORD116 expression. Studies have shown that the use of the Wnt signalling activator CHIR on early cardiomyocytes can induce their re-entry into a proliferative, de-differentiated state (370). Results in this chapter supported this, as cardiomyocyte proliferation was successful after CHIR treatment. This caused a significant increase in cell number and cardiomyocyte purity when compared to the control and may have caused an increase in sarcomeric disassembly and disorganisation. Proliferation and sarcomeric disarray are key signs of de-differentiation in cardiomyocytes. Interestingly, although most of the genes analysed appeared downregulated upon CHIR supplementation, SNORD116 expression appeared to be upregulated. The effects of de-differentiation may have had a non-specific downregulatory effect on the cardiomyocyte

gene expression, but SNORD116 expression is seemingly elevated in this state. As SNORD116 is upregulated during early cardiogenesis, this upregulation in response to Wnt activation may be due to the activation of developmental signalling pathways. Contrastingly, in response to changing the media from glucose-based to fatty acid-based, SNORD116 expression was not affected. This may suggest that SNORD116 is more important during early cardiogenesis rather than cardiomyocyte maturation.

When cultured to day 30 in the standard media for each cell type (glucose-containing for iPSC-CMs and serum-containing for iPSC-CFs), cardiomyocytes have a much higher expression of SNORD116 than cardiac fibroblasts. This change could be due to the absence of serum from cardiomyocyte media. Indeed, the removal of serum from fibroblast media does cause an upregulation of SNORD116 in cardiac fibroblasts. However, this upregulation is only 2.5 to 5-fold higher (depending on the SNORD116 paralogue) and is therefore unlikely to account for the 7 to 17-fold upregulation of SNORD116 in cardiomyocytes compared to cardiac fibroblasts. The higher level of SNORD116 in cardiomyocytes compared to cardiac fibroblasts further suggests that SNORD116 could be important in cardiomyocyte-specific processes such as sarcomere assembly, calcium signalling and contraction. It could also suggest a role in metabolism, as cardiomyocytes are more metabolically active than cardiac fibroblasts. To investigate further, both cell types were manipulated through the induction of cardiac stress to analyse the response in SNORD116 expression.

Chapter 5 Investigating SNORD116 expression in response to cardiac stress

5.1 Introduction

As previously discussed, dysregulation of many cellular processes occurs during heart disease. When using iPSC-derived models to investigate heart disease, there are many strategies that can be used to recapitulate cardiac stress. The diseased heart undergoes metabolic changes that result in increased glycolysis and reduced oxidative phosphorylation, i.e. an increased reliance on anaerobic metabolism. IPSC-CMs can be forced to engage in increased anaerobic metabolism by reducing the level of oxygen they are exposed to. Introducing cardiac cells to a hypoxic environment also partially simulates the ischemic environment that occurs during myocardial infarction, when cardiomyocytes cut off from the blood supply are exposed to drastically lower levels of oxygen. Re-exposure to oxygen after a period of hypoxia simulated ischemic reperfusion that occurs after myocardial infarction.

In addition to hypoxia-related damage, cardiac stress can be induced through the use of cardiotoxic drugs such as doxorubicin. Doxorubicin-induced cardiotoxicity is associated with increased cardiomyocyte apoptosis, increased oxidative stress, reduced mitochondrial biogenesis and disruption of calcium handling (173). Many of the hallmarks of heart failure are seen in doxorubicin-induced cardiomyopathy including chamber dilation, enlarged heart size, interstitial fibrosis and cardiomyocyte death (174,175). In addition to the inhibition of topoisomerase II, doxorubicin interferes with glycolytic enzymes leading to cardiomyocyte death and mitochondrial dysfunction (182,185). The overlapping symptoms between doxorubicin-induced cardiomyopathy and other forms of cardiovascular disease supports the use of doxorubicin as a tool for the *in vitro* modelling of cardiac disease using iPSC-CMs.

Isoprenaline is another drug that can be used to induce cardiac stress. Isoprenaline is a non-selective β-adrenergic receptor agonist that increases the rate of cardiomyocyte contraction by inducing the release of calcium from the sarcoplasmic reticulum (191). This increased workload acts as a form of cardiac stress by forcing a higher demand for ATP production.

There are also many forms of heart disease that exist due to genetic mutation. Hypertrophic cardiomyopathy (HCM) is the most commonly occurring genetic heart disease, affecting 1 in 500 people (80). A strategy of modelling genetic heart diseases such as HCM *in vitro* is to differentiate iPSC lines with HCM-causing mutations into cardiomyocytes. In many cases, these iPSC models successfully recapitulate the phenotypes seen in the clinic such as hypertrophy, impaired metabolism, calcium dysregulation and contractile arrythmia (122,337–340). This work will showcase the use of iPSC-CMs with mutations in the *ACTC1* gene and *MYH7* gene, both sarcomeric genes associated with HCM.

SNORD116 was associated with cardiac stress in an iPSC-derived model of heart disease when iPSC-CMs were differentiated from two iPSC lines, one of which was positive for a HCM-causing mutation and the other was an isogenic control (65). These iPSC-CMs were subjected to cardiac stress via electrical pacing to increase their contraction frequency. Multiple paralogues of SNORD116 were found to be packaged to a greater level in the exosomes released by HCM-positive iPSC-CMs, an effect that was compounded by increased cardiac stress in the form of electrical pacing (65). Additionally, heart disease is often accompanied by a regression towards foetal phenotypes, and data suggests SNORD116 may have a role in cardiac developmental processes. The purpose of this chapter was to investigate how different forms of cardiac stress influences the

expression of SNORD116, which may provide insight into its potential role in heart function and disease.

5.2 The effects of hypoxia on cardiac cell types

5.2.1 The effects of hypoxia on cardiomyocytes

To investigate the effects of hypoxia, iPSC-CMs were cultured in hypoxic (2% O_2 atmosphere) or normoxic (20% O_2 atmosphere) conditions for varying lengths of time. A summary of the different conditions used is shown in Figure 5-1.To investigate the effects of hypoxia on contraction, iPSC-CMs were cultured for 4 days in either normoxic or hypoxic conditions. The cells were fed pre-conditioned media after 2 days to prevent nutrient deficit. After 4 days, the cells were recorded in a temperature-controlled microscope stand for at least 20 seconds. The resulting videos were analysed using the ImageJ plugin MUSCLEMOTION (356,357). According to the results in Figure 5-2, hypoxia caused a decrease in contraction amplitude from 601±123 to 157±129, however due to variation this was not statistically significant. Hypoxia also caused a decrease in contraction frequency from 0.7±0.03 Hz to 0.2±0.07 Hz. Not only did hypoxia cause a decrease in contraction frequency, but it also caused an increase in the frequency of arrhythmogenic-like events from 23±5% to 90±5% of total events. Together these results

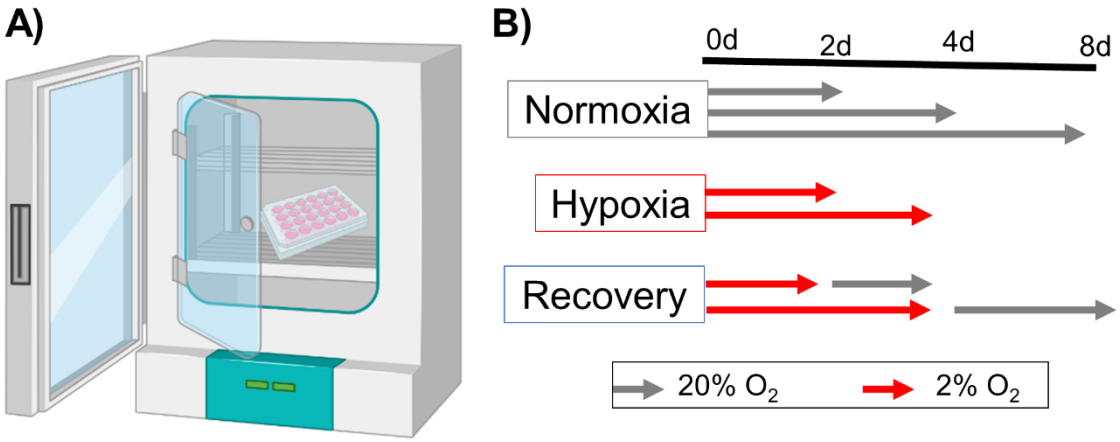

Figure 5-1. Investigating the effects of hypoxia on iPSC-CMs.
A. Example incubator set up wherein the atmosphere can be controlled.
B. Different length of time cells were cultured for in hypoxic or normoxic conditions. (d=days).

demonstrate that hypoxic conditions dysregulate the contraction of iPSC-CMs.

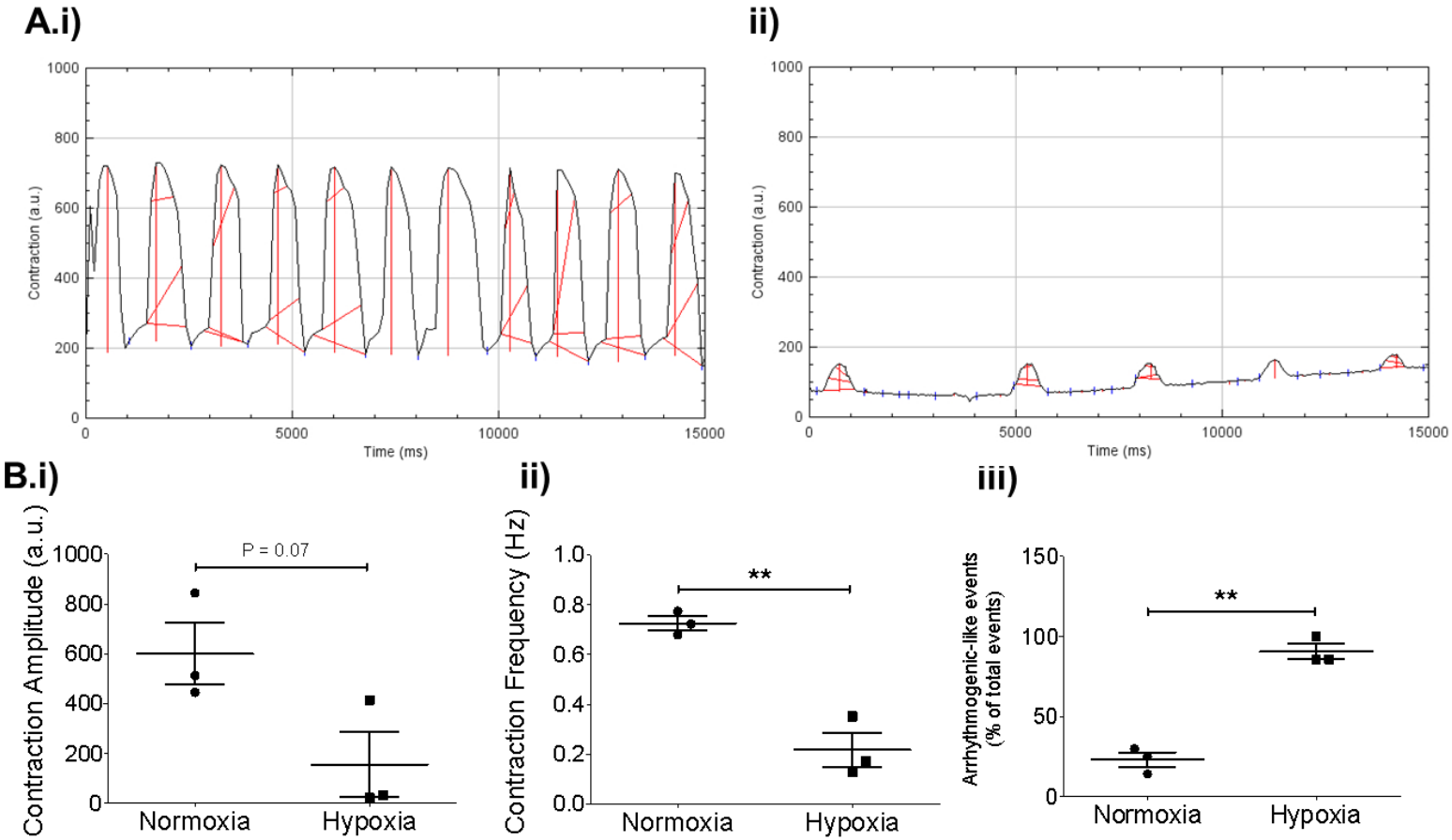

Figure 5-2. The effect of hypoxia on iPSC-CM contraction.

A. Representative contraction traces of cardiomyocytes subjected to i) normoxic and ii) hypoxic atmosphere. Generated using MUSCLEMOTION and ImageJ.

B. The average i) contraction amplitude (in arbitrary units), ii) contraction frequency (in Hz) and iii) percentage of total events that are classed as arrhythmogenic-like events. Statistics calculated using unpaired t-test. * = P≤0.05, ** = P≤0.01, *** = P≤0.001. N=3. Error bars represent SEM.

Hypoxia also caused a disruption to the metabolism of cardiomyocytes. IPSC-CMs were subjected to hypoxic or normoxic conditions (see above) and then metabolism was assessed using the Biolog MitoPlate assay. The results are shown in Figure 5-3 and Figure 5-4. Overall, the percentage contribution of each type of substrate metabolism (glycolysis, TCA, amino acid or fatty acid) did not change under hypoxic conditions. However, total metabolic capacity of the iPSC-CMs was reduced from 1185±142 to

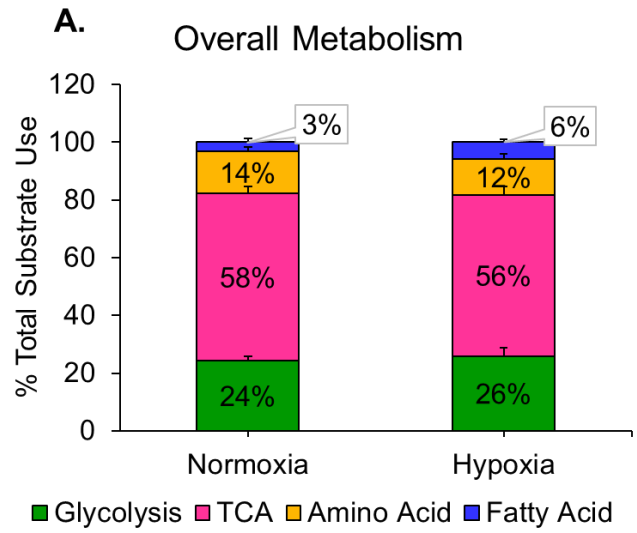

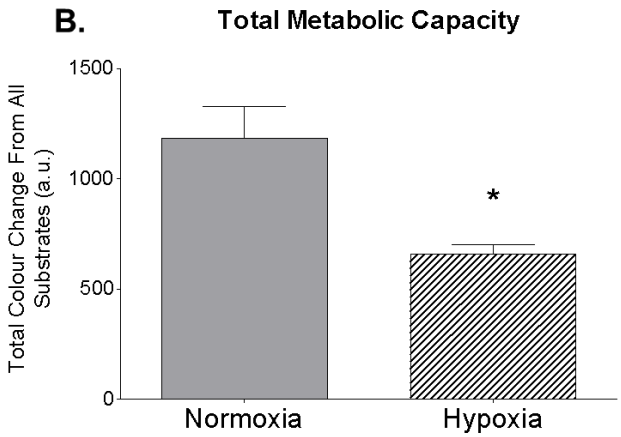

C.

Glycolysis	Normoxia	Hypoxia
NO SUBSTRATE	1.0	0.2
a-D-Glucose	1.0	1.3
Glycogen	1.0	0.5
D-Glucose-1-PO4	1.0	1.0
D-Glucose-6-PO4	1.0	0.7
D-Glutonate-6-PO4	1.0	0.9
D,L-a-Glycerol-PO4	1.0	1.1
L-Lactic Acid	1.0	0.3
Pyruvic Acid	1.0	0.3
Pyruvic Acid + MA	1.0	0.4
TCA		
Citric Acid	1.0	0.7
D,L-Isocitric Acid	1.0	0.5
Cis-Aconitic Acid	1.0	0.4
A-Keto-Glutaric Acid	1.0	0.4
Succinic Acid	1.0	0.5
Fumaric Acid	1.0	0.4
L-Malic Acid	1.0	0.7
A-keto-Butyric Acid	1.0	14.5
Amino Acids		
L-Glutamic Acid	1.0	0.2
L-Glutamine	1.0	0.2
Ala-Gln	1.0	0.2
L-Serine	1.0	3.0
L-Ornithine	1.0	1.5
Tryptamine	1.0	13.2
L-Leucine + MA	1.0	3.9
g-Amino-Butyric Acid + MA	1.0	1.2
a-Keto-Isocaproic Acid + MA	1.0	7.4
Fatty Acids		
Acetyl-L-carnitine + MA	1.0	0.9
L-Octanoylcarnitine + MA	1.0	1.1
L-Palmitoylcarnitine + MA	1.0	1.5
D,L-3-Hydroxybutyric acid	1.0	0.7

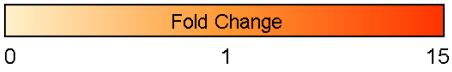

Figure 5-3. Overall metabolism in iPSC-CMs in normoxic and hypoxic conditions.
A. The percentage usage of each metabolic substrate class (based on total colour change). Error bars represent standard deviation.
B. Sum of the total colour change of all substrates in normoxia and hypoxia. Statistical analysis performed using unpaired t-test. * = P≤0.05, ** = P≤0.01, *** = P≤0.001. N=3. Error bars represent SEM.
C. The fold change of substrate usage for each substrate. TCA = The citric acid cycle, MA = L-Malic Acid (100uM).

659±43. Of the 30 substrates tested, 12 showed no change or an increase in usage, with the greatest change seen in A-keto-Butyric Acid that showed a 14.5±6-fold increase in hypoxic compared to normoxic conditions. Six of the 12 substrates that were increased under hypoxia were amino acids, two were in the glycolysis category, two were fatty acids and one was in the TCA category. 18 of the 30 substrates tested showed a decrease in substrate usage, with the greatest change seen in the amino acid glutamine which had a fold change of 0.19±0.05-fold decrease in hypoxia. Of the 18 substrates that were decreased under hypoxia, seven were in the TCA category, six were in the glycolysis category, three were in the amino acid category and two were fatty acids.

Figure 5-4 shows the total colour change in the presence of each individual substrate. Of the glycolysis substrates, only two showed a significant difference between normoxia and hypoxia. These were L-lactic acid and pyruvic acid which decreased from 41±12 to 14±5 and 38±7 to 10±2, respectively. Of the TCA substrates, DL-isocitric acid, succinic acid, fumaric acid and malic acid showed a 50-87 a.u. decrease in total colour normoxic to hypoxic conditions. The amino acids L-glutamic acid, L-glutamine and ala-gln had a total colour change that was 36-48 a.u. higher in normoxia compared to hypoxia. There was no significant difference in the total colour change of any of the fatty acid substrates tested.

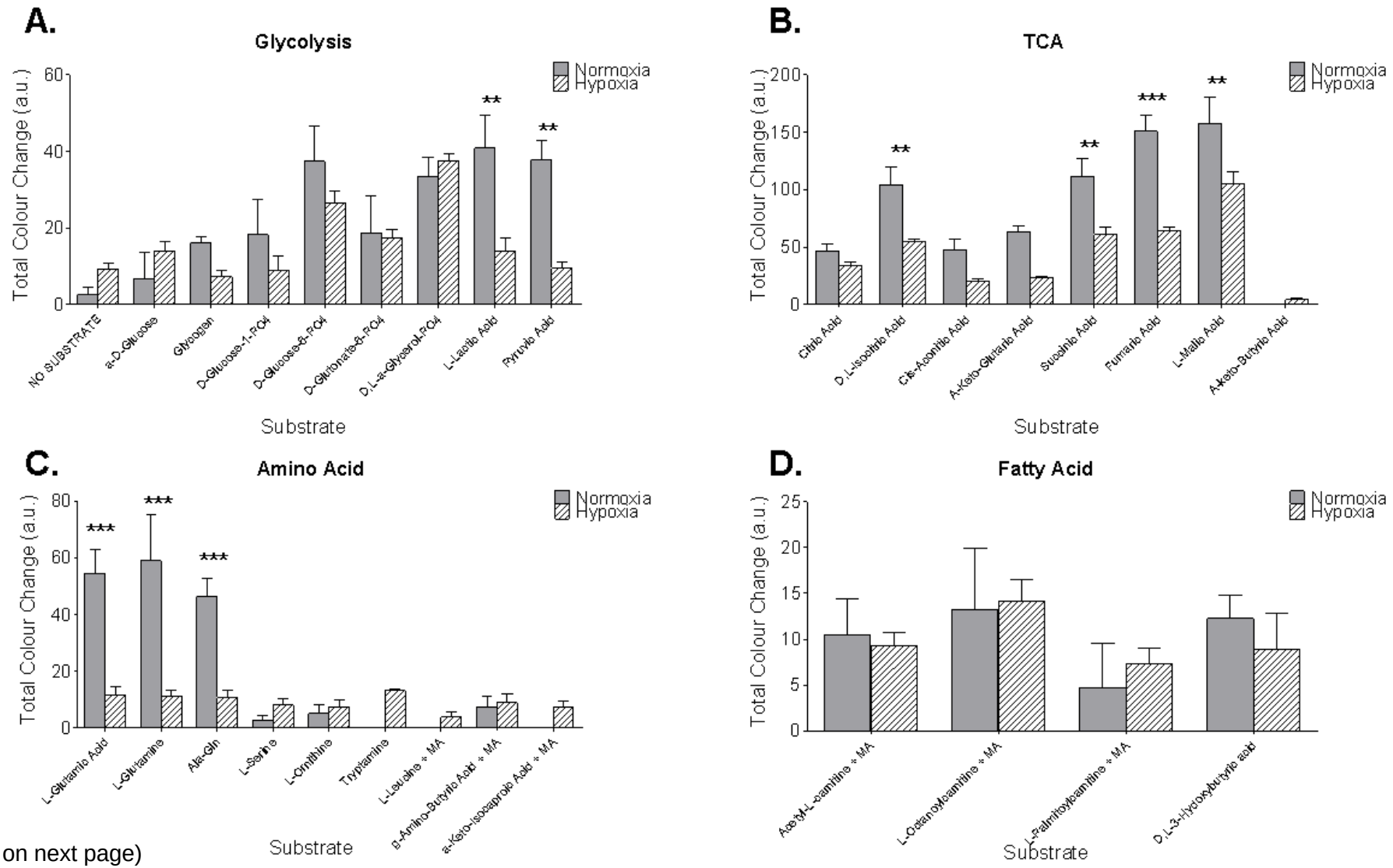

(Legend on next page)

Figure 5-4. Individual substrate metabolism under normoxic and hypoxic conditions. The total colour change of each individual substrate under each metabolic class (A) glycolysis, (B) TCA, (C) amino acid and (D) fatty acid. Statistical analysis performed using two-way ANOVA. * = P≤0.05, ** = P≤0.01, *** = P≤0.001. N=3. Error bars represent SEM. TCA = The citric acid cycle, MA = L-Malic Acid (100uM).

The rate of metabolism can also be calculated using the Biolog MitoPlate assay by calculating the change in colour over time. The maximal rate of colour change was calculated for each substrate and is shown in Figure 5-5. For every substrate tested, the maximal rate was significantly decreased under hypoxic conditions compared to normoxia. This shows that hypoxia had a downregulatory effect the global metabolic rate of iPSC-CMs.

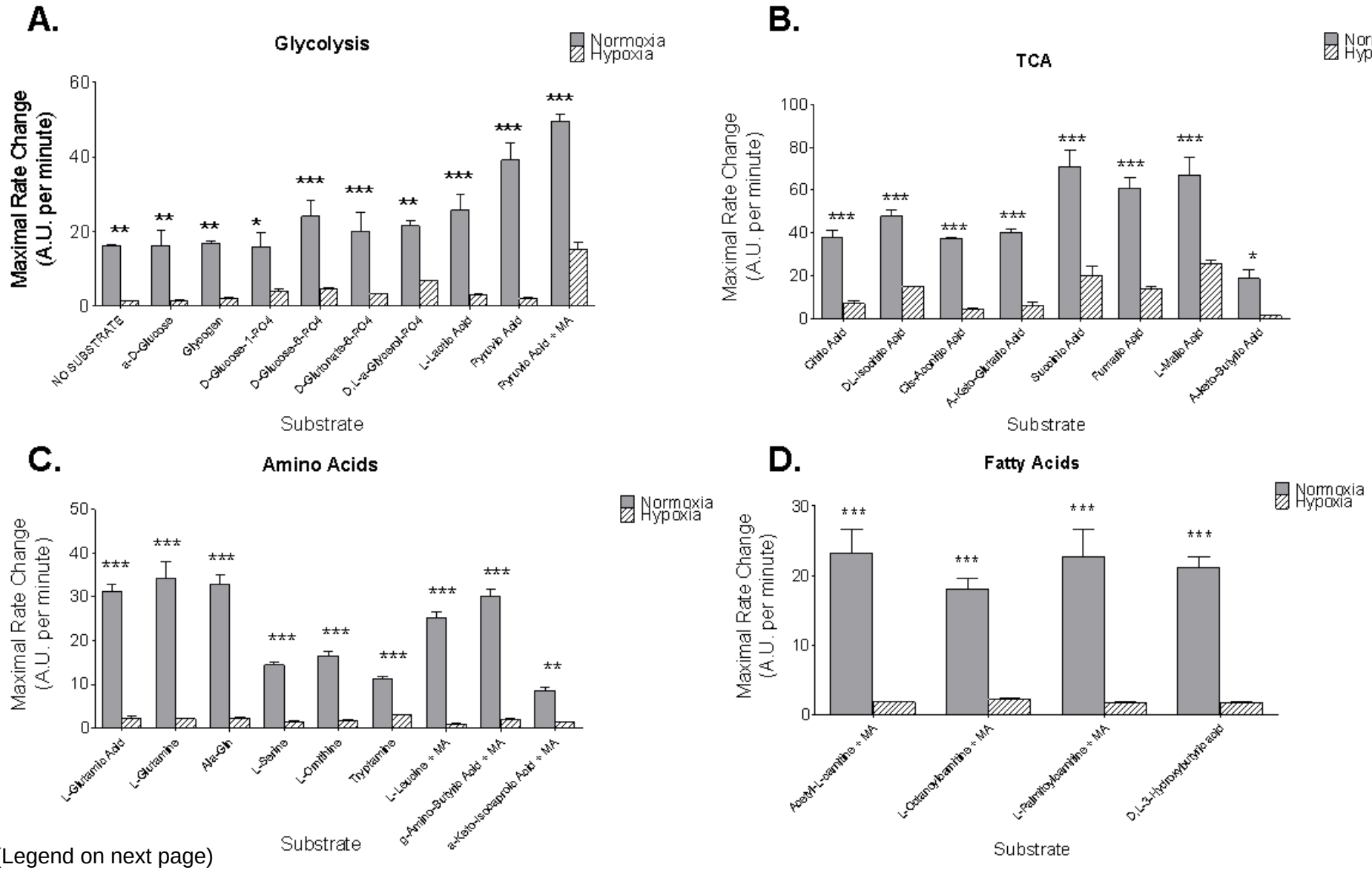

(Legend on next page)

Figure 5-5. Maximal rate of substrate metabolism under normoxic and hypoxic conditions.
The maximal rate in total colour change of each individual substrate under each metabolic class (A) glycolysis, (B) TCA, (C) amino acid and (D) fatty acid. Statistical analysis performed using two-way ANOVA. * = P≤0.05, ** = P≤0.01, *** = P≤0.001. N=3. Error bars represent SEM. TCA = The citric acid cycle, MA = L-Malic Acid (100uM).

In addition to the Biolog MitoPlate assay, metabolism can also be evaluated using the Agilent Seahorse XF96 Cell Mito Stress Test (396). IPSC-CMs were cultured under three conditions: for normoxia, cells were cultured for two days at 37°C, 5% CO_2 and 20% O_2. For hypoxia, cells were cultured for two days at 37°C, 5% CO_2 and 2% O_2. In addition, cells were also cultured for two days under hypoxic conditions, then for two days under normoxic conditions, then a further two days under hypoxic conditions. This was referred to as "conditioned hypoxia". This was done in order to investigate if pre-conditioning iPSC-CMs in hypoxia and allowing their recovery would affect their metabolic response to further hypoxia. The oxygen consumption rate (OCR) and extracellular acidification rate (ECAR) are measured at basal metabolism in Seahorse media (contains glucose, glutamine and pyruvate as metabolic substrates). The OCR and ECAR are measured three times. Each measurement cycle consists of three minutes of mixing followed by three minutes in which the measurement is taken. After 18 minutes, oligomycin is introduced into the media which inhibits ATP synthase, preventing the production of ATP and any proton transport that is not due to proton leak. The respiration taking place during this time is not coupled to ATP-production. After a further 18 minutes, during which time three measurements of OCR and ECAR are taken, the drug Carbonyl cyanide-4 (trifluoromethoxy) Phenylhydrazone (FCCP) is added to the media. This uncoupling agent transports protons across the mitochondrial membrane, stimulating the respiratory chain to operate at maximal capacity and causing the rapid oxidation of substrates. During this time, the cells are operating at their maximum respiratory capacity. After 18 minutes and

three measurement cycles, the drug mixture rotenone and antimycin A are added to inhibit mitochondrial complexes I and II respectively. This effectively inhibits all forms of mitochondrial respiration. After analysis the plate is fixed, stained for DAPI and imaged to provide the number of nuclei per well, which is used to approximate the number of cells per well. The OCR and ECAR measurements are adjusted to be relative to 10,000 cells.

Evaluating the results shown in Figure 5-6, hypoxia caused a significant decrease in the basal OCR of iPSC-CMs from 82±8 pmol/min/10k cells to 34±34 pmol/min/10k cells. Maximal respiration was decreased from 185±43 pmol/min/10k cells in normoxia to 45±47 pmol/min/10k cells in hypoxia. During ATP-inhibited respiration there was no significant difference in OCR across the conditions tested. However, there was a significant difference in the ECAR measured during ATP-inhibited respiration. ECAR decreased from 34±11 mpH/min/10k cells in normoxia to 14±13 mpH/min/10k cells in hypoxia. During maximal respiration, ECAR was decreased from 68±12 mpH/min/10k cells in normoxia to 18±20 mpH/min/10k cells in hypoxia. Although basal ECAR in the conditioned hypoxic cells was higher than that of normoxic and hypoxic cells (48±70 vs 20±9 and 15±15 mpH/min/10k cells), there was too much variation for this to be statistically significant. As such, there was no significant different between the OCR or ECAR of the hypoxic cells compared to the conditioned hypoxic cells during any form of respiration.

Figure 5-7 shows that the number of nuclei decreased from 17,000±1210 nuclei in normoxia to 3230±3450 nuclei in hypoxia. There was no significant difference in nuclei count between the hypoxic and conditioned hypoxic cells. This ~5-fold decrease in cell number reflects the induction of significant cell death in response to hypoxic incubation. Nuclei number was obtained through the counting of attached nuclei with normal

morphology via image analysis. This could be improved with the addition of a live stain to better gauge cell viability.

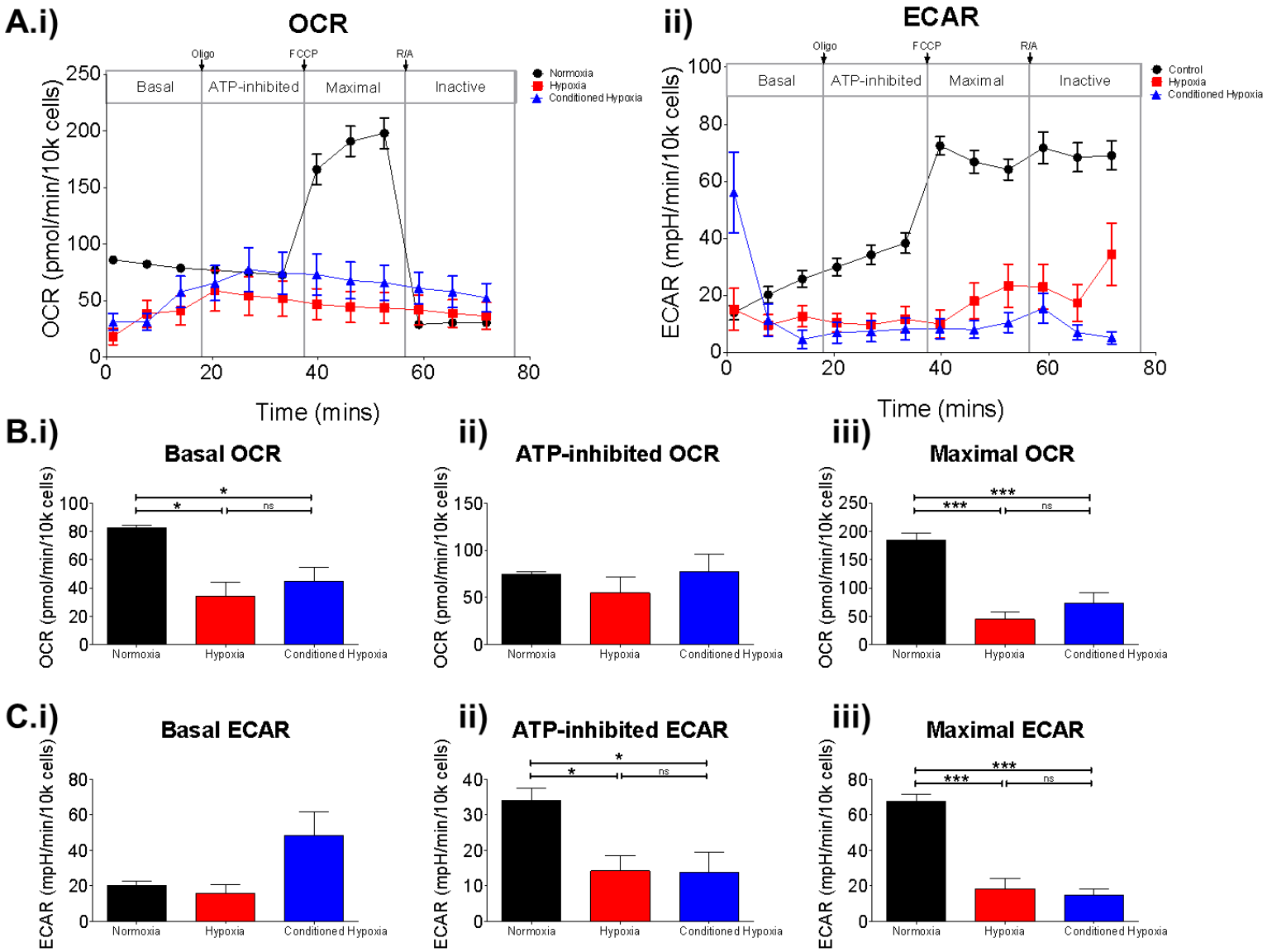

(Legend on next page)

Figure 5-6. The effect of hypoxia on the metabolic performance of iPSC-CMs.
A. The i) OCR and ii) ECAR of iPSCs after exposure to normoxia, hypoxia and conditioned hypoxia over time during various types of metabolism.
B. The OCR of iPSC-CMs in different oxygen conditions during i) basal, ii) ATP-inhibited and iii) maximal metabolism.
C. The ECAR of iPSC-CMs in different oxygen conditions during i) basal, ii) ATP-inhibited and iii) maximal metabolism. Statistical analysis performed using one-way ANOVA. * = P≤0.05, ** = P≤0.01, *** = P≤0.001. Normoxia N = 12, hypoxia N=12, conditioned hypoxia N=30. Error bars represent SEM. OCR = oxygen consumption rate, ECAR = extracellular acidification rate, Oligo = oligomycin (2uM), FCCP = Carbonyl cyanide-4 (trifluoromethoxy) Phenylhydrazone (1uM), R/A = Rotenone/Antimycin A (0.5uM).

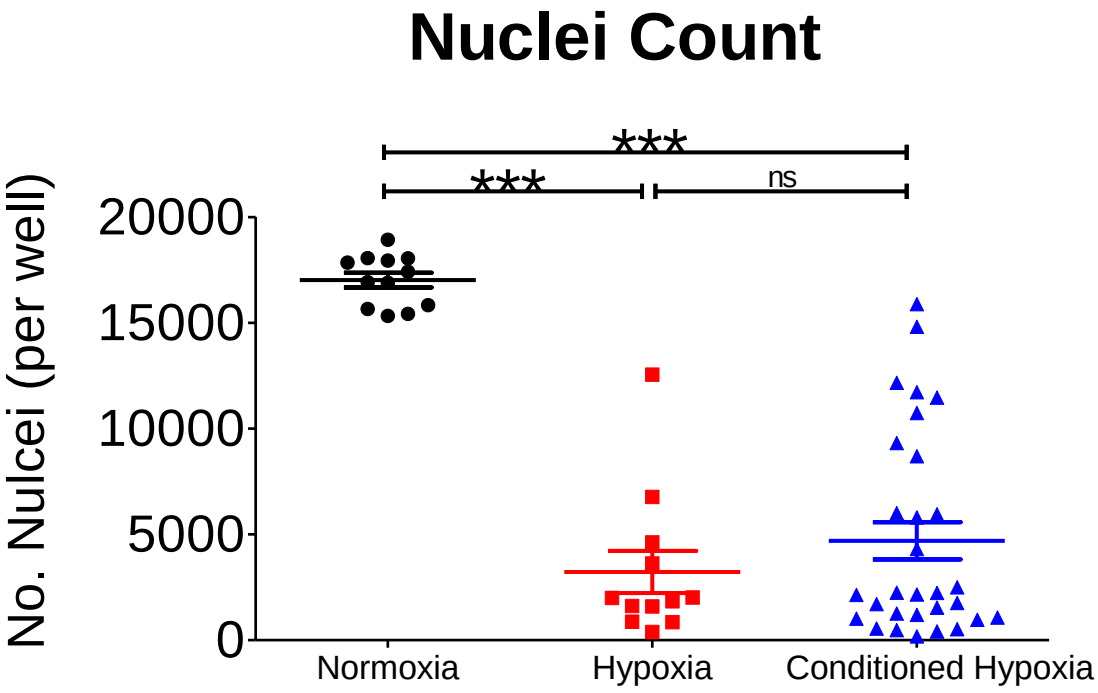

Figure 5-7. The number of nuclei in each condition after Seahorse analysis.
After seahorse analysis, the cells were washed 3x in PBS and fixed in 4% formaldehyde, then stained with DAPI and imaged. ImageJ was used to count the number of nuclei present in a given area in each well and multiplied by the difference factor to find the number of nuclei per well. Statistical analysis performed using one-way ANOVA. * = P≤0.05, ** = P≤0.01, *** = P≤0.001. Normoxia N = 12, hypoxia N=12, conditioned hypoxia N=30. Error bars represent SEM.

Signalling plays an important role in the response of cardiomyocytes to hypoxic stress. An important component of cell-cell communication is the release of specialised extracellular signalling vesicles known as exosomes. SNORD116 exosome packaging has been shown to be affected by cardiac stress in an iPSC-CM model (65). The exoview R100 (nanoView Biosciences) is an advanced automated platform used to detect and characterise exosomes (353). IPSC-CMs were incubated in either hypoxic or normoxic conditions as described previously. After 48 hours, the media was removed, and the exosomes were isolated from the media using the Exo-spin™ exosome purification kit (Cell Guidance Systems). Exosomes are captured onto an analysis chip using an antibody specific to tetraspanin, a universal exosome marker. Captured exosomes are also incubated with fluorescently tagged antibodies that bind the exosome markers CD81, CD9 and CD63. A permeable antibody is used to bind to the interior exosome marker syntenin. The fluorescent wavelength of each of the marker antibodies allows for the quantitation and characterisation of the exosomes. Visualisation of captured exosomes is shown in Figure 5-8.

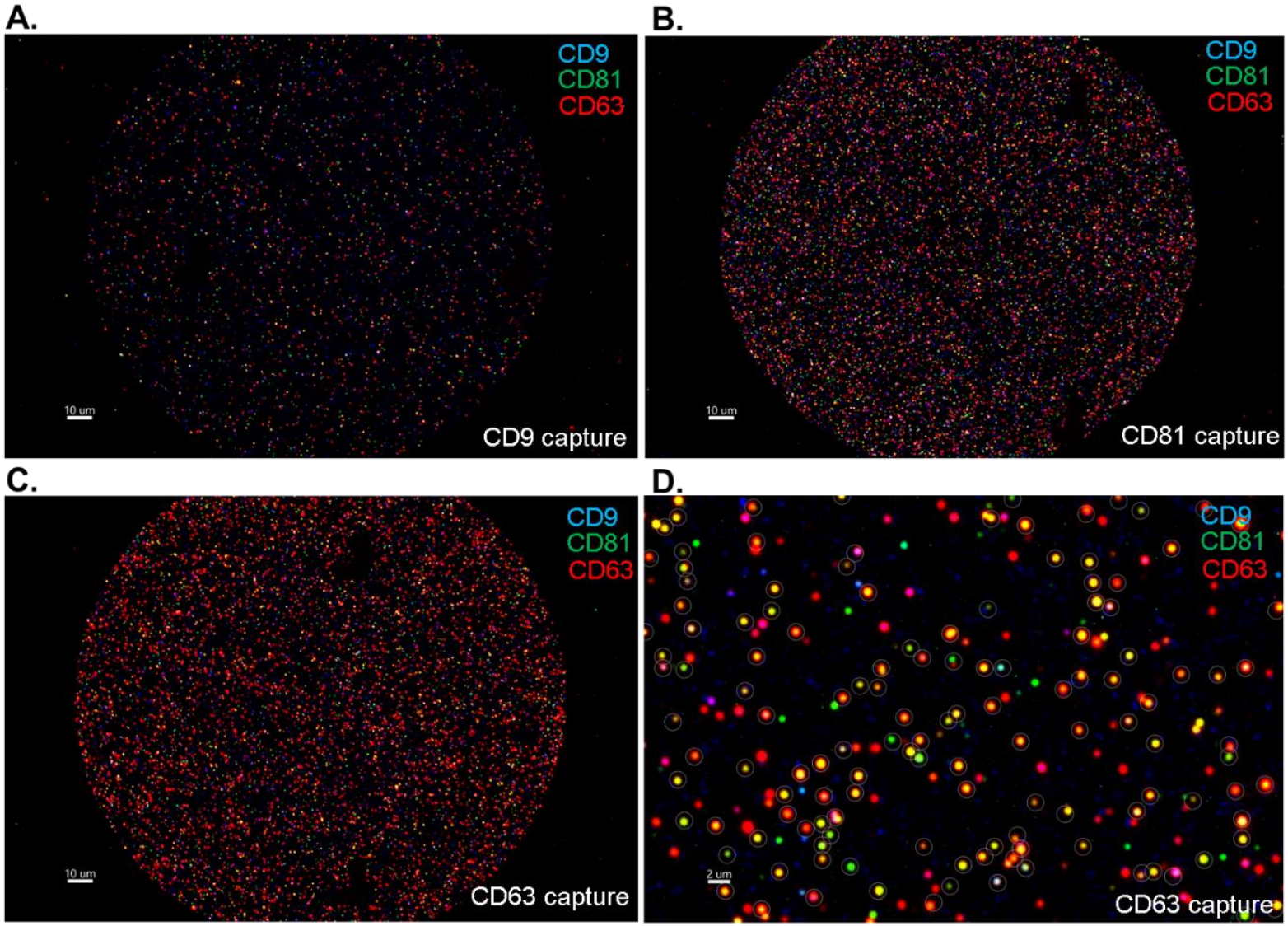

(Legend on next page)

Figure 5-8. Exosome capture and visualisation using the exoview R100.
(A-C) Exosomes tagged with CD9, CD81 or CD63. Blue = CD9, green = CD81, red = CD63. D. Fluorescence co-localisation analysis of exosomes

Figure 5-9 shows the number of exosomes positive for CD63, CD81 and CD9. Exosomes that are positive for multiple markers are included in the count. In hypoxic conditions, exosomes positive for either of the three markers all show an increase in number compared to normoxia. $CD63^+$ exosomes increase from 1.7±0.09 exosomes per 1000 cells in normoxia to 3.1±0.04 exosomes per 1000 cells. $CD81^+$ exosomes increase from 1.9±0.04 to 3.2±0.04 exosomes per 1000 cells in hypoxia, and $CD9^+$ exosomes increase from 0.8±0.1 to 1.2±0.09 exosomes per 1000 cells. $CD81^+$ exosomes were present at the highest level per 1000 cells under normoxic and hypoxic conditions, whereas $CD9^+$ exosomes were the least numerous. The average exosome size under normoxic conditions for CD63, CD81 and CD9 was 56±11nm, 60±18nm and 60±15nm. The average exosome size under hypoxic conditions for CD63, CD81 and CD9 was 55±9nm, 57±12nm and 58±11nm. Neither the exosome marker nor the oxygen conditions appeared to significantly affect exosome size. This may be due to the use of the ExoSpin™ columns to isolate exosomes, which may have reduced the total number of exosomes isolated and selected against exosomes outside a certain size range, therefore skewing the results. Regardless of exosome marker and oxygen conditions, the most frequent size range of exosome was 50-60nm. However, the machine is unable to detect particles smaller than 50nm, therefore any exosomes smaller than 50nm were not quantified. For $CD63^+$ and $CD9^+$ exosomes, a large majority of the population are within the 50-60nm range. However, for $CD81^+$ exosomes there is a more substantial number of exosomes in the 60-70nm range (48% of the number in the 50-60nm range). This could indicate that this marker is more frequently expressed on larger exosomes than the other markers are.

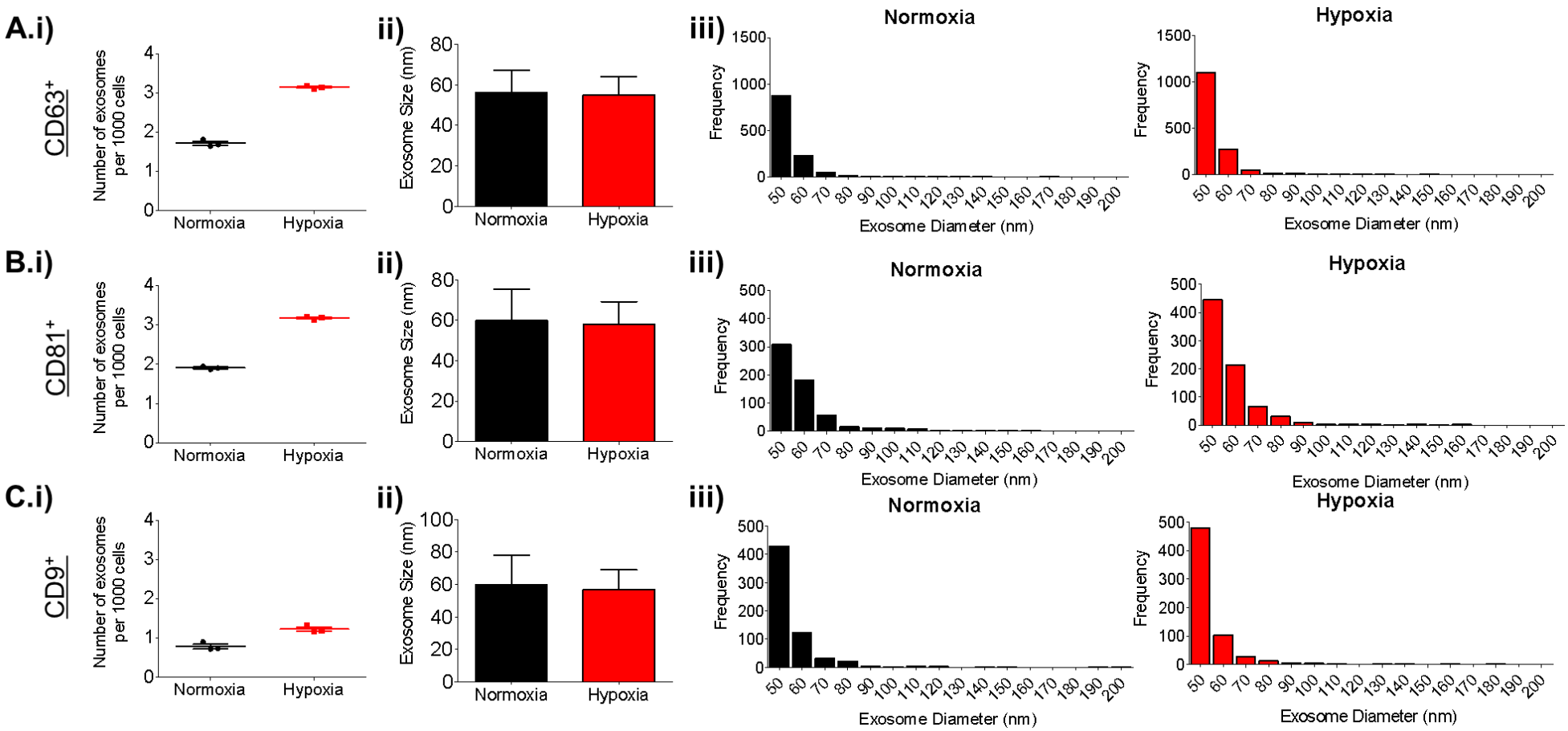

Figure 5-9. Characterisation of exosomes under normoxic and hypoxic conditions.
The i) number, ii) size and iii) size distribution of (A) CD63-positive, (B) CD81-positive and (C) CD9-positive exosomes released from cardiomyocytes under normoxic and hypoxic conditions. N=1. Error bars represent SEM.

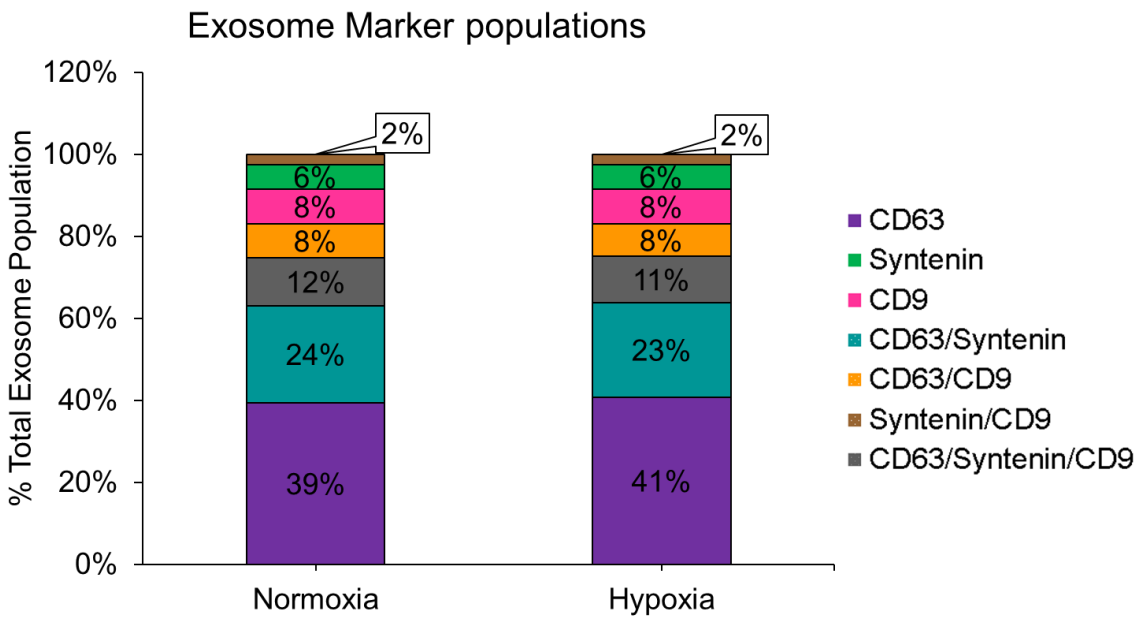

Figure 5-10. Co-localisation of exosome markers.
The co-localisation of the different exosome markers calculated as a percentage of the total exosome population.

The co-localisation of the different markers can be analysed in order to categorise the exosomes into different populations depending on which markers they express. These results are shown in Figure 5-10. Taken as a percentage of total exosomes, the largest population is the CD63-single-positive population which makes up 39% of normoxic exosomes and 41% of hypoxic exosomes. CD9 and syntenin are the smallest of the single-positive populations at 8% and 6% in normoxia, and the CD9/syntenin double-positive population is the smallest percentage of total exosomes. Hypoxia does not appear to affect the size of the various populations.

Overall hypoxia appears to increase the number of exosomes released from cardiomyocytes without changing their size or marker expression.

IPSC-CMs were cultured in various oxygen conditions to analyse the effect of hypoxia on gene expression. Normoxia refers to culture in 37^{O}C, 5% CO_2 and 20% O_2. Hypoxia refers to 37^{O}C, 5% CO_2 and 2% O_2. Cells were cultured for two days in either normoxia or hypoxia. Then to evaluate post-hypoxia recovery, cells were incubated for four days in either hypoxia or normoxia, or for two days in hypoxia followed by two days in normoxia. Then finally to explore the effect of prologued recovery, cells were incubated for either eight days of normoxia or four days of hypoxia followed by four days of normoxia.

Figure 5-11 shows the effect of hypoxia on the expression of genes related to cardiac identity. *RYR2* was downregulated by 0.2±0.4-fold, *ACTC1* was downregulated 0.3±0.02-fold, *MYH6* was downregulated 0.1±0.03-fold and *MYH7* was downregulated 0.05±0.01-fold. Interestingly, when calculated relative to *MYH7* expression, *MYH6* was upregulated 3±0.6-fold in hypoxia. However, after four days in hypoxia, there was no significant difference in *ACTC1* or *MYH6* expression compared to normoxia. Two days of recovery also did not elicit a change in expression. However, *MYH7* was downregulated by 0.17±0.1-fold after two days of hypoxia followed by two days of recovery and was further downregulated by 0.1±0.02-fold after four days of hypoxia compared to normoxia. Relative to *MYH7*, *MYH6* was upregulated 2.7±0.2-fold in the 2-day recovery cells and 5.3±0.8-fold in the hypoxic cells. The ratio of *MYH6* to *MYH7* was increased after four days of hypoxia, but decreased after two days of recovery, though was still not restored to normoxic levels. *RYR2* was downregulated 0.5±0.07-fold after four days in hypoxia, although this is not statistically different to normoxic expression. However, with two days of recovery *RYR2* expression was significantly lower than both the normoxic and hypoxic samples by 0.23±0.14-fold compared to normoxic controls. After four days of recovery following four days of hypoxia, *RYR2* expression was downregulated 0.3±0.1-fold.

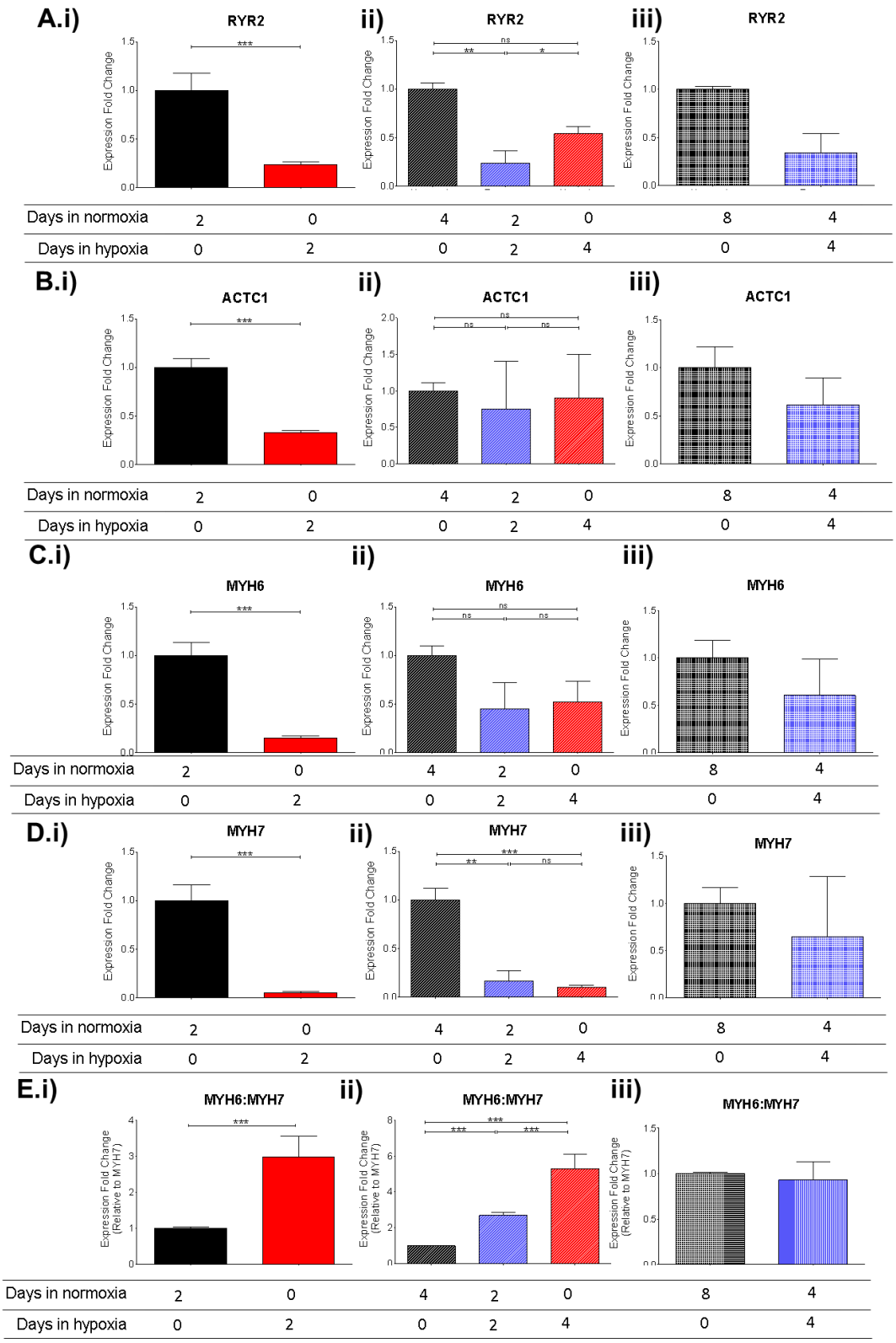

Figure 5-11. Expression of cardiac genes in iPSC-CMs in response to hypoxic conditions.

The expression of A) RYR2, B) *ACTC1*, C) *MYH6* and D) *MYH7* in various oxygen conditions. Plotted as fold change normalised to 18S, calculated using the ddCt method.

E) The expression of *MYH6* in various oxygen conditions, plotted as fold change normalised to *MYH7*, calculated using the ddCt method.

Statistics performed by (i) unpaired t-test and (ii) one-way ANOVA. * = P≤0.05, ** = P≤0.01, *** = P≤0.001 (i) and (ii) N=3, (iii) N=2. Error bars represent SEM.

After prolonged recovery, the expression of *ACTC1*, *MYH6* and *MYH7* appear to be slightly downregulated compared to the normoxic control. *ACTC1* is downregulated 0.6±0.3-fold, *MYH6* is downregulated 0.6±0.4-fold and *MYH7* is downregulated 0.6±0.6-fold. This indicates that prologued recovery after hypoxia may not be sufficient to restore the expression of these genes back to baseline.

The expression of the glycolytic genes hexokinase-2 (*HK2*) and lactate dehydrogenase (*LDHA*), and the FAO gene ATP-citrate lyase (ACLY) were analysed and shown in Figure 5-12. After two days of hypoxia, *HK2* was not significantly changed but *LDHA* was upregulated 5.4±1.9-fold. ACLY was downregulated 0.7±0.15-fold although this was not statistically significant. After four days of hypoxia, *HK2*, *LDHA* and ACLY were upregulated 3.2±1.1-fold, 16±6.3-fold and 3.8±1.3-fold respectively. After two days of recovery, neither *HK2* or *LDHA* were significantly different from the normoxic control, however ACLY was still upregulated 3.2±0.8-fold compared to normoxia. Furthermore, after four days of recovery, ACLY was still upregulated to 2.8±1.4-fold of control, however, *HK2* and *LDHA* were restored to normoxic levels.

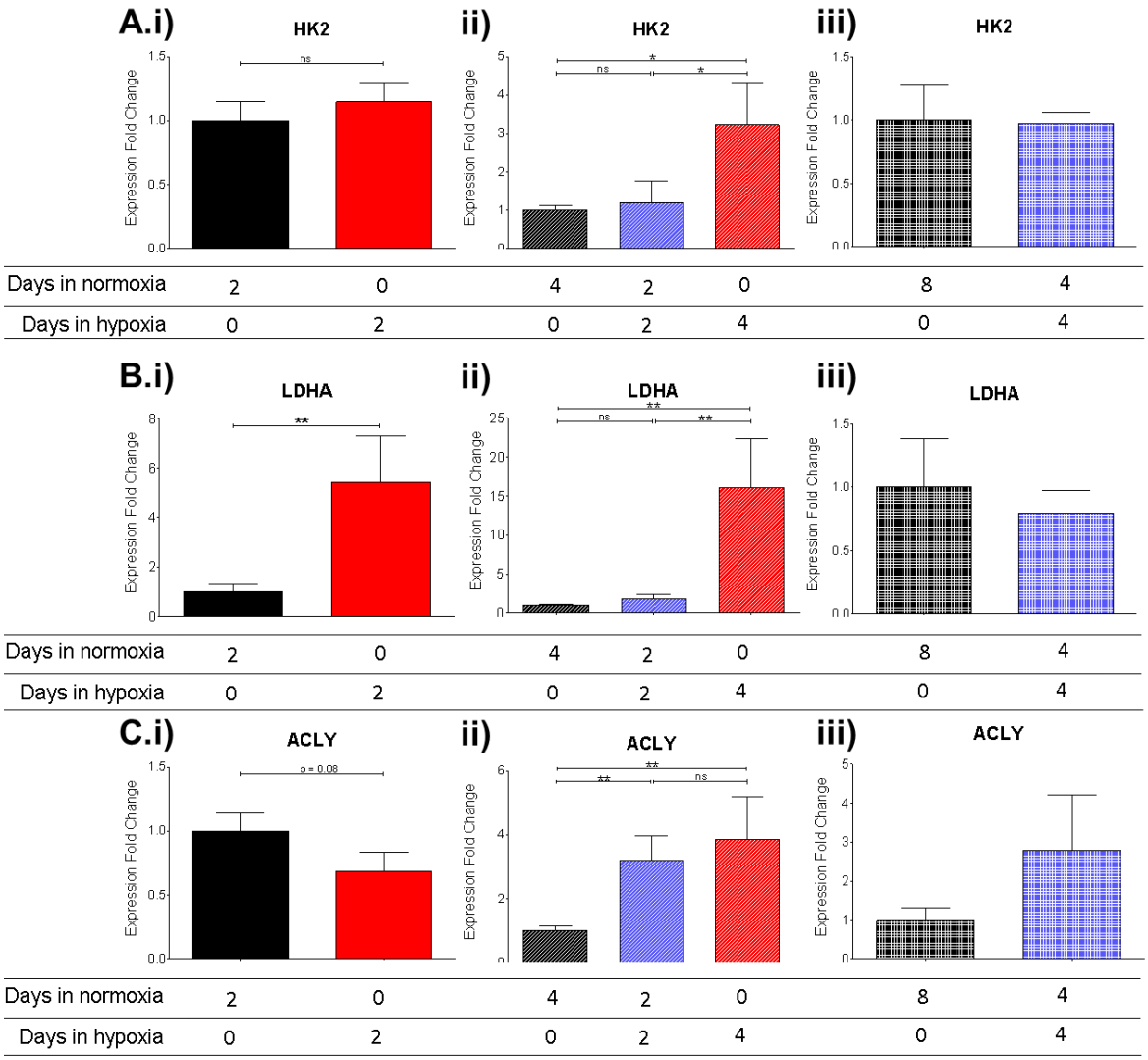

Figure 5-12. Expression of metabolic genes in iPSC-CMs in response to hypoxic conditions.

The expression of A) *HK2*, B) *LDHA* and C) ACLY in various oxygen conditions. Plotted as fold change normalised to 18S, calculated by ddCt. Statistics performed by (i) unpaired t-test and (ii) one-way ANOVA. * = P≤0.05, ** = P≤0.01, *** = P≤0.001 (i) and (ii) N=3, (iii) N=2. Error bars represent SEM.

To assess mitochondrial gene expression, the expression of cytochrome C oxidase subunit 1 (COX1) and the transcriptional co-activator Pparg coactivator 1 alpha (PGC-1a) is shown in Figure 5-13. COX1 is a component of the mitochondrial electron transport chain which is essential for oxidative phosphorylation and ATP production. PGC-1a is a master regulator of mitochondrial biosynthesis. After two days of hypoxia, COX1 is upregulated 4.8±1.1-fold. After four days of hypoxia, COX1 is upregulated even further to 10.9±3 fold compared to normoxia. It remains upregulated after two days of recovery at 3.6±1.2-fold of control, and after four days of recovery COX1 is still upregulated although to a lesser degree by 1.8±0.1-fold of normoxic expression. PGC-1a is downregulated 0.5±0.2-fold after two days of hypoxia although this is not statistically significant. There is no significant difference after four days of hypoxia, two days of recovery or four days of recovery compared to

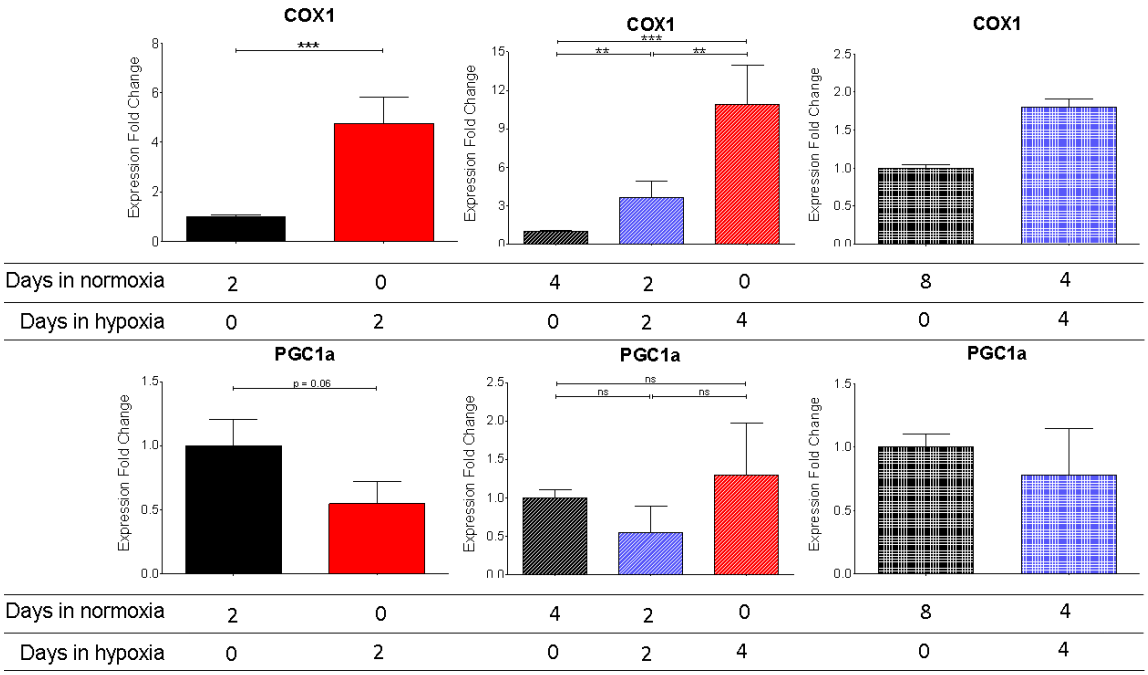

Figure 5-13. Expression of mitochondrial genes in iPSC-CMs in response to hypoxic conditions.
The expression of A) COX1 and B) PGC-1a in various oxygen conditions. Plotted as fold change normalised to 18S, calculated by ddCt. Statistics performed by (i) unpaired t-test and (ii) one-way ANOVA. * = P≤0.05, ** = P≤0.01, *** = P≤0.001 (i) and (ii) N=3, (iii) N=2. Error bars represent SEM.

controls. This indicates that on an expression level, mitochondrial biosynthesis may not have been impacted by the conditions tested, but the upregulation of COX1 suggests oxidative phosphorylation could have been affected by hypoxia.

The expression of the SNORD116 paralogues SNORD116-1, SNORD116-23 and SNORD116-25 in response to hypoxia are shown in Figure 5-14. These paralogues were chosen to represent group I, II and III of SNORD116, respectively. After two days of hypoxia, there is no significant

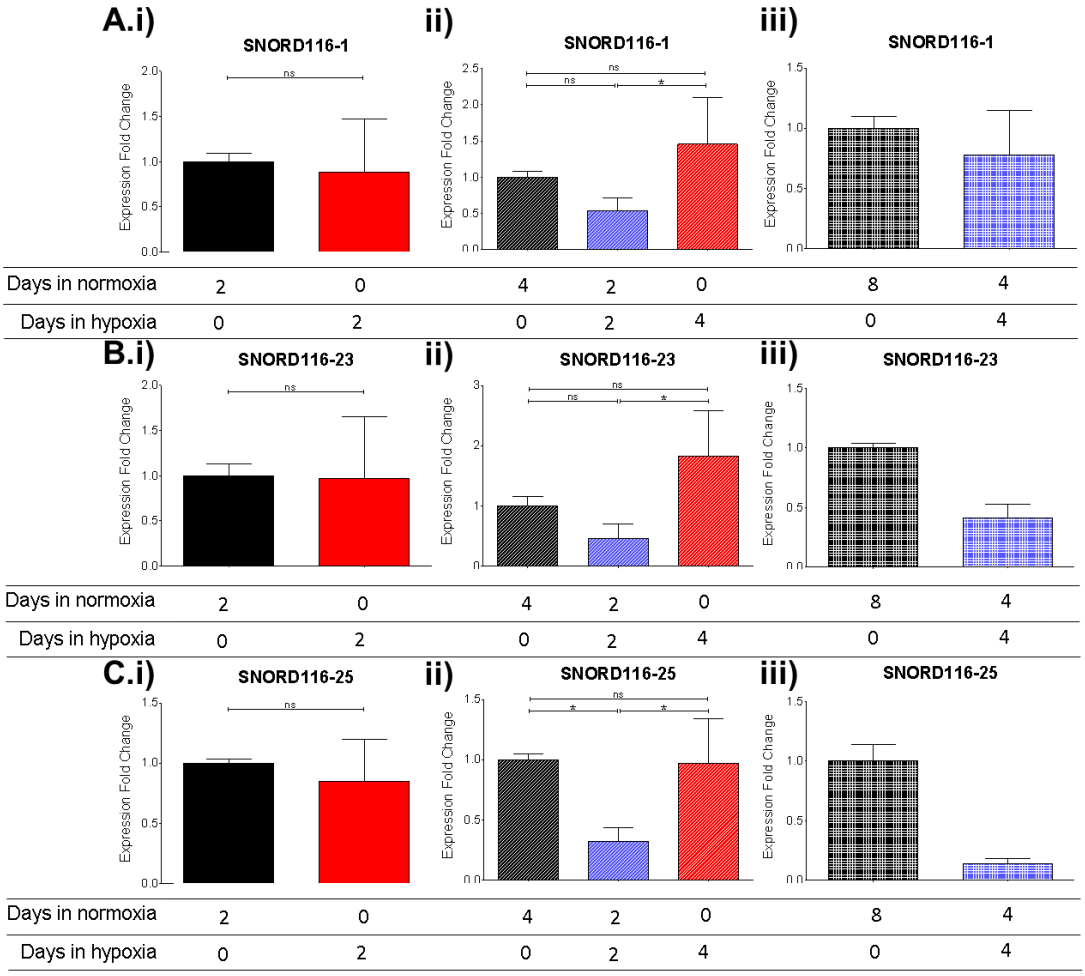

Figure 5-14. Expression of SNORD116 in iPSC-CMs in response to hypoxic conditions.
The expression of A) SNORD116-1, B) SNORD116-23 and C) SNORD116-25 in various oxygen conditions. Plotted as fold change normalised to 18S, calculated by ddCt. Statistics performed by (i) unpaired t-test and (ii) one-way ANOVA. * = P≤0.05, ** = P≤0.01, *** = P≤0.001 (i) and (ii) N=3, (iii) N=2. Error bars represent SEM.

difference in SNORD116 expression. After four days of hypoxia, SNORD116-1 and SNORD116-23 are both upregulated 1.5±0.7-fold and 1.8±0.8-fold compared to control, though this was not statistically significant. SNORD116-25 expression did not change in four days of hypoxia. However, after two days of recovery all three paralogues were downregulated relative to normoxic controls, at 0.3±0.3-fold. Furthermore, all three paralogues remained downregulated compared to controls after four days of recovery. SNORD116-1 was downregulated the least by 0.8±0.4-fold, whereas SNORD116-23 and SNORD116-25 were downregulated 0.4±0.1-fold and 0.1±0.04-fold. These results indicate that hypoxia alone may not dramatically impact SNORD116 expression, but the recovery after exposure to hypoxia appears to involve a downregulation of SNORD116.

To summarise, the results here show that hypoxic stress reduced cardiomyocyte viability and contractility. Cardiomyocyte metabolism was significantly impacted by hypoxia and exhibited overall reduced metabolic capacity. Hypoxic conditions caused cardiomyocytes to release approximately double the number of exosomes than cardiomyocytes in normoxia. This supports previous findings that cardiac stress induces increased exosome output (65). Hypoxia caused a reduction in cardiac gene expression, but an increase in metabolic gene expression. Although SNORD116 expression was not significantly affected by hypoxia alone, cells recovering from hypoxia in normoxic conditions appear to have reduced SNORD116 expression. This suggests that SNORD116 modulation in cardiomyocytes may be important in response and repair pathways post-hypoxic damage. To determine if this was unique to cardiomyocytes or occurred in other cardiac cell types, cardiac fibroblasts were also subjected to hypoxic stress.

5.2.2 The effect of hypoxia on cardiac fibroblasts

IPSC-CFs were cultured in 24-well plates for four days at 37^{O}C, 5% CO_2 in either 20% (normoxic) or 2% (hypoxic) O_2. The media was changed for fresh pre-conditioned media after two days. After four days, the cells were fixed in 4% formaldehyde and stained for aSMA by immunocytochemistry. Representative images are shown in Figure 5-15. CellProfiler was used to quantify the intensity of aSMA. Cells were identified using the OCM stain and the mean intensity of aSMA within each cell was measured. The average cell intensity for each image was calculated. CellProfiler was also used to count the number of nuclei per image using the DAPI stain. Three separate images of each well were used as technical replicates, and three wells were analysed per sample.

The mean intensity of aSMA increased from 0.04±0.01 in normoxia to 0.06±0.004 in hypoxia. The number of nuclei decreased from 164±23 in normoxia to 134±37 in hypoxia, though due to variation in the hypoxic samples this was not statistically significant. Overall, these results show that there is increased expression of aSMA in iPSC-CFs in response to hypoxia, and there may be a reduction in the number of nuclei which could suggest a reduction in viability.

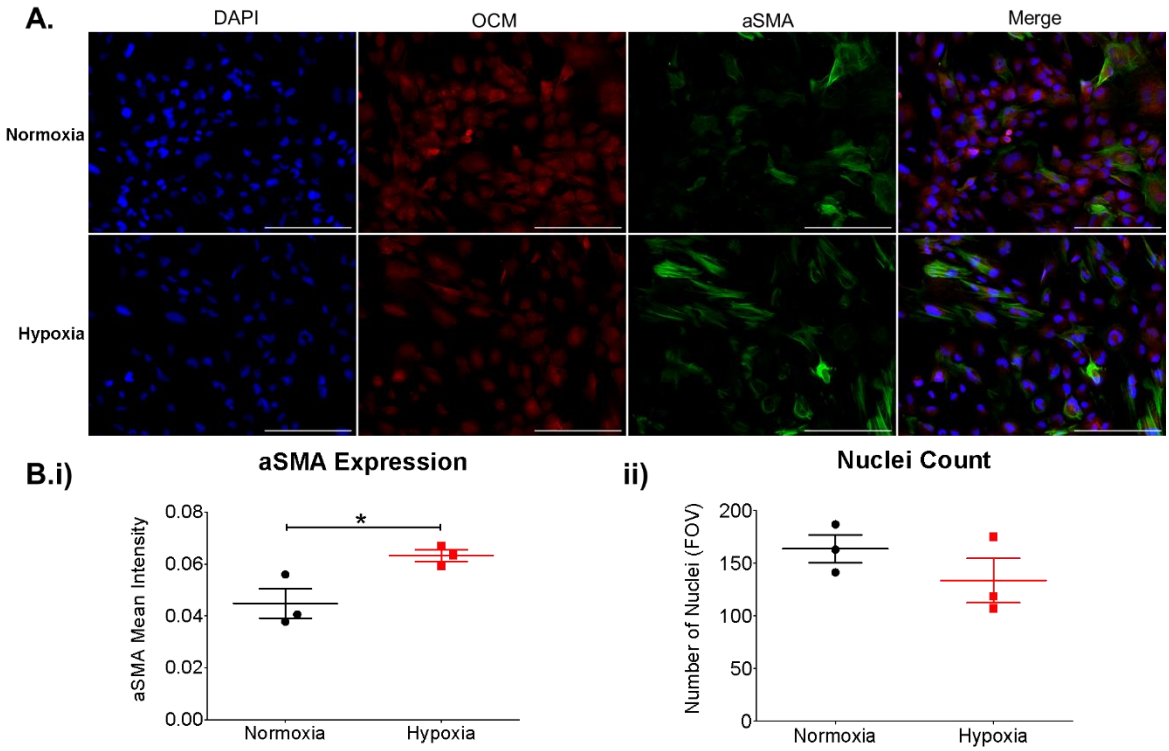

Figure 5-15. The effect of hypoxia on aSMA and nuclei count of iPSC-CFs.
A. Cardiac fibroblasts stained for aSMA under normoxic and hypoxic conditions. Blue = DAPI (1:500), red = OCM (1:1000), green = aSMA. Magnificatiopn = 20x, scale bar = 200um.
B.i) quantification of aSMA intensity and ii) number of nuclei performed using CellProfiler. N=. Error bars represent SEM. OCM = orange cell mask, FOV = field of view.

To investigate the effect of hypoxia on gene expression in IPSC-CFs, the cells were cultured for cultured in 24-well plates for four days at 37^{O}C, 5% CO_2 in either 20% (normoxic) or 2% (hypoxic) O_2. RNA was isolated at day 0, day 2 and day 4 from both the normoxic and hypoxic samples. Figure 5-16 shows the resulting gene expression changes caused by hypoxia. Contrary to protein expression shown in Figure 5-15, the gene expression of *aSMA* does not appear to be affected by hypoxia. The pro-apoptosis genes *BAX* and Caspase 3 are both downregulated 0.7±0.02-fold after two days in hypoxia. After four days of hypoxia, they are upregulated 1.2±0.09 and 1.9±0.1-fold, respectively. The FAO gene ACLY is downregulated 0.4±0.01-fold after two days of hypoxia but is upregulated 1.4±0.04-fold after four days of hypoxia compared to the

normoxic control. The glycolysis gene *LDHA* is upregulated 1.6±0.07-fold after two days and 2.1±0.08-fold after four days of hypoxia compared to the normoxic control.

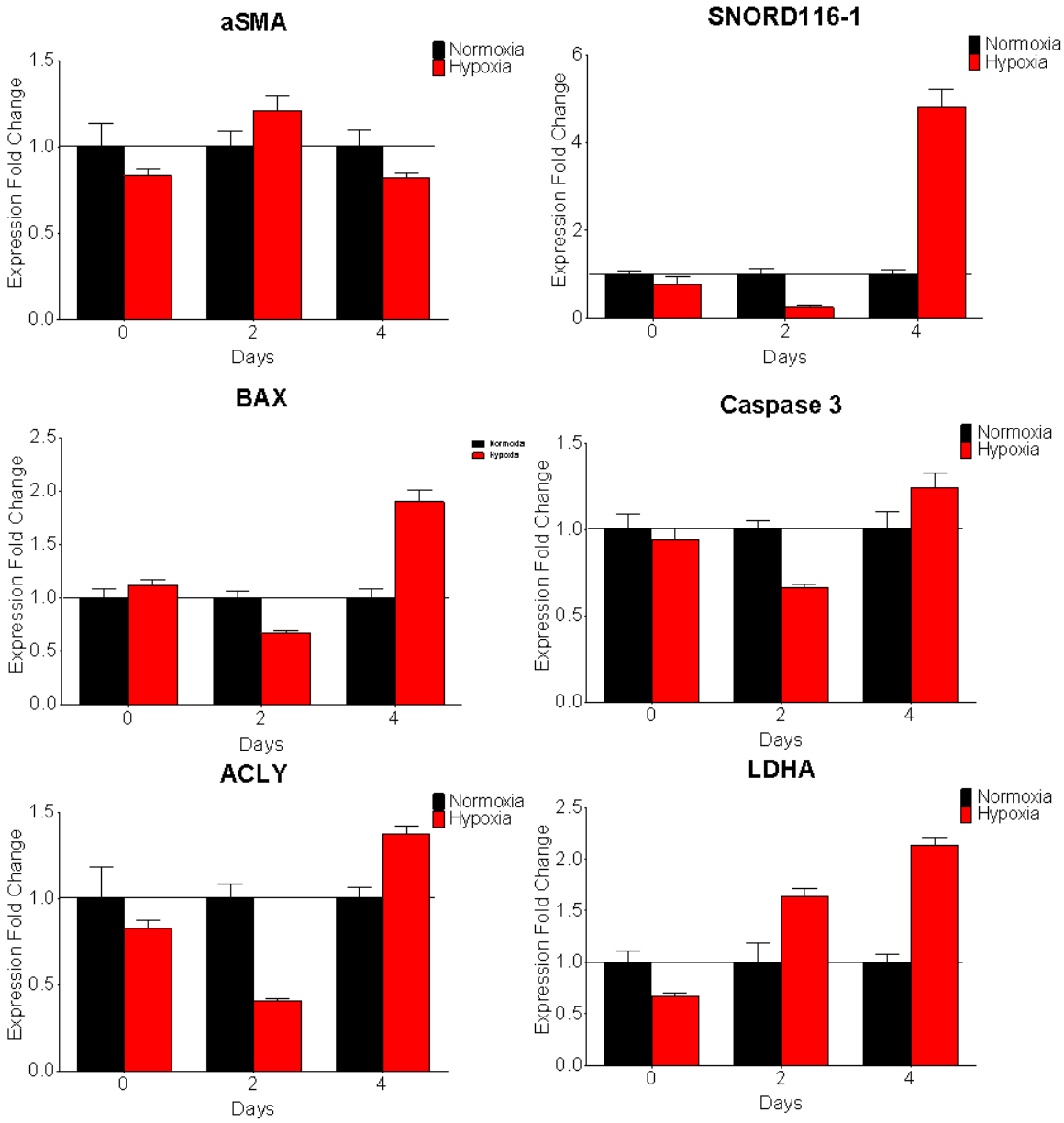

Figure 5-16. IPSC-CF gene expression in response to hypoxia.
The expression of various genes in IPSC-CFs in response to 0, 2 and 4 days of culture in either normoxic or hypoxic conditions. Expression plotted as fold change relative to age-matched normoxic control, calculated using ddCt normalised to GAPDH. N=1. Error bars represent SEM.

SNORD116-1 undergoes the greatest expression changes of the genes analysed. After two days of hypoxia, SNORD116-1 is downregulated 0.2±0.06-fold compared to normoxic expression. However, after four days of hypoxia SNORD116-1 is upregulated 4.8-fold. Interestingly, the trend of expression for SNORD116 appears to follow the same trend as the pro-apoptosis genes *BAX* and Caspase 3 under these conditions, suggesting that the expression of SNORD116 may be linked to apoptosis in hypoxic cardiac fibroblasts. More biological replicates are needed to confirm these findings.

Overall, hypoxia seems to have opposing effects on the expression of SNORD116 in different cardiac cell types, suggesting that its mechanism of action may be cell-type specific. To further investigate this trend, other cardiac stresses were then employed to determine the effect on SNORD116 expression.

5.3 The effects of doxorubicin on cardiac cell types

Doxorubicin (DOX) is a cardiotoxic chemotherapy drug which causes increased DNA damage, ROS and mitochondrial dysfunction in cells. To test the toxicity of doxorubicin on cardiomyocytes, a cell viability assay was performed using cell tire-glo. IPSC-CMs were seeded into a 96-well plate at 100,000 cells/cm^2. After 24-hours, the media (RPMI/B27) was changed for fresh media supplemented with 0uM, 0.5uM, 1uM or 2uM doxorubicin. At 0 hours, 6 hours, 12 hours and 24 hours after treatment with doxorubicin, the cell titre-glo assay was performed to determine cell number. The results are shown in Figure 5-17. Without doxorubicin treatment, cell number increased from 38,000±7,000 to 51,000±1400. Cell number then stayed around this level for the rest of the time course. In 0.5uM doxorubicin, cell number did not increase after 6 hours or 12

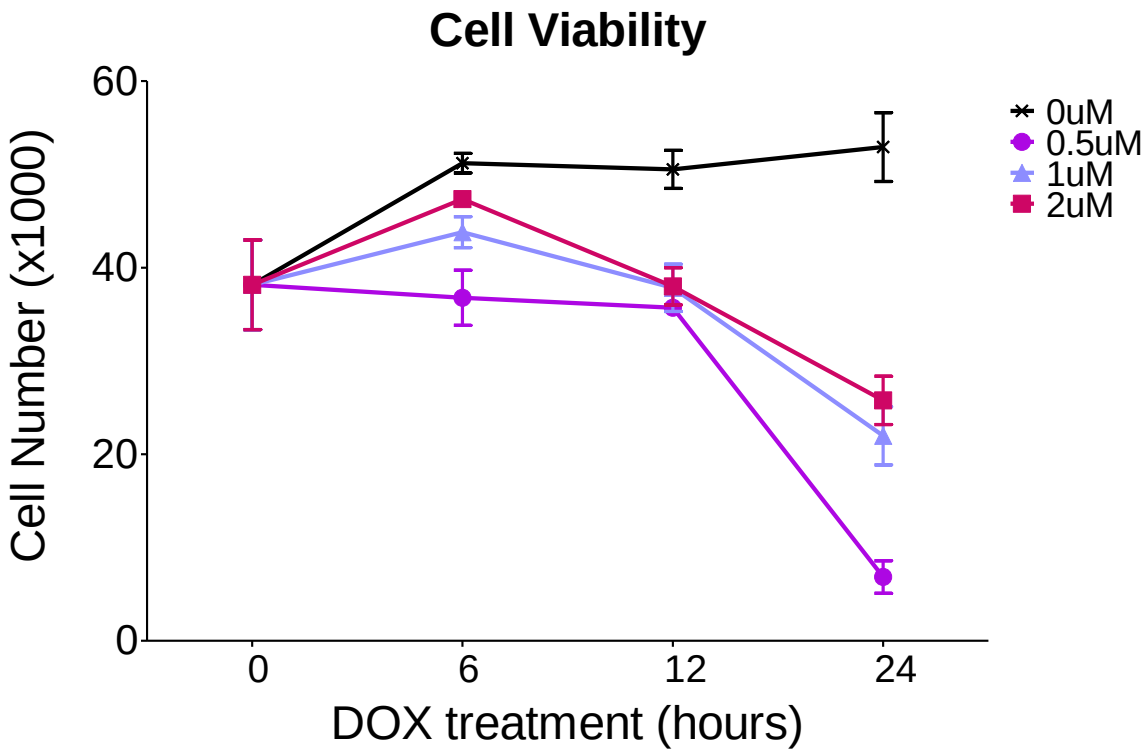

Figure 5-17. The effect of doxorubicin on iPSC-CM viability.
Number of cells present after 0, 6, 12 and 24-hours of 0uM, 0.5uM, 1uM and 2uM doxorubicin. Assessed using Cell titre-glo. N=1. Error bars represent standard deviation between technical replicates.

hours but decreased to 7,000±2,400 cells after 24 hours doxorubicin. After 6 hours in 1uM and 2uM doxorubicin, cell number increased to 44,000±2,300 and 47,000±200 cells, respectively. After 12 hours, cell number had decreased in both 1uM and 2uM doxorubicin to 38,000±2,800 cells. After 24 hours in 1uM doxorubicin, cell number had decreased to 22,000±4,400 cells. After 24 hours in 2uM doxorubicin, cell number had decreased to 26,000±3,700 cells. The apparent increase in cell number after 6 hours in the control, 1uM and 2uM samples could indicate the presence of proliferative cell types within the cardiomyocyte population. The results suggest that 0.5uM doxorubicin has a higher level of toxicity to the cells as it causes the greatest decrease in cell number. However, the cells exposed to 0.5uM doxorubicin also do not show an increase in cell number which could suggest a higher purity of cardiomyocytes. The cardiomyocytes may be more sensitive to doxorubicin than proliferative cell types (or are otherwise unable to account for cell death through cell division), therefore leading to a larger decrease in cell viability. As the 6-hour time point did not show a response in cell viability, it was not used in further experiments. A concentration of 1uM doxorubicin was used in future iPSC-CM experiments as this concentration had the median effect on viability.

To analyse the effect of doxorubicin on contraction, iPSC-CMs were seeded at 100,000 cells/cm^2 into a 96-well plate. The cells were fed RPMI/B27 every other day for four days. 24 hours after the final media change, the media was supplemented doxorubicin to give a final concentration of 1uM (or a vehicle control of 0uM doxorubicin). After 12 hours, the cells were recorded using a temperature-controlled microscope at 37^{O}C for at least ten seconds. The cells were recorded again after 24 hours. The resulting videos were analysed using the ImageJ plugin MUSCLEMOTION (356,357) which uses pixel movement to detect contraction. The results are shown in Figure 5-18. After 12 hours doxorubicin treatment, the cardiomyocytes were not producing any detectable movement and the recordings were therefore not able to be analysed. However, after 24-hours the cardiomyocytes were visibly contractile and therefore able to be analysed. After 24 hours doxorubicin treatment, contraction amplitude was reduced from 38±15 to 13±5. Contraction frequency doubled from 0.5±0.05 Hz to 1±0.3 Hz, and the percentage of events that were classed as arrhythmogenic increased from 8±16% in control conditions to 67±25% in doxorubicin treatment.

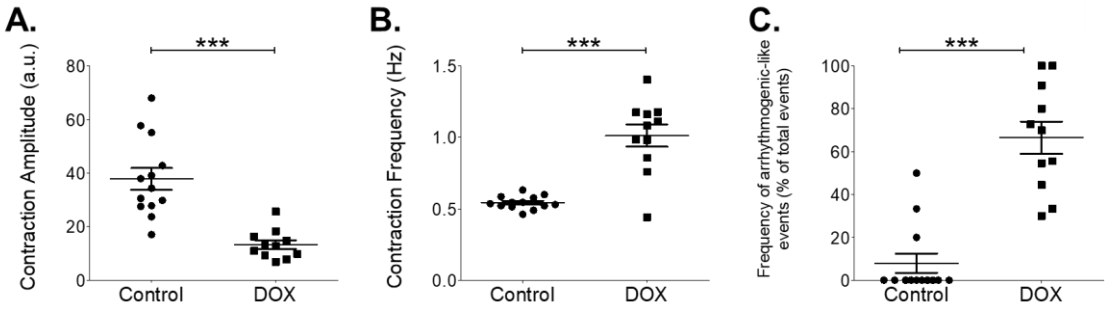

Figure 5-18. The effect of doxorubicin on the contraction of iPSC-CMs.
The average A) contraction amplitude (in arbitrary units), B) contraction frequency (in Hz, or number of contractions per second) and C) percentage of total events that are classed as arrhythmogenic-like events. Statistics calculated using unpaired t-test. * = P≤0.05, ** = P≤0.01, *** = P≤0.001. Control N=13, DOX N=11. Error bars represent SEM.

RNA was isolated from the cells at 0-hour, 12-hour and 24-hour time points during doxorubicin treatment to evaluate the effect of doxorubicin on gene expression. When calculated as relative to GAPDH, *ACTC1* expression decreases 0.5±0.06-fold after 12 hours and is decreased further by 0.4±0.03-fold after 24 hours. The sarcoplasmic calcium channel *RYR2* was downregulated 0.4±0.2-fold and 0.5±0.3-fold after 12 and 24 hours of treatment. The pro-apoptotic gene *BAX* was downregulated 0.5±0.2-fold and 0.4±0.08-fold after 12 and 24 hours of treatment. After 12 hours of doxorubicin treatment, there was no change in the expression of SNORD116-1, 23 or 25. However, after 24 hours of doxorubicin treatment, SNORD116-1, 23 and 25 were upregulated 3±4-fold, 3±3-fold and 3±4-fold, respectively. Due to spread between samples this was not statistically significant.

Doxorubicin has been shown to affect glycolysis through both direct and indirect interactions (182). This could cause doxorubicin treatment to affect the expression of the housekeeper gene GAPDH, which is important in glycolysis. Therefore, gene expression was also calculated relative to *ACTC1*, a structural gene whose expression may be more resistant to doxorubicin treatment. In addition, cell viability data shown in Figure 5-17 indicates that doxorubicin may have a higher toxicity to cardiomyocytes than proliferative cardiac cell types. Therefore, calculating expression fold change relative to *ACTC1* allows the expression changes to be more specific to cardiomyocytes. Relative to *ACTC1*, GAPDH was upregulated 2±0.3-fold and 2.4±0.2-fold after 12 and 24 hours of treatment. Additionally, relative to *ACTC1*, *RYR2* and *BAX* expression was not significantly changed after 12 or 24 hours of doxorubicin treatment. SNORD116-1, 23 and 25 were not significantly changed after 12 hours of treatment, however after 24 hours they were upregulated 10±6-fold, 7±4-fold and 9±5-fold compared to controls. Despite an outlier replicate, this was statistically significant.

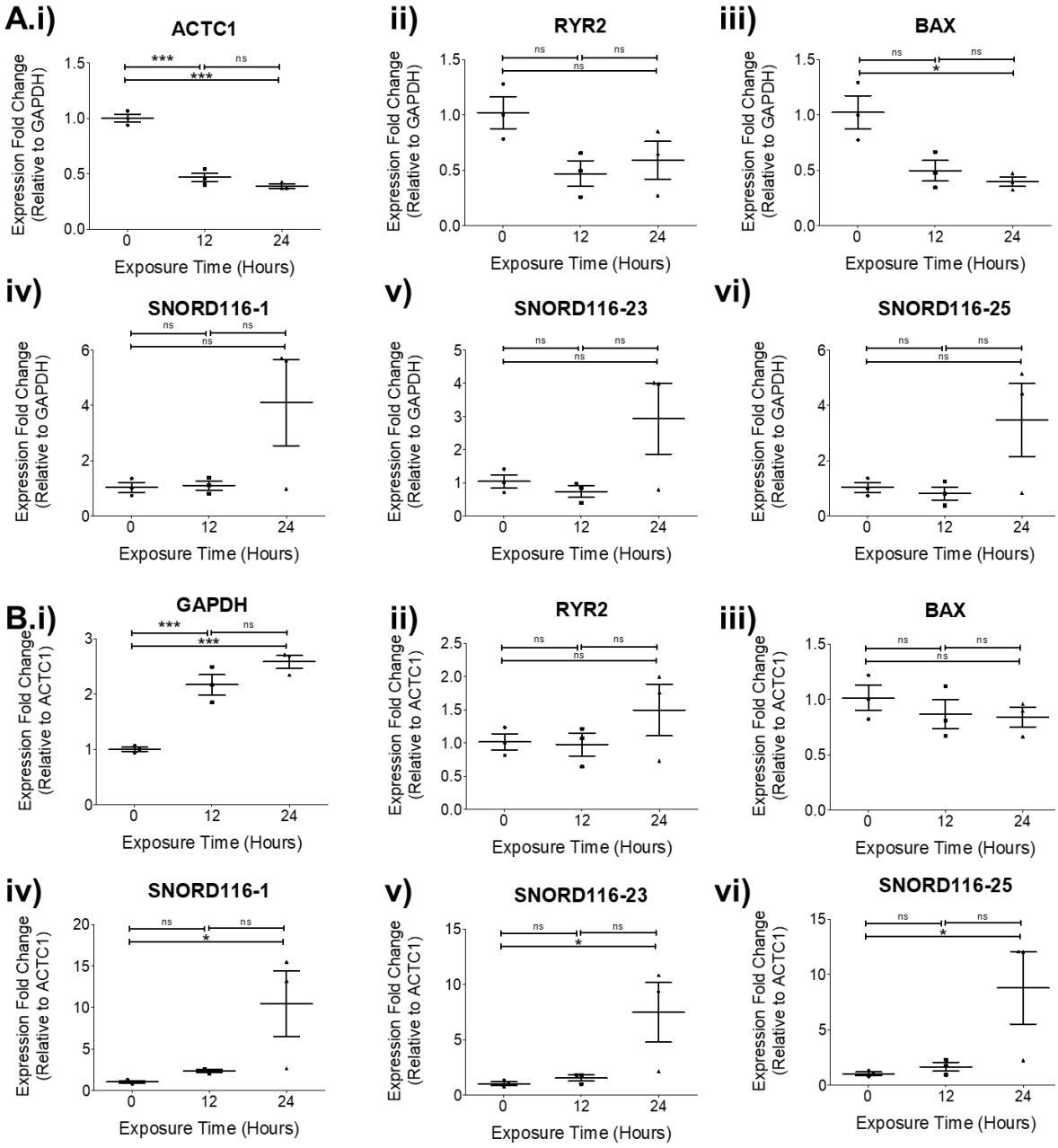

Figure 5-19. The effect of doxorubicin treatment on the gene expression of iPSC-CMs
A. The effect of 0, 12 and 24 hours of doxorubicin treatment on the expression of (i-vi) *ACTC1*, RYR2, *BAX*, SNORD116-1, SNORD116-23 and SNORD116-25. Plotted as expression fold change relative to 0 hours treatment. Calculated using ddCt normalised to GAPDH.
B. The effect of 0, 12 and 24 hours of doxorubicin treatment on the expression of (i-vi) GAPDH, RYR2, *BAX*, SNORD116-1, SNORD116-23 and SNORD116-25. Plotted as expression fold change relative to 0 hours treatment. Calculated using ddCt normalised to *ACTC1*.
Statistics calculated by one-way ANOVA. * = P≤0.05, ** = P≤0.01, *** = P≤0.001. N=3. Error bars represent SEM.

To analyse the effect of doxorubicin on the gene expression of cardiac fibroblasts, iPSC-CFs were seeded into a 24-well plate at 50,000 cells/cm^2. The cells were allowed to grow to confluence for 4 days (with media changes every other day). 24 hours after the final media change, the cells were fed with fibroblast media supplemented with 0uM, 0.5uM, 1uM or 2uM. After 24-hours, the cells were lysed and RNA isolated. Relative to GAPDH, SNORD116-1 expression was upregulated 6±0.5-fold, 7±0.4-fold and 8±0.7-fold in response to 0.5uM, 1uM and 2uM doxorubicin relative to 0uM control. The myofibroblast marker ACTA2 was upregulated 2±0.2-fold, 3±0.21-fold and 3±0.4-fold in 0.5uM, 1uM and 2uM doxorubicin relative to 0uM control. The mitochondrial biogenesis gene PGC-1a was downregulated 0.6±0.04-fold in response to 0.5uM doxorubicin, but otherwise its expression was unchanged relative to 0uM. The oxidative phosphorylation gene COX1 was upregulated in response to 0.5uM and 1uM to 1.4±0.4-fold and 1.4±0.2-fold respectively but did not respond to 2uM doxorubicin. The anti-apoptotic gene BCL2 is downregulated under all three concentrations relative to 0uM, at 0.6±0.2-fold, 0.4±0.1-fold and 0.5±0.1-fold. The proliferation marker KI67 is downregulated 0.7±0.2-fold in response to 0.5uM doxorubicin, but otherwise its expression was unchanged relative to 0uM.

As doxorubicin may influence glycolysis and by extension the expression of GAPDH, expression was also normalised to the gene for smooth muscle alpha actin (ACTA2), a myofibroblast marker. This emphasises the expression changes in myofibroblasts. When relative to ACTA2, SNORD116-1 is upregulated 2.5±0.3-fold in response to 0.5uM, 1uM and 2uM doxorubicin compared to 0uM. GAPDH is downregulated 0.4±0.04-fold, 0.3±0.03-fold and 0.3±0.04-fold in 0.5uM, 1uM and 2uM doxorubicin. PGC-1a is downregulated by 0.3-fold in all doxorubicin concentrations. COX1 is downregulated 0.5±0.03-fold, 0.3±0.02-fold and 0.2±0.02-fold in 0.5uM, 1uM and 2uM. BCL2 is downregulated 0.2±0.04-fold, 0.08±0.02-fold and 0.08±0.02-fold, and Ki67 is downregulated 0.2±0.02-fold in response to all tested concentrations.

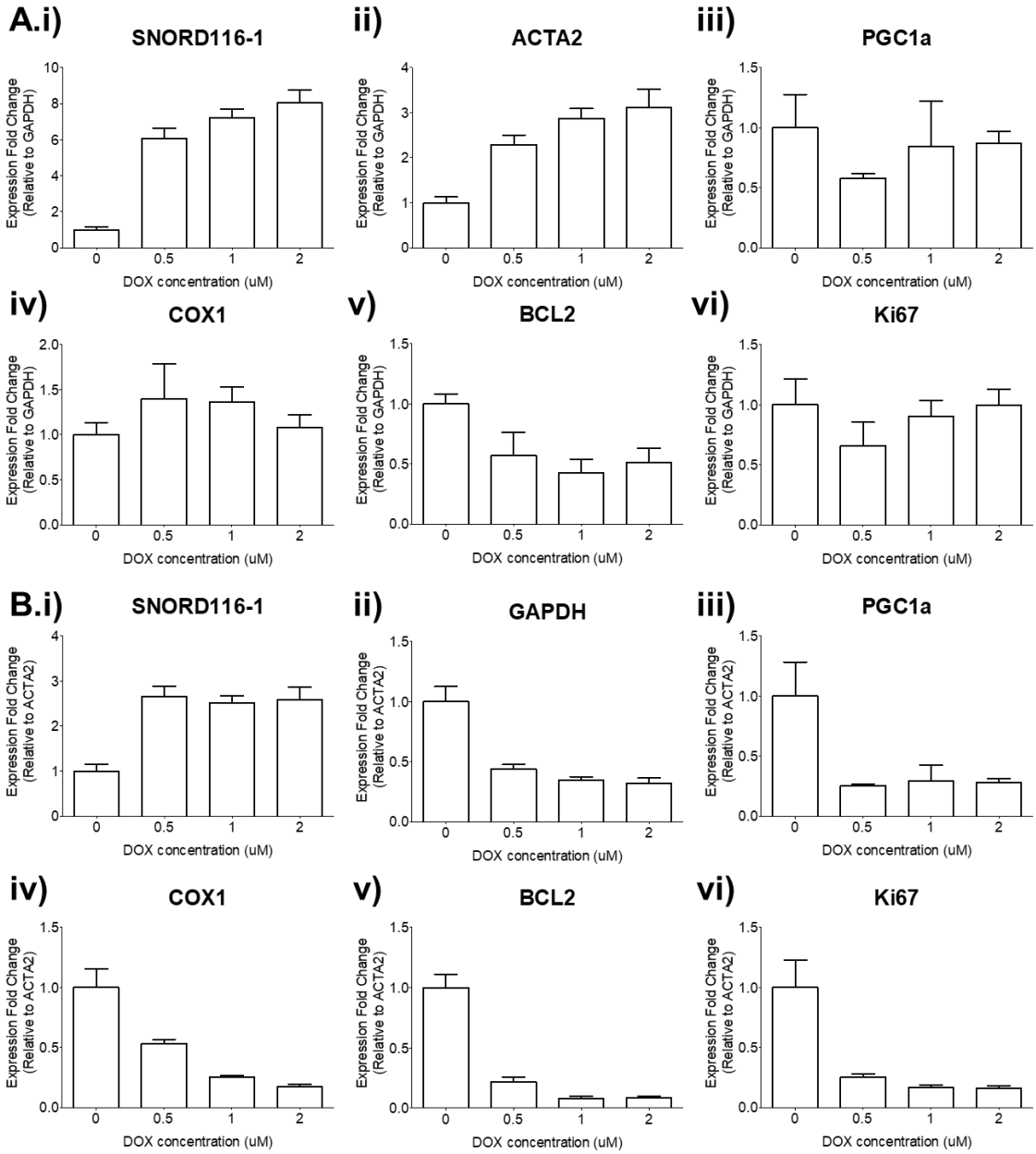

Figure 5-20. The effect of doxorubicin treatment on the gene expression of iPSC-CFs

A. The effect of 0, 0.5, 1 and 2uM of doxorubicin on the expression of (i-vi) SNORD116-1, ACTA2, PGC-1a, COX1, BCL2 and KI67. Plotted as expression fold change relative to 0uM doxorubicin. Calculated using ddCt normalised to GAPDH.

B. The effect of 0, 0.5, 1 and 2uM of doxorubicin on the expression of (i-vi) SNORD116-1, GAPDH, PGC-1a, COX1, BCL2 and KI67. Plotted as expression fold change relative to 0uM doxorubicin. Calculated using ddCt normalised to ACTA2. N=1. Error bars represent SEM.

Overall, in iPSC-CMs, doxorubicin has a negative impact on cell viability and contraction, coupled with a downregulatory effect on gene expression. A similar response is also seen in the gene expression of iPSC-CFs. However, in both cell types SNORD116 expression appears upregulated in response to doxorubicin. This could suggest that doxorubicin-induced cardiotoxicity may involve similar mechanisms regarding SNORD116 function in both cardiac cell types.

It was important to evaluate the effect of non-cardiotoxic drugs on SNORD116 expression to investigate whether the changes observed were as a result of increased energy demand or specifically cardiotoxic effects. Therefore, an alternative non-toxic drug was also used to induce cardiac stress.

5.4 The effect of isoprenaline on cardiac cell types

Isoprenaline is a non-selective β-adrenergic agonist. Historically, isoprenaline has been used in the clinic as a treatment for bradycardia as it has stimulatory effect on heart rate. During increased workload, adrenaline and noradrenaline are released which activate the β-receptors in the heart. In cardiomyocytes, this causes increased contraction frequency. Isoprenaline can be used on iPSC-CMs to mimic the signalling of increased workload in the heart. To test if isoprenaline is toxic in cardiomyocytes, a cell viability assay was performed using cell tire-glo. IPSC-CMs were seeded into a 96-well plate at 100,000 cells/cm^2. After 24-hours, the media (RPMI/B27) was changed for fresh media supplemented with 0uM, 2uM, 5uM or 10uM isoprenaline. At 0 hours, 6 hours, and 12 hours after treatment with isoprenaline, the cell titre-glo assay was performed to determine cell number. The results are shown in Figure 5-21 shows that overall, there was no decrease in cell viability in

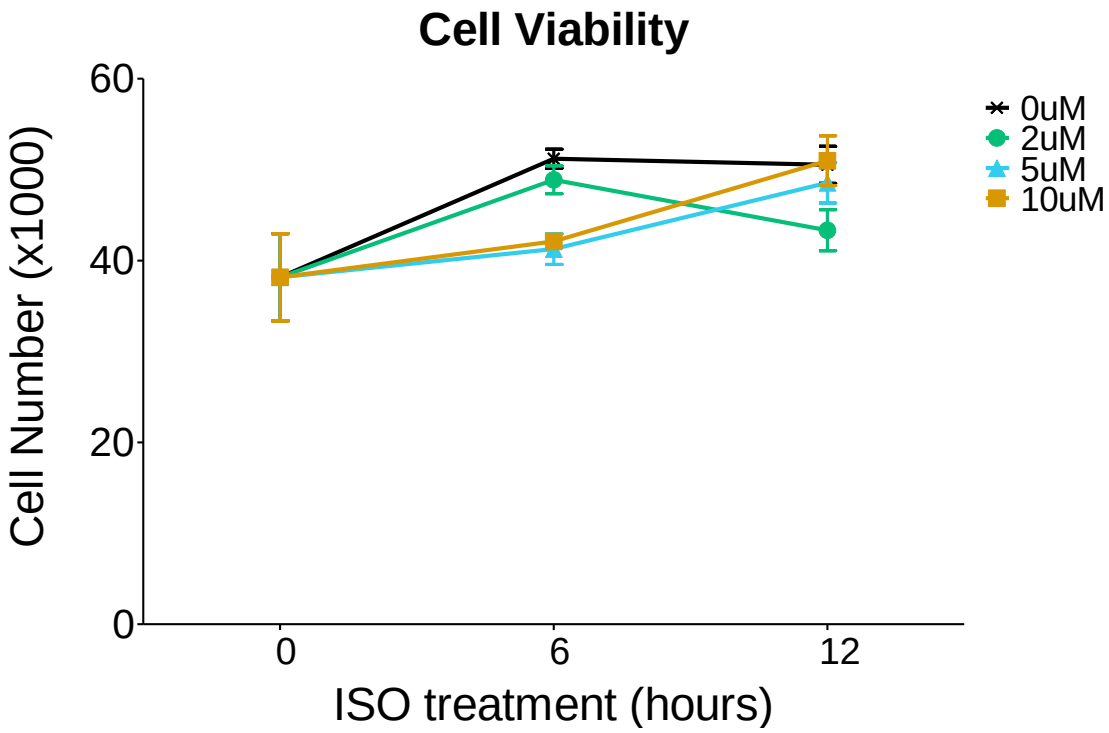

Figure 5-21. The effect of isoprenaline on iPSC-CM viability.
Number of cells present after 0, 6 and 12-hours of 0uM, 2uM, 5uM and 10uM isoprenaline. Assessed using Cell titre-glo. N=1. Error bars represent standard deviation between technical replicates.

response to isoprenaline treatment. After 6 hours, the control increased from 38,000±7,000 cells to 51,000±1400. Cell number then stayed at this level for the rest of the time course. In 2uM isoprenaline, cell number increased to 49,000±2,000 after 6 hours but decreased to 43,000±3,000 cells after 12 hours of treatment. In both 5uM and 10uM isoprenaline, cell number increased to 42,000±2,000 cells after 6 hours. After 12 hours, cells in 5uM isoprenaline had grown to 49,000±3,000 cells. In 10uM isoprenaline, cell number increased to 51,000±4,000 cells. The increase in cell number in all samples compared to the 0-hour time point could indicate the presence of proliferative cell types in the cardiomyocyte samples. Overall, isoprenaline was not found to be toxic to the cells.

Isoprenaline is a fast-acting drug which takes effect almost immediately. Therefore, the effects of isoprenaline were analysed after short-term exposure to the drug. IPSC-CMs were seeded at 100,000 cells/cm^2 into a 96-well plate. The cells were fed RPMI/B27 every other day for four days. 24 hours after the final media change, the media was supplemented with isoprenaline to give a final concentration of 5uM (or a vehicle control of 0uM isoprenaline). After 5 minutes, the cells were recorded using a temperature-controlled microscope at 37^{O}C for at least ten seconds. The cells were recorded again after 1 hour. The resulting videos were analysed using the ImageJ plugin MUSCLEMOTION. The results are shown in Figure 5-22. After 5 minutes contraction amplitude was unchanged. However, contraction frequency had increased from 0.9±0.2 Hz in the control to 1.2±0.3 Hz in response to isoprenaline. One hour after treatment, contraction frequency had increased from 0.7±0.06 Hz in the

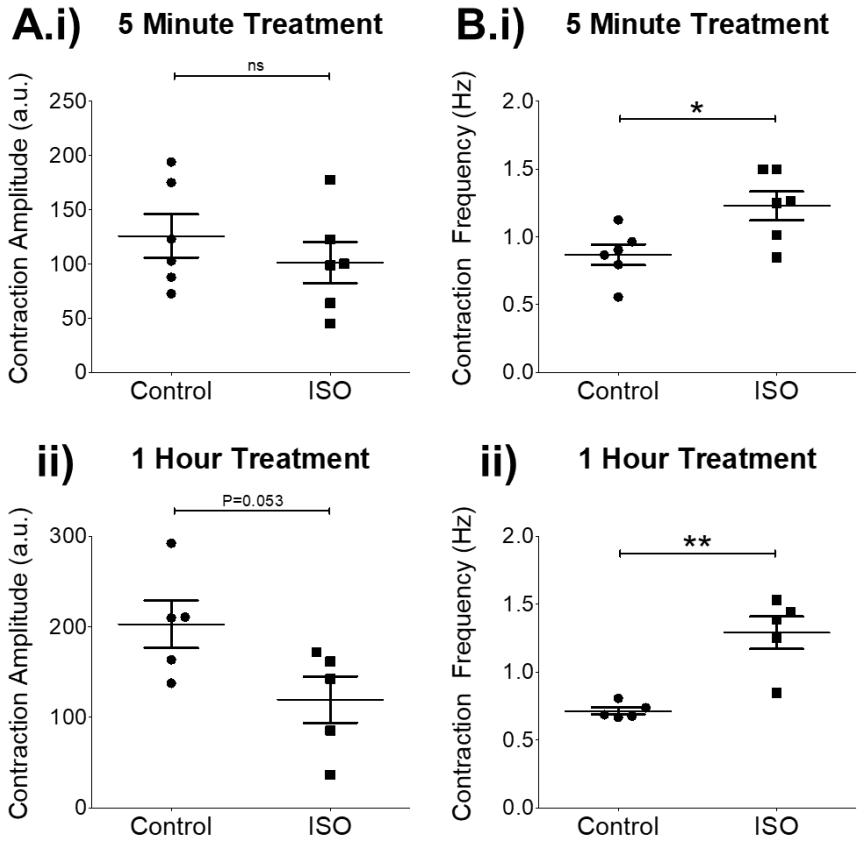

Figure 5-22. The effect of isoprenaline on the contraction of iPSC-CMs.
The average A) contraction amplitude (in arbitrary units) and B) contraction frequency (in Hz, or number of contractions per second) after (i) 5 minutes or (ii) 1 hour of isoprenaline treatment. Statistics calculated using unpaired t-test. * = P≤0.05, ** = P≤0.01, *** = P≤0.001. N=6 (5 min), N=5 (1 hour). Error bars represent SEM.

control to 1.3±0.3 Hz in response to isoprenaline. Contrary to the expected response to isoprenaline, contraction amplitude had decreased from 126±49 in the control to 101±47, though this was not statistically significant. Overall, isoprenaline mainly appeared to have a stimulatory effect on contraction frequency.

RNA was isolated from the cells at 0-minute, 5 minute and 60 minute time points during isoprenaline treatment to evaluate the effect of short-term isoprenaline treatment on the gene expression of iPSC-CMs. Overall, none of the genes analysed were significantly upregulated in response to isoprenaline treatment. SNORD116-1, 23 and 25 showed a slight upregulation of ~2-fold in response to 5 minutes of isoprenaline treatment but the variation between samples was too great for this to be statistically significant. Although isoprenaline appears to have an immediate effect on contraction, it does not appear to have an immediate effect on gene expression. This may be because, for all the genes analysed, the cells did not have enough time to transcribe or degrade the mRNA present before RNA isolation was performed.

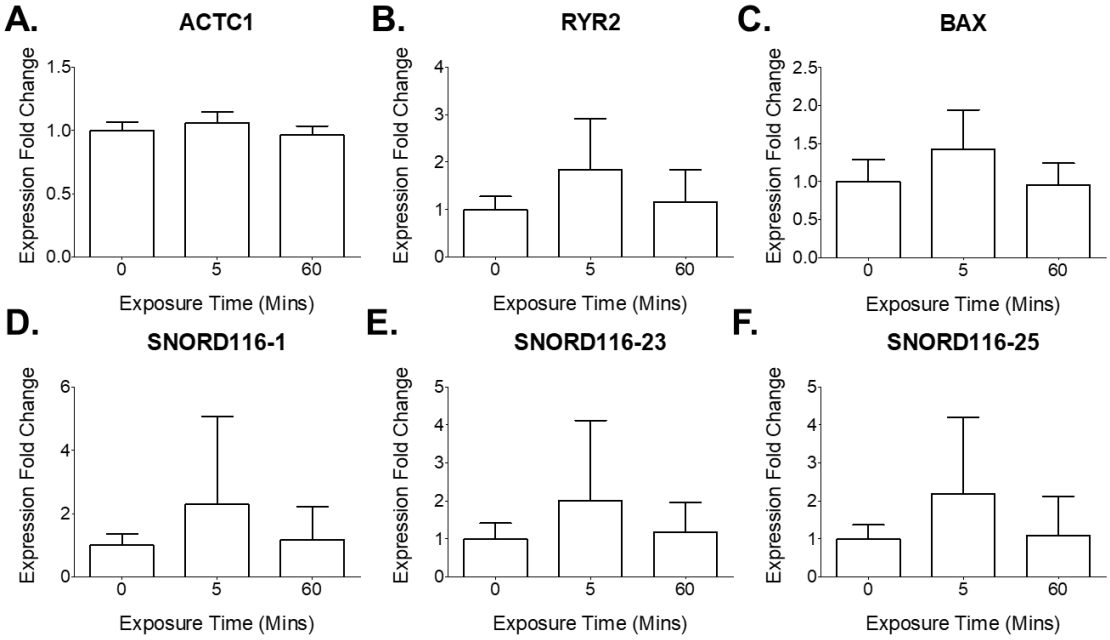

Figure 5-23. The effect of isoprenaline treatment on the gene expression of iPSC-CMs
The effect of 0, 5 and 60 minutes of isoprenaline treatment on the expression of (A-F) *ACTC1*, RYR2, *BAX*, SNORD116-1, SNORD116-23 and SNORD116-25. Plotted as expression fold change relative to 0 minutes treatment. Calculated using ddCt normalised to GAPDH. N = 3. Error bars represent SEM. Statistics calculated using one-way ANOVA.

During increased workload, β-adrenergic receptor activators are released in the heart. The primary effect is to increase cardiomyocyte contraction. However, cardiac fibroblasts also express β-adrenergic receptors. Therefore, it is important to also evaluate the effect of increased workload on cardiac fibroblasts. IPSC-CFs were seeded into a 24-well plate at 50,000 cells/cm^2. The cells were allowed to grow to confluence for 4 days (with media changes every other day). 24 hours after the final media change, the cells were fed with fibroblast media supplemented with 0uM, 2uM, 5uM or 10uM isoprenaline. Based on the short-term isoprenaline treatment gene expression results presented in Figure 5-23, it was assumed that short-term treatment of isoprenaline on cardiac fibroblasts would also result in insignificant changes to gene expression. Therefore, RNA was isolated 12 hours after isoprenaline treatment. The results are shown in Figure 5-24.

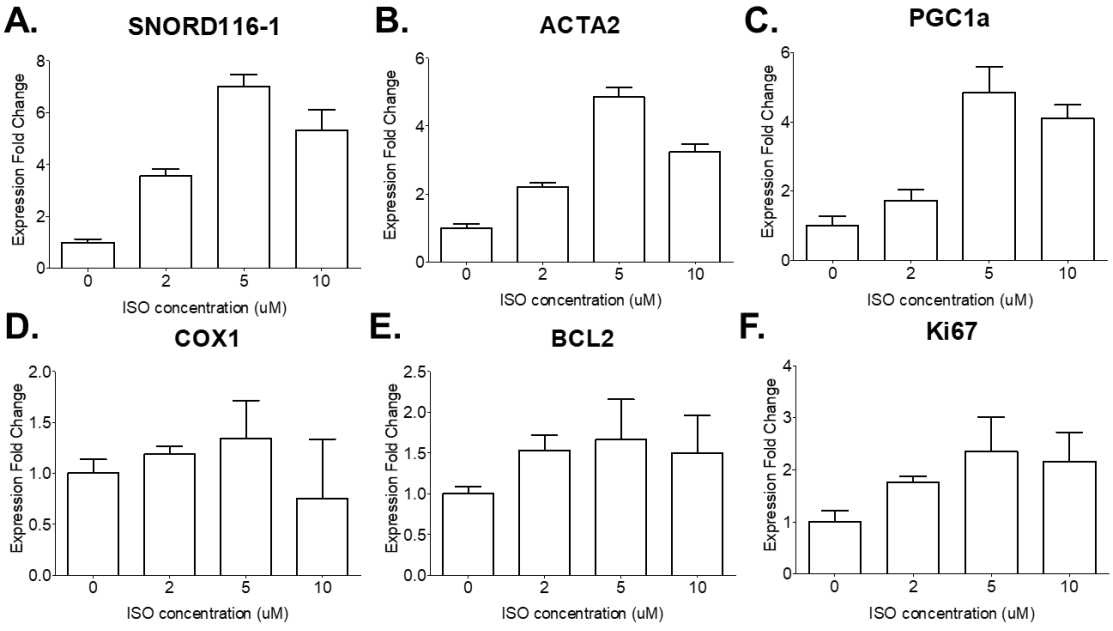

Figure 5-24. The effect of isoprenaline treatment on the gene expression of iPSC-CFs
A. The effect of 0, 2, 5 and 10uM of isoprenaline on the expression of (A-F) SNORD116-1, ACTA2, PGC-1a, COX1, BCL2 and KI67. Plotted as expression fold change relative to 0uM isoprenaline. Calculated using ddCt normalised to GAPDH. N = 1. Error bars represent SEM.

Relative to 0uM and normalised to GAPDH, SNORD116-1 was upregulated 3.5±0.3-fold, 7±0.5-fold and 5.3±0.8-fold in response to 2uM, 5uM and 10uM isoprenaline. ACTA2 was upregulated 2.2-4.9-fold. PGC-1a was upregulated 1.7-4.8±0.7-fold. COX1 did not fluctuate more than ~0.3-fold relative to 0uM isoprenaline. BCL2 was upregulated 1.5±0.5-fold and Ki67 expression was upregulated 1.8-2.4-fold in response to isoprenaline treatment.

To summarise, isoprenaline had the expected stimulatory effect on cardiomyocyte contraction frequency, however it did not appear to immediately affect the expression of SNORD116 in iPSC-CMs. Interestingly, SNORD116 did appear to be upregulated in iSPC-CFs in response to isoprenaline, although further replicates are needed to confirm this.

The similarities and differences between cardiomyocytes and cardiac fibroblasts in response to various cardiac stresses demonstrates the need for further investigation into the cross-talk between the two cell types. As a potential cardiac stress signal, SNORD116 may influence the stress response through communication mechanisms between cardiomyocytes and cardiac fibroblasts. Therefore, the impact of signals released from stressed cardiomyocytes on cardiac fibroblasts was evaluated.

5.5 The effect of conditioned media on cardiac fibroblasts

In the heart, cardiomyocytes and cardiac fibroblasts co-exist and signal to each other. Under stress conditions, cardiomyocytes can release different signals to cardiac fibroblasts in order to elicit various responses. To evaluate the effect of stressed cardiomyocyte signalling on cardiac fibroblasts, doxorubicin and isoprenaline were used to mimic this scenario *in vitro*. IPSC-CMs were cultured in 1 uM doxorubicin-supplemented media, 5uM isoprenaline-supplemented media or drug-free media. The same concentrations were also placed into an empty 24-well plate to obtain a drug-positive CM-free control media. The length of time the CMs were in the drug-supplemented media is referred to as the "conditioning time". For doxorubicin, this was 12 and 24 hours, for isoprenaline this was 6 and 12 hours. Afterwards, the media was transferred to iPSC-CFs, which were cultured in the conditioned media for 12 hours before RNA isolation. Cell-density-equivalent 96-well plates were set up with the same conditions to perform a cell titre-glo assay. The results are shown in Figure 5-25.

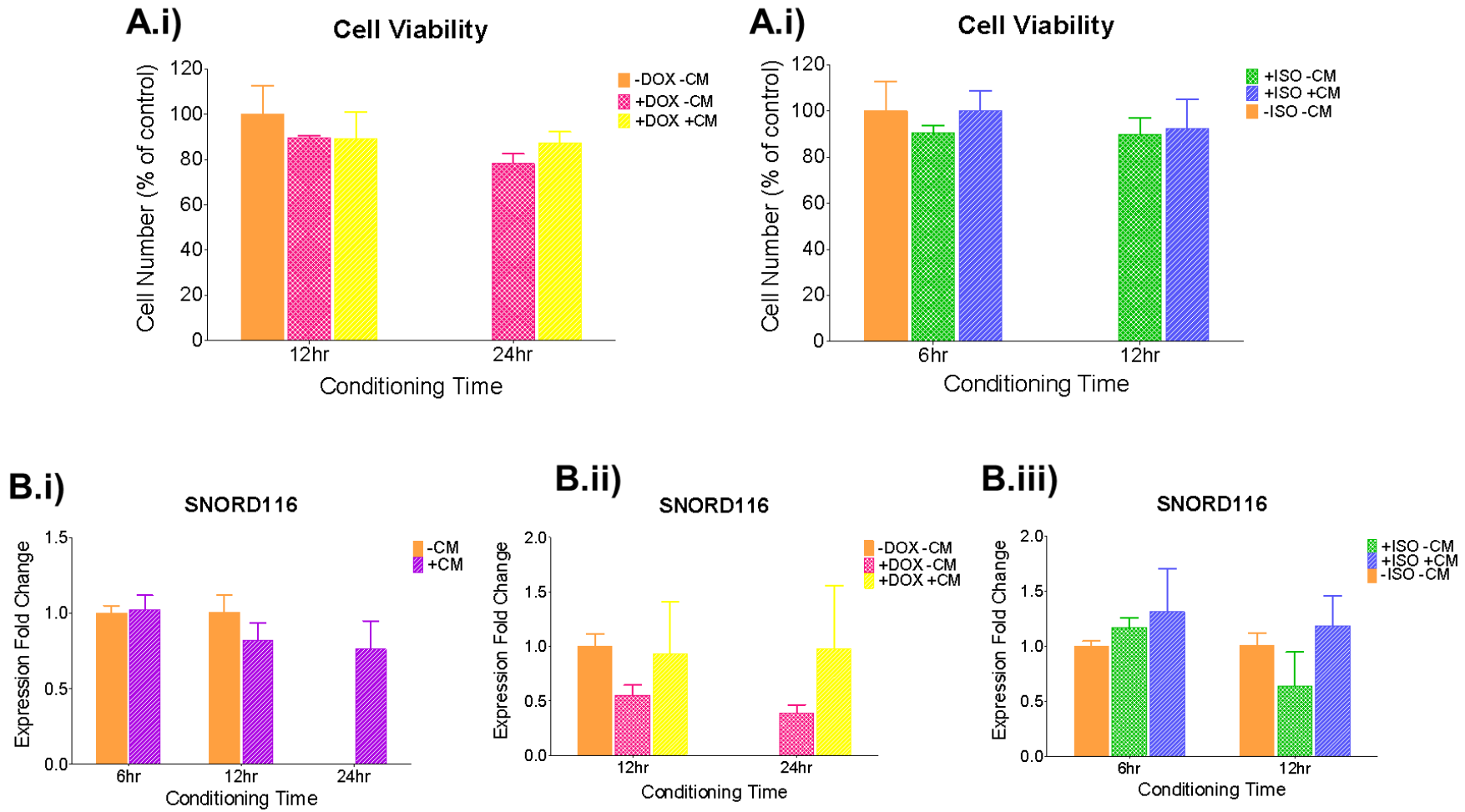

Figure 5-25. The effect of conditioned media on iPSC-CFs.
A. Cell number as a percentage of the unconditioned control in response to (i) doxorubicin and (ii) isoprenaline with and without the presence of CMs.
B. The effect of (i) drug-fee, (ii) doxorubicin-conditioned and (iii) isoprenaline-conditioned media on iPSC-CF SNORD116-1 expression. Calculated using ddCt normalised to GAPDH. N=1, error bars represent SEM.

Overall, cell viability did not decrease more than 25% below control levels. The largest decrease in viability was caused by 24 hour-conditioned CM-free doxorubicin-supplemented media which caused viability to decrease to 78±1.9% of controls. By contrast, the 12 hour-conditioned CM-free doxorubicin-supplemented media only caused a 10±0.3% reduction in viability. The CM-positive doxorubicin-supplemented media caused a reduction in viability to 89±4% with 12 hours of conditioning, and 87±2% with 24 hours of conditioning. Six hours of CM-free isoprenaline-supplemented conditioning caused a reduction in viability to 91±1% compared to the CM-free drug-free control, and 12 hours reduced viability to 90±2%. Contrastingly, six hours of CM-positive isoprenaline-supplemented conditioning caused no reduction in viability, although 12 hours caused a 7.5±4% reduction in viability.

Due to contamination, the 24-hour conditioned CM-free drug-free sample was unable to be analysed. Figure 5-25B shows the effect of conditioned media on SNORD116 expression. Relative to six hours of conditioning with no CMs present, SNORD116 expression showed no change after six hours of conditioning with CMs present or after 12 hours conditioning without CMs present. However, 12 hours and 24 hours of conditioning with CMs present both caused a downregulation of SNORD116 by 0.8±0.2-fold. Compared to 12 hours of CM-free drug-free conditioning, 12 hours of CM-free DOX-supplemented conditioning caused a downregulation of 0.6±0.1-fold in SNORD116 expression. However, the same length of DOX-supplemented conditioning with CMs present caused no change in SNORD116 expression. There was also no change in SNORD116 expression after 24 hours of DOX-supplemented conditioning with CMs present, however without CMs present SNORD116 was downregulated by 0.4±0.1-fold.

Relative to six hours of drug-free CM-free conditioning, six hours of CM-free ISO conditioning caused an upregulation of SNORD116 expression by 1.2±0.1-fold. Six hours of ISO conditioning with CMs present caused a further upregulation by 1.3±0.4-fold. 12 hours of CM-free drug-free condition caused no change in SNORD116 expression, however 12 hours of CM-free ISO conditioning caused a downregulation of 0.6±0.3-fold. Contrastingly, 12 hours of ISO conditioning with CMs present caused an upregulation of 1.2±0.3-fold in SNORD116 expression

Overall, contrastingly to previous results, doxorubicin-supplemented media appeared to cause a downregulation of SNORD116 expression in iPSC-CFs. This downregulation was attenuated by the cardiomyocyte-conditioned media. The same trend was seen in response to isoprenaline, where the presence of cardiomyocytes attenuated the downregulatory effect of isoprenaline on SNORD116 expression. Further replicates are necessary to confirm these findings.

The results of this section demonstrate that external factors can be used to induce cardiac stress in both cardiomyocytes and cardiac fibroblasts *in vitro*. However, many forms of cardiac disease arise due to internal factors, namely genetics. Therefore, the effect of genetic mutation on SNORD116 expression was also investigated.

5.6 The effect of HCM-linked genetic variants on SNORD116 expression in cardiomyocytes

Stress can be induced in cardiomyocytes by changing their oxygen levels, or by exposing them to a drug that induces cardiac stress. However, genetic variants can also lead to cardiac stress in cardiomyocytes, and many forms of heart disease are caused by genetic mutation. The E99K mutation in the *ACTC1* gene can give rise to HCM in some individuals (114,397). This variant is caused by a single nucleotide base change from guanidine to adenosine. The D1HCM iPSC line was derived from a $E99K^{+/-}$ HCM patient. The D1WT iPSC line was generated using CRISPR-Cas9 to correct the mutation in the D1HCM line (340). Figure 5-26 shows the region of *ACTC1* where the E99K mutation is located. CDNA isolated from the D1WT cells contains a guanidine base at the E99K locus, but the D1HCM sample contains 50% adenosine at the same locus demonstrating the presence of the heterozygous mutation. The sequences are otherwise identical.

In addition to these two lines, the D3WT iPSC line was obtained from an $E99K^{-/-}$ individual directly related to the D1HCM patient as a non-isogenic wild-type control. Due to the difficulty of differentiating the D1WT line into cardiomyocytes, as shown in later results, the D3WT line was typically used as a wild-type control for D1HCM iPSC-CMs.

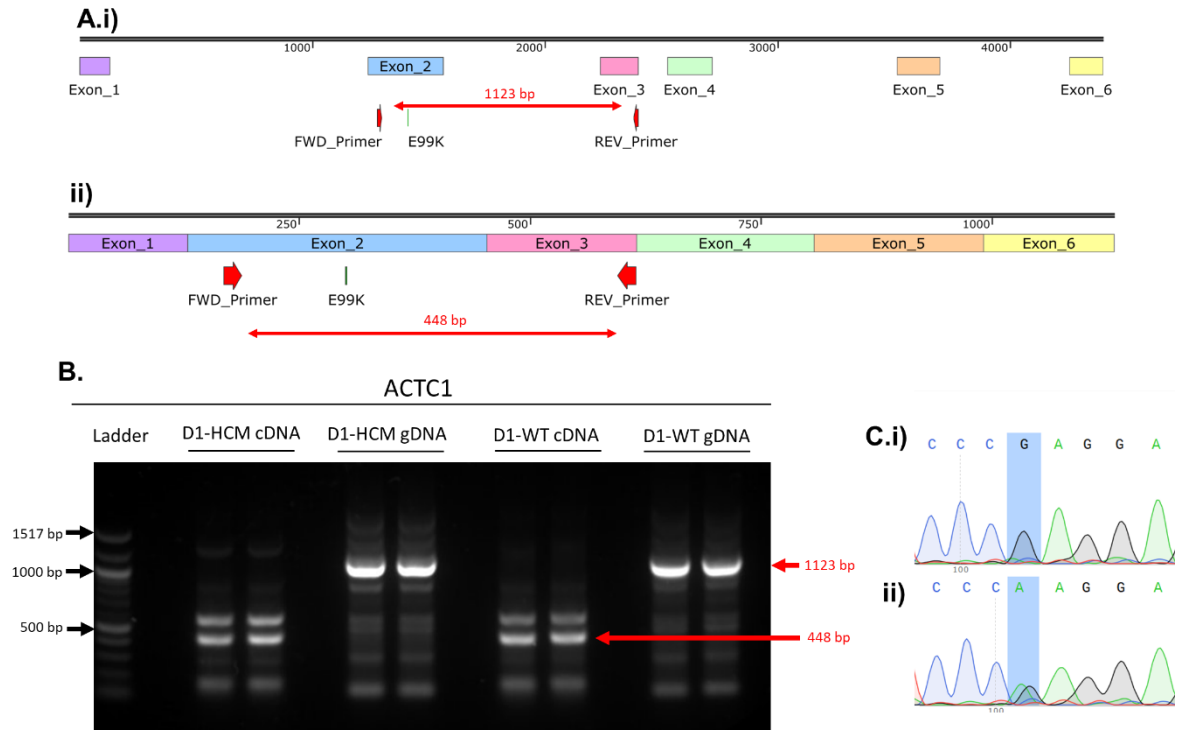

Figure 5-26. Characterising the E99K mutation in the *ACTC1* locus.
A. The (i) genomic and (ii) cDNA sequence of the human *ACTC1* gene with the exons labelled. The forward and reverse primers used to amplify the region of DNA containing the E99K mutation are indicated by red arrows. The size of the resulting DNA sequence is denoted in red.
B. Agarose gel electrophoresis of the *ACTC1*-E99K region of DNA amplified using the primer pair shown in (A) using gDNA and cDNA isolated from the E99K$^{+/-}$ D1HCM iPSC line and the E99K$^{-/-}$ D1WT iPSC line.
C. Sequencing results of the cDNA bands shown in (B) where (i) resulted from the D1WT cDNA and (ii) resulted from the D1HCM cDNA

5.6.1 The exosome characteristics of a HCM genetic variant

SNORD116 has been previously discovered to be packaged to a greater extent into the exosomes of iPSC-CMs with the *ACTC1*-E99K mutation (65). Therefore, further research was carried out to evaluate the effect of the E99K mutation on the exosome profile of iPSC-CMs.

As described previously, the exoview R100 (nanoView Biosciences) was used to quantify and characterise the exosomes released from D3WT and D1HCM iPSC-CMs at day 8 and day 16 of the differentiation. Exosomes were isolated using the Exo-spin™ exosome purification kit (Cell Guidance Systems). The number of exosomes was normalised to cell number. Figure 5-27 shows that D3WT-CMs release 0.79±0.01 $CD63^+$ exosomes per 1000 cells at day 8, which increases to 1.72±0.08 exosomes per 1000 cells at day 16. Similarly, D1HCM-CMs release 0.69±0.02 $CD63^+$ exosomes per 1000 cells at day 8 which increases to 1.48±0.07 exosomes per 1000 cells at day 16. D3WT and D1HCM iPSC-CMs both release 0.9±0.11 $CD81^+$ exosomes per 1000 cells at day 8 which increases at day 16 to 1.91±0.03 for D3WT and 2.10±0.06 for D1HCM. Both D3WT and D1HCM iPSC-CMs release 0.20±0.04 $CD9^+$ exosomes per 1000 cells at day 8, which increases to 0.8±0.02 exosomes per 1000 cells at day 16. Overall, ageing from day 8 to day 16 causes the number of exosomes released by the cells to double, though this does not appear to be affected by the presence of the E99K mutation. Figure 5-27 shows that the average size of $CD63^+$ exosomes was 56.5±0.9 nm, whilst $CD81^+$ and $CD9^+$ exosomes were 60±1.6 nm. There was no difference in size between day 8 and day 16 or D3WT and D1HCM. This may be due to the use of the ExoSpin columns during exosome isolation which may reduce the number of exosomes isolated and select for exosomes of a certain size.

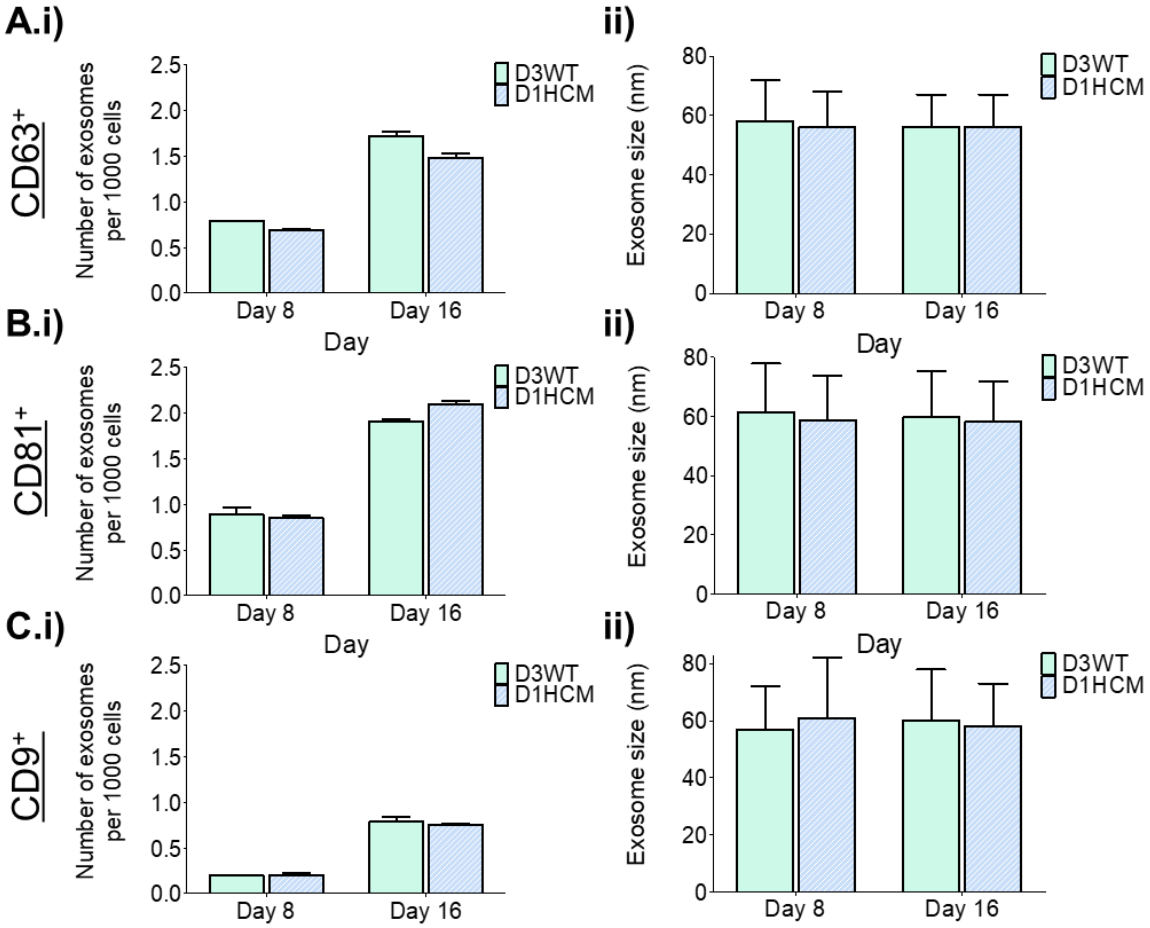

Figure 5-27. Number and size of exosomes released from D3WT and D1HCM iPSC-CMs at days 8 and 16 of the differentiation.

The number (i) and size (ii) of (A) CD63-positive, (B) CD81-positive and (C) CD9-positive exosomes released from D3WT and D1HCM iPSC-CMs at day 8 and 16 of the differentiation. N=1. Error bars represent SEM.

Figure 5-28 show how the size of the exosomes is distributed. Under all conditions tested, exosomes were most frequently between 50 and 60nm in size. However, there was some variation in the size of the 60-70nm range across the different conditions.

At day 9, the D3WT cells released a larger number of 60-70nm sized $CD63^+$ exosomes compared to the other conditions. Additionally, the size of 60-70nm $CD81^+$ exosome population released from D1HCM iPSC-CMs at both time points was smaller than that of the D3WT-iPSC-CMs. There were no other noticeable differences in the size distribution of exosomes across the different conditions.

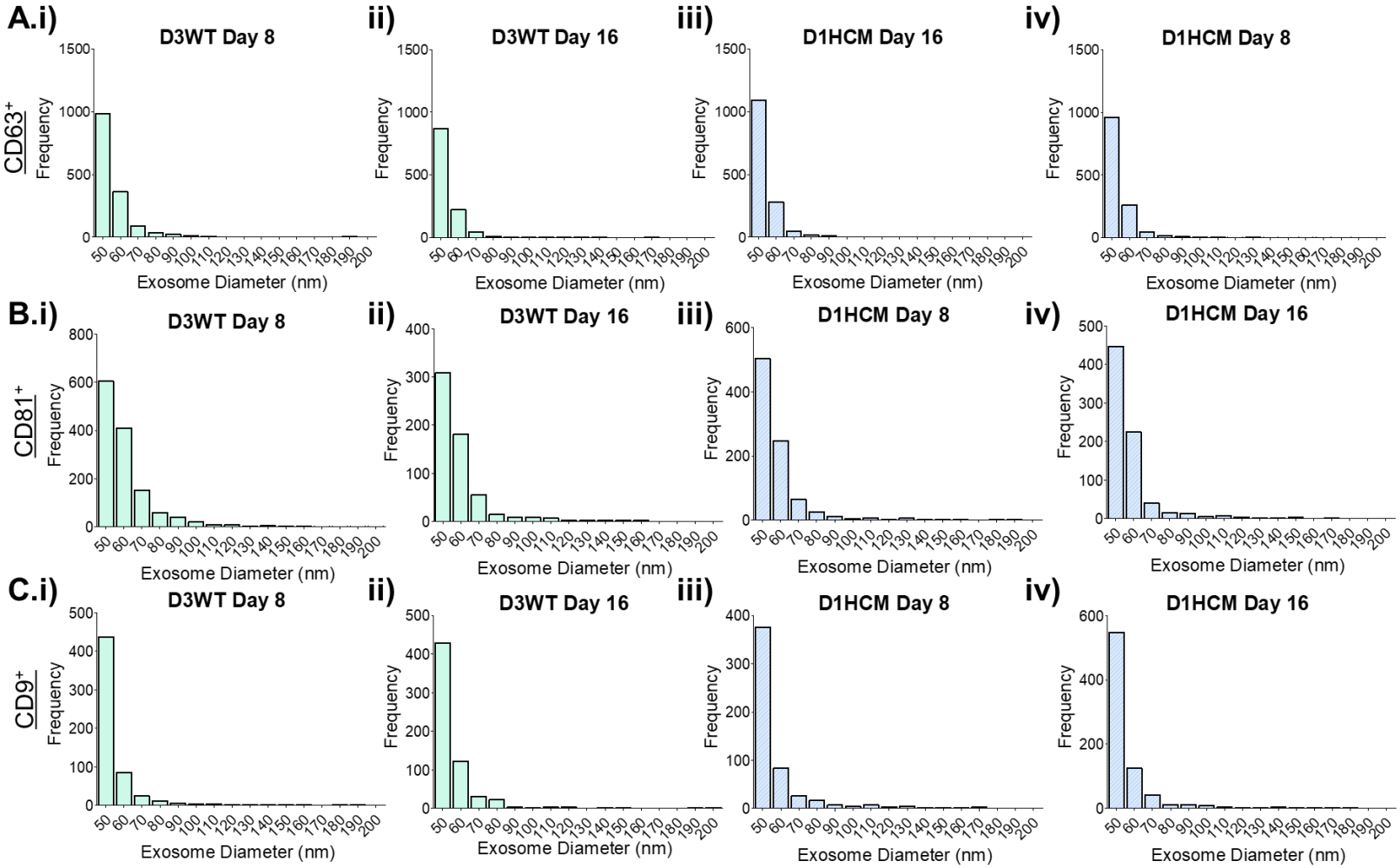

Figure 5-28. Size distribution of exosomes released from D3WT and D1HCM iPSC-CMs at day 8 and 16 of the differentiation.
The size distribution of (A) CD63-positive, (B) CD81-positive and (C) CD9-positive exosomes released from (i-iv) day 8 D3WT, day 16 D3WT, day 8 D1HCM and day 16 D1HCM iPSC-CMs. N=1.

Additional cardiac stress was previously found to compound the effect of the mutation and increase the packaging of SNORD116 by E99K$^{+/-}$ iPSC-CMs (65). Therefore, the effect of additional cardiac stress in the form of hypoxia was evaluated. Day 14 cardiomyocytes were incubated at 37^{O}C, 5% CO_2 in either 20% (normoxic) or 2% (hypoxic) O_2. After 48 hours, the media was removed, and the exosomes were isolated from the media using the Exo-spin^{TM} exosome purification kit. The exoview R100 (nanoView Biosciences) was used to quantify and characterise the exosomes released from D3WT and D1HCM iPSC-CMs under normoxic and hypoxic conditions. The number and size of exosomes released under normoxic and hypoxic conditions is shown in Figure 5-28.

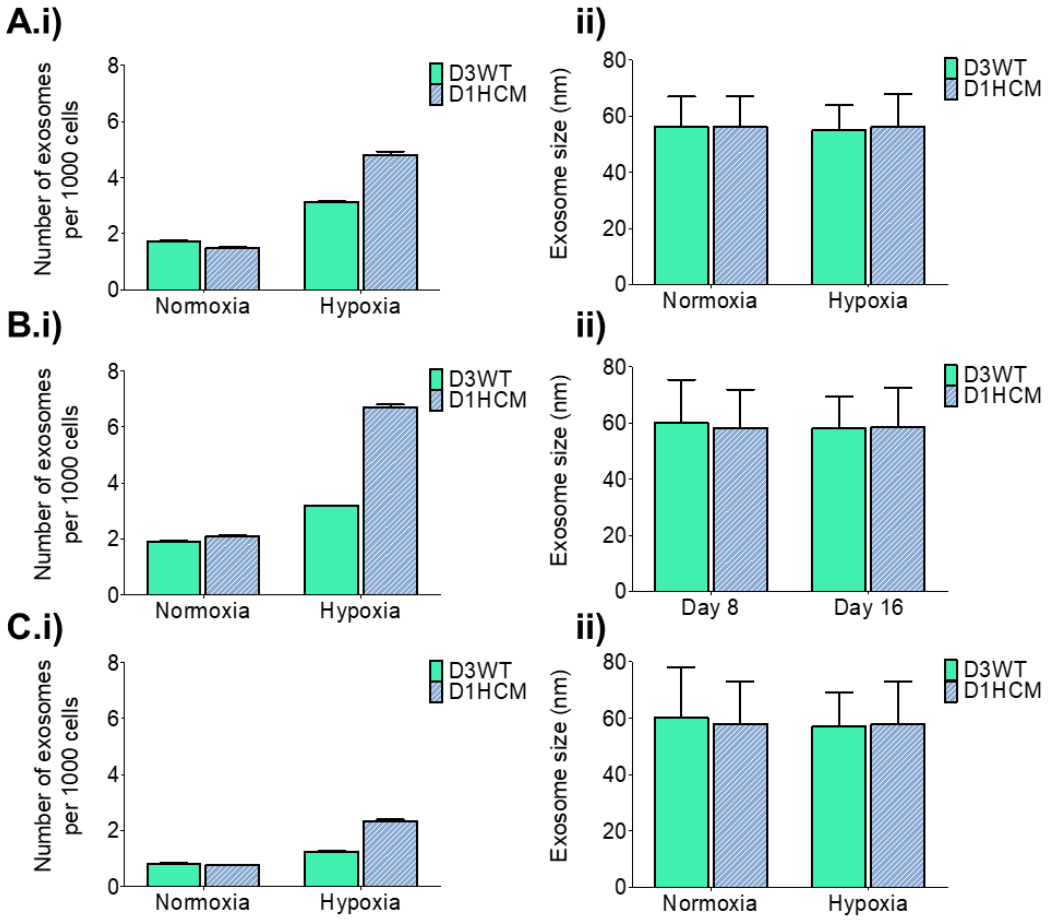

Figure 5-29. Number and size of exosomes released from D3WT and D1HCM iPSC-CMs under normoxic and hypoxic conditions.
The number (i) and size (ii) of (A) CD63-positive, (B) CD81-positive and (C) CD9-positive exosomes released from D3WT and D1HCM iPSC-CMs under normoxic and hypoxic conditions. N=1. Error bars represent SEM.

In normoxic conditions, D3WT cells released 1.72±0.08 $CD63^+$ exosomes per 1000 cells, which increased to 3.14±0.03 exosomes per 1000 cells in hypoxia. In comparison, D1HCM cells released 1.48±0.07 $CD63^+$ exosomes per 1000 cells under normoxia which increased to 4.81±0.15 exosomes per 1000 cells under hypoxic conditions. D3WT and D1HCM cells released similar numbers of $CD81^+$ exosomes under normoxia at 1.91±0.03 and 2.10±0.06 exosomes per 1000 cells, respectively. However, hypoxia caused the number of $CD81^+$ exosomes released by D3WT cells to increase to 3.18±0.04 per 1000 cells, whereas D1HCM cells released more than double that amount at 6.69±0.16 per 1000 cells. Both D3WT and D1HCM cells released 0.8±0.09 $CD9^+$ exosomes per 1000 cells in normoxia. Hypoxia caused a small increase in the number of $CD9^+$ exosomes released from D3WT cells to 1.23±0.07 per 1000 cells, whereas D1HCM cells released more than double the amount released under normoxia at 2.32±0.11 exosomes per 1000 cells. Overall, hypoxia appeared to cause iPSC-CMs of both cell lines to release a greater number of exosomes. However, the presence of the $E99K^{+/-}$ mutation had an additive effect on the increase in exosome release.

As shown in Figure 5-30, the average size and size distribution of exosomes released was not affected by any of the conditions tested.

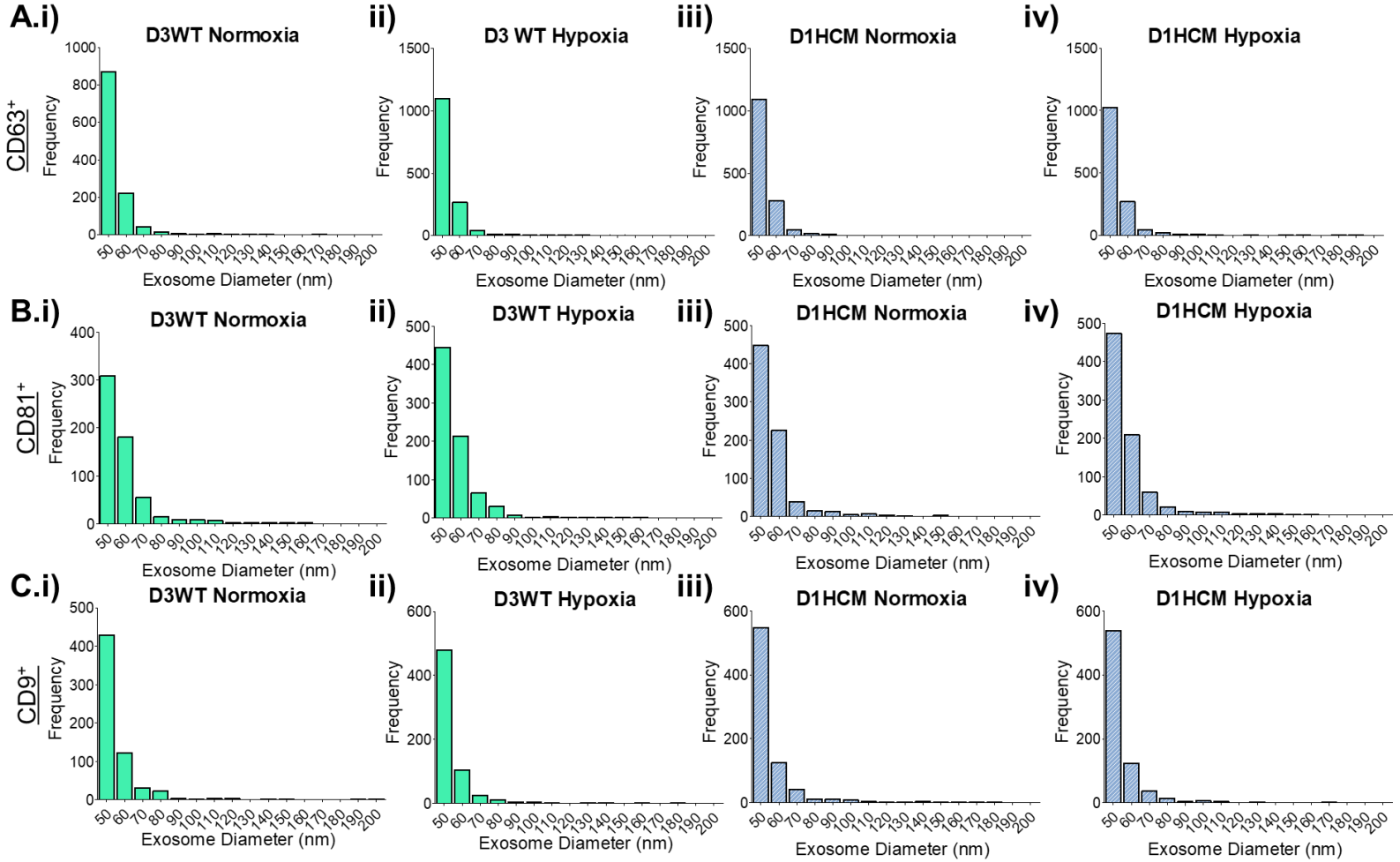

Figure 5-30. Size distribution of exosomes released from D3WT and D1HCM iPSC-CMs under normoxic and hypoxic conditions.

The size distribution of (A) CD63-positive, (B) CD81-positive and (C) CD9-positive exosomes released from (i-iv) Normoxic D3WT, Hypoxic D3WT, normoxic D1HCM and hypoxic D1HCM iPSC-CMs. N=1. Error bars represent SEM.

The expression of the different exosome markers can co-localise giving rise to seven unique exosome populations within the total population. The differential expression of the various exosome markers can influence the downstream signalling effect that the exosome elicits. Therefore, changes to the marker profile of the exosomes can indicate differences in the state of the cells. When D3WT iPSC-CMs develop from day 8 to day 16 in normoxic conditions, the percentage of CD63 single-positive exosomes increases from 28% to 39% of the total population. This corresponds with a decrease in the proportion of other populations. There is no notable change to the population proportions of exosomes released from D3WT cells under hypoxia compared to normoxia.

When D1HCM iPSC-CMs develop from day 8 to day 16 under normoxic conditions, the percentage of the CD63 single-positive exosomes increases from 32% to 47% of the total population. This corresponds with a decrease in the proportion of other populations. At day 16 under normoxic conditions, the proportion of the CD63 single-positive population is 8% larger in the D1CHM sample compared to the D3WT sample. However, under hypoxic conditions, the proportions of exosome populations released by D3WT cells is largely similar to the proportions released by D1HCM cells. The largest differences are seen in the CD63/syntenin double-positive population which is 23% for D3WT and 20% for D1HCM, and the CD69 single-positive population which is 41% for D3WT and 38% for D1HCM.

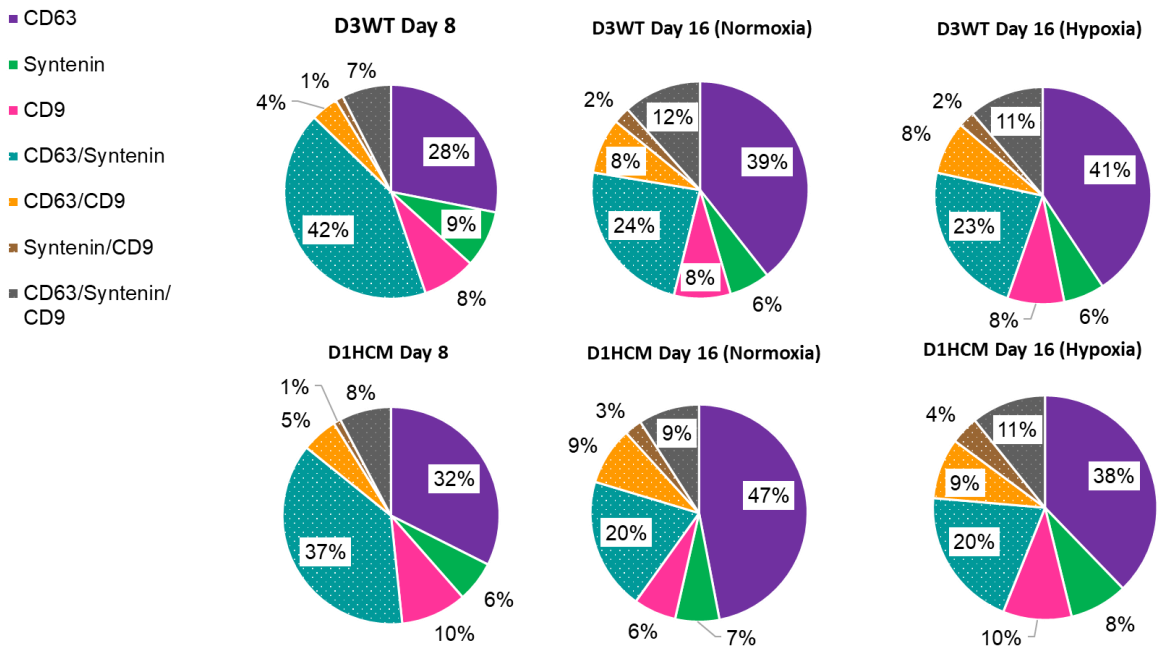

Figure 5-31. Co-localisation of exosome markers released by D3WT and D1HCM iPSC-CMs.
The percentage break down of the different exosome populations released from D3WT and D1HCM iPSC-CMs at day 8 and 16 of the differentiation under normoxia, and day 16 under hypoxia. Calculated as a percentage of the total exosome population.

Overall these results show that the stage of development can affect the number of exosomes released by iPSC-CMs, as day 16 cells release approximately double the number of exosomes released by day 8 cells. Under normoxic conditions, the presence of the E99K mutation within iPSC-CMs does not appear to affect the size or number of exosomes released, but may impact the size distribution and marker expression of exosomes released. Hypoxia causes both cell lines to increase their exosome output, however the increase is greater in iPSC-CMs with the E99K mutation.

As HCM is a genetic disorder, and SNORD116 has been previously identified as a potential cardiac stress signal in HCM iPSC-CM exosomes, the consequences of this potential signalling relationship during cardiac development was explored.

5.6.2 The effect of HCM-linked genetic variants on cardiac development

To understand the effect of the E99K genetic variant on SNORD116 expression during iPSC-CM differentiation, D1HCM, D1WT and D3WT cells were differentiated into cardiomyocytes. RNA was isolated on days 0, 2, 4, 8 and 17. In all three cell lines, *nanog* is downregulated from day 2 onwards. *GATA4* appears upregulated at day 4 and appears to peak at day 8, although all of the lines show a high degree of variation. In D1HCM and D3WT, *NKX2-5* is upregulated 20±19-fold and 18±6-fold at day 8. *TNNI1* is upregulated at day 8 to 7.5±6-fold in D1HCM and 6±0.4-fold in D3WT. There is no significant difference between the expression of *NKX2-5* or *TNNI1* at day 17 compared to day eight in either the D1HCM line or the D3WT line.

In the D1WT line *NKX2-5* and *TNNI1* are not significantly upregulated from stem cell levels during the differentiation. This cell line failed to generate contractile cells. Interestingly, SNORD116-1 expression in the D1WT line appears to be downregulated (although this is not statistically significant due to variation) and followed a similar trend to SNORD116 expression during iPSC-CF differentiation shown in Figure 4-13. During D1HCM iPSC-CM differentiation, SNORD116-1 is downregulated 0.2±0.2-fold and 0.3±0.2-fold at days two and four of the differentiation compared to day zero. However, at day eight, SNORD116-1 expression is 0.8±0.2-fold that of stem cell levels meaning its expression had increased between days four and eight. By day 17, the expression of SNORD116 had decreased to 0.2±0.1-fold that of stem cell expression. Expression of SNORD116 in the D3WT line followed the same trend as the D1HCM line. In none of the three cell lines tested was SNORD116-1 expression higher than stem cell level.

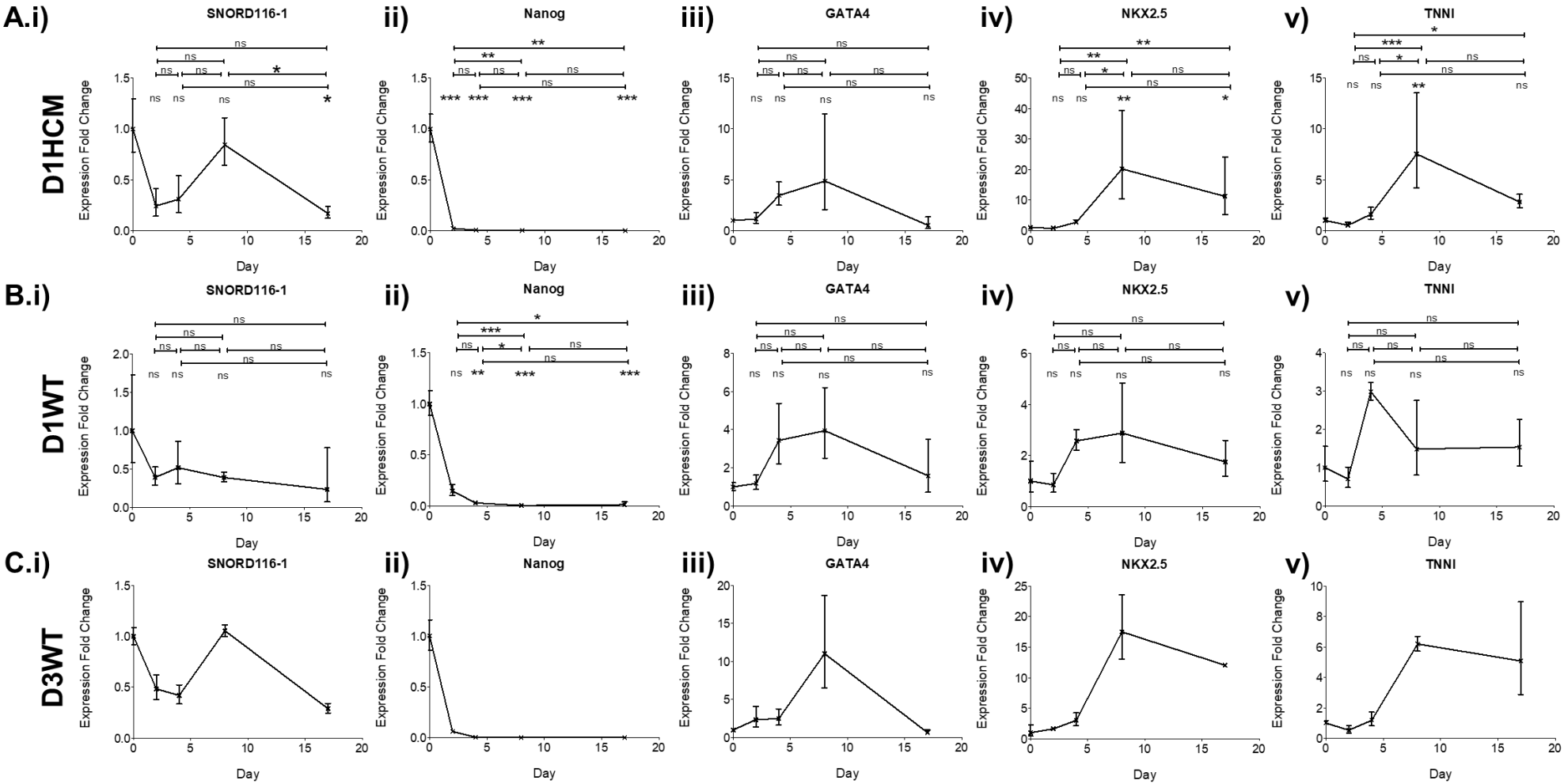

Figure 5-32. The expression of genes during the differentiation of E99K-associated iPSC-lines.
The expression of (i-v) SNORD116-1, *nanog*, *GATA4*, *NKX2-5* and TNNI1 on days 0, 2, 4, 8 and 17 of iPSC-CM differentiation in the (A) D1HCM, (B) D1WT and (C) D3WT iPSC lines. Expression plotted as fold change relative to day 0. Calculated using ddCt normalised to GAPDH. Statistics calculated using one-way ANOVA, * = P≤0.05, ** = P≤0.01, *** = P≤0.001. (A,B) N=3, (C) N=2. Error bars represent SEM.

The E99K variant is not the only sarcomeric mutation that can give rise to HCM. Genetic variants within the *MYH7* gene is commonly associated with HCM. A wild-type iPSC line was genetically modified to introduce a heterozygous and homozygous p.C9123T mutation in the *MYH7* gene (122). To evaluate the effect of this genetic variant on SNORD116 expression, all three iPSC lines were differentiated into cardiomyocytes. RNA was isolated on days 0, 2, 4, 6, 8 and 17 of the differentiation. Gene expression analysis is shown in Figure 5-33.

In all three lines, *nanog* is downregulated from day 2 onwards. *GATA4* expression peaks at day 6 in all three cell lines at 24±2-fold, 19±5-fold and 52±4-fold relative to stem cell levels in the C9123T$^{-/-}$, C9123T$^{+/-}$ and C9123$^{+/+}$ lines. *NKX2-5* expression is first upregulated at day 6 in all three cell lines and peaks at day 8 in the C9123T$^{-/-}$ and C9123T$^{+/-}$ lines at 20±3-fold and 68±11-fold respectively. In the C9123$^{+/+}$ line, *NKX2-5* is highest at day 17 at 14±4-fold relative to stem cell levels. *TNNI1* is upregulated in all three cell lines from day 6 onwards and is expressed the highest at day 17 at 3±0.3-fold, 13±2-fold and 7±0.5-fold in the C9123T$^{-/-}$, C9123T$^{+/-}$ and C9123$^{+/+}$ lines, respectively. In the C9123T$^{-/-}$ line, SNORD116-1 expression is downregulated from day 2 onwards, with its lowest expression of 0.1±0.01-fold of stem cell levels at day 17. SNORD116-1 expression follows the same downregulatory trend in the C9123$^{+/+}$ line. However, the C9123T$^{+/-}$ line diverts slightly from this trend in that SNORD116-1 expression is lowest at day 2 of the differentiation by 0.3±0.06-fold that of stem cell levels, which increases to 0.5±0.06-fold, 0.6±0.05-fold and 0.6±0.05-fold at days 4, 6 and 8. By day 17 expression had reduced to 0.5±0.06-fold. Overall, in all three cell lines SNORD116 expression appears highest at day 0 compared to the rest of the time points.

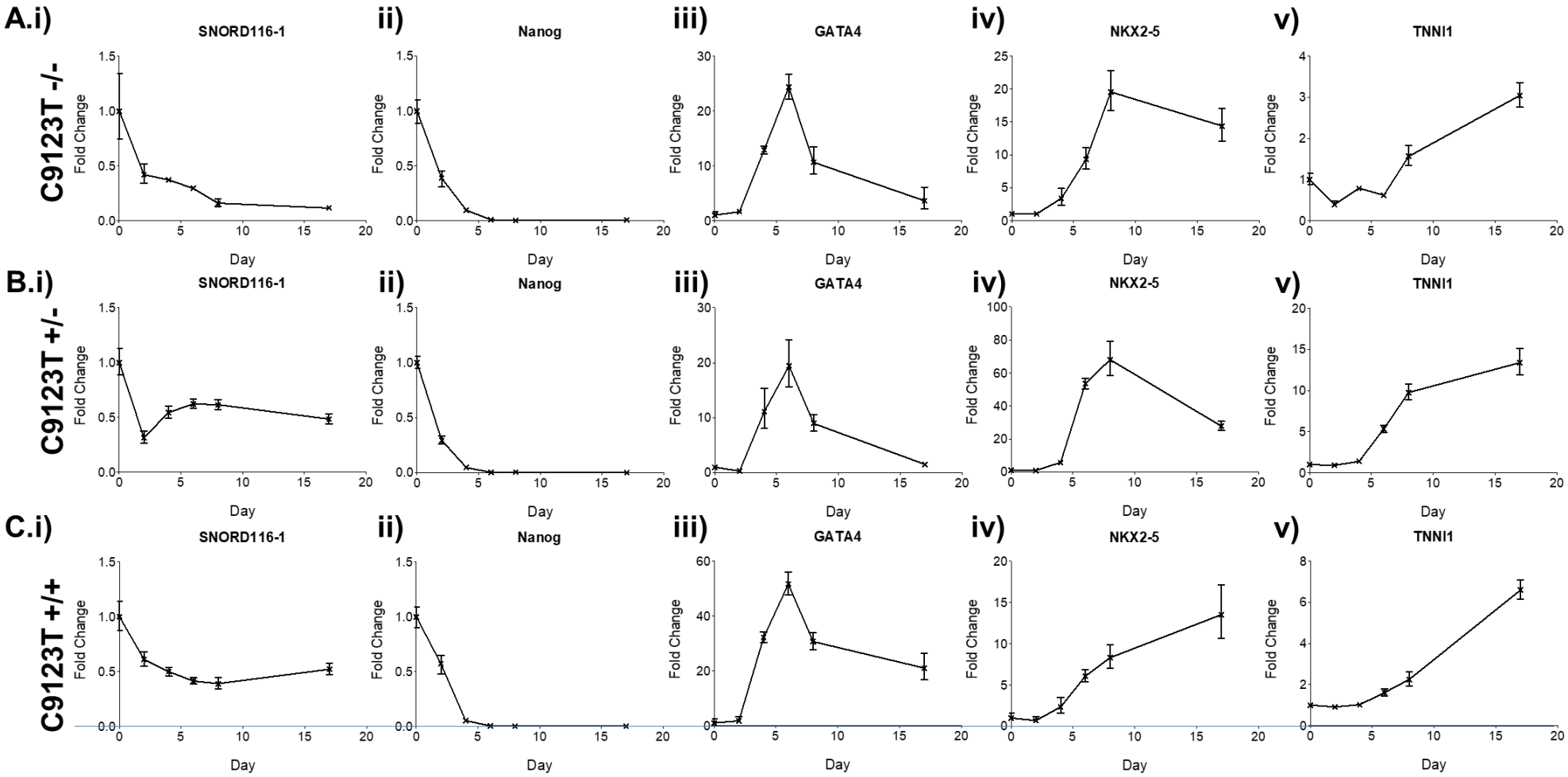

Figure 5-33. The expression of genes during the differentiation of *MYH7*-C9123T-associated iPSC-lines.
The expression of (i-v) SNORD116-1, *nanog*, *GATA4*, *NKX2-5* and TNNI1 on days 0, 2, 4, 6, 8 and 17 of iPSC-CM differentiation in the (A) C9123T$^{-/-}$, (B) C9123T$^{-/+}$ and (C) C9123T$^{+/+}$ iPSC lines. Expression plotted as fold change relative to day 0. Calculated using ddCt normalised to GAPDH. N=1, Error bars represent SEM.

The overall effect of the presence of a sarcomeric gene mutation on SNORD116-1 expression in different cell types is shown in Figure 5-34. Among the D3WT, D1WT and D1HCM cell lines, SNORD116-1 expression is lowest in iPSC-CFs compared to iPSC-CMs and iPSCs. Relative to D3WT-CF expression, SNORD116-1 is downregulated 0.4±0.1-fold and 0.3±0.1-fold in D1WT and D1HCM iPSC-CFs. Contrastingly, SNORD116-1 expression is 3.4±3.8-fold and 2.9±9.6-fold higher in D3WT and D1HCM iPSC-CMs. Across the three cell lines, SNORD116-1 expression levels are highest in iPSCs compared to iPSC-CF and iPSC-CM cells. Relative to D3WT-CF expression, SNORD116-1 is 236±26-fold, 244±17-fold and 288±26-fold higher in D3WT, D1WT and D1HCM iPSC-CMs.

Among the *MYH7*-C9123T cell lines, SNORD116-1 expression is again higher in iPSCs, although the difference is less dramatic that in the *ACTC1*-E99K lines. Relative to C9123T$^{-/-}$-CM expression, SNORD116 is 8.7±3-fold, 8.9±1.1-fold and 7.6±1-fold higher in C9123T$^{-/-}$, C9123T$^{-/+}$ and C9123T$^{+/+}$ iPSCs. Interestingly, SNORD116-1 is upregulated 4±0.4-fold in both C9123T$^{-/+}$ and C9123T$^{+/+}$ iPSC-CM compared to C9123T$^{-/-}$ iPSC-CMs.

Overall, the presence of the *ACTC1*-E99K mutation in iPSC-CMs does not appear to significantly affect the cellular expression levels of SNORD116-1 during or after iPSC-CM differentiation The presence of the *MYH7*-C0123T mutation does not appear to affect the trend of SNORD116 expression during iPSC-CM differentiation but may cause an upregulation in SNORD116 expression in differentiated iPSC-CMs. This indicates that different genetic variants may have a different effect on SNORD116 expression.

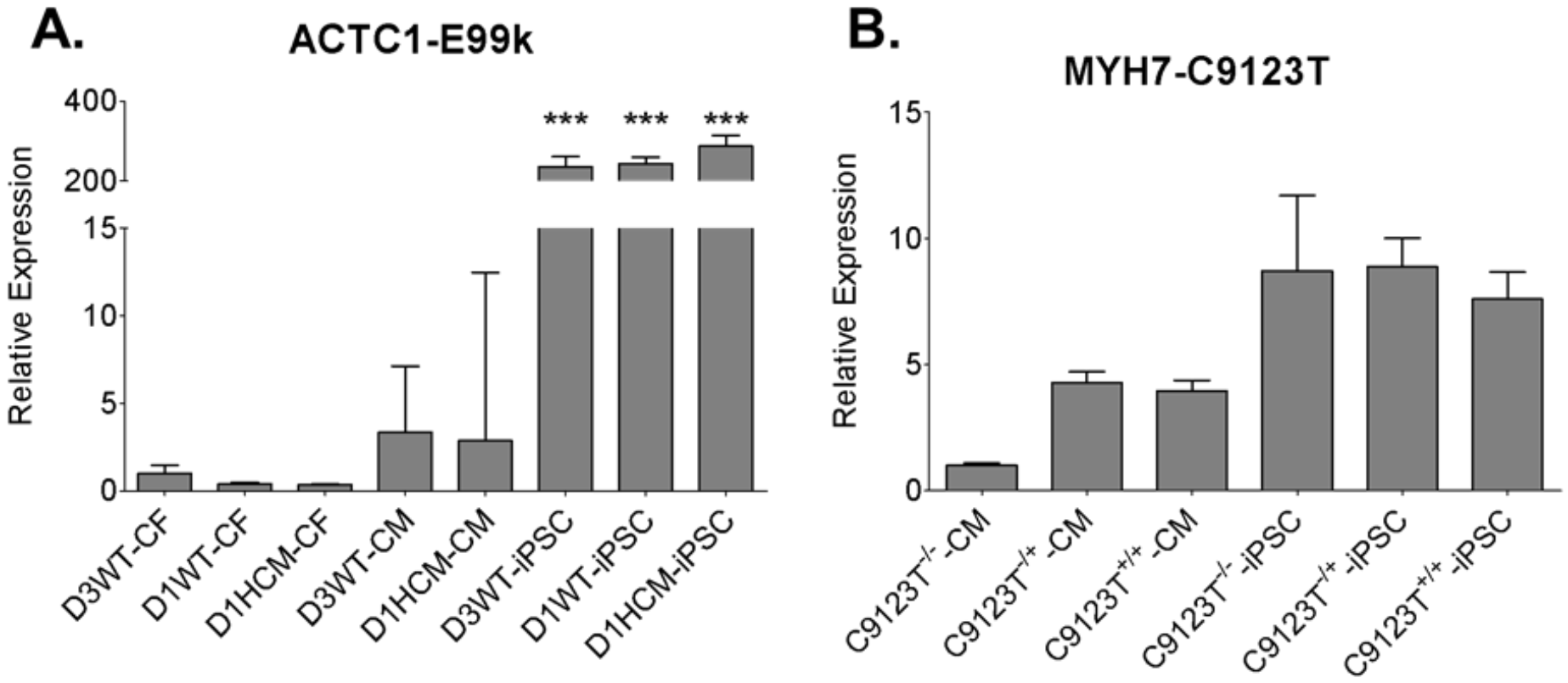

Figure 5-34. The effect of sarcomeric gene mutations on SNORD116 expression across different cell types.
A. The relative expression of SNORD116-1 in iPSC-CF, iPSC-CM and iPSCs derived from the D3WT, D1WT and D1HCM lines which are E99k$^{-/-}$, E99K$^{-/-}$ and E99K$^{-/+}$ in the *ACTC1* gene. Expression was calculated relative to expression in D3WT-CFs using ddCt normalised to GAPDH. The CF samples were lysed at day 30, the CM samples were lysed at day 30 and the iPSCs were lysed at passage 31. Statistics were calculated as significant to D3WT-CF using one-way ANOVA. * = P≤0.05, ** = P≤0.01, *** = P≤0.001. N=3. Error bars represent SEM.
B. The relative expression of SNORD116-1 in iPSC-CMs and iPSCs derived from the *MYH7*-C9123T$^{-/-}$, *MYH7*-C9123T$^{-/+}$ and *MYH7*-C9123T$^{+/+}$ lines. Expression was calculated relative to expression in C9123T$^{-/-}$-CMs using ddCt normalised to GAPDH. The CM samples were lysed at day 17 and the iPSC samples were lysed at passage 28. N=1, error bars represent SEM.

5.7 Discussion

The aim of this chapter was to induce stress in cardiac cell types and evaluate the effect on SNORD116 expression. Various strategies of inducing stress in cardiac cell types were used to investigate SNORD116 expression in iPSC-derived models of heart disease. Genetic models indicated that differentiation and exosome signalling may be affected by HCM-linked genetic variants. Culture conditions were manipulated to cause stress-induced changes in contraction, metabolism and gene expression. Hypoxia and doxorubicin-induced cardiotoxicity appeared to cause increased cell death and frequency of arrhythmogenic contraction in iPSC-CMs. IPSC-CFs appeared to be less sensitive to hypoxia than iPSC-CMs in terms of viability, but were shown to increase their expression of aSMA protein, indicating some activation into myofibroblasts.

Hypoxia in particular had a significant detrimental effect on iPSC-CM contraction frequency and metabolism. Contraction frequency has been shown to decrease in response to hypoxia in other studies (398–400). The reduction in contraction frequency in iPSC-CMs may be linked to the metabolic effects of hypoxia, as contraction relies on the production of ATP. According to substrate usage analysis performed using the Biolog MitoPlate assay, overall metabolic capacity was reduced as a result of hypoxia, and the total substrate usage of several key glycolytic, TCA and amino acid substrates was significantly reduced. Additionally, in all substrates tested, the rate of metabolism was significantly reduced under hypoxia. Therefore, the results presented here align with previously established effects of hypoxia.

Metabolic output was also measured by Agilent Seahorse analysis, which also indicated a reduction in metabolic capacity as a result of hypoxia. Both basal OCR and maximal OCR were significantly reduced by hypoxia.

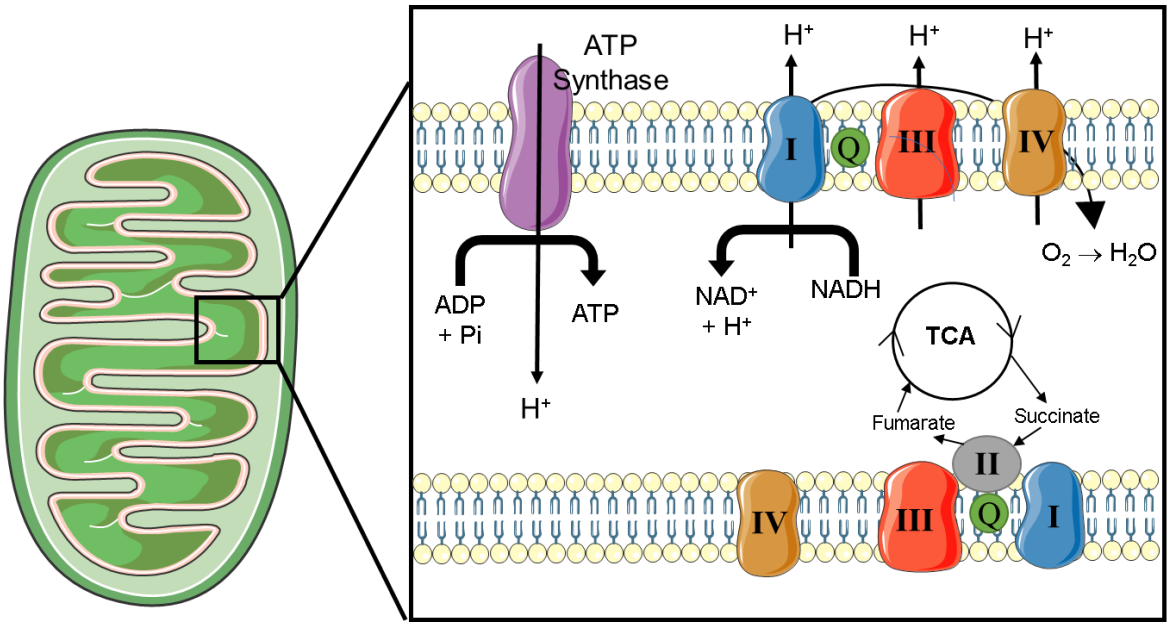

Figure 5-35. Oxidative phosphorylation and the mitochondrial electron transport chain.
Rendered using Servier Medical Art.

During basal respiration, the mitochondrial transport chain performs oxidative phosphorylation, using ATP-synthase to power the active transport of protons across the mitochondrial membrane. An overview of this process is shown in Figure 5-35. During this process, oxygen is reduced to water. Because there is less oxygen available for reduction in a hypoxic atmosphere, the rate of oxygen consumption is expectedly lower in hypoxic cells. Although the assay was performed in a normoxic atmosphere, exposure to hypoxia may have caused damage to mitochondrial components and reduced the cell's ability to perform oxidative phosphorylation. Upon the addition of oligomycin, ATP synthase-powered proton transport is inhibited. Interestingly, in both the hypoxic and pre-conditioned hypoxic samples, the OCR appears to increase at this point, although in the normoxic samples it does not change. It is unclear why the rate of oxygen consumption should increase in the hypoxic samples upon the inhibition of ATP-synthase. Any O_2 that is reduced during this time can only occur due to proton leak. Increased ROS caused by hypoxia may have caused damage to the mitochondrial

membrane, allowing more proton leak to occur thus resulting in increased OCR during ATP-inhibited respiration in hypoxic cells.

To achieve maximal respiration, the uncoupling agent FCCP is added to the cells which transports protons across the mitochondrial membrane allowing the rapid oxidation of substrates. The OCR of the normoxic cells increases to ~200 pmol/min/10k cells, however neither of the hypoxic samples show an increase in OCR. This further emphasises the adverse effects of hypoxia on the cells' ability to perform oxidative phosphorylation.

The extracellular acidification rate (ECAR) is primarily an indicator of the rate of metabolism of non-oxygen consuming forms of metabolism such as glycolysis which produces lactic acid. During basal respiration, there is no significant difference in the ECAR of normoxic, hypoxic or pre-conditioned hypoxic cells. In normoxic cells, the inhibition of ATP synthase causes an increase in the ECAR, indicating that the cells increase their usage of metabolic pathways disconnected from the electron transport chain (such as glycolysis). ECAR is increased even further upon addition of FCCP, which may be due to the increase in proton movement, causing higher levels of acidity. The increase in ECAR under maximal respiration may also be due to the accumulation of CO_2 (a product of the citric acid cycle) breaking down into bicarbonate (401).

Interestingly, the ECAR of hypoxic cells fails to increase upon addition of either oligomycin or FCCP. This indicates that hypoxia impairs not only oxygen-dependent forms of metabolism, but also anaerobic respiration as well. Overall, the results from the seahorse analysis support the results from the Biolog MitoPlate analysis in demonstrating that hypoxia has a global downregulatory effect on metabolism in iPSC-CMs. Additionally, nuclei number – an indicator of cell number – was significantly reduced in cells exposed to hypoxic conditions and pre-conditioned hypoxic cells.

This suggests a higher rate of cell death compared to normoxic conditions. In terms of their metabolic output and viability, the pre-conditioning of iPSC-CMs to hypoxia did not affect their sensitivity to hypoxia.

Changes in metabolism in response to hypoxia coincided with changes in exosome signalling. The number of exosomes released per 1000 cells increased in iPSC-CMs exposed to hypoxic conditions, suggesting that hypoxia-induced cardiac stress promotes an increase in exosome signalling in iPSC-CMs. This supports previous findings that demonstrated increased cardiac stress through electrical pacing caused an increase in exosome release from iPSC-CMs (65). In further agreement with the findings of this study, the presence of the *ACTC1*-E99K mutation in iPSC-CMs compounded the effect of cardiac stress causing an even greater increase in the number of exosomes released. This further supports the theory that there may be mutation-specific pathological signalling pathways that affect the heart's response to stress.

The average size and size distribution of exosomes did not change in response to hypoxia. However, this may be due to the use of ExoSpin™ columns during exosome isolation which may have reduced the number of exosomes isolated and selected for exosomes in a specific size range.

Interestingly, the presence of the mutation may have affected the size distribution of certain exosome populations. For example, D3WT iPSC-CMs released a larger proportion of $CD81^+$ exosomes in the 60-70nm size range compared to D1HCM cells at both days 8 and 16. Additionally, at day 16 under normoxic conditions, the CD63 single-positive population was 8% larger in the D1HCM sample compared to the D3WT sample. This could indicate a link between the CD63 exosome marker and the *ACTC1*-E99K mutation. The CD63/syntenin double positive population is also 4%

smaller, which could indicate less packaging of exosome cargo into the CD63 population by E99K$^{+/-}$ iPSC-CMs.

Changes to exosome marker profile has been shown to be involved in disease pathogenesis. For example, plasma exosomes from HIV-positive patients have increased levels of CD9 and CD63 positive exosomes compared to HIV-negative patients (402). Similarly, malignant pancreatic cancer cells release higher numbers of CD9 and CD63-positive exosomes compared to non-malignant controls (403). This demonstrates a potential link between these exosome markers and disease signalling pathways. It is therefore interesting that results in this chapter indicate that iPSC-CMs positive for a HCM-associated genetic variant appear to express a larger population of CD63-positive exosomes compared to the wild-type variant.

Overall, although analysis of exosomes by the ExoView R100 did not analyse RNA cargo, the results demonstrate a potential link between the sarcomeric mutation E99K and the exosome profile of iPSC-CMs. And as SNORD116 packaging has previously been confirmed to be increased as a result of this genetic variation, this work further supports the potential relationship between cardiac stress, exosome release and SNORD116 signalling.

Pivoting towards intracellular pathways, gene expression analysis was carried out to better understand the relationship between cardiac stress and SNORD116 expression. The expression of several functional cardiac genes was downregulated in response to hypoxia and doxorubicin-induced cardiac stress in iPSC-CMs. This supports previous findings that cardiac stress causes a downregulation of cardiac gene expression (404). The expression of the foetal isoform of myosin heavy chain *MYH6* relative to its adult isoform *MYH7* increases in response to hypoxia. This demonstrates the reactivation of the foetal gene program in response to cardiac stress. Interestingly, when given a longer period to recover from

hypoxia, many of the cardiac genes appear restored to normoxic expression levels. However, the gene for the sarcoplasmic calcium channel *RYR2* is still downregulated even after extended recovery, suggesting hypoxic stress may cause long-term impairment to calcium handling and contraction. Hypoxia and doxorubicin-induced cardiac stress also appeared to have an up regulatory effect on pro-apoptotic and *aSMA* gene expression in iPSC-CFs. This indicates the activation of disease signalling pathways in both cardiac cell types in response to these stressors.

In iPSC-CMs, the glycolysis genes *HK2* and *LDHA* are upregulated in response to hypoxia. *LDHA* is also upregulated in hypoxic iPSC-CFs. This supports previous established findings that glycolytic metabolism is increased in response to cardiac stress (75,77,182). However, this seemingly contradicts the metabolic data which indicate that all forms of metabolism are reduced in hypoxia. Therefore, the upregulation of these genes may be a compensatory mechanism. COX1 (important in oxidative phosphorylation) is also upregulated in response to hypoxia, which supports the theory that hypoxia causes the upregulation genes important for respiration in an effort to cope with the reduced oxygen environment.

Interestingly, the FAO gene ACLY is also upregulated in cardiac cells under extended hypoxic conditions (although less so in iPSC-CFs), which counteracts established findings that FAO is reduced in response to cardiac stress. Again, this may be part of a compensatory mechanism to stimulate all forms of metabolism in a low oxygen environment. In cardiomyocytes, although both *HK2* and *LDHA* are restored to normoxic expression levels after two days of recovery, ACLY is still upregulated after extended recovery from hypoxia. As FAO is linked to iPSC-CM maturity, this could indicate that hypoxic stress may have a pro-maturation effect on cardiomyocytes or may select for cardiomyocytes

that are more metabolically mature. However, it is important to note that gene transcription is not wholly representative of cellular metabolism and that other processes such as protein translation, modification and localisation can also influence metabolism, and would not be detected by RT-qPCR alone.

Surprisingly, PGC-1a expression in iPSC-CMs did not significantly change in response to cardiac stress. It is possible that mitochondrial biogenesis is already at high levels in and is therefore not further upregulated. PGC-1a was upregulated in iPSC-CFs in response to isoprenaline. The expression of *aSMA* also appeared upregulated in iPSC-CFs in response to isoprenaline, which may indicate the activation of pro-fibrotic pathways. The activation of these genes may be part of a support mechanism wherein increased activation of β-adrenoreceptors promotes activation and mitochondrial biogenesis in cardiac fibroblasts to boost the supply of ATP and ECM proteins, providing support to cardiomyocytes with an increased workload. Although iPSC-CM contraction frequency was increased, short-term isoprenaline exposure failed to elicit a significant change in gene expression in iPSC-CMs. This may be because RNA isolation was carried out too soon after treatment and mRNA levels may not have had time to respond. Although isoprenaline has been shown to cause an increase in contraction force of iPSC-CMs (405), results here indicated that contraction amplitude had not increased. This may indicate that the contraction amplitude calculated by the MUSCLEMOTION software is not fully representative of contraction force. Alternative software such as SarcTrac (406) could be used to improve the assay.

Overall these gene expression changes demonstrate a response to cardiac stress that generally aligns with the contraction, metabolism and protein expression analysis in demonstrating cardiac dysfunction.

In general, SNORD116 expression appeared upregulated in response to cardiac stress in both iPSC-CMs and iPSC-CFs. In iPSC-CMs, SNORD116 expression levels were not changed after two days of hypoxia. However after four days of hypoxia, SNORD116-1 and SNORD116-23 both appeared to be upregulated, although this was not significant due to variation in the hypoxic replicates likely stemming from reduced viability. SNORD116-1 was also found to be upregulated after four days of hypoxia in iPSC-CFs. Interestingly, given two days of recovery, the expression of all three SNORD116 paralogues in iPSC-CMs was downregulated, and also appeared to be downregulated after an extended period of recovery. This could suggest that the restoration of oxidative metabolism in iPSC-CMs is linked with the downregulation of SNORD116, which therefore may be important in the initiation of repair pathways in iPSC-CMs. Additionally, doxorubicin also caused an upregulation of SNORD116 in both cell types. This could indicate a common cardiac stress response pathway that is shared by both cardiomyocytes and cardiac fibroblasts involving SNORD116 upregulation.

In investigating the cross-talk between cardiomyocytes and cardiac fibroblasts during cardiac stress, conditioned media was supplied to cardiac fibroblasts to evaluate the effect on SNORD116. Doxorubicin-supplemented media appeared to cause a downregulation in SNORD116 expression in iPSC-CFs, which contrasts with the previous results that show an increase in response to doxorubicin. However, conditioning of the drug may have altered the properties of the drug and its effect in cardiac fibroblasts. In addition, the absence of serum from the conditioned media may have also contributed to the altered response to doxorubicin in cardiac fibroblasts. Interestingly, the presence of cardiomyocyte-derived signals seemed to ameliorate the downregulatory effect of doxorubicin on iPSC-CF SNORD116 expression. A similar trend was also seen with isoprenaline-supplemented conditioning. This may suggest that the signals released by cardiomyocytes in the presence of isoprenaline and doxorubicin are protective against the downregulatory

effects of these drugs on SNORD116 in cardiac fibroblasts. This demonstrates how communication between cardiomyocytes and cardiac fibroblasts during cardiac stress can alter the expression of SNORD116, further highlighting its potential role in the cardiac stress response.

In addition to environmental cardiac stress, the presence of HCM genetic variants was can affect the expression of SNORD116. During cardiomyocyte differentiation of the *ACTC1*-E99K iPSC lines, SNORD116 follows the same trend of expression in both the D3WT and D1HCM cells. The D1WT line appears to show a slightly different expression trend, but this is likely due to its failure to generate cardiomyocytes, as demonstrated by the absence of cardiac marker gene activation. It is interesting that the two lines capable of generating cardiomyocytes showed an increase in SNORD116 expression at day 8 compared to days 2 and 4, when no such increase was seen in the D1WT line. This reinforces the postulation that SNORD116 is important in processes specific to cardiomyocyte differentiation.

An additional HCM-causing genetic variant was investigated to further explore the potential effect of genetic mutation on SNORD116 expression. Expression of SNORD116 during the differentiation of cardiomyocytes from the C9123T$^{-/-}$, C9123T$^{-/+}$ and C9123T$^{+/+}$ iPSC lines followed a different trend to that seen in the *ACTC1*-E99K lines. There was no large increase of expression at day 8 despite increases in cardiac marker genes that indicates the successful generation of cardiomyocytes. However, expression of SNORD116 did appear to be upregulated in day 17 iPSC-CMs derived from the heterozygous and homozygous *MYH7*-C0123T mutant lines compared to the wild-type line.

Overall, within the different cell lines SNORD116 expression was highest in iPSCs. In iPSC-CMs, the E99K variant did not appear to affect SNORD116 expression, however the C9123T variant did appear to

upregulate SNORD116. Further replicates are needed to confirm this trend.

To summarise, SNORD116 expression is altered response to cardiac stress in both cardiomyocytes and cardiac fibroblasts. In most cases, cardiac stress appears to cause an up-regulatory response on SNORD116 expression, although it has also shown to be downregulated under certain conditions, such as during recovery after hypoxia. Taken together, these results may indicate that SNORD116 is plays a role in the heart's response to stress. However, it is not clear whether SNORD116 expression is linked to the metabolic, contractile or transcriptional changes that occur during cardiac stress. Therefore, future chapters employ alternate strategies in investigating the role of SNORD116 in further detail.

Chapter 6 Modulating the expression of SNORD116 in cardiac cells

6.1 Introduction

A classic approach in investigating the function of a gene is to modulate the expression of that gene and observe the resulting changes that occur. There are multiple strategies of modulating gene expression that have different biological and practical advantages.

One strategy of modulating gene expression is through use of an overexpression vector. Often these are circular plasmids of DNA that are synthesised to contain the sequence of the gene of interest alongside a promotor and sometimes a reporter gene. The pcDNA3.1(+)MBII85 plasmid (heretofore referred to as the MBII85 plasmid) was a gift from Stefan Stamm (Addgene plasmid #67643; http://n2t.net/addgene:67643; RRID:Addgene_67643). This plasmid (shown in Figure 6-1) contains the mouse copy of SNORD116, and was shown to cause overexpression of SNORD116 in HEK 293T cells (407). The plasmid was designed based on the sequence from *Mus musculus* BAC clone RP24-177J9 from chromosome 7 (GenBank accession AC172750.1), a region of the mouse genome containing the SNORD116 cluster. The insert was designed to contain the natural exons and introns that are found at the SNORD116 locus to facilitate normal transcription and modification of the pre-mRNA. The mouse SNORD116 transcript encoded on the MBII85 plasmid corresponds to the SNORD116-1 mouse transcript, however all mouse SNORD116 paralogues are >94% identical to each other. Additionally, mouse SNORD116 is >80% identical to most human SNORD116 paralogues. Moreover, the key functional C/D box sequences are conserved across the human and mouse SNORD116 transcripts.

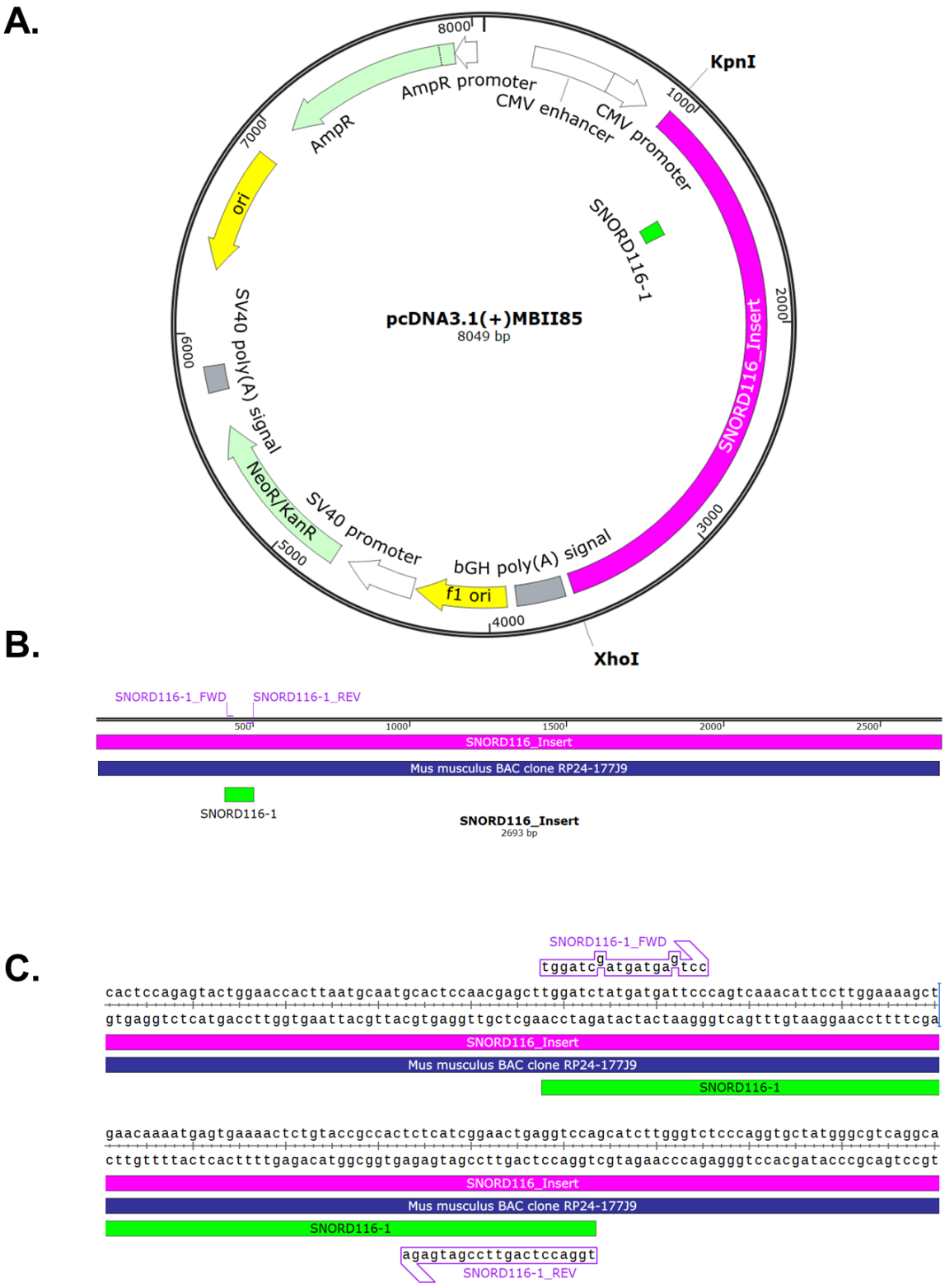

Figure 6-1. Plasmid map of the MBII85 plasmid used for SNORD116 overexpression.
A. Plasmid map of Addgene plasmid #67643 pcDNA3.1(+)MBII85. The SNORD116-conatining insert is highlighted in pink.
B. Map of the SNORD116 gene insert within the MBII85 plasmid. The sequence highlighted in blue shares 100% identity with the *Mus musculus* BAC clone RP24-177J9 sequence. The sequence in green corresponds to the mouse SNORD116-1 transcript. Forward (FWD) and reverse (REV) primers used to detect SNORD116-1 expression are indicated in purple
C. Detailed sequence of SNORD116-1 gene within the MBII86 insert.

Gene knock-out is an alternative strategy for modulating gene expression. This is commonly achieved in iPSCs using CRISPR-Cas9, wherein the gene is enzymatically cleaved out of the genome and thereby no longer expressed. To enable directed cleavage, a guide RNA (gRNA) is designed with complementarity to the target cut site. To remove the gene entirely, two target sites must be cut, one either side of the gene. The Cas9 endonuclease forms a ribonucleoprotein (RNP) complex with the gRNA and target genomic DNA (gDNA). Cas9 induces a double-stranded break at the target site within the gDNA. These breaks can be repaired by non-homologous end joining or through homology-directed repair. The latter can be exploited to facilitate the incorporation of a positive selection cassette into the target site. The selection cassette is flanked by regions homologous to sequences at the target cut sites. An overview of this process is presented in Figure 6-2 . Importantly, a target cut site must be directly adjacent to a protospacer adjacent motif (PAM) sequence (5'-NGG-3') to facilitate Cas9 binding.

This chapter will describe the employment of these gene modulation strategies in the investigation of SNORD116.

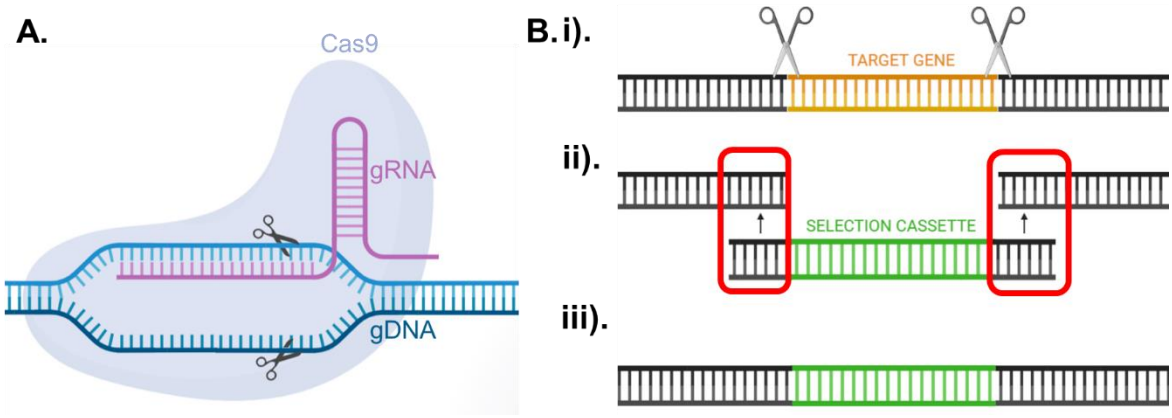

Figure 6-2. Principle of gene knockout using CRISPR-Cas9.
A. Ribonucleoprotein complex of cas9, gRNA and target gDNA.
B. i) Cas9-mediated removal of the target gene followed by (ii) insertion of selction cassette by homology-directed repair resulting in (iii) replacement of the target gene with the selection cassette at the target site in the genome. Figure generated using BioRender.com.

6.2 Overexpression of SNORD116

6.2.1 Overexpression of SNORD116 in iPSC-CFs

Cardiac fibroblasts were differentiated from iPSCs and seeded into a 24-well plate at a seeding density of 100,000 cells/cm^2. After two days of recovery, the cells were transfected with 600ng per well of either the MBII85 plasmid or a transfection control plasmid. After 72 hours the cells were lysed and analysed by RT-qPCR. The results are shown in Figure 6-3. SNORD116 was expressed at 2.4±0.2-fold that of control levels. The expression of *aSMA* appeared upregulated by 1.9±0.1-fold in response to SNORD116 overexpression. The expression of *COL1A1*, CyclinD2, ki67 and caspase 3 did not appear to be affected by SNORD116 overexpression.

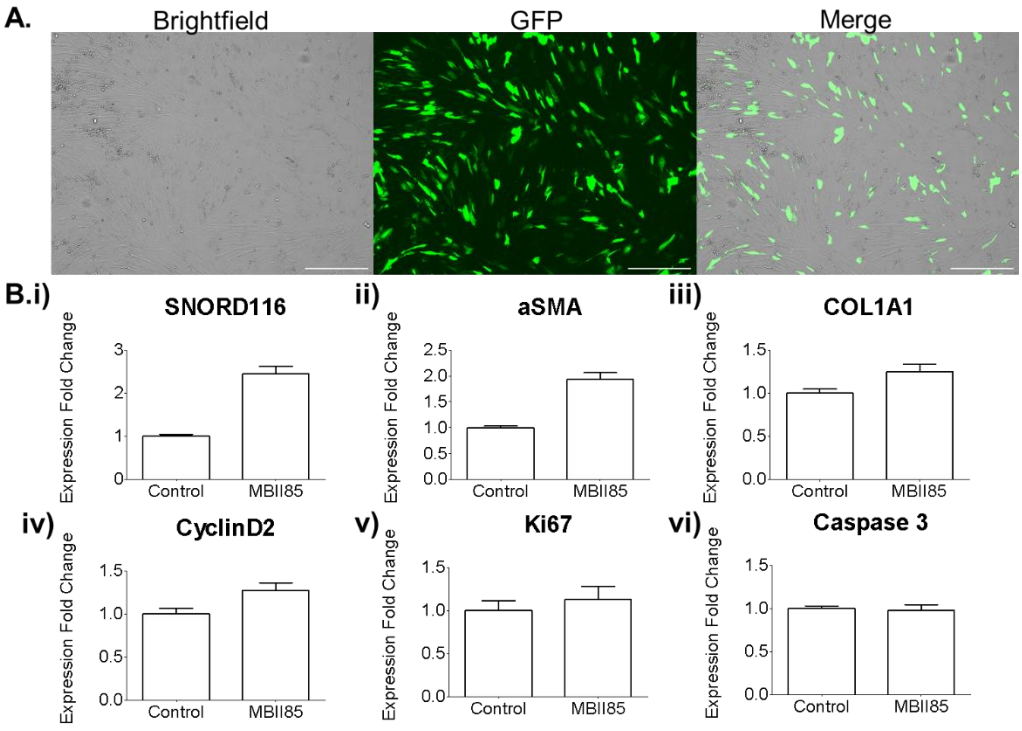

Figure 6-3. Overexpression of SNORD116 in iPSC-CFs.
A. Images taken in the brightfield and GFP channels of iPSC-CFs 24hrs post-transfection by lipofection with a GFP control plasmid. Magnification = 4x, scale bar = 500um.
B. Gene expression of iPSC-CFs transfected with the control and MBII85 plasmids 72 hours post-transfection. Expression plotted as fold change relative to control, calculated using the ddCt method normalised to GAPDH. N=1. Error bars represent SEM.

The effect of SNORD116 overexpression on iPSC-CF viability was measured using cell titre-glo. In addition, transfected CFs were also dissociated, fixed and stained for aSMA expression 72 hours post-transfection. The expression of aSMA was analysed using flow cytometry. The results shown in Figure 6-4 indicated that there was no difference in viability between the control and MBII85 plasmid transfections. Also, there was no apparent change in aSMA protein expression as a result of SNORD116 overexpression. The percentage of aSMA-positive fibroblasts was 38% in the transfection control sample and 39% in the MBII85-transfected sample.

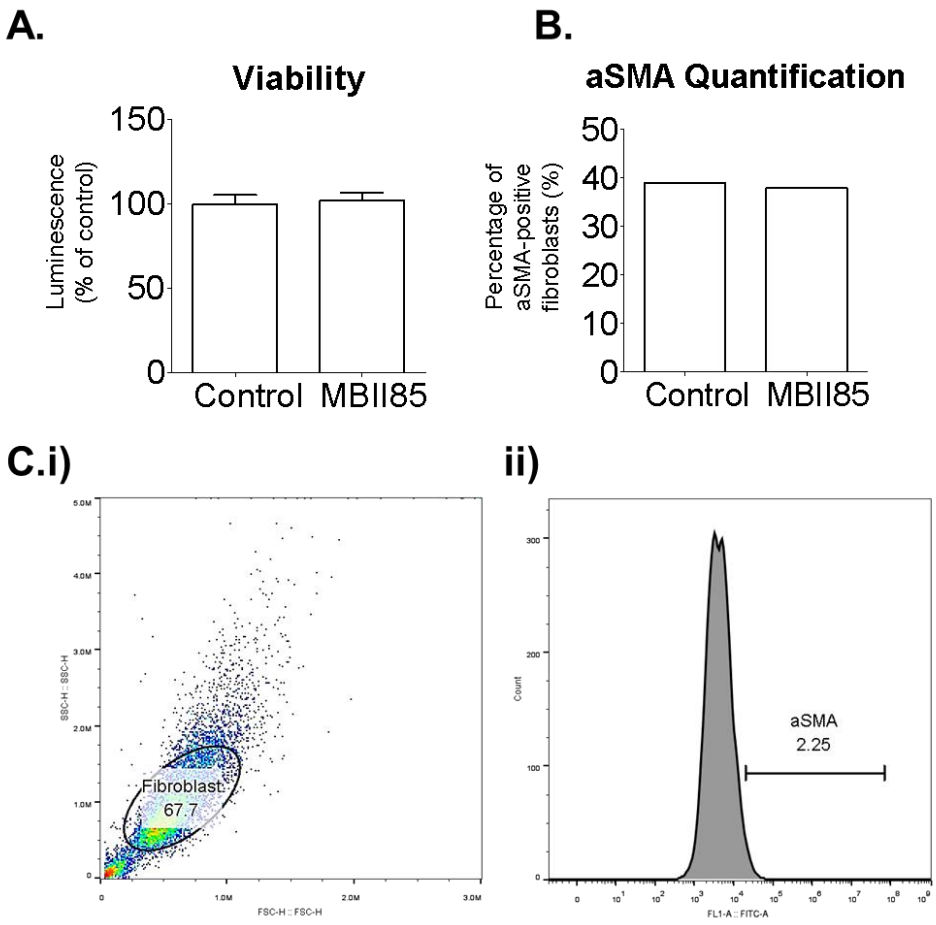

Figure 6-4. IPSC-CF response in viability and aSMA expression to SNORD116 overexpression.

A. Cell viability of iPSC-CFs after transfection measured using cell titre-glo. N=1.Error bars represent standard deviation between technical replicates.

B.The percentage of cardiac fibroblasts that are positive for aSMA expression 72hrs post-transfection of either the control or MBII85 plasmid. N=1.Number of total events = 10,000 per sample.

C. Gates used for aSMA expression quantification. (i) The fibroblast population was gated using the forward and side scatter. (ii) The aSMA+ population was gated using FITC-A fluorescence of cells stained with the secondary antibody only.

Transfected iPSC-CFs were also analysed by immunocytochemistry to quantify the expression of aSMA expression and nuclear ki67 expression. Cells were fixed and permeabilised 72 hours post-transfection and stained for aSMA (green) and ki67 (red). The level of aSMA expression indicates activation, and the level of nuclear ki67 indicates cell proliferation. CellProfiler was used to quantify the mean intensity of aSMA expression relative to the background level. CellProfiler was also used to outline the nuclei and measure the mean intensity of ki67 relative to the number of nuclei. The results are shown in Figure 6-5. Consistent with the flow cytometry results in Figure 6-4, there was no apparent change in the protein expression of aSMA in response to SNORD116 overexpression. There was also no significant difference in the number of nuclei relative to the control. However, nuclear ki67 expression was significantly lower in response to SNORD116 overexpression. The average mean intensity of nuclear ki67 per number of nuclei present was $5.6x10^{-4}\pm1.4x10^{-5}$ in control samples, which decreased to $2.5x10^{-4}\pm9.8x10^{-5}$ in response to SNORD116 overexpression.

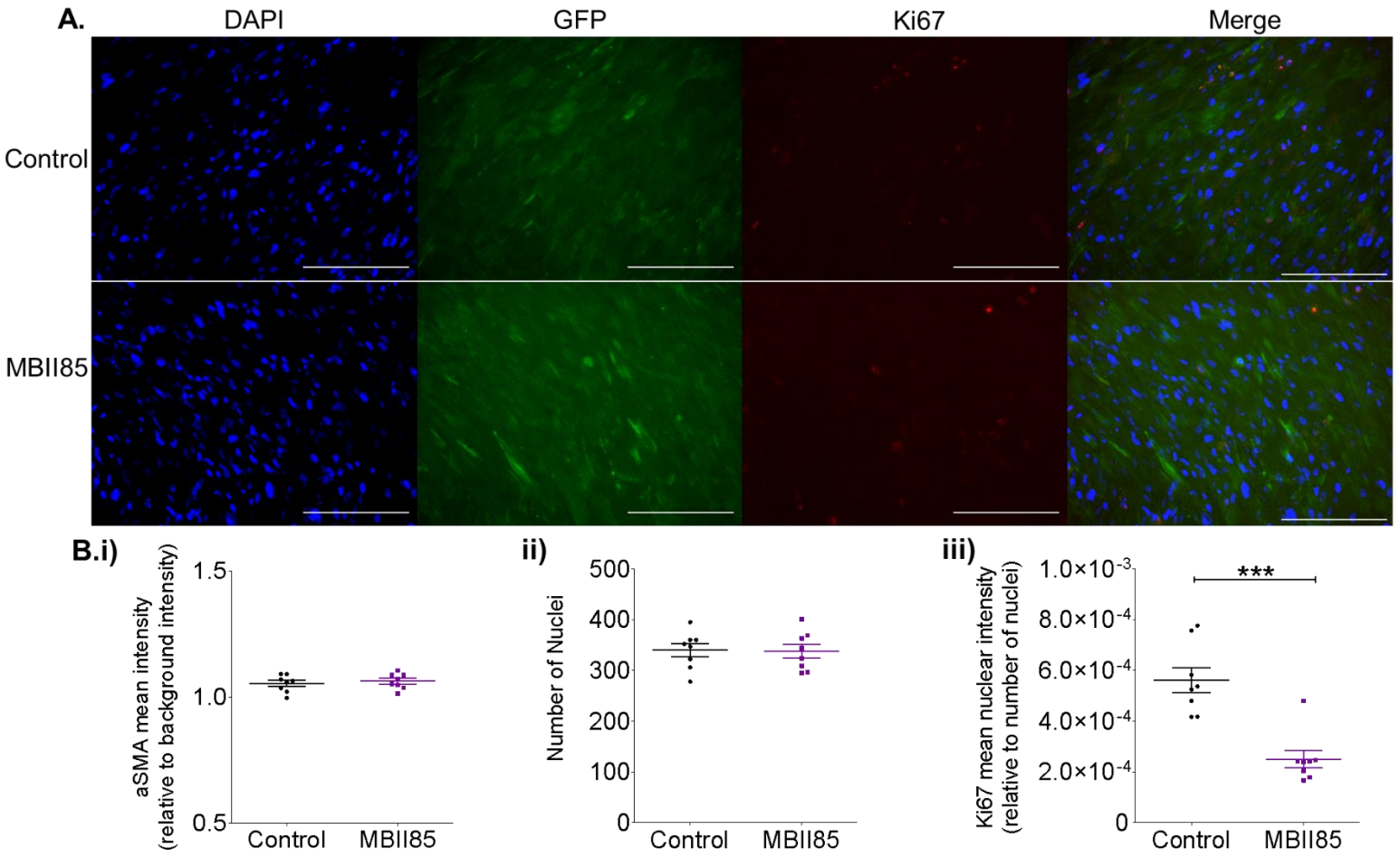

Figure 6-5. Immunocytochemistry of iPSC-CFs transfected with MBII85.
A. The expression of DAPI (blue), aSMA (green) and ki67 (red) in iPSC-CFs transfected with either a transfection control plasmid or the MBII85 plasmid. Magnification = 20x, scale bar = 200um.
B.i) The mean intensity of aSMA relative to the background level. (ii) the number of nuclei per sample. (iii) The mean intensity of nuclear ki67 relative to the number of nuclei. N=8. Error bars represent SEM.

To investigate the effect of SNORD116 overexpression on the metabolism of iPSC-CFs, transfected CFs were analysed using the Biolog MitoPlate assay. Eight individual substrates were selected to be analysed: three glycolytic substrates (glucose, lactate, pyruvate), one ketone (β-hydroxybutyrate or B-OBH), one amino acid (glutamine), one TCA substrate (citric acid) and one fatty acid (oleic acid). Oleic acid was combined with carnitine to facilitate uptake into the cells, therefore the metabolism of carnitine on its own was also assessed. The results are presented in Figure 6-6.

In terms of substrate usage capacity, there was no significant effect of SNORD116 overexpression on the total substrate use of any of the substrates tested. Glutamine, citric acid and oleic acid did not produce a colour change greater than the no-substrate control, suggesting they were not taken up and/or metabolised by the CFs. Pyruvate caused the largest total colour change under both conditions at 46±6 in the control sample and 56±10 in the MBII85 sample. Interestingly, when analysing the rate of colour change per substrate, there were some differences caused by SNORD116 overexpression although this was not significant due to variation in the MBII85 sample replicates. Despite having a smaller total colour change, the rate of lactate metabolism appeared higher in the MBII85 transfected cells at 10±18 a.u/min compared to 0 rate change above the no substrate control in the transfection control sample. Pyruvate also appeared to have a higher rate of metabolism upon SNORD116 expression, with a rate of 9±2 a.u/min in the control cells and 23±22 a.u/min in the MBII85 cells. The only substrate tested that showed a lower rate of metabolism as a result of SNORD116 overexpression was glucose, which had a rate of 14±1 a.u/min in the control cells and 0.8±1 in the MBII85 cells. Once again, glutamine, citric acid and oleic acid did not produce a rate change higher than the no-substrate control, further indicating that they were not metabolised by the cells in either sample.

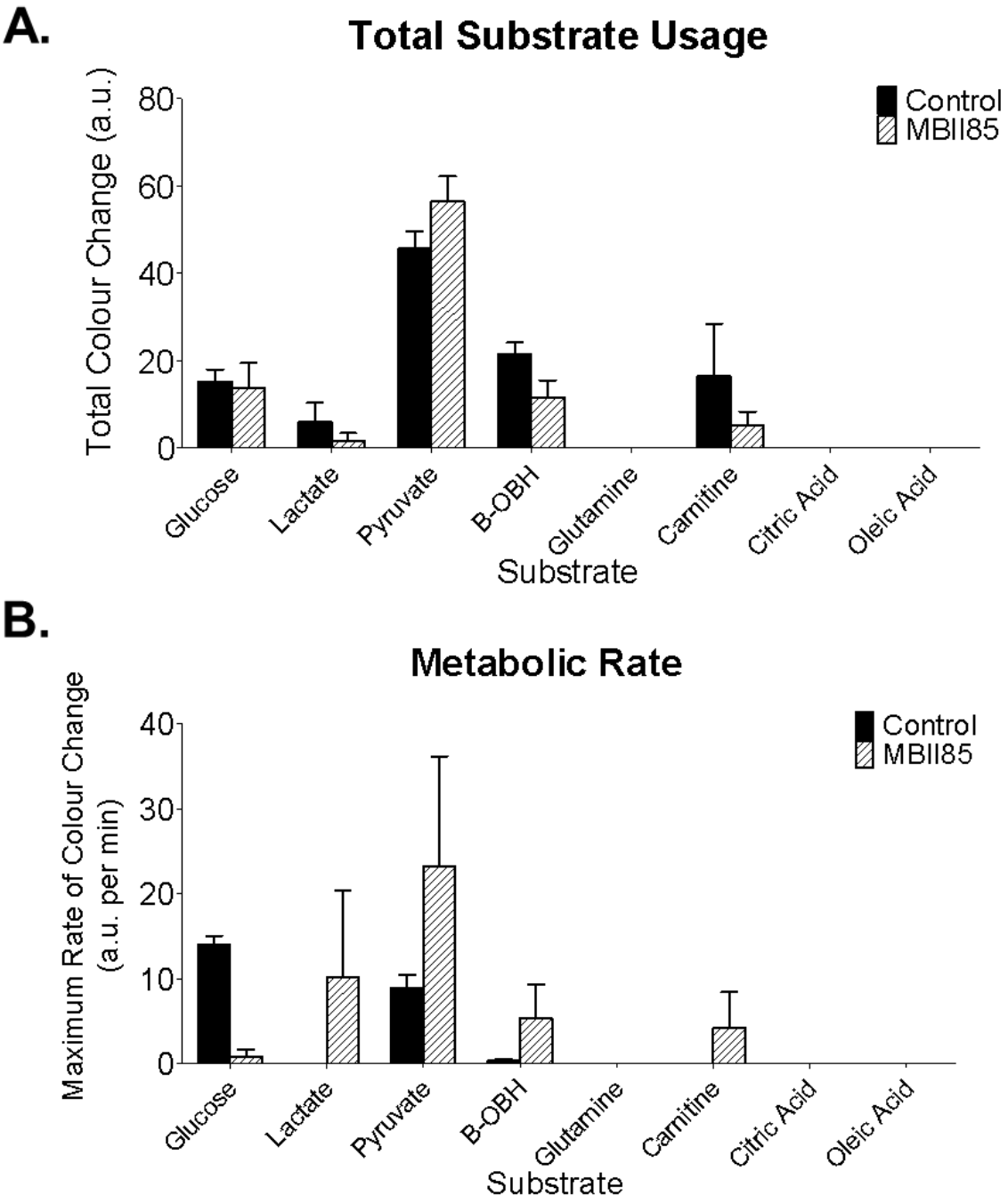

Figure 6-6. Substrate metabolism of iPSC-CFs in response toSNORD116 overexpression.
The (A) total colour change and (B) maximal rate of colour change as a result of metabolism of individual substrates by iPSC-CFs transfected with either the control or MBII85 plasmid. Normalised to the average no substrate control of each sample. N=3 (Control), N=4 (MBII85). Statistics calculated by two-way ANOVA. Error bars represent SEM.

Overall, SNORD116 overexpression can be achieved in iPSC-CFs by means of lipofection of an overexpression plasmid (MBII85). The overexpression of SNORD116 in cardiac fibroblasts does not appear to affect cell viability or cause significant upregulation of *aSMA*, a marker of activation. However, SNORD116 overexpression did appear to cause a reduction in the amount of nuclear ki67 expression, which could indicate that cell proliferation pathways were affected. This could be investigated further using cell growth assays. The total capacity to metabolise various substrates did not appear to be affected by SNORD116 overexpression in cardiac fibroblasts. However, the rate of metabolism of certain substrates did appear affected although the large variation in some substrates prevented this from being significant. Most notably, the rate of glucose metabolism appeared slower in response to SNORD116 overexpression. The same overexpression system was used to investigate if similar effects could be observed in cardiomyocytes in response to SNORD116 overexpression.

6.2.2 Overexpression of SNORD116 in iPSC-CMs

6.2.2.1 : Effect of SNORD116 overexpression on gene and protein expression

On day 15 of the iPSC-CM differentiation protocol, the cells were dissociated and seeded at 175,000 cells/cm^2 into 24-well plates in RPMI/B27 media supplemented with 10% FBS. The media was replaced the next day. The following day, the iPSC-CMs were transfected by lipofection with 600ng per well of the MBII85 plasmid or a transfection control plasmid expressing GFP. RNA was isolated 72-hours post-transfection. In addition, the media was harvested three, five and seven days after transfection and pooled. Extracellular vesicles were isolated by ultracentrifugation and the expression was analysed by RT-qPCR. Figure 6-7 shows the expression fold change of SNORD116-1 at both the cellular and extracellular vesicle level as a result of transfection. The MBII85 plasmid caused SNORD116 expression to be upregulated 3±0.2-fold higher compared to the control three days post-transfection. It also appeared to be packaged 9±0.8-fold more into EVs compared to the transfection control. Additionally, the effect of the MBII85 plasmid on iPSC-CM viability was analysed using cell titre-glo. There was no difference in viability between the control and MBII85 transfection samples.

Overall, the MBII85 plasmid appeared successful in achieving overexpression and increased packaging of SNORD116. Therefore, the MBII85 plasmid was taken further to be used in subsequent overexpression analysis.

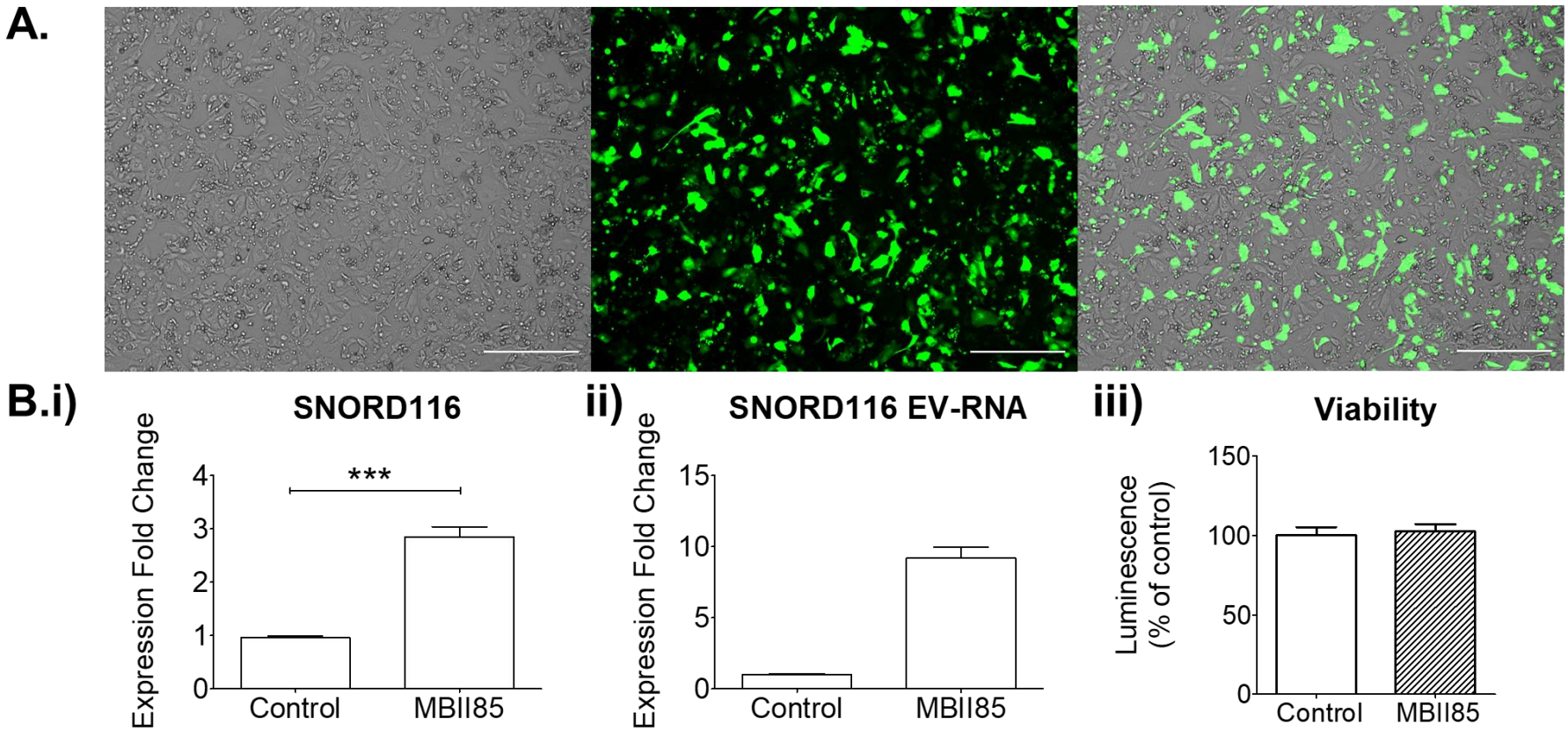

Figure 6-7. Overexpression of SNORD116 in iPSC-CMs

A. Images of transfected iPSC-CMs taken in the GFP and brightfield channels 72-hours post-transfection. Magnification = 4x, scale bar = 500um.

B.i) Expression of SNORD116 72-hours post-transfection with the MBII85 plasmid relative to the transfection control plasmid. Expression plotted as fold change relative to control, calculated by ddCt method normalised to 18S. N=3, error bars = SEM. Statistics calculated by unpaired t-test, *** = P<0.001.

B.ii) Expression of SNORD116 packaged inside extracellular vesicles isolated by ultracentrifugation from pooled iPSC-CM media harvested 3, 5 and 7 days after transfection. Expression fold change relative to control, calculated by ddCt method normalised to 18S. N=1, error bars = SEM

B.iii) Cell viability of iPSC-CMs 72 hours post-transfection with the MBII85 plasmid relative to the transfection control plasmid. Measured using cell titre-glo. N=3. Error bars represent standard deviation. Statistics calculated by unpaired t-test.

To investigate the transcriptomic effect of SNORD116 overexpression, iPSC-CMs were dissociated at day 15 and seeded into a 24-well plate at a density of 175,000 cells/cm^2. After 48 hours, the cells were transfected with 600ng per well of either the control plasmid or the MBII85 plasmid. RNA was isolated using the Qiagen miRNeasy Kit. RNA sequencing and bioinformatic analysis was performed by Harris Papadopoulou and Jon Price of the University of Cambridge Department of Medicine. Bulk analysis of the transcriptomic results is shown in Figure 6-8.

Principal component analysis showed that the control and MBII85-transfected cells were clearly defined as two separate clusters. However, there was a large amount of variance between the individual replicates within each sample. In total, 705 genes were upregulated, and 376 genes were downregulated as a result of SNORD116 overexpression. There were 241 total genes that were significantly ($P<0.05$) upregulated, and 163 genes that were significantly downregulated (fold change > 1.2). Gene expression changes ranged from -2 log_2 to 2 log_2 fold change, with most significant changes occurring between -1 log_2 and 1 log_2 fold change with normalised counts of 5-10 log_2 mean count.

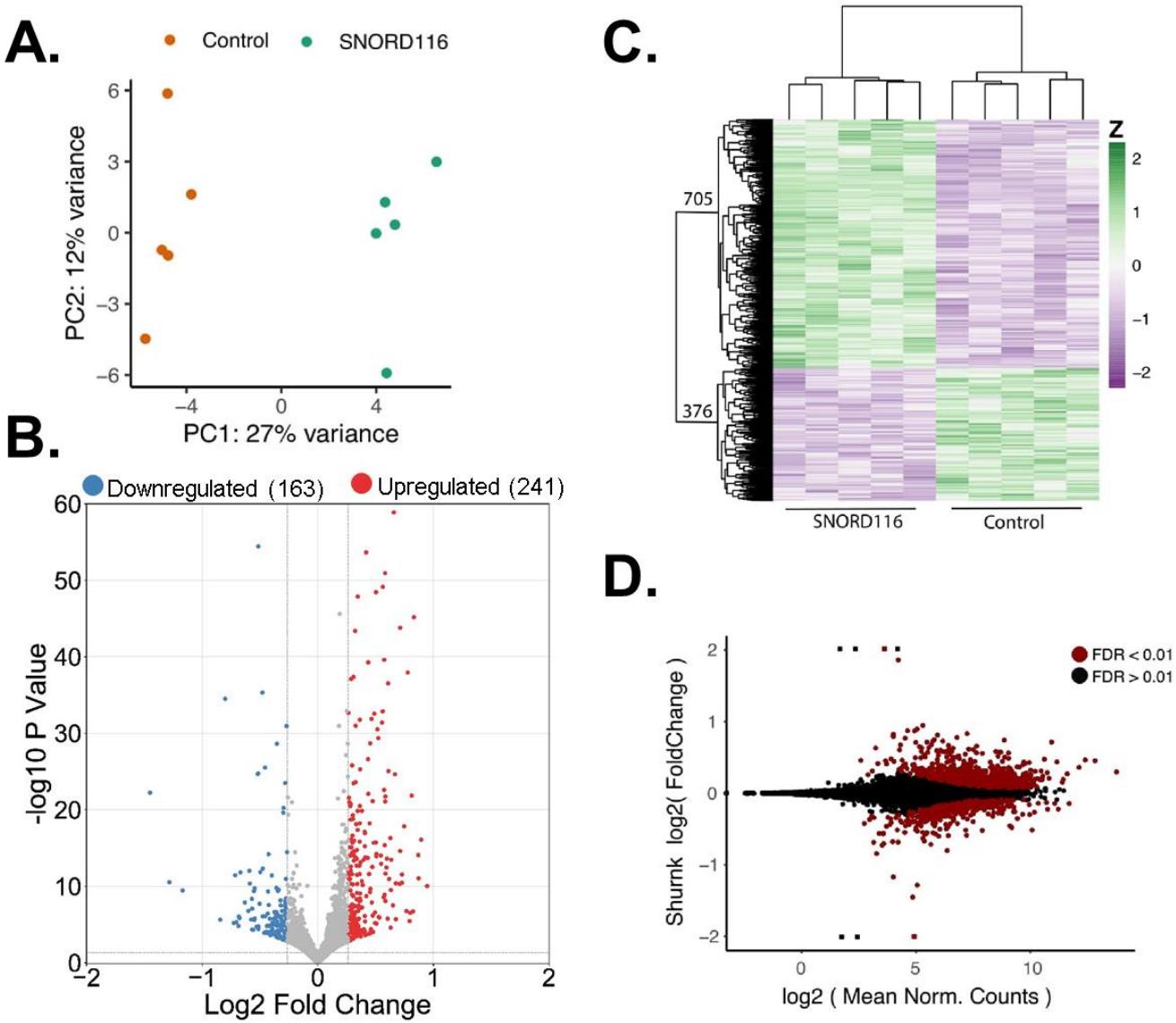

(Legend on next page)

Figure 6-8. Bulk analysis of the RNAseq dataset produced by SNORD116 overexpression.
A. Principal component analysis of the dataset. PC1 and PC2 variance expression between the transfection control samples (Control, orange) and the SNORD116 overexpression samples (SNORD116, green).
B. Volcano plot of the RNAseq data. Fold change cut off = -1.2 > Log2 FC > 1.2. P min = $1e^{-100}$. plotted using http://www.bioinformatics.com.cn/srplot, an online platform for data analysis and visualization.
C. Clustered heatmap of RNA-Seq expression z-scores computed for genes that are significantly differentially expressed Benjamini-Hochberg adjusted p-Value ($p < 0.05$) in any comparison. The genes (rows) and samples (columns) are clustered using the Pearson Correlation distance and complete linkage hierarchical clustering. The colour code shows the differential gene expression (as z-score), with a green colour indicating higher expression of a gene and purple colour indicating lower expression of a gene.
Analysis performed by Jon Price using DESEQ2. N=5.
D. MA plot showing the mean of the normalized counts versus the log2 foldchanges for all genes tested.

The list of differentially expressed genes (DEGs) as a result of SNORD116 overexpression (where $P<0.05$) was subjected to Kyoto Encyclopaedia of Genes and Genomes (KEGG) pathway enrichment analysis. The results are shown in Figure 6-9. The pathway enriched with the highest degree of significance was the focal adhesion pathway which contained 47 DEGs, 42 of which were downregulated as a result of SNORD116 overexpression. The pathway with the highest number of DEGs was pathways in cancer with 67 genes. The PI3K-Akt signalling pathway contained the second-highest number of DEGs with 52 genes. Focusing specifically on cardiomyopathy pathways, the arrhythmogenic right ventricular cardiomyopathy (ARVC) pathway was the most significantly enriched of the cardiomyopathy pathways. With a $-\log_{10}P$ of 4.9, the ARVC pathway contained 20 DEGs, 15 of which were downregulated as a result of SNORD116 overexpression. Other cardiomyopathy-associated pathways identified were the dilated cardiomyopathy (DCM) and hypertrophic cardiomyopathy (HCM) pathways. The fold changes of the DEGs in these three pathways was plotted as a heatmap in Figure 6-9.

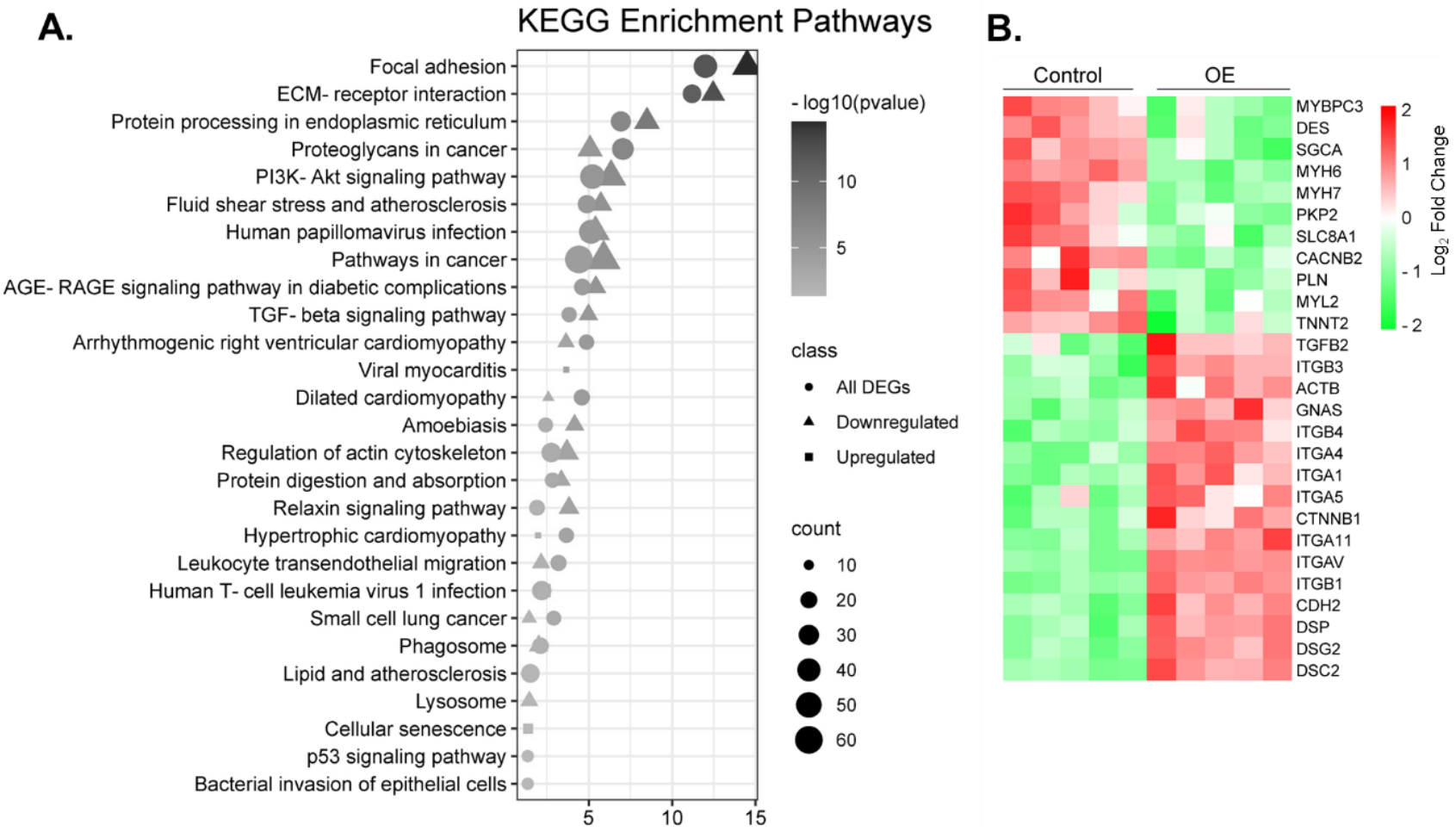

Figure 6-9. KEGG Pathway Enrichment analysis of DEGs resulting from SNORD116 overexpression.
A. List of KEGG pathways identified as enriched from list of differentially expressed genes (where P<0.05). -log10 P value is plotted on the x axis and indicated by shading intensity, the size of each point indicates the gene count and the shape indicates the fold change direction of genes in the pathway. B. Heatmap showing the expression changes of genes from the ARVC, DC and HCM pathways as a result of SNORD116 overexpression. Fold change indicated by the colour scale (downregulated = green, upregulated = red

The DEGs of the ARVC pathway is expanded in detail in Figure 6-10. The majority of genes within the ARVC, HCM and DCM pathways that were downregulated as a result of SNORD116 expression were associated with either cardiac ion channels – such as CACNB2, SLC8A1, *RYR2* and HCN4 – or they were genes associated with intracellular cardiomyocyte structures such as *MYH6* and 7, *TNNT2*, *MYL2* and MYBPCL3. Contrastingly, the majority of DEGs that were upregulated as a result of SNORD116 overexpression were associated with the desmosome, adherens junction or gap junction such as DSG2, DSC2, CDH2 and GJA1.

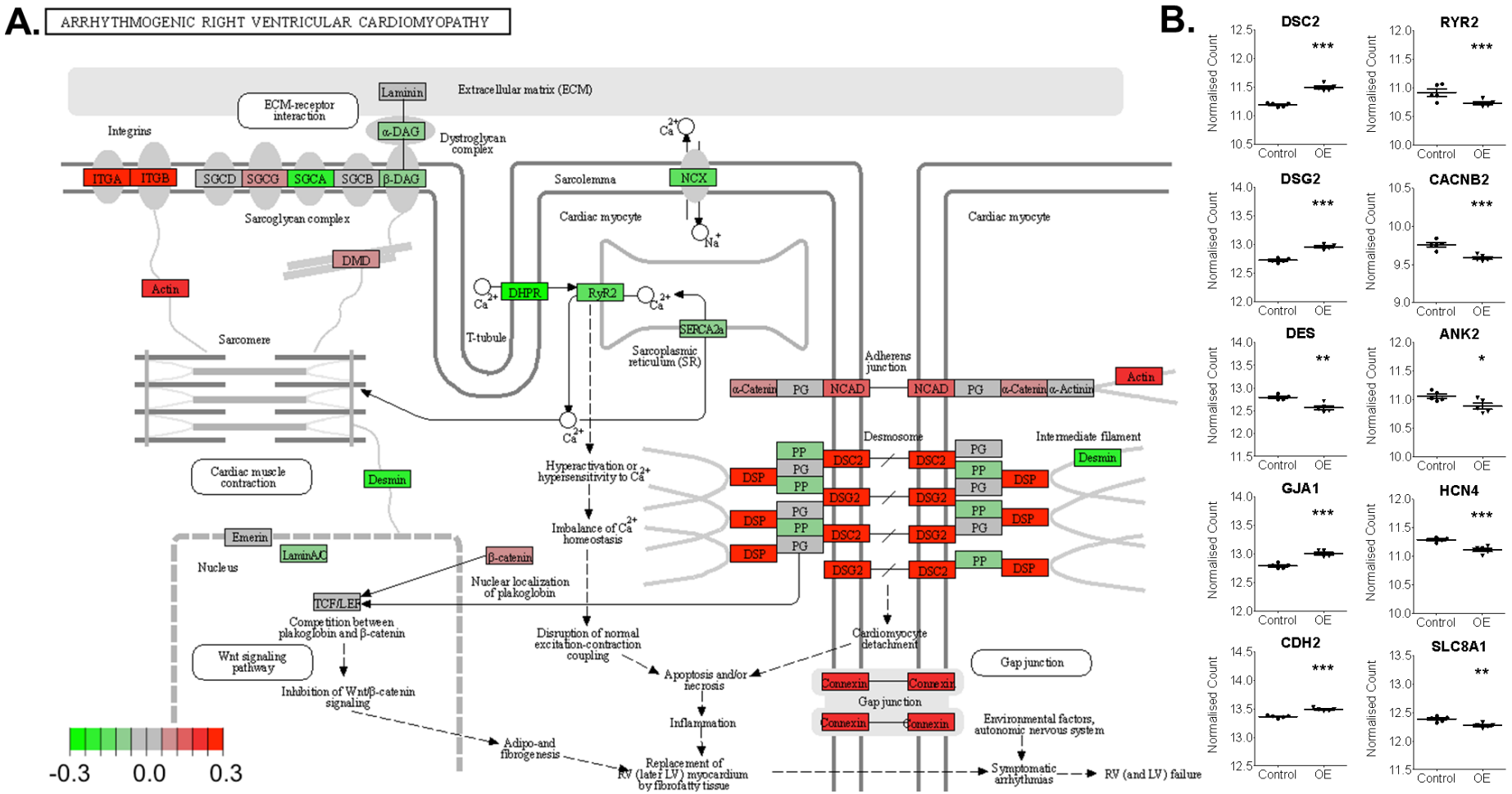

Figure 6-10. ARVC Pathway DEGs as a result of SNORD116 overexpression in iPSC-CMs.

A. Pathway map of the arrhythmogenic right ventricular cardiomyopathy gene pathway with fold changes resulting from SNORD116 overexpression indicated by the colour scale (downregulated = green, upregulated = red). Rendered by Jon Price using Pathview.

C. Normalised counts of genes identified from the ARVC pathway in cells transfected with either the transfection control plasmid (control) or MBII85 plasmid (OE). Statistics calculated by unpaired t-test. * = P<0.05, ** = P<0.01, *** = P<0.001. N=5. Error bars represent SEM.

The list of differentially expressed genes was subjected to Ingenuity Pathway Analysis (IPA) (Qiagen) in order to assess the gene pathways that were predicted to be activated or inhibited by SNORD116 overexpression. The list of DEGs as a result of SNORD116 overexpression was thresholded at $p<0.001$ and inputted into the IPA software for analysis. The IPA software generated a list of canonical pathways that were predicted to be activated or inhibited by SNORD116 overexpression. Each predicted pathway has an associated Z score which indicates whether the pathway is activated (+Z) or inhibited (-Z), and a P-value indicating the statistical significance of that pathways' activation or inhibition. In total, 201 different pathways were predicted to be affected, where 160 were activated and 41 were inhibited. The results are presented in Figure 6-11.

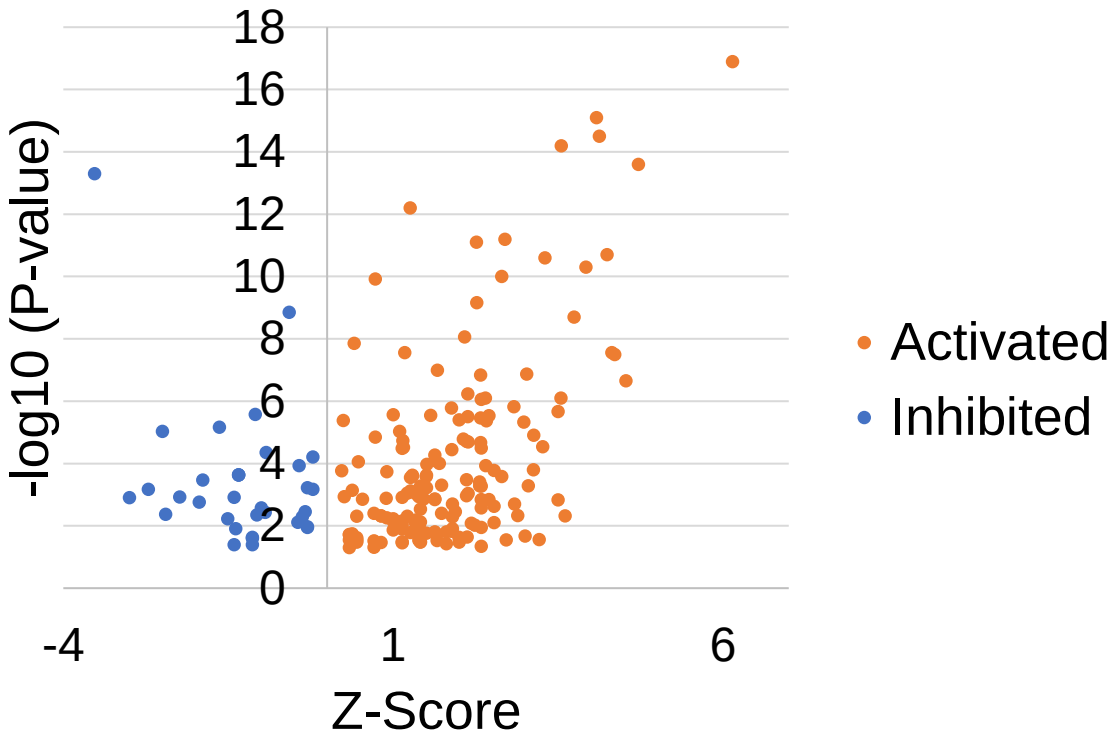

Figure 6-11. IPA canonical pathways predicted to be affected by SNORD116 expression based on transcriptomic data.
The list of DEGs was thresholded to p<0.001 and inputted into IPA. The list of canonical pathways generated was thresholded to p<0.05. N=5.

The IPA software is capable of generating expanded pathway maps that detail the specific interactions between molecules within a pathway. The cardiac hypertrophy signalling pathway was predicted to be activated by SNORD116 overexpression, which is shown in Figure 6-12. Genes within this pathway that were upregulated include TGFβ, IGF1R, calmodulin and JUN. These were predicted to cause the activation of a hypertrophic response. Contrastingly to this, the cardiomyocyte differentiation pathway was predicted to be inhibited by SNORD116 overexpression, as shown in Figure 6-13. The genes for NPPB, NPPA, *MYH7* and *MYL2* were all downregulated, contributing to the predicted inhibition of cardiomyocyte differentiation as a result of SNORD116 overexpression.

Cardiac Hypertrophy Signalling

P = 2.88403E-06
Z = 2.45 (Activated)

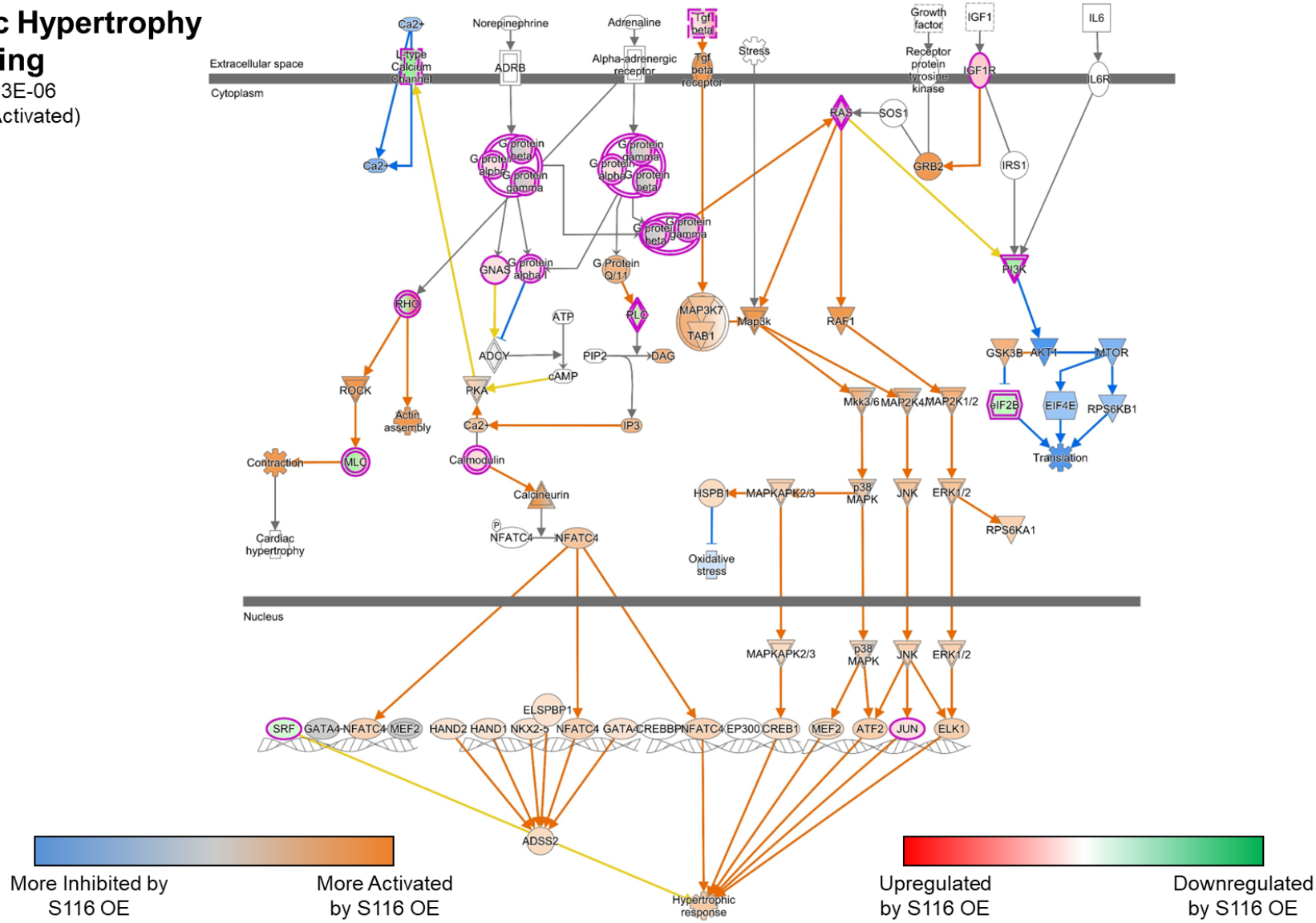

(Legend on next page)

Figure 6-12. IPA expanded pathway of cardiac hypertrophy signalling.
Genes that are upregulated or downregulated by S116 overexpression (S116 OE) are colour coded red/green. Molecules that are predicted to be activated or inhibited are colour coded blue/orange. DEGs present in the dataset are highlighted by double pink line. Orange arrows = leads to activation, blue arrows = leads to inhibition, yellow arrows = findings inconsistent with state of downstream molecule, grey arrows = effect not predicted. Image generated by IPA software. N=5.

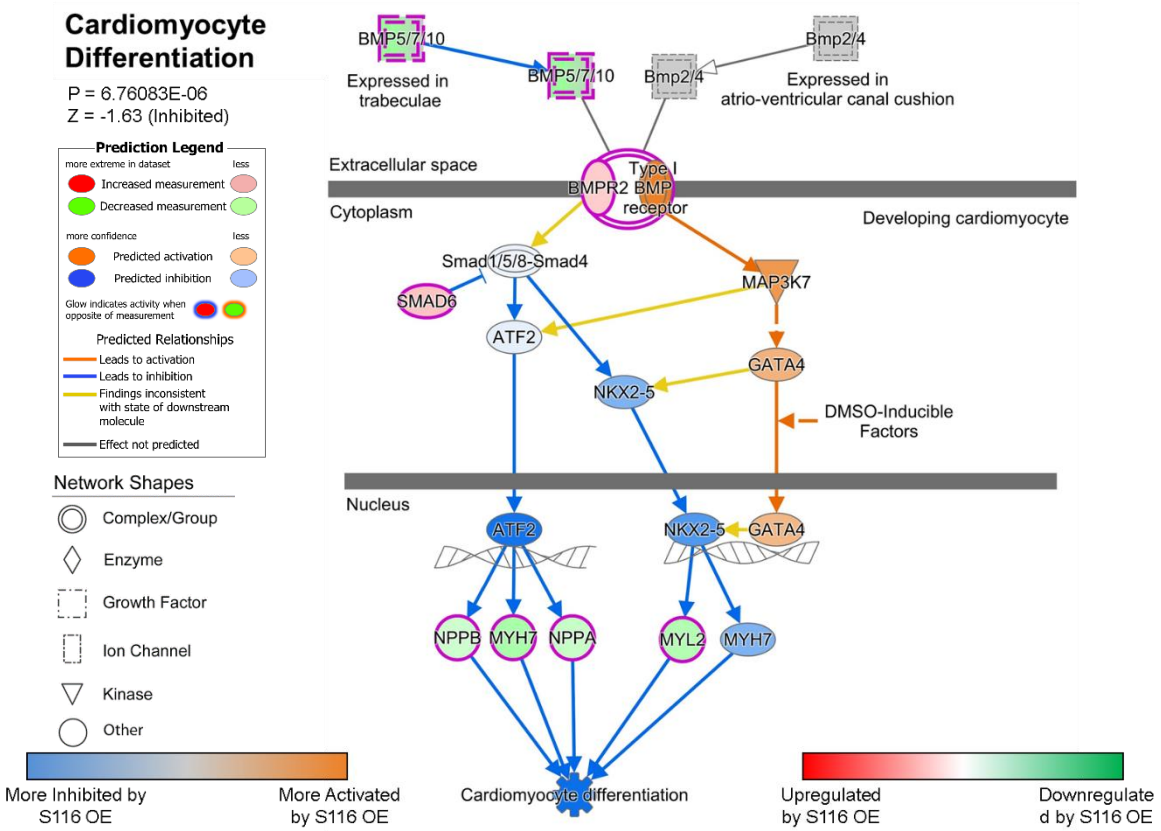

Figure 6-13. IPA expanded pathway of cardiomyocyte differentiation.
Genes that are upregulated or downregulated by S116 overexpression (S116 OE) are colour coded red/green. Molecules that are predicted to be activated or inhibited are colour coded blue/orange. DEGs present in the dataset are highlighted by double pink line. Orange arrows = leads to activation, blue arrows = leads to inhibition, yellow arrows = findings inconsistent with state of downstream molecule, grey arrows = effect not predicted. Image generated by IPA software. N=5.

To evaluate the effect of SNORD116 overexpression on protein expression, iPSC-CMs that had been cultured in fatty acid media (371) were transfected with either the MBII85 plasmid or a control plasmid. After 72 hours, the cells were scraped, pelleted and sent for proteomic analysis. Proteomic analysis was performed by Mandy Peffers and James Anderson of the University of Liverpool Institute of Life Courses and Medical Sciences. The results are shown in Figure 6-14. Of the proteins identified with at least one unique peptide, 872 were differentially expressed by SNORD116 overexpression with a $p<0.05$. Of these, 404 had a positive fold change and 468 had a negative fold change. When thresholded to $-1.5 > \log_2$ fold change > 1.5, 51 proteins had increased abundance and 31 had decreased abundance when SNORD116 was overexpressed. The three most upregulated proteins were CTP synthase 1 (CTPS1), NCK-interacting protein with SH3 domain (NCKIPSD) and Chromosome 6 open reading frame 136 (C6orf136) with $\log_2$ fold changes of 4.9, 6.3 and 13.4 respectively. The three most downregulated proteins were Keratin 17 (KRT17), S100 Calcium Binding Protein A14 (S100A14) and Plakophillin-1 (PKP1) with $\log_2$ fold changes of -3.2, -3.2 and -6.0, respectively.

The 872 differentially expressed proteins were inputted into IPA to predict which pathways were activated or inhibited by SNORD116 overexpression. Top pathways are listed in Figure 6-14. SNARE signalling and glycolysis I were the top two pathways predicted to be inhibited by SNORD116 overexpression. HIPPO signalling and Dilated Cardiomyopathy signalling were two of the top four pathways predicted to be activated by SNORD116 overexpression.

A.

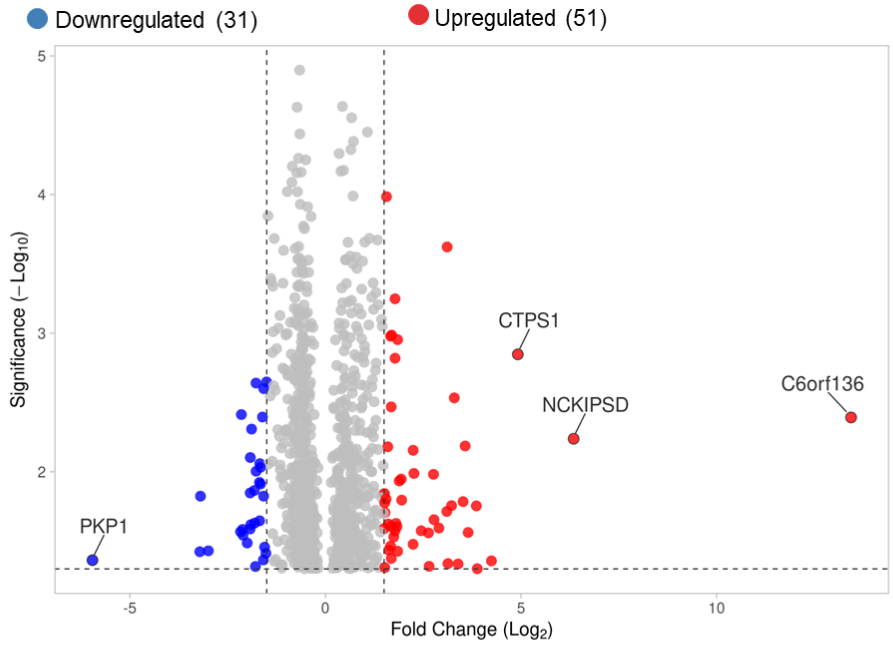

B.

Pathway	-LOG10(P-value)	Z-score
HIPPO signaling	1.48	2.828427
Aryl Hydrocarbon Receptor Signaling	1.65	2
Xenobiotic Metabolism AHR Signaling Pathway	1.51	1.666667
Dilated Cardiomyopathy Signaling Pathway	2.04	1.527525
Neuroprotective Role of THOP1 in Alzheimer's Disease	2.01	0.816497
mTOR Signaling	1.51	0.816497
Semaphorin Neuronal Repulsive Signaling Pathway	1.39	0.27735
Xenobiotic Metabolism CAR Signaling Pathway	1.61	-0.57735
Factors Promoting Cardiogenesis in Vertebrates	1.46	-0.816497
HIF1α Signaling	2.56	-1
ILK Signaling	1.31	-1.147079
PI3K/AKT Signaling	2.7	-1.807392
Glycogen Biosynthesis II	2.58	-2
ERK5 Signaling	1.31	-2.645751
Glycolysis I	2.03	-2.828427
SNARE Signaling Pathway	1.58	-3.5

Figure 6-14. Proteomic analysis of SNORD116 overexpression in iPSC-CMs.
A. Volcano plot showing the differentially expressed proteins as a result of SNORD116 overexpression. Only proteins with at least one unique peptide were included. The top four hits are labelled. Fold change cut off = -2 > Log2 FC > 2. Significance at off at P<0.05. Plot generated using VolcaNoseR.
B. IPA canonical pathways predicted to be affected by SNORD116 expression based on proteomic data. The list of differentially expressed proteins was thresholded to those with two unique peptides and p<0.05. The list of canonical pathways was thresholded to p<0.05. N=5..

Figure 6-16 shows the expanded glycolysis I pathway. The proteins in this pathway are enzymes important in the glycolytic break down of glucose. All the enzymes that were differentially expressed showed a decrease in abundance in response to SNORD116 overexpression. This decreased abundance led to the predicted decrease in ATP and NADH production, and an overall predicted inhibition of glycolysis. Figure 6-16 shows the expanded HIPPO signalling pathway. Within this pathway, the MST, KRS and LATS kinases are predicted to be activated. The predicted activation of these kinases contributes to the subsequent predicted inhibition of YAP/TAZ and therefore a predicted decrease in cell proliferation. Figure 6-17 outlines a summary of the expression changes of proteins identified in the SNARE Signalling, DCM, Glycolysis I and HIPPO Signalling pathways as a result of SNORD116 overexpression.

Glycolysis I

P = 0.0093

Z = -2.83 (Inhibited)

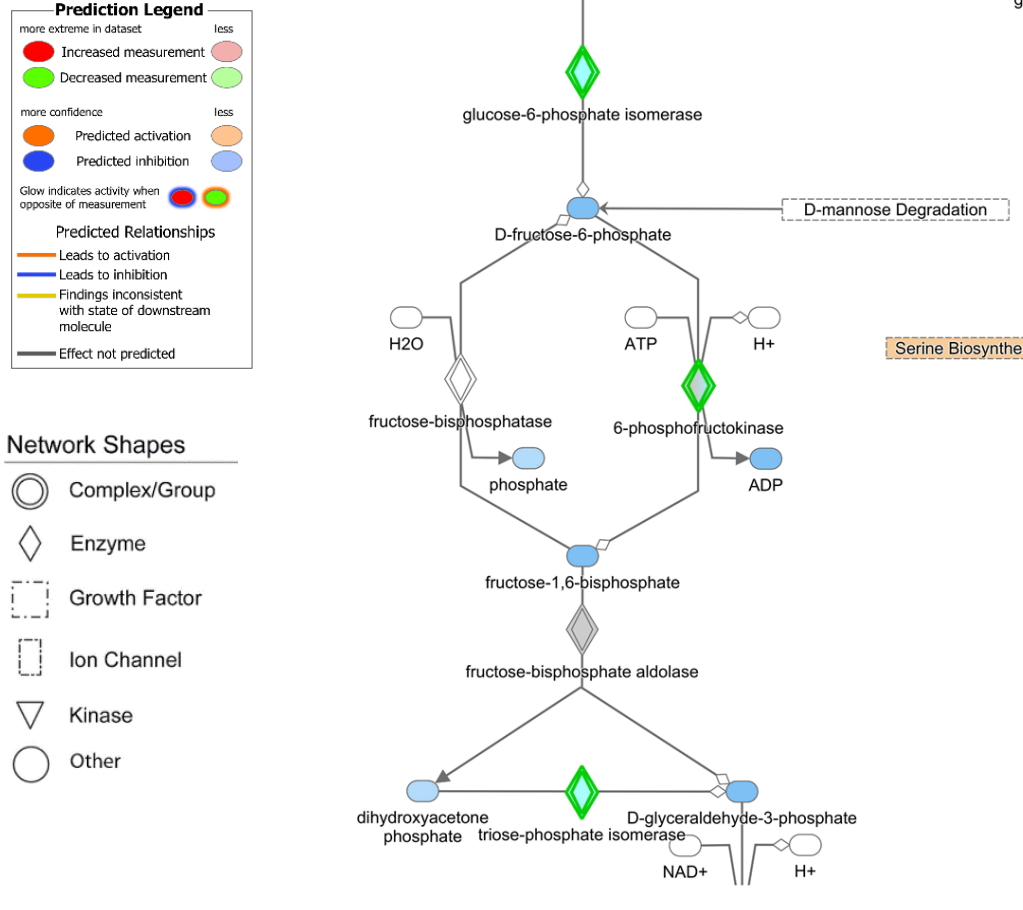

More Inhibited by S116 OE — More Activated by S116 OE

Upregulated by S116 OE — Downregulated by S116 OE

(Legend on next page)

Figure 6-15. IPA expanded pathway of Glycolysis I.
Genes that are upregulated or downregulated by S116 overexpression (S116 OE) are colour coded red/green. Molecules that are predicted to be activated or inhibited are colour coded blue/orange. DEGs present in the dataset are highlighted by double green line. Orange arrows = leads to activation, blue arrows = leads to inhibition, yellow arrows = findings inconsistent with state of downstream molecule, grey arrows = effect not predicted. Image generated by IPA software.N=5.

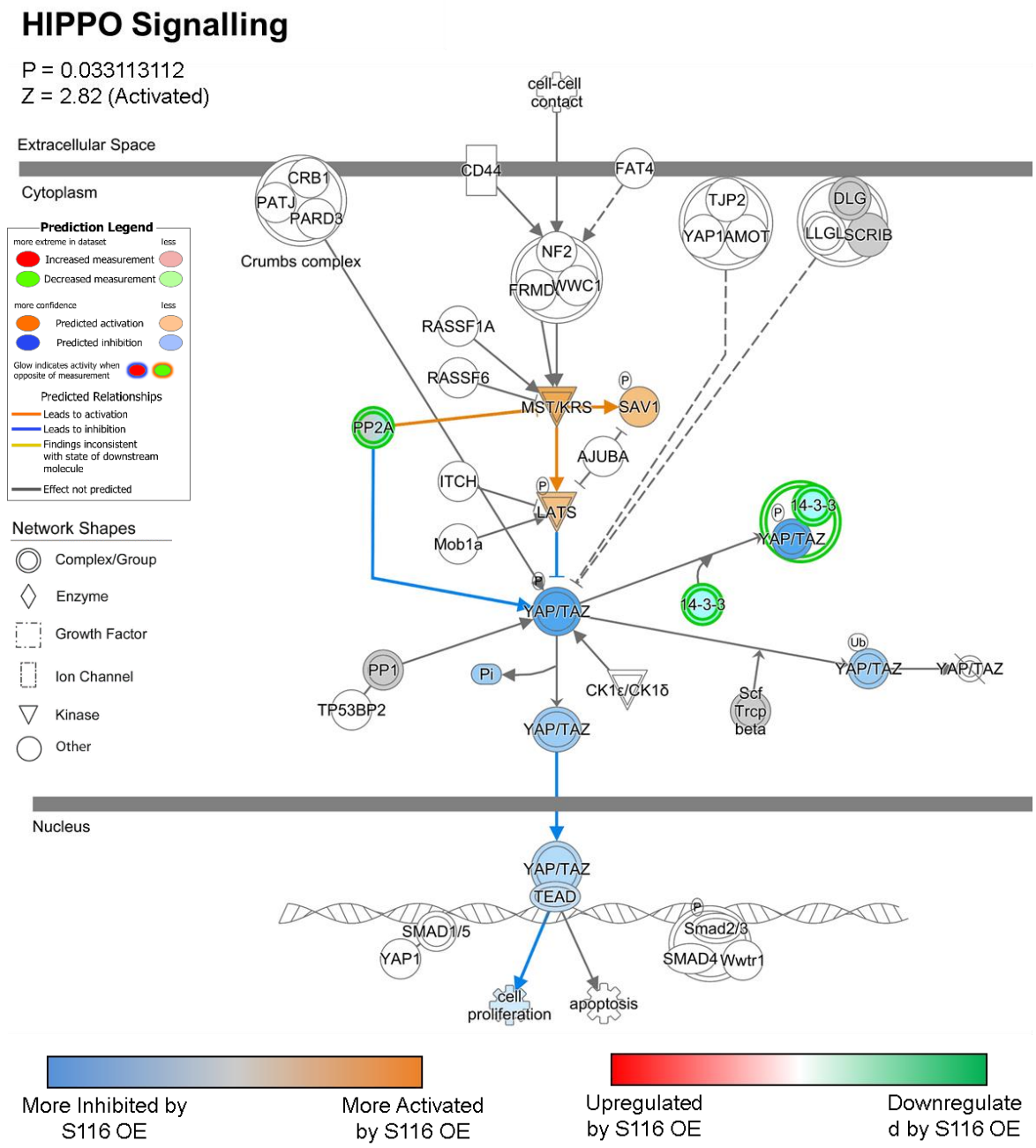

Figure 6-16. IPA expanded pathway of HIPPO Signalling.
Genes that are upregulated or downregulated by S116 overexpression (S116 OE) are colour coded red/green. Molecules that are predicted to be activated or inhibited are colour coded blue/orange. DEGs present in the dataset are highlighted by double green line. Orange arrows = leads to activation, blue arrows = leads to inhibition, yellow arrows = findings inconsistent with state of downstream molecule, grey arrows = effect not predicted. Image generated by IPA software=5.

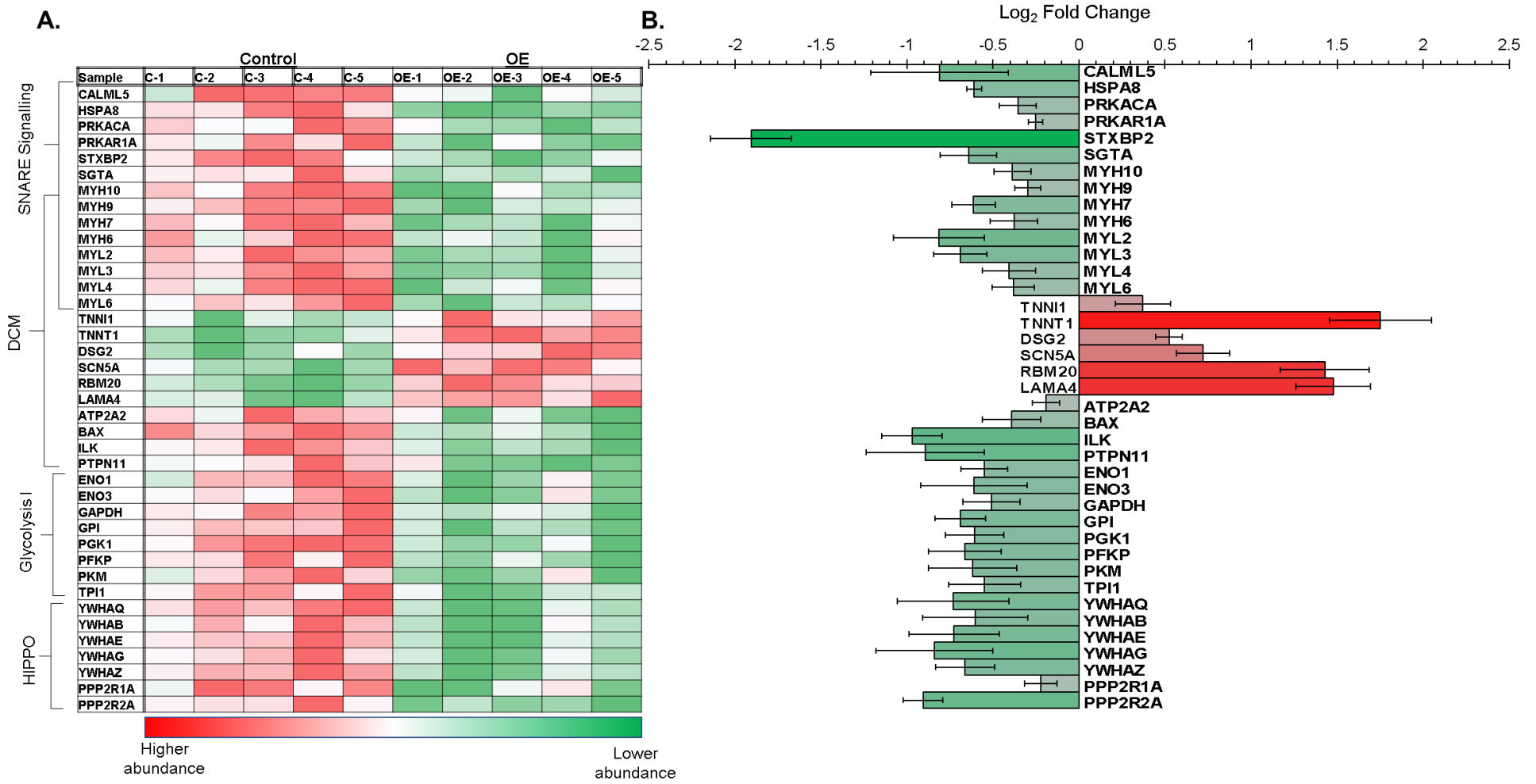

Figure 6-17. Expression changes of proteins within the top pathways predicted to be activated or inhibited by SNORD116 overexpression.
A. Heatmap based on the normalised counts of proteins expressed in the control vs MBII85 (OE) transfected cells.
B. Average Log_2 fold changes of proteins in the OE samples relative to the control samples corresponding with the list of proteins shown in (A), Error bars represent standard deviation. N=5.

There were 14 differentially expressed proteins identified within the SNARE signalling pathway. Eight of these proteins were also identified as part of the DCM signalling pathway, which contained a total of 18 differentially expressed proteins. The glycolysis I and HIPPO signalling pathways each contained 8 differentially expressed proteins. All of the proteins identified as part of the SNARE signalling, glycolysis I and HIPPO signalling pathways were downregulated as a result of SNORD116 overexpression. The eight proteins identified in both the SNARE signalling and DCM pathways (MYH10, MYH9, *MYH7*, *MYH6*, *MYL2*, *MYL3*, MYL4 and MYL6) were downregulated in response to SNORD116 overexpression. *ATP2A2*, *BAX*, ILK and PTPN11 were also DCM-related proteins that were downregulated by SNORD116 overexpression. However, *TNNI1*, TNNT1, DSG2, SCN5A, RBM20 and LAMA4 were proteins identified in the DCM pathway that showed increased abundance resulting from SNORD116 overexpression.

To understand how gene expression changes on a transcriptomic level and protein changes on a proteomic level compare in response to SNORD116 overexpression, molecules in the glycolysis I and dilated cardiomyopathy pathways were mapped out and colour coded according to their transcriptomic and proteomic fold changes. The results are presented in Figure 6-18 and Figure 6-19. In the glycolysis I pathway, all the proteins that were differentially expressed were decreased in abundance in response to SNORD116 overexpression. However, the corresponding mRNA expression showed the opposite trend i.e., they were either unchanged or upregulated.

When investigating the dilated cardiomyopathy pathway, the protein and mRNA levels of each molecule generally followed the same trend in response to SNORD116 overexpression. Cardiac ion channels such as SCN5A, *ATP2A2* and CACNB1 were either unchanged or decreased in abundance at both the mRNA and protein level. The exception to this was

RYR2 which showed increased abundance at a protein level but was downregulated at an mRNA level. Genes associated with apoptosis such as GAB1, PTPN11 and *BAX* were unchanged or downregulated at both an mRNA and protein level. Interestingly, many sarcomeric genes were downregulated at both an mRNA and protein level in response to SNORD116 overexpression, including *MYH6*, *MYH7*, *MYL2* and MYL6. MYH10 and MYL6 were also decreased at a protein level but their mRNA was upregulated. Contrastingly, the *TNNI1* and TNNT1 proteins were increased in abundance in response to SNORD116 overexpression but their gene expression was downregulated. RBM20, a protein that controls the splicing of titin, was upregulated at a protein level in response to SNORD116 overexpression expression but the mRNA expression was unchanged. Molecules important to the connection of the cell to its environment and neighbouring cells such as LAMA4 and the desmosomal proteins DSC2 and DSG2 were unchanged or upregulated in response to SNORD116 overexpression at both a mRNA and protein level.

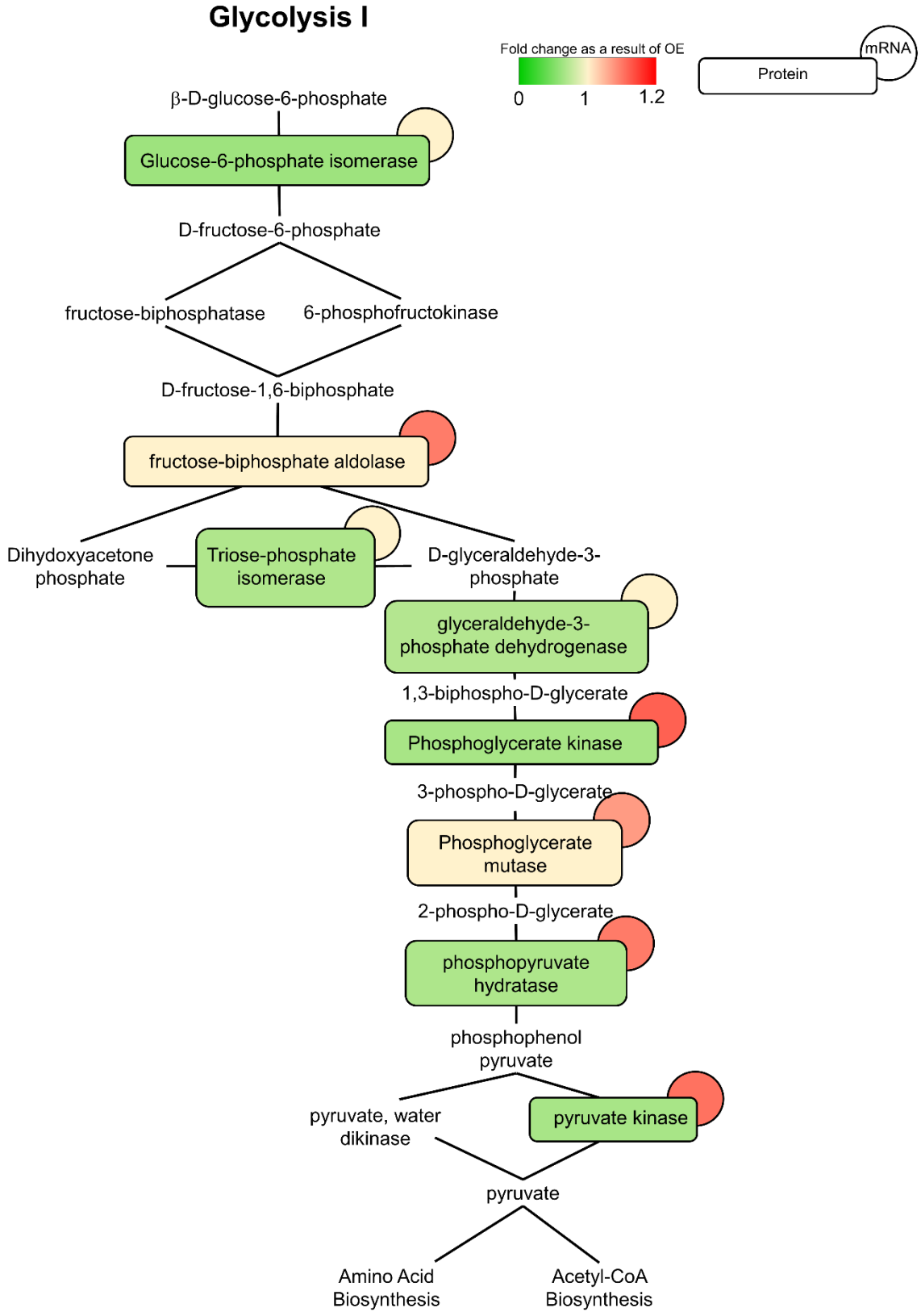

Figure 6-18. Comparative analysis of transcriptomic and proteomic abundance of molecules in the Glycolysis I pathway in response to SNORD116 overexpression. Pathway design based on IPA Glycolysis I pathway map. Molecules present in the proteomic dataset (N=5) are represented by rectangles; molecules present in the RNAseq dataset (N=5) are represented by circles. Molecules that increase in abundance are shaded red; molecules that decrease in abundance are shaded green. Pathway map adapted from IPA software.

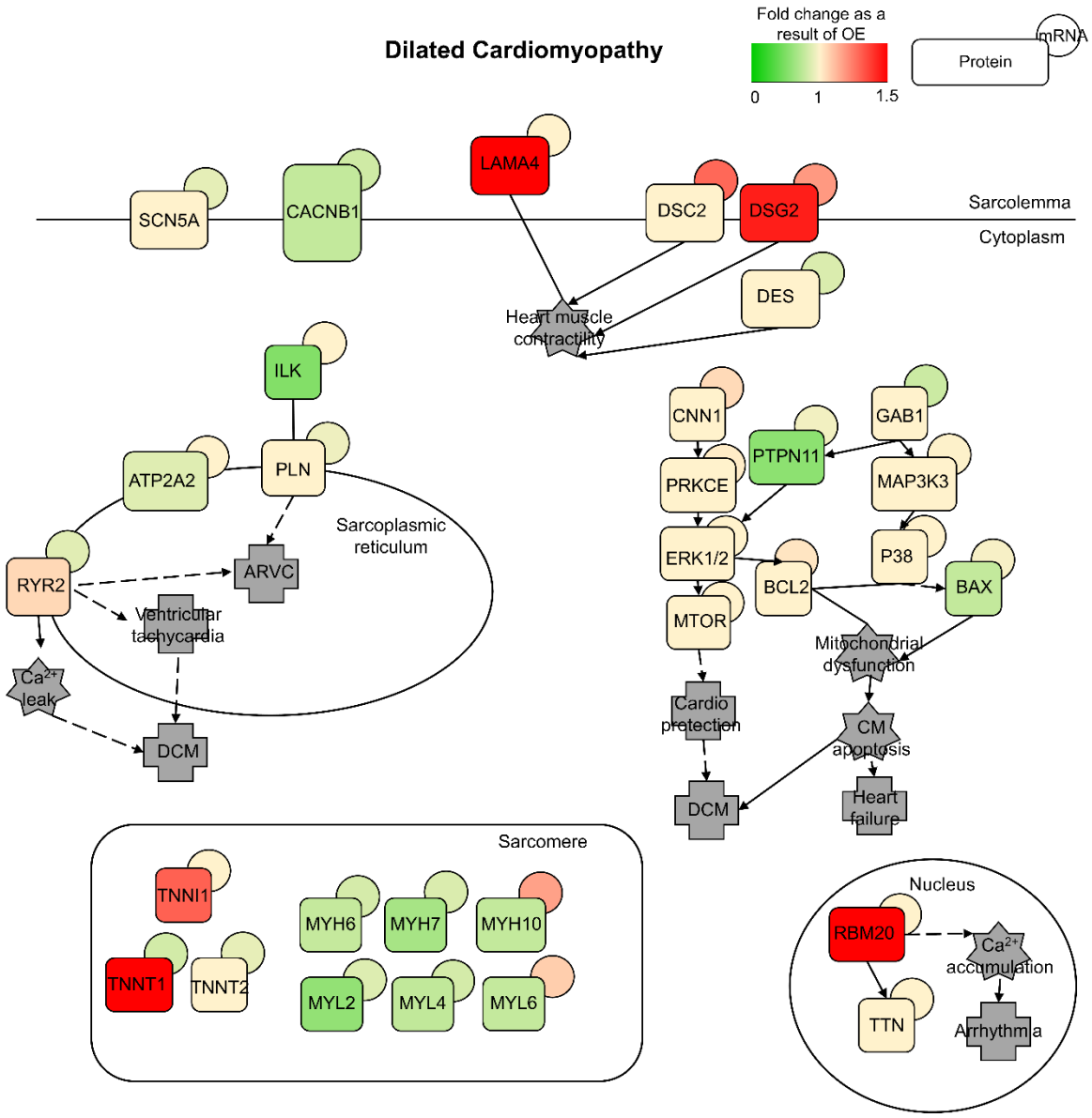

Figure 6-19. Comparative analysis of transcriptomic and proteomic abundance of molecules in the Dilated Cardiomyopathy pathway in response to SNORD116 overexpression.

Pathway design based on IPA Dilated Cardiomyopathy signalling pathway map. Molecules present in the proteomic dataset (N=5) are represented by rectangles; molecules present in the RNAseq dataset (N=5) are represented by circles. Molecules that increase in abundance are shaded red; molecules that decrease in abundance are shaded green. Biological processes are represented by grey stars, disease conditions are represented by grey plus signs. Pathway map adapted from IPA software.

In summary, SNORD116 was overexpressed in iPSC-CMs by means of lipofection of the MBII85 plasmid. On a transcriptomic level this caused dysregulation of multiple cardiomyopathy-related gene pathways including ARVC. In addition, cardiomyopathy pathways were also dysregulated on a proteomic level. Proteomic analysis also revealed a decrease in glycolytic enzymes as a result of SNORD116 overexpression. However, the greatest decrease caused by SNORD116 overexpression was the downregulation of PKP1 protein, which was 62-fold lower as a result of SNORD116 overexpression. This identified PKP1 as a potential target of SNORD116. Interestingly, PKP1 mRNA levels were not affected by SNORD116 overexpression, which may suggest a mechanism of regulation on the part of SNORD116 that affects PKP1 protein level but not mRNA level. To explore the outcome of these gene and protein expression changes on cardiomyocyte function, contraction and metabolic assessment was performed using the MBII85 plasmid.

6.2.2.2 Functional effects of SNORD116 overexpression

Following these omics results, the functional effect of SNORD116 overexpression in cardiomyocytes was then investigated. To analyse the effect of SNORD116 overexpression on contraction, iPSC-CMs were transfected with 600ng of either a control plasmid or the MBII85 plasmid by means of lipofection. 72 hours after transfection, the cells were recorded in a temperature-controlled microscope chamber at 37^{O}C for at least 20 seconds. Three different areas of each well were recorded so that each biological replicate had three technical replicates. The resulting recordings were analysed using MUSCLEMOTION as described in Figure 5-2. The results are presented in Figure 6-20. Overall, due to spread between replicates there was no statistically significant difference in the contraction amplitude or frequency of the iPSC-CMs transfected with either the control plasmid or the MBII85 plasmid. However, the contraction amplitude appeared to increase from 157±60 to 215±60 as a result of SNORD116 overexpression. Contraction frequency appeared to decrease from 0.5±0.1 Hz to 0.4±0.1 Hz. Overall, the overexpression of SNORD116 may have affected the contraction of iPSC-CMs, but further replicates and/or a higher transfection efficiency are needed to confirm this.

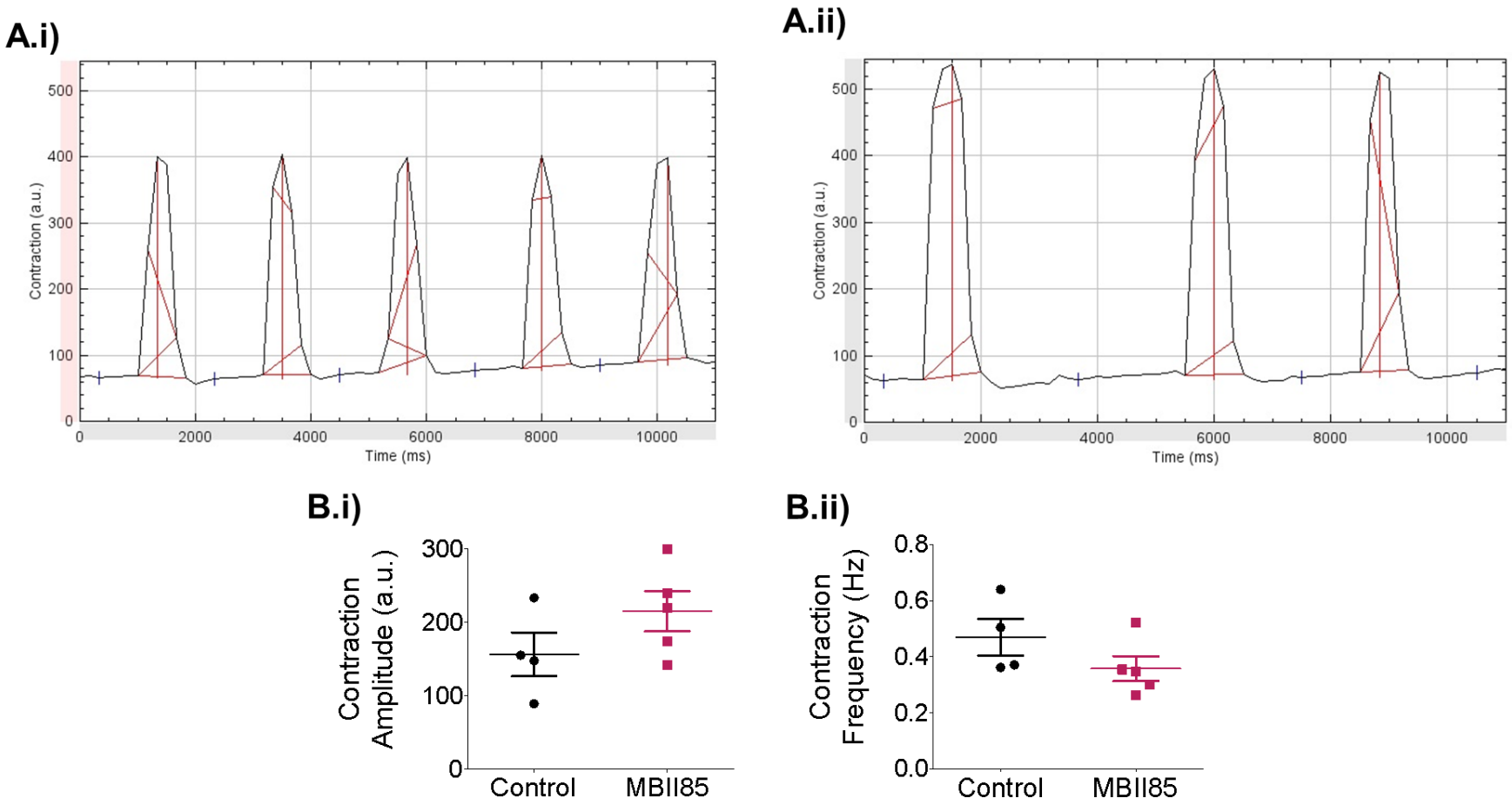

Figure 6-20. The effect of SNORD116 overexpression on the contraction of iPSC-CMs.
A. Representative contraction analysis traces of iPSC-CMs transfected with i) a transfection control plasmid and ii) the MBII85 plasmid. Generated using ImageJ and the MUSCLEMOTION plugin.
B. The (i) contraction amplitude and (ii) contraction frequency of iPSC-CMs transfected with either a transfection control plasmid or the MBII85 plasmid. Statistics calculated by unpaired t-test. (i-ii) Control N=4, MBII85 N=5

IPSC-CMs were seeded into a 96-well Agilent Seahorse analysis plate at a density of 30,000 cells per well. Each well was transfected with 100ng of either the MBII85 plasmid or a GFP control plasmid. The cells were then cultured in either normoxia (37^{o}C, 5% CO_2, 20% O_2) or hypoxia (37^{O}C, 5% CO_2, 2% O_2). 72 hours post-transfection, metabolism was analysed using the Agilent Seahorse XF96 Cell Mito Stress Test which measured the OCR and ECAR. For each sample, the ratio of OCR over ECAR was calculated by dividing the OCR of each replicate at each time point by the average ECAR of that timepoint. The results are shown in Figure 6-21 and Figure 6-22.

Overall, under normoxic conditions there was no statistically significant difference in the OCR of iPSC-CMs transfected with the control plasmid or the MBII85 plasmid. However, the MBII85 plasmid did cause a reduction in the ECAR of transfected iPSC-CMs. During basal respiration, SNORD116 overexpression caused the ECAR to be reduced from 22±12 to 15±7 mpH/min/10k cells, although this was not statistically significant. During ATP-inhibited and maximal respiration, SNORD116 overexpression caused the ECAR to be reduced from 62±13 to 52±8 mpH/min/10k cells and 64±10 to 55±8 mpH/min/10k cells respectively. Correspondingly, the ratio of OCR over ECAR was higher in the MBII85 transfected iPSC-CMs compared to the control, reflecting the decreased ECAR in the overexpression samples. During basal respiration, OCR/ECAR was increased from 5.4±0.3 in the control to 7.6±1 in response to the MBII85 plasmid. During ATP-inhibited respiration, OCR/ECAR increased from 0.7±0.05 to 0.8±0.1, and during maximal respiration the OCR/ECAR increased from 4.7±0.7 to 5.7±1.1. mpH/min/10k cells.

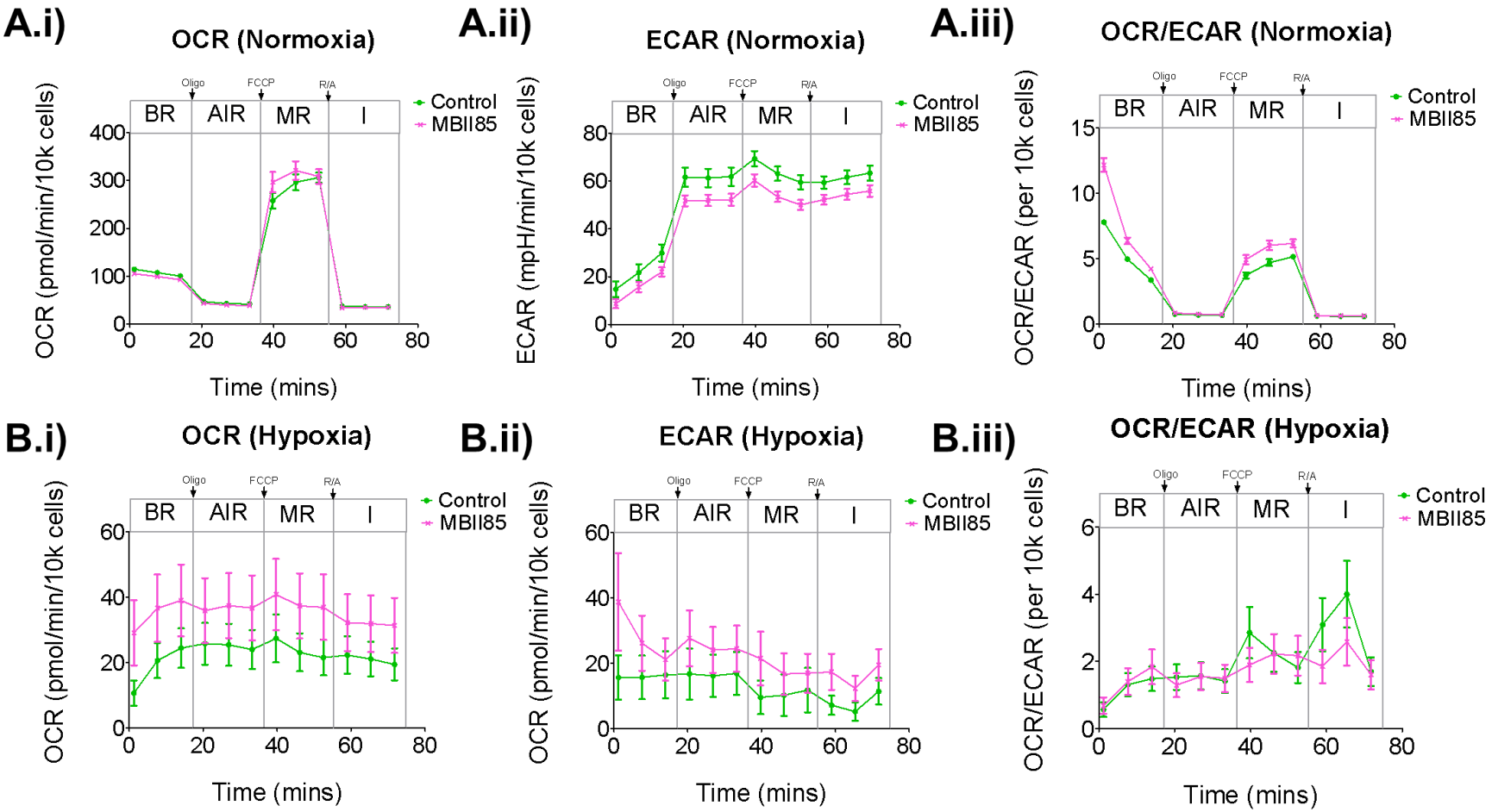

Figure 6-21. The effect of SNORD116 overexpression and hypoxia on iPSC-CM OCR and ECAR over time.
The effect of the control plasmid and the MBII85 plasmid on the i) OCR, ii) ECAR and iii) OCR/ECAR of iPSC-CMs cultured in (A) normoxia or (B) hypoxia. OCR = oxygen consumption rate, ECAR = extracellular acidification rate, Oligo = oligomycin (2uM), FCCP = Carbonyl cyanide-4 (trifluoromethoxy) Phenylhydrazone (1uM), R/A = Rotenone/Antimycin A (0.5uM). BR = basal respiration, AIR = ATP-inhibited respiration, MR = maximal respiration, I = inactivated. N=12.

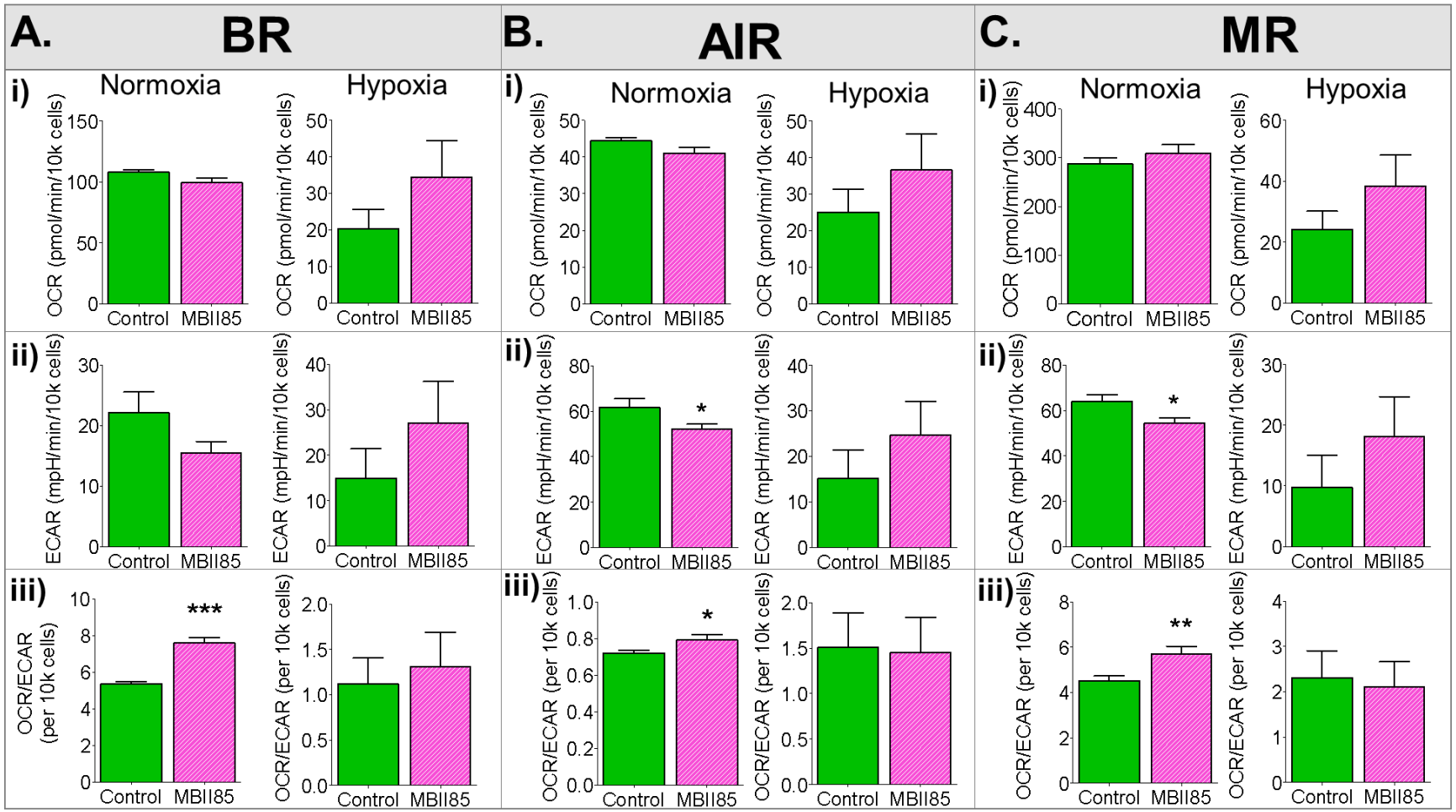

Figure 6-22. The effect of SNORD116 overexpression and hypoxia on OCR and ECAR during different types of respiration.
The i) OCR, ii) ECAR and iii)OCR/ECAR of iPSC-CMs transfected with the control plasmid and the MBII85 plasmid cultured in normoxic and hypoxic conditions during (A) basal, (B) ATP-inhibited and (C) maximal respiration. BR = basal respiration, AIR = ATP-inhibited respiration, MR = maximal respiration. Statistics calculated by unpaired t-test. * = P≤0.05, ** = P≤0.01, *** = P≤0.001. N=12.

Under hypoxic conditions, the MBII85 plasmid appears to have had the opposite effect as seen in normoxia, in that it seems to have caused an increase in metabolic output compared to the control. In the hypoxic cells during basal respiration, OCR is increased from 20±18 to 34±34 pmol/min/10k cells in response to SNORD116 overexpression. In addition, ECAR increases from 15±20 to 27±30 mpH/min/10k cells compared to the transfection control. Variation between replicates prevented this from being statistically significant. Similarly, during ATP-inhibited respiration of hypoxic cells, OCR was 25±22 pmol/min/10k cells in the transfection control and 37±34 pmol/min/10k cells in the MBII85 transfected cells. During maximal respiration, OCR was 24±22 pmol/min/10k cells in the transfection control and 38±35 pmol/min/10k cells in the MBII85 transfected cells.

ECAR during ATP-inhibited respiration of hypoxic cells was 24±22 mpH/min/10k cells in the transfection control and 38±35 mpH/min/10k cells in the MBII85 transfected sample. Curiously, when transitioning from ATP-inhibited to maximal respiration, the ECAR appeared to decrease during maximal respiration for both transfection samples, at 10±15 mpH/min/10k cells in the transfection control and 18±22 mpH/min/10k cells in the MBII85 transfected sample. However, it still appeared higher in response to SNORD116 overexpression compared to the transfection control. Overall, overexpression of SNORD116 under normoxic conditions appears to cause a decrease in ECAR without affecting OCR of iPSC-CMs. However, under hypoxic conditions, SNORD116 expression does not appear to cause a decrease in ECAR, and may in fact cause an increase in both OCR and ECAR compared to the transfection control.

In summary, one of the most dysregulated cardiomyopathy-related gene pathways affected by SNORD116 overexpression was the ARVC pathway. Therefore, the effect of SNORD116 overexpression on contraction was analysed. Although contraction was not significantly affected by SNORD116 overexpression, there was a trend of decreased contraction frequency and increased contraction amplitude resulting from SNORD116 overexpression. In terms of metabolism, proteomics analysis also revealed a decrease in multiple glucose-metabolising enzymes. Correspondingly, a decrease in ECAR under normoxic conditions was observed using seahorse analysis. This suggests that SNORD116 overexpression caused a reduction in glucose metabolism in iPSC-CMs.

Among all the changes in protein expression as a result of SNORD116 overexpression, PKP1 was the most downregulated, with a 62-fold lower abundance compared to the transfection control. This exciting novel finding presented PKP1 as a potential target of SNORD116. Further investigation was performed in an effort to validate PKP1 as a direct target of SNORD116 and to explore the significance of this potential interaction in cardiac cells.

6.2.3 Investigating the potential of PKP1 as a target of SNORD116

To corroborate the proteomics finding that PKP1 protein was downregulated by SNORD116 overexpression, iPSC-CMs were transfected with 600ng per well of either the MBII85 plasmid or a control plasmid. After 72-hours post-transfection, the cells were lysed and proteins separated using SDS-PAGE. The expression of PKP1 was analysed by western blotting and the results are presented in Figure 6-23. Both samples produced a band at ~70 kDa. Although the band produced by MBII85-transfected cells appears more intense than the control, when calculated relative to total protein present, the intensity of PKP1 is 0.12 a.u. in the MBII85 sample and 0.24 a.u. in the control sample. This supports the finding that SNORD116 overexpression causes decreased abundance of PKP1 protein in iPSC-CMs.

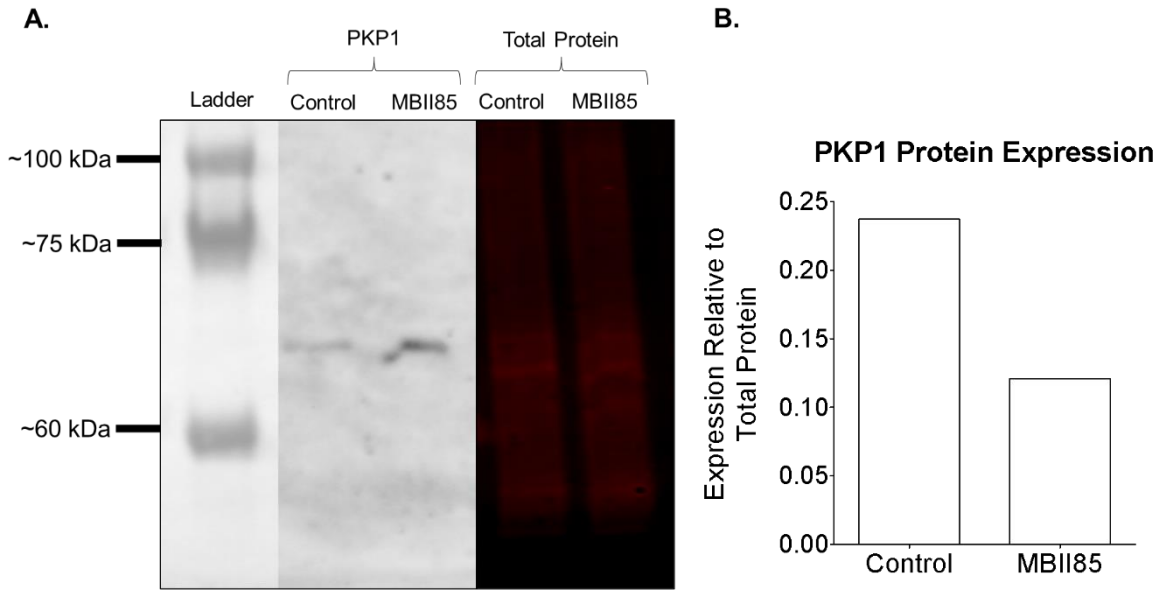

Figure 6-23. Expression of PKP1 in response to SNORD116 overexpression by western blot analysis.
A. Western blot showing PKP1 expression and total protein expression of iPSC-CM protein 72 hours post-transfection with either the MBII85 plasmid or a control plasmid. Proteins extracted and separated using SDS-PAGE. Total protein stained using REVERT™ 700 Total Protein Stain. PKP1 stained using Invitrogen PKP1 Monoclonal Antibody (10B2).
B. Protein expression calculated by band intensity relative to total protein intensity. N=1

A cartilage-specific knockout of SNORD116 in mice was generated by collaborators Mandy Peffers *et al.* (55,408) at the of the University of Liverpool Institute of Life Courses and Medical Sciences, who kindly shared the list of differentially expressed proteins between the knockout and wild-type cartilage. In total, there were 624 differentially expressed proteins with a P<0.05 and a maximum fold change greater than 1.5. In addition, the target prediction software SnoTARGET generated a list of 571 potential targets of SNORD116 based on sequence analysis (32). Both of these datasets were compared to the list of differentially expressed proteins as a result of SNORD116 overexpression in cardiomyocytes (thresholded at P<0.05 and -1.5> fold change > 1.5). The resulting overlap between datasets is shown in Figure 6-24..

A.

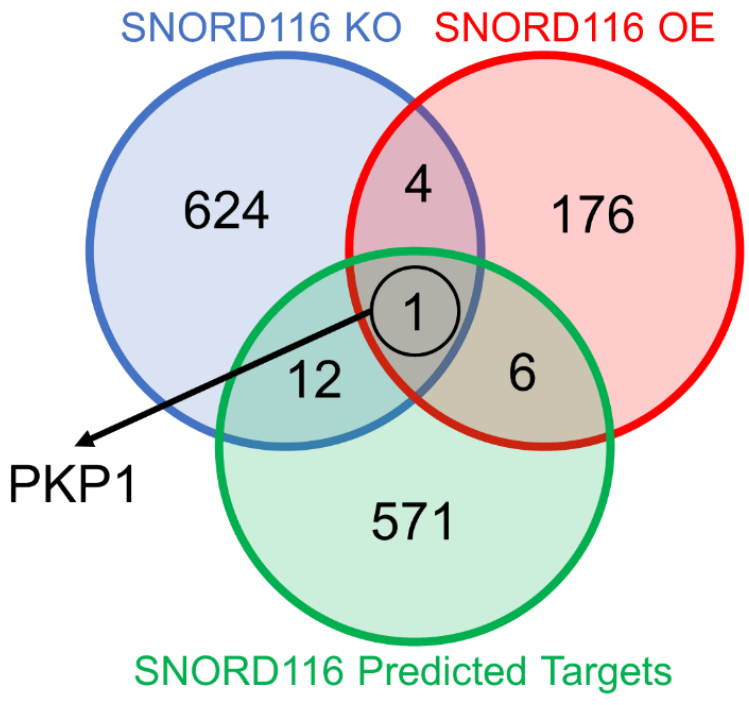

B.

Max fold change compared to control	
Cartilage KO	Cardiomyocyte OE
+2	-62

Figure 6-24. Comparing multiple datasets to identify universal SNORD116 targets.
A. Venn diagram of proteins from three datasets showing the number of proteins in each dataset along with the number of proteins overlapping between datasets.
B. The maximum fold change of PKP1 protein expression as a result of cartilage specific SNORD116 knockout and SNORD116 overexpression in cardiomyocytes.

In total, there was only one common target present in all three datasets. PKP1 was predicted to be a target of SNORD116 using bioinformatics, and it was greatly reduced by SNORD116 overexpression. In addition, it was also found to be elevated upon SNORD116 knockout.

In an effort to understand the mechanism behind the targeting of PKP1, the sequences of both SNORD116 and PKP1 were compared for homology. Figure 6-25 shows the cDNA sequence maps of SNORD116-1 and PKP1. Within both sequences exists a homologous region of 13 base pairs (AGCTGAACAAAATG) that is almost identical, with the exception of a G insertion in the PKP1 sequence. A proposed binding interaction between these sequences is shown in Figure 6-26. To summarise, when the two molecules come into proximity, the protruding stem loop of SNORD116 opens to allow hydrogen bonds to form between complementary base pairs within the PKP1 mRNA. This interaction occurs between the D’ and C’ boxes of the SNORD116 sequence and leaves a single unbound G base protruding within the PKP1 mRNA. This base is free to bind to a free C base on the other side of the loop structure within SNORD116, leading to the formation of a total of 14 hydrogen bonds between the two molecules. To ensure that this potential binding interaction was not specific to the human SNORD116-1 paralogue, the mouse SNORD116-1 paralogue from within the MBII85 overexpression plasmid was substituted in and also forms the same complementary base pairing.

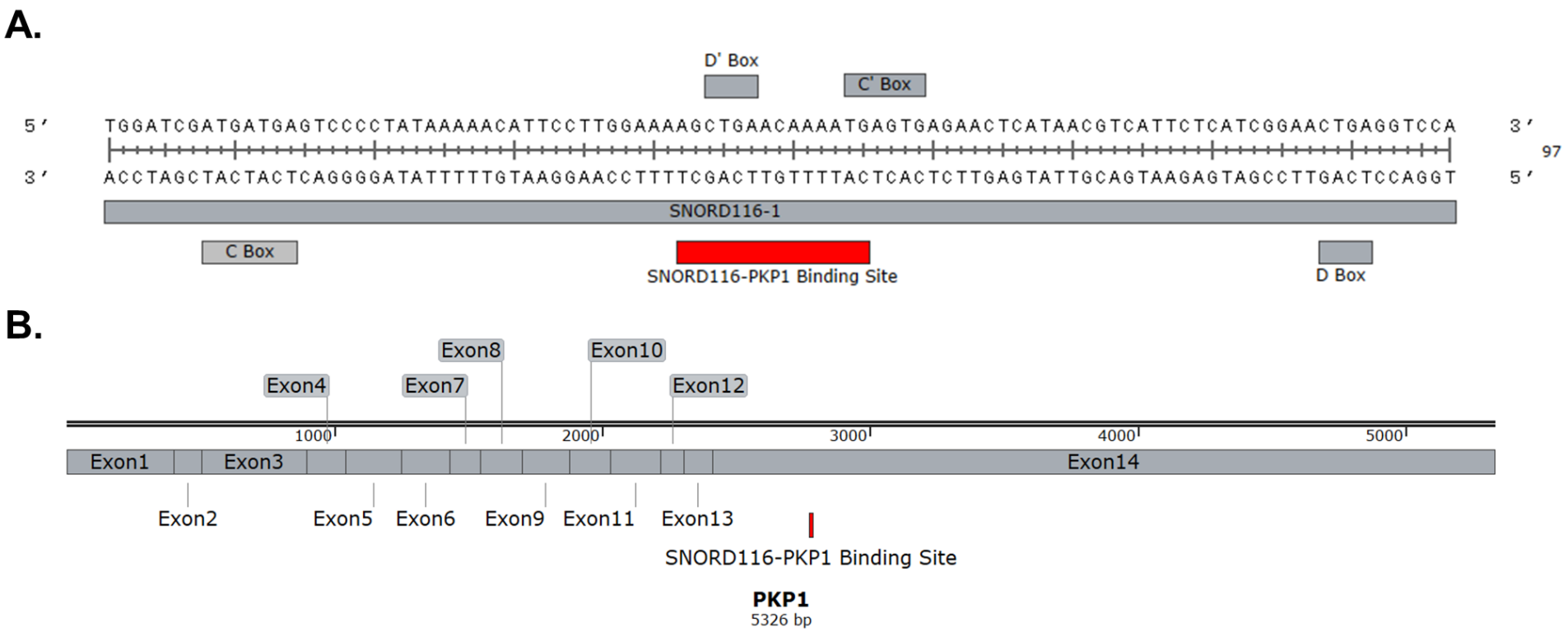

Figure 6-25. Identifying a potential binding site between SNORD116 and PKP1.
A. The cDNA sequence of human SNORD116-1 with the C and D boxes highlighted and the SNORD116-PKP1 binding site coloured in red.
B. The cDNA sequence of PKP1 with the exons labelled and the SNORD116-PKP1 binding site coloured in red

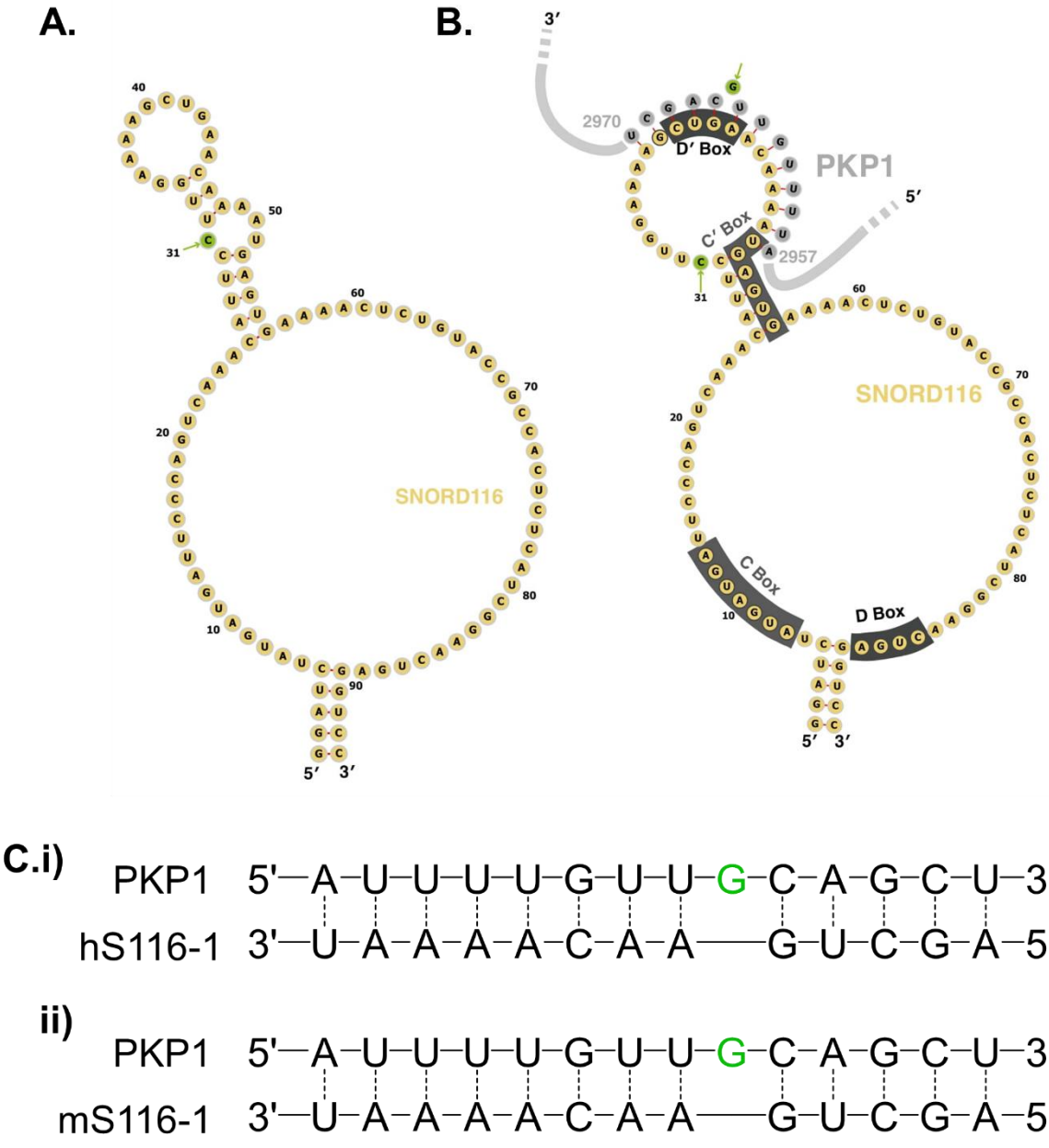

Figure 6-26. Proposed mechanism of SNORD116 binding to PKP1.
A. Predicted secondary structure of SNORD116-1 snoRNA
B. SNORD116 binding to PKP1 mRNA. Predicted base-pair bonds are shown in red. Base pairs predicted to bind across the structure are highlighted in green.
Figure rendered by ViennaRNA and used with permission from Jon Price, University of Cambridge.
C. Schematic of PKP1 binding region between PKP1 mRNA and (i) human SNORD116-1 mRNA and (ii) mouse SNORD116-1 mRNA

Once a proposed mechanism for the interaction between SNORD116 and PKP1 was conceived, the role and expression of PKP1 was further investigated. Expression data from the NCBI (409) and Human Protein Atlas (410) was used to plot the mRNA and protein expression of plakophilin throughout the various organs of the body. The results are shown in Figure 6-27. To provide additional context, the expression of the other three isoforms of plakophilin (*PKP2*, *PKP3* and *PKP4*) are also shown. The level of RNA expression was reported as RPKM (reads per kilobase million) based on results from publicly available RNAseq data. The Protein Atlas scored protein levels as high (3), medium (2), low (1) or undetected (0). The level of protein expression was quantified by immunocytochemistry/immunofluorescence (ICC-IF), and the intensity of the staining determined the score. The results are publicly available on the human protein atlas website (https://www.proteinatlas.org/).

The highest expression of PKP1 mRNA was reported to be in skin tissue with an RPKM of 355. PKP1 was also reported to be expressed with an RPKM of 151 in esophagus tissue. Lower expression levels was reported in fat tissue, placenta, prostate and salivary gland tissue at RPKMs of 8, 4, 16 and 2 respectively. Contrastingly, PKP1 protein expression was reported to be highest in cervical tissue. The RNA expression of PKP1 in cervical tissue was not tested and is therefore unknown. Esophagus, oral mucosa, skin and vaginal tissue showed medium levels of PKP1 protein expression. Low levels of PKP1 protein were also found in breast tissue, tonsil tissue and the cerebral cortex. Overall, the expression of PKP1 appeared restricted to epithelial tissue types. Contrastingly to this, the other isoforms show a more diffuse expression pattern and are found to be expressed in most tissues to some level. Interestingly, *PKP2* appears to be the dominant form of plakophilin expressed in the heart at both an mRNA and protein level.

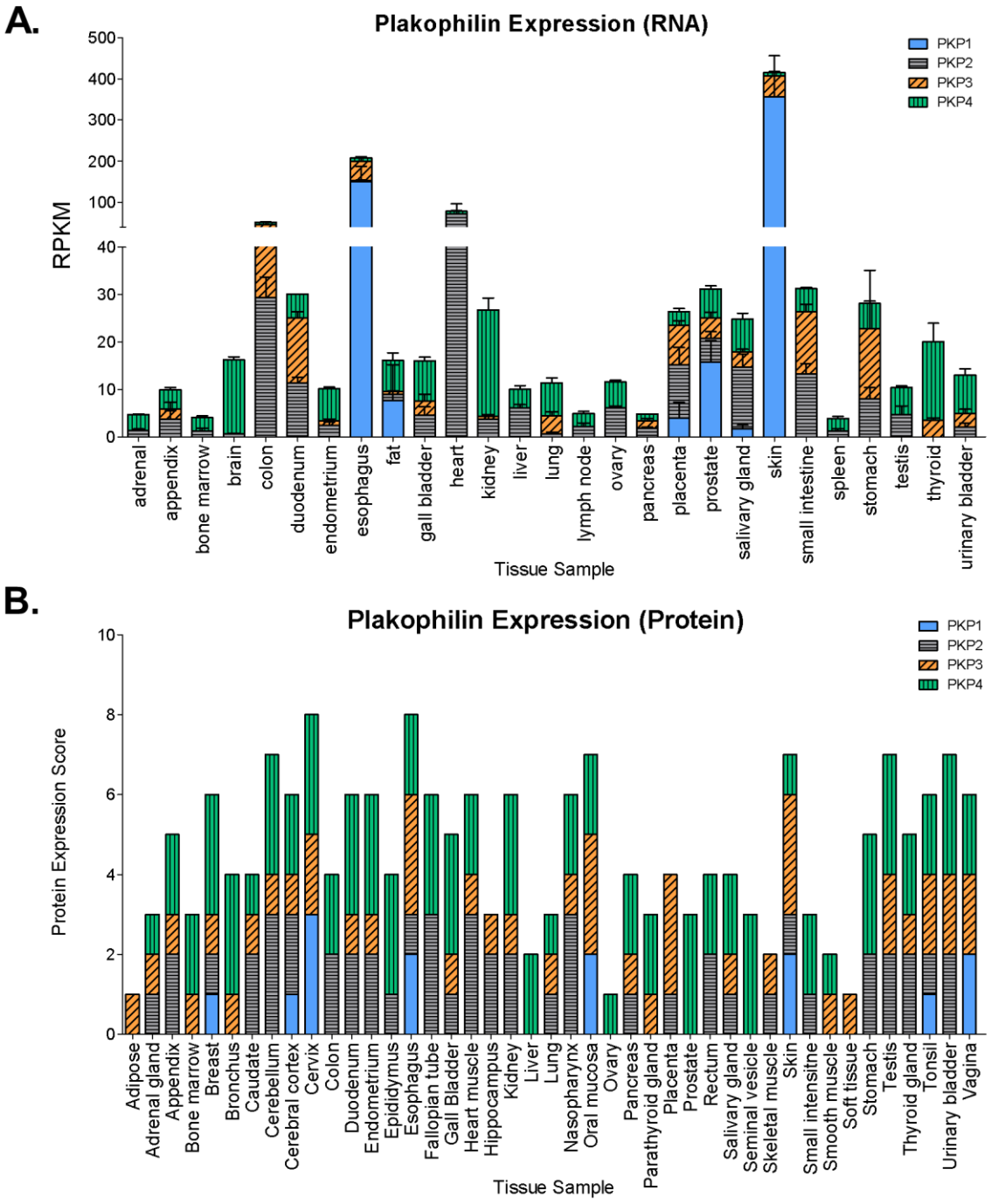

Figure 6-27. Expression of plakophilin in the human body.
A. RNA expression of the plakophilin isoforms based on public expression data from the NCBI. Data gathered from the HPA RNA-seq of normal tissues project PRJEB4337, PMID 24309898. Available at https://www-ncbi-nlm-nih-gov.uea.idm.oclc.org/gene/5317
B. Protein expression of the plakophilin isoforms based on public expression data from the Human Protein Atlas available at https://www.proteinatlas.org/ENSG00000081277-PKP1/tissue

In addition to investigating plakophilin expression across different tissue types *in vivo*, it was important to explore how expression changed across different cell types that are cultured *in vitro*. Figure 6-28 shows the expression of SNORD116 and plakophilin in primary CFs, iPSC-CMs, iPSCs, chondrocytes and neurones relative to the expression in primary skin fibroblasts. The expression of SNORD116 is not significantly different between primary skin fibroblasts, primary cardiac fibroblasts, iPSC-CMs and chondrocytes. The exception to this is SNORD116-1, which is 4-fold higher in primary cardiac fibroblasts and iPSC-CMs than in skin fibroblasts. However, in iPSCs, SNORD116 levels are elevated relative to skin fibroblast expression, with the SNORD116-1 paralogue showing the greatest fold change at 22-fold that of skin fibroblasts. Across all the cell types tested, neurones showed the greatest level of SNORD116 expression at 77-fold, 43-fold and 49-fold that of skin fibroblast level for SNORD116-1, SNORD116-23 and SNORD116-25. These results are consistent with the finding that group I paralogues are more highly expressed than group II or group III, and that brain tissue shows the highest level of SNORD116 expression (31,45,411).

The expression of PKP1 was very low in most cell types tested, resulting in large variance between replicates. IPSCs showed the greatest level of PKP1 expression at 3-fold that of skin fibroblasts. PKP1 was 2-fold higher in neurones relative to skin fibroblasts, though the other cell types tested did not show a difference in expression compared to skin fibroblasts. *PKP2* was downregulated in chondrocytes compared to skin fibroblasts, at 0.1-fold. However, it was elevated in all other cell types tested and showed the highest degree of expression in iPSC-CMs at 1,600-fold that of skin fibroblasts. This reinforces the finding that *PKP2* is the dominant plakophilin isoform expressed in heart tissue. *PKP3* is expressed highly in chondrocytes and cardiac fibroblasts, at 35-fold and 23-fold that of skin fibroblasts, although its expression is greatly downregulated in neurones to 0.3-fold that of skin fibroblasts. *PKP4* expression is generally similar across all cell types tested, though is elevated by 2-fold in iPSCs.

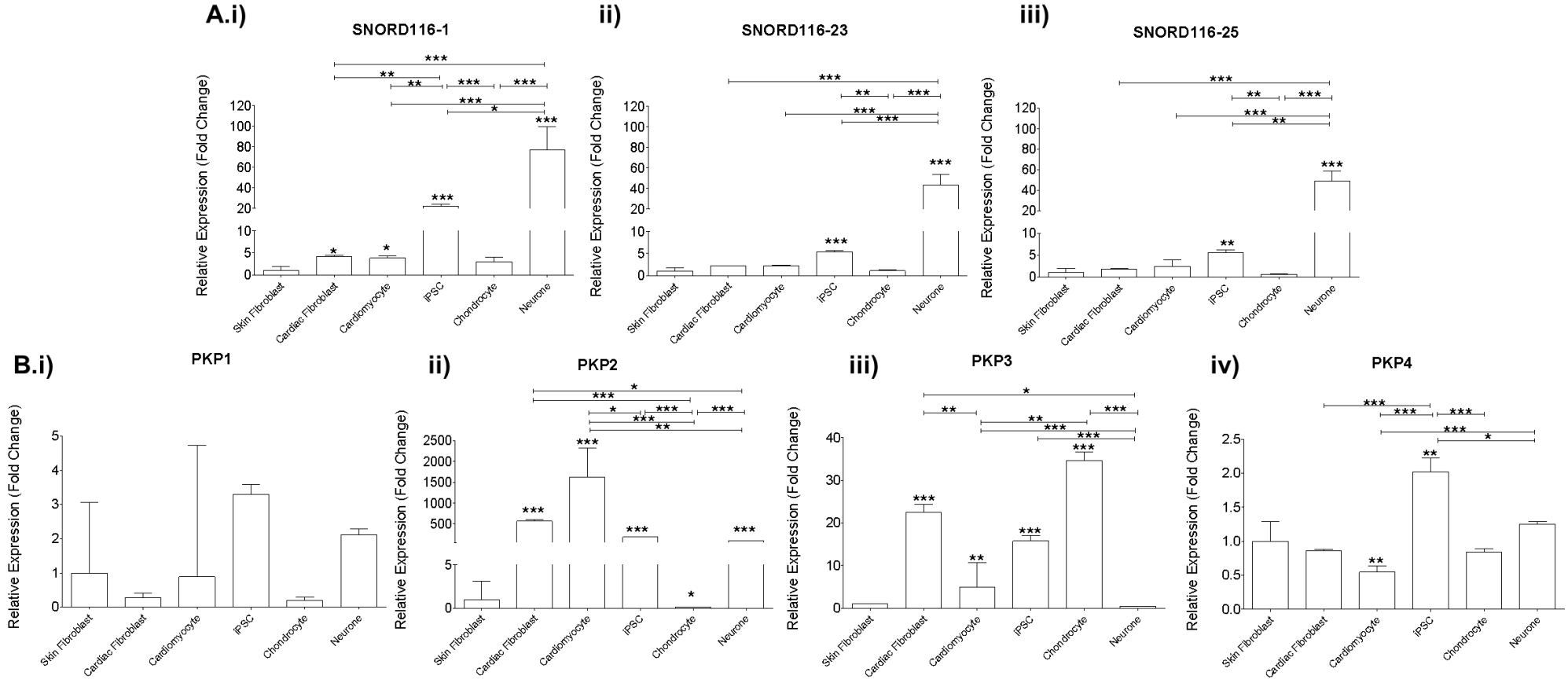

Figure 6-28. Expression of SNORD116 and plakophilin in various cell types.
A. The expression of (i) SNORD16-1, (ii) SNORD116-23 and (iii) SNORD116-25 across various cell types.
B. The expression of (i-iv) PKP1, PKP2, PKP3 and PKP4 in various cell types.
Expression calculated using the ddCt method relative to the expression level in skin fibroblasts, normalised to GAPDH. N=3. Statistics calculated by one-way ANOVA, * = P<0.05, ** = P<0.01, *** = P<0.001.

To gain a better understanding of the how a potential SNORD116-PKP1 axis may influence cardiac function, the expression of PKP1 during cardiac development was investigated. Protein was isolated and separated using SDS-PAGE from iPSC-CMs during days 0, 2, 4 and 8 of the differentiation. PKP1 protein was quantified as intensity relative to total protein as shown in Figure 6-29. On each consecutive day tested, PKP1 expression increased from an intensity relative to total protein of 0.14, 0.22, 0.75 and 0.97 a.u. These results indicate that total PKP1 expression increases during early cardiomyocyte development.

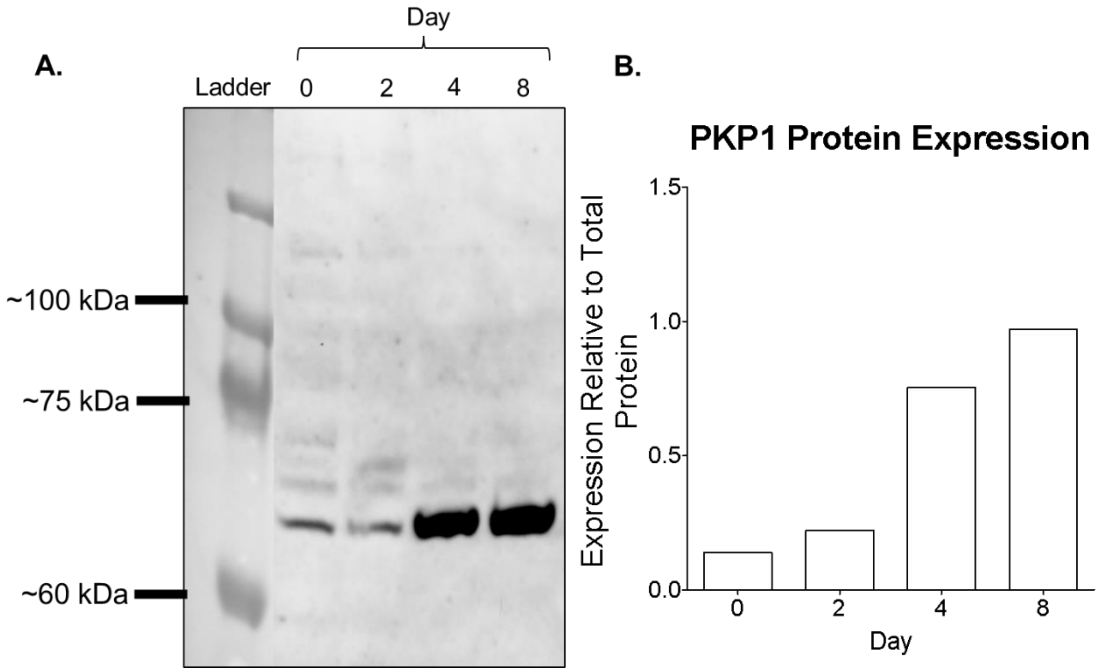

Figure 6-29. PKP1 expression during cardiac development by western blot analysis.
A. Western blot showing PKP1 expression on days 0, 2, 4 and 8 of the iPSC-CM differentiation. Proteins extracted and separated using SDS-PAGE. Total protein stained using REVERT^{TM} 700 Total Protein Stain. PKP1 stained using Invitrogen PKP1 Monoclonal Antibody (10B2).
B. Protein expression calculated by band intensity relative to total protein intensity. N=1

Western blotting allows the quantification of total protein, however it does not describe the localisation of the protein. Therefore, PKP1 expression was analysed by immunocytochemistry. To provide additional context to this data, the expression of PKP2 – the dominant cardiac isoform of plakophilin – was also analysed. Cells were fixed on days 0, 2 and 4 of iPSC-CM differentiation and stained for either PKP1 or PKP2. The resulting images are shown in Figure 6-30 and Figure 6-31. These images were also analysed using CellProfiler to gauge the level of nuclearization of PKP1 and PKP2 during differentiation. The intensity of expression within the nucleus was compared to the perinuclear intensity, which was determined by a region of 10 pixels surrounding the nucleus. The ratio of mean nuclear to perinuclear intensity was calculated. In addition, background intensity was used as a threshold to determine the percentage of cells that showed expression in the nucleus that was greater than background intensity. The results are presented in Figure 6-32. Both PKP1 and PKP2 are expressed in a pattern that appears largely peri-nuclear at day 0. The ratio of nuclear/perinuclear signal is 0.8±0.05 for PKP1 and 0.8±0.03 for PKP2 at day 0. However, after day 0 the expression pattern adopts an appearance that suggests localisation to the nucleus takes place. The ratio of nuclear/perinuclear signal is 1.5±0.01 for PKP1 and 1.1±0.03 for PKP2 at day 2. By day 4, PKP2 expression also appears to localise to a region outside the nuclear and perinuclear regions which could be the desmosome. Additionally, the ratio of nuclear/perinuclear signal decreases to 1±0.01. PKP1 does not share this desmosomal-like expression pattern and appears highly restricted to the nucleus by day 4 with a nuclear/perinuclear signal of 1.2±0.02. The percentage of nuclei positive for PKP1 signal increases from 8±5% on day 0 to 59±1% on day 2 and 72±1% on day 4. The percentage of PKP2-positive nuclei increases from 8±1% on day 0 to 44±25% on day 2 and 52±2% on day 4. Overall, the percentage of nuclei positive for PKP1 and PKP2 expression increases as the differentiation progresses.

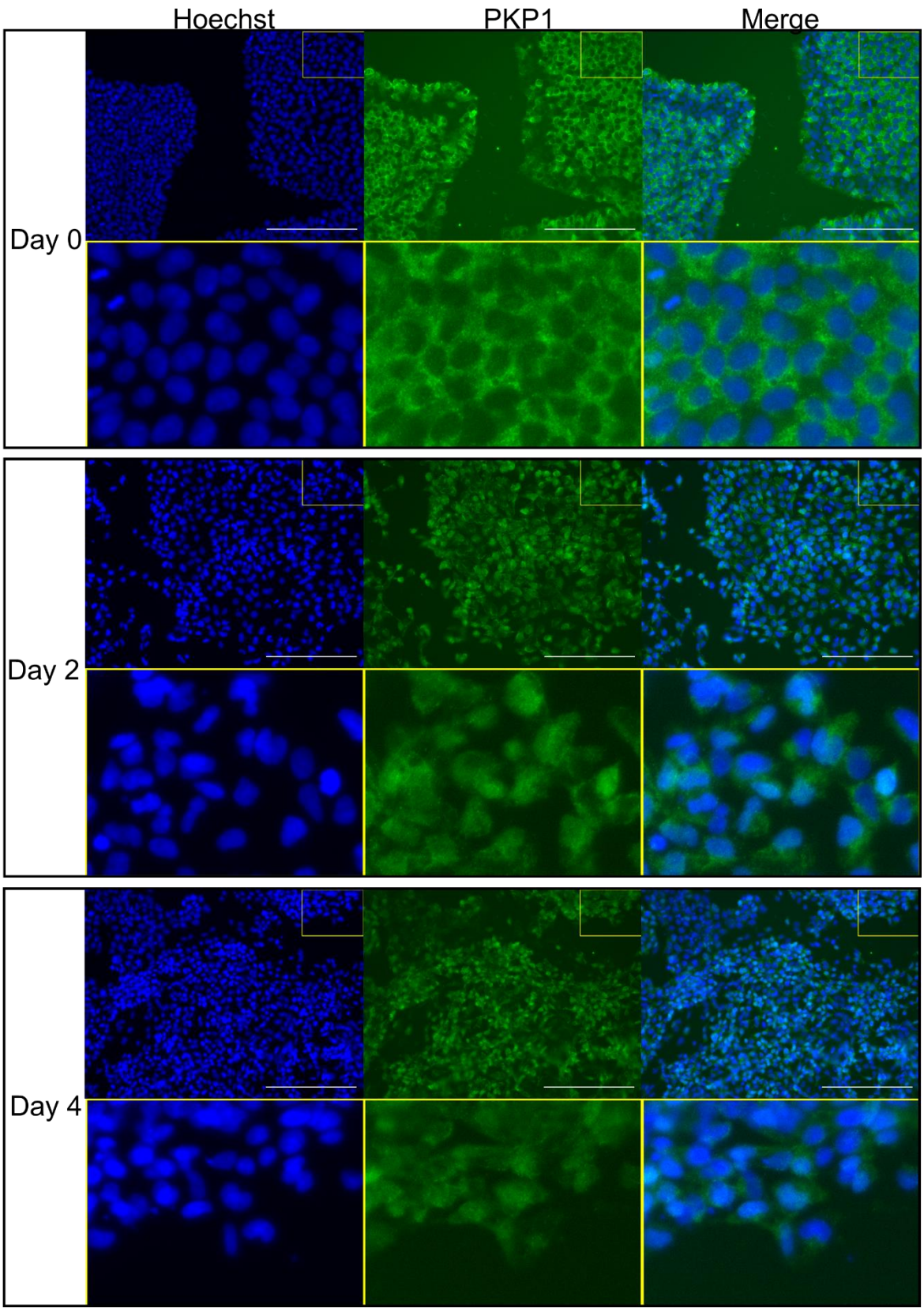

Figure 6-30. Immunocytochemistry of PKP1 expression during early cardiomyocyte differentiation.
Visualisation of the nuclei (blue) and PKP1 (green) of cells on days 0, 2 and 4 of iPSC-CM differentiation. Magnification = 20x, scale bar = 200um. The top right corner of each image was blown up x5 and is outlined in yellow.

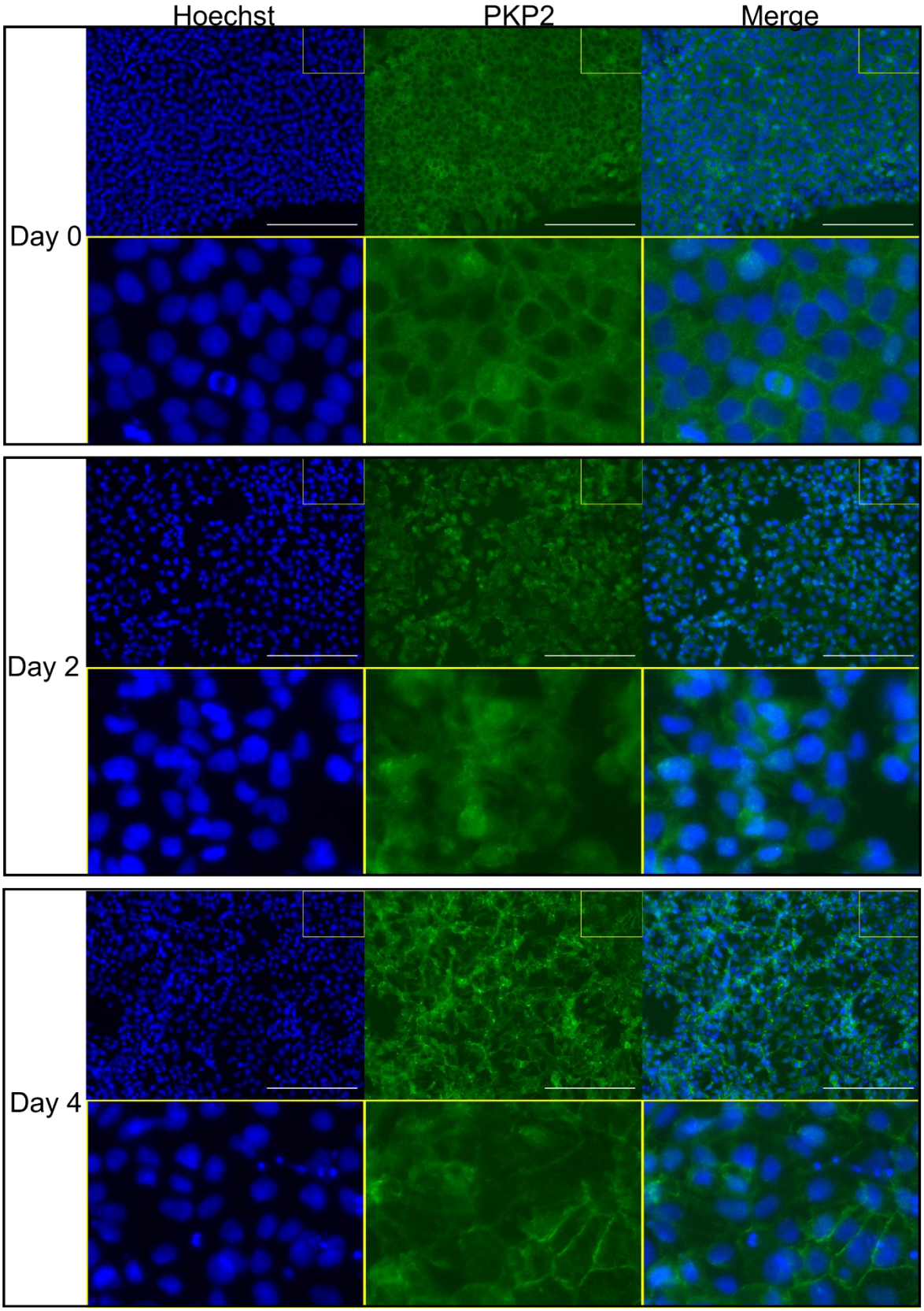

Figure 6-31 Immunocytochemistry of PKP2 expression during early cardiomyocyte differentiation.
Visualisation of the nuclei (blue) and PKP2 (green) of cells on days 0, 2 and 4 of iPSC-CM differentiation. Magnification = 20x, scale bar = 200um. The top right corner of each image was blown up x5 and is outlined in yellow.

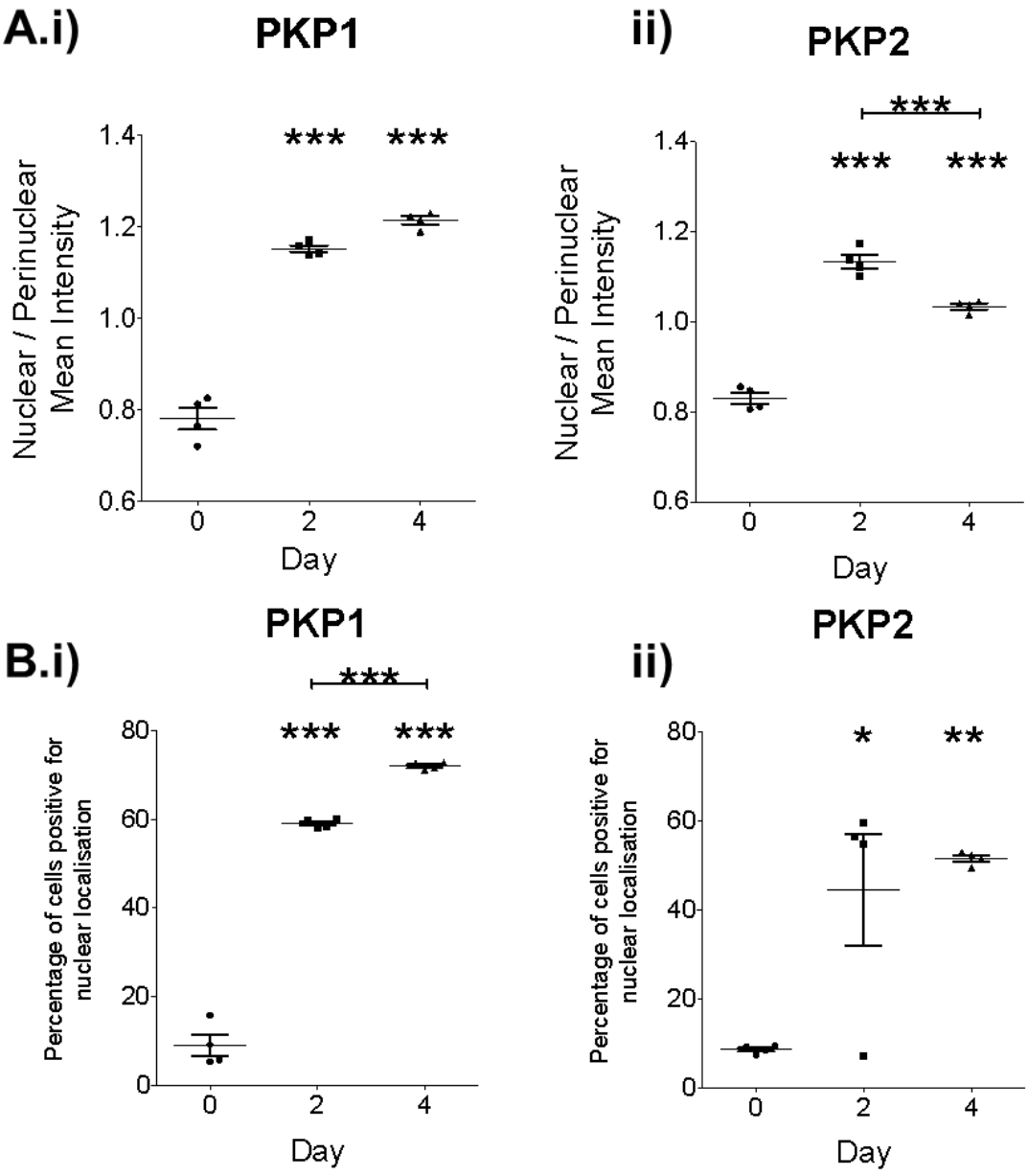

Figure 6-32. Nuclear localisation of PKP1 and PKP2 during early cardiomyocyte differentiation.

A. The ratio of mean nuclear/perinuclear intensity of (i) PKP1 and (ii) PKP2 at days 0, 2 and 4 of the iPSC-CM differentiation.

B. The percentage of nuclei positive for (i) PKP1 and (ii) PKP2 expression at days 0, 2 and 4 of the iPSC-CM differentiation.

N=4, statistics calculated by one-way ANOVA. * = P<0.05, ** = P<0.01, *** = P<0.001.

To investigate the expression pattern of plakophilin in fully differentiated cardiomyocytes, iPSC-CMs were differentiated and cultured from day 20 to day 30 in either glucose-based media (+glucose) or glucose-free fatty acid-based media (-glucose). The expression of PKP1 and PKP2 was visualised using immunocytochemistry, as shown in Figure 6-33 and Figure 6-34. By qualitative comparison, overall PKP2 expression appears higher and more diffuse than PKP1 expression. PKP1 expression appears mostly nuclear, but signal also appears in regions surrounding the nucleus. There appears to be more signal in the cells treated with glucose-based media compared to glucose-free, but this may be due to background fluorescence. PKP2 expression appears both nuclear and cytoplasmic under both conditions. CellProfiler was used to gauge the level of nuclearization of PKP1 and PKP2 and the percentage of nuclei positive for signal. The results are shown in Figure 6-35. The ratio of nuclear/perinuclear PKP1 expression is 1±0.04 in glucose-based media and 1.1 ±0.04 in glucose-free media. The ratio of nuclear/perinuclear PKP2 signal is 1.2±0.08 in glucose-based media and 1.4 ±0.2 in glucose-free media. The percentage of nuclei positive for PKP1 signal decreases from 99±1% in glucose-based media to 85±4% in glucose-free media. The percentage of nuclei positive for PKP2 signal increases from 94±5% to 96±1%, though this is not statistically significant.

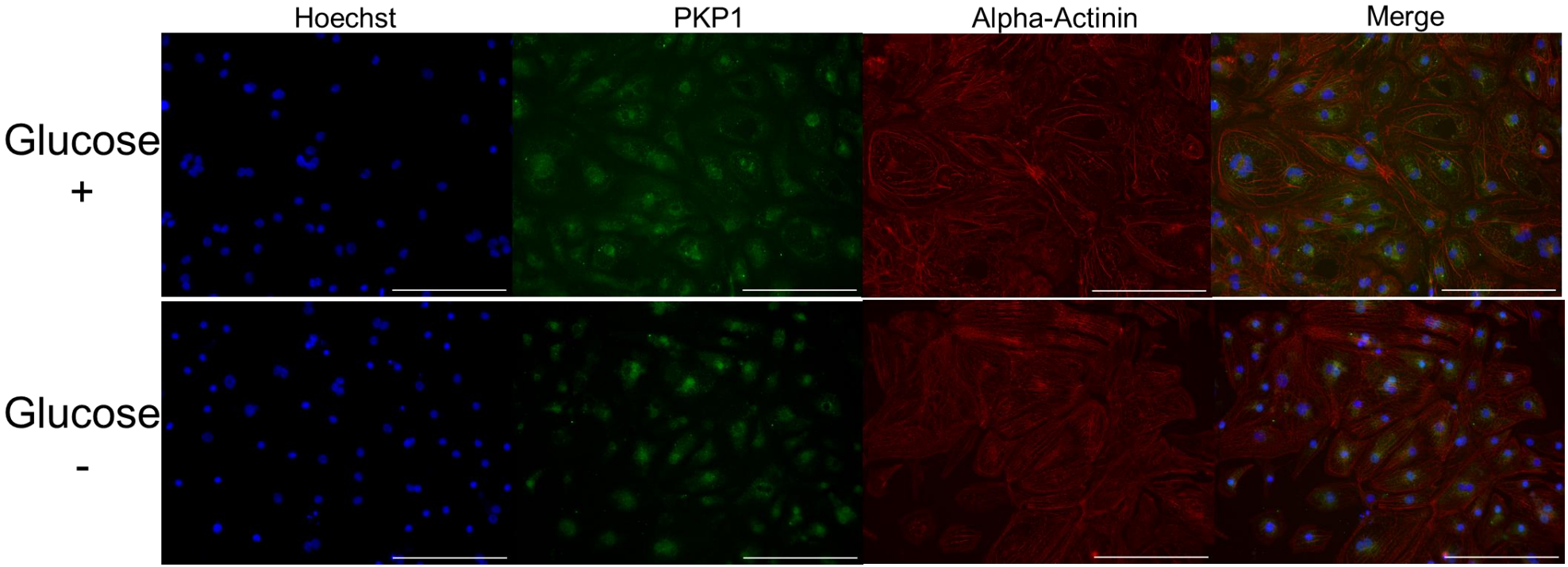

Figure 6-33 Immunocytochemistry of PKP1 expression in day 30 iPSC-CMs.
Visualisation of the nuclei (blue), PKP1 (green) and alpha-actinin (red) of day 30 iPSC-CMs cultured in glucose-based or glucose-free media. Magnification = 20x, scale bar = 200um.

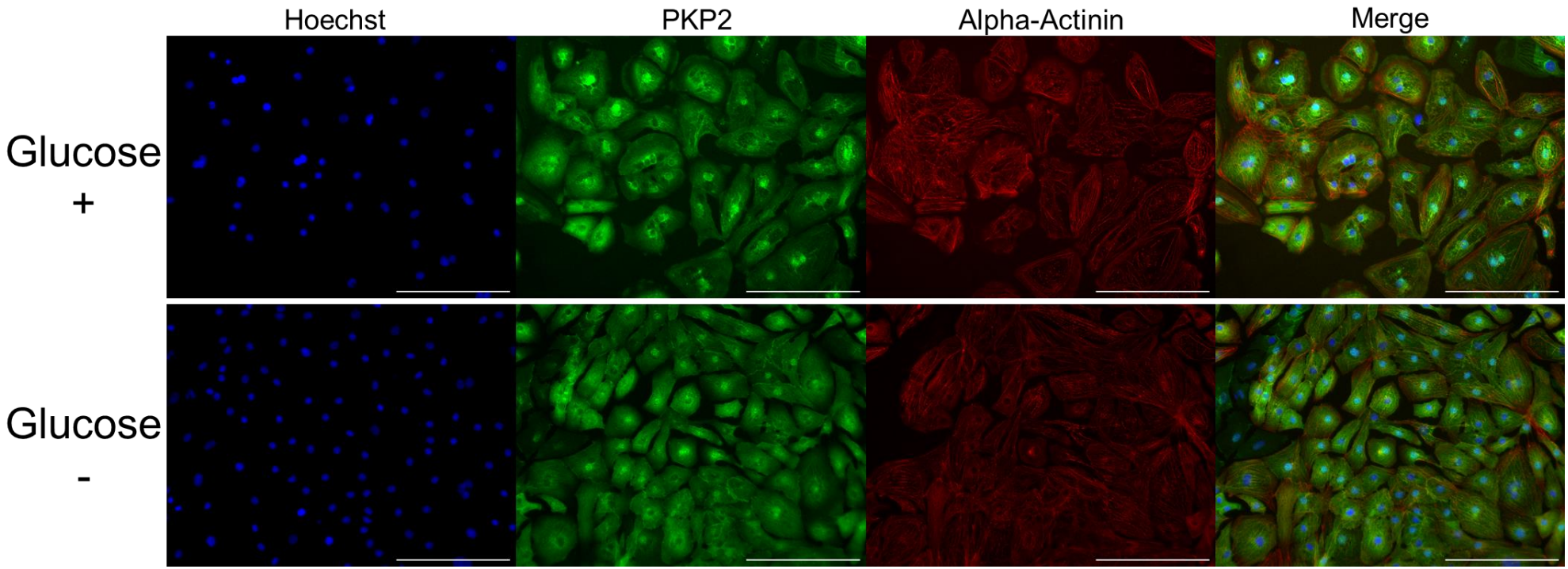

Figure 6-34 Immunocytochemistry of PKP1 expression in day 30 iPSC-CMs.
Visualisation of the nuclei (blue), PKP2 (green) and alpha-actinin (red) of day 30 iPSC-CMs cultured in glucose-based or glucose-free media. Magnification = 20x, scale bar = 200um.

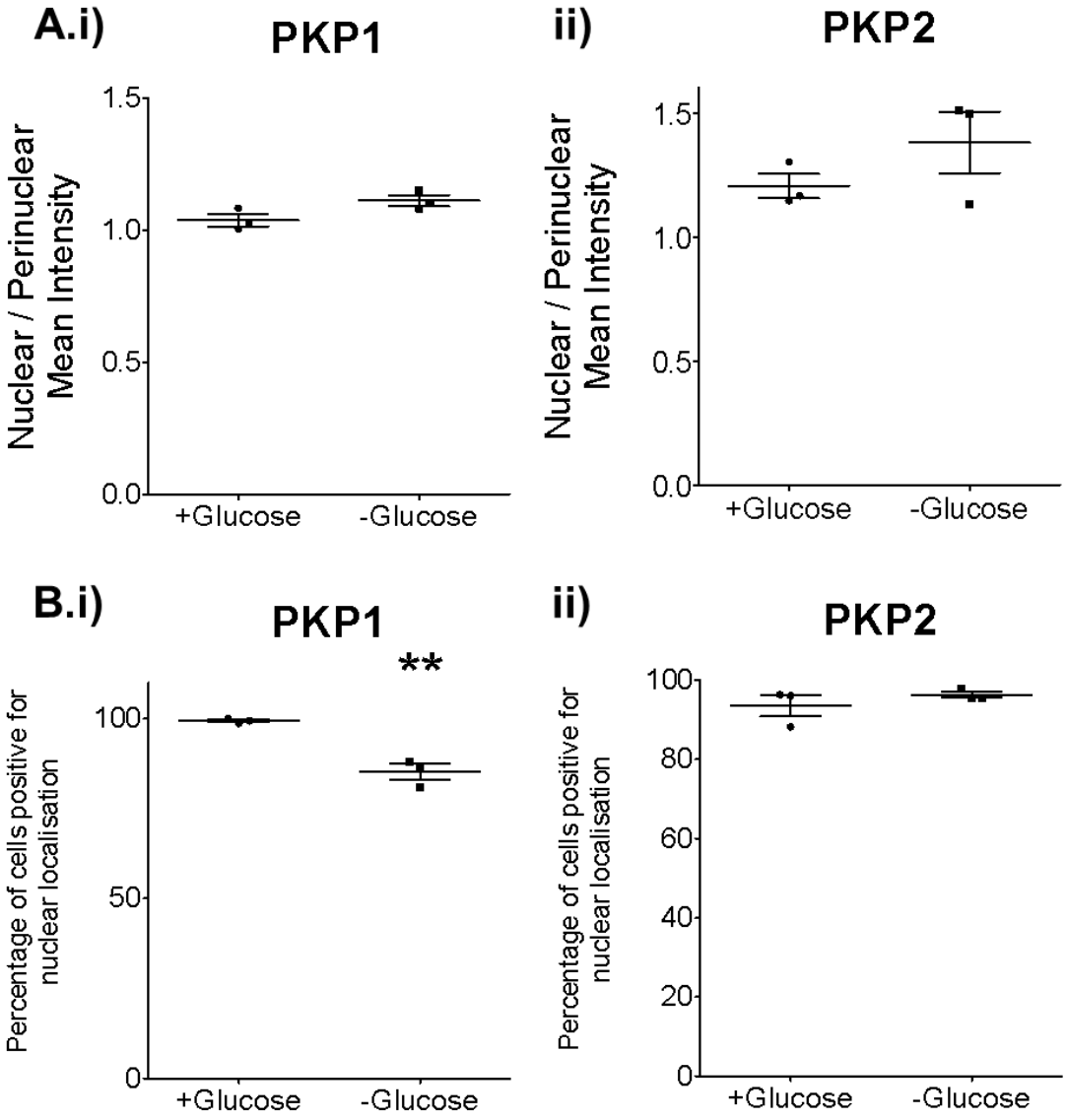

Figure 6-35. Nuclear localisation of PKP1 and PKP2 in day 30 iPSC-CMs.
A. The ratio of mean nuclear/perinuclear intensity of (i) PKP1 and (ii) PKP2 in day 30 iPSC-CMs cultured in glucose-based and glucose-free media.
B. The percentage of nuclei positive for (i) PKP1 and (ii) PKP2 expression in day 30 iPSC-CMs cultured in glucose-based and glucose-free media
N=3, statistics calculated by unpaired t-test. * = P<0.05, ** = P<0.01, *** = P<0.001.

To investigate the localisation of PKP1 in response to wnt signalling activation, day 20 iPSC-CMs were cultured in glucose-based media and treated for four days with 2uM CHIR or a vehicle control. After treatment the cells were fixed and PKP1 expression was analysed using immunocytochemistry and CellProfiler. The results are shown in Figure 6-36. Overall, there was no significant difference in the number of nuclei between CHIR-treated and control cells, which could indicate that the CHIR treatment was insufficient in causing increased cell proliferation. Similarly, there was no significant difference in the ratio of nuclear/perinuclear PKP1 signal. The percentage of nuclei positive for PKP1 did decrease from 83±16% to 66±23% in response to CHIR treatment, however this was not statistically significant due to variation between replicates.

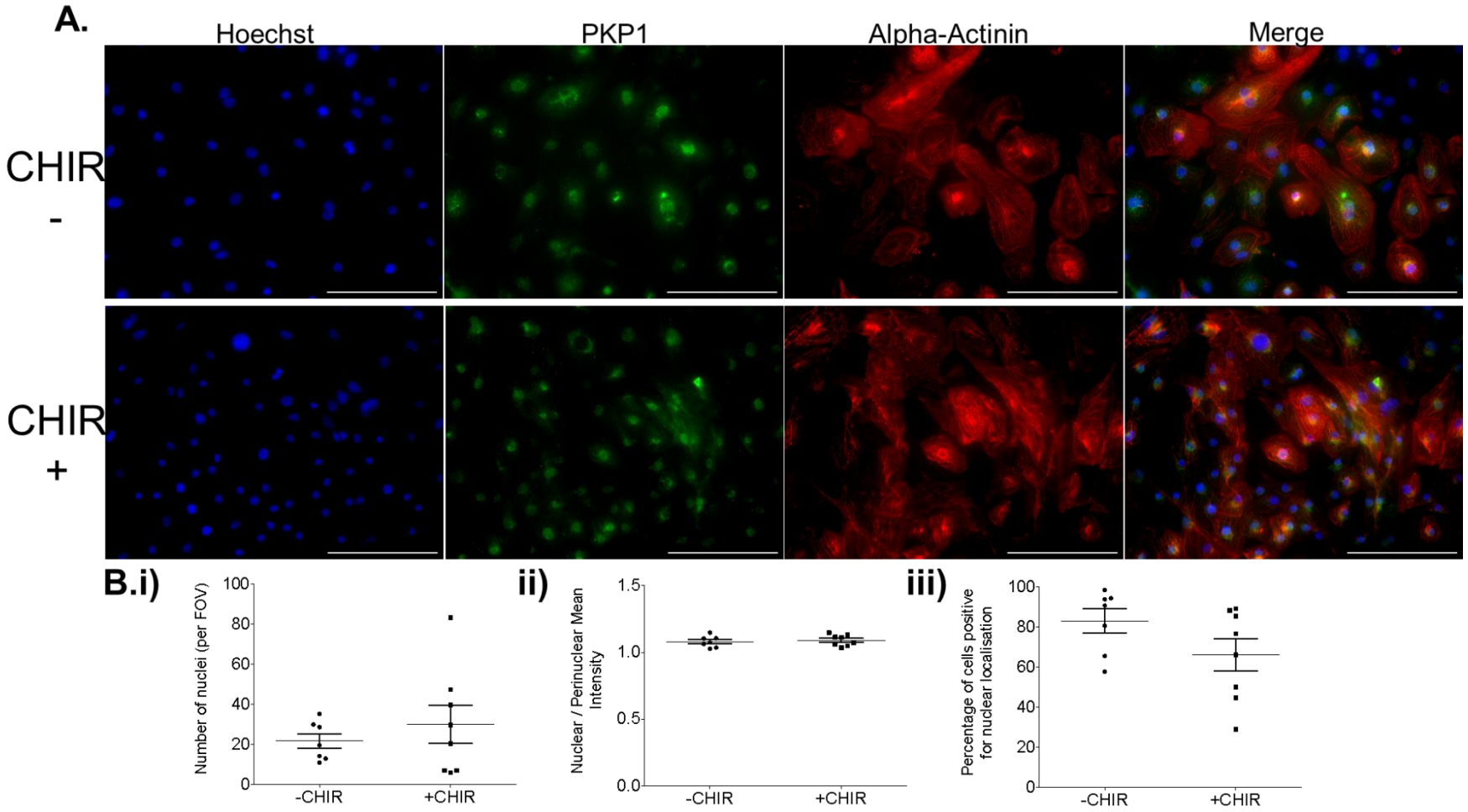

Figure 6-36. Nuclear expression of PKP1 in iPSC-CMs in response to CHIR treatment.
A. Visualisation of the nuclei (blue), PKP1 (green) and alpha-actinin (red) of day 30 iPSC-CMs treated with CHIR or a vehicle control. Magnification = 20x, scale bar = 200um.
B. (i) Number of nuclei, (ii) Nuclear/perinuclear signal intensity of PKP1 and (iii) percentage of nuclei positive for PKP1 signal in iPSC-CMs treated with CHIR or a vehicle control. Statistics calculated by unpaired t-test.N= 7 (control), N = 8 (CHIR).

To investigate how SNORD116 overexpression affects the localisation of PKP1, iPSC-CMs were seeded into a 96-well plate at a density of 100,000 cells/cm^2 and transfected with 100ng per well of either the MBII85 plasmid or a control plasmid. After 72-hours post-transfection the cells were fixed and PKP1 expression was analysed using immunocytochemistry and CellProfiler. Qualitatively, there was no visible difference in the expression pattern of PKP1 between control samples and MBII85-transfected cells. Additionally, there was no difference in the number of nuclei, the ratio of nuclear/perinuclear signal or the percentage of nuclei that were positive for PKP1. For both transfection samples, the ratio of nuclear/perinuclear signal intensity was 1.1±0.04. The percentage of nuclei that were positive for PKP1 signal was .95±7% in both samples. Overall, these result indicate that SNORD116 overexpression did not cause a change in the localisation of PKP1 in iPSC-CMs

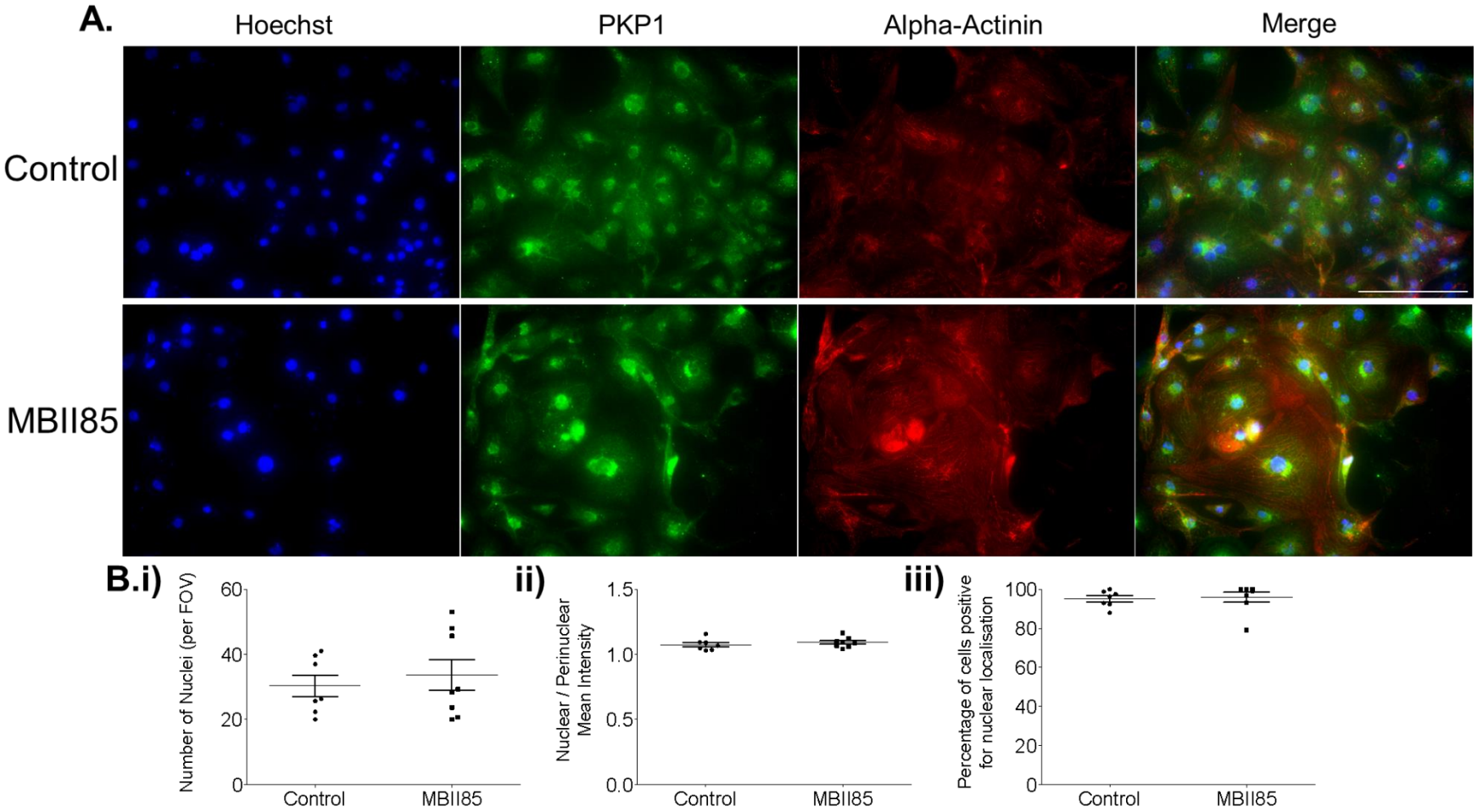

Figure 6-37. Nuclear expression of PKP1 in iPSC-CMs in response to SNORD116 overexpression.
A. Visualisation of the nuclei (blue), PKP1 (green) and alpha-actinin (red) of iPSC-CMs transfected with the MBII85 plasmid or a control plasmid. Magnification = 20x, scale bar = 200um.
B. (i) Number of nuclei, (ii) Nuclear/perinuclear signal intensity of PKP1 and (iii) percentage of nuclei positive for PKP1 signal in of iPSC-CMs transfected with the MBII85 plasmid or a control plasmid. Statistics calculated by unpaired t-test.N= 7 (control), N = 8 (MBII85).

Because SNORD116 is expressed highly in neurones, this warranted further investigation of the potential SNORD116-PKP1 axis in neural cell types. Neural stem cells (NSCs) were obtained from Axol (product number ax0015) and differentiated according to the product manual into neural progenitors. These cells were seeded into a 24-well plate and transfected with 600ng per well of either the MBII85 plasmid or a control plasmid. Images of the transfected cells are shown in Figure 6-38. After 72 hours, the cells were scraped, pelleted and sent for proteomic analysis. Proteomic analysis was performed by Mandy Peffers and James Anderson of the University of Liverpool Institute of Life Courses and Medical Sciences. Figure 6-38 shows the transfected cells, the number of differentially expressed proteins and the amount of protein analysed per sample.

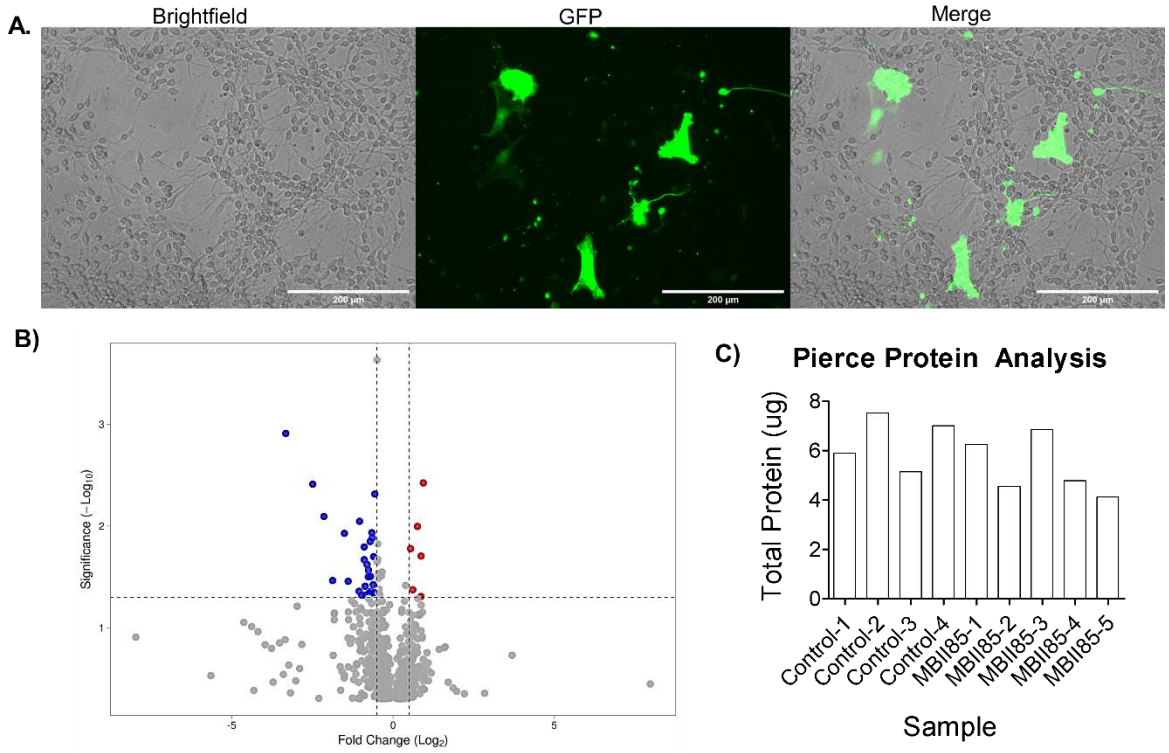

Figure 6-38. SNORD116 overexpression in neural cells.
A. . NPCs transfected with a GFP control plasmid 72 hours post-transfection. Magnification = 20x, scale bar = 200um.
B. Volcano plot of differentiability expressed proteins were thresholded to -0.5 > log_2 fold change > 0.5 and P<0.05. Proteins found in lower abundance as a result of SNORD116 overexpression are coloured blue and proteins found in higher abundance as a result of SNORD116 overexpression are coloured red.N=4 (control), N=5 (MBII85).
C. Total protein per sample, measured by Pierce test.

The amount of protein analysed was 4-8 ug per sample. PKP1 was not detected in these samples. In total, 1,690 proteins were identified, however only 45 were differentially expressed with a $P < 0.05$. These proteins were inputted into IPA to predict biological pathways that may have been affected by SNORD116 overexpression. The top two pathways predicted to be affected by SNORD116 overexpression were gluconeogenesis I and glycolysis I. Although the IPA software was unable to generate a z-score for these pathways due to insufficient entries, the proteins within this pathway that are present in the dataset (ENO2 and GPI) were downregulated by 0.6-fold and 0.8-fold of control levels.

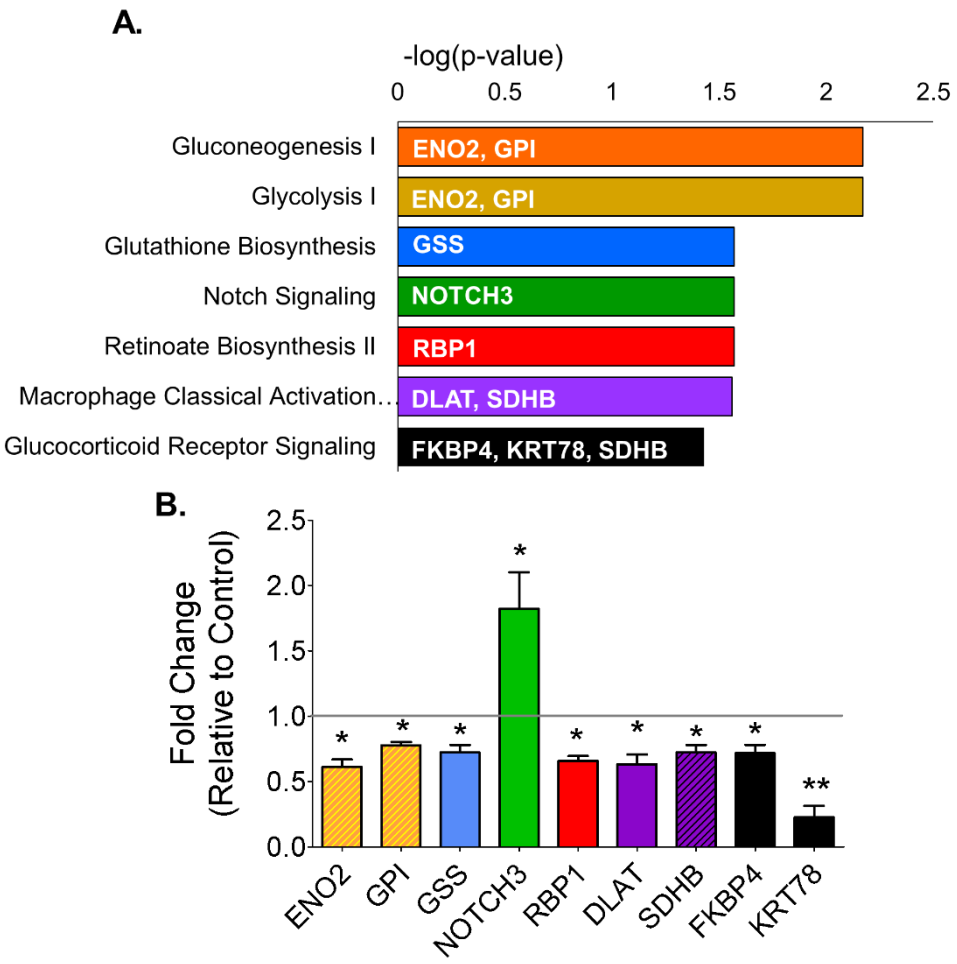

Figure 6-39. Pathway analysis of neural cell proteomic results.
A. IPA pathways predicted to be affected by SNORD116 overexpression. Genes within the pathway that were changed in the dataset are shown in white.
B. Fold changes of proteins in each of the predicted pathways. N=4 (control), N=5 (MBII85). Statistics calculated by one-way ANOVA. * = P<5, ** = P<0.01

To summarise the results of this section, SNORD116 overexpression was achieved in multiple cell types. using an overexpression plasmid by means of lipofection. A consistent finding across all cell types was that glucose metabolism appeared to be inhibited by SNORD116 overexpression. This was reflected in proteomic and Seahorse analysis of iPSC-CMs, Biolog substrate analysis of iPSC-CFs and proteomic analysis of neural cells. Proteomic analysis of iPSC-CMs revealed PKP1 as a potential direct target of SNORD116. Sequence analysis of PKP1 and SNORD116 uncovered a potential binding site between the two RNA molecules that may explain the dramatic downregulation of PKP1 upon SNORD116 overexpression. Following this discovery, the role of PKP1 in a cardiac context was explored. PKP1 was found to be scarcely expressed in many cell types including cardiac cells. Immunocytochemistry revealed an expression pattern of PKP1 that suggested the protein localises to the nucleus in differentiated cardiomyocytes. Culture of iPSC-CMs in a glucose-free fatty acid-based media caused a reduction in the percentage of nuclei that express PKP1, however Wnt signalling activation and SNORD116 overexpression in iPSC-CMs did not cause a change in PKP1 localisation. To further investigate the SNORD116-PKP1 axis, SNORD116 was overexpressed in neural cells. PKP1 was not detected by mass spectrometry of the neural cells. However, SNORD116 overexpression did result in the dysregulation of several pathways including glucose metabolism. In order to further support these findings, an overexpression plasmid that would overexpress a human paralogue of SNORD116 was built.

6.2.4 Building human SNORD116 overexpression plasmids

The MBII85 plasmid was useful in revealing potential targets and mechanisms of SNORD116, however it was not 100% identical to human SNORD116. Additionally, previous exosome analysis had identified preferential packaging of specific SNORD116 paralogues by iPSC-CMs under stress conditions, some of which do not share high sequence similarity with mouse SNORD116 (65). Therefore, the MBII85 plasmid was adapted to contain specific human SNORD116 paralogue sequences. An overview of the strategy is shown in Figure 6-40. In summation, the mouse SNORD116 insert was digested out using the restriction enzymes KpnI and XhoI. The human SNORD116 sequence was inserted in its place via ligation.

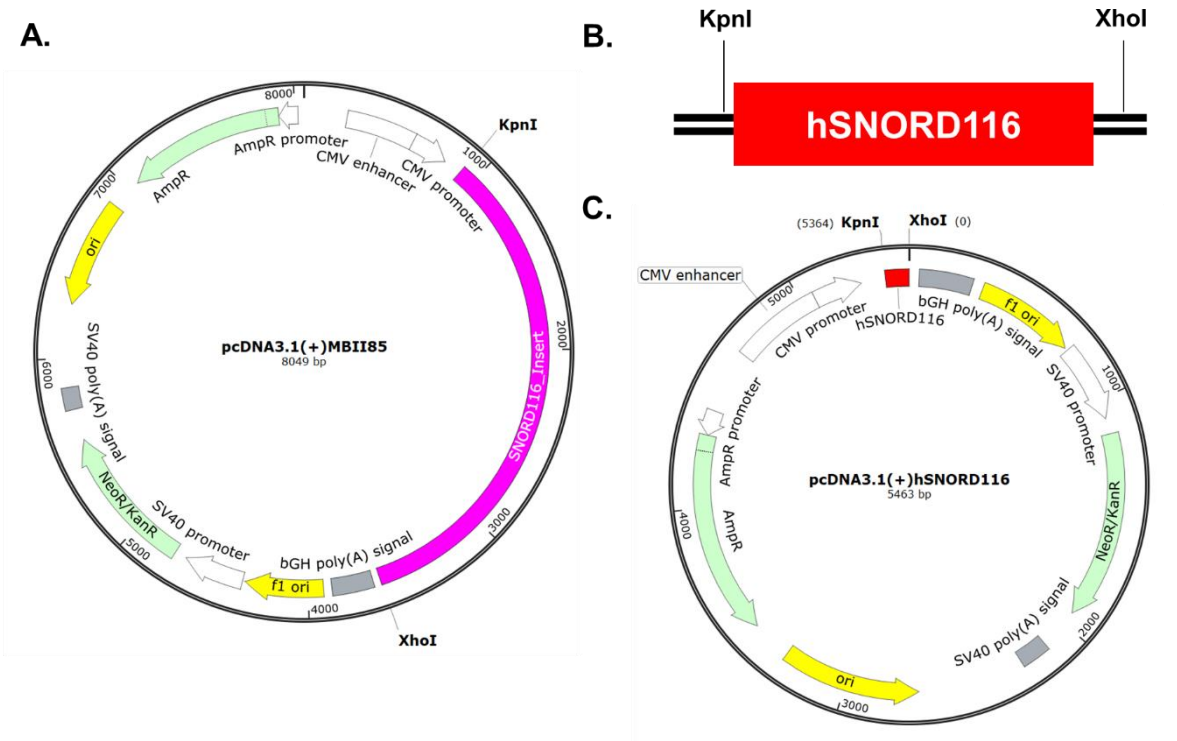

Figure 6-40. Adaptation of the MBII85 plasmid.
A. Plasmid map of the MBII85 plasmid
B. Human SNORD116 insert flanked by KpnI and XhoI sites
C. Plasmid map of the resulting hSNORD116 plasmid after digestion of MBII85 and ligation of the hSNORD116 insert.

As there are 30 different human SNORD116 paralogues, SNORD116-23 was selected as the initial paralogue to use it shares ~80% sequence identity with the mouse sequence in the MBII85 plasmid, and was previously found to be differentially packaged by cardiomyocytes under stress conditions (65). Figure 6-41 shows the design and isolation of the SNORD116-23 insert, and the digestion of the MBII85 plasmid to remove the mouse SNORD116 sequence (mSNORD116). The SNORD116-23 insert was ligated into the digested MBII85 vector. The resulting SNORD116-23 plasmid was midi-prepped and a diagnostic digest was performed to confirm the present of the SNORD116-23 insert. This was further confirmed by sequencing. The plasmid was transfected into hiPSC-CMs to test is overexpression of SNORD116-23 could be induced by the SNORD116-23 plasmid. The results are presented in Figure 6-42. The SNORD116-23 plasmid caused a 3232±155 overexpression of SNORD116-23.

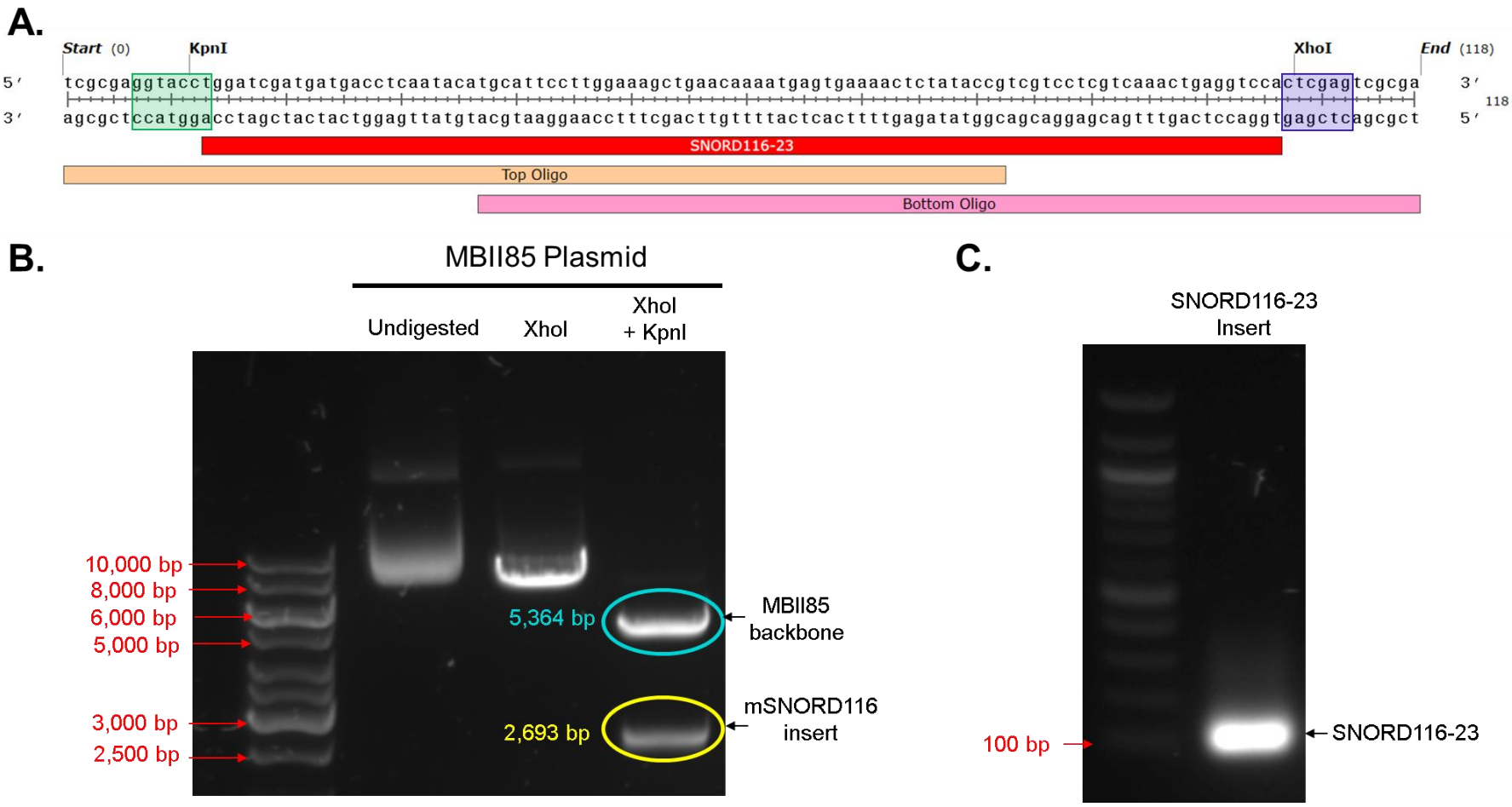

Figure 6-41. Preparation of the MBII85 plasmid vector and SNORD116-23 insert for ligation.
A. Design of the SNORD116-23 insert. The hSNORD116-23 transcript is highlighted in red. The top oligo is highlighted in orange and the bottom oligo is highlighted in pink. The KpnI restriction site is highlighted in green and the XhoI restriction site is highlighted in blue.
B. Functional digest of the MBII85 plasmid to remove the mSNORD116 insert
C. PCR product of the SNORD116-23 insert after PCR amplification.

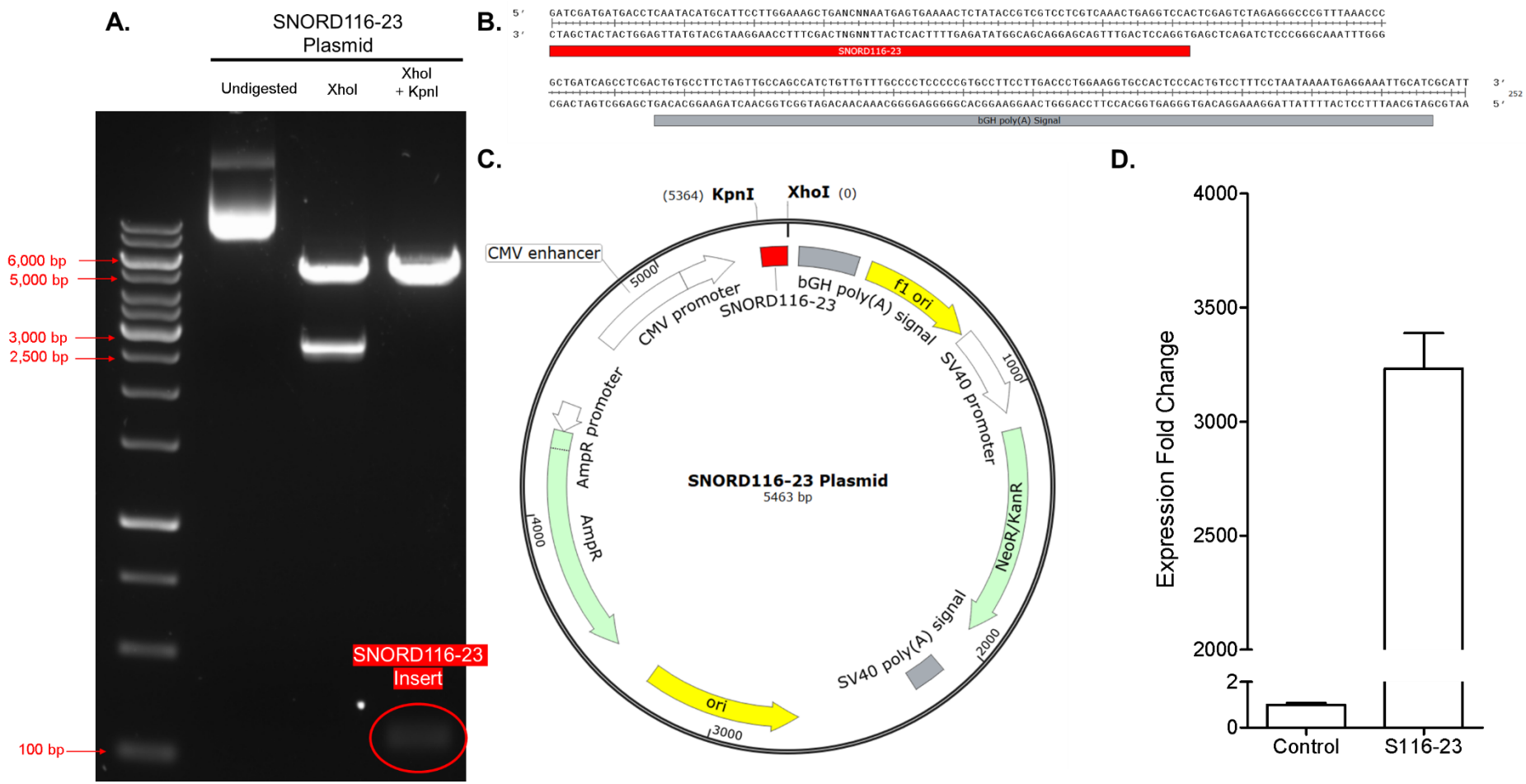

Figure 6-42. Validation of the SNORD116-23 plasmid.

A. Diagnostic digest of the SNORD116-23 plasmid.

B. Sequencing results of the SNORD116-23 plasmid confirming the presence of the SNORD116-23 insert before the poly(A) tail.

C. Map of the SNORD116-23 plasmid

D. Overexpression of SNORD116-23 72 hours post-transfection in hiPSC-CMs. Fold change calculated by ddCt method, normalised to GAPDH. N=1.

To further investigate the effect of SNORD116-23 overexpression on iPSC-CMs, gene analysis was performed by RT-qPCR 72 hours post-transfection with 600ng of either the SNORD116-23 plasmid or a control plasmid. The results are shown in Figure 6-43. To ensure that other SNORD116 paralogues had not been overexpressed, the expression of SNOD116-1 was measured and did not appear to change in response to SNORD116-23 overexpression. The expression of titin appeared upregulated by 1.8±0.04-fold relative to the control. However, another cardiac structural gene, TNNI3, did not appear to have altered expression. The expression of the metabolic genes *LDHA* and ACLY did not appear affected by SNORD116-23 overexpression. The calcium channel RYR was also not affected by SNORD116-23 overexpression, however CACNA1D appeared downregulated by 0.4±0.2-fold relative to the control.

In summary, the results of this section demonstrate that the overexpression of a human paralogue of SNORD116 can be achieved by adapting the MBII85 primer. Preliminary expression analysis suggests that some genes may be affected by the overexpression of SNORD116-23 in hiPSC-CMs, however further analysis is needed to confirm this.

Overall, SNORD116 overexpression was helpful in identifying a potential target of SNORD116 and revealed interesting potential pathways and mechanisms for SNORD116 signalling. However, it was also important to explore other methods of modulating SNORD116 expression to validate these findings.

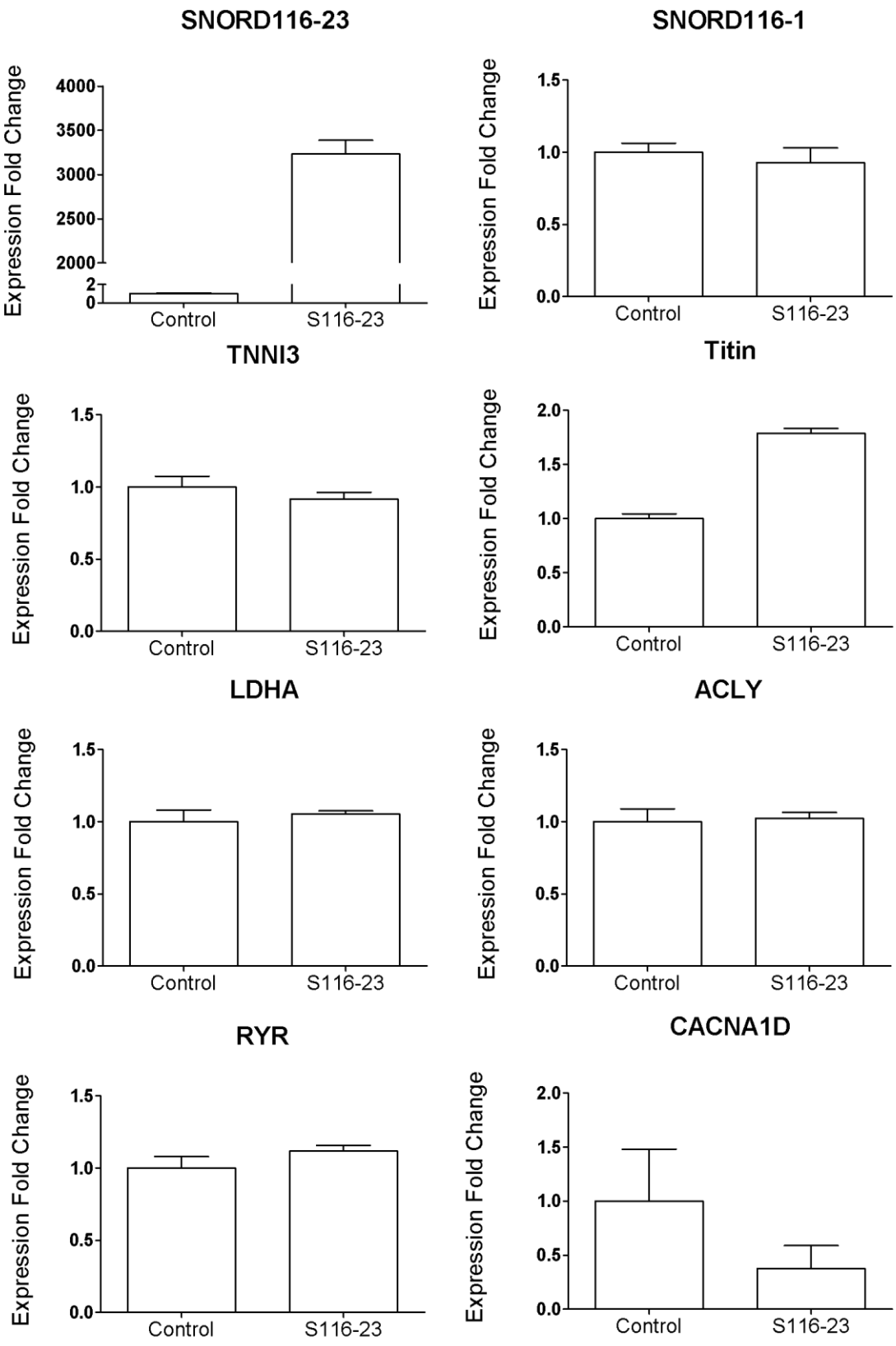

Figure 6-43. Gene expression analysis of iPSC-CMs transfected with the SNORD116-23 plasmid.

Expression calculated as fold change relative to transfection control using the ddCt method, normalised to GAPDH. N=1, error bars represent SEM.

6.3 Generation of a SNORD116 knockout iPSC line

To generate a SNORD116 knockout iPSC line, several plasmids needed to be constructed. Firstly, a plasmid encoding the guide RNA that would direct the Cas9 protein to the target cut site. In order to achieve complete removal of the SNORD116 cluster, two double-stranded breaks would be required: one upstream of the cluster and one downstream. This had been achieved previously for SNORD116 in a human neuroblastoma line (51). The DNA breaks can be repaired by the cell through non-homologous end-joining. However, this would not enable subsequent identification of successfully targeted cells. Therefore, a positive selection cassette was designed to replace the SNORD116 cluster through homology-directed repair. An overview of this strategy is depicted in Figure 6-44. The selection cassette must contain a gene to allow for selection, in this case the gene confers puromycin resistance (puroR). In addition, the selection cassette must be flanked by regions that are homologous to the sequences at the target cut sites to allow for homologous recombination.

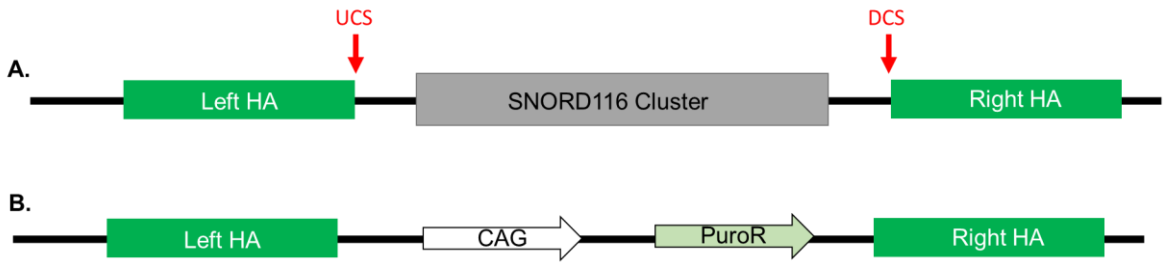

Figure 6-44. Targeting strategy for the removal of SNORD116 from the genome.
A. SNORD116 cluster with the left arm of homology (Left HA) and right arm of homology (Right HA) flanking the cluster. The uprestream CRISPR-Cas9 cut site (UCS) and downstream cut site (DCS) are indicated by red arrows.
B. The selection cassette in the place of SNORD116 between the two arms of homology. CAG = synthetic promoter, PuroR = gene for puromycin resistance

The online software CRISPick (412) was used to design the upstream and downstream target site guide RNAs. The CRISPR-Cas9 guide plasmid U6 was used as the template plasmid into which the guide RNA could be ligated. The top CRISPRPick results were used to synthesise the guide sequences, with BsaI restriction site overhangs added to ensure ligation into the plasmid. Successful ligation of the guide into the plasmid would result in destruction of the restriction site. Figure 6-45 shows the template guide map and guide sequences.

A.

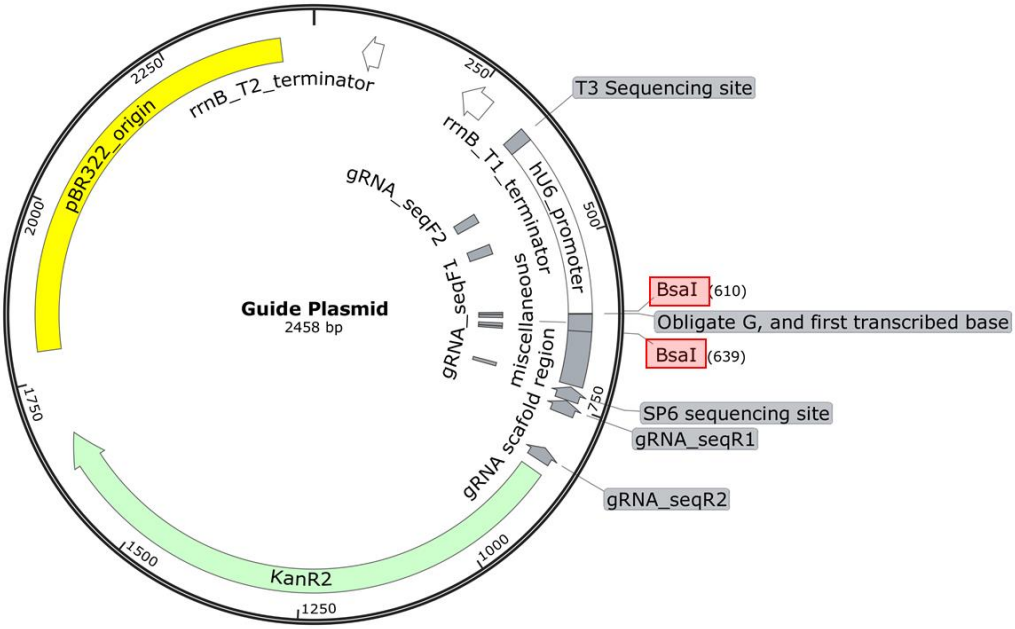

B.

	SNORD116
Upstream Guide Annealed	5'-A-C-C-G-a-c-g-t-g-c-t-g-a-a-t-g-a-g-a-g-t-g-g-3' 3'-t-g-c-a-c-g-a-c-t-t-a-c-t -c-t-c-a-c-c-G-T-T-T-5'
Downstream Guide Annealed	5'-A-C-C-G-g-a-g-c-c-a-t-c-c-a-t-a-a-g-t-t-a-t-c-t-3' 3'-c-t-c-g-g-t-a-g-g-t-a-t-t-c-a-a-t-a-g-a-G-T-T-T-5'

Figure 6-45. SNORD116 CRISPR-Cas9 guide design.
A. U6 guide RNA template plasmid. The BSAI restriction sites are highlighted in red.
B. Annealed sequences for the upstream and downstream guides with the restriction site overhangs shown in red.

The guide oligoes were annealed, amplified and digested with BsaI. The U6 plasmid was digested with BsaI. The digested plasmid and insert fragments were ligated together and midi-prepped. A diagnostic digest using BsaI was performed to confirm the successful ligation indicated by the loss of the BsaI restriction site. Sequencing was also performed to confirm successful generation of the upstream and downstream guide plasmids. The results are shown in Figure 6-46.

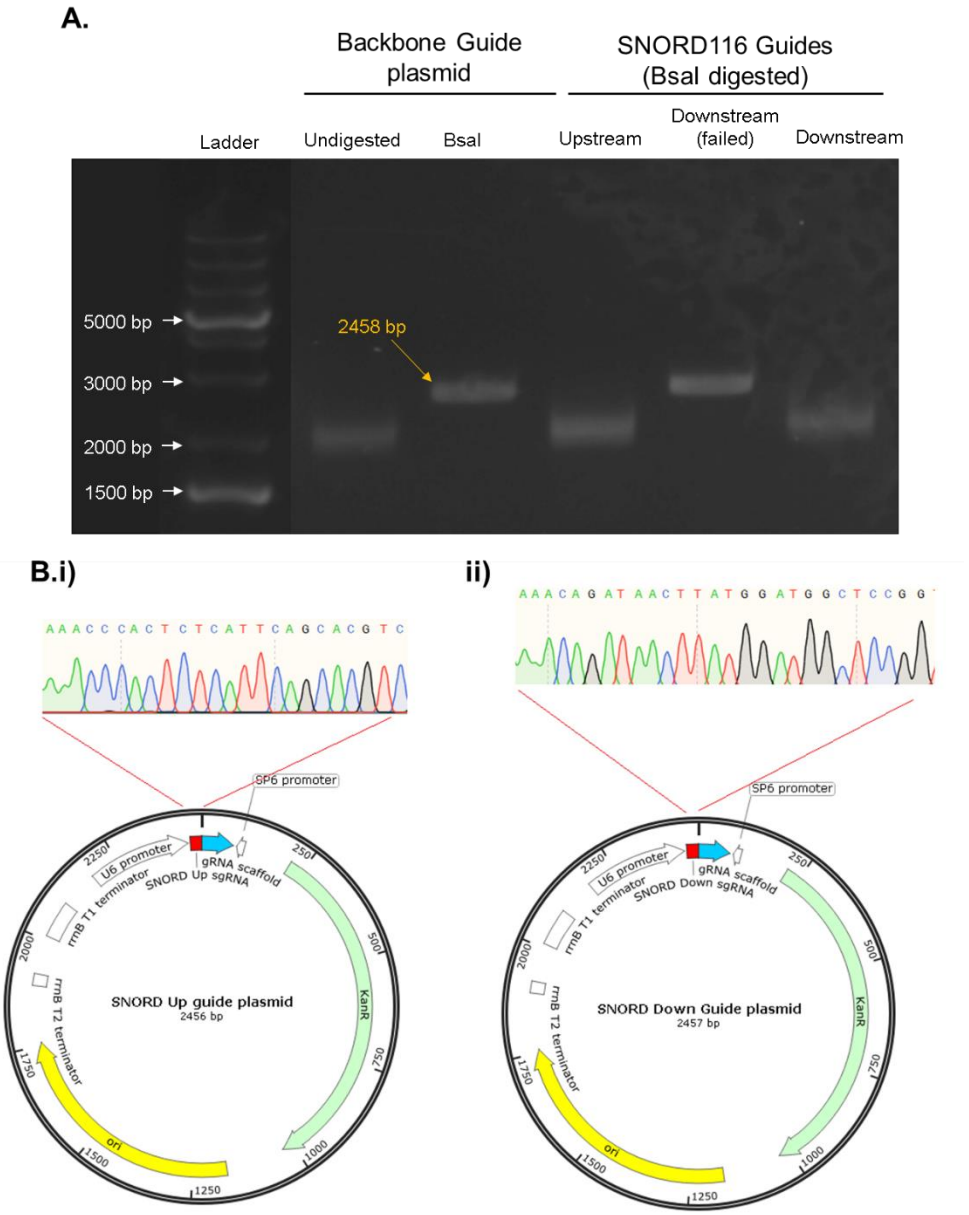

Figure 6-46. Constructing the CRISPR-Cas9 guide plasmids.
A. Diagnostic digest of the upstream and downstream guide plasmids
B. Guide plasmids with sequencing to confirm the integration of the guide insert into the plasmid

In addition to the guide plasmids, a targeting plasmid must also be constructed that contains the selection cassette flanked by arms of homology to allow for homology-directed integration into the target site. An existing targeting plasmid (the AAVS targeting plasmid) was used as a template. This plasmid contained the PuroR selection cassette and was designed to target the AAVS1 safe harbour site within the genome, and therefore contained arms of homology appropriate for this target. To target SNORD116, these arms were removed using restriction enzymes and replaced with arms homologous to the SNORD116 target sites. Figure 6-47 shows a schematic of these plasmids. The AAVS targeting plasmid was digested with SalI and PacI to remove the left arm, and NotI and XhoI to remove the right arm. This functional digest is depicted in Figure 6-48. PCR of iPSC genomic DNA was used to amplify the left and right arms of homology. Primers were designed based on the regions of homology and included the appropriate restriction sites that would facilitate ligation into the targeting plasmid. Isolation of the SNORD116 arms of homology are shown in Figure 6-49.

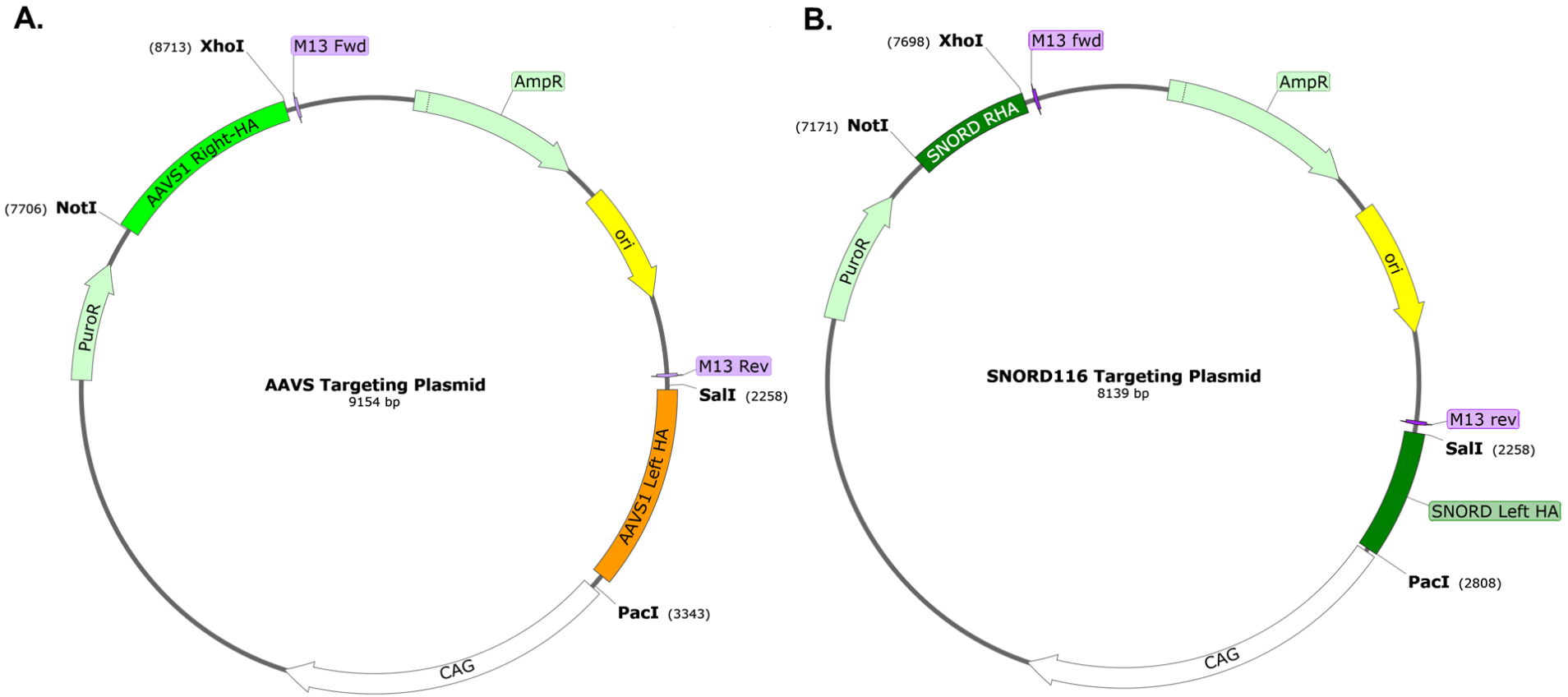

Figure 6-47. Designing the SNORD116 targeting plasmid.
A. Targeting plasmid with puromycin resistance selection cassette with arms of homology for the AAVS1 safe harbour locus.
(B) Targeting plasmid with puromycin resistance selection cassette with arms of homology for the SNORD116 locus.
CAG = synthetic promoter, PuroR = gene for puromycin resistance, AmpR = gene for ampicillin resistance, HA = arm of homology, M13 fwd = validation primer for Right HA, M13 Rev = validation primer for Left HA

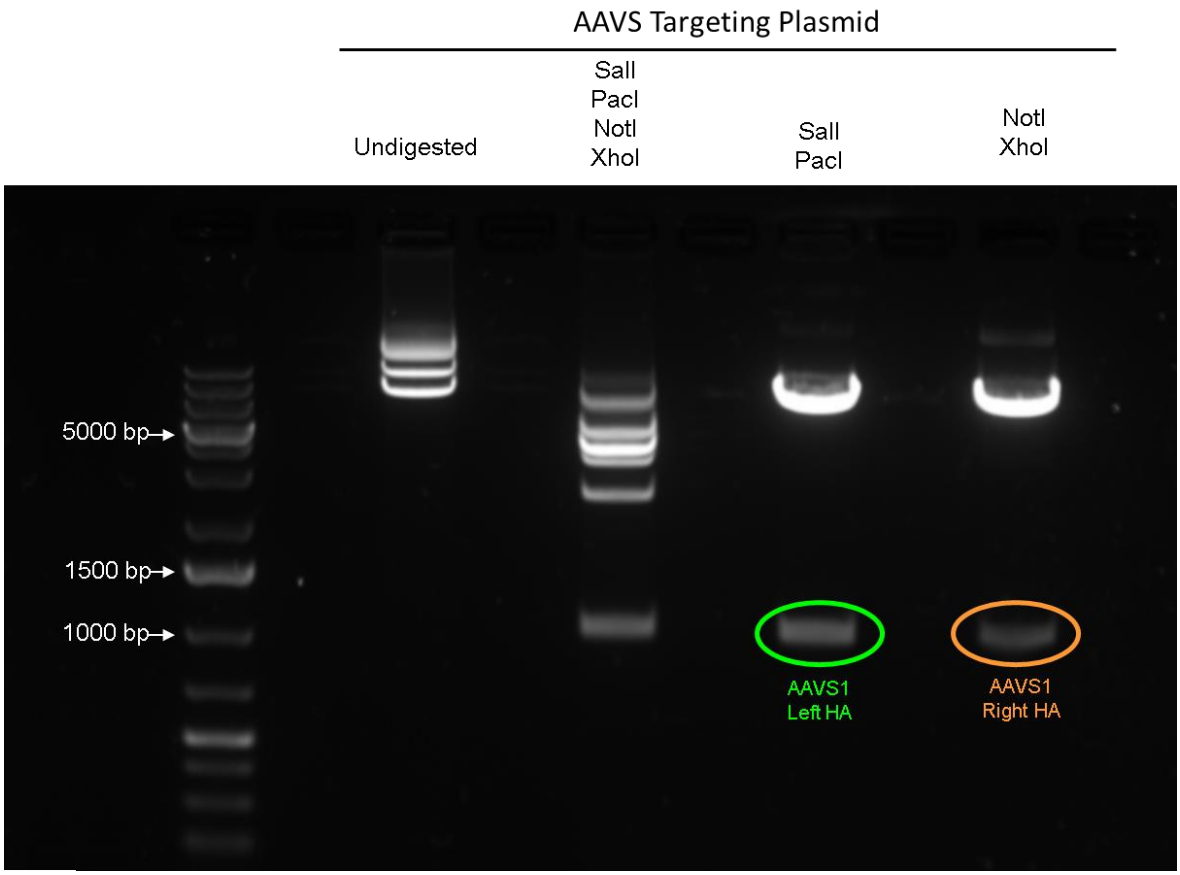

Figure 6-48. Removal of the AAVS1 arms of homology.
Functional digest of the AAVS targeting plasmid to remove the arms of homology.

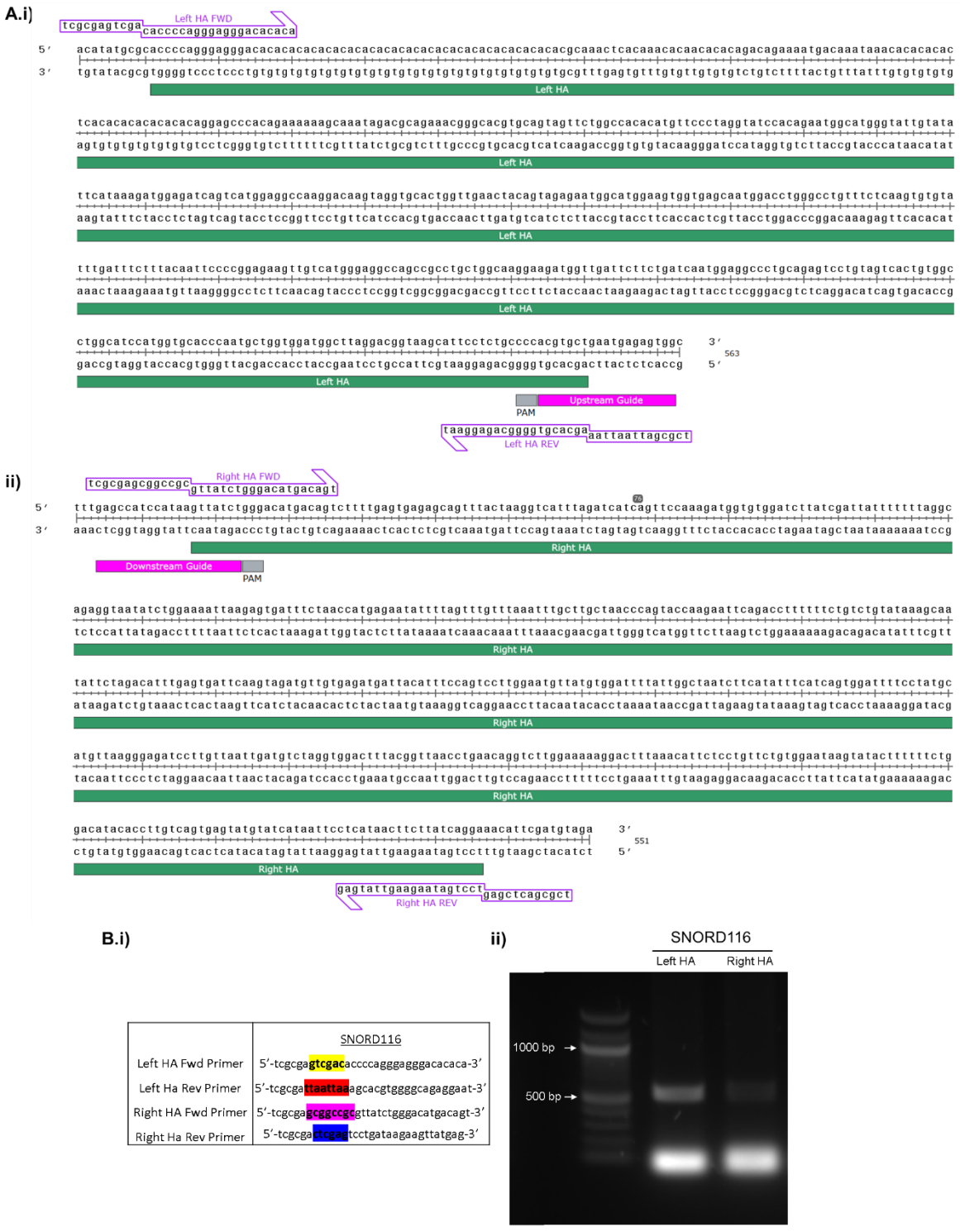

Figure 6-49. Isolating the SNORD115 arms of homology.
A. The (i) left and (ii) right arms of homology with the froward (FWD) and reverse (REV) primer sequences added and the guide sequences highlighted in pink. The PAM sites are highlighted in grey.
B. (i) forward and reverse primer sequences used to PCR amplify the SNORD116 arms of homology. Restriction sites are colour coded (yellow = SalI, red = PacI, pink = NotI, blue = XhoI). B.(ii) shows the gel image of the PCR products generated using the primer sequences.

The arms of homology were ligated into the targeting plasmid in step-wise fashion, starting with the left arm. The AAVS left HA was digested out and the SNORD116 left HA (which is ~500bp smaller) was ligated in. Figure 6-50 shows a diagnostic digest of the resulting plasmid confirming the presence of the SNORD116 left HA

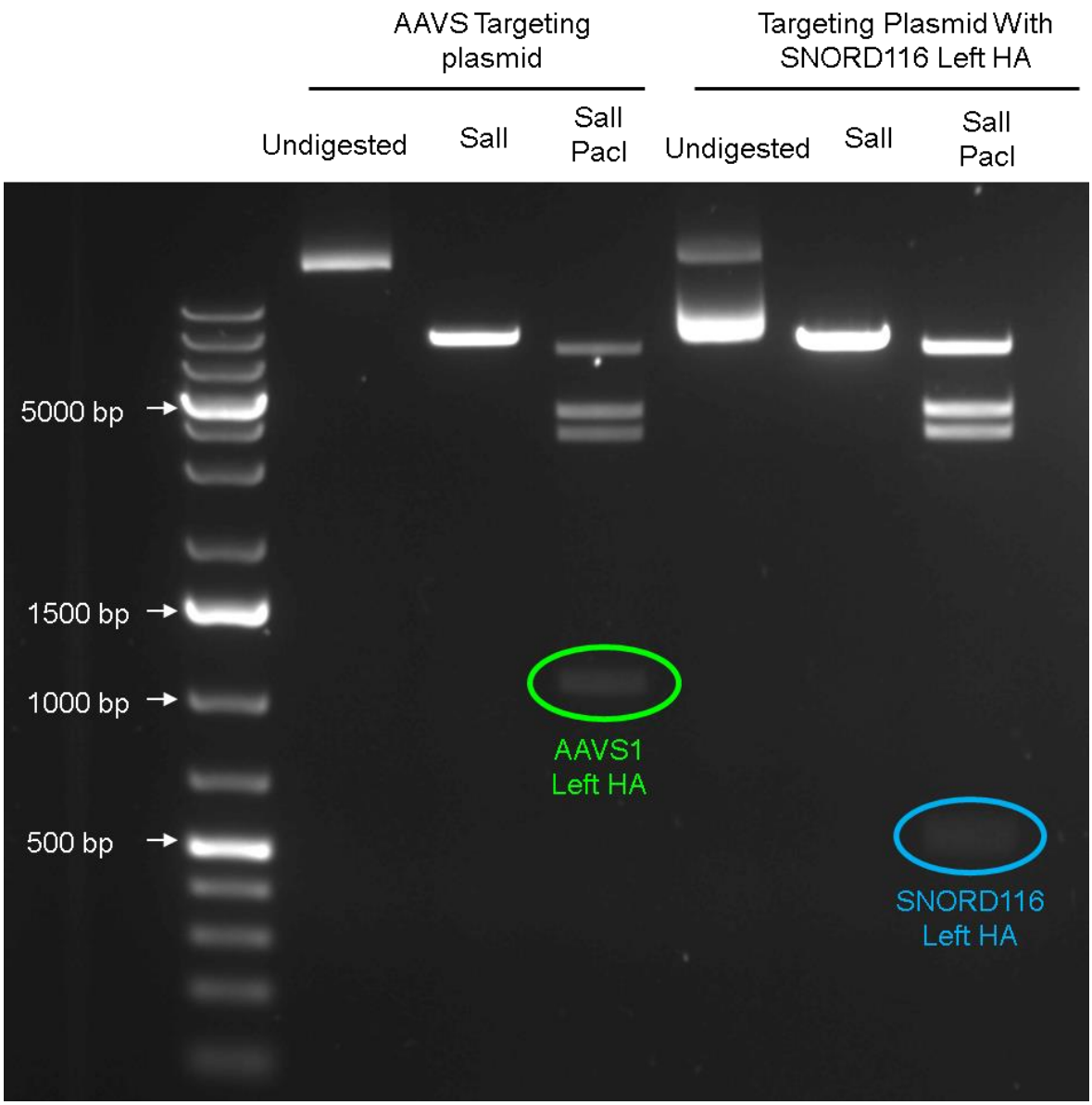

Figure 6-50. Diagnostic digest of targeting plasmid with SNORD116 left HA.
Band at 500bp confirms the presence of the SNORD116 left HA.

The resulting plasmid was digested with NotI and XhoI to remove the AAVS right HA, resulting in a plasmid containing the SNORD116 right HA. A diagnostic digest confirming this is shown in Figure 6-51.

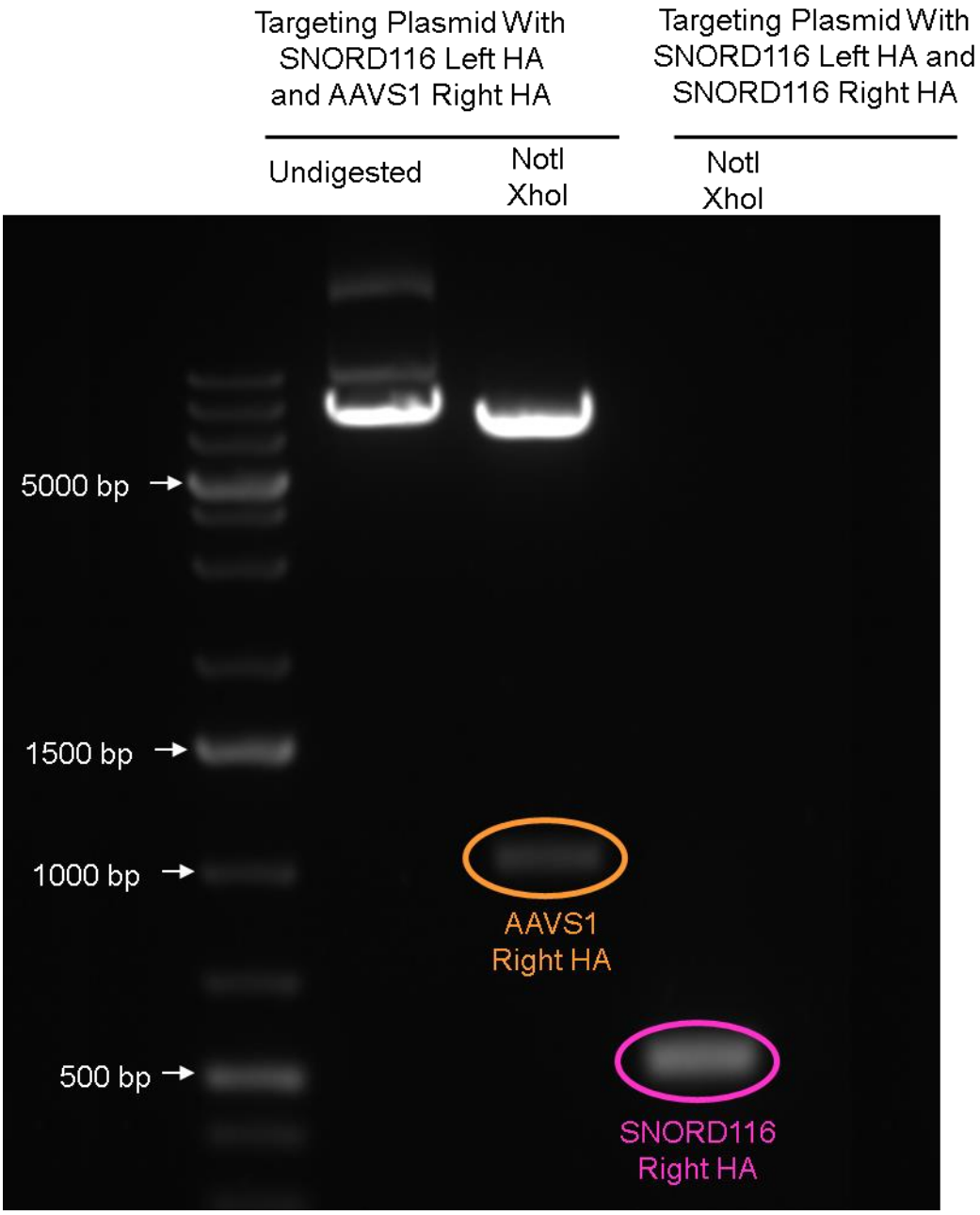

Figure 6-51. Diagnostic digest of targeting plasmid with SNORD116 right HA. Band at 500bp confirms the presence of the SNORD116 right HA

The SNORD116 targeting plasmid was sequenced using the M13 forward primer to validate the right arm of homology and the M13 reverse primer to validate the left arm of homology. Sequencing was performed by GENEWIZ. The sequencing results were blasted against the predicted SNORD116 targeting plasmid sequence using Nucleotide BLAST (361). The validated sequence regions are shown in Figure 6-52. Sequencing confirmed the successful integration of the SNORD116 left and right arms of homology into the targeting plasmid.

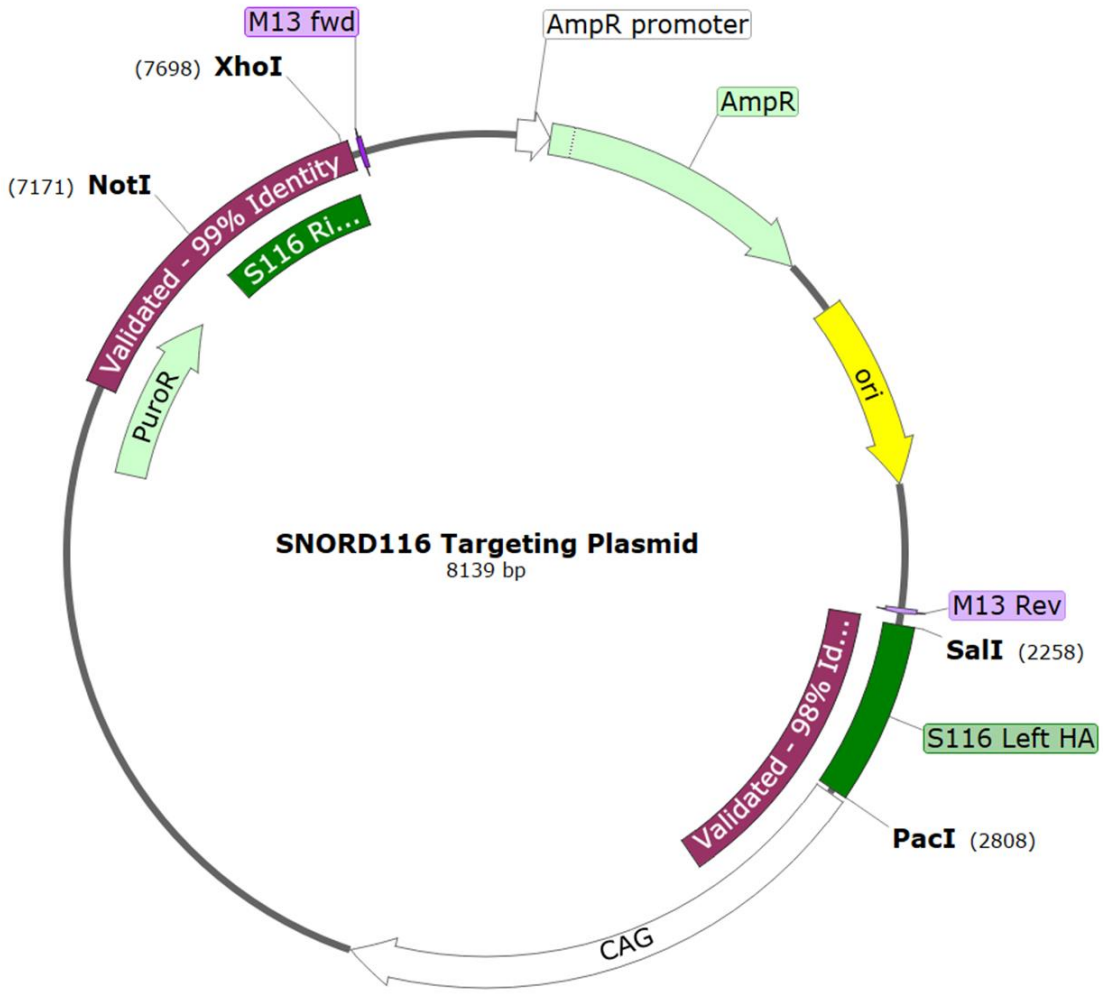

Figure 6-52. SNORD116 targeting plasmid with sequence validation.
Sequenced regions are shown in purple with the % identity between the true sequencing results and the predicted SNORD116 targeting plasmid sequence.

Once the necessary plasmids were successfully constructed, they were ready to be transfected into stem cells. IPSCs were transfected by nucleofection using the Lonza Amaxa 4D-Nucleofector. In total, 1,000,000 iPSCs were transfected with 1,000 ng of the Cas9 plasmid, 1,000ng of the SNORD116 targeting plasmid, 500ng of the upstream guide plasmid and 500ng of the downstream plasmid. The transfected cells were seeded into a 6-well plate at a range of densities: 5,000 cells/cm^2, 10,000 cells/cm^2, 15,000 cells/cm^2 and 20,000 cells/cm^2. 1,000,000 iPSCs were also transfected with 3,000ng of a GFP control plasmid. GFP-transfected cells were seeded at a density of 10,000 cells/cm^2. These cells were imaged 48 hours post-transfection, as shown in Figure 6-53. To select for positively targeted cells, from 48-hours post-transfection onwards the iPSCs were cultured in media supplemented with 0.33ug/mL of puromycin. To ensure that untargeted iPSCs were not resistant to puromycin, an untargeted control was also cultured in puromycin supplemented media alongside the target cells. An antibiotic-free culture of untargeted cells was cultured for comparison. Figure 6-53 demonstrates that 48 hours of puromycin exposure is lethal to untargeted iPSCs.

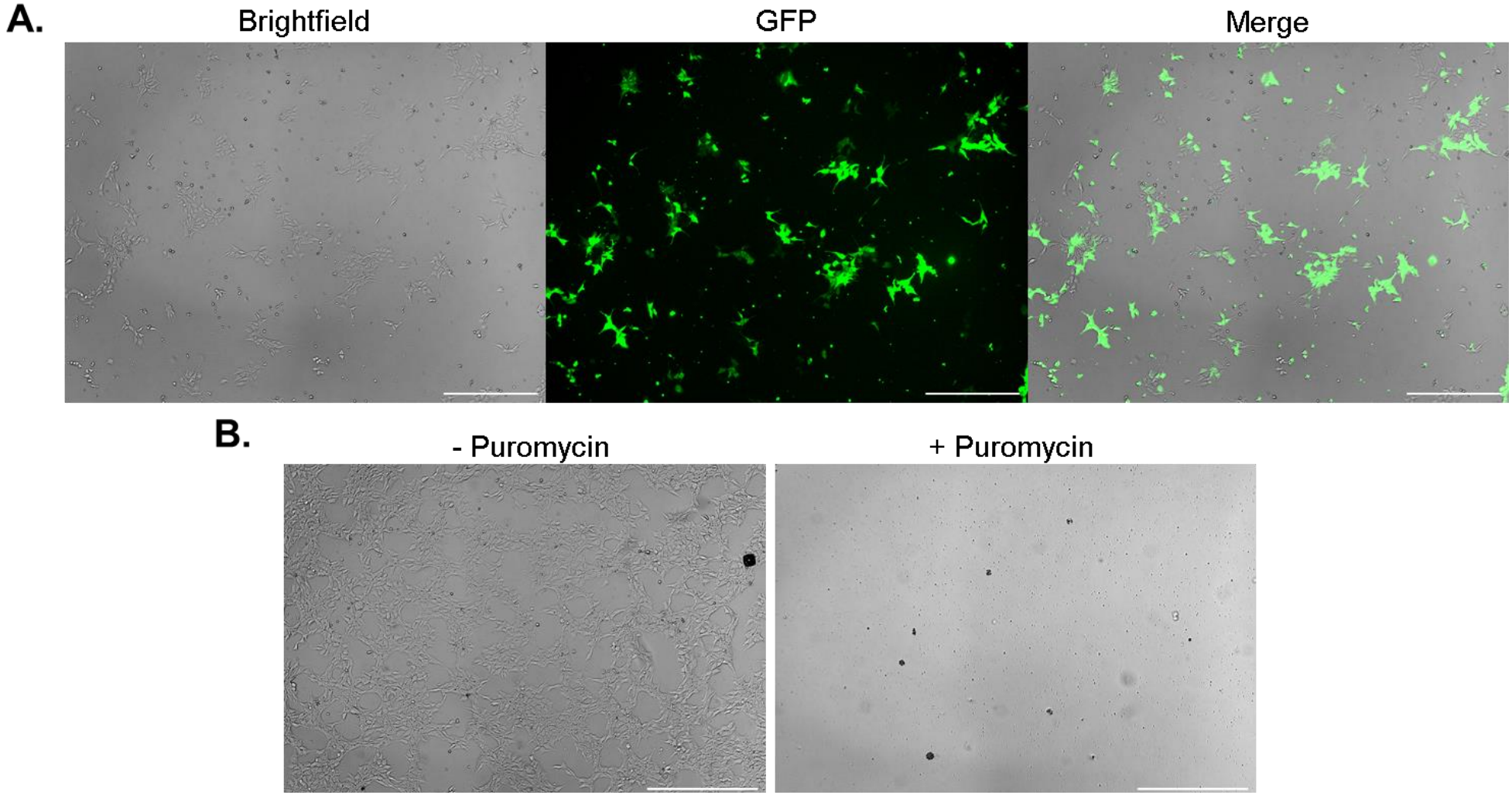

Figure 6-53. Transfection and antibiotic selection.
A. IPSCs 24-hours post-transfection by nucleofection with a GFP control plasmid.
B. The effect of 48 hours of puromycin exposure on untargeted iPSCs.

Targeted iPSCs were cultured in puromycin supplemented media until the colonies had reached a size of ~800um in diameter, which took a total of seven days. Figure 6-54 depicts the growth in colony size of targeted iPSCs. Once the colonies were large enough, they were manually picked using a p20 pipette and re-seeded individually into a 96-well plate. The individual clones were expanded until they were large enough to extract genomic DNA from. At this stage, the clones could be screened using PCR amplification.

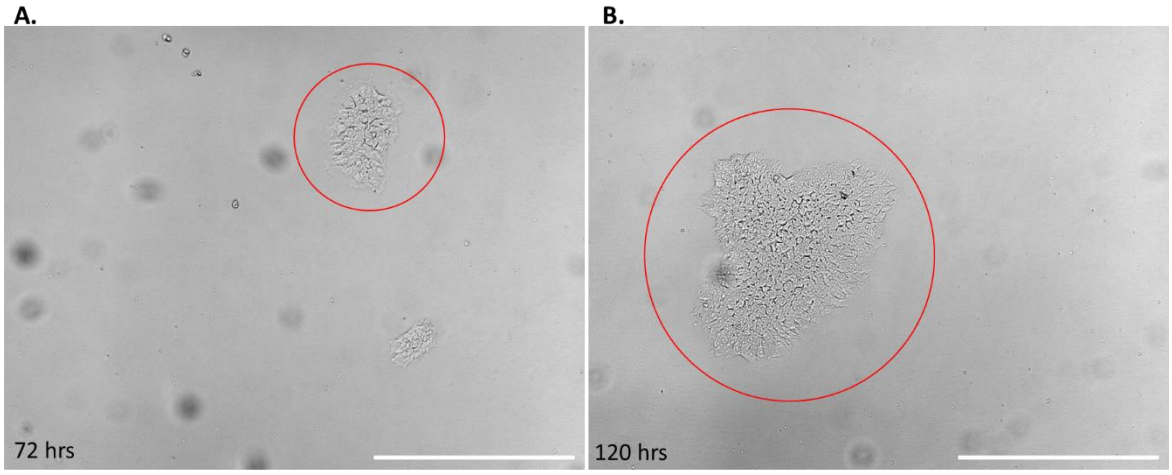

Figure 6-54. Colony growth of SNORD116 targeted iPSCs.
A. IPSC colony after 72 hours of growth in puromycin (96 hours post-transfection).
B. IPSC colony after 120 hours of growth in puromycin (144 hours post-transfection).
Scale bar = 500um.

Firstly, gDNA from all puromycin-resistant clones was pooled to generate a mixed targeted selected population. Primer pairs were designed that would amplify a 1,340bp region within the cassette to confirm integration of the cassette into the genome.

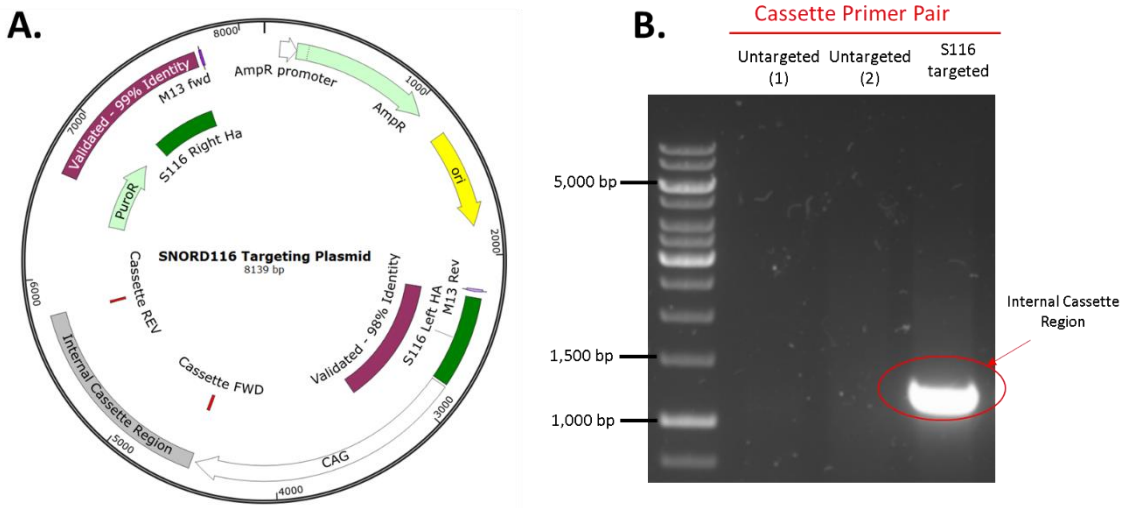

Figure 6-55. Isolation of the selection cassette from gDNA of targeted iPSCs.
A. Targeting plasmid with the internal selection cassette and its PCR primers annotated in red.
B. Diagnostic gel of gDNA isolated from two untargeted populations and the mixed targeted population amplified using the cassette primer pair.

These results indicate that the selection cassette had been integrated into cells within the targeted population, but this may be due to random integration or amplification of the plasmid. To screen for targeted integration, primer pairs were designed that would amplify a region of the genome spanning from outside the left arm of homology across to the inside onside of the selection cassette i.e. across the 5' or upstream target site. Four primer pairs were designed. Genomic DNA from two separate untargeted populations and the mixed targeted populations were screened. The resulting diagnostic gels are shown in Figure 6-56. Unfortunately, none of the primer pairs were able to amplify a band that was unique to the SNORD116 targeted population.

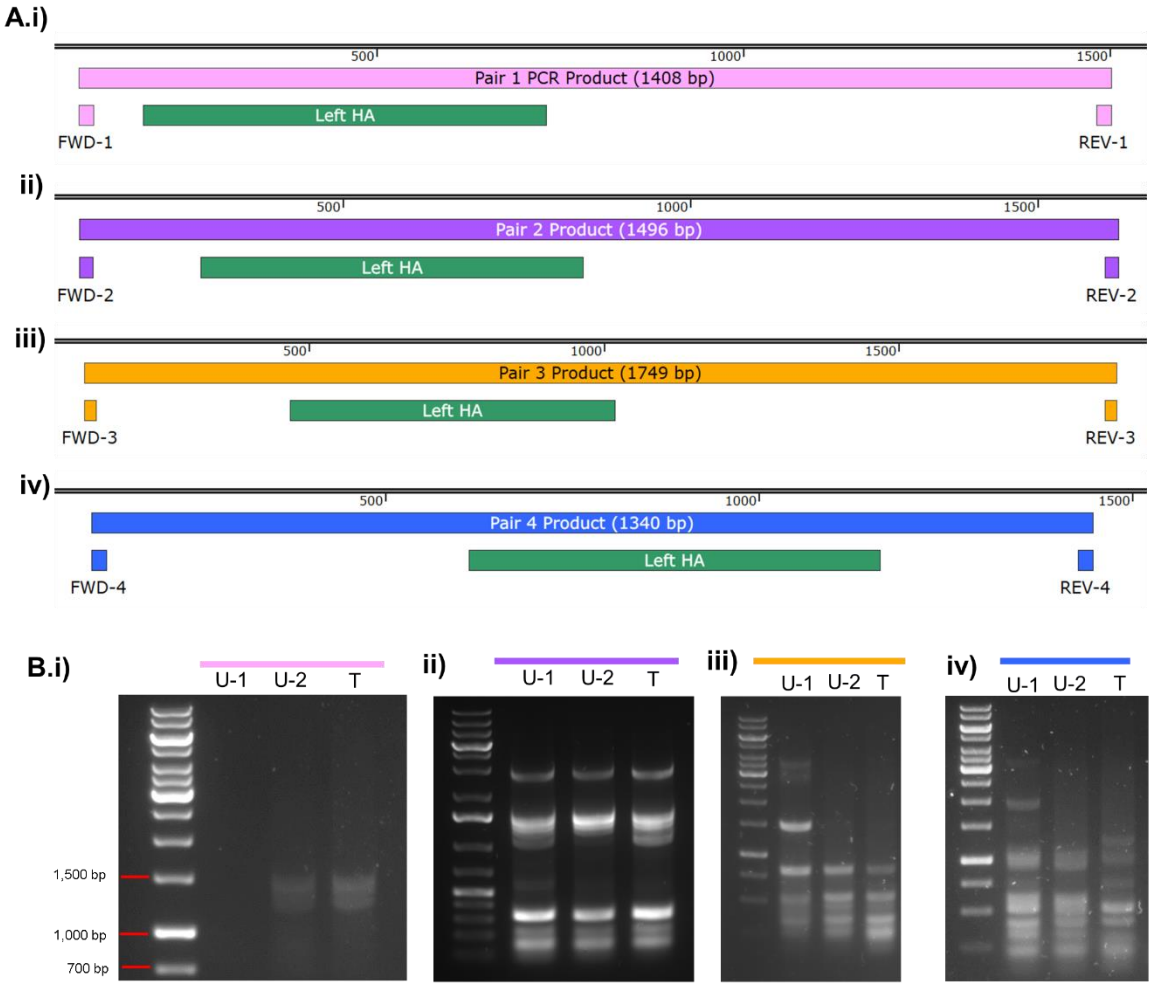

Figure 6-56. Screening for 5' integration of the selection cassette.
A. Sequence map showing the forward and reverse primers and PCR products resulting from (i-iv) primer pairs 1-4.
B. Diagnostic digest showing the PCR amplification of gDNA isolated from two untargeted populations (U1 and U2) and the S116 targeted mixed population (T) using primers pairs (i-iv) 1-4.

As an alternative strategy, primer pairs were designed to amplify the region from inside the cassette across to the outside of the right arm of homology, i.e. the 3’ or downstream target site. Two primer pairs were designed. The diagnostic gels are shown in Figure 6-57. Neither of the primer pairs were capable of producing a band.

As both the 5’ and 3’ screening primer sets failed to generate a unique band in the targeted population, a primer pair was designed that spanned from outside the left HA across the selection cassette to outside the right HA. This arm-spanning PCR product would total 6072 bp in length. The resulting PCR is shown in Figure 6-58. Unfortunately, this primer pair also failed to generate a unique band in the SNORD116 targeted population, and no bands larger than 6 kb was produced. This could suggest that 6kb is too long a product to be generated by PCR, or the selection cassette was not integrated into the SNORD116 at the targeted cut sites.

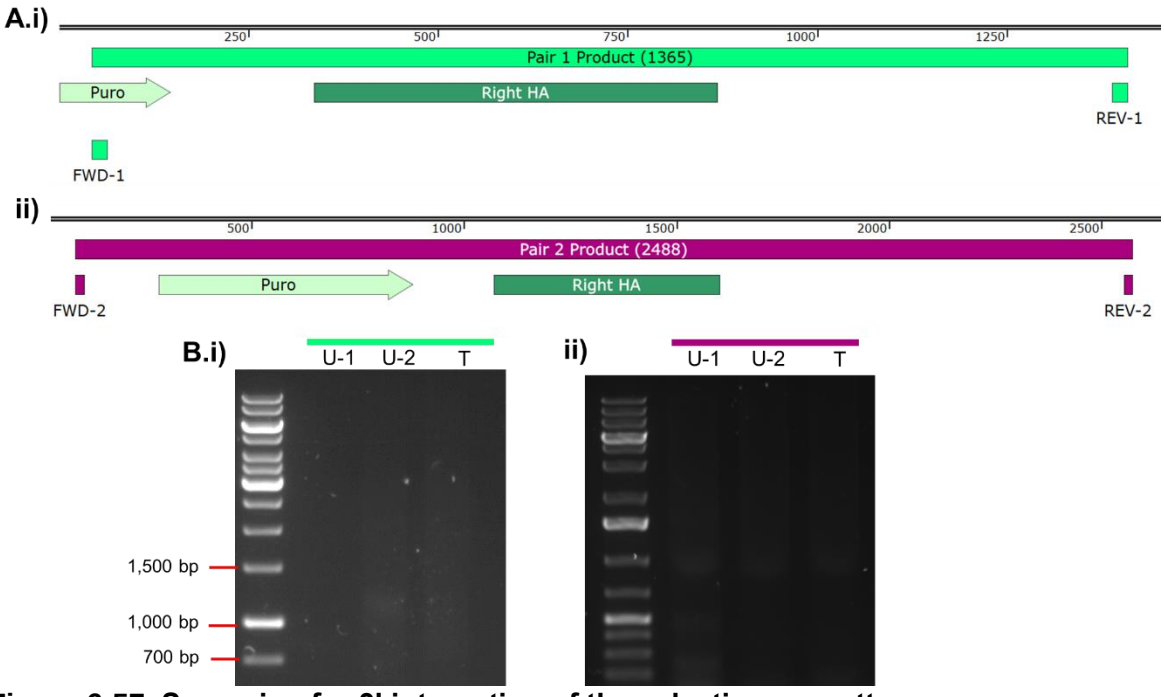

Figure 6-57. Screening for 3’ integration of the selection cassette.
A. Sequence map showing the forward and reverse primers and PCR products resulting from (i) primer pair 1 and (ii) primer pair 2.
B. Diagnostic digest showing the PCR amplification of gDNA isolated from two untargeted populations (U1 and U2) and the S116 targeted mixed population (T) using (i) primer pair 1 and (ii) primer pair 2.

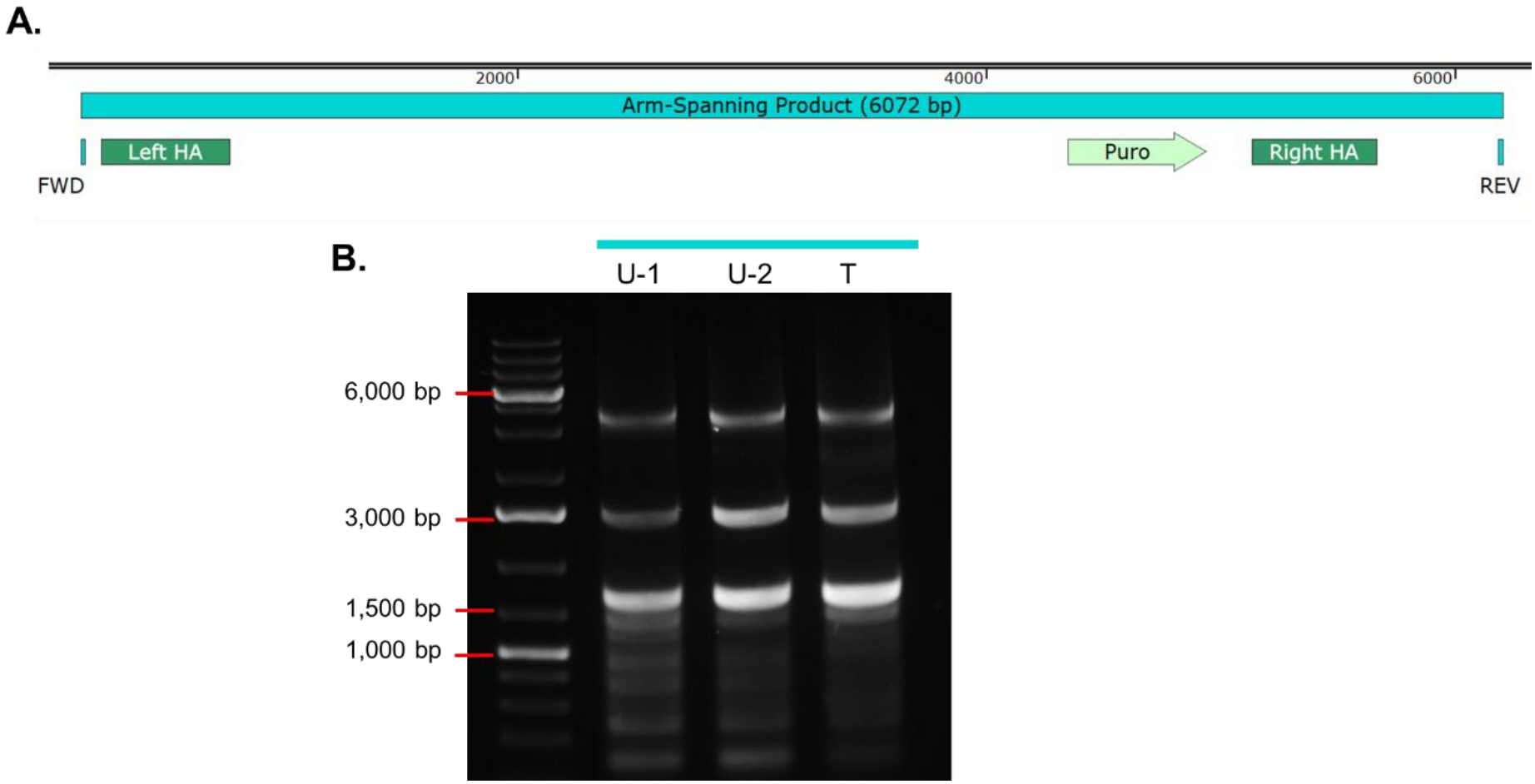

Figure 6-58. Screening for the integration of the selection cassette across both arms of homology.
A. Sequence map showing the forward and reverse primers and PCR product
B. Diagnostic digest showing the PCR amplification of gDNA isolated from untargeted populations (U1 and U2) and the S116 targeted mixed population (T) using the primers shown in (A).

It was also possible that off-target primer binding in the mixed population was generating large amounts of PCR products that were obscuring any unique bands from targeted gDNA. Therefore, individual clones were screened for cassette integration. A total of 9 clones survived to the point of gDNA isolation. The clones were first screened for the presence of the internal selection cassette region. All clones except clone 6 and clone 9 contained the selection cassette region, as shown in Figure 6-59. Clones 1-5, 7 and 8 were then screened using the 5' primer pair 1. Unfortunately, none of the clones generated a unique band suggesting that SNORD116 targeting had not been successful in these clones.

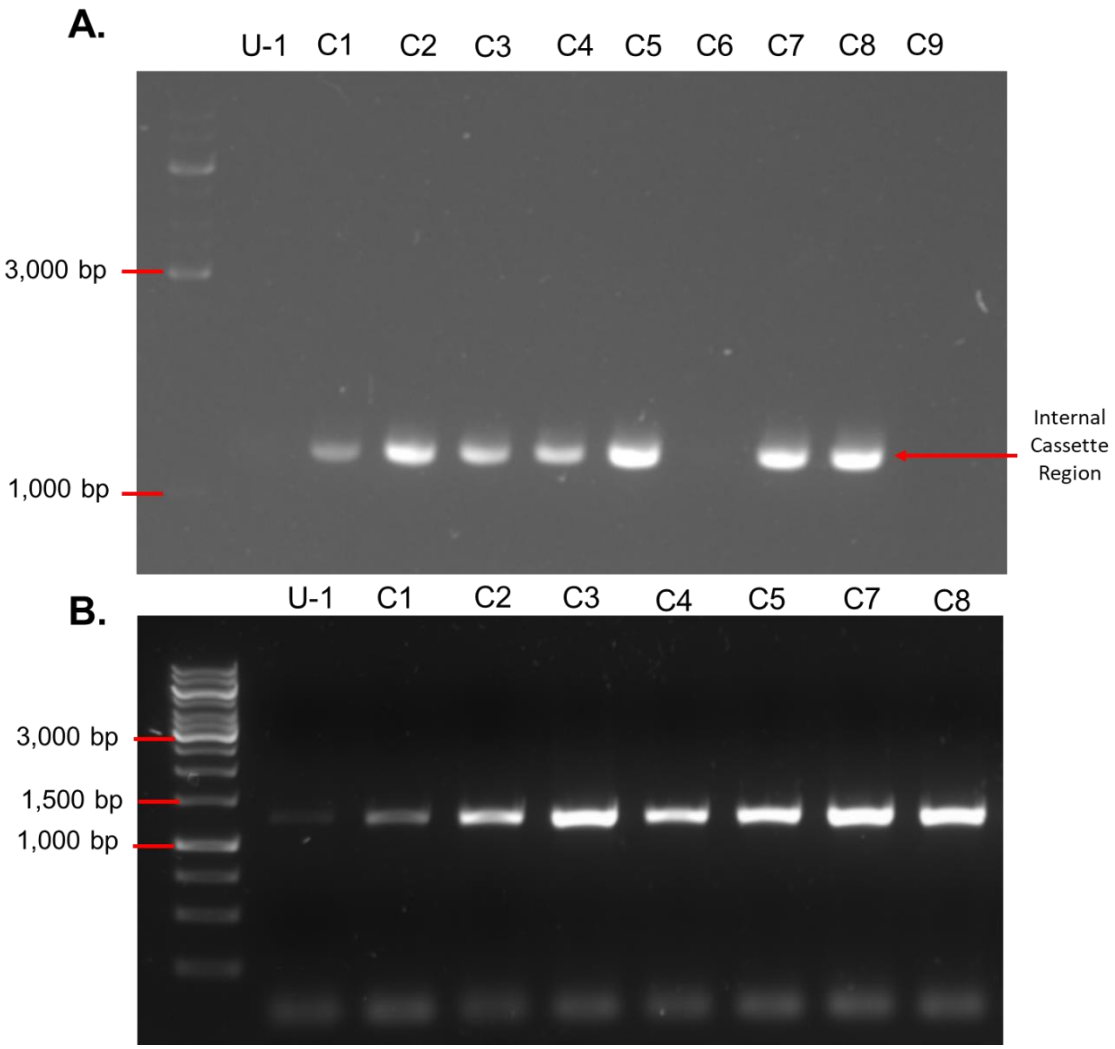

Figure 6-59. Individual clone screening.
A. Screening of SNORD116 targeted clones using the internal cassette region primer pair. B. Screening of clones using the 5' primer pair 1. U = untransfected, C = targeted clone.

As the clones did generate a PCR product that corresponded to the correct band size for the screening primer, this suggested the potential of contamination in the untargeted genomic DNA sample. Therefore, the untargeted cells and clones were lysed for RNA to screen for loss SNORD116 expression. The results presented in Figure 6-60 show that none of the clones appear to have reduced SNORD116 expression.

To summarise the result of this section, a targeting plasmid and guide plasmids for CRISPR-Cas9 knockout of SNORD116 were designed and validated. IPSCs were transfected by nucleofection and puromycin selection was successful in eliminating cells that had not taken up the selection plasmid. However, after selection and clonal expansion was carried out, no conclusive evidence was found indicating successful integration of the selection cassette into the target site. Other groups have since successfully developed SNORD116 knockout iPSC lines that could be used as an alternative approach (Tai *et al.,* publication in review).

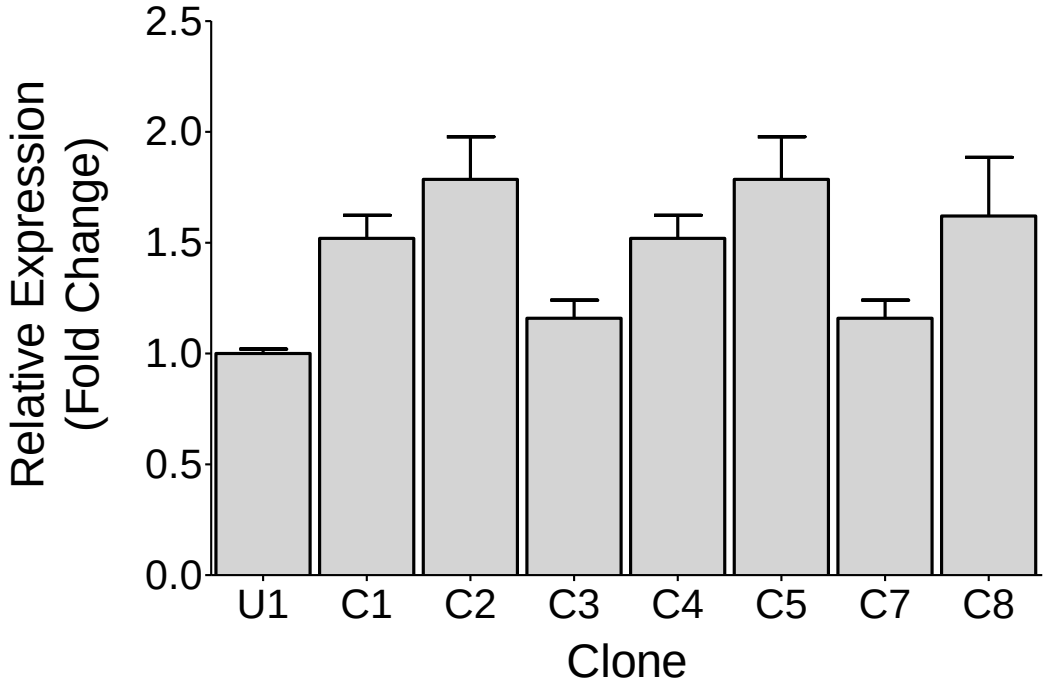

Figure 6-60. RT-qPCR screening of SNORD116 clones.
Expression of SNORD116 measured by RT-qPCR using the SNORD116-1 primer pair. Calculated as fold change relative to the untargeted sample by ddCt method, normalised to GAPDH.

6.4 Discussion

The aim of this chapter was to evaluate the effect of modulating SNORD116 expression in cardiac cells in order to ascertain its function in a cardiac context. Expression modulation is a useful strategy in the investigation into the function of a novel gene. Results from previous chapters demonstrate that SNORD116 appears to play a role in cardiac development and response to stress, however the target and mechanism behind this role was unclear. Modulating the expression of SNORD116 was important in determining the specific pathways and targets that SNORD116 interacts with. However, in the case of SNORD116, this was no simple task. As discussed previously, there are 30 different paralogue sequences within the SNORD116 cluster, very few of which share 100% sequence identity. Choosing a strategy of expression modulation that encompassed all 30 paralogues of SNORD116 presented a practical challenge.

One strategy to overcome this was to overexpress SNORD116 using a publicly available and validated overexpression vector. This plasmid had been previously used to overexpress SNORD116 in human cells in the context of researching human disease (407). In addition to this, the mouse SNORD116 sequence present in the overexpression plasmid is at least 75% identical to 21 of the 30 human paralogues and contains the conserved C and D boxes that are important in canonical snoRNA function. Therefore, this plasmid was used in the overexpression of SNORD116. However, the presence of mouse sequences within the plasmid present a risk of interference within human cells, and it is possible that some of the effects produced by the plasmid transfection are caused by these non-human sequences. This notwithstanding, the non-human sequences encoded on the plasmid make up a minority of the total transcript according to the original authors (407). Therefore, due to the overwhelming similarity between the mouse and human transcripts,

this risk was considered acceptable although may limit the scope of the results.

The results of this chapter demonstrate that the MBII85 plasmid was successfully transfected into human cells and was effective in causing SNORD116 overexpression. Overexpression of SNORD116 as a result of MBII85 transfection was 3-fold higher than controls. Transfection efficiency was assessed using the transfection of a commercial GFP plasmid. However, although providing an approximation of transfection efficiency, differences in plasmid size may have resulted in a different transfection efficiency.

RNAseq data showed that the overexpression of SNORD116 in iPSC-CMs affected a number of cardiomyopathy-related gene pathways. This supports previous findings that SNORD116 is involved the response to cardiac stress, as it demonstrates the capacity to modulate the expression of genes important to the function of the heart. Similar pathways were also affected on a proteomic level, as proteins such as *MYH6*, *MYH7*, *MYL2* and MYL4 were downregulated at an RNA and protein level by SNORD116 overexpression. Predictive pathway analysis suggested that cardiac hypertrophy and dilated cardiomyopathy signalling was activated in response to SNORD116 overexpression. Aligning with this, contraction analysis indicated that SNORD116 overexpression may have reduced the contraction frequency of cardiomyocytes and increased the contraction amplitude, which may further reflect a hypertrophic response to SNORD116 overexpression. The effect on contraction may be due to the changes in sarcomeric gene expression seen on both an mRNA and protein level.

Transcriptomic and proteomic pathway analysis also suggested multiple key signalling pathways such as TGFβ signalling, HIPPO signalling and mTOR signalling had been activated by SNORD116 overexpression. TGFβ

signalling is a classic signalling pathway important in the response of cardiac cells to stress and is typically elevated in heart disease (223,413–415). The HIPPO signalling pathway is a widely established regulator of organ size (416,417), and contributes to cardiac development by restricting cardiomyocyte proliferation (418,419). The mTOR pathway is also a widely established component of the cardiac stress response (420–423) and is also known to be a regulator of metabolism in cardiac cells (424,425). This is of particular interest, as the metabolism of cardiac cells does appear to be affected by SNORD116 overexpression.

Proteomics results revealed that multiple proteins important in the metabolism of glucose were reduced upon SNORD116 overexpression. By contrast, transcriptomic data showed that many of these genes were in fact upregulated by SNORD116 overexpression. Both RNA and protein extraction occurred 72-hours post-transfection. As gene expression changes typically occur on a much faster timescale than protein changes, the discrepancy between the transcriptomic and proteomic dataset could reflect a compensatory upregulation of glycolysis-related genes to counteract their reduction at a protein level. Functionally, glucose metabolism in cardiomyocytes was reduced in response to SNORD116 overexpression, as shown by Seahorse analysis. This reduction in glucose metabolism may have caused an energy deficit that could have contributed to the apparent reduction in contraction frequency. In addition, the rate of glucose metabolism by cardiac fibroblasts also appeared reduced when SNORD116 was overexpressed. Proteins important in glucose metabolism were also downregulated upon SNORD116 overexpression in neural cells. These observations indicate that SNORD116 is capable of modulating glucose metabolism and appears overall inhibitory to the breakdown of glucose in multiple different cell types.

In addition to reducing glucose metabolism, SNORD116 overexpression caused a dramatic downregulation of PKP1 protein levels, which presented *PKP1* as a potential primary target of SNORD116. Data mined from SNORD116 overexpression in hiPSC-CMs, SNORD116 knock-out in mouse cartilage and predictive bioinformatic targeting software was collated together. Despite using different systems of expression modulation in different tissues from different species, *PKP1* was still the only target conserved across the datasets. This suggests that SNORD116 may target *PKP1* not just in cardiomyocytes, but in multiple tissues.

Sequence interrogation revealed a potential 14-base pair binding interaction between SNORD116 and PKP1 mRNA. The binding of SNORD116 to PKP1 mRNA could cause the inhibition of PKP1 translation, thus leading to the reduction of PKP1 protein when SNORD116 is overexpressed. The unchanged levels of PKP1 in the transcriptomic results suggest that the SNORD116-PKP1 binding interaction is non-destructive, allowing the sequencing of PKP1 mRNA to be unaffected. PKP1 protein expression was not detected in the proteomic analysis of neural cells. This could be due to the naturally low expression of *PKP1* in brain tissue combined with the low amount of protein inputted into the mass spectrometry analysis. However, glucose metabolism was still reduced by SNORD116 overexpression. This could indicate that the modulation of glucose metabolism by SNORD116 occurs independently of the targeting of PKP1. However, an alternative explanation is that PKP1 was targeted by SNORD116 which did result in the reduction of glycolysis-related proteins, but the levels of PKP1 protein were too low to be detectable by mass spectrometry, and so only the consequence of the interaction was reflected in the results. The amount of protein analysed in the neural overexpression samples was 4-8 ug which is significantly lower than the optimal for mass spectrometry (>20 ug), which likely contributed to the low number of significantly differentially expressed proteins and wide variation between replicates.

Upon further investigation into the role of PKP1 in cardiac cell types, immunocytochemistry revealed that PKP1 expression was largely perinuclear in stem cells, with a very similar expression pattern displayed by PKP2. However, as the stem cells differentiated down a cardiac mesoderm pathway, the ratio of nuclear to perinuclear expression increased. Day 30 cardiomyocytes displayed a mostly nuclear expression pattern of PKP1. This heavily contrasted with the expression of PKP2 in day 30 cardiomyocytes, which appeared far more diffused throughout the nucleus, cytoplasm and membrane. PKP1 expression has previously been shown to translocate to the nucleus upon Wnt signalling during tooth development (426). As Wnt signalling activation is a key component during the initiation of cardiomyocyte differentiation, this may explain the apparent localisation of PKP1 to the nucleus by day two of the differentiation. Further Wnt activation through CHIR supplementation in later-stage cardiomyocytes did not affect the localisation pattern. Overall, in cardiac cells, the role of PKP1 appears to be specific to the nucleus which could suggest its function as a transcriptional regulator. Future experiments could improve upon this assay by using pre-fixation triton treatment to improve the clarity of signal from desmosomal proteins (427,428).

Public databanks were analysed, and RT-qPCR was performed to analyse the expression profile of plakophilin across various tissues. The key findings from these results showed that PKP1 showed low expression in the majority of tissues analysed. However, previous RNAseq results from iPSC-CM differentiation could be mined to explore how plakophilin expression changes during cardiac development.

Western blotting was carried out to analyse the expression of PKP1 during differentiation and in response to SNORD116 overexpression. These western blots produced bands around 65kDa. However, other

publications have shown PKP1 to produce bands closer to 75kDa (429,430). The difference in size may be due to differences in sample preparation or protein extraction. Future results could be improved by the use of a different antibody and a positive PKP1 control sample.

An alternative strategy to overexpressing a gene is the employment of genetic modification tools to remove it from the genome so that it can no longer be expressed. In pursuit of this, CRISPR-Cas9 is a widely-used tool for generating knock-out lines. As previously stated, there are 30 different paralogues of SNORD116. To ensure the complete knock-out of all SNORD116 paralogues, the entire cluster should be removed from the genome. This had been achieved previously in a human neuroblastoma cell line (51) but until very recently had not been achieved in human iPSCs. To achieve this required the design of two Cas9 gRNA sequences to target upstream and downstream of the SNORD116 cluster. To allow for selection of targeted cells, a targeting plasmid containing a puromycin resistance selection cassette flanked by regions of homology was designed. Upon transfection of stem cells with the necessary plasmids, puromycin-resistant clones were isolated for screening.

Only 9 individual clones survived the clonal expansion phase. Of these 9, 7 contained the selection cassette. However, none of these clones showed definitive evidence that the selection cassette has been integrated into the target site. Random integration can account for the off-target integration of the selection cassette (431). However, contamination of the untargeted genomic DNA sample may have led to deceptive screening results, therefore RT-qPCR was employed as an alternative screening strategy. However, these results failed to identify a clone with reduced SNORD116 expression. This is not an ideal screening strategy, as targeting and clonal expansion could affect the expression of SNORD116. Furthermore, SNORD116 has the additional caveat of being paternally imprinted, which means that even if successful knockout had occurred on

one chromosome, it will not affect SNORD116 expression unless it is removed specifically from the paternal chromosome. Ultimately, the most reliable screening strategy would have been to send each individual clone for sequencing at the target locus. However, cost and time restraints prevented further development in this area.

Clonal survival was generally low after targeting. Nucleofection, CRISPR-Cas9 targeting and clonal isolation and expansion subject iPSCs to stressful conditions that increase the likelihood of cell death. In addition, it may be possible that the absence of SNORD116 expression may impact stem cell survivability and growth rate as SNORD116 has been shown in previous chapters to affect glucose metabolism among other key signalling pathways. These factors may have reduced the chances of isolating a correctly targeted clone. Modifying culture conditions such as the use of pro-survival reagents like CloneR (432) or changing the post-transfection seeding density (433) have been shown to improve survival after transfection. Conditions of the transfection such as plasmid concentration could be optimised to improve targeting efficiency. Alternatively, different gRNAs may need to be designed to improve binding of the RNP, or switching to a single-guide approach coupled with the insertion of a stop codon to prevent expression of the cluster instead of its removal entirely. This strategy of CRISPR-Cas9 mediated genome editing to generate knock-out iPSC lines had been used successfully in many different contexts (432,434,435). Modification of the targeting strategy coupled with improved iPSC clonal culture techniques would improve the probability of successfully generating a SNORD116 iPSC knock-out line.

Overall, SNORD116 has been shown to be involved in metabolic and cardiomyopathy pathways, and the potential target PKP1 has been uncovered. However, the majority of the work completed so far has been carried out with *in vitro* cell models. These models have many advantages

including ease of culture and expression modulation. However, it was important to integrate clinical research in order to strengthen the findings of this work and fully explore the potential role of SNORD116 in heart disease.

Chapter 7 The expression of SNORD116 in HCM patient samples

7.1 Introduction

The results presented so far have been gathered using mostly iPSC-derived cell models to investigate the role of SNORD116 in the heart. However, it is necessary to emphasise the importance of integrating these results with data gathered from clinical samples. This will provide a greater insight into the relationship between SNORD116 and heart disease and enhances the clinical relevance of these findings. Moreover, it will be important in determining if SNORD116 or its specific paralogues could be used as biomarkers of heart disease states.

Within the Norfolk and Norwich University hospital cardiology department is the inherited cardiac conditions service run by Dr Sunil Nair and specialist nurses Emma Hughes and Caroline Hall. Collaboration with their team and the UEA Biorepository has allowed access to blood samples taken from patients diagnosed with HCM. Although patient information has been completely anonymised, details such as age, gender, symptoms, and in some cases genotype have been included in the results. The serum was analysed for the presence of SNORD116, and the white blood cells were analysed for inflammatory markers. These results were integrated with the anonymised patient information to explore the relationship between circulating SNORD116 levels and HCM.

7.2 HCM patient sample background

Cardiology outpatients were assessed in the inherited cardiac conditions clinic. A summary of patient information is shown in Table 7-1. The background of each patient was recorded which included age, sex, family history of HCM, and the presence of any co-morbidities. Four of the six patients were older than 60 years. The youngest patient was 48 years old, and the oldest was 72. Three of the patients had no reported family history of HCM, the others had reported HCM in a direct male family member. Five of the six patients were male. All of the patients had some form of co-morbidity. Two of the patients had suffered a past stroke and one patient was on immunosuppressants to treat an inflammatory disease. All but one of the patients exhibited left ventricular hypertrophy (LVH) that was otherwise unexplained. Only one of the six patients suffered with syncope. Morphology was classed as asymmetric septal for three of the six patients, apical for one, septal for one and undefined for one. Three of the six patients showed electrocardiogram (ECG) evidence for LVH, three did not. The maximum wall thickness in millimetres was measured for all patients. This ranged from 16mm to 30mm. The left atrial size was only measured for three of the patients and was reported as 39mm, 41mm and 48mm. The left ventricle diameter was only measured for two patients and was reported as 49/32 mm and 40/29 mm. The left ventricular outflow tract pressure gradient (LVOT grad) was measured in three of the patients as 10mmHg, 12-52mmHg and 113mmHg. Only one of the six patients reported non-sustained ventricular tachycardia (VT) in the form of ventricular fibrillation (VF) arrest. Four of the six patients displayed left ventricular fibrosis through cardiac magnetic resonance (CMR). Two of the patients were found to be positive for a HCM-associated genetic variant, one patient had a *MYBPC3* c.3713T>C substitution and one patient had a *MYBPC3* c.2716 deletion. The genotype results for the remaining four patients had not been revealed at time of writing.

Table 7-1. HCM Patient Information.
Patient information corresponding to each sample is listed. Information that is unknown or not gathered is denoted by "-".

Sample	Family History	Age (yrs)	Sex	Co-morbitisies	Un-explained LVH	Presence of Syncope	Morphology	ECG Evidence LVH	Max wall thickness (mm)	Left atrial size (mm)	Left ventricle Diameter (end diastolic / end systolic) (mm)	Max LVOT grad (mmHg)	Non-sustained VT?	LV Fibrosis on CMR	Genetics
HCM-1	Non	72	M	CVA	Yes	No	Septal	-	16	41	-	None	VF arrest	Yes	MYBPC3 3713T>C (Leu1238>Pro)
HCM-2	None	56	M	Ankylosing spondylitis	Yes	No	Asymmetrical septal	-	25	39	49 / 32	10	No	Patchy enhancement on CMR	MYBPC3 2716 del (Val906Trpfs)
HCM-3	Possible HCM in brother	48	M	Cerebellar stroke 2020	Yes	No	Asymmetrical septal (ASH)	Yes	30	48	40 / 29	12 (prev peak 52)	No	Patchy enhancement basal / anterior / septal	Results Pending
HCM-4	None	66	F	Hypothyroidism, rheumatoid arthritis (on methotrexate)	Yes	No	Asymmetrical septal (ASH)	Yes	21mm	-	-	113	No	Yes	Results Pending
HCM-5	LVH and LV Impairment in father	62	M	HTN, paraprotein anaemia, mild coronary disease	-	Yes	Apical	Yes	17mm	-	-	-	No	No	Results Pending
HCM-6	Brother died age 14 in sleep due to heart condition	62	M	Peripheral arterial disease, COPD	Yes	No		No	16mm	-	-	Nil	No	No	Results Pending

7.3 Levels of circulating SNORD116 in HCM patient serum

The blood of six HCM patients was harvested into EDTA collection tubes. Approximately 6mL of blood was harvested per patient. Blood samples were also taken from two separate individuals (both male, ages 58 and 54) with no history of cardiac disease to provide healthy controls. The blood was separated by histopaque and ultracentrifugation. The serum was isolated, aliquoted and frozen at -80^{o}C until analysis. Serum samples were lysed directly to provide whole serum RNA. In addition, exosomes were isolated from the serum and lysed using the ExoQuick serum isolation and RNA extraction kit (System Biosciences). Expression was analysed using RT-qPCR. The results are shown in Figure 7-1.

Looking firstly at whole serum RNA, SNORD116-1 is found at similar levels to the control samples in most of the HCM samples. HCM-1 and HCM-2, the two samples with known HCM-causing genetic variants, express SNORD116-1 at 0.2±0.4-fold and 0.3±0.3-fold relative to control-1. Control-2, HCM-3, HCM-4 and HCM-6 are within 0.5-fold of control-1 expression levels. HCM-5 is the only sample that appears to have increased SNORD116-1 at 8.2±1.1-fold of control-1. SNORD116-23 is lower in all samples relative to control-1. SNORD116-23 is decreased to less than 0.2-fold of control-1 levels in control-2, HCM-2, HCM-3, HCM-4 and HCM-6. In HCM-1 and HCM-5, SNORD116-23 is decreased by 0.4±0.1-fold and 0.8±0.2-fold, respectively. SNORD116-25 is increased 6.2±1.1-fold and 3.4±2.5-fold in HCM-5 and HCM-6, but is otherwise within 0.5-fold of control-1 expression levels.

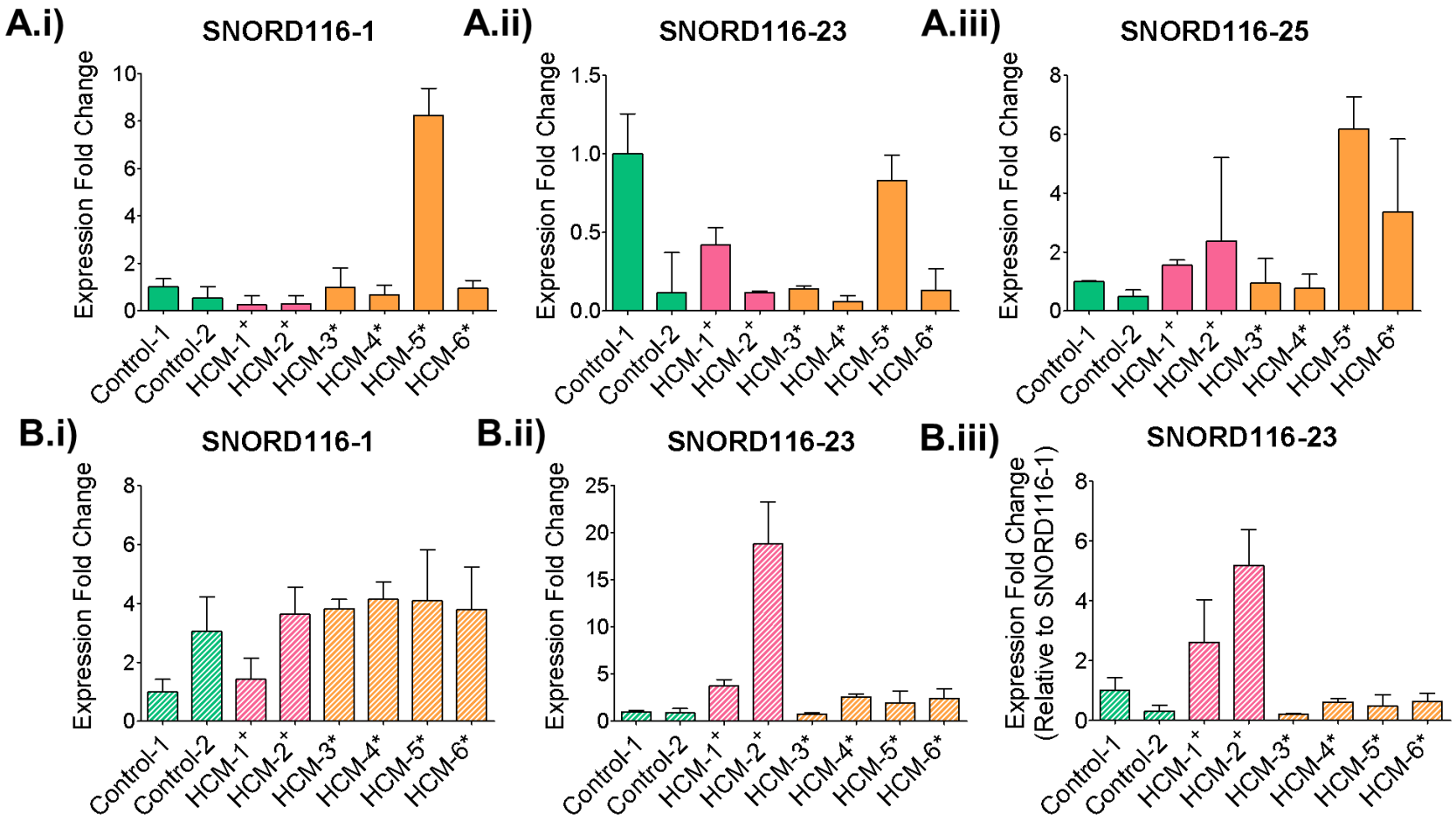

Figure 7-1. Relative levels of circulating SNORD116 in the serum of HCM patients.

A. Expression of SNORD116- (i) 1, (ii) 23 and (iii) 25 in the whole serum of HCM patient blood and non-HCM controls.

B. Expression of SNORD116- (i) 1 and (ii) 23 in the exosomes of serum isolated from HCM patient blood and non-HCM controls. (iii) SNORD116-23 exosome expression relative to SNORD116-1

Expression calculated as fold change using the ddCT method relative to control sample 1, normalised to 18S (or SNORD116-1). N=3 (technical), error bars represent SEM.+ = HCM patients with a known mutation, * = HCM patients with no known genotype information.

When analysing serum exosome RNA, SNORD116-25 was not detectable in any of the samples tested. Relative to control-1, SNORD116-1 was increased by 4±2-fold in HCM-2, HCM-3, HCM-4, HCM-5 and HCM-6. SNORD116-1 was also increased by 3±1-fold in control-2 relative to control-1. SNORD116-1 was unchanged in HCM-1 relative to control-1. When normalised to 18S, SNORD116-23 was present at similar levels in control-1, control-2 and HCM-3. However, SNORD116-23 was 2±1-fold higher in HCM-4, HCM-5 and HCM-6. In HCM-1 and HCM-2, the samples from patients with confirmed HCM-causing genetic variants, SNORD116-23 was increased by 4±1-fold and 19±4-fold respectively. Interestingly, when SNORD116-23 levels were normalised to SNORD116-1 levels, SNORD116-23 was still highest in HCM-1 and HCM-2 by 3±1-fold and 5±1-fold respectively. However, when normalised to SNORD116-1 and relative to control-1, SNORD116-23 was 0.3±0.2-fold lower in control-2 and HCM-3. HCM-4, HCM-5 and HCM-6 showed SNORD116-23 levels that were within 0.5-fold of control-1 when normalised to SNORD116-1.

Overall, expression levels of the different SNORD116 paralogues appears highly variable between different samples. In whole serum RNA, SNORD116 appears mostly downregulated in HCM patient blood relative to healthy controls. The exception to this trend is SNORD116-25, which is upregulated in four of the six HCM samples relative to the control samples. SNORD116-23 is also expressed most highly of all samples in control-1 but is comparatively downregulated in the control-2 sample. The whole serum RNA analysis shows the greatest level of variation between samples. When isolating exosomal RNA expression, there is less variability between samples. SNORD116-1 is expressed at relatively similar levels across the samples except in control-1 and HCM-1, where it appears downregulated. However, SNORD116-23 shows an interesting trend of upregulation across the HCM samples relative to the controls, particularly in the samples with known HCM-causing genetic variants. To link SNORD116 expression with the health of the patient, markers of inflammation were invested in the blood samples.

7.4 Inflammatory markers in HCM patient blood

In addition to analysing the serum, the white blood cell population was also analysed to investigate the prevalence of inflammation among the HCM patients. Flow cytometry was used to characterise different white blood cell populations in HCM patient blood based on CD14 and CD16 marker expression. CD14 is a marker expressed generally by monocytes in the peripheral blood cell population (436). Monocytes that are both CD14-positive and CD16-positive represent monocytes that have been activated into macrophages (437). The three different classes of monocyte populations based on CD14 and CD16 expression are classical monocytes (CD14+/CD16-), intermediate monocytes or macrophages (CD14+/ CD16+) and non-classical monocytes (CD14-/CD16+) (438,439).

A FITC-conjugated anti-CD14 antibody was used to stain CD14-positive cells, and an APC-conjugated anti-CD16 antibody was used to stain cells expressing CD16. Unstained and single-stained populations were used to set the gates for each sample. Example gating is shown in Figure 7-2. The proportion of each cell population (non-monocyte, classical monocyte, macrophage and non-classical monocyte) was calculated as a percentage of the total cell population. The results are shown in Figure 7-3.

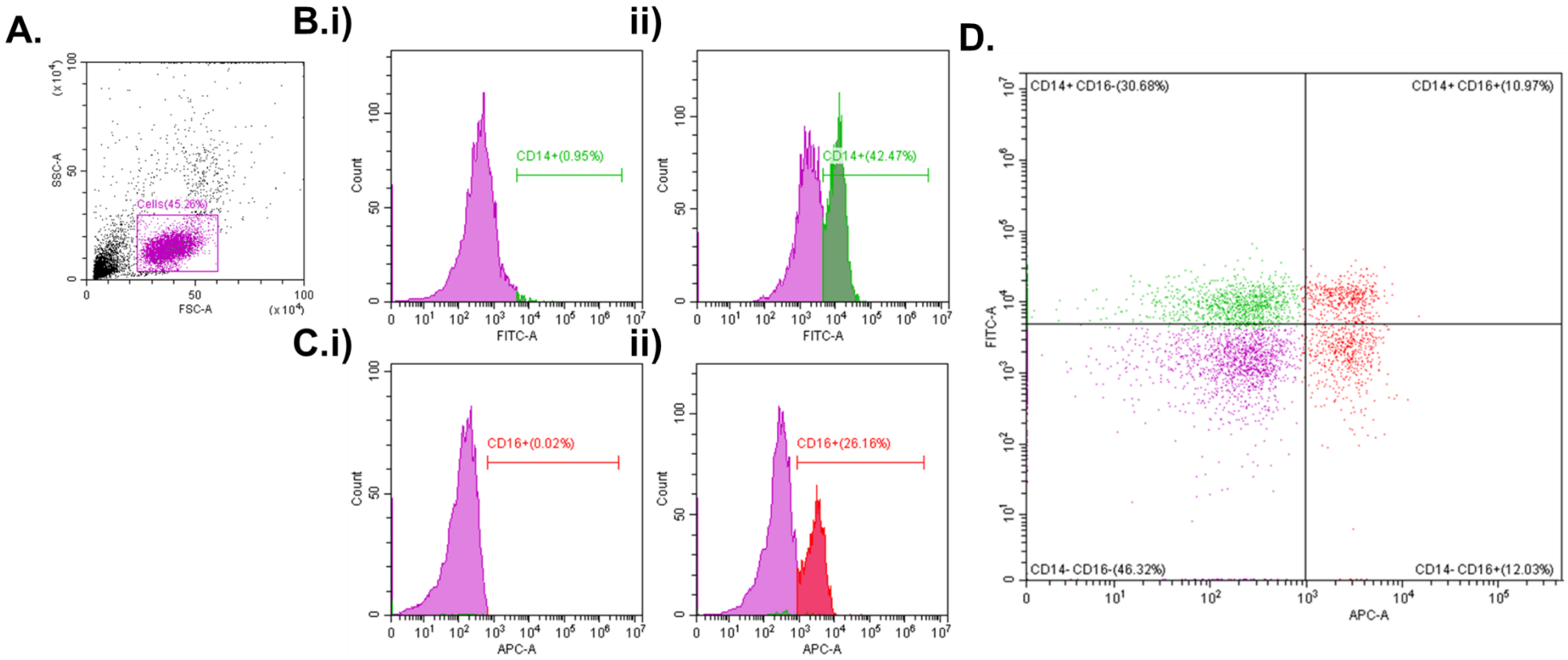

Figure 7-2. Gating HCM blood samples for flow cytometry analysis.
A. Forward and side scatter used to isolate the cell population
B. FITC fluorescence used to gate the CD14+ cells in an (i) unstained versus (ii) CD14 stained population
C. APC fluorescence used to gate the CD16+ cells in an (i) unstained versus (ii) CD16 stained population
D. Usage of the gate to define the double negative, CD14 single-positive, CD16 single positive and double populations of dual-stained cells.

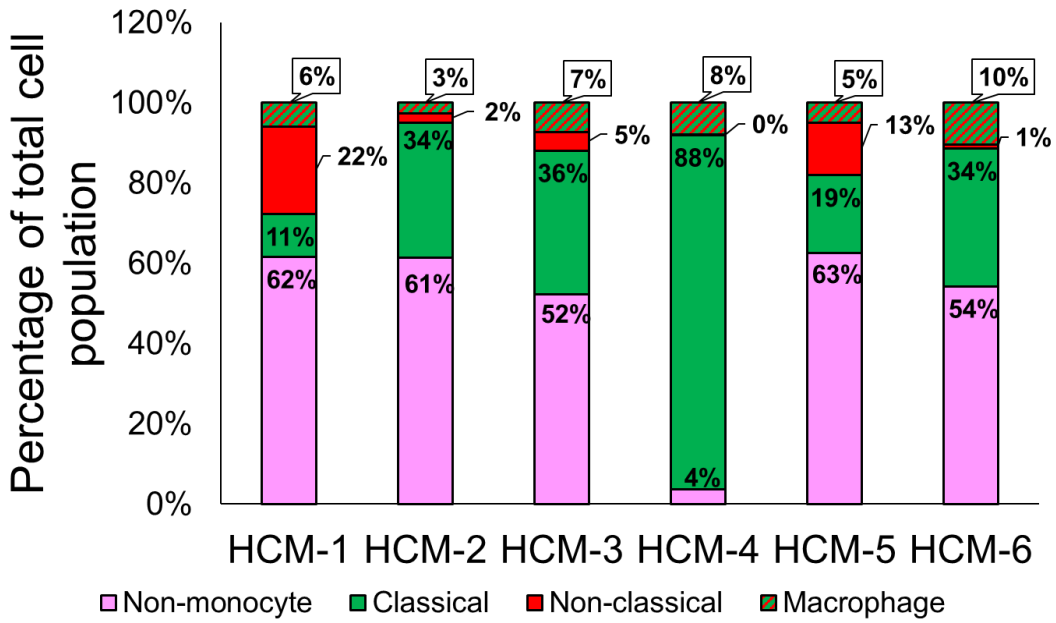

Figure 7-3. Percentage of different cell populations within the white blood cells of HCM patients.
Isolated white blood cells were stained for CD14 and CD16. The percentage of each population based on the expression of these markers was calculated for each blood sample. Non-monocyte = CD14-/CD16-, Classical = CD14+/CD16-, Non-classical = CD14-/CD16+, Macrophage = CD14+/CD16+.

For the majority of the samples, the non-monocyte population was the largest of the four populations. The average size of the non-monocyte population across the HCM samples was 49±21%. The large variation stemmed from the outlier sample HCM-4 which only showed a non-monocyte population of 4%. For five out of six of the HCM samples, the second largest population was the classical monocyte population. This had an average size of 37±25%, again with variation stemming from HCM-4 sample which exhibited a classical monocyte population size of 88%. The average non-classical monocyte population was 7±8% of the total population in the HCM samples. HCM-1 and HCM-5 exhibited sizes of 22% and 13%, respectively, but the other samples produced proportions of <5% of the total cell population. The macrophage population was more consistently sized across the samples with an average of 6±2% of the total cell population. HCM-6 showed the biggest macrophage population at 10%. The smallest macrophage population was produced by HCM-2 which was 3% of the total cell population.

In addition to analysis by flow cytometry, the CD14+ population of white blood cells were isolated and lysed for RNA. The expression of tumour necrosis factor alpha (TNFa) and pentraxin-3 (PTX3) was analysed using RT-qPCR. The results are shown in Figure 7-4. Expression of TNFa was 1±0.1-fold and 1.2±0.2-fold for control-1 and control-2. However, relative to these levels, TNFa was upregulated in all the HCM samples. In HCM-1 and HCM-2, TNFa was upregulated 3±0.4-fold and 4±0.5-fold. In HCM-3 and HCM-4, TNFa was upregulated 8±0.5-fold and 7±1-fold. HCM-5 and HCM-6 showed the greatest level of upregulation at 13±0.7-fold and 21±11-fold respectively. Similar to TNFa, PTX3 was also upregulated in all the HCM samples relative to the control samples. HCM-4 and HCM-2 showed the smallest upregulation at 5±1-fold and 6±0.7-fold relative to control-1. HCM-1 and HCM-5 were upregulated 11±1-fold and 15±3-fold. HCM-3 and HCM-6 showed the greatest level of PTX3 upregulation at 27±1 and 41±24-fold relative to control levels.

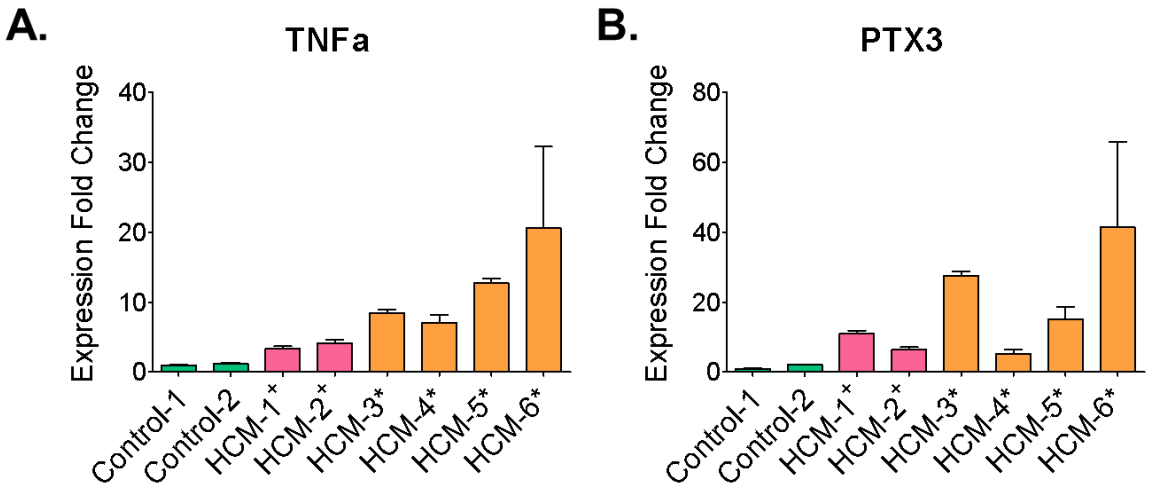

Figure 7-4. The expression of inflammation genes in CD14+ isolated blood cells. The expression fold change of (A) TNFa and (B) PTX3 in CD14-positive blood cells isolated from HCM patients and non-HCM controls. Calculated using the ddCt method relative to control-1, normalised to 18S. Error bars represent SEM of technical replicates.

Overall, gene expression data indicate that there is increased inflammatory gene expression in HCM monocytes compared to the control samples. All of the HCM samples exhibited CD14+ and CD14+/CD16+ monocyte populations to varying levels, which further supports the finding that HCM blood samples express markers of inflammation.

7.5 Discussion

The aim of this chapter was to investigate SNORD116 expression in clinical samples in order to better understand its role in the body. Blood samples from six HCM patients were analysed for SNORD116 levels. The average age of the patients tested was 60.6±8 years old, which is slightly older than the average patient diagnosed with HCM being of 51±16 years (440). Although, the average reported here reflects the age of the patient at the time of sample collection and not age at diagnosis. Five of the six HCM patients and both control patients were male, which is a more severe ratio than the average of 3:2 male: female HCM patients (440) Overall, this cohort does slightly deviate from the average age and gender of HCM patients, but limitations in patient recruitment and sample processing prevented expansion of the cohort size.

All patients were diagnosed with otherwise unexplained LVH or displayed ECG evidence of LVH, and five of the six patients displayed hypertrophic morphology classed as either apical, septal or asymmetric septal. All patients displayed a maximum wall thickness of ≥16mm, which is larger than the average of 13.6mm for a healthy male (441). These observations illustrate the HCM diagnosis and reinforce the cohort as representative of HCM. However, it is also important to note that all of the HCM patients exhibited at least one other pre-existing condition that may have contributed to the results collected.

Blood serum was analysed for whole serum RNA and exosome RNA, which produced strikingly different results. SNORD116-1 expression in whole serum RNA was generally within 0.5-1-fold of the control, except for HCM-1 and HCM-2 where it was downregulated ~0.2-fold, and HCM-5 where it was upregulated 8-fold. Increased expression of cytokines such as TNFa and PTX3 have previously been associated with HCM (442–444), therefore their expression in the clinical blood samples was analysed.

HCM-1 and HCM-2 both showed the lowest TNFa monocyte expression of the HCM samples and are also the only two samples with confirmed HCM-causing genetic variants. These factors may be linked to decreased whole serum SNORD116-1 expression. HCM-5 exhibited one of the highest expression levels of TNFa, which may explain why whole serum SNORD116-1 is upregulated. However, contrary to this HCM-6 also exhibited high TNFa expression but whole serum SNORD116-1 expression was comparable to control levels. In contrast to the whole serum expression levels, SNORD116-1 was expressed in exosomes approximately to comparable levels across all of the samples. This may suggest that SNORD116-1 packaged into exosomes plays a different role to SNORD116-1 non-specifically expressed in serum. It could also suggest that exosomal SNORD116-1 expression is not linked with inflammation or HCM.

SNORD116-23 shows a different expression pattern to SNORD116-1 in both whole serum and exosome-specific RNA. In whole serum, SNORD116-23 is notably decreased in most of the samples relative to control-1, including control-2. Unfortunately, with only two controls, there is no way to identify the outlier and is therefore difficult to comment on any HCM-specific trends. However, exosome-specific expression of SNORD116-23 is consistent across both controls. Five of the six HCM samples exhibit increased packaging of SNORD116-23 relative to the controls. The highest levels of SNORD116-23 were seen in the two HCM samples with confirmed HCM-causing genetic variants. This was true when normalised to both 18S and SNORD116-1. This suggests that exosomal SNORD116-23 expression may be linked to HCM, and that the level of packaging may be influenced by the presence of sarcomeric mutations. This is supported by previous findings that showed increased packaging of SNORD116-23 in the exosomes of iPSC-CMs with HCM-causing genetic variants under stress conditions (65).

SNORD116-25 expression was detected in whole serum RNA but not exosome-specific RNA, which again suggests that generally circulating versus exosome-packaged forms of SNORD116 may be involved in different pathways. SNORD116-25 is present at higher levels in the serum of four of the six HCM samples relative to the controls, which may suggest a link between HCM and circulating SNORD116-25.

Flow cytometry was used to characterise different white blood cell populations in HCM patient blood based on CD14 and CD16 marker expression. CD14 is a marker expressed generally by monocytes in the peripheral blood cell population (436). Monocytes that are both CD14-positive and CD16-positive represent monocytes that have been activated into macrophages (437). In the literature, CD14+/CD16- monocytes are termed classical monocytes and are reported to be the largest proportion of the total monocyte population (445). This is mostly reflected in the results of HCM patient blood, with the exception of HCM-1 which shows a classical monocyte population of 11% and a CD14-/CD16+ population of 22%. This population is termed the non-classical monocyte population and has been shown to be anti-inflammatory and maintain vascular homeostasis (446), although it has also been shown to produce pro-inflammatory cytokines and expand in response to infection (445,447). This population is generally the smallest across the HCM patients with the exception of HCM-1 and HCM-5. These samples both exhibit relatively high levels of whole serum SNORD116-23 and SNORD116-25 suggesting there may be a connection between circulating SNORD116 and non-classical monocyte expansion.

The macrophage population was the most consistently sized across the HCM samples, averaging ~6% of the total population. This is higher than previously reported populations which averaged closer to 2% of the total white blood cell population in healthy individuals (448). This may indicate

that all of the HCM patients were exhibiting a low-level inflammatory response.

HCM-1 was the only female HCM patient and displayed the largest population of classical monocytes, which is contrary to a previous study that showed women have decreased numbers of classical monocytes compared to men (449). However, this study was carried out in lupus patients and not HCM patients. These results could indicate that there may be a relationship between classical monocyte expansion in female vs male HCM patients, although much larger cohort numbers would be needed to confirm this.

Interestingly, CD14+ monocyte gene expression showed that TNFa and PTX3 – both important components of pro-inflammatory signalling (450)– were upregulated in all of the HCM samples relative to the controls. This may suggest an increase in inflammation in patients with HCM compared to healthy individuals, which is supported by previous studies (451–453).

Analysis of patient blood serum was the only occasion where the different SNORD116 paralogues exhibited dissimilar and sometimes completely opposing expression patterns. This suggests that *in vivo*, the different SNORD116 paralogues may perform markedly different roles. These findings emphasise the importance of incorporating clinical and *in vivo* research above relying solely on single cell type *in vitro* models, and demonstrates how a multi-tissue environment can provide richer and more detailed results.

Chapter 8 Discussion

8.1 General Discussion

Heart disease afflicts millions of people across the world and presents a substantial financial burden to the healthcare system. Part of the challenge in understanding and treating heart disease is its significant variability and heterogeneity. From congenital defects and sarcomeric mutations to contractile dysfunction and signalling perturbation, there are many distinct molecular mechanisms that underscore cardiac pathophysiology. However, there are some common threads that weave together the different aspects of heart disease. Metabolism is a key component to the functionality of any tissue, but is especially crucial to the heart. Cardiomyocytes are one of the most metabolically active cell types in the body, and virtually every form of heart disease features the dysregulation of cardiac metabolism. These changes are intricately linked with changes that occur in cardiac gene transcription, and reflect the pathological reactivation of developmental programmes. Researchers are challenged with innovating methods of modelling heart disease to better understand the mechanisms behind these processes in order to discover and develop improved treatment strategies for patients.

This work has illustrated the use of iPSCs to model and investigate aspects of cardiac development and disease. Results presented here have demonstrated how cardiac stressors designed to simulate the stress of heart disease had a drastic impact on metabolism and gene transcription. This shows how heart disease can be successfully modelled *in vitro* using human iPSC-derived cells in the investigation of novel gene pathways. Supplementing this is the analysis of clinical samples from heart disease patients that, although preliminary, has yielded promising results.

A huge portion of the human transcriptome is not translated into protein but is important in the regulation of vital gene and signalling pathways. There's growing evidence that dysregulation in the expression of these non-coding RNAs contributes to the progression of many human diseases, including cardiovascular disease (454,455). It is also speculated that differences in the abundance of particular non-coding RNAs may partially explain the heterogeneity in disease penetrance and symptom presentation between patients with the same affliction, and may even act as molecular markers with predictive potential (30,138).

SNORD116 is a non-coding RNA that was implicated in cardiac disease when it was found to be packaged in greater abundance by HCM cardiomyocytes under stress conditions (65). Although it was one of several non-coding RNAs affected in the study, SNORD116 was of particular interest as multiple paralogues were detected, and it had already been implicated in a human disease with metabolic and cardiac features (33,62). SNORD116 has been explored in the literature to some extent, albeit in a heavily neurological context, but presents a challenging – although fascinating – RNA to investigate. Its multiple paralogues and paternal imprinting lead to difficulties in the analysis and modulation of its expression. However, through innovative techniques and the power and utility of iPSC-derived models, there is now a much clearer picture of the role of SNORD116 in cardiac development and disease. The results presented here provide a foundation of knowledge from which further work can be conducted into the potential of SNORD116 as a biomarker of heart disease, or even as potential target for RNA-based therapies.

8.2 Key findings

8.2.1 PKP1 identified as the putative target of SNORD116

SNORD116 has been investigated in a largely neuronal context due to its importance in Prader-Willi Syndrome. However, despite decades of extensive investigation, no direct interaction between SNORD116 and a predicted target has been found. As such, the mechanism of SNORD116 actin in PWS and other contexts remains elusive. Here, a human iPSC-based model – combined with data from animal and *in silico* studies – has been used to identify PKP1 as a potential target of SNORD116.

Upon SNORD116 overexpression in cardiomyocytes, the protein with the largest decrease in abundance was the desmosomal armadillo protein PKP1. Separate studies performed by collaborators using mouse models showed an increase in PKP1 expression upon SNORD116 knockout (55,56,408), and the bioinformatic sequence analysis software snoTARGET predicted the targeting of PKP1 by SNORD116 (32). Contrastingly with this, RNA-seq results did not show a significant change in PKP1 mRNA levels. This may be due to technical limitations such as the low expression of PKP1 mRNA in cardiomyocytes, or differences in transfection efficiency between the proteomic and transcriptomic samples.

However, there were some other notable discrepancies between the RNA and protein changes that occurred as a result of SNORD116 overexpression. For example, after three days post-transfection many glycolysis-related genes were increased at an mRNA level but decreased at a protein level, possibly due to a compensatory mechanism. This could suggest that changes in the RNA expression of certain genes occurred at a different rate than changes to protein expression. Therefore, a decrease in PKP1 mRNA may have occurred earlier or later than the 72-hour time

point and was therefore missed in the RNA-seq results. Additionally, the transcriptomic analysis of SNORD116 overexpression was carried out on day 15 iPSC-CMs that had not been subjected to pro-maturation fatty acid-based media. Contrastingly, the proteomic analysis was carried out on day 30 iPSC-CMs that had been subjected to pro-maturation media. The maturation state of the cells may have influenced the effect of SNORD116 overexpression.

Assuming that there was no change in PKP1 mRNA expression upon SNORD116 overexpression, this could suggest that SNORD116 had an inhibitory effect on the translation of PKP1 protein through a method of post-transcriptional modification that was non-destructive, as opposed to mechanisms such as RNAi that prevent translation through the depletion of target mRNA. An example of one such method could be the SNORD116-directed methylation of PKP1 mRNA leading to steric inhibition of translation. Other C/D box snoRNAs have been shown to perform this method of regulation through 2'-O-methylation of target mRNA, such as in the case of Bim by SNORD89 (19), and PXDN by U32A and U51 (20). Sequence analysis identified one potential binding site between SNORD116 and PKP1 mRNA that may facilitate binding and subsequent methylation.

An alternative method of regulation could be SNORD116-directed alternative splicing of PKP1 mRNA. SNORD115 exists in the same gene cluster as SNORD116 and has been shown to regulate the expression of serotonin receptor 2C (5-HT_{2C}R) by promoting alternative splicing of its pre-mRNA (22). The alternatively spliced form of 5-GT_{2C}R generates a non-functional protein (22–24). There are two splice variants of *PKP1*, denoted *PKP1a* and *PKP1b*. The latter is longer and contains an additional 63 base pairs between exons 6 and 7. Although the effect of this insertion on the functionality of the protein is not well understood, it does appear to change the localisation of the protein, as PKP1b is found exclusively in

the nucleus (149). Results presented in chapter 6.2.3 show that the expression of *PKP1* in differentiated cardiomyocytes appears largely nuclear and is therefore likely to be the *PKP1b* isoform, although the antibody used cannot distinguish between splice variants. Western blot analysis indicated the generation of multiple differently-sized bands during early cardiomyocyte differentiation, but a single ~65kDa band in differentiated cardiomyocytes, supporting the proposition that cardiomyocytes only express one isoform of *PKP1* which is likely to be the nuclear *PKP1b* isoform. However, publications have shown PKP1 to produce bands closer to 75kDa (429,430). The difference in size may be due to differences in sample preparation or protein extraction. Future results could be improved by the use of a different antibody and a positive PKP1 control sample.

PKP1 mRNA expression in cardiomyocytes was too low to be evaluated using RT-qPCR. The form of *PKP1* identified by mass spectrometry in the proteomics results was also not able to distinguish between *PKP1* isoforms. It is possible that SNORD116-directed alternative splicing of *PKP1* may result in reduced expression of one of the *PKP1* isoforms, leading to a decrease in PKP1 protein abundance in cardiomyocytes upon SNORD116 overexpression. The potential binding interaction identified between SNORD116 and *PKP1* shown in Figure 6-26 does not align near the exon 6-7 splice junction, but there may be other binding sites between the two molecules not yet identified. This was suggested by data presented in the paper describing the snoTARGET software (32), although the exact binding site identified was not specified and the software is no longer available for use. In addition, it is important to remember the existence of multiple SNORD116 paralogues. The proposed 14 base-pair binding site occurs within canonical regions conserved across SNORD116 paralogues, but there may be binding sites within less well-conserved regions that facilitate paralogue-specific binding interactions. Results

from clinical samples certainly suggests the possibility of paralogue-specific SNORD116 functions in human disease.

The loss of the potential SNORD116-PKP1 interaction may explain some of the phenotypes seen in PWS. Separate from its role in the desmosome where it may influence cell adhesion, communication and migration, PKP1 ca also translocate to the cytoplasm and nucleus (149). Activation of the PI3K/Akt signalling pathway causes PKP1 to be phosphorylated. translocate to the cytoplasm and promote proliferation (456,457). SNORD116 may be important in regulating this pathway, suggesting that its absence during development may dysregulate cell growth. Cell growth was not thoroughly assayed during this project as cardiomyocytes are post-mitotic, however preliminary results performed in cardiac fibroblasts did show a change in Ki67 nuclearization in response to SNORD116 overexpression. Additionally, the PI3K/Akt pathway has been shown to regulate glycolysis (458,459), and glucose metabolism was consistently found to be dysregulated by SNORD116 overexpression. This supports the proposal that PKP1 participates in intracellular signalling pathways and that loss of SNORD116 leads to dysregulation of these pathways during development, thus contributing to PWS pathogenesis. Public databanks with information of embryonic RNA/protein expression (such as https://www.informatics.jax.org/) could be used to evaluate the expression profile of PKP1 during development to explore these hypotheses further.

Although further work is needed to validate the potential binding interaction between SNORD116 and *PKP1*, identification of a putative SNORD116 target will have a resounding impact on SNORD116 research in Prader-Willi Syndrome and other fields. Although SNORD116 has been shown to dysregulate key cellular pathways in multiple tissue types, so far there are no known targets of SNORD116 which has inhibited a detailed understanding of its function. The detection of *PKP1* as a

candidate target of SNORD116 has implications in multiple tissues and disease states beyond the cardiac context.

8.2.2 SNORD116 is upregulated in early cardiac development

The expression of multiple SNORD116 paralogues is upregulated 2-3 fold on day 4 of cardiomyocyte and cardiac fibroblast differentiation. This is the point during differentiation where mesoderm markers such as *GATA4* and EOMES show peak expression. The upregulation of cardiac transcription factor *NKX2-5* is first seen at this point, alongside the activation of various cardiac structural genes. The cardiac metabolism gene *PPARa* is also first upregulated on day 4. These are the early gene transcription events that are essential for cardiac development. The upregulation of SNORD116 at this stage indicates that it may be important in the specification of early cardiac mesoderm induction. Results presented in Chapter 4 showed that the activation of Wnt signalling using CHIR appeared to increase the expression of SNORD116 and promote cardiomyocyte proliferation. Therefore, the manipulation of Wnt signalling during early iPSC-CM differentiation may contribute to the changes seen in SNORD116 expression.

The expression of SNORD116-1 during cardiomyocyte differentiation was analysed using multiple iPSC lines, and the peak in expression at day 4 was not always observed. In the D1HCM and D3WT lines, SNORD116-1 expression was downregulated during days 2 and 4 of the differentiation, although expression was elevated at day 8. These cell lines typically formed contractile cells around day 10-12 of the differentiation protocol in contrast to the AA-tagged iPSC line which produced contractile cells around day 5-6. The delayed elevation of SNORD116-1 expression in the E99K lines may relate to their delayed cardiomyocyte development. Additionally, these lines responded with less consistency to the differentiation protocol and produced populations of reduced

cardiomyocyte purity (60-70%) which may have influenced the expression of SNORD116 and caused variation in the results. These observations emphasise how discrepant responses can be triggered in cell lines from different genetic backgrounds. As SNORD116 expression during the differentiation was always plotted as relative to stem cell levels, differential expression levels between stem cells of different genetic backgrounds would affect the results. Reinforcing this, the C9123T lines again showed a contrastive expression pattern to the AA-tagged and E99K lines. Interestingly in the case of C9123T, the presence of the mutation appeared to cause higher levels of SNORD116 in day 17 cardiomyocytes, although further replicates are needed to confirm this.

Overall the AA-tagged line produced the highest purity cardiomyocyte populations with the most consistency, and so this line was used to demonstrate how multiple SNORD116 paralogues also show peak expression at day 4 of the differentiation. Interestingly, work carried out by Dr Jefferey Spees and his team at the University of Vermont has found that SNORD116 is elevated in epicardial progenitor cells during heart development in mice (manuscript in preparation). This demonstrates that multiple models provide evidence that SNORD116 may play an important role during cardiac development.

Western blot analysis and immunocytochemistry showed that in stem cells, PKP1 may be expressed as multiple isoforms and displays a perinuclear localisation pattern, although there was still some nuclear expression. However, by day 4, PKP1 appears to display a predominantly nuclear localisation pattern. In addition, western blotting indicated that there appears to be fewer differently-sized isoforms of PKP1 expressed as the cardiomyocytes differentiate. As the different isoforms of PKP1 are known to localise to different regions of the cell, these changes in PKP1 localisation could indicate that alternative splicing of the PKP1 pre-mRNA occurs during early cardiac development. Studies in tooth development

have shown that activation of Wnt signalling by either Wnt3a supplementation or GSK3β inhibition caused PKP1 to translocate from the plasma membrane to the nucleus of dental epithelial cells (426).

Wnt signalling and mesoderm induction also appears to influence SNORD116 expression. If SNORD116 directly affects the expression or splicing of PKP1, then the changes in SNORD116 expression in response to Wnt signalling modulation may contribute to the changes in PKP1 localisation seen during early cardiac differentiation. Alternatively, as the nuclear localisation of PKP1 appears to begin around day 2 and the upregulation of SNORD116 occurs around day 4, it is possible that PKP1 localises to the nucleus upon Wnt activation, which then promotes the upregulation of SNORD116. This then acts on PKP1 pre-mRNA to ensure the expression of specific PKP1 isoforms during later stages of cardiac development. The apparent nuclear localisation of PKP1 could suggest the protein may act in the capacity of a novel transcription factor. The potential SNORD116-PKP1 axis may influence important transcriptional and metabolic events that contribute to the transition from foetal to adult cardiomyocyte. This same axis may play a role in the reactivation of foetal phenotypes seen in cardiovascular disease.

8.2.3 SNORD116 is affected by cardiac stress

Loss of SNORD116 in both mice and humans has been shown to increase levels of IGFBP7, a regulator of insulin-like growth factor (IGF) binding (460). Increased levels of IGFBP7 have been linked with heart failure and associated with ROS production, cardiac inflammatory injury, tissue fibrosis and cellular senescence (461). Clinically, patients with PWS have a significantly higher chance of experiencing cardiac dysfunction (60,62,64). Additionally, SNORD116 was found to be packaged at greater levels into the exosomes of HCM cardiomyocytes under increased

workload (65). Taken together, this evidence suggested that SNORD116 may be important in the signalling pathways involved in cardiac stress.

Both hypoxic stress and doxorubicin-induced cardiotoxicity appeared to have an upregulatory effect on SNORD116 expression in iPSC-CMs and (in the case of doxorubicin) iPSC-CFs. Interestingly, cardiomyocytes recovering after exposure to hypoxia had significantly lower expression levels of SNORD116, suggesting that the reduction of SNORD116 may be important in the activation of repair pathways. Prologued exposure to isoprenaline, which has been shown to induce cardiac hypertrophy (194–196), had an upregulatory effect on SNORD116 in iPSC-CFs. Additionally, activated myofibroblasts express SNORD116 at greater levels compared to less activated fibroblasts.

Taken together, these observations suggested that SNORD116 expression appears to be elevated in response to oxidative and cardiac stress This relationship was further supported by the dysregulation of several cardiomyopathy pathways at both an mRNA and protein level upon SNORD116 overexpression in cardiomyocytes. Key structural and ion-transport-related cardiac genes were downregulated, resulting in the dysregulation of the ARVC and DCM pathways. Additionally, a number of genes important in cardiac cell adhesion were upregulated, although this may be in compensation for the dramatic decrease in PKP1 protein. It is unclear whether the changes in cardiac expression occur as a result of direct targeting of PKP1 by SNORD116, or if these genes are secondary targets unrelated to the ablation of PKP1. However, it is clear that modulating SNORD116 expression influences the cardiac expression profile of cardiomyocytes, and increased SNORD116 expression may have a pro-pathological effect on cardiac cells.

8.2.4 SNORD116 modulates cardiac metabolism

Patients with PWS experience a number of clinical outcomes including a dysregulation of metabolism (33,57,62,462). A SNORD116 knock out mouse model of PWS demonstrated several metabolic abnormalities that resulted in post-natal lethality (463). This evidence indicated that SNORD116 may be a modulator of metabolism.

Results presented here show that SNORD116 overexpression significantly reduced the ECAR of cardiomyocytes and caused a reduction in numerous glycolysis-related proteins in cardiomyocytes and neural cells – both highly metabolic cell types. It also appeared to cause a reduction in the rate of glucose metabolism in cardiac fibroblasts. Moreover, a cardiac-specific SNORD116 knockout in mice was shown to cause significant dysregulation to several key metabolic proteins (68). Metabolism is crucial to the functionality of the heart due to the energy demands of contraction, therefore any reduction in metabolic capacity will reduce the cell's ability to manage increased workload. This could lead to an energy deficit, a common feature of many forms of heart disease that often has fatal consequences (76,464). Increased levels of SNORD116 associated with cardiac stress may reduce the metabolic capacity of cardiac cells and impair their ability to meet the energy demands of the heart. The exact mechanistic relationship between SNORD116 and glucose metabolism is still unclear. However, culturing cardiomyocytes in a glucose-free media appeared to affect the localisation of PKP1. This may indicate that SNORD116 affects glucose metabolism in cardiac cells by changing the expression or localisation of PKP1. This potential interaction is entirely novel and may have significant clinical implications beyond heart disease.

8.3 Limitations

There are several limitations to this work that should be addressed. Firstly, the conclusion that SNORD116 may directly target and suppress PKP1 protein expression was based largely on overexpression studies. This is highly reliant on high transfection efficiencies that are not always consistently achieved. Secondly, although data from SNORD116 knockout mouse models was kindly provided by collaborators (55,68), SNORD116 knockout in human cardiomyocytes was not carried out. Therefore, the effect of decreased SNORD116 expression in human cardiac cells was not investigated. Additionally, the overexpression plasmid used to generate transcriptomic and proteomic data transcribed a mouse orthologue of SNORD116 that – although highly similar in sequence and containing the conserved C/D box sequences speculated to be involved in targeting – did not express a human copy of SNORD116. Although an alternative overexpression plasmid was constructed to express a human paralogue of SNORD116, time constraints limited the implementation of this plasmid. Furthermore, the overexpression studies conducted here were restricted to 72-hour time-point analysis to maintain consistency across transfections. Multiple time-points could have been analysed to find the optimal time of overexpression, and gain a better understanding of how SNORD116 overexpression affect cardiomyocytes over time.

Multiple strategies were employed to induce cardiac stress in the investigation of SNORD116 expression. Although multiple concentrations of doxorubicin were used to widen the scope of these experiments, only one concentration of oxygen was used to induce hypoxia in cells. Although this was effective in inducing oxidative stress as demonstrated by metabolic assays, multiple different concentrations and time points could have tested. For example, short-burst 0% oxygen exposure may have more effectively simulated the environment of a myocardial infarction, whereas prologued exposure to 5-10% oxygen may have

succeeded in inducing oxidative stress without the dramatic loss in viability. Additionally, in cardiomyocytes, isoprenaline was effective in increasing contraction frequency and arrythmia but did not result in changes to gene expression. A longer time point, or multiple time-points, may have allowed for the detection of expression changes in response to the effects of isoprenaline in cardiomyocytes, as it did in cardiac fibroblasts.

Human iPSC-based models are generally limited in their ability to recapitulate the *in vivo* primary tissue environment due to the lack of maturity. Fatty acid-based media was used to culture iPSC-CMs in a pro-maturation culture medium, however the resulting iPSC-CMs were still unable to fully achieve the mature phenotype of adult primary cardiomyocytes. However, the immature phenotype of iPSC-CMs used throughout this work may have been advantageous, in that this may have allowed the exposure of a potential developmental role of SNORD116 that would be missed in later stages of development or from the use of animal models.

In addition to limitations in maturity, iPSC models can present a lack of consistency in differentiation efficiency which can lead to variation in results. This is particularly apparent when comparing expression profiles across multiple different genetic backgrounds. However, to improve this, more time can be spent optimising the differentiation protocol by changing culture conditions such as seeding density and growth factor concentration .

8.4 Future work

The investigation into the potential SNORD116-PKP1 axis in cardiac development and disease was challenging due to the low expression of *PKP1* in differentiated cardiac cells. Of the cell types analysed, iPSCs appeared to show the highest expression levels of *PKP1*. To validate the proteomic results and show that SNORD116 targets *PKP1*, further overexpression studies followed by proteomic analysis could be conducted in iPSCs and early mesoderm progenitors, which can typically be transfected to a high degree of efficiency (>80%) (465).

Additionally, the potential 2'O-methylation of *PKP1* mRNA can be detected using a modified method of RT-qPCR analysis (466). Isoform-specific primer pairs could be used to determine whether SNORD116 causes the alternative splicing of *PKP1*. In terms of validating the binding interaction between SNORD116 and *PKP1*, there are several biochemical methods of detecting RNA-RNA interactions. Electrophoretic mobility shift assay (EMSA) uses radio-labelled probes and polyacrylamide gel electrophoresis to demonstrate the change in mobility of a bound versus unbound RNA molecule (467,468). Single-molecule Förster resonance energy transfer (smFRET) is a fluorophore-based method of detecting binding between two RNA molecules, that can be combined with microscopy techniques to allow live-imaging of binding interactions (469,470). The luciferase reporter assay has been widely used in the validation of miRNA targeting (471), but could be adapted to investigate the potential SNORD116-PKP1 interaction.

Once a method of validating the interaction between SNORD116 and *PKP1* has been successfully implemented, bioinformatic sequence analysis could be employed to aid in the determination of multiple binding sites between the two RNA molecules. Software such as snoTARGET have previously been developed to identify potential binding interactions

between SNORD116 and the entire human transcriptome (32), therefore modifying these parameters to search specifically within *PKP1* should be feasible. Upon the identification of potential binding sites, site-directed mutagenesis can be employed to validate these binding interactions. This strategy can also be used to explore the effects of disrupting the interaction between SNORD116 and PKP1 and how that affects cell signalling and function.

Preliminary investigation into the potential function of *PKP1* in a cardiac context was carried out, and results indicated that there may be a nuclear role of PKP1 during early cardiac differentiation. However, future investigations could be improved through the use of antibodies specific to certain isoforms of *PKP1*, revealing the potential role of alternative splicing and cellular localisation during cardiac development. Nuclear fractionation and western blotting could also be used to quantify abundance and localisation of PKP1.

SNORD116 was upregulated during early cardiac differentiation and SNORD116 overexpression appeared to affect multiple cardiomyopathy pathways. However, it is important to observe the effects of loss-of-expression to complement these overexpression studies. Despite continued effort, a SNORD116 knockout iPSC line was not able to be successfully generated in this work. However, during the final stages of this work, a project funded by the Foundation for Prader-Willi Research (led by Dr. Derek Tai, Havard, USA) has successfully generated human iPSC lines wherein SNORD116 expression is knocked out. Soon to be available through the PWS iPSC Biobank (https://www.fpwr.org/ipsc-biobank), these iPSC lines could be used to differentiate human cardiomyocytes and determine the effect of loss of SNORD116 expression on cardiac development and response to stress.

8.5 Conclusion

Evidence suggests that SNORD116 plays a role in both cardiac development and disease. This may be through the post-transcriptional modification of *PKP1*, with potential consequences in differentiation and metabolism, although further investigation is needed to confirm this. Clinical evidence is highly preliminary but does suggest a connection between sarcomeric mutation and elevated SNORD116 levels, although interestingly this appears to be paralogue-specific. This reinforces the need to integrate animal studies, human *in vitro* research, and clinical analysis to gain comprehensive understanding of the role of SNORD116 in cardiac development and disease.

References

1. Cheng J, Kapranov P, Drenkow J, Dike S, Brubaker S, Patel S, et al. Transcriptional maps of 10 human chromosomes at 5-nucleotide resolution. Science (1979) [Internet]. 2005 May 20 [cited 2022 Nov 16];308(5725):1149–54. Available from: https://www.science.org
2. Huang W, Li H, Yu Q, Xiao W, Wang DO. LncRNA-mediated DNA methylation: an emerging mechanism in cancer and beyond [Internet]. Vol. 41, Journal of Experimental and Clinical Cancer Research. BioMed Central Ltd; 2022 [cited 2022 Nov 16]. p. 100. Available from: https://doi.org/10.1186/s13046-022-02319-z
3. Yoon JH, Abdelmohsen K, Gorospe M. Posttranscriptional gene regulation by long noncoding RNA [Internet]. Vol. 425, Journal of Molecular Biology. Academic Press; 2013 [cited 2022 Nov 16]. p. 3723–30. Available from: /pmc/articles/PMC3594629/
4. He RZ, Luo DX, Mo YY. Emerging roles of lncRNAs in the post-transcriptional regulation in cancer [Internet]. Vol. 6, Genes and Diseases. Chongqing yi ke da xue, di 2 lin chuang xue yuan Bing du xing gan yan yan jiu suo; 2019 [cited 2022 Nov 16]. p. 6–15. Available from: /pmc/articles/PMC6411652/
5. Tan YT, Lin JF, Li T, Li JJ, Xu RH, Ju HQ. LncRNA-mediated posttranslational modifications and reprogramming of energy metabolism in cancer [Internet]. Vol. 41, Cancer Communications. John Wiley and Sons Inc; 2021 [cited 2022 Nov 16]. p. 109–20. Available from: https://onlinelibrary-wiley-com.uea.idm.oclc.org/doi/full/10.1002/cac2.12108
6. Gill T, Cai T, Aulds J, Wierzbicki S, Schmitt ME. RNase MRP Cleaves the CLB2 mRNA To Promote Cell Cycle Progression: Novel Method of mRNA Degradation. Mol Cell Biol [Internet]. 2004 Feb 1 [cited 2020 Oct 16];24(3):945–53. Available from: /pmc/articles/PMC321458/?report=abstract

7. Tyc K, Steitz JA. U3, U8 and U13 comprise a new class of mammalian snRNPs localized in the cell nucleolus. EMBO Journal [Internet]. 1989 Oct 1 [cited 2022 Nov 16];8(10):3113–9. Available from: https://onlinelibrary.wiley.com/doi/10.1002/j.1460-2075.1989.tb08463.x

8. Kass S, Tyc K, Steitz JA, Sollner-Webb B. The U3 small nucleolar ribonucleoprotein functions in the first step of preribosomal RNA processing. Cell. 1990 Mar 23;60(6):897–908.

9. Balakin AG, Smith L, Fournier MJ. The RNA world of the nucleolus: Two major families of small RNAs defined by different box elements with related functions. Cell. 1996 Sep 6;86(5):823–34.

10. Bratkovič T, Bozič J, Rogelj B. Functional diversity of small nucleolar RNAs. Nucleic Acids Res [Internet]. 2020 Feb 28 [cited 2022 Nov 16];48(4):1627–51. Available from: https://academic-oup-com.uea.idm.oclc.org/nar/article/48/4/1627/5673630

11. Rimer JM, Lee J, Holley CL, Crowder RJ, Chen DL, Hanson PI, et al. Long-range function of secreted small nucleolar RNAs that direct 2-O-methylation. Journal of Biological Chemistry [Internet]. 2018 Aug 24 [cited 2022 Nov 16];293(34):13284–96. Available from: /pmc/articles/PMC6109910/

12. Jorjani H, Kehr S, Jedlinski DJ, Gumienny R, Hertel J, Stadler PF, et al. An updated human snoRNAome. Nucleic Acids Res [Internet]. 2016 Jun 20 [cited 2020 Dec 11];44(11):5068–82. Available from: https://pubmed.ncbi.nlm.nih.gov/27174936/

13. Kiss-László Z, Henry Y, Kiss T. Sequence and structural elements of methylation guide snoRNAs essential for site-specific ribose methylation of pre-rRNA. EMBO Journal [Internet]. 1998 Feb 2 [cited 2022 Nov 16];17(3):797–807. Available from: /pmc/articles/PMC1170428/?report=abstract

14. Hirose T, Steitz JA. Position within the host intron is critical for efficient processing of box C/D snoRNAs in mammalian cells. Proc

Natl Acad Sci U S A [Internet]. 2001 Nov 6 [cited 2021 Jan 17];98(23):12914–9. Available from: www.pnas.orgcgidoi10.1073pnas.231490998

15. Lestrade L, Weber MJ. snoRNA-LBME-db, a comprehensive database of human H/ACA and C/D box snoRNAs. Nucleic Acids Res [Internet]. 2006 Jan 1 [cited 2021 Jan 17];34(Database issue):D158–62. Available from: http://www-snorna.biotoul.

16. Matera AG, Terns RM, Terns MP. Non-coding RNAs: Lessons from the small nuclear and small nucleolar RNAs [Internet]. Vol. 8, Nature Reviews Molecular Cell Biology. Nature Publishing Group; 2007 [cited 2021 Jan 17]. p. 209–20. Available from: https://www-nature-com.uea.idm.oclc.org/articles/nrm2124

17. Pauli C, Liu Y, Rohde C, Cui C, Fijalkowska D, Gerloff D, et al. Site-specific methylation of 18S ribosomal RNA by SNORD42A is required for acute myeloid leukemia cell proliferation. Blood [Internet]. 2020 Jun 4 [cited 2022 Nov 16];135(23):2059–70. Available from: https://www-snorna.biotoul.fr.

18. Higa-Nakamine S, Suzuki TT, Uechi T, Chakraborty A, Nakajima Y, Nakamura M, et al. Loss of ribosomal RNA modification causes developmental defects in zebrafish. Nucleic Acids Res [Internet]. 2012 Jan 1 [cited 2021 Jan 17];40(1):391–8. Available from: https://academic.oup.com/nar/article/40/1/391/1278217

19. Bao H juan, Chen X, Liu X, Wu W, Li Q hui, Xian J yuan, et al. Box C/D snoRNA SNORD89 influences the occurrence and development of endometrial cancer through 2′-O-methylation modification of Bim. Cell Death Discov. 2022;8(1):1–10.

20. Elliott BA, Ho HT, Ranganathan S V., Vangaveti S, Ilkayeva O, Abou Assi H, et al. Modification of messenger RNA by 2′-O-methylation regulates gene expression in vivo. Nat Commun [Internet]. 2019 Dec 1 [cited 2020 May 13];10(1):1–9. Available from: https://doi.org/10.1038/s41467-019-11375-7

21. Scott MS, Ono M. From snoRNA to miRNA: Dual function regulatory non-coding RNAs. Vol. 93, Biochimie. Elsevier; 2011. p. 1987–92.

22. Kishore S, Stamm S. The snoRNA HBII-52 regulates alternative splicing of the serotonin receptor 2C. Science (1979) [Internet]. 2006 Jan 13 [cited 2021 Jan 17];311(5758):230–2. Available from: http://science.sciencemag.org/

23. Wang Q, O'Brien PJ, Chen CX, Cho DSC, Murray JM, Nishikura K. Altered G Protein-Coupling Functions of RNA Editing Isoform and Splicing Variant Serotonin2C Receptors. J Neurochem [Internet]. 2000 Mar 1 [cited 2022 Nov 16];74(3):1290–300. Available from: http://doi.wiley.com/10.1046/j.1471-4159.2000.741290.x

24. Wang Z, Rolish ME, Yeo G, Tung V, Mawson M, Burge CB. Systematic identification and analysis of exonic splicing silencers. Cell [Internet]. 2004 Dec 17 [cited 2022 Nov 16];119(6):831–45. Available from: https://pubmed-ncbi-nlm-nih-gov.uea.idm.oclc.org/15607979/

25. Jade H, Virginie M, Jean P, Pascale M, Nicolai K, Henrik N, et al. Re-assessment of the involvement of snord115 in the serotonin 2c receptor pathway in a genetically relevant mouse model. Elife. 2020 Oct 1;9:1–34.

26. Good DJ, Kocher MA. Phylogenetic analysis of the SNORD116 locus [Internet]. Vol. 8, Genes. MDPI AG; 2017 [cited 2020 Dec 11]. Available from: /pmc/articles/PMC5748676/?report=abstract

27. Ding F, Li HH, Zhang S, Solomon NM, Camper SA, Cohen P, et al. SnoRNA Snord116 (Pwcr1/MBII-85) deletion causes growth deficiency and hyperphagia in mice. PLoS One [Internet]. 2008 Mar 5 [cited 2020 Dec 11];3(3). Available from: https://pubmed.ncbi.nlm.nih.gov/18320030/

28. Scott MS, Ono M, Yamada K, Endo A, Barton GJ, Lamond AI. Human box C/D snoRNA processing conservation across multiple cell types. Nucleic Acids Res [Internet]. 2012 Apr 1 [cited 2022 Nov

16];40(8):3676–88. Available from: https://academic-oup-com.uea.idm.oclc.org/nar/article/40/8/3676/2411371

29. O'Leary NA, Wright MW, Brister JR, Ciufo S, Haddad D, McVeigh R, et al. Reference sequence (RefSeq) database at NCBI: Current status, taxonomic expansion, and functional annotation. Nucleic Acids Res [Internet]. 2016 [cited 2020 Dec 18];44(D1):D733–45. Available from: https://pubmed.ncbi.nlm.nih.gov/26553804/

30. De Almeida RA, Fraczek MG, Parker S, Delneri D, O'keefe RT. Non-coding RNAs and disease: The classical ncRNAs make a comeback. Biochem Soc Trans [Internet]. 2016 Aug 15 [cited 2021 Jan 17];44(4):1073–8. Available from: /pmc/articles/PMC6042638/?report=abstract

31. Bortolin-Cavaillé ML, Cavaillé J. The SNORD115 (H/MBII-52) and SNORD116 (H/MBII-85) gene clusters at the imprinted Prader-Willi locus generate canonical box C/D snoRNAs. Nucleic Acids Res [Internet]. 2012 Aug [cited 2021 Jan 17];40(14):6800–7. Available from: /pmc/articles/PMC3413130/?report=abstract

32. Bazeley PS, Shepelev V, Talebizadeh Z, Butler MG, Fedorova L, Filatov V, et al. snoTARGET shows that human orphan snoRNA targets locate close to alternative splice junctions. Gene [Internet]. 2008 Jan 31 [cited 2021 Jan 17];408(1–2):172–9. Available from: /pmc/articles/PMC6800007/?report=abstract

33. Cassidy SB, Schwartz S, Miller JL, Driscoll DJ. Prader-Willi syndrome [Internet]. Vol. 14, Genetics in Medicine. Nature Publishing Group; 2012 [cited 2021 Jan 12]. p. 10–26. Available from: https://www.nature.com/articles/gim0b013e31822bead0

34. Farooqi IS, O'Rahilly S. Monogenic Obesity in Humans. Annu Rev Med [Internet]. 2005 Feb 19 [cited 2021 Jan 12];56(1):443–58. Available from: http://www.annualreviews.org/doi/10.1146/annurev.med.56.062904.144924

35. Reik W, Walter J. Genomic imprinting: Parental influence on the genome [Internet]. Vol. 2, Nature Reviews Genetics. Nature Publishing Group; 2001 [cited 2021 Jan 12]. p. 21–32. Available from: https://www.nature.com/articles/35047554

36. Frietze S, O'Geen H, Blahnik KR, Jin VX, Farnham PJ. ZNF274 Recruits the Histone Methyltransferase SETDB1 to the 3' Ends of ZNF Genes. Defossez PA, editor. PLoS One [Internet]. 2010 Dec 8 [cited 2021 Jan 17];5(12):e15082. Available from: https://dx.plos.org/10.1371/journal.pone.0015082

37. Butler MG, Fischer W, Kibiryeva N, Bittel DC. Array comparative genomic hybridization (aCGH) analysis in Prader-Willi syndrome. Am J Med Genet A [Internet]. 2008 Apr 1 [cited 2021 Jan 13];146(7):854–60. Available from: https://pubmed-ncbi-nlm-nih-gov.uea.idm.oclc.org/18266248/

38. Butler MG, Bittel DC, Kibiryeva N, Talebizadeh Z, Thompson T. Behavioral Differences among Subjects with Prader-Willi Syndrome and Type I or Type II Deletion and Maternal Disomy. Pediatrics [Internet]. 2004 Mar [cited 2021 Jan 13];113(3 I):565–73. Available from: /pmc/articles/PMC6743499/?report=abstract

39. Driscoll DJ, Miller JL, Schwartz S. Prader-Willi Syndrome. 1998.

40. Fontana P, Grasso M, Acquaviva F, Gennaro E, Galli ML, Falco M, et al. SNORD116 deletions cause Prader-Willi syndrome with a mild phenotype and macrocephaly. Clin Genet [Internet]. 2017 Oct 1 [cited 2023 Mar 27];92(4):440–3. Available from: https://onlinelibrary-wiley-com.uea.idm.oclc.org/doi/full/10.1111/cge.13005

41. Bieth E, Eddiry S, Gaston V, Lorenzini F, Buffet A, Conte Auriol F, et al. Highly restricted deletion of the SNORD116 region is implicated in Prader–Willi Syndrome. European Journal of Human Genetics [Internet]. 2015 Feb 20 [cited 2023 Mar 27];23(2):252. Available from: /pmc/articles/PMC4297892/

42. Duker AL, Ballif BC, Bawle E V., Person RE, Mahadevan S, Alliman S, et al. Paternally inherited microdeletion at 15q11.2 confirms a significant role for the SNORD116 C/D box snoRNA cluster in Prader-Willi syndrome. Eur J Hum Genet [Internet]. 2010 Nov [cited 2023 Mar 27];18(11):1196–201. Available from: https://pubmed.ncbi.nlm.nih.gov/20588305/

43. Gabriel JM, Merchant M, Ohta T, Ji Y, Caldwelli RG, Ramsey MJ, et al. A transgene insertion creating a heritable chromosome deletion mouse model of Prader-Willi and Angelman syndromes. Proc Natl Acad Sci U S A [Internet]. 1999 Aug 3 [cited 2021 Jan 14];96(16):9258–63. Available from: www.pnas.org.

44. Watrin F, Le Meur E, Roeckel N, Ripoche MA, Dandolo L, Muscatelli F. The Prader-Willi syndrome murine imprinting center is not involved in the spatio-temporal transcriptional regulation of the Necdin gene. BMC Genet [Internet]. 2005 Jan 5 [cited 2021 Jan 16];6(1):1–12. Available from: https://link-springer-com.uea.idm.oclc.org/articles/10.1186/1471-2156-6-1

45. Zhang Q, Bouma GJ, McClellan K, Tobet S. Hypothalamic expression of snoRNA Snord116 is consistent with a link to the hyperphagia and obesity symptoms of Prader-Willi syndrome. International Journal of Developmental Neuroscience. 2012 Oct 1;30(6):479–85.

46. Castle JC, Armour CD, Löwer M, Haynor D, Biery M, Bouzek H, et al. Digital Genome-Wide ncRNA Expression, Including SnoRNAs, across 11 Human Tissues Using PolyA-Neutral Amplification. Creighton C, editor. PLoS One [Internet]. 2010 Jul 26 [cited 2021 Jan 16];5(7):e11779. Available from: https://dx.plos.org/10.1371/journal.pone.0011779

47. Galiveti CR, Raabe CA, Konthur Z, Rozhdestvensky TS. Differential regulation of non-protein coding RNAs from Prader-Willi Syndrome locus. Sci Rep [Internet]. 2014 Sep 23 [cited 2021 Jan 16];4(September):1–9. Available from: www.nature.com/scientificreports

48. Yang T, Adamson TE, Resnick JL, Leff S, Wevrick R, Francke U, et al. A mouse model for Prader-Willi syndrome imprinting-centre mutations. Nat Genet [Internet]. 1998 [cited 2021 Jan 14];19(1):25–31. Available from: https://pubmed-ncbi-nlm-nih-gov.uea.idm.oclc.org/9590284/

49. Skryabin B V, Gubar L V, Seeger B, Pfeiffer J, Handel S, Robeck T, et al. Deletion of the MBII-85 snoRNA Gene Cluster in Mice Results in Postnatal Growth Retardation. Ferguson-Smith AC, editor. PLoS Genet [Internet]. 2007 Dec 28 [cited 2021 Jan 14];3(12):e235. Available from: https://dx.plos.org/10.1371/journal.pgen.0030235

50. Burnett LC, LeDuc CA, Sulsona CR, Paull D, Eddiry S, Levy B, et al. Induced pluripotent stem cells (iPSC) created from skin fibroblasts of patients with Prader-Willi syndrome (PWS) retain the molecular signature of PWS. Stem Cell Res. 2016 Nov 1;17(3):526–30.

51. Bochukova EG, Lawler K, Croizier S, Keogh JM, Patel N, Strohbehn G, et al. A Transcriptomic Signature of the Hypothalamic Response to Fasting and BDNF Deficiency in Prader-Willi Syndrome. Cell Rep. 2018 Mar 27;22(13):3401–8.

52. Gray J, Yeo GSH, Cox JJ, Morton J, Adlam ALR, Keogh JM, et al. Hyperphagia, severe obesity, impaired cognitive function, and hyperactivity associated with functional loss of one copy of the brain-derived neurotrophic factor (BDNF) gene. Diabetes [Internet]. 2006 Dec 1 [cited 2021 Jan 13];55(12):3366–71. Available from: http://diabetes.diabetesjournals.org]

53. Bahamonde ME, Lyons KM. BMP3: to be or not to be a BMP. Vol. 83 A Suppl 1, The Journal of bone and joint surgery. American volume. 2001.

54. Ilnytska O, Argyropoulos G. The role of the Agouti-related protein in energy balance regulation [Internet]. Vol. 65, Cellular and Molecular Life Sciences. NIH Public Access; 2008 [cited 2021 Jan 13]. p. 2721–31. Available from: /pmc/articles/PMC2748318/?report=abstract

55. Peffers MJ, Dale AG, Clough H, Dyer P, Ellis J, Tew S, et al. The role of SNORD116 in cartilage ageing and osteoarthritis. Osteoarthritis Cartilage. 2020 Apr 1;28:S342–3.

56. Steinbusch MMF, Fang Y, Milner PI, Clegg PD, Young DA, Welting TJM, et al. Serum snoRNAs as biomarkers for joint ageing and post traumatic osteoarthritis. Sci Rep [Internet]. 2017 Mar 2 [cited 2021 Jan 17];7(1):1–11. Available from: www.nature.com/scientificreports

57. Hurren BJ, Flack NAMS. Prader-Willi Syndrome: A spectrum of anatomical and clinical features. Clinical Anatomy [Internet]. 2016 Jul 1 [cited 2022 Nov 17];29(5):590–605. Available from: https://onlinelibrary.wiley.com/doi/10.1002/ca.22686

58. Smith A, Loughnan G, Steinbeck K. Death in adults with Prader-Willi syndrome may be correlated with maternal uniparental disomy. [Internet]. Vol. 40, Journal of medical genetics. BMJ Publishing Group Ltd; 2003 [cited 2022 Nov 17]. p. 63. Available from: http://www.jmedgenet.com/cgi/content/full/40/5/e63

59. Schrander-Stumpel CThRM, Curfs LMG, Sastrowijoto P, Cassidy SB, Schrander JJP, Fryns JP. Prader-Willi syndrome: Causes of death in an international series of 27 cases. Am J Med Genet [Internet]. 2004 Feb 1 [cited 2022 Nov 17];124A(4):333–8. Available from: https://onlinelibrary.wiley.com/doi/10.1002/ajmg.a.20371

60. Pomara C, D'Errico S, Riezzo I, De Cillis GP, Fineschi V. Sudden cardiac death in a child affected by Prader-Willi syndrome. Int J Legal Med [Internet]. 2005 May 5 [cited 2022 Nov 17];119(3):153–7. Available from: https://link-springer-com.uea.idm.oclc.org/article/10.1007/s00414-004-0513-9

61. Grugni G, Crinò A, Bosio L, Corrias A, Cuttini M, De Toni T, et al. The Italian National Survey for Prader–Willi syndrome: An epidemiologic study. Am J Med Genet A [Internet]. 2008 Apr 1 [cited 2022 Nov 17];146A(7):861–72. Available from: https://onlinelibrary.wiley.com/doi/10.1002/ajmg.a.32133

62. Marcus KA, van Alfen-van der Velden JA, Otten BJ, Weijers G, Yntema HG, de Korte CL, et al. Cardiac evaluation in children with Prader-Willi syndrome. Acta Paediatr [Internet]. 2012 May 1 [cited 2022 Nov 17];101(5):e225–31. Available from: https://onlinelibrary.wiley.com/doi/10.1111/j.1651-2227.2011.02570.x

63. Patel S, Harmer JA, Loughnan G, Skilton MR, Steinbeck K, Celermajer DS. Characteristics of cardiac and vascular structure and function in Prader?Willi syndrome. Clin Endocrinol (Oxf) [Internet]. 2007 Jun 1 [cited 2022 Nov 17];66(6):771–7. Available from: https://onlinelibrary.wiley.com/doi/10.1111/j.1365-2265.2007.02808.x

64. Marzullo P, Marcassa C, Campini R, Eleuteri E, Minocci A, Sartorio A, et al. Conditional Cardiovascular Response to Growth Hormone Therapy in Adult Patients with Prader-Willi Syndrome. J Clin Endocrinol Metab [Internet]. 2007 Apr 1 [cited 2022 Nov 17];92(4):1364–71. Available from: https://academic.oup.com/jcem/article/92/4/1364/2597289

65. James V, Nizamudeen ZA, Lea D, Dottorini T, Holmes TL, Johnson BB, et al. Transcriptomic Analysis of Cardiomyocyte Extracellular Vesicles in Hypertrophic Cardiomyopathy Reveals Differential snoRNA Cargo. Stem Cells Dev [Internet]. 2021 Dec 15 [cited 2022 May 3];30(24):1215–27. Available from: https://www-liebertpub-com.uea.idm.oclc.org/doi/full/10.1089/scd.2021.0202

66. Ibrahim AGE, Cheng K, Marbán E. Exosomes as critical agents of cardiac regeneration triggered by cell therapy. Stem Cell Reports. 2014 May 6;2(5):606–19.

67. Johnstone RM. Exosomes biological significance: A concise review. Blood Cells Mol Dis. 2006 Mar 1;36(2):315–21.

68. Pilcher L (University of V, McElroy-Yaggy K (University of V, Soloman L (University of V, Spees J (Univesity of V. LOSS OF SNORD116 LNCRNA REDUCED PATHOLOGICAL REMODELING

AFTER MYOCARDIAL INFARCTION IN MICE. In: International Society for Stem Cell Research. San Francisco; 2022. p. 863.

69. Tsao CW, Aday AW, Almarzooq ZI, Alonso A, Beaton AZ, Bittencourt MS, et al. Heart Disease and Stroke Statistics-2022 Update: A Report from the American Heart Association. Vol. 145, Circulation. 2022. 153–639 p.

70. Wilkins E, Wilson L, Wickramasinghe K, Bhatnagar P. European Cardiovascular Disease Statistics 2017. European Heart Network [Internet]. 2017;94–100. Available from: www.ehnheart.org

71. Petrich BG, Wang Y. Stress-Activated MAP Kinases in Cardiac Remodeling and Heart Failure: New Insights from Transgenic Studies. Trends Cardiovasc Med. 2004 Feb 1;14(2):50–5.

72. Molkentin JD, Dorn GW. Cytoplasmic Signaling Pathways That Regulate Cardiac Hypertrophy. http://dx.doi.org/101146/annurev.physiol631391 [Internet]. 2003 Nov 28 [cited 2022 Oct 13];63:391–426. Available from: https://www.annualreviews.org/doi/abs/10.1146/annurev.physiol.63.1.391

73. Frey N, Olson EN. Cardiac Hypertrophy: The Good, the Bad, and the Ugly. Annu Rev Physiol. 2003;65:45–79.

74. Sweet ME, Cocciolo A, Slavov D, Jones KL, Sweet JR, Graw SL, et al. Transcriptome analysis of human heart failure reveals dysregulated cell adhesion in dilated cardiomyopathy and activated immune pathways in ischemic heart failure. BMC Genomics [Internet]. 2018 Nov 12 [cited 2022 Oct 13];19(1):1–14. Available from: https://bmcgenomics.biomedcentral.com/articles/10.1186/s12864-018-5213-9

75. Lopaschuk GD, Karwi QG, Tian R, Wende AR, Abel ED. Cardiac Energy Metabolism in Heart Failure. Circ Res [Internet]. 2021 May 14 [cited 2022 Oct 13];128(10):1487–513. Available from:

https://www.ahajournals.org/doi/abs/10.1161/CIRCRESAHA.121.318241

76. Lopaschuk GD, Jaswal JS. Energy Metabolic Phenotype of the Cardiomyocyte During Development, Differentiation, and Postnatal Maturation. J Cardiovasc Pharmacol [Internet]. 2010 Aug [cited 2020 Mar 25];56(2):130–40. Available from: http://journals.lww.com/00005344-201008000-00003

77. Ascuitto RJ, Ross-Ascuitto NT. Substrate metabolism in the developing heart. Semin Perinatol. 1996 Dec 1;20(6):542–63.

78. Piquereau J, Ventura-Clapier R. Maturation of cardiac energy metabolism during perinatal development. Vol. 9, Frontiers in Physiology. Frontiers Media S.A.; 2018. p. 959.

79. Houten SM, Violante S, Ventura F V., Wanders RJA. The Biochemistry and Physiology of Mitochondrial Fatty Acid β-Oxidation and Its Genetic Disorders. Annu Rev Physiol [Internet]. 2016 Feb 10 [cited 2022 Sep 21];78(1):23–44. Available from: https://www.annualreviews.org/doi/10.1146/annurev-physiol-021115-105045

80. Maron BJ, Gardin JM, Flack JM, Gidding SS, Kurosaki TT, Bild DE. Prevalence of hypertrophic cardiomyopathy in a general population of young adults: Echocardiographic analysis of 4111 subjects in the CARDIA study. Circulation [Internet]. 1995 Aug 15 [cited 2020 Feb 27];92(4):785–9. Available from: https://pubmed-ncbi-nlm-nih-gov.uea.idm.oclc.org/7641357/

81. Díez-López C, Salazar-Mendiguchía J. Clinical presentations of hypertrophic cardiomyopathy and implications for therapy. In: Global Cardiology Science and Practice [Internet]. HBKU Press; 2018 [cited 2022 Nov 22]. Available from: /pmc/articles/PMC6209433/

82. Kelly BS, Mattu A, Brady WJ. Hypertrophic cardiomyopathy: electrocardiographic manifestations and other important

considerations for the emergency physician. American Journal of Emergency Medicine. 2007 Jan 1;25(1):72–9.

83. Gersh BJ, Maron BJ, Bonow RO, Dearani JA, Fifer MA, Link MS, et al. 2011 ACCF/AHA guideline for the diagnosis and treatment of hypertrophic cardiomyopathy: A report of the American College of cardiology foundation/American heart association task force on practice guidelines [Internet]. Vol. 124, Circulation. Lippincott Williams & Wilkins Hagerstown, MD ; 2011 [cited 2022 Nov 23]. p. 783–831. Available from: http://circ.ahajournals.org/lookup/suppl/doi:10.1161/CIR.0b013e318223e2bd/-/DC1.

84. Noureldin RA, Liu S, Nacif MS, Judge DP, Halushka MK, Abraham TP, et al. The diagnosis of hypertrophic cardiomyopathy by cardiovascular magnetic resonance [Internet]. Vol. 14, Journal of Cardiovascular Magnetic Resonance. J Cardiovasc Magn Reson; 2012 [cited 2022 Nov 23]. Available from: https://pubmed-ncbi-nlm-nih-gov.uea.idm.oclc.org/22348519/

85. Zaiser E, Sehnert AJ, Duenas A, Saberi S, Brookes E, Reaney M. Patient experiences with hypertrophic cardiomyopathy: a conceptual model of symptoms and impacts on quality of life. J Patient Rep Outcomes [Internet]. 2020 Dec 1 [cited 2022 Nov 22];4(1):102. Available from: https://jpro.springeropen.com/articles/10.1186/s41687-020-00269-8

86. Maron BJ. Sudden Death in Young Competitive Athletes. JAMA [Internet]. 1996 Jul 17 [cited 2022 Nov 22];276(3):199. Available from: http://jama.jamanetwork.com/article.aspx?doi=10.1001/jama.1996.03540030033028

87. Wolf CM, Cordula MW. Hypertrophic cardiomyopathy: genetics and clinical perspectives. Cardiovasc Diagn Ther [Internet]. 2019 Oct 1

[cited 2022 Dec 13];0(0):S388–415. Available from: https://cdt.amegroups.com/article/view/24557/html

88. Pagiatakis C, Di Mauro V. The Emerging Role of Epigenetics in Therapeutic Targeting of Cardiomyopathies. Int J Mol Sci [Internet]. 2021 Aug 2 [cited 2022 Dec 13];22(16). Available from: /pmc/articles/PMC8395924/

89. Pradeep R, Akram A, Proute MC, Kothur NR, Georgiou P, Serhiyenia T, et al. Understanding the Genetic and Molecular Basis of Familial Hypertrophic Cardiomyopathy and the Current Trends in Gene Therapy for Its Management. Cureus [Internet]. 2021 Aug 30 [cited 2022 Dec 13];13(8). Available from: /pmc/articles/PMC8481153/

90. Maron BJ, Maron MS, Semsarian C. Genetics of hypertrophic cardiomyopathy after 20 years: Clinical perspectives [Internet]. Vol. 60, Journal of the American College of Cardiology. American College of Cardiology FoundationWashington, D.C.; 2012 [cited 2022 Oct 13]. p. 705–15. Available from: http://dx.doi.org/10.1016/j.jacc.2012.02.068

91. Walsh R, Offerhaus JA, Tadros R, Bezzina CR. Minor hypertrophic cardiomyopathy genes, major insights into the genetics of cardiomyopathies [Internet]. Vol. 19, Nature Reviews Cardiology. Nature Research; 2022 [cited 2022 Oct 13]. p. 151–67. Available from: https://www-nature-com.uea.idm.oclc.org/articles/s41569-021-00608-2

92. Wong AYK. Myocardial mechanics: Application of sliding-filament theory to isovolumic concentration of the left ventricle. J Biomech. 1973 Sep 1;6(5):565–81.

93. Smith DA. The sliding-filament theory of muscle contraction. The Sliding-Filament Theory of Muscle Contraction. Springer International Publishing; 2019. 1–426 p.

94. Tyska MJ, Warshaw DM. The myosin power stroke. Cell Motil Cytoskeleton [Internet]. 2002 Jan 1 [cited 2022 Nov 22];51(1):1–

15. Available from: https://onlinelibrary.wiley.com/doi/10.1002/cm.10014

95. England J, Loughna S. Heavy and light roles: Myosin in the morphogenesis of the heart. Cellular and Molecular Life Sciences. 2013;70(7):1221–39.

96. Vibert P, Craig R, Lehman W. Steric-model for activation of muscle thin filaments. J Mol Biol [Internet]. 1997 Feb [cited 2022 Nov 22];266(1):8–14. Available from: https://linkinghub.elsevier.com/retrieve/pii/S0022283696908001

97. Vio R, Angelini A, Basso C, Cipriani A, Zorzi A, Melacini P, et al. Hypertrophic cardiomyopathy and primary restrictive cardiomyopathy: Similarities, differences and phenocopies [Internet]. Vol. 10, Journal of Clinical Medicine. MDPI; 2021 [cited 2022 Oct 13]. p. 10. Available from: https://www.mdpi.com/2077-0383/10/9/1954/htm

98. Chou C, Chin MT. Pathogenic mechanisms of hypertrophic cardiomyopathy beyond sarcomere dysfunction [Internet]. Vol. 22, International Journal of Molecular Sciences. MDPI; 2021 [cited 2022 Nov 22]. p. 8933. Available from: https://www.mdpi.com/1422-0067/22/16/8933/htm

99. Marian AJ, Braunwald E. Hypertrophic cardiomyopathy: Genetics, pathogenesis, clinical manifestations, diagnosis, and therapy. Circ Res [Internet]. 2017 Sep 1 [cited 2022 Nov 22];121(7):749–70. Available from: /pmc/articles/PMC5654557/

100. Marston SB. How do mutations in contractile proteins cause the primary familial cardiomyopathies? Vol. 4, Journal of Cardiovascular Translational Research. Springer; 2011. p. 245–55.

101. Marsiglia JDC, Pereira AC. Cardiomiopatia hipertrófica: Como as mutações levam à doença?. Arq Bras Cardiol. 2014;102(3):295–303.

102. Marston S, Copeland O, Jacques A, Livesey K, Tsang V, McKenna WJ, et al. Evidence from human myectomy samples that MYBPC3 mutations cause hypertrophic cardiomyopathy through haploinsufficiency*. Circ Res [Internet]. 2009 Jul 31 [cited 2022 Nov 23];105(3):219–22. Available from: http://circres.ahajournals.org.

103. Sommese RF, Sung J, Nag S, Sutton S, Deacon JC, Choe E, et al. Molecular consequences of the R453C hypertrophic cardiomyopathy mutation on human β-cardiac myosin motor function. Proc Natl Acad Sci U S A. 2013 Jul 30;110(31):12607–12.

104. Kron SJ, Toyoshima YY, Uyeda TQP, Spudich JA. Assays for Actin Sliding Movement over Myosin-Coated Surfaces. Methods Enzymol. 1991;196(C):399–416.

105. Spudich JA, Rice SE, Rock RS, Purcell TJ, Warrick HM. Optical Traps to Study Properties of Molecular Motors. Cold Spring Harb Protoc [Internet]. 2011 Nov [cited 2022 Dec 13];2011(11):1305. Available from: /pmc/articles/PMC4784437/

106. Despond EA, Dawson JF. Classifying cardiac actin mutations associated with hypertrophic cardiomyopathy [Internet]. Vol. 9, Frontiers in Physiology. Frontiers Media S.A.; 2018 [cited 2022 Nov 23]. Available from: /pmc/articles/PMC5913282/

107. Risi C, Eisner J, Belknap B, Heeley DH, White HD, Schröder GF, et al. Ca2+-induced movement of tropomyosin on native cardiac thin filaments revealed by cryoelectron microscopy. Proc Natl Acad Sci U S A. 2017;114(26):6782–7.

108. Olson TM, Doan TP, Kishimoto NY, Whitby FG, Ackerman MJ, Fananapazir L. Inherited and de novo mutations in the cardiac actin gene cause hypertrophic cardiomyopathy. J Mol Cell Cardiol. 2000 Sep 1;32(9):1687–94.

109. Monserrat L, Hermida-Prieto M, Fernandez X, Rodríguez I, Dumont C, Cazón L, et al. Mutation in the alpha-cardiac actin gene associated with apical hypertrophic cardiomyopathy, left ventricular

non-compaction, and septal defects. Eur Heart J [Internet]. 2007 Feb 6 [cited 2022 Nov 23];28(16):1953–61. Available from: https://academic.oup.com/eurheartj/article-lookup/doi/10.1093/eurheartj/ehm239

110. Bookwalter CS, Trybus KM. Functional consequences of a mutation in an expressed human α-cardiac actin at a site implicated in familial hypertrophic cardiomyopathy. Journal of Biological Chemistry [Internet]. 2006 Jun 16 [cited 2022 Nov 23];281(24):16777–84. Available from: http://www.jbc.org/article/S0021925820558602/fulltext

111. Dahari M, Dawson JF. Do cardiac actin mutations lead to altered actomyosin interactions? Biochemistry and Cell Biology [Internet]. 2015 Mar 18 [cited 2022 Nov 23];93(4):330–4. Available from: https://cdnsciencepub-com.uea.idm.oclc.org/doi/10.1139/bcb-2014-0156

112. Debold EP, Saber W, Cheema Y, Bookwalter CS, Trybus KM, Warshaw DM, et al. Human actin mutations associated with hypertrophic and dilated cardiomyopathies demonstrate distinct thin filament regulatory properties in vitro. J Mol Cell Cardiol. 2010 Feb 1;48(2):286–92.

113. Song W, Vikhorev PG, Kashyap MN, Rowlands C, Ferenczi MA, Woledge RC, et al. Mechanical and energetic properties of papillary muscle from *ACTC* E99K transgenic mouse models of hypertrophic cardiomyopathy. American Journal of Physiology-Heart and Circulatory Physiology [Internet]. 2013 Jun 1 [cited 2020 Mar 30];304(11):H1513–24. Available from: https://www.physiology.org/doi/10.1152/ajpheart.00951.2012

114. Bai F, Caster HM, Dawson JF, Kawai M. The immediate effect of HCM causing actin mutants E99K and A230V on actin-Tm-myosin interaction in thin-filament reconstituted myocardium. J Mol Cell Cardiol. 2015 Feb 1;79:123–32.

115. Van Dijk SJ, Paalberends ER, Najafi A, Michels M, Sadayappan S, Carrier L, et al. Contractile dysfunction irrespective of the mutant protein in human hypertrophic cardiomyopathy with normal systolic function. Circ Heart Fail [Internet]. 2012 Jan [cited 2020 Mar 25];5(1):36–46. Available from: http://www.ncbi.nlm.nih.gov/pubmed/22178992

116. Robinson P, Griffiths PJ, Watkins H, Redwood CS. Dilated and hypertrophic cardiomyopathy mutations in troponin and α-tropomyosin have opposing effects on the calcium affinity of cardiac thin filaments. Circ Res [Internet]. 2007 Dec 7 [cited 2020 Mar 25];101(12):1266–73. Available from: http://www.ncbi.nlm.nih.gov/pubmed/17932326

117. Morimoto S. Sarcomeric proteins and inherited cardiomyopathies. Cardiovasc Res. 2008;77(4):659–66.

118. Waldmller S, Erdmann J, Binner P, Gelbrich G, Pankuweit S, Geier C, et al. Novel correlations between the genotype and the phenotype of hypertrophic and dilated cardiomyopathy: Results from the German Competence Network Heart Failure. Eur J Heart Fail [Internet]. 2011 Nov 18 [cited 2022 Nov 22];13(11):1185–92. Available from: https://onlinelibrary.wiley.com/doi/10.1093/eurjhf/hfr074

119. Tafelmeier M, Baessler A, Wagner S, Unsoeld B, Preveden A, Barlocco F, et al. Design of the SILICOFCM study: Effect of sacubitril/valsartan vs lifestyle intervention on functional capacity in patients with hypertrophic cardiomyopathy. Clin Cardiol [Internet]. 2020 May 3 [cited 2022 Nov 22];43(5):430–40. Available from: https://onlinelibrary.wiley.com/doi/10.1002/clc.23346

120. Millat G, Bouvagnet P, Chevalier P, Dauphin C, Simon Jouk P, Da Costa A, et al. Prevalence and spectrum of mutations in a cohort of 192 unrelated patients with hypertrophic cardiomyopathy. Eur J Med Genet. 2010 Sep 1;53(5):261–7.

121. Velicki L, Jakovljevic DG, Preveden A, Golubovic M, Bjelobrk M, Ilic A, et al. Genetic determinants of clinical phenotype in hypertrophic cardiomyopathy. BMC Cardiovasc Disord [Internet]. 2020 Dec 1 [cited 2022 Nov 23];20(1):516. Available from: https://bmccardiovascdisord.biomedcentral.com/articles/10.1186/s12872-020-01807-4

122. Mosqueira D, Mannhardt I, Bhagwan JR, Lis-Slimak K, Katili P, Scott E, et al. CRISPR/Cas9 editing in human pluripotent stemcell-cardiomyocytes highlights arrhythmias, hypocontractility, and energy depletion as potential therapeutic targets for hypertrophic cardiomyopathy. Eur Heart J. 2018;39(43):3879–92.

123. Sylvester J, Seidenberg P, Silvis M. The Dilemma of Genotype Positive-Phenotype Negative Hypertrophic Cardiomyopathy. Curr Sports Med Rep [Internet]. 2014 [cited 2022 Nov 23];13(2):94–9. Available from: http://journals.lww.com/00149619-201403000-00010

124. Sweet M, Taylor MRG, Mestroni L. Diagnosis, prevalence, and screening of familial dilated cardiomyopathy.

125. Watkins H, Ashrafian H, Redwood C. Inherited Cardiomyopathies. Schwartz RS, editor. New England Journal of Medicine [Internet]. 2011 Apr 28 [cited 2022 Nov 23];364(17):1643–56. Available from: http://www.nejm.org/doi/10.1056/NEJMra0902923

126. Kayvanpour E, Katus HA, Meder B. Determined to Fail—the Role of Genetic Mechanisms in Heart Failure [Internet]. Vol. 12, Current Heart Failure Reports. Current Science Inc.; 2015 [cited 2022 Nov 23]. p. 333–8. Available from: https://link-springer-com.uea.idm.oclc.org/article/10.1007/s11897-015-0264-6

127. McNally EM, Golbus JR, Puckelwartz MJ. Genetic mutations and mechanisms in dilated cardiomyopathy [Internet]. Vol. 123, Journal of Clinical Investigation. American Society for Clinical Investigation; 2013 [cited 2022 Nov 23]. p. 19–26. Available from: /pmc/articles/PMC3533274/

128. Teekakirikul P, Kelly MA, Rehm HL, Lakdawala NK, Funke BH. Inherited cardiomyopathies: Molecular genetics and clinical genetic testing in the postgenomic era [Internet]. Vol. 15, Journal of Molecular Diagnostics. J Mol Diagn; 2013 [cited 2022 Nov 23]. p. 158–70. Available from: https://pubmed-ncbi-nlm-nih-gov.uea.idm.oclc.org/23274168/

129. Herman DS, Lam L, Taylor MRG, Wang L, Teekakirikul P, Christodoulou D, et al. Truncations of Titin Causing Dilated Cardiomyopathy. New England Journal of Medicine [Internet]. 2012 Feb 16 [cited 2022 Nov 23];366(7):619–28. Available from: http://www.nejm.org/doi/abs/10.1056/NEJMoa1110186

130. Van Der Ven PFM, Bartsch JW, Gautel M, Jockusch H, Fürst DO. A functional knock-out of titin results in defective myofibril assembly. J Cell Sci [Internet]. 2000 Apr 15 [cited 2022 Nov 23];113(8):1405–14. Available from: http://www.embl.heidelberg.de

131. Musa H, Meek S, Gautel M, Peddie D, Smith AJH, Peckham M. Targeted homozygous deletion of M-band titin in cardiomyocytes prevents sarcomere formation. J Cell Sci [Internet]. 2006 Oct 15 [cited 2022 Nov 23];119(20):4322–31. Available from: https://journals-biologists-com.uea.idm.oclc.org/jcs/article/119/20/4322/29396/Targeted-homozygous-deletion-of-M-band-titin-in

132. Gramlich M, Michely B, Krohne C, Heuser A, Erdmann B, Klaassen S, et al. Stress-induced dilated cardiomyopathy in a knock-in mouse model mimicking human titin-based disease. J Mol Cell Cardiol. 2009 Sep 1;47(3):352–8.

133. Gräter F, Shen J, Jiang H, Gautel M, Grubmüller H. Mechanically induced titin kinase activation studied by force-probe molecular dynamics simulations. Biophys J. 2005 Feb 1;88(2):790–804.

134. Willis MS, Ike C, Li L, Wang DZ, Glass DJ, Patterson C. Muscle ring finger 1, but not muscle ring finger 2, regulates cardiac hypertrophy

in vivo. Circ Res [Internet]. 2007 Mar 2 [cited 2022 Nov 23];100(4):456–9. Available from: http://www.circulationaha.org

135. Peng J, Raddatz K, Molkentin JD, Wu Y, Labeit S, Granzier H, et al. Cardiac hypertrophy and reduced contractility in hearts deficient in the titin kinase region. Circulation [Internet]. 2007 Feb 13 [cited 2022 Nov 23];115(6):743–51. Available from: http://www.circulationaha.org

136. Arbustini E, Diegoli M, Fasani R, Grasso M, Morbini P, Banchieri N, et al. Mitochondrial DNA mutations and mitochondrial abnormalities in dilated cardiomyopathy. American Journal of Pathology [Internet]. 1998 [cited 2022 Nov 23];153(5):1501–10. Available from: /pmc/articles/PMC1853408/

137. Alimadadi A, Munroe PB, Joe B, Cheng X. Meta-Analysis of Dilated Cardiomyopathy Using Cardiac RNA-Seq Transcriptomic Datasets. [cited 2022 Nov 23]; Available from: https://www.ncbi.nlm.nih.gov/geo/

138. Chen YX, Ding J, Zhou WE, Zhang X, Sun XT, Wang XY, et al. Identification and Functional Prediction of Long Non-Coding RNAs in Dilated Cardiomyopathy by Bioinformatics Analysis. Front Genet [Internet]. 2021 Apr 16 [cited 2022 Nov 23];12. Available from: /pmc/articles/PMC8085533/

139. Corrado D, Basso C, Thiene G. Arrhythmogenic right ventricular cardiomyopathy: an update. Heart [Internet]. 2009 May 1 [cited 2022 Nov 25];95(9):766–73. Available from: http://heart.bmj.com/

140. Basso C, Thiene G, Corrado D, Angelini A, Nava A, Valente M. Arrhythmogenic right ventricular cardiomyopathy: Dysplasia, dystrophy, or myocarditis? Circulation [Internet]. 1996 Sep 1 [cited 2022 Nov 25];94(5):983–91. Available from: https://www-ahajournals-org.uea.idm.oclc.org/doi/abs/10.1161/01.CIR.94.5.983

141. Corrado D, Link MS, Calkins H. Arrhythmogenic Right Ventricular Cardiomyopathy. Jarcho JA, editor. New England Journal of Medicine [Internet]. 2017 Jan 5 [cited 2022 Nov 25];376(1):61–72. Available from: http://www.nejm.org/doi/10.1056/NEJMra1509267

142. Corrado D, Basso C, Thiene G, McKenna WJ, Davies MJ, Fontaliran F, et al. Spectrum of clinicopathologic manifestations of arrhythmogenic right ventricular cardiomyopathy/dysplasia: A multicenter study. J Am Coll Cardiol [Internet]. 1997 Nov 15 [cited 2022 Nov 25];30(6):1512–20. Available from: https://www.jacc.org/doi/10.1016/S0735-1097(97)00332-X

143. Thiene G, Nava A, Corrado D, Rossi L, Pennelli N. Right Ventricular Cardiomyopathy and Sudden Death in Young People. New England Journal of Medicine [Internet]. 1988 Jan 21 [cited 2022 Nov 25];318(3):129–33. Available from: http://www.nejm.org/doi/abs/10.1056/NEJM198801213180301

144. Lemery R, Brugada P, Bella PD, Dugernier T, Van den Dool A, Wellens HJJ. Nonischemic ventricular tachycardia. Clinical course and long-term follow-up in patients without clinically overt heart disease. Circulation [Internet]. 1989 [cited 2022 Nov 25];79(5):990–9. Available from: http://ahajournals.org

145. Wilber DJ, Baerman J, Olshansky B, Kall J, Kopp D. Adenosine-sensitive ventricular tachycardia: Clinical characteristics and response to catheter ablation. Circulation [Internet]. 1993 [cited 2022 Nov 25];87(1):126–34. Available from: http://ahajournals.org

146. Sen-Chowdhry S, Lowe MD, Sporton SC, McKenna WJ. Arrhythmogenic right ventricular cardiomyopathy: Clinical presentation, diagnosis, and management. Vol. 117, American Journal of Medicine. Elsevier Inc.; 2004. p. 685–95.

147. Zhao G, Qiu Y, Zhang HM, Yang D. Intercalated discs: cellular adhesion and signaling in heart health and diseases. Heart Fail Rev [Internet]. 2019 Jan 1 [cited 2022 Jun 29];24(1):115–32. Available

from: https://link-springer-com.uea.idm.oclc.org/article/10.1007/s10741-018-9743-7

148. Patel DM, Green KJ. Desmosomes in the Heart: A Review of Clinical and Mechanistic Analyses. http://dx.doi.org.uea.idm.oclc.org/103109/154190612014906533 [Internet]. 2014 [cited 2022 Jun 28];21(3):109–28. Available from: https://www-tandfonline-com.uea.idm.oclc.org/doi/abs/10.3109/15419061.2014.906533

149. Schmidt A, Langbein L, Rode M, Prätzel S, Zimbelmann R, Franke WW. Plakophilins 1a and 1b: Widespread nuclear proteins recruited in specific epithelial cells as desmosomal plaque components. Cell Tissue Res [Internet]. 1997 [cited 2022 Nov 25];290(3):481–99. Available from: https://pubmed-ncbi-nlm-nih-gov.uea.idm.oclc.org/9369526/

150. Bass-Zubek AE, Godsel LM, Delmar M, Green KJ. Plakophilins: multifunctional scaffolds for adhesion and signaling. Vol. 21, Current Opinion in Cell Biology. Elsevier Current Trends; 2009. p. 708–16.

151. Sonnenberg A, Liem RKH. Plakins in development and disease. Vol. 313, Experimental Cell Research. Academic Press Inc.; 2007. p. 2189–203.

152. Green KJ, Gaudry CA. Are desmosomes more than tethers for intermediate filaments? [Internet]. Vol. 1, Nature Reviews Molecular Cell Biology. European Association for Cardio-Thoracic Surgery; 2000 [cited 2022 Nov 25]. p. 208–16. Available from: https://www-nature-com.uea.idm.oclc.org/articles/35043032

153. Rampazzo A, Nava A, Malacrida S, Beffagna G, Bauce B, Rossi V, et al. Mutation in human desmoplakin domain binding to plakoglobin causes a dominant form of arrhythmogenic right ventricular cardiomyopathy. Am J Hum Genet. 2002 Nov 1;71(5):1200–6.

154. Gerull B, Heuser A, Wichter T, Paul M, Basson CT, McDermott DA, et al. Mutations in the desmosomal protein plakophilin-2 are

common in arrhythmogenic right ventricular cardiomyopathy. Nat Genet [Internet]. 2004 Nov 17 [cited 2022 Nov 25];36(11):1162–4. Available from: http://www.nature.com/naturegenetics/

155. Pilichou K, Nava A, Basso C, Beffagna G, Bauce B, Lorenzon A, et al. Mutations in desmoglein-2 gene are associated with arrhythmogenic right ventricular cardiomyopathy. Circulation [Internet]. 2006 Mar 7 [cited 2022 Nov 25];113(9):1171–9. Available from: http://www.circulationaha.org

156. Gehmlich K, Lambiase PD, Asimaki A, Ciaccio EJ, Ehler E, Syrris P, et al. A novel desmocollin-2 mutation reveals insights into the molecular link between desmosomes and gap junctions. Heart Rhythm. 2011 May 1;8(5):711–8.

157. Ohno S, Nagaoka I, Fukuyama M, Kimura H, Itoh H, Makiyama T, et al. Age-Dependent Clinical and Genetic Characteristics in Japanese Patients With Arrhythmogenic Right Ventricular Cardiomyopathy/Dysplasia. Circulation Journal [Internet]. 2013 [cited 2022 Nov 25];77(6):CJ-12-1446. Available from: https://www.jstage.jst.go.jp/article/circj/77/6/77_CJ-12-1446/_article

158. Bao J, Wang J, Yao Y, Wang Y, Fan X, Sun K, et al. Correlation of ventricular arrhythmias with genotype in arrhythmogenic right ventricular cardiomyopathy. Circ Cardiovasc Genet [Internet]. 2013 Dec [cited 2022 Nov 25];6(6):552–6. Available from: http://circgenetics.ahajournals.org/lookup/suppl/doi:10.1161/CIRCGENETICS.113.000122/-/DC1.

159. Asimaki A, Tandri H, Huang H, Halushka MK, Gautam S, Basso C, et al. A New Diagnostic Test for Arrhythmogenic Right Ventricular Cardiomyopathy. New England Journal of Medicine [Internet]. 2009 Mar 12 [cited 2022 Nov 25];360(11):1075–84. Available from: http://www.nejm.org/doi/abs/10.1056/NEJMoa0808138

160. Kirchner F, Schuetz A, Boldt LH, Martens K, Dittmar G, Haverkamp W, et al. Molecular insights into arrhythmogenic right ventricular

cardiomyopathy caused by plakophilin-2 missense mutations. Circ Cardiovasc Genet [Internet]. 2012 Aug [cited 2022 Nov 25];5(4):400–11. Available from: http://circgenetics.ahajournals.org/lookup/suppl/doi:10.1161/CIRCGENETICS.111.961854/-/DC1.

161. Cerrone M, Montnach J, Lin X, Zhao YT, Zhang M, Agullo-Pascual E, et al. Plakophilin-2 is required for transcription of genes that control calcium cycling and cardiac rhythm. Nat Commun [Internet]. 2017 Dec 1 [cited 2022 Nov 25];8(1):1–16. Available from: www.nature.com/naturecommunications

162. Mertens C, Kulm C, Franke WW. Plakophilins 2a and 2b: Constitutive Proteins of Dual Location in the Karyoplasm and the Desmosomal Plaque.

163. Gandjbakhch E, Fressard V, Charron P, Lorin De La Grandmaison G, Simon F, Gary F, et al. 252 Plakophilin2b is not expressed in the heart: consequences for the genetic screening of arrhythmogenic right ventricular cardiomyopathy. Archives of Cardiovascular Diseases Supplements. 2011 Jan 1;3(1):83.

164. Gandjbakhch E, Charron P, Fressart V, Lorin De La Grandmaison G, Simon F, Gary F, et al. Plakophilin 2A is the dominant isoform in human heart tissue: consequences for the genetic screening of arrhythmogenic right ventricular cardiomyopathy. [cited 2022 Nov 25]; Available from: http://heart.bmj.com/

165. Mertens C, Hofmann I, Wang Z, Teichmann M, Chong SS, Schnölzer M, et al. Nuclear particles containing RNA polymerase III complexes associated with the junctional plaque protein plakophilin 2. Proc Natl Acad Sci U S A [Internet]. 2001 Jul 3 [cited 2022 Nov 25];98(14):7795–800. Available from: https://www.pnas.org

166. Bernard J, Jacquillat C, Boiron M, Najean Y, Seligmann M, Tanzer J, et al. Essai de traitement des leucémies aiguës lymphoblastiques et myéloblastiques par un antibiotique nouveau: la rubidomycine

(13,057 RP). Etude de 61 observations. Presse Med. 1967;75(19):951–5.

167. Bonadonna G, Monfardini S. CARDIAC TOXICITY OF DAUNORUBICIN. The Lancet. 1969 Apr 19;293(7599):837–8.

168. Arcamone F, Cassinelli G, Fantini G, Grein A, Orezzi P, Pol C, et al. Adriamycin, 14-hydroxydaunomycin, a new antitumor antibiotic from S. peucetius var. caesius. Biotechnol Bioeng [Internet]. 1969 [cited 2022 Oct 13];11(6):1101–10. Available from: https://pubmed.ncbi.nlm.nih.gov/5365804/

169. Lefrak EA, Pitha J, Rosenheim S, Gottlieb JA. A CLINICOPATHOLOGIC ANALYSIS OF ADRIAMYCIN CARDIOTOXICITY. [cited 2022 Oct 13]; Available from: https://acsjournals.onlinelibrary.wiley.com/doi/10.1002/1097-0142

170. Vitfell-Rasmussen J, Krarup-Hansen A, Vaage-Nilsen M, Kümler T, Zerahn B. Real-life incidence of cardiotoxicity and associated risk factors in sarcoma patients receiving doxorubicin. Acta Oncol (Madr) [Internet]. 2022 [cited 2022 Nov 25];61(7):801–8. Available from: https://www.tandfonline.com/doi/abs/10.1080/0284186X.2022.2082884

171. Swain SM, Whaley FS, Ewer MS. Congestive heart failure in patients treated with doxorubicin. Cancer [Internet]. 2003 Jun 1 [cited 2022 Nov 25];97(11):2869–79. Available from: https://onlinelibrary.wiley.com/doi/10.1002/cncr.11407

172. Bodley A, Liu LF, Israel M, Seshadri R, Koseki Y, Giuliani FC, et al. DNA Topoisomerase II-mediated Interaction of Doxorubicin and Daunorubicin Congeners with DNA. Cancer Res. 1989;49(21):5969–78.

173. Rawat PS, Jaiswal A, Khurana A, Bhatti JS, Navik U. Doxorubicin-induced cardiotoxicity: An update on the molecular mechanism and

novel therapeutic strategies for effective management. Biomedicine & Pharmacotherapy. 2021 Jul 1;139:111708.

174. Kajihara H, Yokozaki H, Yamahara M, Kadomoto Y, Tahara E. Anthracycline induced myocardial damage: An analysis of 16 autopsy cases. Pathol Res Pract. 1986 Aug 1;181(4):434–41.

175. Fitter W, DeSa DJ, Pai KRM. Adriamycin cardiotoxicity: report of an unusual case with features resembling endomyocardial fibrosis. J Clin Pathol [Internet]. 1981 Jun 1 [cited 2022 Oct 13];34(6):602–5. Available from: https://jcp.bmj.com/content/34/6/602

176. Zhao Y, McLaughlin D, Robinson E, Harvey AP, Hookham MB, Shah AM, et al. Nox2 NADPH oxidase promotes pathologic cardiac remodeling associated with doxorubicin chemotherapy. Cancer Res [Internet]. 2010 Nov 15 [cited 2022 Dec 13];70(22):9287–97. Available from: https://aacrjournals.org/cancerres/article/70/22/9287/560193/Nox2-NADPH-Oxidase-Promotes-Pathologic-Cardiac

177. Ma J, Wang Y, Zheng D, Wei M, Xu H, Peng T. Rac1 signalling mediates doxorubicin-induced cardiotoxicity through both reactive oxygen species-dependent and -independent pathways. Cardiovasc Res [Internet]. 2013 Jan 1 [cited 2022 Dec 13];97(1):77–87. Available from: https://pubmed.ncbi.nlm.nih.gov/23027656/

178. Zhu H, Sarkar S, Scott L, Danelisen I, Trush MA, Jia Z, et al. Doxorubicin Redox Biology: Redox Cycling, Topoisomerase Inhibition, and Oxidative Stress. React Oxyg Species (Apex) [Internet]. 2016 May [cited 2022 Dec 13];1(3):189. Available from: /pmc/articles/PMC5921833/

179. Hopkins R. Hydrogen Peroxide in Biology and Medicine: An Overview. Reactive Oxygen Species. 2017;1(2):99–109.

180. Trush MA, G. Mimnaugh E, Gram TE. Activation of pharmacologic agents to radical intermediates. Implications for the role of free

radicals in drug action and toxicity. Biochem Pharmacol. 1982;31(21):3335–46.

181. Mimnaugh EG, Trush MA, Ginsburg E, Gram TE. Differential Effects of Anthracycline Drugs on Rat Heart and Liver Microsomal Reduced Nicotinamide Adenine Dinucleotide Phosphate-dependent Lipid Peroxidation. Cancer Res. 1982;42(9):3574–82.

182. Mohan UP, Kunjiappan S, Tirupathi PPB, Arunachalam S. Disruption of glycolysis, tca cycle, respiratory chain, calcium and iron homeostasis in doxorubicin induced cardiomyopathy-an in-silico approach. Biointerface Res Appl Chem. 2022;12(6):8527–42.

183. Jeyaseelan R, Poizat C, Wu HY, Kedes L. Molecular Mechanisms of Doxorubicin-induced Cardiomyopathy: SELECTIVE SUPPRESSION OF REISKE IRON-SULFUR PROTEIN, ADP/ATP TRANSLOCASE, AND PHOSPHOFRUCTOKINASE GENES IS ASSOCIATED WITH ATP DEPLETION IN RAT CARDIOMYOCYTES. Journal of Biological Chemistry. 1997 Feb 28;272(9):5828–32.

184. García M, Pujol A, Ruzo A, Riu E, Ruberte J, Arbós A, et al. Phosphofructo-1-Kinase Deficiency Leads to a Severe Cardiac and Hematological Disorder in Addition to Skeletal Muscle Glycogenosis. PLoS Genet [Internet]. 2009 Aug [cited 2022 Oct 13];5(8):e1000615. Available from: https://journals.plos.org/plosgenetics/article?id=10.1371/journal.pgen.1000615

185. Gao S, Li H, Feng X jun, Li M, Liu Z ping, Cai Y, et al. α-Enolase plays a catalytically independent role in doxorubicin-induced cardiomyocyte apoptosis and mitochondrial dysfunction. J Mol Cell Cardiol. 2015 Feb 1;79:92–103.

186. Karwi QG, Uddin GM, Ho KL, Lopaschuk GD. Loss of Metabolic Flexibility in the Failing Heart. Front Cardiovasc Med. 2018 Jun 6;5:68.

187. Lopaschuk GD, Ussher JR, Folmes CDL, Jaswal JS, Stanley WC. Myocardial fatty acid metabolism in health and disease. Physiol Rev [Internet]. 2010 [cited 2022 Oct 13];90(1):207–58. Available from: https://journals.physiology.org/doi/10.1152/physrev.00015.2009

188. Tariq M, Al-Badr AA. ISOPROTERENOL. In: ANALYTICAL PROFILES OF DRUG SUBSTANCES. Riyadh: Americal Pharmaceutical Association; 1985. p. 391–420.

189. Brembilla-Perrot B, Terrier De La Chaise A, Pichene M, Aliot E, Cherrier F, Pernot C. Isoprenaline as an aid to the induction of catecholamine dependent supraventricular tachycardias during programmed stimulation. Heart [Internet]. 1989 Apr 1 [cited 2022 Oct 13];61(4):348–55. Available from: https://heart.bmj.com/content/61/4/348

190. Fleming HA, Mirams JA. A CLINICAL TRIAL OF A SUSTAINED-ACTION PREPARATION OF ISOPRENALINE IN THE TREATMENT OF HEART-BLOCK. The Lancet [Internet]. 1963 Aug 3 [cited 2022 Oct 13];282(7301):214–7. Available from: http://www.thelancet.com/article/S0140673663901144/fulltext

191. Wachter SB, Gilbert EM. Beta-Adrenergic Receptors, from Their Discovery and Characterization through Their Manipulation to Beneficial Clinical Application. Cardiology [Internet]. 2012 Aug [cited 2022 Oct 13];122(2):104–12. Available from: https://www.karger.com/Article/FullText/339271

192. Patel PJ, Segar R, Patel JK, Padanilam BJ, Prystowsky EN. Arrhythmia induction using isoproterenol or epinephrine during electrophysiology study for supraventricular tachycardia. J Cardiovasc Electrophysiol [Internet]. 2018 Dec 1 [cited 2022 Nov 25];29(12):1635–40. Available from: https://pubmed-ncbi-nlm-nih-gov.uea.idm.oclc.org/30192033/

193. Feng Y, Cheng J, Wei B, Wang Y. CaMKII inhibition reduces isoproterenol-induced ischemia and arrhythmias in hypertrophic

mice. Oncotarget [Internet]. 2017 Mar 3 [cited 2022 Nov 25];8(11):17504–9. Available from: /pmc/articles/PMC5392265/

194. Shin E, Ko KS, Rhee BD, Han J, Kim N. Different effects of prolonged β-adrenergic stimulation on heart and cerebral artery. Integr Med Res [Internet]. 2014 Dec [cited 2022 Nov 25];3(4):204–10. Available from: /pmc/articles/PMC5481746/

195. Osadchii OE. Cardiac hypertrophy induced by sustained β-adrenoreceptor activation: Pathophysiological aspects. Heart Fail Rev [Internet]. 2007 Mar 27 [cited 2022 Nov 25];12(1):66–86. Available from: https://link.springer.com/article/10.1007/s10741-007-9007-4

196. Zhang W, Elimban V, Nijjar MS, Gupta SK, Dhalla NS. Role of mitogen-activated protein kinase in cardiac hypertrophy and heart failure [Internet]. Vol. 8, Experimental and Clinical Cardiology. Pulsus Group; 2003 [cited 2022 Nov 25]. p. 173–83. Available from: /pmc/articles/PMC2719157/

197. Chowdhury D, Tangutur AD, Khatua TN, Saxena P, Banerjee SK, Bhadra MP. A proteomic view of isoproterenol induced cardiac hypertrophy: Prohibitin identified as a potential biomarker in rats. J Transl Med [Internet]. 2013 May 24 [cited 2022 Nov 25];11(1):130. Available from: https://translational-medicine.biomedcentral.com/articles/10.1186/1479-5876-11-130

198. Allawadhi P, Khurana A, Sayed N, Kumari P, Godugu C. Isoproterenol-induced cardiac ischemia and fibrosis: Plant-based approaches for intervention. Phytotherapy Research [Internet]. 2018 Oct 1 [cited 2022 Nov 25];32(10):1908–32. Available from: https://onlinelibrary.wiley.com/doi/10.1002/ptr.6152

199. Thygesen K, Alpert JS, White HD. Universal definition of myocardial infarction. Circulation. 2007;116(22):2634–53.

200. British Heart Foundation. UK Factsheet. British Heart Foundation [Internet]. 2022;(August):1–21. Available from:

https://www.bhf.org.uk/-/media/files/research/heart-statistics/bhf-cvd-statistics-uk-factsheet.pdf?rev=4b0be2cd03eb412f8f2703b63a3b4ebb&hash=E6965279D61DEA4CBD0C97E176CAA671

201. Mozaffarian S, Etemad K, Aghaali M, Khodakarim S, Ghorbani SS, Nazari SSH. Short and long-term survival rates following myocardial infarction and its predictive factors: A study using national registry data. Journal of Tehran University Heart Center [Internet]. 2021 [cited 2022 Nov 25];16(2):68–74. Available from: /pmc/articles/PMC8742861/

202. Mechanic OJ, Grossman SA. Myocardial Infarction, Acute [Internet]. StatPearls. StatPearls Publishing; 2018 [cited 2022 Nov 25]. Available from: https://www.ncbi.nlm.nih.gov/books/NBK459269/

203. Van De Werf F, Bax J, Betriu A, Blomstrom-Lundqvist C, Crea F, Falk V, et al. Management of acute myocardial infarction in patients presenting with persistent ST-segment elevation [Internet]. Vol. 29, European Heart Journal. Oxford University Press; 2008 [cited 2022 Nov 25]. p. 2909–45. Available from: https://academic.oup.com/eurheartj/article/29/23/2909/496390

204. Reed GW, Rossi JE, Cannon CP. Acute myocardial infarction. Vol. 389, The Lancet. Lancet Publishing Group; 2017. p. 197–210.

205. Thygesen K, Alpert JS, Jaffe AS, Chaitman BR, Bax JJ, Morrow DA, et al. Fourth Universal Definition of Myocardial Infarction (2018). Vol. 138, Circulation. 2018. 618–651 p.

206. Saleh M, Ambrose JA. Understanding myocardial infarction [version 1; referees: 2 approved] [Internet]. Vol. 7, F1000Research. F1000 Research Ltd; 2018 [cited 2022 Nov 25]. Available from: /pmc/articles/PMC6124376/

207. Jennings RB. Early phase of myocardial ischemic injury and infarction. Am J Cardiol. 1969 Dec 1;24(6):753–65.

208. Burke AP, Virmani R. Pathophysiology of Acute Myocardial Infarction. Vol. 91, Medical Clinics of North America. Elsevier; 2007. p. 553–72.

209. Vakeva AP, Agah A, Rollins SA, Matis LA, Li L, Stahl GL. Myocardial infarction and apoptosis after myocardial ischemia and reperfusion: Role of the terminal complement components and inhibition by anti-C5 therapy. Circulation [Internet]. 1998 Jun 9 [cited 2022 Nov 25];97(22):2259–67. Available from: http://ahajournals.org

210. Frangogiannis NG, Smith CW, Entman ML. The inflammatory response in myocardial infarction [Internet]. Vol. 53, Cardiovascular Research. Oxford Academic; 2002 [cited 2022 Nov 25]. p. 31–47. Available from: www.elsevier.com/locate/cardiores

211. Hashmi S, Al-Salam S. Acute myocardial infarction and myocardial ischemia-reperfusion injury: A comparison. Int J Clin Exp Pathol [Internet]. 2015 [cited 2022 Nov 25];8(8):8786–96. Available from: /pmc/articles/PMC4583853/

212. Krijnen PAJ, Meischl C, Hack CE, Meijer CJLM, Visser CA, Roos D, et al. Increased Nox2 expression in human cardiomyocytes after acute myocardial infarction. J Clin Pathol [Internet]. 2003 Mar 1 [cited 2022 Nov 25];56(3):194–9. Available from: www.jclinpath.com

213. Braunersreuther V, Montecucco F, Ashri M, Pelli G, Galan K, Frias M, et al. Role of NADPH oxidase isoforms NOX1, NOX2 and NOX4 in myocardial ischemia/reperfusion injury. J Mol Cell Cardiol [Internet]. 2013 Nov 1 [cited 2022 Nov 25];64:99–107. Available from: https://linkinghub.elsevier.com/retrieve/pii/S0022282813002708

214. Xu Y, Huo Y, Toufektsian MC, Ramos SI, Ma Y, Tejani AD, et al. Activated platelets contribute importantly to myocardial reperfusion injury. Am J Physiol Heart Circ Physiol [Internet]. 2006 Feb [cited 2022 Nov 25];290(2):692–9. Available from: www.ajpheart.org

215. Zhao W, Zhao D, Yan R, Sun Y. Cardiac oxidative stress and remodeling following infarction: role of NADPH oxidase. Cardiovascular Pathology. 2009 May 1;18(3):156–66.

216. Brod J. Pathogenesis of cardiac oedema. Br Med J [Internet]. 1972 Jan 22 [cited 2022 Dec 13];1(5794):222–8. Available from: https://pubmed-ncbi-nlm-nih-gov.uea.idm.oclc.org/5058735/

217. Terentyev D, Györke I, Belevych AE, Terentyeva R, Sridhar A, Nishijima Y, et al. Redox modification of ryanodine receptors contributes to sarcoplasmic reticulum Ca2+ leak in chronic heart failure. Circ Res [Internet]. 2008 Dec 5 [cited 2022 Nov 25];103(12):1466–72. Available from: http://circres.ahajournals.org

218. Jennings R, Reimer K. Factors involved in salvaging ischemic myocardium: effect of reperfusion of arterial blood. Circulation. 1983;68(2):25–36.

219. Mao S, Liang Y, Chen P, Zhang Y, Yin X, Zhang M. In-depth proteomics approach reveals novel biomarkers of cardiac remodelling after myocardial infarction: An exploratory analysis. J Cell Mol Med [Internet]. 2020 Sep 23 [cited 2022 Nov 25];24(17):10042–51. Available from: https://onlinelibrary.wiley.com/doi/10.1111/jcmm.15611

220. Jacobs M, Staufenberger S, Gergs U, Meuter K, Brandstätter K, Hafner M, et al. Tumor necrosis factor-α at acute myocardial infarction in rats and effects on cardiac fibroblasts. J Mol Cell Cardiol. 1999 Nov 1;31(11):1949–59.

221. Turner NA, Mughal RS, Warburton P, O'Regan DJ, Ball SG, Porter KE. Mechanism of TNFα-induced IL-1α, IL-1β and IL-6 expression in human cardiac fibroblasts: Effects of statins and thiazolidinediones. Cardiovasc Res [Internet]. 2007 Oct 1 [cited 2022 Nov 25];76(1):81–90. Available from: https://academic.oup.com/cardiovascres/article-lookup/doi/10.1016/j.cardiores.2007.06.003

222. Dobaczewski M, Bujak M, Li N, Gonzalez-Quesada C, Mendoza LH, Wang XF, et al. Smad3 signaling critically regulates fibroblast phenotype and function in healing myocardial infarction. Circ Res [Internet]. 2010 Aug 6 [cited 2022 Nov 25];107(3):418–28. Available from: http://circres.ahajournals.org

223. Bujak M, Frangogiannis NG. The role of TGF-β signaling in myocardial infarction and cardiac remodeling [Internet]. Vol. 74, Cardiovascular Research. Oxford Academic; 2007 [cited 2022 Nov 8]. p. 184–95. Available from: https://academic.oup.com/cardiovascres/article-lookup/doi/10.1016/j.cardiores.2006.10.002

224. van Putten S, Shafieyan Y, Hinz B. Mechanical control of cardiac myofibroblasts. Vol. 93, Journal of Molecular and Cellular Cardiology. Academic Press; 2016. p. 133–42.

225. Chen W, Frangogiannis NG. Fibroblasts in post-infarction inflammation and cardiac repair. Vol. 1833, Biochimica et Biophysica Acta - Molecular Cell Research. Elsevier; 2013. p. 945–53.

226. Willems IEMG, Havenith MG, De Mey JGR, Daemen MJAP. The α-smooth muscle actin-positive cells in healing human myocardial scars. American Journal of Pathology [Internet]. 1994 Oct [cited 2022 Nov 25];145(4):868–75. Available from: /pmc/articles/PMC1887334/?report=abstract

227. Poulsom R, Alison MR, Forbes SJ, Wright NA. Adult stem cell plasticity. J Pathol [Internet]. 2002 Jul 1 [cited 2022 Nov 26];197(4):441–56. Available from: https://onlinelibrary-wiley-com.uea.idm.oclc.org/doi/full/10.1002/path.1176

228. Tarnowski M, Sieron AL. Adult stem cells and their ability to differentiate. Medical Science Monitor. 2006;12(8):154–64.

229. Tocci A, Forte L. Mesenchymal stem cell: Use and perspective. Hematology Journal. 2003;4(2):92–6.

230. Hernández R, Jiménez-Luna C, Perales-Adán J, Perazzoli G, Melguizo C, Prados J. Differentiation of Human Mesenchymal Stem Cells towards Neuronal Lineage: Clinical Trials in Nervous System Disorders. Biomol Ther (Seoul) [Internet]. 2020 [cited 2022 Nov 26];28(1):34. Available from: /pmc/articles/PMC6939692/

231. Ferrand J, Noël D, Lehours P, Prochazkova-Carlotti M, Chambonnier L, Ménard A, et al. Human Bone Marrow-Derived Stem Cells Acquire Epithelial Characteristics through Fusion with Gastrointestinal Epithelial Cells. PLoS One [Internet]. 2011 [cited 2022 Nov 26];6(5):e19569. Available from: https://journals-plos-org.uea.idm.oclc.org/plosone/article?id=10.1371/journal.pone.0019569

232. Chu DT, Phuong TNT, Tien NLB, Tran DK, Thanh V Van, Quang TL, et al. An Update on the Progress of Isolation, Culture, Storage, and Clinical Application of Human Bone Marrow Mesenchymal Stem/Stromal Cells. Int J Mol Sci [Internet]. 2020 Feb 1 [cited 2022 Nov 27];21(3). Available from: https://pubmed.ncbi.nlm.nih.gov/31973182/

233. Hwang NS, Zhang C, Hwang YS, Varghese S. Mesenchymal stem cell differentiation and roles in regenerative medicine. Wiley Interdiscip Rev Syst Biol Med [Internet]. 2009 Jul 1 [cited 2022 Nov 27];1(1):97–106. Available from: https://onlinelibrary-wiley-com.uea.idm.oclc.org/doi/full/10.1002/wsbm.26

234. Kretlow JD, Jin YQ, Liu W, Zhang WJ, Hong TH, Zhou G, et al. Donor age and cell passage affects differentiation potential of murine bone marrow-derived stem cells. BMC Cell Biol [Internet]. 2008 Oct 28 [cited 2022 Nov 27];9(1):1–13. Available from: https://link.springer.com/articles/10.1186/1471-2121-9-60

235. Turinetto V, Vitale E, Giachino C. Senescence in Human Mesenchymal Stem Cells: Functional Changes and Implications in Stem Cell-Based Therapy. International Journal of Molecular Sciences 2016, Vol 17, Page 1164 [Internet]. 2016 Jul 19 [cited

2022 Nov 27];17(7):1164. Available from: https://www.mdpi.com/1422-0067/17/7/1164/htm

236. Sylvester KG, Longaker MT. Stem Cells: Review and Update. Archives of Surgery [Internet]. 2004 Jan 1 [cited 2022 Nov 27];139(1):93–9. Available from: https://jamanetwork.com/journals/jamasurgery/fullarticle/396233

237. Research IS for SC. ISSCR guidelines 2021. International Society for Stem Cell Research. 2021;(May).

238. Act E. HUMAN FERTILISATION AND EMBRYOLOGY The Human Fertilisation and Embryology (Research Purposes) Regulations 2001. 2001;2001(188):1–2. Available from: http://www.legislation.gov.uk/uksi/2001/188/pdfs/uksi_20010188_en.pdf

239. Takahashi K, Yamanaka S. Induction of Pluripotent Stem Cells from Mouse Embryonic and Adult Fibroblast Cultures by Defined Factors. Cell. 2006 Aug 25;126(4):663–76.

240. Malik N, Rao MS. A review of the methods for human iPSC derivation. In: Methods in Molecular Biology. NIH Public Access; 2013. p. 23–33.

241. Zhao XY, Li W, Lv Z, Liu L, Tong M, Hai T, et al. iPS cells produce viable mice through tetraploid complementation. Nature 2009 461:7260 [Internet]. 2009 Jul 23 [cited 2022 Nov 27];461(7260):86–90. Available from: https://www.nature.com/articles/nature08267

242. Boland MJ, Hazen JL, Nazor KL, Rodriguez AR, Gifford W, Martin G, et al. Adult mice generated from induced pluripotent stem cells. Nature 2009 461:7260 [Internet]. 2009 Aug 2 [cited 2022 Nov 27];461(7260):91–4. Available from: https://www.nature.com/articles/nature08310

243. Guenther MG, Frampton GM, Soldner F, Hockemeyer D, Mitalipova M, Jaenisch R, et al. Chromatin Structure and Gene Expression

Programs of Human Embryonic and Induced Pluripotent Stem Cells. Cell Stem Cell. 2010 Aug 6;7(2):249–57.

244. Chin MH, Pellegrini M, Plath K, Lowry WE. Molecular Analyses of Human Induced Pluripotent Stem Cells and Embryonic Stem Cells. Cell Stem Cell. 2010 Aug 6;7(2):263–9.

245. Mikkelsen TS, Hanna J, Zhang X, Ku M, Wernig M, Schorderet P, et al. Dissecting direct reprogramming through integrative genomic analysis. Nature 2008 454:7200 [Internet]. 2008 May 28 [cited 2022 Nov 27];454(7200):49–55. Available from: https://www.nature.com/articles/nature07056

246. Maherali N, Sridharan R, Xie W, Utikal J, Eminli S, Arnold K, et al. Directly Reprogrammed Fibroblasts Show Global Epigenetic Remodeling and Widespread Tissue Contribution. Cell Stem Cell. 2007 Jun 7;1(1):55–70.

247. Cao H, Yang P, Pu Y, Sun X, Yin H, Zhang Y, et al. Characterization of bovine induced pluripotent stem cells by lentiviral transduction of reprogramming factor fusion proteins. Int J Biol Sci. 2012 Mar 21;8(4):498–511.

248. Soldner F, Hockemeyer D, Beard C, Gao Q, Bell GW, Cook EG, et al. Parkinson's Disease Patient-Derived Induced Pluripotent Stem Cells Free of Viral Reprogramming Factors. Cell [Internet]. 2009 Mar 6 [cited 2020 Mar 13];136(5):964–77. Available from: http://www.ncbi.nlm.nih.gov/pubmed/19269371

249. Stadtfeld M, Nagaya M, Utikal J, Weir G, Hochedlinger K. Induced pluripotent stem cells generated without viral integration. Science (1979). 2008 Nov 7;322(5903):945–9.

250. Zhou W, Freed CR. Adenoviral gene delivery can reprogram human fibroblasts to induced pluripotent stem cells. Stem Cells [Internet]. 2009 Nov [cited 2020 Mar 21];27(11):2667–74. Available from: http://www.ncbi.nlm.nih.gov/pubmed/19697349

251. He TC, Zhou S, Da Costa LT, Yu J, Kinzler KW, Vogelstein B. A simplified system for generating recombinant adenoviruses. In: Proceedings of the National Academy of Sciences of the United States of America. 1998. p. 2509–14.

252. Ban H, Nishishita N, Fusaki N, Tabata T, Saeki K, Shikamura M, et al. Efficient generation of transgene-free human induced pluripotent stem cells (iPSCs) by temperature-sensitive Sendai virus vectors. Proc Natl Acad Sci U S A. 2011 Aug 23;108(34):14234–9.

253. Fusaki N, Ban H, Nishiyama A, Saeki K, Hasegawa M. Efficient induction of transgene-free human pluripotent stem cells using a vector based on Sendai virus, an RNA virus that does not integrate into the host genome. Proc Jpn Acad Ser B Phys Biol Sci. 2009 Oct;85(8):348–62.

254. Ding S, Wu X, Li G, Han M, Zhuang Y, Xu T. Efficient transposition of the piggyBac (PB) transposon in mammalian cells and mice. Cell [Internet]. 2005 Aug 12 [cited 2020 Mar 21];122(3):473–83. Available from: http://www.ncbi.nlm.nih.gov/pubmed/16096065

255. Yusa K, Rad R, Takeda J, Bradley A. Generation of transgene-free induced pluripotent mouse stem cells by the piggyBac transposon. Nat Methods. 2009;6(5):363–9.

256. Mali P, Chou BK, Yen J, Ye Z, Zou J, Dowey S, et al. Butyrate greatly enhances derivation of human induced pluripotent stem cells by promoting epigenetic remodeling and the expression of pluripotency-associated genes. Stem Cells [Internet]. 2010 Apr [cited 2020 Mar 21];28(4):713–20. Available from: http://www.ncbi.nlm.nih.gov/pubmed/20201064

257. Okita K, Nakagawa M, Hyenjong H, Ichisaka T, Yamanaka S. Generation of mouse induced pluripotent stem cells without viral vectors. Science (1979) [Internet]. 2008 Nov 7 [cited 2020 Mar 23];322(5903):949–53. Available from: http://www.ncbi.nlm.nih.gov/pubmed/18845712

258. Yu J, Vodyanik MA, Smuga-Otto K, Antosiewicz-Bourget J, Frane JL, Tian S, et al. Induced pluripotent stem cell lines derived from human somatic cells. Science (1979). 2007 Dec 21;318(5858):1917–20.

259. Chou BK, Mali P, Huang X, Ye Z, Dowey SN, Resar LMS, et al. Efficient human iPS cell derivation by a non-integrating plasmid from blood cells with unique epigenetic and gene expression signatures. Cell Res. 2011 Mar;21(3):518–29.

260. Junying Y, Kejin H, Kim SO, Shulan T, Stewart R, Slukvin II, et al. Human induced pluripotent stem cells free of vector and transgene sequences. Science (1979) [Internet]. 2009 May 8 [cited 2020 Mar 23];324(5928):797–801. Available from: http://www.ncbi.nlm.nih.gov/pubmed/19325077

261. Warren L, Manos PD, Ahfeldt T, Loh YH, Li H, Lau F, et al. Highly efficient reprogramming to pluripotency and directed differentiation of human cells with synthetic modified mRNA. Cell Stem Cell. 2010 Nov 5;7(5):618–30.

262. Krishnan A, Samtani R, Dhanantwari P, Lee E, Yamada S, Shiota K, et al. A detailed comparison of mouse and human cardiac development. Pediatric Research 2014 76:6 [Internet]. 2014 Aug 28 [cited 2022 Nov 28];76(6):500–7. Available from: https://www-nature-com.uea.idm.oclc.org/articles/pr2014128

263. Moretti A, Laugwitz KL, Dorn T, Sinnecker D, Mummery C. Pluripotent Stem Cell Models of Human Heart Disease. Cold Spring Harb Perspect Med [Internet]. 2013 [cited 2022 Nov 28];3(11). Available from: /pmc/articles/PMC3808770/

264. Mestas J, Hughes CCW. Of mice and not men: differences between mouse and human immunology. J Immunol [Internet]. 2004 Mar 1 [cited 2022 Nov 28];172(5):2731–8. Available from: https://pubmed-ncbi-nlm-nih-gov.uea.idm.oclc.org/14978070/

265. Bruneau BG. Signaling and transcriptional networks in heart development and regeneration. Cold Spring Harb Perspect Biol

[Internet]. 2013 Mar [cited 2022 Nov 18];5(3). Available from: /pmc/articles/PMC3578359/

266. Doyle MJ, Lohr JL, Chapman CS, Koyano-Nakagawa N, Garry MG, Garry DJ. Human Induced Pluripotent Stem Cell-Derived Cardiomyocytes as a Model for Heart Development and Congenital Heart Disease. Stem Cell Rev Rep. 2015;11(5):710–27.

267. Sizarov A, Ya J, De Boer BA, Lamers WH, Christoffels VM, Moorman AFM. Formation of the building plan of the human heart: Morphogenesis, growth, and differentiation. Circulation [Internet]. 2011 Mar 15 [cited 2022 Nov 18];123(10):1125–35. Available from: http://circ.ahajournals.org

268. Cao Y, Duca S, Cao J. Epicardium in Heart Development. Cold Spring Harb Perspect Biol [Internet]. 2020 Feb 1 [cited 2022 Nov 28];12(2). Available from: /pmc/articles/PMC6996450/

269. Harris IS, Black BL. Development of the Endocardium. Pediatr Cardiol [Internet]. 2010 [cited 2022 Nov 28];31(3):391. Available from: /pmc/articles/PMC2836465/

270. Bruneau BG. The developmental genetics of congenital heart disease [Internet]. Vol. 451, Nature. Nature Publishing Group; 2008 [cited 2022 Nov 18]. p. 943–8. Available from: http://pie.med.utoronto.ca/HTBG/

271. Benson DW, Silberbach GM, Kavanaugh-McHugh A, Cottrill C, Zhang Y, Riggs S, et al. Mutations in the cardiac transcription factor NKX2.5 affect diverse cardiac developmental pathways. Journal of Clinical Investigation. 1999 Dec 1;104(11):1567–73.

272. Garg V, Kathiriya IS, Barnes R, Schluterman MK, King IN, Butler CA, et al. GATA4 mutations cause human congenital heart defects and reveal an interaction with TBX5. Nature [Internet]. 2003 Jul 24 [cited 2022 Nov 18];424(6947):443–7. Available from: www.nature.com/nature.

273. Merscher S, Funke B, Epstein JA, Heyer J, Puech A, Lu MM, et al. TBX1 is responsible for cardiovascular defects in velo-cardio-facial/DiGeorge syndrome. Cell. 2001 Feb 23;104(4):619–29.

274. Bedada FB, Chan SSK, Metzger SK, Zhang L, Zhang J, Garry DJ, et al. Acquisition of a quantitative, stoichiometrically conserved ratiometric marker of maturation status in stem cell-derived cardiac myocytes. Stem Cell Reports. 2014 Oct 14;3(4):594–605.

275. Burridge PW, Holmström A, Wu JC. Chemically Defined Culture and Cardiomyocyte Differentiation of Human Pluripotent Stem Cells. Curr Protoc Hum Genet [Internet]. 2015 Oct 1 [cited 2020 Apr 28];87(1):21.3.1-21.3.15. Available from: http://www.ncbi.nlm.nih.gov/pubmed/26439715

276. Cao N, Liang H, Huang J, Wang J, Chen Y, Chen Z, et al. Highly efficient induction and long-term maintenance of multipotent cardiovascular progenitors from human pluripotent stem cells under defined conditions. Cell Res [Internet]. 2013 Sep [cited 2021 Mar 8];23(9):1119–32. Available from: /pmc/articles/PMC3773575/

277. Laflamme MA, Chen KY, Naumova A V., Muskheli V, Fugate JA, Dupras SK, et al. Cardiomyocytes derived from human embryonic stem cells in pro-survival factors enhance function of infarcted rat hearts. Nat Biotechnol [Internet]. 2007 Sep 26 [cited 2021 Mar 8];25(9):1015–24. Available from: https://www-nature-com.uea.idm.oclc.org/articles/nbt1327

278. Lian X, Hsiao C, Wilson G, Zhu K, Hazeltine LB, Azarin SM, et al. Robust cardiomyocyte differentiation from human pluripotent stem cells via temporal modulation of canonical Wnt signaling. Proc Natl Acad Sci U S A [Internet]. 2012 Jul 3 [cited 2021 Mar 8];109(27). Available from: https://pubmed-ncbi-nlm-nih-gov.uea.idm.oclc.org/22645348/

279. Zhang J, Tao R, Campbell KF, Carvalho JL, Ruiz EC, Kim GC, et al. Functional cardiac fibroblasts derived from human pluripotent stem cells via second heart field progenitors. Nat Commun [Internet].

2019 Dec 1 [cited 2022 Sep 15];10(1):1–15. Available from: https://doi.org/10.1038/s41467-019-09831-5

280. Burridge PW, Matsa E, Shukla P, Lin ZC, Churko JM, Ebert AD, et al. Chemically defined generation of human cardiomyocytes. Nat Methods. 2014;11(8):855–60.

281. Sharma A, Zhang Y, Buikema JW, Serpooshan V, Chirikian O, Kosaric N, et al. Stage-specific Effects of Bioactive Lipids on Human iPSC Cardiac Differentiation and Cardiomyocyte Proliferation. Sci Rep [Internet]. 2018 Dec 1 [cited 2020 May 13];8(1). Available from: /pmc/articles/PMC5920079/

282. Tu C, Chao BS, Wu JC. Strategies for improving the maturity of human induced pluripotent stem cell-derived cardiomyocytes. Circ Res [Internet]. 2018 [cited 2022 Nov 28];123(5):512–4. Available from: https://www-ahajournals-org.uea.idm.oclc.org/doi/abs/10.1161/CIRCRESAHA.118.313472

283. Rhee JW, Wu JC. Cardiac Cell Cycle Activation as a Strategy to Improve iPSC-derived Cardiomyocyte Therapy. Circ Res [Internet]. 2018 Jan 1 [cited 2022 Nov 28];122(1):14. Available from: /pmc/articles/PMC5773069/

284. Liu J, Wang P, He L, Li Y, Luo J, Cheng L, et al. Cardiomyocyte-restricted deletion of PPARβ/δ in PPARα-null mice causes impaired mitochondrial biogenesis and defense, but no further depression of myocardial fatty acid oxidation. PPAR Res [Internet]. 2011 [cited 2022 Sep 21];2011:13. Available from: /pmc/articles/PMC3167180/

285. Cheng L, Ding G, Qin Q, Huang Y, Lewis W, He N, et al. Cardiomyocyte-restricted peroxisome proliferator-activated receptor-δ deletion perturbs myocardial fatty acid oxidation and leads to cardiomyopathy. Nat Med [Internet]. 2004 Nov 10 [cited 2022 Sep 21];10(11):1245–50. Available from: http://www.nature.com/naturemedicine

286. Sharifpanah F, Wartenberg M, Hannig M, Piper HM, Sauer H. Peroxisome Proliferator-Activated Receptor α Agonists Enhance Cardiomyogenesis of Mouse ES Cells by Utilization of a Reactive Oxygen Species-Dependent Mechanism. Stem Cells [Internet]. 2008 Jan 1 [cited 2022 Sep 21];26(1):64–71. Available from: https://academic.oup.com/stmcls/article/26/1/64-71/6401848

287. Braissant O, Wahli W. Differential Expression of Peroxisome Proliferator-Activated Receptor-α, -β, and -γ during Rat Embryonic Development*. Endocrinology [Internet]. 1998 Jun 1 [cited 2022 Sep 21];139(6):2748–54. Available from: https://academic.oup.com/endo/article/139/6/2748/2986977

288. Kliewer SA, Forman BM, Blumberg B, Ong ES, Borgmeyer U, Mangelsdorf DJ, et al. Differential expression and activation of a family of murine peroxisome proliferator-activated receptors. Proc Natl Acad Sci U S A [Internet]. 1994 Jul 19 [cited 2022 Sep 21];91(15):7355–9. Available from: https://www.pnas.org

289. Peymani M, Ghaedi K, Irani S, Nasr-Esfahani MH. Peroxisome proliferator-activated receptor γ activity is required for appropriate cardiomyocyte differentiation. Cell J [Internet]. 2016 Jul 1 [cited 2022 Sep 21];18(2):221–8. Available from: /pmc/articles/PMC4988421/

290. Wickramasinghe NM, Sachs D, Shewale B, Gonzalez DM, Dhanan-Krishnan P, Torre D, et al. PPARdelta activation induces metabolic and contractile maturation of human pluripotent stem cell-derived cardiomyocytes. Cell Stem Cell. 2022 Apr 7;29(4):559-576.e7.

291. Wu P, Deng G, Sai X, Guo H, Huang H, Zhu P. Maturation strategies and limitations of induced pluripotent stem cell-derived cardiomyocytes [Internet]. Vol. 41, Bioscience Reports. Portland Press Ltd; 2021 [cited 2022 Sep 27]. Available from: https://pubmed-ncbi-nlm-nih-gov.uea.idm.oclc.org/33057659/

292. Tu C, Chao BS, Wu JC. Strategies for improving the maturity of human induced pluripotent stem cell-derived cardiomyocytes. Vol.

123, Circulation Research. Lippincott Williams and Wilkins; 2018. p. 512–4.

293. Ahmed RE, Anzai T, Chanthra N, Uosaki H. A Brief Review of Current Maturation Methods for Human Induced Pluripotent Stem Cells-Derived Cardiomyocytes. Vol. 8, Frontiers in Cell and Developmental Biology. Frontiers Media S.A.; 2020. p. 178.

294. Koivumäki JT, Naumenko N, Tuomainen T, Takalo J, Oksanen M, Puttonen KA, et al. Structural Immaturity of Human iPSC-Derived Cardiomyocytes: In Silico Investigation of Effects on Function and Disease Modeling. Front Physiol [Internet]. 2018 Feb 7 [cited 2022 Sep 27];9(FEB):80. Available from: http://journal.frontiersin.org/article/10.3389/fphys.2018.00080/full

295. Hwang HS, Kryshtal DO, Feaster TK, Sánchez-Freire V, Zhang J, Kamp TJ, et al. Comparable calcium handling of human iPSC-derived cardiomyocytes generated by multiple laboratories. J Mol Cell Cardiol. 2015 Aug 1;85:79–88.

296. Kane C, Couch L, Terracciano CMN. Excitation–contraction coupling of human induced pluripotent stem cell-derived cardiomyocytes. Front Cell Dev Biol [Internet]. 2015 Sep 29 [cited 2022 Sep 27];3(SEP):59. Available from: http://journal.frontiersin.org/Article/10.3389/fcell.2015.00059/abstract

297. Gherghiceanu M, Barad L, Novak A, Reiter I, Itskovitz-Eldor J, Binah O, et al. Cardiomyocytes derived from human embryonic and induced pluripotent stem cells: comparative ultrastructure. J Cell Mol Med [Internet]. 2011 Nov 1 [cited 2022 Sep 27];15(11):2539–51. Available from: https://onlinelibrary.wiley.com/doi/10.1111/j.1582-4934.2011.01417.x

298. Canfield SG, Zaja I, Godshaw B, Twaroski D, Bai X, Bosnjak ZJ. High Glucose Attenuates Anesthetic Cardioprotection in Stem-Cell-

Derived Cardiomyocytes: The Role of Reactive Oxygen Species and Mitochondrial Fission. Anesth Analg [Internet]. 2016 May 1 [cited 2022 Nov 28];122(5):1269. Available from: /pmc/articles/PMC5189917/

299. Granéli C, Hicks R, Brolén G, Synnergren J, Sartipy P. Diabetic Cardiomyopathy Modelling Using Induced Pluripotent Stem Cell Derived Cardiomyocytes: Recent Advances and Emerging Models. Stem Cell Rev Rep [Internet]. 2019 Feb 15 [cited 2022 Nov 28];15(1):13–22. Available from: https://link-springer-com.uea.idm.oclc.org/article/10.1007/s12015-018-9858-1

300. Correia C, Koshkin A, Duarte P, Hu D, Teixeira A, Domian I, et al. Distinct carbon sources affect structural and functional maturation of cardiomyocytes derived from human pluripotent stem cells. 2017 [cited 2022 Sep 27];7(1):1–17. Available from: www.nature.com/scientificreports/

301. Tu C, Chao BS, Wu JC. Strategies for improving the maturity of human induced pluripotent stem cell-derived cardiomyocytes [Internet]. Circulation Research Lippincott Williams and Wilkins; 2018 p. 512–4. Available from: https://stemcellsjournals.onlinelibrary.wiley.com/

302. Ng KM, Lau YM, Dhandhania V, Cai ZJ, Lee YK, Lai WH, et al. Empagliflozin Ammeliorates High Glucose Induced-Cardiac Dysfuntion in Human iPSC-Derived Cardiomyocytes. Sci Rep [Internet]. 2018 Dec 1 [cited 2022 Nov 28];8(1). Available from: https://pubmed-ncbi-nlm-nih-gov.uea.idm.oclc.org/30291295/

303. Acharya A, Baek ST, Huang G, Eskiocak B, Goetsch S, Sung CY, et al. The bHLH transcription factor Tcf21 is required for lineage-specific EMT of cardiac fibroblast progenitors. Development [Internet]. 2012 Jun 15 [cited 2022 Nov 28];139(12):2139–49. Available from: https://journals-biologists-com.uea.idm.oclc.org/dev/article/139/12/2139/45057/The-bHLH-transcription-factor-Tcf21-is-required

304. Smith CL, Baek ST, Sung CY, Tallquist MD. Epicardial-Derived Cell Epithelial-to-Mesenchymal Transition and Fate Specification Require PDGF Receptor Signaling. Circ Res [Internet]. 2011 Jun 10 [cited 2022 Nov 28];108(12). Available from: https://www-ahajournals-org.uea.idm.oclc.org/doi/abs/10.1161/CIRCRESAHA.110.235531

305. Moore-Morris T, Cattaneo P, Puceat M, Evans SM. Origins of Cardiac Fibroblasts. J Mol Cell Cardiol [Internet]. 2016 Feb 1 [cited 2022 Nov 28];91:1. Available from: /pmc/articles/PMC4764439/

306. Ali SR, Ranjbarvaziri S, Talkhabi M, Zhao P, Subat A, Hojjat A, et al. Developmental Heterogeneity of Cardiac Fibroblasts Does Not Predict Pathological Proliferation and Activation. Circ Res [Internet]. 2014 [cited 2022 Nov 28]; Available from: https://www-ahajournals-org.uea.idm.oclc.org/doi/abs/10.1161/CIRCRESAHA.115.303794

307. Wessels A, van den Hoff MJB, Adamo RF, Phelps AL, Lockhart MM, Sauls K, et al. Epicardially derived fibroblasts preferentially contribute to the parietal leaflets of the atrioventricular valves in the murine heart. Dev Biol. 2012 Jun 15;366(2):111–24.

308. Moore-Morris T, Guimarães-Camboa N, Banerjee I, Zambon AC, Kisseleva T, Velayoudon A, et al. Resident fibroblast lineages mediate pressure overload–induced cardiac fibrosis. J Clin Invest [Internet]. 2014 Jul 1 [cited 2022 Nov 28];124(7):2921–34. Available from: http://www.jci.org

309. Furtado MB, Costa MW, Pranoto EA, Salimova E, Pinto AR, Lam NT, et al. Cardiogenic genes expressed in cardiac fibroblasts contribute to heart development and repair. Circ Res [Internet]. 2014 Apr 25 [cited 2023 Jan 12];114(9):1422–34. Available from: https://pubmed-ncbi-nlm-nih-gov.uea.idm.oclc.org/24650916/

310. Furtado MB, Costa MW, Rosenthal NA. The cardiac fibroblast: Origin, identity and role in homeostasis and disease. Differentiation [Internet]. 2016 Sep 1 [cited 2023 Jan 12];92(3):93–101. Available

from: https://pubmed-ncbi-nlm-nih-gov.uea.idm.oclc.org/27421610/

311. von Gise A, Zhou B, Honor LB, Ma Q, Petryk A, Pu WT. WT1 regulates epicardial epithelial to mesenchymal transition through β-catenin and retinoic acid signaling pathways. Dev Biol. 2011 Aug 15;356(2):421–31.

312. Zhang H, Tian L, Shen M, Tu C, Wu H, Gu M, et al. Generation of Quiescent Cardiac Fibroblasts from Human Induced Pluripotent Stem Cells for In Vitro Modeling of Cardiac Fibrosis. 2019 Aug 16 [cited 2022 May 9];125(5):552–66. Available from: /pmc/articles/PMC6768436/

313. Zhang J, Tao R, Campbell KF, Carvalho JL, Ruiz EC, Kim GC, et al. Functional cardiac fibroblasts derived from human pluripotent stem cells via second heart field progenitors. 2019 [cited 2022 Sep 15];10(1):1–15. Available from: https://www-nature-com.uea.idm.oclc.org/articles/s41467-019-09831-5

314. Zhao L, Zhang B. Doxorubicin induces cardiotoxicity through upregulation of death receptors mediated apoptosis in cardiomyocytes. Sci Rep [Internet]. 2017 Mar 16 [cited 2022 Nov 28];7. Available from: https://pubmed-ncbi-nlm-nih-gov.uea.idm.oclc.org/28300219/

315. Burridge PW, Li YF, Matsa E, Wu H, Ong SG, Sharma A, et al. Human Induced Pluripotent Stem Cell–Derived Cardiomyocytes Recapitulate the Predilection of Breast Cancer Patients to Doxorubicin–Induced Cardiotoxicity. Nat Med [Internet]. 2016 May 1 [cited 2022 Nov 28];22(5):547. Available from: /pmc/articles/PMC5086256/

316. Hoekstra M, Mummery CL, Wilde AAM, Bezzina CR, Verkerk AO. Induced pluripotent stem cell derived cardiomyocytes as models for cardiac arrhythmias. Front Physiol. 2012;3 AUG:346.

317. Mehta A, Chung YY, Ng A, Iskandar F, Atan S, Wei H, et al. Pharmacological response of human cardiomyocytes derived from virus-free induced pluripotent stem cells. Cardiovasc Res [Internet]. 2011 Sep 1 [cited 2022 Nov 28];91(4):577–86. Available from: https://academic-oup-com.uea.idm.oclc.org/cardiovascres/article/91/4/577/347509

318. Matsa E, Rajamohan D, Dick E, Young L, Mellor I, Staniforth A, et al. Drug evaluation in cardiomyocytes derived from human induced pluripotent stem cells carrying a long QT syndrome type 2 mutation. Eur Heart J [Internet]. 2011 Apr 1 [cited 2022 Nov 28];32(8):952–62. Available from: https://academic-oup-com.uea.idm.oclc.org/eurheartj/article/32/8/952/2398453

319. Hidalgo A, Glass N, Ovchinnikov D, Yang SK, Zhang X, Mazzone S, et al. Modelling ischemia-reperfusion injury (IRI) in vitro using metabolically matured induced pluripotent stem cell-derived cardiomyocytes. APL Bioeng [Internet]. 2018 Mar 20 [cited 2022 Nov 28];2(2):026102. Available from: https://aip-scitation-org.uea.idm.oclc.org/doi/abs/10.1063/1.5000746

320. Chen T, Vunjak-Novakovic G. Human Tissue-Engineered Model of Myocardial Ischemia–Reperfusion Injury. https://home-liebertpub-com.uea.idm.oclc.org/tea [Internet]. 2019 May 10 [cited 2022 Nov 28];25(9–10):711–24. Available from: https://www-liebertpub-com.uea.idm.oclc.org/doi/10.1089/ten.tea.2018.0212

321. Sebastião MJ, Gomes-Alves P, Reis I, Sanchez B, Palacios I, Serra M, et al. Bioreactor-based 3D human myocardial ischemia/reperfusion in vitro model: a novel tool to unveil key paracrine factors upon acute myocardial infarction. Translational Research. 2020 Jan 1;215:57–74.

322. Wei W, Liu Y, Zhang Q, Wang Y, Zhang X, Zhang H. Danshen-Enhanced Cardioprotective Effect of Cardioplegia on Ischemia Reperfusion Injury in a Human-Induced Pluripotent Stem Cell-Derived Cardiomyocytes Model. Artif Organs [Internet]. 2017 May

1 [cited 2022 Nov 28];41(5):452–60. Available from: https://onlinelibrary-wiley-com.uea.idm.oclc.org/doi/full/10.1111/aor.12801

323. Välimäki H, Verho J, Kreutzer J, Kattipparambil Rajan D, Ryynänen T, Pekkanen-Mattila M, et al. Fluorimetric oxygen sensor with an efficient optical read-out for in vitro cell models. Sens Actuators B Chem. 2017 Oct 1;249:738–46.

324. Shah D, Virtanen L, Prajapati C, Kiamehr M, Gullmets J, West G, et al. Modeling of LMNA-Related Dilated Cardiomyopathy Using Human Induced Pluripotent Stem Cells. Cells 2019, Vol 8, Page 594 [Internet]. 2019 Jun 15 [cited 2022 Nov 28];8(6):594. Available from: https://www.mdpi.com/2073-4409/8/6/594/htm

325. Peters MC, Maas RGC, van Adrichem I, Doevendans PAM, Mercola M, Šarić T, et al. Metabolic Maturation Increases Susceptibility to Hypoxia-induced Damage in Human iPSC-derived Cardiomyocytes. Stem Cells Transl Med [Internet]. 2022 Oct 21 [cited 2022 Nov 28];11(10):1040–51. Available from: https://academic-oup-com.uea.idm.oclc.org/stcltm/article/11/10/1040/6677141

326. Häkli M, Kreutzer J, Mäki AJ, Välimäki H, Lappi H, Huhtala H, et al. Human induced pluripotent stem cell-based platform for modeling cardiac ischemia. Scientific Reports 2021 11:1 [Internet]. 2021 Feb 18 [cited 2022 Nov 28];11(1):1–13. Available from: https://www-nature-com.uea.idm.oclc.org/articles/s41598-021-83740-w

327. Ward MC, Gilad Y. A generally conserved response to hypoxia in iPSC-derived cardiomyocytes from humans and chimpanzees. Elife [Internet]. 2019 Apr 1 [cited 2022 Nov 28];8. Available from: /pmc/articles/PMC6538380/

328. Veldhuizen J, Chavan R, Moghadas B, Park JG, Kodibagkar VD, Migrino RQ, et al. Cardiac ischemia on-a-chip to investigate cellular and molecular response of myocardial tissue under hypoxia. Biomaterials. 2022 Feb 1;281:121336.

329. Semenza GL. Hypoxia-Inducible Factor 1 and Cardiovascular Disease. Annu Rev Physiol [Internet]. 2014 Feb [cited 2022 Nov 28];76:39. Available from: /pmc/articles/PMC4696033/

330. Moncrieff J, Lindsay MM, Dunn FG. Hypertensive heart disease and fibrosis. Vol. 19, Current Opinion in Cardiology. 2004. p. 326–31.

331. Khan R, Sheppard R. Fibrosis in heart disease: understanding the role of transforming growth factor-beta1 in cardiomyopathy, valvular disease and arrhythmia. Immunology [Internet]. 2006 May 1 [cited 2022 Oct 9];118(1):10–24. Available from: https://onlinelibrary.wiley.com/doi/10.1111/j.1365-2567.2006.02336.x

332. Bacmeister L, Schwarzl M, Warnke S, Stoffers B, Blankenberg S, Westermann D, et al. Inflammation and fibrosis in murine models of heart failure [Internet]. Vol. 114, Basic Research in Cardiology. Dr. Dietrich Steinkopff Verlag GmbH and Co. KG; 2019 [cited 2022 Oct 9]. p. 19. Available from: https://doi.org/10.1007/s00395-019-0722-5

333. Segura AM, Frazier OH, Buja LM. Fibrosis and heart failure. Heart Fail Rev [Internet]. 2014 Mar 4 [cited 2022 Oct 9];19(2):173–85. Available from: https://link.springer.com/article/10.1007/s10741-012-9365-4

334. Lu L, Guo J, Hua Y, Huang K, Magaye R, Cornell J, et al. Cardiac fibrosis in the ageing heart: Contributors and mechanisms. Clin Exp Pharmacol Physiol [Internet]. 2017 Dec 1 [cited 2022 Oct 9];44:55–63. Available from: https://onlinelibrary.wiley.com/doi/10.1111/1440-1681.12753

335. Swaney JS, Roth DM, Olson ER, Naugle JE, Meszaros JG, Insel PA. Inhibition of cardiac myofibroblast formation and collagen synthesis by activation and overexpression of adenylyl cyclase. Proceedings of the National Academy of Sciences [Internet]. 2005 Jan 11 [cited 2022 Nov 28];102(2):437–42. Available from: https://www-pnas-org.uea.idm.oclc.org/doi/abs/10.1073/pnas.0408704102

336. Giacomelli E, Meraviglia V, Campostrini G, Cochrane A, Cao X, van Helden RWJ, et al. Human-iPSC-Derived Cardiac Stromal Cells Enhance Maturation in 3D Cardiac Microtissues and Reveal Non-cardiomyocyte Contributions to Heart Disease. Cell Stem Cell. 2020 Jun 4;26(6):862-879.e11.

337. Li J, Feng X, Wei X. Modeling hypertrophic cardiomyopathy with human cardiomyocytes derived from induced pluripotent stem cells. Vol. 13, Stem Cell Research and Therapy. BioMed Central Ltd; 2022. p. 1–20.

338. Zhou W, Bos JM, Ye D, Tester DJ, Hrstka S, Maleszewski JJ, et al. Induced Pluripotent Stem Cell–Derived Cardiomyocytes from a Patient with MYL2-R58Q-Mediated Apical Hypertrophic Cardiomyopathy Show Hypertrophy, Myofibrillar Disarray, and Calcium Perturbations. J Cardiovasc Transl Res [Internet]. 2019 Oct 1 [cited 2022 Oct 13];12(5):394–403. Available from: https://doi.org/10.1007/s12265-019-09873-6

339. Lan F, Lee AS, Liang P, Sanchez-Freire V, Nguyen PK, Wang L, et al. Abnormal calcium handling properties underlie familial hypertrophic cardiomyopathy pathology in patient-specific induced pluripotent stem cells. Cell Stem Cell. 2013 Jan 3;12(1):101–13.

340. Smith JGW, Owen T, Bhagwan JR, Mosqueira D, Scott E, Mannhardt I, et al. Isogenic Pairs of hiPSC-CMs with Hypertrophic Cardiomyopathy/LVNC-Associated ACTC1 E99K Mutation Unveil Differential Functional Deficits. Stem Cell Reports. 2018 Nov 13;11(5):1226–43.

341. Fontaine V, Duboscq-Bidot L, Jouve C, Hamlin M, Curjol A, Briand V, et al. Generation of iPSC line from MYH7 R403L mutation carrier with severe hypertrophic cardiomyopathy and isogenic CRISPR/Cas9 corrected control. Stem Cell Res. 2021 Apr 1;52:102245.

342. Mosqueira D, Mannhardt I, Bhagwan JR, Lis-Slimak K, Katili P, Scott E, et al. CRISPR/Cas9 editing in human pluripotent stem cell-

cardiomyocytes highlights arrhythmias, hypocontractility, and energy depletion as potential therapeutic targets for hypertrophic cardiomyopathy. Eur Heart J [Internet]. 2018 Nov 11 [cited 2022 Nov 28];39(43):3879. Available from: /pmc/articles/PMC6234851/

343. Seok H, Deng R, Cowan DB, Wang DZ. Application of CRISPR-Cas9 gene editing for congenital heart disease. Clin Exp Pediatr [Internet]. 2021 [cited 2022 Nov 28];64(6):269–79. Available from: http://www.e-cep.org/journal/view.php?doi=10.3345/cep.2020.02096

344. Li J, Feng X, Wei X. Modeling hypertrophic cardiomyopathy with human cardiomyocytes derived from induced pluripotent stem cells [Internet]. 2022 p. 1–20. Available from: https://stemcellres-biomedcentral-com.uea.idm.oclc.org/articles/10.1186/s13287-022-02905-0

345. Ben Jehuda R, Shemer Y, Binah O. Genome Editing in Induced Pluripotent Stem Cells using CRISPR/Cas9. Vol. 14, Stem Cell Reviews and Reports. Humana Press Inc.; 2018. p. 323–36.

346. Poon A, Schmid B, Pires C, Nielsen TT, Hjermind LE, Nielsen JE, et al. Generation of a gene-corrected isogenic control hiPSC line derived from a familial Alzheimer's disease patient carrying a L150P mutation in presenilin 1. Stem Cell Res. 2016 Nov 1;17(3):466–9.

347. Grobarczyk B, Franco B, Hanon K, Malgrange B. Generation of Isogenic Human iPS Cell Line Precisely Corrected by Genome Editing Using the CRISPR/Cas9 System. Stem Cell Rev Rep. 2015 Oct 10;11(5):774–87.

348. Mosqueira D, Mannhardt I, Bhagwan JR, Lis-Slimak K, Katili P, Scott E, et al. CRISPR/Cas9 editing in human pluripotent stemcell-cardiomyocytes highlights arrhythmias, hypocontractility, and energy depletion as potential therapeutic targets for hypertrophic cardiomyopathy. Eur Heart J [Internet]. 2018 Nov 14 [cited 2020 Mar 28];39(43):3879–92. Available from: http://www.ncbi.nlm.nih.gov/pubmed/29741611

349. Han Z. Generate Better Hypertrophic Cardiomyopathy Model Using Induced Pluripotent Stem Cells and Crispr / Cas9. 2019;15(3):79–83.

350. Cohn R, Thakar K, Lowe A, Ladha FA, Pettinato AM, Romano R, et al. A Contraction Stress Model of Hypertrophic Cardiomyopathy due to Sarcomere Mutations. Stem Cell Reports. 2019 Jan 8;12(1):71–83.

351. Bodbin SE, Denning C, Mosqueira D. Transfection of hpsc-cardiomyocytes using viafect™ transfection reagent. Methods Protoc. 2020;3(3):1–10.

352. Johnson BB, Reinhold J, Holmes TL, Moore JA, Cowell V, Bernardo AS, et al. Modelling Metabolic Shifts during Cardiomyocyte Differentiation, Iron Deficiency and Transferrin Rescue Using Human Pluripotent Stem Cells. Metabolites 2022, Vol 12, Page 9 [Internet]. 2021 Dec 22 [cited 2022 May 3];12(1):9. Available from: https://www.mdpi.com/2218-1989/12/1/9/htm

353. Breitwieser K, Koch LF, Tertel T, Proestler E, Burgers LD, Lipps C, et al. Detailed Characterization of Small Extracellular Vesicles from Different Cell Types Based on Tetraspanin Composition by ExoView R100 Platform. Int J Mol Sci [Internet]. 2022 Aug 1 [cited 2023 Jan 13];23(15):8544. Available from: https://www.mdpi.com/1422-0067/23/15/8544/htm

354. Escola JM, Kleijmeer MJ, Stoorvogel W, Griffith JM, Yoshie O, Geuze HJ. Selective enrichment of tetraspan proteins on the internal vesicles of multivesicular endosomes and on exosomes secreted by human B-lymphocytes. J Biol Chem [Internet]. 1998 Aug 7 [cited 2023 Jan 17];273(32):20121–7. Available from: https://pubmed-ncbi-nlm-nih-gov.uea.idm.oclc.org/9685355/

355. Simpson RJ, Kalra H, Mathivanan S. ExoCarta as a resource for exosomal research. J Extracell Vesicles [Internet]. 2012 [cited 2023 Jan 17];1(1). Available from: https://pubmed-ncbi-nlm-nih-gov.uea.idm.oclc.org/24009883/

356. Schindelin J, Arganda-Carreras I, Frise E, Kaynig V, Longair M, Pietzsch T, et al. Fiji: An open-source platform for biological-image analysis. Nat Methods [Internet]. 2012 Jul [cited 2019 Apr 2];9(7):676–82. Available from: http://www.ncbi.nlm.nih.gov/pubmed/22743772

357. Sala L, Van Meer BJ, Tertoolen LGJ, Bakkers J, Bellin M, Davis RP, et al. Musclemotion: A versatile open software tool to quantify cardiomyocyte and cardiac muscle contraction in vitro and in vivo. Circ Res [Internet]. 2018 Feb 2 [cited 2022 Oct 5];122(3):e5–16. Available from: /pmc/articles/PMC5805275/

358. Stirling DR, Swain-Bowden MJ, Lucas AM, Carpenter AE, Cimini BA, Goodman A. CellProfiler 4: improvements in speed, utility and usability. BMC Bioinformatics [Internet]. 2021 Dec 1 [cited 2023 Jan 17];22(1):1–11. Available from: https://bmcbioinformatics-biomedcentral-com.uea.idm.oclc.org/articles/10.1186/s12859-021-04344-9

359. R Core Team. R: A Language and Environment for Statistical Computing [Internet]. R Foundation for Statistical Computing. 2021. Available from: https://www.r-project.org/

360. Perkins DN, Pappin DJC, Creasy DM, Cottrell JS. Probability-based protein identification by searching sequence databases using mass spectrometry data. [cited 2023 Jan 18]; Available from: http://www.matrixscience.com.

361. Altschul SF, Gish W, Miller W, Myers EW, Lipman DJ. Basic local alignment search tool. J Mol Biol [Internet]. 1990 Oct 5 [cited 2018 Feb 11];215(3):403–10. Available from: https://www.sciencedirect.com/science/article/pii/S0022283605803602?via%3Dihub

362. Sikkel MB, Francis DP, Howard J, Gordon F, Rowlands C, Peters NS, et al. Hierarchical statistical techniques are necessary to draw reliable conclusions from analysis of isolated cardiomyocyte studies. Cardiovasc Res [Internet]. 2017 Dec 1 [cited 2023 Apr

11];113(14):1743–52. Available from: https://pubmed.ncbi.nlm.nih.gov/29016722/

363. Rupert CE, Irofuala C, Coulombeid KLK. Practical adoption of state-of-the-art hiPSC-cardiomyocyte differentiation techniques. 2020 [cited 2022 Oct 14]; Available from: https://doi.org/10.1371/journal.pone.0230001.t001

364. Balafkan N, Mostafavi S, Schubert M, Siller R, Liang KX, Sullivan G, et al. A method for differentiating human induced pluripotent stem cells toward functional cardiomyocytes in 96-well microplates. Sci Rep [Internet]. 2020 Dec 1 [cited 2022 Oct 14];10(1):18498. Available from: https://doi.org/10.1038/s41598-020-73656-2

365. Fuerstenau-Sharp M, Zimmermann ME, Stark K, Jentsch N, Klingenstein M, Drzymalski M, et al. Generation of highly purified human cardiomyocytes from peripheral blood mononuclear cell-derived induced pluripotent stem cells. PLoS One [Internet]. 2015 May 13 [cited 2022 Oct 14];10(5). Available from: /pmc/articles/PMC4430251/

366. Tohyama S, Hattori F, Sano M, Hishiki T, Nagahata Y, Matsuura T, et al. Distinct metabolic flow enables large-scale purification of mouse and human pluripotent stem cell-derived cardiomyocytes. Cell Stem Cell. 2013 Jan 3;12(1):127–37.

367. Ordoño J, Pérez-Amodio S, Ball K, Aguirre A, Engel E. The generation of a lactate-rich environment stimulates cell cycle progression and modulates gene expression on neonatal and hiPSC-derived cardiomyocytes. Biomaterials Advances. 2022 Aug 1;139:213035.

368. Makinde AO, Kantor PF, Lopaschuk GD. Maturation of fatty acid and carbohydrate metabolism in the newborn heart. In: Molecular and Cellular Effects of Nutrition on Disease Processes [Internet]. Springer US; 1998 [cited 2022 Sep 27]. p. 49–56. Available from: https://link-springer-com.uea.idm.oclc.org/chapter/10.1007/978-1-4615-5763-0_6

369. Maas RGC, Lee S, Harakalova M, Snijders Blok CJB, Goodyer WR, Hjortnaes J, et al. Massive expansion and cryopreservation of functional human induced pluripotent stem cell-derived cardiomyocytes. STAR Protoc [Internet]. 2021;2(1):100334. Available from: https://doi.org/10.1016/j.xpro.2021.100334

370. Buikema JW, Lee S, Goodyer WR, Maas RG, Chirikian O, Li G, et al. Wnt Activation and Reduced Cell-Cell Contact Synergistically Induce Massive Expansion of Functional Human iPSC-Derived Cardiomyocytes. Cell Stem Cell [Internet]. 2020 Jul 2 [cited 2022 Sep 27];27(1):50-63.e5. Available from: /pmc/articles/PMC7334437/

371. Hu D, Linders A, Yamak A, Correia C, Kijlstra JD, Garakani A, et al. Metabolic maturation of human pluripotent stem cellderived cardiomyocytes by inhibition of HIF1α and LDHA. Circ Res [Internet]. 2018 Oct [cited 2021 Feb 25];123(9):1066–79. Available from: /pmc/articles/PMC6208155/

372. Correia C, Koshkin A, Duarte P, Hu D, Teixeira A, Domian I, et al. Distinct carbon sources affect structural and functional maturation of cardiomyocytes derived from human pluripotent stem cells. Sci Rep. 2017 Dec 1;7(1):1–17.

373. Yang X, Rodriguez ML, Leonard A, Sun L, Fischer KA, Wang Y, et al. Fatty Acids Enhance the Maturation of Cardiomyocytes Derived from Human Pluripotent Stem Cells. Stem Cell Reports. 2019 Oct 8;13(4):657–68.

374. Horikoshi Y, Yan Y, Terashvili M, Wells C, Horikoshi H, Fujita S, et al. Fatty acid-treated induced pluripotent stem cell-derived human cardiomyocytes exhibit adult cardiomyocyte-like energy metabolism phenotypes. Cells [Internet]. 2019 Sep 1 [cited 2022 Sep 27];8(9). Available from: /pmc/articles/PMC6769886/

375. Adachi K, Suemori H, Yasuda S ya, Nakatsuji N, Kawase E. Role of *SOX2* in maintaining pluripotency of human embryonic stem cells. Genes to Cells [Internet]. 2010 Apr 1 [cited 2022 Sep

20];15(5):455–70. Available from: https://onlinelibrary.wiley.com/doi/10.1111/j.1365-2443.2010.01400.x

376. Swain N, Thakur M, Pathak J, Swain B. SOX2, OCT4 and NANOG: The core embryonic stem cell pluripotency regulators in oral carcinogenesis. Journal of Oral and Maxillofacial Pathology [Internet]. 2020 [cited 2022 Sep 20];24(2):368. Available from: /pmc/articles/PMC7802841/

377. Watt AJ, Battle MA, Li J, Duncan SA. GATA4 is essential for formation of the proepicardium and regulates cardiogenesis. Proc Natl Acad Sci U S A [Internet]. 2004 Aug 24 [cited 2022 Sep 20];101(34):12573–8. Available from: www.pnas.orgcgidoi10.1073pnas.0400752101

378. Zhang L, Nomura-Kitabayashi A, Sultana N, Cai W, Cai X, Moon AM, et al. Mesodermal Nkx2.5 is necessary and sufficient for early second heart field development. Dev Biol. 2014 Jun 1;390(1):68–79.

379. Guo X, Xu Y, Wang Z, Wu Y, Chen J, Wang G, et al. A Linc1405/Eomes Complex Promotes Cardiac Mesoderm Specification and Cardiogenesis. Cell Stem Cell. 2018 Jun 1;22(6):893-908.e6.

380. Czarnowska E, Domal-Kwiatkowska D, Reichman-Warmusz E, Bierla JB, Sowinska A, Ratajska A, et al. The correlation of PPAR α activity and cardiomyocyte metabolism and structure in idiopathic dilated cardiomyopathy during heart failure progression. PPAR Res. 2016;2016.

381. Braissant O, Foufelle F, Scotto C, Dauça M, Wahli W. Differential expression of peroxisome proliferator-activated receptors (PPARs): tissue distribution of PPAR-alpha, -beta, and -gamma in the adult rat. Endocrinology [Internet]. 1996 Jan 1 [cited 2022 Oct 5];137(1):354–66. Available from:

https://academic.oup.com/endo/article-lookup/doi/10.1210/endo.137.1.8536636

382. Guo Y, Pu WT. Cardiomyocyte maturation: New phase in development [Internet]. Circulation Research. Lippincott Williams and Wilkins; 2020 [cited 2021 Feb 25]. p. 1086–106. Available from: www.ahajournals.org/journal/res

383. Zhang Z, Schwartz S, Wagner L, Miller W. A greedy algorithm for aligning DNA sequences. J Comput Biol [Internet]. 2000 [cited 2022 Oct 4];7(1–2):203–14. Available from: https://pubmed-ncbi-nlm-nih-gov.uea.idm.oclc.org/10890397/

384. Zhu H, Scharnhorst KS, Stieg AZ, Gimzewski JK, Minami I, Nakatsuji N, et al. Two dimensional electrophysiological characterization of human pluripotent stem cell-derived cardiomyocyte system. Scientific Reports 2017 7:1 [Internet]. 2017 Mar 7 [cited 2023 Mar 27];7(1):1–9. Available from: https://www-nature-com.uea.idm.oclc.org/articles/srep43210

385. Mauritz C, Schwanke K, Reppel M, Neef S, Katsirntaki K, Maier LS, et al. Generation of Functional Murine Cardiac Myocytes From Induced Pluripotent Stem Cells. Circulation [Internet]. 2008 Jul 29 [cited 2023 Mar 27];118(5):507–17. Available from: https://www-ahajournals-org.uea.idm.oclc.org/doi/abs/10.1161/circulationaha.108.778795

386. Zhang J, Wilson GF, Soerens AG, Koonce CH, Yu J, Palecek SP, et al. Functional Cardiomyocytes Derived From Human Induced Pluripotent Stem Cells. Circ Res [Internet]. 2009 Feb 27 [cited 2023 Mar 27];104(4). Available from: https://www-ahajournals-org.uea.idm.oclc.org/doi/abs/10.1161/CIRCRESAHA.108.192237

387. Zhang J, Tao R, Campbell KF, Carvalho JL, Ruiz EC, Kim GC, et al. Functional cardiac fibroblasts derived from human pluripotent stem cells via second heart field progenitors. Nature Communications 2019 10:1 [Internet]. 2019 May 20 [cited 2023 Mar 27];10(1):1–

15. Available from: https://www-nature-com.uea.idm.oclc.org/articles/s41467-019-09831-5

388. Zhang H, Tian L, Shen M, Tu C, Wu H, Gu M, et al. Generation of Quiescent Cardiac Fibroblasts From Human Induced Pluripotent Stem Cells for In Vitro Modeling of Cardiac Fibrosis. Circ Res [Internet]. 2019 Aug 16 [cited 2023 Mar 27];125(5):552–66. Available from: https://pubmed.ncbi.nlm.nih.gov/31288631/

389. Meyyappan M, Wong H, Hull C, Riabowol KT. Increased Expression of Cyclin D2 during Multiple States of Growth Arrest in Primary and Established Cells. Mol Cell Biol [Internet]. 1998 Jun [cited 2022 Oct 4];18(6):3163–72. Available from: https://journals-asm-org.uea.idm.oclc.org/doi/10.1128/MCB.18.6.3163

390. Montaigne D, Butruille L, Staels B. PPAR control of metabolism and cardiovascular functions [Internet]. Vol. 18, Nature Reviews Cardiology. Nature Research; 2021 [cited 2022 Oct 5]. p. 809–23. Available from: https://www-nature-com.uea.idm.oclc.org/articles/s41569-021-00569-6

391. Liu J, Wang P, Luo J, Huang Y, He L, Yang H, et al. Peroxisome proliferator-activated receptor β/δ activation in adult hearts facilitates mitochondrial function and cardiac performance under pressure-overload condition. Hypertension [Internet]. 2011 Feb [cited 2022 Oct 5];57(2):223–30. Available from: https://pubmed-ncbi-nlm-nih-gov.uea.idm.oclc.org/21220704/

392. Fang X, Stroud MJ, Ouyang K, Fang L, Zhang J, Dalton ND, et al. Adipocyte-specific loss of PPARγ attenuates cardiac hypertrophy. JCI Insight [Internet]. 2016 Oct 6 [cited 2020 Mar 30];1(16):e89908. Available from: http://www.ncbi.nlm.nih.gov/pubmed/27734035

393. Traaseth N, Elfering S, Solien J, Haynes V, Giulivi C. Role of calcium signaling in the activation of mitochondrial nitric oxide synthase and citric acid cycle. Vol. 1658, Biochimica et Biophysica Acta - Bioenergetics. Elsevier; 2004. p. 64–71.

394. LaNoue K, Nicklas WJ, Williamson JR. Control of citric acid cycle activity in rat heart mitochondria. Journal of Biological Chemistry. 1970 Jan 10;245(1):102–11.

395. Baranyi U, Winter B, Gugerell A, Hegedus B, Brostjan C, Laufer G, et al. Primary human fibroblasts in culture switch to a myofibroblast-like phenotype independently of TGF beta. Cells. 2019;8(7).

396. Gu X, Ma Y, Liu Y, Wan Q. Measurement of mitochondrial respiration in adherent cells by Seahorse XF96 Cell Mito Stress Test. STAR Protoc. 2021 Mar 19;2(1):100245.

397. Song W, Dyer E, Stuckey DJ, Copeland O, Leung MC, Bayliss C, et al. Molecular mechanism of the E99K mutation in cardiac actin (ACTC Gene) that causes apical hypertrophy in man and mouse. Journal of Biological Chemistry. 2011 Aug 5;286(31):27582–93.

398. Salameh A, Zöbisch H, Schröder B, Vigelahn J, Jahn M, Abraham G, et al. Effects of Hypoxia and Acidosis on Cardiac Electrophysiology and Hemodynamics. Is NHE-Inhibition by Cariporide Still Advantageous? Front Physiol. 2020 Mar 19;11:224.

399. Duranteau J, Chandel NS, Kulisz A, Shao Z, Schumacker PT. Intracellular Signaling by Reactive Oxygen Species during Hypoxia in Cardiomyocytes. Journal of Biological Chemistry. 1998 May 8;273(19):11619–24.

400. Metabolic Regulation of Cardiac Differentiation and Maturation in Pluripotent Stem Cells: A Lesson from Heart Development. JMA J. 2020 Jul 31;3(3):193–200.

401. Mookerjee SA, Goncalves RLS, Gerencser AA, Nicholls DG, Brand MD. The contributions of respiration and glycolysis to extracellular acid production. Biochim Biophys Acta Bioenerg. 2015 Feb 1;1847(2):171–81.

402. Chettimada S, Lorenz DR, Misra V, Dillon ST, Reeves RK, Manickam C, et al. Exosome markers associated with immune activation and oxidative stress in HIV patients on antiretroviral therapy. Scientific

Reports 2018 8:1 [Internet]. 2018 May 8 [cited 2023 Mar 28];8(1):1–16. Available from: https://www-nature-com.uea.idm.oclc.org/articles/s41598-018-25515-4

403. Khushman M, Bhardwaj A, Patel GK, Laurini JA, Roveda K, Tan MC, et al. Exosomal Markers (CD63 and CD9) Expression Pattern Using Immunohistochemistry in Resected Malignant and Non-malignant Pancreatic Specimens. Pancreas [Internet]. 2017 [cited 2023 Mar 28];46(6):782. Available from: /pmc/articles/PMC5494969/

404. Razeghi P, Young ME, Alcorn JL, Moravec CS, Frazier OH, Taegtmeyer H. Metabolic gene expression in fetal and failing human heart. Circulation [Internet]. 2001 Dec 11 [cited 2022 Oct 13];104(24):2923–31. Available from: https://pubmed.ncbi.nlm.nih.gov/11739307/

405. Blazeski A, Zhu R, Hunter DW, Weinberg SH, Zambidis ET, Tung L. Cardiomyocytes derived from human induced pluripotent stem cells as models for normal and diseased cardiac electrophysiology and contractility. Prog Biophys Mol Biol [Internet]. 2012 Oct [cited 2023 Mar 28];110(0):166. Available from: /pmc/articles/PMC3910285/

406. Toepfer CN, Sharma A, Cicconet M, Garfinkel AC, Mücke M, Neyazi M, et al. SarcTrack. Circ Res [Internet]. 2019 Apr 12 [cited 2023 Mar 28];124(8):1172–83. Available from: https://pubmed.ncbi.nlm.nih.gov/30700234/

407. Falaleeva M, Surface J, Shen M, de la Grange P, Stamm S. SNORD116 and SNORD115 change expression of multiple genes and modify each other's activity. Gene. 2015 Nov 10;572(2):266–73.

408. Peffers MJ, Chabronova A, Balaskas P, Fang Y, Dyer P, Cremers A, et al. SnoRNA signatures in cartilage ageing and osteoarthritis. Sci Rep [Internet]. 2020 Dec 1 [cited 2021 Jan 17];10(1):1–10. Available from: https://doi.org/10.1038/s41598-020-67446-z

409. Fagerberg L, Hallstrom BM, Oksvold P, Kampf C, Djureinovic D, Odeberg J, et al. Analysis of the human tissue-specific expression by genome-wide integration of transcriptomics and antibody-based proteomics. Molecular and Cellular Proteomics [Internet]. 2014 Feb [cited 2022 Nov 2];13(2):397–406. Available from: https://pubmed-ncbi-nlm-nih-gov.uea.idm.oclc.org/24309898/

410. Uhlén M, Fagerberg L, Hallström BM, Lindskog C, Oksvold P, Mardinoglu A, et al. Tissue-based map of the human proteome. Science (1979) [Internet]. 2015 Jan 23 [cited 2022 Nov 2];347(6220). Available from: http://dx.doi.

411. Coulson RL, Powell WT, Yasui DH, Dileep G, Resnick J, LaSalle JM. Prader-Willi locus Snord116 RNA processing requires an active endogenous allele and neuron-specific splicing by Rbfox3/NeuN. Hum Mol Genet [Internet]. 2018 Dec 1 [cited 2022 Oct 13];27(23):4051–60. Available from: https://academic-oup-com.uea.idm.oclc.org/hmg/article/27/23/4051/5074296

412. Doench JG, Fusi N, Sullender M, Hegde M, Vaimberg EW, Donovan KF, et al. Optimized sgRNA design to maximize activity and minimize off-target effects of CRISPR-Cas9. Nat Biotechnol [Internet]. 2016 Feb 1 [cited 2022 Nov 3];34(2):184–91. Available from: https://www-nature-com.uea.idm.oclc.org/articles/nbt.3437

413. Saadat S, Noureddini M, Mahjoubin-Tehran M, Nazemi S, Shojaie L, Aschner M, et al. Pivotal Role of TGF-β/Smad Signaling in Cardiac Fibrosis: Non-coding RNAs as Effectual Players. Vol. 7, Frontiers in Cardiovascular Medicine. Frontiers Media S.A.; 2021. p. 256.

414. Kapur NK. Transforming growth factor-β governing the transition from inflammation to fibrosis in heart failure with preserved left ventricular function [Internet]. Vol. 4, Circulation: Heart Failure. Lippincott Williams & Wilkins Hagerstown, MD; 2011 [cited 2022 Nov 8]. p. 5–7. Available from: http://circheartfailure.ahajournals.org

415. Thompson NL, Bazoberry F, Speir EH, Casscells W, Ferrans VJ, Flanders KC, et al. Transforming growth factor beta-1 in acute myocardial infarction in rats. Growth Factors [Internet]. 1988 [cited 2022 Nov 8];1(1):91–9. Available from: https://www-tandfonline-com.uea.idm.oclc.org/doi/abs/10.3109/08977198809000251

416. Edgar BA. From cell structure to transcription: Hippo Forges a new path. Vol. 124, Cell. Elsevier B.V.; 2006. p. 267–73.

417. Varelas X. The hippo pathway effectors TAZ and YAP in development, homeostasis and disease [Internet]. Vol. 141, Development (Cambridge). Company of Biologists Ltd; 2014 [cited 2022 Nov 8]. p. 1614–26. Available from: https://journals-biologists-com.uea.idm.oclc.org/dev/article/141/8/1614/46642/The-Hippo-pathway-effectors-TAZ-and-YAP-in

418. Heallen T, Zhang M, Wang J, Bonilla-Claudio M, Klysik E, Johnson RL, et al. Hippo pathway inhibits wnt signaling to restrain cardiomyocyte proliferation and heart size. Science (1979) [Internet]. 2011 Apr 22 [cited 2022 Nov 8];332(6028):458–61. Available from: www.sciencemag.org/cgi/content/full/332/6028/455/DC1

419. Xiao Y, Leach J, Wang J, Martin JF. Hippo/Yap Signaling in Cardiac Development and Regeneration [Internet]. Vol. 18, Current Treatment Options in Cardiovascular Medicine. Springer Healthcare; 2016 [cited 2022 Nov 8]. p. 38. Available from: https://link-springer-com.uea.idm.oclc.org/article/10.1007/s11936-016-0461-y

420. Zhang D, Contu R, Latronico MVG, Zhang JL, Rizzi R, Catalucci D, et al. MTORC1 regulates cardiac function and myocyte survival through 4E-BP1 inhibition in mice. Journal of Clinical Investigation [Internet]. 2010 Aug 2 [cited 2022 Nov 8];120(8):2805–16. Available from: http://www.jci.org

421. Shende P, Plaisance I, Morandi C, Pellieux C, Berthonneche C, Zorzato F, et al. Cardiac raptor ablation impairs adaptive hypertrophy, alters metabolic gene expression, and causes heart failure in mice. Circulation [Internet]. 2011 Mar 15 [cited 2022 Nov 8];123(10):1073–82. Available from: http://circ.ahajournals.org/cgi/content/full/CIRCULATIONAHA.110.977066/DC1.

422. Zhu Y, Pires KMP, Whitehead KJ, Olsen CD, Wayment B, Zhang YC, et al. Mechanistic Target of Rapamycin (Mtor) Is Essential for Murine Embryonic Heart Development and Growth. Mallo M, editor. PLoS One [Internet]. 2013 Jan 14 [cited 2022 Nov 8];8(1):e54221. Available from: https://dx.plos.org/10.1371/journal.pone.0054221

423. Sciarretta S, Volpe M, Sadoshima J. mTOR Signaling in Cardiac Physiology and Disease: Sciarretta et al. mTOR signaling in the cardiovascular system. Circ Res. 2014;114(3):549–64.

424. Sen S, Kundu BK, Wu HCJ, Hashmi SS, Guthrie P, Locke LW, et al. Glucose regulation of load-induced mTOR signaling and ER stress in mammalian heart. J Am Heart Assoc [Internet]. 2013 May 17 [cited 2022 Nov 8];2(3). Available from: http://ahajournals.org

425. Schisler JC, Grevengoed TJ, Pascual F, Cooper DE, Ellis JM, Paul DS, et al. Cardiac energy dependence on glucose increases metabolites related to glutathione and activates metabolic genes controlled by mechanistic target of rapamycin. J Am Heart Assoc [Internet]. 2015 Feb 24 [cited 2022 Nov 8];4(2). Available from: http://jaha.ahajournals.org/

426. Miyazaki K, Yoshizaki K, Arai C, Yamada A, Saito K, Ishikawa M, et al. Plakophilin-1, a novel Wnt signaling regulator, is critical for tooth development and ameloblast differentiation. PLoS One [Internet]. 2016 Mar 1 [cited 2022 Nov 8];11(3). Available from: https://pubmed-ncbi-nlm-nih-gov.uea.idm.oclc.org/27015268/

427. FRANKE WW, SCHMID E, GRUND C, MÜLLER H, ENGELBRECHT I, MOLL R, et al. Antibodies to High Molecular Weight Polypeptides of

Desmosomes: Specific Localization of a Class of Junctional Proteins in Cells and Tissues. Differentiation. 1981 Dec 1;20(1–3):217–41.

428. Geier C, Gehmlich K, Ehler E, Hassfeld S, Perrot A, Hayess K, et al. Beyond the sarcomere: CSRP3 mutations cause hypertrophic cardiomyopathy. Hum Mol Genet [Internet]. 2008 Sep 15 [cited 2023 Mar 28];17(18):2753–65. Available from: https://academic-oup-com.uea.idm.oclc.org/hmg/article/17/18/2753/2527213

429. Bonné S, Gilbert B, Hatzfeld M, Chen X, Green KJ, Van Roy F. Defining desmosomal plakophilin-3 interactions. J Cell Biol [Internet]. 2003 Apr 28 [cited 2023 Mar 28];161(2):403–16. Available from: https://pubmed.ncbi.nlm.nih.gov/12707304/

430. Lee P, Jiang S, Li Y, Yue J, Gou X, Chen SY, et al. Phosphorylation of Pkp1 by RIPK4 regulates epidermal differentiation and skin tumorigenesis. EMBO J [Internet]. 2017 Jul 3 [cited 2023 Mar 28];36(13):1963–80. Available from: https://onlinelibrary-wiley-com.uea.idm.oclc.org/doi/full/10.15252/embj.201695679

431. Kim S, Kim D, Cho SW, Kim J, Kim JS. Highly efficient RNA-guided genome editing in human cells via delivery of purified Cas9 ribonucleoproteins. Genome Res. 2014;24(6):1012–9.

432. Sanjurjo-Soriano C, Erkilic N, Mamaeva D, Kalatzis V. CRISPR/Cas9-Mediated Genome Editing to Generate Clonal iPSC Lines. In: Methods in Molecular Biology [Internet]. Humana Press Inc.; 2022 [cited 2022 Nov 8]. p. 589–606. Available from: https://link-springer-com.uea.idm.oclc.org/protocol/10.1007/7651_2021_362

433. Goullée H, Taylor RL, Forrest ARR, Laing NG, Ravenscroft G, Clayton JS. Improved CRISPR/Cas9 gene editing in primary human myoblasts using low confluency cultures on Matrigel. Skelet Muscle [Internet]. 2021 Dec 1 [cited 2022 Nov 8];11(1):23. Available from: https://skeletalmusclejournal.biomedcentral.com/articles/10.1186/s13395-021-00278-1

434. De Masi C, Spitalieri P, Murdocca M, Novelli G, Sangiuolo F. Application of CRISPR/Cas9 to human-induced pluripotent stem cells: From gene editing to drug discovery [Internet]. Vol. 14, Human Genomics. BioMed Central; 2020 [cited 2022 Nov 8]. p. 25. Available from: https://humgenomics.biomedcentral.com/articles/10.1186/s40246-020-00276-2

435. Geng B chuan, Choi KH, Wang S zhi, Chen P, Pan X di, Dong N guo, et al. A simple, quick, and efficient CRISPR/Cas9 genome editing method for human induced pluripotent stem cells. Acta Pharmacol Sin [Internet]. 2020 Nov 18 [cited 2022 Nov 8];41(11):1427–32. Available from: http://www.nature.com/articles/s41401-020-0452-0

436. Passlick B, Flieger D, Ziegler-Heitbrock H. Identification and characterization of a novel monocyte subpopulation in human peripheral blood. Blood [Internet]. 1989 Nov 15 [cited 2022 Nov 11];74(7):2527–34. Available from: http://ashpublications.org/blood/article-pdf/74/7/2527/601475/2527.pdf

437. Ziegler-Heitbrock HWL, Fingerle G, Ströbel M, Schraut W, Stelter F, Schütt C, et al. The novel subset of CD14+/CD16+ blood monocytes exhibits features of tissue macrophages. Eur J Immunol [Internet]. 1993 Sep 1 [cited 2022 Nov 11];23(9):2053–8. Available from: https://onlinelibrary.wiley.com/doi/10.1002/eji.1830230902

438. Mossanen JC, Jansen TU, Pracht J, Liepelt A, Buendgens L, Stoppe C, et al. Elevated circulating CD14++CD16+ intermediate monocytes are independently associated with extracardiac complications after cardiac surgery. Sci Rep [Internet]. 2020 Dec 1 [cited 2022 Nov 14];10(1):1–11. Available from: https://www-nature-com.uea.idm.oclc.org/articles/s41598-020-57700-9

439. Ziegler-Heitbrock L, Ancuta P, Crowe S, Dalod M, Grau V, Hart DN, et al. Nomenclature of monocytes and dendritic cells in blood

[Internet]. Vol. 116, Blood. American Society of Hematology; 2010 [cited 2022 Nov 14]. p. e74–80. Available from: http://ashpublications.org/blood/article-pdf/116/16/e74/1332100/zh804210000e74.pdf

440. Canepa M, Fumagalli C, Tini G, Vincent-Tompkins J, Day SM, Ashley EA, et al. Temporal Trend of Age at Diagnosis in Hypertrophic Cardiomyopathy: An Analysis of the International Sarcomeric Human Cardiomyopathy Registry. Circ Heart Fail [Internet]. 2020 Sep 1 [cited 2022 Nov 11];13(9):E007230. Available from: http://ahajournals.org

441. Walpot J, Juneau D, Massalha S, Dwivedi G, Rybicki FJ, Chow BJW, et al. Left Ventricular Mid-Diastolic Wall Thickness: Normal Values for Coronary CT Angiography. Radiol Cardiothorac Imaging [Internet]. 2019 Dec 1 [cited 2022 Nov 11];1(5):e190034. Available from: http://pubs.rsna.org/doi/10.1148/ryct.2019190034

442. Schumacher SM, Naga Prasad S V. Tumor Necrosis Factor-α in Heart Failure: An updated review. Curr Cardiol Rep [Internet]. 2018 Sep 9 [cited 2023 Mar 28];20(11):117. Available from: /pmc/articles/PMC6311126/

443. Farini A, Villa C, Di Silvestre D, Bella P, Tripodi L, Rossi R, et al. PTX3 Predicts Myocardial Damage and Fibrosis in Duchenne Muscular Dystrophy. Front Physiol [Internet]. 2020 May 19 [cited 2023 Mar 28];11:403. Available from: /pmc/articles/PMC7248204/

444. Kuusisto J, Kärjä V, Sipola P, Kholová I, Peuhkurinen K, Jääskeläinen P, et al. Low-grade inflammation and the phenotypic expression of myocardial fibrosis in hypertrophic cardiomyopathy. Heart [Internet]. 2012 Jul 1 [cited 2023 Mar 28];98(13):1007–13. Available from: https://heart-bmj-com.uea.idm.oclc.org/content/98/13/1007

445. Mukherjee R, Kanti Barman P, Kumar Thatoi P, Tripathy R, Kumar Das B, Ravindran B. Non-Classical monocytes display inflammatory features: Validation in Sepsis and Systemic Lupus Erythematous.

Sci Rep [Internet]. 2015 Sep 11 [cited 2022 Nov 11];5(1):1–14. Available from: www.nature.com/scientificreports/

446. Narasimhan PB, Marcovecchio P, Hamers AAJ, Hedrick CC. Nonclassical Monocytes in Health and Disease [Internet]. Vol. 37, Annual Review of Immunology. Annual Reviews Inc.; 2019 [cited 2022 Nov 11]. p. 439–56. Available from: https://www-annualreviews-org.uea.idm.oclc.org/doi/abs/10.1146/annurev-immunol-042617-053119

447. Sampath P, Moideen K, Ranganathan UD, Bethunaickan R. Monocyte Subsets: Phenotypes and Function in Tuberculosis Infection. Vol. 9, Frontiers in Immunology. Frontiers Media S.A.; 2018. p. 1726.

448. Ren X, Mou W, Su C, Chen X, Zhang H, Cao B, et al. Increase in peripheral blood intermediate monocytes is associated with the development of recent-onset type 1 diabetes mellitus in children. Int J Biol Sci [Internet]. 2017 [cited 2022 Nov 14];13(2):209–18. Available from: /pmc/articles/PMC5332875/

449. Jiang W, Zhang L, Lang R, Li Z, Gilkeson G. Sex Differences in Monocyte Activation in Systemic Lupus Erythematosus (SLE). Crispin J, editor. PLoS One [Internet]. 2014 Dec 8 [cited 2022 Nov 11];9(12):e114589. Available from: https://dx.plos.org/10.1371/journal.pone.0114589

450. Cui X, Zhang H, Cao A, Cao L, Hu X. Cytokine TNF-α promotes invasion and metastasis of gastric cancer by down-regulating Pentraxin3. J Cancer [Internet]. 2020 [cited 2022 Nov 11];11(7):1800–7. Available from: /pmc/articles/PMC7052870/

451. Ismail TF, Mistry N, Jabbour A, Hewins B, He T, Wage R, et al. Role of inflammation in the pathogenesis of hypertrophic cardiomyopathy: a T2-mapping CMR study. Journal of Cardiovascular Magnetic Resonance [Internet]. 2012 Dec 1 [cited 2022 Nov 11];14(S1):P167. Available from: https://jcmr-

online.biomedcentral.com/articles/10.1186/1532-429X-14-S1-P167

452. Kuusisto J, Kärjä V, Sipola P, Kholová I, Peuhkurinen K, Jääskeläinen P, et al. Low-grade inflammation and the phenotypic expression of myocardial fibrosis in hypertrophic cardiomyopathy. Heart [Internet]. 2012 Jul 1 [cited 2022 Nov 11];98(13):1007–13. Available from: http://heart.bmj.com/

453. Fang L, Ellims AH, Beale AL, Taylor AJ, Murphy A, Dart AM. Systemic inflammation is associated with myocardial fibrosis, diastolic dysfunction, and cardiac hypertrophy in patients with hypertrophic cardiomyopathy. Am J Transl Res [Internet]. 2017 [cited 2022 Nov 11];9(11):5063–73. Available from: /pmc/articles/PMC5714791/

454. Hobuß L, Bär C, Thum T. Long Non-coding RNAs: At the Heart of Cardiac Dysfunction? Front Physiol [Internet]. 2019 Jan 29 [cited 2021 Sep 16];10(JAN):30. Available from: https://www.frontiersin.org/article/10.3389/fphys.2019.00030/full

455. Shen S, Jiang H, Bei Y, Xiao J, Li X. Long Non-Coding RNAs in Cardiac Remodeling. Cellular Physiology and Biochemistry [Internet]. 2017 Jun 1 [cited 2020 Mar 30];41(5):1830–7. Available from: https://www.karger.com/Article/FullText/471913

456. Wolf A, Rietscher K, Glaß M, Hüttelmaier S, Schutkowski M, Ihling C, et al. Insulin signaling via Akt2 switches plakophilin 1 function from stabilizing cell adhesion to promoting cell proliferation. J Cell Sci. 2013;126(8):1832–44.

457. Müller L, Hatzfeld M, Keil R. Desmosomes as Signaling Hubs in the Regulation of Cell Behavior. Front Cell Dev Biol. 2021 Sep 23;9:2636.

458. Xie Y, Shi X, Sheng K, Han G, Li W, Zhao Q, et al. PI3K/Akt signaling transduction pathway, erythropoiesis and glycolysis in hypoxia (Review). Mol Med Rep [Internet]. 2019 Feb 1 [cited 2023 Mar

28];19(2):783–91. Available from: http://www.spandidos-publications.com/10.3892/mmr.2018.9713/abstract

459. Hu H, Juvekar A, Lyssiotis CA, Lien EC, Albeck JG, Oh D, et al. Phosphoinositide 3-Kinase Regulates Glycolysis through Mobilization of Aldolase from the Actin cytoskeleton. Cell [Internet]. 2016 Jan 1 [cited 2023 Mar 28];164(3):433. Available from: /pmc/articles/PMC4898774/

460. Eddiry S, Diene G, Molinas C, Salles J, Auriol FC, Gennero I, et al. SNORD116 and growth hormone therapy impact IGFBP7 in Prader–Willi syndrome. Genetics in Medicine. 2021 Sep 1;23(9):1664–72.

461. Zhang L, Smyth D, Al-Khalaf M, Blet A, Du Q, Bernick J, et al. Insulin-like growth factor-binding protein-7 (IGFBP7) links senescence to heart failure. Nature Cardiovascular Research 2022 1:12 [Internet]. 2022 Dec 22 [cited 2023 Jan 26];1(12):1195–214. Available from: https://www-nature-com.uea.idm.oclc.org/articles/s44161-022-00181-y

462. G. Butler M. Prader-Willi Syndrome: Obesity due to Genomic Imprinting. Curr Genomics [Internet]. 2012 Aug 2 [cited 2021 Jan 13];12(3):204–15. Available from: /pmc/articles/PMC3137005/?report=abstract

463. Stefan M, Ji H, Simmons RA, Cummings DE, Ahima RS, Friedman MI, et al. Hormonal and Metabolic Defects in a Prader-Willi Syndrome Mouse Model with Neonatal Failure to Thrive. Endocrinology [Internet]. 2005 Oct 1 [cited 2021 Jan 14];146(10):4377–85. Available from: https://academic.oup.com/endo/article/146/10/4377/2499924

464. Vogt AM, Kübler W. Heart failure: is there an energy deficit contributing to contractile dysfunction? Basic Res Cardiol [Internet]. 1998 Feb [cited 2023 Jan 26];93(1):1–10. Available from: https://pubmed-ncbi-nlm-nih-gov.uea.idm.oclc.org/9538931/

465. Braam SR, Denning C, van den Brink S, Kats P, Hochstenbach R, Passier R, et al. Improved genetic manipulation of human embryonic stem cells. Nature Methods 2008 5:5 [Internet]. 2008 Apr 6 [cited 2022 Dec 16];5(5):389–92. Available from: https://www-nature-com.uea.idm.oclc.org/articles/nmeth.1200

466. Elliott BA, Holley CL. Assessing 2'-O-Methylation of mRNA Using Quantitative PCR. Methods Mol Biol [Internet]. 2021 [cited 2022 Dec 16];2298:171–84. Available from: https://pubmed-ncbi-nlm-nih-gov.uea.idm.oclc.org/34085245/

467. Li Y, Jiang Z, Chen H, Ma WJ. A modified quantitative EMSA and its application in the study of RNA–protein interactions. J Biochem Biophys Methods. 2004 Aug 31;60(2):85–96.

468. Bak G, Han K, Kim KS, Lee Y. Electrophoretic mobility shift assay of RNA-RNA complexes. Methods in Molecular Biology [Internet]. 2015 [cited 2022 Dec 16];1240:153–63. Available from: https://link-springer-com.uea.idm.oclc.org/protocol/10.1007/978-1-4939-1896-6_12

469. Miyawaki A. Development of Probes for Cellular Functions Using Fluorescent Proteins and Fluorescence Resonance Energy Transfer. https://doi-org.uea.idm.oclc.org/101146/annurev-biochem-072909-094736 [Internet]. 2011 Jun 15 [cited 2022 Dec 16];80:357–73. Available from: https://www-annualreviews-org.uea.idm.oclc.org/doi/abs/10.1146/annurev-biochem-072909-094736

470. Helm M, Kobitski AY, Nienhaus GU. Single-molecule Förster resonance energy transfer studies of RNA structure, dynamics and function. Biophys Rev [Internet]. 2009 Nov 10 [cited 2022 Dec 16];1(4):161–76. Available from: https://link-springer-com.uea.idm.oclc.org/article/10.1007/s12551-009-0018-3

471. Smale ST. Luciferase Assay. Cold Spring Harb Protoc [Internet]. 2010 May 1 [cited 2022 Dec 16];2010(5):pdb.prot5421. Available from:

http://cshprotocols.cshlp.org.uea.idm.oclc.org/content/2010/5/pdb.prot5421.full